THE UNIVERSITY OF HULL
Department of Computer Science

Robotic Assisted Laser Bone Ablation for Orthopaedic Surgery

being a Thesis submitted for the Degree of Doctor of Philosophy

in the University of Hull

by

Fadi Odeh Ahwal, MSc Bio-Eng, BSc EE

May, 2006

Abstract

The needs for better quality patient care and improved surgical procedures drive the development of new surgical tools and techniques that can augment the human surgeon capabilities. Over the past decade or so there have been significant advances in the design and development of computer assisted image guided surgery systems that can potentially perform complex tasks with high dexterity, speed and flexibility.

The aim of this research work is to investigate various aspects in the design of a new computer assisted surgical tool capable of sawing, drilling and sculpturing of bone in support of image guided surgery that aims to reduce invasiveness, minimise blood loss and improve surgical outcome. The research of this thesis focuses on the design of an active positioning system (robotic end-effector) that uses a laser to cut bone to replace some of the currently available tools.

This thesis starts by reviewing medical lasers and laser delivery systems, and discussing the effects of different lasers and lasers' parameters on tissue ablation time, rate and depth. It then defines criterion for the selection of the most appropriate laser and laser delivery system for bone cutting, drilling and sculpturing applications.

Secondly, the thesis presents a unique design of a robotic laser end-effector. This end-effector is designed to provide accurate laser guidance for precise surgical performance (tissue ablation). This design is supported by an in-depth forward and inverse kinematic analysis to determine the end-effector workspace, resolution, positioning accuracy and manipulation flexibility.

Thirdly and perhaps most importantly, the thesis presents two innovative laser feedback techniques, developed by the author, to determine the laser ablation depth and rate in real time during laser tissue interaction. These techniques are presented with complete analysis and supported by real time feedback examples. The techniques showed high measurement accuracy and reliability.

Finally the thesis reviews the overall system performance supported by an error analysis model to determine the effects of different errors on the manipulation and positioning performance of the laser end-effector. It also presents some possible end-effector design modifications, alternative feedback techniques and suggestions for future work.

ACKNOWLEDGMENTS

I wish first to acknowledge my wife Hanan for her love, support and encouragement, and even the editing assistance she gave me throughout this PhD research work. Hanan was always there whenever I needed her and I believe that this work could not have done without her support. I wish also to thank my lovely son Suhayd and daughter to be Lujayn for their love and understanding especially during those times when the research came first.

I wish to thank my supervisor, Professor Roger Phillips, for his encouragement and guidance through the research work. He gave me the freedom to pursue this research, even though it didn't quite fit into the other projects in the department.

I would like to thank the other members of my panel committee Dr. Chandra Kambhampati and Mr. Warren Viant for the assistance they provided at all levels of the research project.

I would like to acknowledge other members of computer science department who assisted me over the course of my studies. Very special thanks goes out to James Ward and Mike Bielby who was right there when I had questions at the early stage of my research work.

Many thanks go to the physics departments at The University of Manchester and the University of Hull for the use of their laser facilities. Special thanks go to Dr. Mark Dickenson - University of Manchester, Professor P. Dyer and the late Mr. P. Monk-University of Hull for their support and advice.

Finally, I would like to thank my parents and the whole family for the support they provided me through my entire life and in particular, my father who was looking forward to seeing me finishing my PhD but he unfortunately died before that.

In conclusion, I recognize that this research work would not have been possible without the financial assistance of Al-Quds University and The University of Hull.

Table of Contents

Table of Figures

Table of Tables

Chapter 1

Introduction

1.1 Robotic System for Computer Assisted Orthopaedic Surgery

The needs for better quality patient care, improved surgical procedures and reducing healthcare costs are driving the development of new surgical tools. Some of these tools support new surgical techniques that can augment the human surgeon capabilities which can reduce surgical invasiveness, blood loss, and exposure to X-ray radiation. They may also reduce surgical and post hospitalisation time.

Over the past decade or so there have been significant advances in the design and development of computer assisted surgical robot systems. For example surgical robots can potentially perform complex tasks with high dexterity. One of the main advantages of active surgical robots is the increased precision and repeatability in carrying out surgical procedures where it is often difficult for the surgeon to operate consistently with such a high level of precision.

The aim of this project is to investigate the design of a new orthopaedic surgical tool capable of sawing, drilling and sculpturing of bone in support of image guided surgery in orthopaedics. The research of this thesis involves the design of an active positioning system (robotic End-Effector) that uses an emergent technology for bone cutting; namely a laser. Such a system may potentially replace some of the currently available surgical tools.

The End-Effector provides the physical link between a computer based pre-operative or intra-operative surgical plan and the patient anatomy. It also provides accurate tool guidance for precise surgical performance. The End-Effector would considerably enhance the currently available computer assisted orthopaedic surgery system (CAOSS) [PHIL[1] 00][PHIL[2] 00][VIAN 97], developed at the University of Hull, by providing robotic positioning of the proposed new surgical cutting tool. The main objectives of the research presented in this thesis are

- to define the set of requirement for the design of a robotic End-Effector
- to investigate emergent technologies for bone cutting and study the different characteristics of these technologies and their surgical capabilities
- to select one of these emergent technologies as a component of the robotic End-Effector
- to design an End-Effector prototype that is capable of delivering the new surgical tool to the surgical site
- to design the End-Effector's control and feedback mechanisms
- to investigate a suitable feedback mechanism for the new surgical tool

1.2 Thesis Structure

The thesis comprises of eight chapters and six appendices. The first two chapters are introductory chapters. Chapter 2 provides a literature review of computer assisted surgery systems as well as a brief review of the emergent technologies for bone cutting in the medical field. More specifically it presents the basic principles of computer assisted surgery systems, the different techniques used and some examples of computer assisted surgery systems. It also presents the steps of the surgical procedures involving surgical robots. Finally Chapter 2 discusses emergent techniques for cutting bone, namely: medical lasers, water-jet and ultrasonic drilling, and presents their use in different surgical applications.

As it was decided to use a laser for this project, Chapter 3 studies the different aspects of medical laser and their surgical applications focussing on laser bone cutting, drilling and sculpturing in orthopaedic surgery. The chapter starts by a short summary on lasers and their operating principles. This is followed by explaining laser tissue ablation and tissue interaction. It then presents different types of lasers, their medical applications and tissue interaction mechanisms. The chapter also studies the suitability of these for hard tissue ablation in terms of cut quality, damage to the surrounding tissue, and laser-tissue ablation depth and ablation rate. Furthermore, the chapter presents selection criteria for the most appropriate laser for specific surgical applications. Moreover, it investigates the different types of laser delivery systems and identifies the most appropriate one for such application. Finally this chapter suggests the most appropriate laser, the type of the laser delivery system, the different laser parameters (laser energy level, spot-size and pulse rate), and the manipulation speed for further development of the robotic End-Effector of this thesis.

Chapter 4 starts by introducing the different laser parameters of the most appropriate laser (namely Er: YAG laser) and physical laws that govern its effects on biological tissue during laser tissue interaction. It presents an in depth analysis of the effect of different Er: YAG laser parameters on biological tissue during laser tissue interaction. Also presented in this chapter is a modified equation of Beer's law for predicting the laser tissue ablation depth according to the given laser type and laser parameters as foreseen by the author. This chapter also presents laser bone cutting and drilling techniques and identifies the requirements for the design of a suitable laser End-Effector in terms of laser safety and laser beam manipulation speed. Finally the chapter presents an experiment prepared by the author to validate the laser tissue interaction predictions and prove the modification of Beer's law followed by some experimental results and concluding remarks.

Chapter 5 Investigates the robotic delivery for laser cutting of bone for image guided orthopaedic surgery. It introduces a new laser based surgical tool namely the 'laser End-Effector'. This chapter provides the blue prints of the proposed design of a prototype laser End-Effector, which should be capable of performing the basic tasks of bone cutting and drilling with a high degree of accuracy. This chapter first identifies the mandatory design requirements and shows the overall system design as foreseen by the author. It presents a complete design procedure and design analysis for a laser End-Effector prototype. The laser End-Effector prototype presented in this chapter is a 3 DOF device featuring a novel and unique design. This chapter also presents an in depth analysis of the laser End-Effector's forward and inverse kinematics (dynamic model) and explains its use for cutting and drilling techniques. The chapter ends by summarising the major features of the laser End-Effector prototype and setting proposed future development phases to attain a clinically approved commercial laser End-Effector.

The topic of Chapter 6 is feedback techniques for laser tissue interaction. The chapter starts by identifying the basic feedback and control requirements for the laser End-Effector control unit. These include all surgical and functional requirements. It then proceeds in investigating the different feedback techniques. These include innovated photo-acoustic feedback techniques devised by the author to measure the laser ablation depth and ablation rate inside bone during laser bone interaction. These techniques are based on measuring the acoustic time of flight (ATOF) and the phase shift (APH) between the laser-induced photo-acoustic waves during laser tissue ablation. This chapter present an in depth analysis of theses techniques supported by two illustrated examples. The chapter ends by presenting alternative laser feedback techniques followed by an overall summery.

Chapter 7 presents an overall system error analysis performance evaluation of the laser End-Effector. It highlights and analyses the possible sources of errors within the laser End-Effector system (i.e. End-Effector, control unit, and feedback mechanisms) during Front End positioning and laser tissue ablation. This chapter presents an error analysis model derived by the author to analyse and quantify the effect of physical errors within the End-Effector system on the position and orientation of the laser cutting tool. This error analysis model is an important aspect of the End-Effector design. It is a useful tool for performance accuracy analysis and End-Effector calibration process. The chapter ends by a performance and accuracy evaluation of the proposed laser End-Effector and some concluding remarks for the proposed future work.

Finally, concluding remarks regarding this thesis and the author's contribution are presented in Chapter 8. The chapter also presents some design recommendations for the developments of a fully functional clinical laser End-Effector.

1.3 Practical achievements of the research

The full implementation of the proposed laser End-Effector is beyond the scope of this thesis project. To set the contest of this thesis, it is worthwhile to summarise some of the key practical achievements of the research. These include:

1. Selection of the laser type and the laser delivery system
2. Preparation for various practical laser experiments
3. Design of the laser End-Effector
4. Deriving a geometric approach to determine the forward and inverse kinematics of the proposed laser End-Effector
5. Design of a high level control and feedback system
6. Devising an innovative photo-acoustic feedback technique to measure the depth of the laser front position inside bone and the laser bone ablation rate during laser tissue interaction.
7. Design and implementation of a photo-acoustic feedback circuit.
8. Practical experiments in support of the design and the proposed feedback techniques for laser ablation
9. An in-depth error analysis, positioning accuracy evaluation and evaluation of the overall End-Effector system
10. A general error analysis model equation which can be used to quantify the effects of structural and other physical errors on the positioning and orientation of the laser Front and the End-Effector's workspace

Chapter 2

Literature Review: Computer Assisted Surgery

2.1 Objective

This chapter reviews various different Computer Assisted Surgery systems, the technology behind them, and their uses in Orthopaedic surgery. Furthermore, this chapter reviews the potential of emerging technologies for tissue cutting in surgery that were initially considered as alternatives to laser technology for bone cutting.

2.2 Introduction

Computer assisted surgery (CAS) systems provide quantitative information for the surgical site. Furthermore, CAS typically deskills surgical techniques that are difficult to apply, allowing less experienced surgeons to perform complex surgical tasks. It also enables the development of new surgical procedures that typically reduce invasiveness of surgery and reduce hospitalisation time of surgery [VIAN 97][NOLT 04].

CAS systems typically involve components for imaging, measurement and position control of surgical tools. These include fluoroscopes, CT or MRI scanners, robots (manipulators), and positioning tracking systems. Together, these components enable a surgeon to position surgical tools relative to a patient's anatomy with more accuracy and often with less invasiveness than conventional techniques [LEA 98].

Robots in computer-assisted surgery should be used to perform complementary tasks [MOHS 95] that typically require high complexity and precision, be based on a surgical plan designed by the surgeon and always be under the control of surgeons [MOHS 95][PROU 96][PHIL[1] 00]. In the operating theatre, safety of both patient and medical staff is paramount. However, it is unlikely that robots will ever replace surgeons in performing surgery.

Presented in this literature review are the basic principles of CAS systems, the different techniques used and some of the CAS systems currently available [LAHM 99][MAI 00][ORTH 99][UNIV[1] nd]. These include: CAOSS [MOHS 95][PHIL[1] 00][PHIL[2] 00] the Computer Assisted Orthopaedic Surgery System developed at the University of Hull [MOHS 95][PHIL[1] 00].

Emerging technologies that may be suitable for bone cutting and drilling include water-jet, ultrasonic and laser. The first two are reviewed in this chapter with the latter being discussed in Chapter 4 as this was the technology selected to develop a new generation of cutting tools for orthopaedic surgery. This review discusses the different applications of these technologies and their advantages and disadvantages relative to the traditional tools currently in use for surgery.

2.3 CAS Categorization

Computer Assisted Surgeries systems may be categorized as including one or more of the following functional elements [LEA 98][NOLT 04]:

- Surgical planning
- Surgical navigation
- Delivery of treatment

2.3.1 Surgical planning

Surgical planning typically involves image processing, visualization, image registration and surgical simulation. Images are normally used to help surgeons determine the required relative positions of bones and implants. Images are also used to navigate surgical tools as surgery progresses [ABDE 97][LEA 94][LEA 95][HOWE 99], but the imaging modality for planning and navigating may be different. Imaging systems used in CAS include 2D and 3D fluoroscopy, Computerised Tomography (CT) and Magnetic Resonance Imaging (MRI). Surgical planning using 2D fluoroscopes typically involves a small number of 2D images where the surgeon mentally reconstructs the 3D anatomy of the patient during surgery [LEA 95][NOLT 04]. On the other hand CT and MRI provide 3D images of patient anatomy, which give surgeons more information for creating and exploring alternative surgical plans [LEA' 95][NOLT 04]. Surgical planning could be categorized according to the time of application. Planning could be performed prior or during a surgical procedure (pre-surgical planning or intra-surgical planning respectively).

Pre-surgical planning typically starts with 2D or 3D medical images together with information about the surgical site [TAYL 03][LEA 94][LEA' 95]. It involves image processing, visualization, image registration and surgical simulation using image information for optimal surgical procedure [LEA 95][LEA 98]. During the pre-surgical planning phase 3D CT, 3D MRI or 2D X-Ray images are used to display a graphical model (virtual image dataset) of the patient's anatomy [NOLT 04]. A surgical procedure is then planned (trajectory plan) on this model and the numerical coordinates which describe the procedure may then be used to derive the manipulator's equation of motion [TAYL 03].

Intra-surgical planning, on the other hand, could be a computer based image guided approach which utilizes a mobile C-arm 3D fluoroscopic image intensifier in a technique known as virtual fluoroscopy (VF) [PHIL1 02][PHIL2 02]. This technique produces a 3D virtual image dataset of the patient's anatomy and the surgical tool. In such VF systems a number of equally spaced 2D images of the operating site are taken using a C-arm image intensifier, typically there are 50 to 200 such fluoroscopic images. [PHIL1 02][PHIL2 02][HAZA 03][NOLT 04]. The Siremobile ISO C 3-D imaging fluoroscope [NOLT 04] is shown in Figure 2.1.

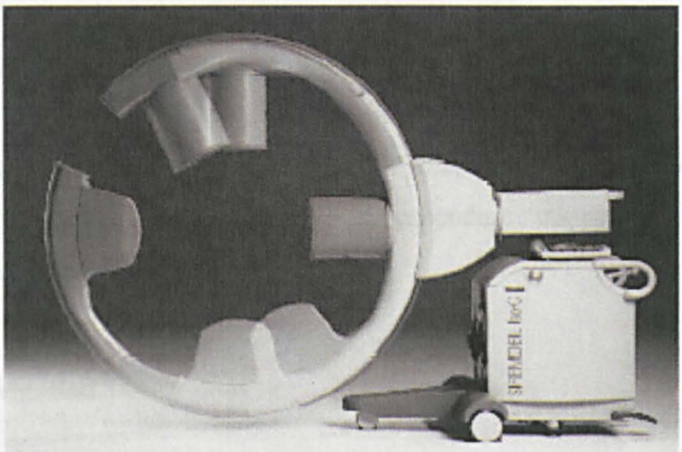

Figure 2.1: Siemens SIREMOBIL ISO-C 3D image intensifier [NOLT 04]

The ISO C 3-D has a stepper motor that provides a high precision 190° orbital rotation around the surgical site for capture of the equally spaced 2D fluoroscopic images. These images are reconstructed to give a high-resolution 3D image dataset with a volume of approximately 12.5 cm^3 and a voxel size of about 0.5 mm (Figure 2.2). This reconstruction uses a cone beam reconstruction algorithm. A recent laboratory study showed that 3D fluoroscopic navigation using this device has an accuracy of 1.18 mm (maximum error) [NOLT 02][NOLT 04].

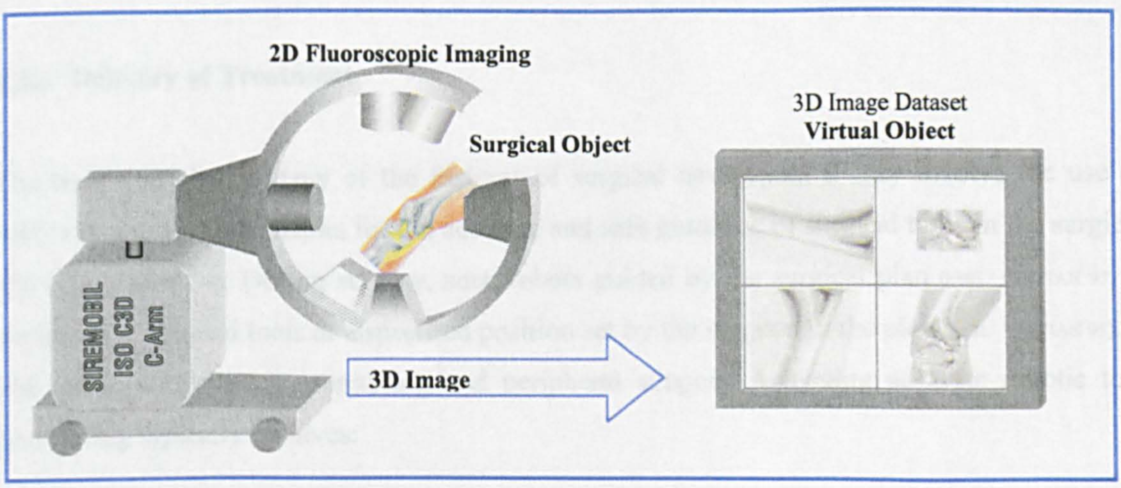

Figure 2.2: 2D fluoroscopic images to form 3D dataset using the ISO C3D

The resulting 3D image dataset for the virtual object (VO) may be loaded into a planning / navigation system (based on optical tracking system) using a standard DICOM format [NOLT 04][EULE 03]. During actual navigation system the mobile C-arm is removed from the operation field.

During planning / navigation the position and orientation of the surgical tool are tracked optically though a rigid arrangement of at least three optical markers (reference frame) [PHIL[1,2] 02][NOLT 04][HOFS 99]. The planning / navigation system typically provides a visual overlay in real time of the surgical tool onto a visualization of the 3D virtual image dataset. This image overlay requires immobilization (fixation) of the surgical object. To cater for movement of the surgical object an optically tracked dynamic reference frame (DRF) is attached to the bony anatomy of the surgical object. Using the 3D virtual image dataset and the overlaid projection of the surgical tool, the surgeon plans the surgical procedure taking appropriate anatomical measurements if required.

2.3.2 Surgical navigation

Surgical navigation concerns the precise guidance of surgical tools to specified locations in the operating theatre during surgery [DIGI[2] 98][JOSK 00][LIAO 04]. Surgical navigation systems may include:

- Optical tracking systems and devices [BRUC 02][WILE[1] 04][RIBO 01][FRAN 04][LEA 95]
- Electromagnetic tracking systems [BRUC 02]
- Acoustic feedback [WEGN 98]
- Intra-operative imaging such as fluoroscopy, ultrasonography and interventional CT/ MRI [MURP 02][PHIL[1] 02][PHIL[2] 02][JOSK 00][GRÜT 04][NOLT 04][MESS 04][[LIAO 04]
- Image free navigation [NOLT 04]

2.3.3 Delivery of Treatment

The treatment shares many of the features of surgical navigation. It may involve the use of robots or active manipulators for the accurate and safe guidance of surgical tools in the surgical site [VIAN 95][PHIL[1] 95]. During surgery, such robots guided by the surgical plan [PHIL[1] 95][VIAN 95] to position the surgical tools at a specified position set by the surgeon in the plan [PHIL[1] 95][VIAN 95]. It also deals with patient monitoring and peripheral support. Achieving accurate robotic tool positioning typically involves:

- Registration
- Immobilization or fixation.

2.3.3.1 Registration

Registration is a key technique in CAS. Basically registration is the mapping of one coordinate space to another. This registration is required to map a set of 2D images to a 3D space, and also to map a 3D image space to 3D patient space [KIMI 00][SIMO 97]. Typically it consists of finding a rigid transformation from one coordinate system to another so that all features in one of the coordinate systems can be mapped and shown in the other coordinate systems. Registration also determines the spatial relationship between the robot coordinate system and the coordinate system associated with the patient's anatomy in the robot's workspace [KIMI 00. Registration must account for patient movements and interchange of surgical tools during surgery.

The registration process can occur prior or during surgery (pre-surgical and intra-surgical registration, respectively). When registration is completed, a designated position and orientation of the surgical object on the 3D virtual image can be translated into a set of control commands to control the positioning of the surgical tool [LEA 94][LEA 95].

For pre-surgical planning image data registration of patient's anatomy can be used to find the correspondence between points in the preoperative image data and points on the patient's anatomy on the operating table. The general approaches currently used for patient's anatomy registration include [WEST 01][FITZ 01]:

- Fiducial-based registration
- Shape-based registration [PIEP 97][NISH 03]

For fiducial-based registration, fiducials refer to reference features (landmarks) that are present in the computer-based image reconstructed models and on the patient's anatomy [TRAX 01]. These fiducials are used to register the coordinate frames of the computer-based model of the surgical site with that of the patient's anatomy [LEA 95][PHIL² 95][PETE 00].

Firstly fiducials are identified within the computer based model of the surgical site. Then, during surgery the positions of these fiducials are determined using some sensing systems [LEA 95][SCHL 98]. Sensing systems used to locate fiducials include optical, magnetic and ultrasonic detection. In addition fiducials may be physically located with the aid of a probe attached to a robot's end-effector [LEA 95].

Artificial fiducials [LAVA 94] are also used in CAS systems to establish the anatomic object's reference frame [LEA¹ 95]. These artificial fiducials are easily located in the preoperative images as well as by the intraoperative locating device. For example, "N"-shaped fiducials have been used in neurosurgery [LEA 95][LAVA 94][NASS 98]. However, anatomical fiducials are preferable since they are inherently non-invasive, not subject to movement during surgery and they are intrinsically safe.

Typically, fiducials registration uses a solid registration technique (linear transformation technique) between corresponding pairs of fiducials (landmarks). This requires that the surgeon identifies three or more 3D landmarks in the preoperative image and the corresponding 3D landmarks in the patient during surgery. Then a transformation matrix is calculated to register the 3D patient model with the patient in theatre [TRAX 01]. These methods of registration often has limited accuracy [KIMI 00] because the 3D landmarks are often difficult to define with high accuracy.

At the University of Hull a number of discrete data matching algorithms have been investigated. They include 3D point to 3D points, 3D surface to 3D volume and 2D projections to 3D volume [VIAN 00][Li].

Shape-based registration is an alternative to fiducial registration. It is used in many CAS applications such as in HipNav and Navitrak [SUGA 00][HOWE 99]. Shape-based registration is generally image based and one such technique uses a "cloud-of-points". This shape-based registration surface matches [GLOZ 01] the shape of the bone surface model, generated from the preoperative images with the surface data points collected during surgery. The intra-operative data points can be collected, by direct contact with percutaneous probes [SUGA 00][GLOZ 01]. Alternatively they can also be collected using ultrasonic or fluoroscopic images [SUGA 00].

Several techniques are used to sample the large number of points {P1,P2......Pn} from the actual bone surface. These techniques include direct touching of points on the bone surface by a probe attached to the end-effector of the surgical robot arm [YANI 00] and on optically tracked probe [KUMA 04]).

A drawback of the cloud-of-points is that only the accessible portion of the bone can be sampled. Hence small inaccuracies in matching this portion to image extracted surfaces may lead to large inaccuracies for inaccessible portions [TRAX 01].

Other less adopted techniques are laser scanning registration where exposed bone is laser scanned [FADD 94][TRAX 01] and ultrasound registration which provides a non-invasive acquisition of a patient's internal bone structure [KIMI 00].

2.3.3.2 Immobilization

It is clearly important that registration is maintained during surgery. The two primary methods for maintaining registration are: immobilization and motion tracking of the patient's anatomy.

Immobilization or fixation involves fixing the bones with respect to the registered surgical site. In many orthopaedic procedures immobilization is applied to large bones of the skeletal system. This is done by clamping the bone by some rigid structure.

However, in some cases where bone movement occurs (e.g. due to breathing), such as in the case of pedicle screw placement, an alternative technique is required. This involves tracking in real time the motion of the surgical site. In this case, a registration reference frame with infrared LED array is placed on a vertebra during spinal surgery which optically tracks vertebral motion [LAVA 94].

Two examples of immobilization are in Total Knee Replacement (TKR) and pelvic surgery.

For TKR , an intramedullary bone clamp is used which comprises a stainless steel rod 40 cm in length and 9.5 mm in diameter and a tapered stainless steel cone which slides along the rod. The rod is driven into the intramedullary canal and the cone wedged into the bone and locked to the rod [LEA' 95]. A fixation arm is connected to the outside end of the rod and locked down which provides very rigid fixation of the knee joint [LEA 95].

For pelvic surgery the pelvis is immobilized [LEA' 95] using a vacuum pack and foam covered aluminium blocks. The vacuum pack is placed under the patient's lower back during surgery to help prevent pressure sore development. The anatomically controlled foam covered aluminium blocks apply a download pressure to the pelvis.

2.3.4 Navigation

Navigation of tools and implants within the surgical site is a critical issue in CAS [SUGA 00]. Navigation (tracking) systems typically provide the surgeon with numerical and visual feedback on the position of tools and implants within the surgical site during the surgical procedure [SUGA 00]. This navigation is achieved by attaching tracking devices to the surgical tools (drills, guides, etc) during surgery.

The most common tracking devices used in CAS is optical tracking cameras and infrared light emitting diodes (IREDs). Optical sensors are easy to set up, very accurate, have a sufficiently fast sensing rate [SUGA 00][KIMI 00][MITT 94][PHIL[1] 95] and they can track multiple tools simultaneously. However, these devices have a major disadvantage that they require direct line of sight during the course of the surgical procedure. They also can be expensive if a very high level of accuracy (in the range of 0.1 mm) is required [SUGA 00].

Other tracking technologies include acoustic (Ultrasound) or magnetic sensors [HUMM 02]. The latter create a field around the surgical site. This field is altered by magnetic coils attached to surgical tools as they move within it. Such devices do not require direct line of sight but they are typically not as accurate as the infrared trackers (Optical Trackers) [SUGA 00] [BRUC 02][WILE[2] 04][RIBO 01][FRAN 04]. Furthermore, these tracking techniques are affected by moving metal objects and they have difficulties tracking multiple tools simultaneously. They are thus of limited utility for CAS.

The following paragraphs present two examples of surgery planning and navigation systems, namely: HipNav and KneeNav TKR.

HipNav (Hip Navigation system) is a navigation system that uses optical tracking cameras and IREDs to track tools for Total Hip Replacement (THR) surgery. It has been developed to permit accurate placement of the acetabular component during total hip replacement. It comprises of three components [MRCA 96][SUGA 00], namely: a preoperative planner, a range of motion simulator and an intra-operative tracking and guidance system

The preoperative planner allows the surgeon to specify the alignment of the acetabular component within the pelvis based upon preoperative CT images [MRCA 96][SUGA 00]. The range of motion simulator [MRCA 96] determines the range of motion based upon the specific bone and implant geometry and alignment. The feedback provided by the simulator permits the surgeon to determine the optimal, patient-specific acetabular implant alignment system.

KneeNav-TKR (see Figure 2.3) is a CT-based surgical planning and navigation system. The planar cuts for the femoral component of the TKR prosthesis are planned preoperatively using a CT of the patient. The saw cuts are made using the usual TKR mechanical guide [WOLF 04]. However, to position the guide a hand held tracking device is first placed in the saw slot of the guide. As the guide is moved intra-operative measurements of alignment are provided. Once the guides are properly aligned bone cuts are made using a traditional oscillating saw [WOLF 04][DIGI nd].

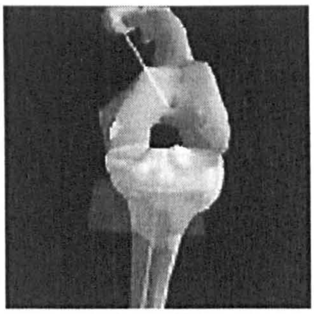

Figure 2.3: KneeNav-TKR navigation [WOLF 04]

2.4 Review of some Orthopaedic Computer Assisted Surgery systems

This literature review is mainly concerned with CAS systems for Orthopaedics. These include CAS systems for Total Knee Replacement (TKR), Total Hip Replacement (THR) and hip trauma surgery. In some of these CAS systems a computer-controlled robot performs the surgery with some degree of human intervention. Robotic systems commercially available in orthopaedics include [NOBU 00] [TRAX 01]: ROBODOC, CASPAR and Navitrack.

2.4.1 ROBODOC

ROBODOC was the first active robot used in medical application. This system is intended for primary cementless Total Hip Arthroplasty (THA) [TRAX 01]. The ROBODOC system (Figure 2.4) consists of; a preoperative planning system and a five axis robotic arm with a high-speed end milling device that prepares the femoral canal for the femoral component of the THA prosthesis according to the planned position.

ROBODOC SYSTEM COMPONENTS

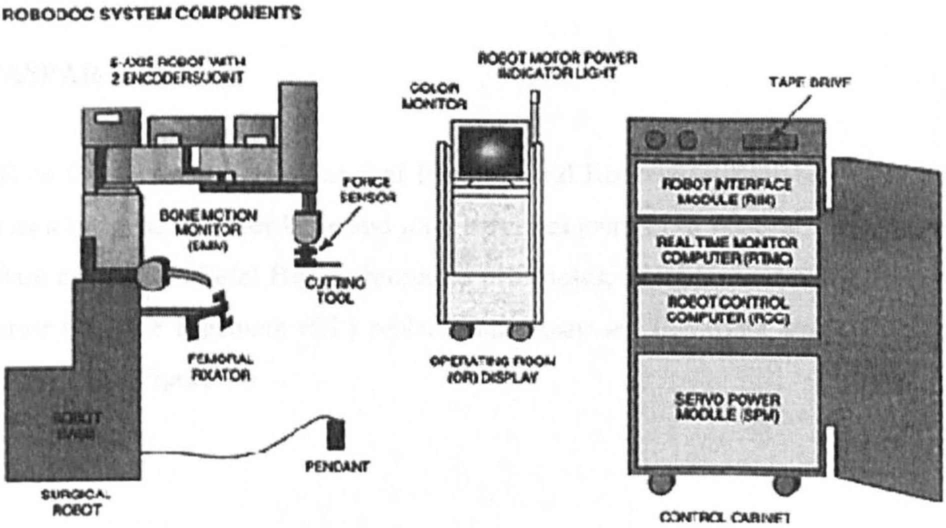

Figure 2.4: ROBODOC system components [MITT 94]

The ROBODOC system is supposed to be safe and effective in producing superior implant fit and positioning while eliminating femoral fractures [SUGA 00]. It offers complete preoperative planning of the femoral implant procedure. This includes surgeon-controlled selection of prosthesis size, shape, and placement. It also offers controlled milling of the femur in preparation for prosthesis [STUL 00].

Early ROBODOC systems used rigid fiducial pins for registration between the preoperative planning and navigation during surgery [SUGA 00]. ROBODOC later adopted a matched points method for anatomy based registration, thus removing the need for these fiducial pins [LAHM 99].

ROBODOC system uses a preoperative planning software called ORTHODOC (developed by Integrated Surgical System). This is a CT-based planning software that allows the surgeons to develop a plan of the femoral component placement in THA [SUGA 00][HICK 98][STUL 00]. The surgeon can check the developed plan by referring to the geometric relationship between the implant and the endosteal cortical contour in the coronal, sagittal and axial planes. After the surgical plan is completed, a tape of the milling plan for the robot is created by ORTHODOC [HICK 98][STUL 00].

During surgery an incision is made, the bone exposed and the femur head removed. A bone clamp (Bone Fixation Device) is then used for femur fixation. This prevents movement of the femur during bone milling. The milling tape then guides the surgical robot arm of ROBODOC to accurately mill a cavity in the femur to within an accuracy of 0.1 mm. This allows surgeons to properly orient and align the implant [HICK 98].

The second generation of ROBODOC features a monitor for bone motion during surgery. This monitor comprised of a spring loaded probe that securely attached to the proximal femur. The 3D displacement of the probe is measured relative to the robot base [MITT 94].

2.4.2 CASPAR

CASPAR or Computer Assisted Surgical Planning and Robotics system has been designed to function as a universal tool for bone and joint surgeries [UNIV[2] nd]. It enables surgeons to plan for and implant cementless Total Hip Arthroplasty prostheses, Total Knee Arthroplasty prostheses and anterior Cruciate Ligament (CL) replacements [UNIV[2] nd]. The robot used by the CASPAR system is shown in Figure 2.5.

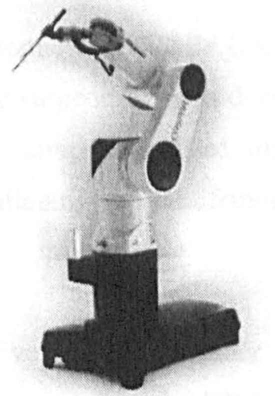

Figure 2.5: Computer Assisted Surgical Planning and Robotics [URS 00][PHIL nd]

Planning in CASPAR is based on 3D CT images using CAD data for the prosthetics [UNIV² nd]. The robot control plan is saved on an EPROM chip, which is then transferred to the surgery robot [UNIV¹ nd]. The CASPAR system uses CT-based planning software called (PROTON). This software includes biomedical simulation, for example for THA this checks the perprosthetic stress distribution and the rotational stability of the femoral component using finite element analysis [SUGA 00].

Registration in the CASPAR system can either be by shape registration by matching surface geometry [VERS 00] or by implanted fiducials that serve as references on the CT scans. The positions of these fiducials are measured by the robot during surgery and matched with the positions on the CT images [PETE 00].

For immobilization of the surgical site a fixation device is connected to the robot that rigidly fixes the bone (femur and tibia) by a special clamp (Figure 2.6) [PETE 00][UNIV² nd]. The CASPAR system has bone-motion sensors which detect excessive motion of the bone and automatically stops the drilling process [PETE 00].

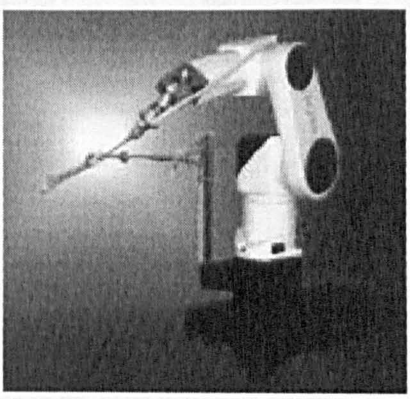

Figure 2.6: Fixation with CASPAR system [UNIV² nd]

2.4.3 Navitrack

Navitrack is a very compact ergonomic and mobile CAS system that was developed by an orthopaedic surgeon for orthopaedic surgeons. It was developed by Sulzer Medical and CAS-partner Orthosoft Inc [SULZ nd] for computer-assisted implants of Total Knee Arthroplasty prosthesis. It allows precise positioning of the femoral and tibial components without intramedullary instrumentation.

Navitrack currently has a preoperative CT-based planner [SUGA 00] from which the patient's CT scans are transferred to the workstation using the DICOM interchange format [SULZ^2 nd]. The Navitrack then reconstructs a 3D model of the surgical site automatically [SULZ^2 nd]. Navitrack uses an image matching technique for registration. In this technique a CT-based 3D model of patient anatomical structure is constructed preoperatively. During surgery the instruments are calibrated and the patient's anatomy is matched with the 3D model.

Navitrack provides visual representations for tool navigation during surgery. It provides surgeons with a real-time display of the 3D CT images during surgery with the display of the tool overlaid. This enables surgeons to track instruments, implants and patient's bone structure throughout the surgical procedure [ORTH 99]. For increased flexibility the system can be equipped with either optical or electromagnetic (EM) tracking systems [AMIO 00].

In addition to the TKA surgery, Navitrack can be used for ACL/PCL reconstruction, pedicle screw insertion [SULZ nd][SULZ^2 nd] and Total Hip Arthroplasty. Figure 2.7 and Figure 2.8 show some of Navitrack's applications.

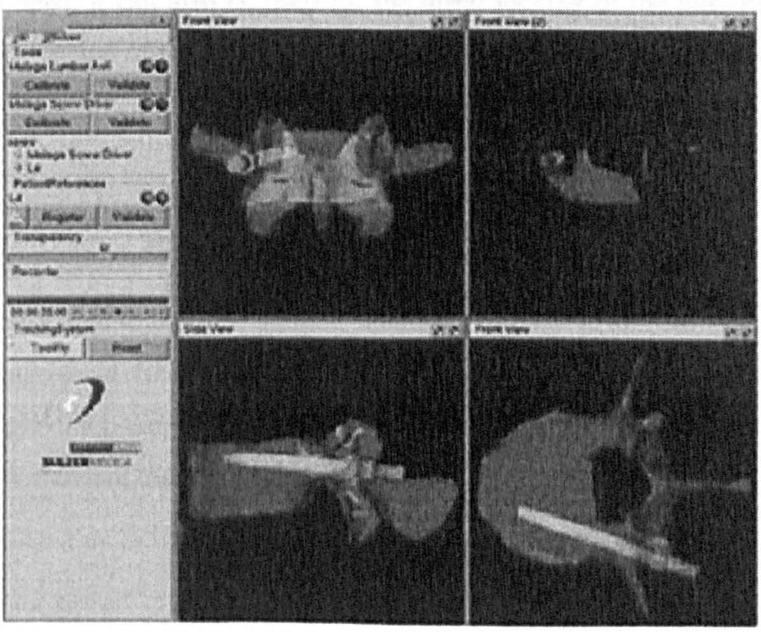

Figure 2.7: Spinal Surgery: Pedicle Screw Placement, Cage Placement, DYNESYS [SULZ^2 nd]

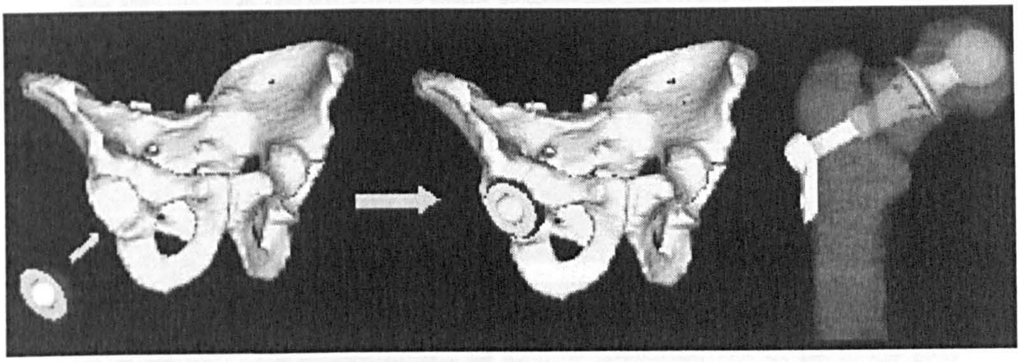

Figure 2.8: THA Surgery: Pre-operative Planning and Interoperative Navigation of Acetbular Cups and Femoral Stems [SULZ² nd]

2.4.4 Computer Assisted Orthopaedic Surgery System - CAOSS

The University of Hull in collaboration with local hospitals has been developing CAS for orthopaedics since 1992. They identified a basic principle in orthopaedic surgery which can be stated as the "Placement of an object (Guide wire, Screw, Tube, Scope,… etc) at a specific site within a region via a trajectory planned from X-ray based 2D images and other imaging modalities and governed by 3D anatomical constrains". [PHIL² 95][HAFE nd]. The CAS system they developed is known as the Computer Assisted Orthopaedic Surgery System (CAOSS). This system provides computer based intra-operative surgical planning using a fluoroscopic image intensifier and a self-supporting passive arm for tool positioning during surgery [PHIL¹ 00][PHIL² 00][MOHS 95]

CAOSS is a pre-production prototype of CAOS. It was used to evaluate the efficacy of the intra-operative image guided surgery approach via a clinical trial [SULZ nd]. CAOSS aims to assist orthopaedic surgeons to accurately drill bones for the insertion of dynamic hip screw (DHS) into the femoral head. It can also be used for the distal locking of the intramedullary femoral nails and for the insertion of the cannulated screws for repair of the neck of the femur fractures [PHIL¹ 00] [PHIL² 00].

CAOSS comprises of a passive arm and an end-effector for holding the guided cannula (Figure 2.9A) [PHIL² 00]. The passive arm is commercially available where as the end-effector (Figure 2.9B) is specifically built to hold the guiding cannula. The passive arm comprises of three joints that provide 6 degrees of freedom (6 DOF). This passive arm can be locked to position by tightening a single knob [PHIL² 00][PHIL¹ 00]. Moreover, it can be attached to the rails on the operating table by standard theatre clamps [PHIL² 00].

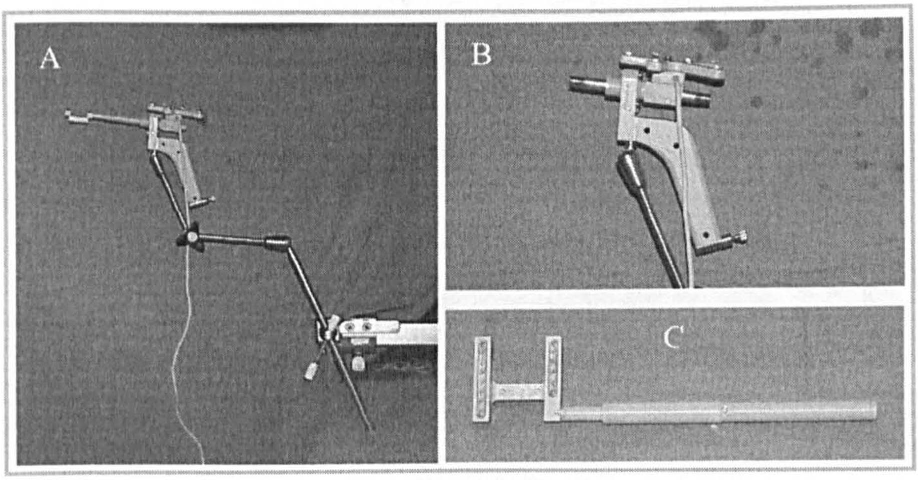

Figure 2.9: (A) CAOSS equipment set up showing the end-effector with the registration phantom. The end-effector is held by a lockable passive arm which is attached to the operating table using a Maquet clamp. (B) The end-effector with guiding cannula. (C) The registration phantom. [PHIL² 00]

Patient anatomy is localized using a registration phantom (Figure 2.9C) which contains 21 metallic balls that is placed in the fluoroscopic image beam when imaging the patient [PHIL¹ 00][PHIL² 00]. Through back projection of the phantom's balls and the optical tracking of the phantom, anatomy can be localised and registered with the image intensifier [PHIL² 00].

A 3D surgical plan is constructed from a number of 2D fluoroscopic images. To achieve accurate reconstruction of the 3D surgical images, accurate calibration of the 2D fluoroscopic images is required. Image calibration involves preoperative imaging of an x-ray translucent grid containing an evenly spaced grid of 64 x 64 balls [PHIL² 00]. This calibration plate is placed on the x-ray receptor cover of the C-arm and an image is taken. Software automatically detects the grid and calculates a "distortion-undistortion matrix" [PHIL² 00]. Intra-operatively, the distortion from each fluoroscopic image is removed before using it for planning and display. This calibration need only to be performed monthly.

Surgical planning in CAOSS uses anatomical features acquired by AP and lateral fluoroscopic images of the fracture site taken after fracture reduction [PHIL¹ 00][PHIL² 00]. For the Compession Hip Screw procedure these anatomical features include the shaft axis of the proximal femur, the femoral neck and the femoral head [VERS 00]. The 2D projection of the femur shaft axis and the femoral neck and head centres is then determined. These 2D projections are then reconstructed to create a 3D surgical plan [PHIL² 00] [PHIL¹ 00].

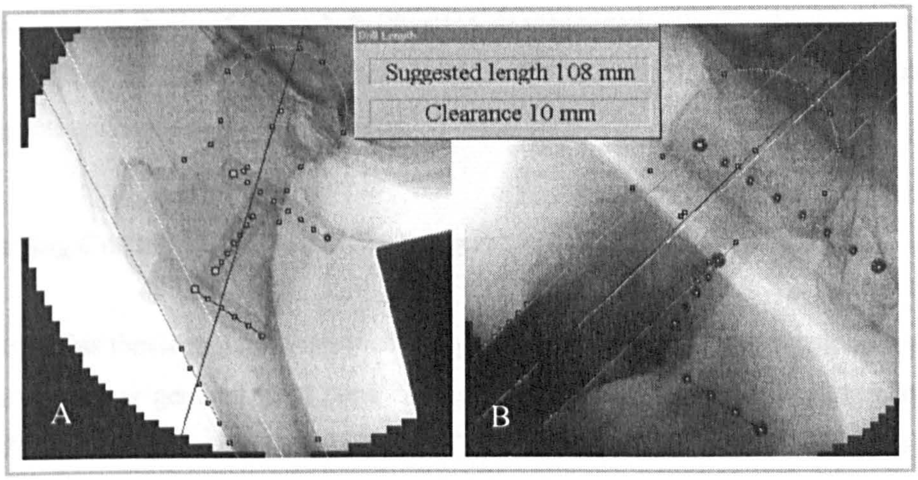

Figure 2.10: (A) AP and (B) lateral fluoroscopic image for compression hip screw planning. Both figures show: points for the femoral shaft, neck and head, the planned trajectory for the guide wire, the projection and detection of the registration phantom.

The implementation of the surgical plan in CAOSS is a passive approach. A passive manipulator arm is holding a specifically built end-effector. Guided by a computer display, the surgeon manually positions a guiding cannula, mounted in the end-effector, at the surgical site. The position of the guiding cannula and the end-effector is optically tracked by means of an optical tracking system and infrared emitting diodes attached to the end-effector [PHIL[1] 00] [PHIL[2] 00]. When the desired position of the cannula is achieved, the surgeon locks the passive arm joints rigidly holding the cannula in place. An orthopaedic drill is then used to implant the guide wire along the planned trajectory. Further fluoroscopic images may be taken to monitor the progress on the insertion of the guide wire [PHIL[2] 00].

2.5 Summary

There are potential advantages to using CAS in orthopaedics, for example improved surgical accuracy, reducing surgical complexity, reduced surgical invasiveness and dosage reduction of the X-ray radiation exposure in orthopaedics. However, there are countering disadvantages. To illustrate this point of view, one or more of the CAS systems detailed above suffer from one or more of the following disadvantages [SUGA 00].

1. Increase surgical invasiveness through additional operations for markers implantation
2. Elongate the surgical time
3. Increase blood losses

CAS technologies are relatively immature. They still offer much potential to reduce invasiveness through the integration of newly emerging technology such as Laser, Water-Jet and Ultrasound for bone cutting. This could lead to a new generation of surgical tools and instruments, new methods of image hybridization or visualization and perhaps new methods of registration. Some of these emerging technologies are discussed in more depth later in this chapter and other chapters within this thesis.

2.6 Emerging Cutting Technologies for Surgery

At the start of this thesis project, three technologies for bone cutting were considered as possible candidates for a new generation of bone cutting tools for CAS in orthopaedics. Water-jet and ultrasound are reviewed within this section. The other technology considered was laser and since this was the technology selected this is reviewed in considerable detail in Chapter 3.

2.6.1 Water-Jet Technology in Medicine

High-pressure liquid jets can be used for cutting or fragmentation of a wide range of materials. This section discusses the potential of a high-pressure water jet as a surgical tool. Water-jet technology has been used for more than 30 years in industrial cutting and drilling applications. It was first used in medical applications in the early 1980s [PAPA 82][HATA 94][KOTA 01], and pioneering work was continued by doctors in Sweden, Japan, Germany and Switzerland. [HONL 99][SAPH 98]

In the early 1980s, thewater-jet cutting process was utilized for cutting of organs. In a recent study, Honl, M. et al. [HONL 99] investigated the usage of water-jet cutting technology for revision surgery of prostheses, where bone and bone cement (Polymethylmethacrylate or PMMA) samples were cut at varied pressure using an industrial jet cutting device.

The results showed that using plain water below 400 bar, PMMA was cut selectively without any damage to bone, and by increasing the pressure to above 400 bar the bone was cut yet the cutting depth was significantly lower than that of the PMMA (Figure 2.11).

When a water-soluble abrasive disaccharide was added to the water the results showed a significantly higher removal rate for bone and PMMA at the same pressure levels and the quality of cuts were better for both materials. [HONL 99]

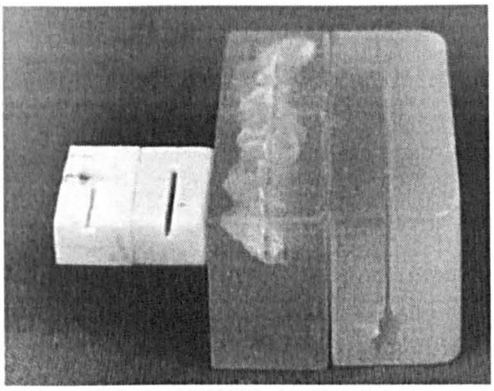

Figure 2.11: Samples of bone (left) and PMMA (right) after cutting with different water pressures [HONL 99]

Water-jet devices have been investigated for dentistry. Many devices are currently used for removing tooth decay. These devices include high-speed-drill (most commonly used), air abrasion (AA) unit (uses compressed air to propel and direct small abrasive particles [HANS 00], and Laser Technology (approved by the FDA in 1998) [HANS 00]. Based on a study in 2000 for the use of water-jet stream for removing tooth decay by [HANS 00] it appears that water-jet has a great potential in comparison with the existing methods for removing tooth decay (see Figure 2.12). During these studies, variations in fluid pressure, orifice size and type, abrasive type (none, baking soda, aluminium oxide), abrasive size and abrasive concentration were investigated. Results showed that tooth material can be effectively removed with a water jet stream and because decayed tooth material is softer than healthy teeth the appropriate ranges whereby a water jet system can effectively remove both healthy and decayed tooth materials were identified [HANS 00].

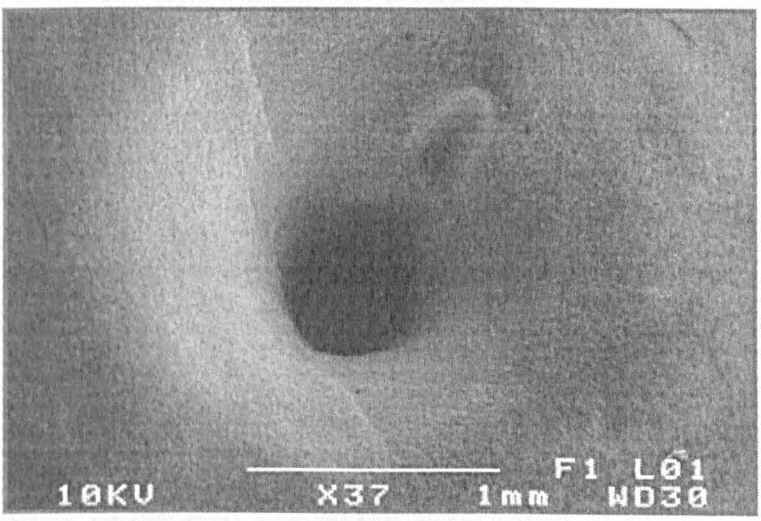

Figure 2.12: A cut made into a tooth using water jet stream with a 0.152 mm round orifice, a 17% volumetric concentration of 27-micron aluminium oxide, 3.4 MPa, and for a 30 second test duration [HANS 00].

2.6.1.1 Handy-jet™ dissector

One of the water-jet products currently available for medical use is the Handy-jet™ dissector, a multifunctional saline-jet dissector, developed by SAPHIR Medical-Germany. Handy-jet™ was optimally designed for the dissection of parenchymal organs, with a working pressure up to 35 bar and a jet-diameter of 0.15 mm. In the Handy-jet the water-jet abrasion is integrated with a suction system (Figure 2.13) and this combination makes the Handy-jet highly selective, gentle and efficient in use. In this system tissue damage is prevented by the avoidance of heat and the use of the isotonic saline solution as the jet-medium.

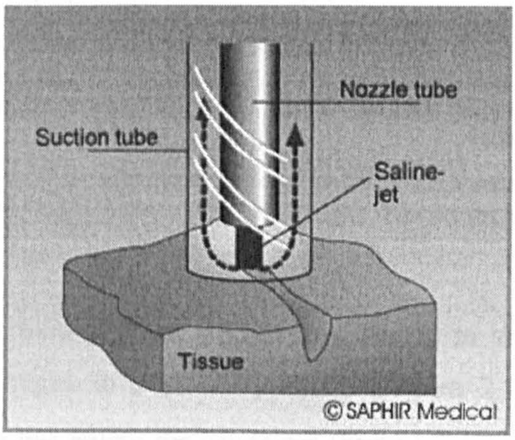

Figure 2.13: Working principle of the Handy-jet™ handpiece [SAPH 98]

According to SAPHIR Medical, the Handy-jet™ was tested and certified at 120 bar and has an integrated isomatic heating system (37°C). Dissection pressure can be adjusted from 0 to 35 bar and the flow rate can be adjusted from 0 to 1500 ml/min. The Handy-jet™ was used for dissection of parenchymal organs where it resulted in less bleeding, significantly shorter operating times and minimized tissue damage (Figure 2.14 and Figure 2.15)

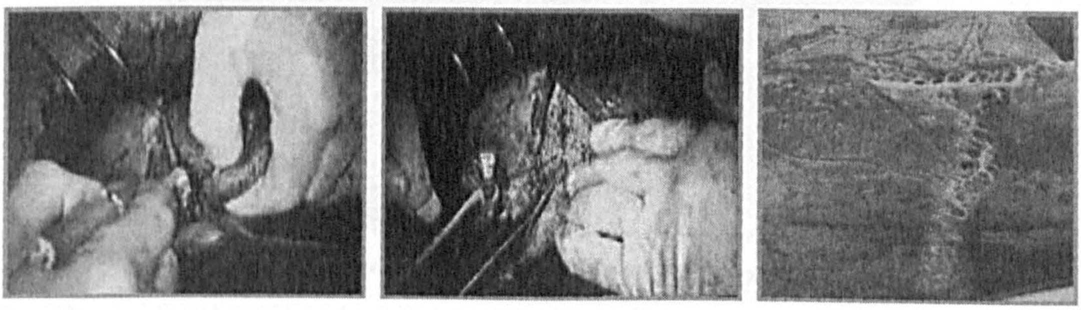

Figure 2.14: Handy-jet™ in Practice, on the right Liver parenchyma selective preparation of the vasculature with the Handy-jet™ [SAPH 98]

In comparison with different technologies such as Nd: YAG laser and High Frequency Electrosurgical system, from the histological effects of the three different technologies, one can see that water jet cause no damage to the surrounding tissue compared with the other systems (Figure 2.15).

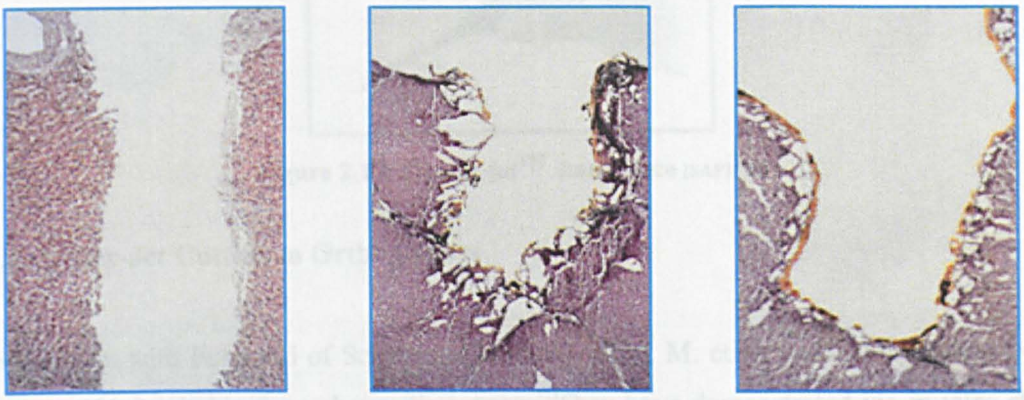

Water jet lesion in the hepatic parenchyma. H.E.x 200. Note the completely intact cell structure without any necrotic margins.

Lesion in the hepatic parenchyma caused by a monopolar electrode at 60 watts. H.E. x 200. Note the irregular and partly fissural margins.

Lesion in the hepatic parenchyma caused by Nd: YAG laser at 45 watts. H.E x 200. Note the caramelised surface and the regular margins.

Figure 2.15: Schurr M.O. et al: Histologic Effects of Different Technologies for Dissection in Endoscopic Surgery: Nd: YAG Laser, High Frequency Electrosurgical unit and Water-Jet. [SAPH 98]

The handy-jet technology uses a saline solution bag placed in high-pressure container and compressed with pure nitrogen to raise the pressure (Figure 2.16). A high-pressure tube connects the bag with a nozzle within the handpiece (Figure 2.17). A sapphire with a pinhole of 0.15 mm in diameter produces the cutting jet. The pressure can be adjusted to suit the application. [SAPH 98]. The most effective distance for tissue cutting is within 40 mm, where the jet stream is uniform in diameter (i.e features consistent pressure force). This in effect reduces the possibility of lateral damage to tissue and provides more control over the cutting depth.

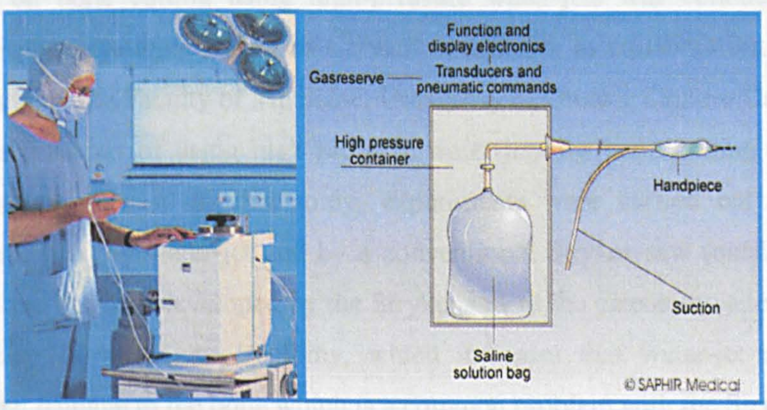

Figure 2.16: Concept of the of the Handy-jet^{TM} system [SAPH 98]

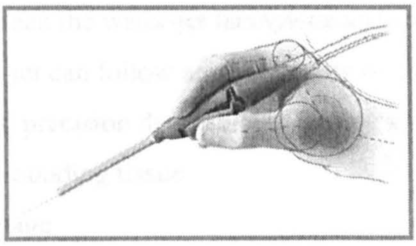

Figure 2.17: Handy-jet™ handpiece [SAPH 98]

2.6.1.2 Water-Jet Cutting in Orthopaedics

In cooperation with Euromed of Schwerin-Germany, Honl, M. et al. [HONL nd] have developed a water jet scalpel suitable for orthopaedic surgery. They have demonstrated via in vitro studies the characteristics of this scalpel in terms of; selectivity, efficiency and cutting speed in bones cartilage and meniscus tissue. The results acquired showed no thermal damage to the surrounding tissue. [HONL nd]

A study regarding intervertebral discs using three different techniques for spinal discectomy [HONL nd]; namely laser, APLD (automated percutaneous lumber discectomy) and hydro-jet (water-jet) discectomy, were conducted on 60 sections of intervertebral columns of young pigs. The results showed the selectivity of the water-jet discectomy technique over the other two techniques. In comparison with the other techniques, a significantly higher amount of nucleus tissue was found to have been removed with hydro-jet discectomy than by laser and APLD. Moreover, water-jet discectomy was found to be 10 times faster than APLD and 4 times Faster than laser with no damage to the surrounding tissue [HONL nd].

Another study on bone cutting using high-pressure water-jets was conducted by the Gas Dynamic Laboratory, National Research Council of Canada in collaboration with a team of medical doctors from the Faculty of Medicine, University of Ottawa, Ontario Canada. The study investigated the potential of using high pressure water-jets for bone cutting (osteotomies) in orthopaedic surgery [VIJA nd]. In this study, experiments were carried out to compare the osteotomies performed by water-jet and by a conventional Stryker saw (oscillating saw). The results showed that the heat developed by the Stryker saw at the osteotomy site was found to be greater than that for water-jet osteotomy, which indicates that water-jet might reduce or eliminate thermal damage to the bone which is a common problem with the Stryker saw [VIJA nd].

2.6.1.3 An Evaluation of the Water-Jet technology

The potential major advantages of water-jet as a surgical tool over the traditional tools used for surgery may include the following:

- No mechanical contact between the water-jet handpiece and tissue
- Being a point cut the water -jet can follow any cut profile or shape (cutting and drilling)
- Features high selectivity and precision during tissue cutting and drilling
- Cause no damage to the surrounding tissue
- Reduced thermal tissue damage
- Reduce blood loss
- Environmentally Safe: cause no environmental hazards
- Can easily be integrated with robotic systems
- Water-jet temperature can be regulated and set to be equal to the human body temperature
- Faster than other technologies (eg. APLD and laser)

On the other hand, water-jet technology has some potential disadvantages. These include:

- May exert pressure on tissue during surgery, which may cause tissue movement (undesirable in computer assisted surgery)
- May cause infection due to direct tissue contact
- High-cost: high pressure pumps are relatively expensive

In general a high-pressure water-jet has the potential to be effective for bone cutting and drilling with high selectivity, efficiency and reduced tissue damage in comparison to traditional surgical tools. Water jet can be applied using flexible high-pressure water tubes and lightweight cutting tools; these could be mounted to a robot's end-effecter for computer assisted surgery.

2.6.2 A Ultrasonic Sonic Driller Corer (USDC)

In orthopaedics the current practice of using power driven rotating drills can cause significant stress, strain and excessive heating of the bone sufficient enough to kill it (i.e. bone necrosis). Since dead bone will not hold screws securely and will not heal, the type of drill plays a significant role in determining the success of the orthopaedic surgery. Some of the problems associated with the currently used rotational drills may include:

1. Tissue vibration; if the target surface is too hard for the drill bit.
2. A drill bit tends to drift from its initial (target) position as it gathers speed.
3. Jammed drill bits attempt to rotate exerting rotational torque on its holder (e.g. the surgeon's arm)
4. Drill bits tend to brake or bend inside bone.

As a solution for all these problems and the control problem of the traditional drill used in orthopaedics surgery, NASA's Jet Propulsion Laboratory (JPL) in consultation with

Cybersonics developed a robust low power Ultrasonic Sonic Driller Corer (USDC). It is a drill and core sampler.

2.6.2.1 USDC Operating Principle and Applications

The USDC works like a jackhammer [BARC 01] [R&D 00]. It has no gears or motors and only two moving piezoelectric parts, which can change their shape under the application of an electric field. As the current is switched ON and OFF, the piston-like piezoelectric actuator causes ultrasonic and sonic vibration which in turn performs the drilling by forcing the drill bit up and down into the object. Figure 2.18 shows the USDC in action where very little torque (i.e. holding force to prevent the drill from movement) is applied to produce effective drilling.

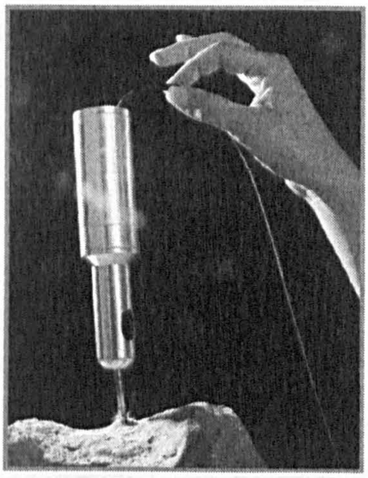

Figure 2.18: The USDC, "Less Torque, More Action" [BARC 01]

The head mechanism is a mechanical frequency transformer that converts a 20 kHz ultrasonic drive frequency to a combination of high drive signal and 60-100 Hz sonic hammering action required for the drilling mechanism [SHER 01]. Figure 2.19 shows a photograph and schematic of the USDC mechanism.

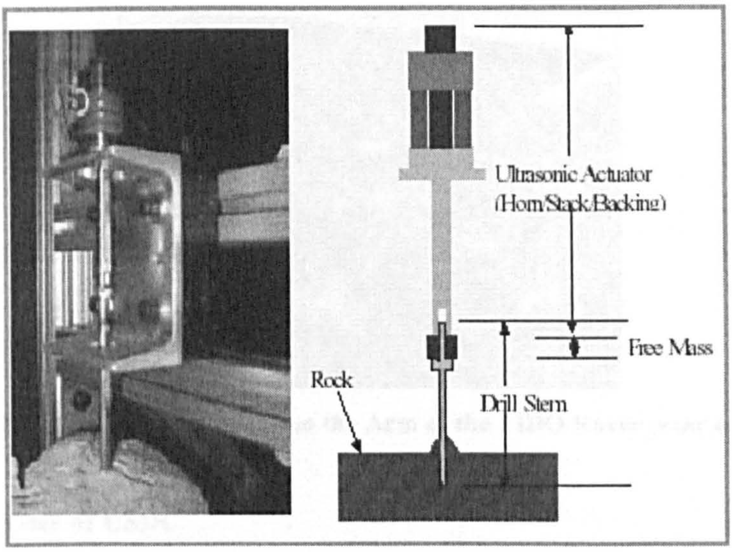

Figure 2.19: A Photograph and Schematic of the USDC mechanism [SHER 01]

The USDC can create holes that are slightly larger than the bit diameter which reduces the chances of jamming which is a key problem encountered in conventional drills. Different shape and size drill bits can be utilized with no need for sharpening. The drill can be safely guided by hand or by an active manipulator with very little axial force (Figure 2.20).

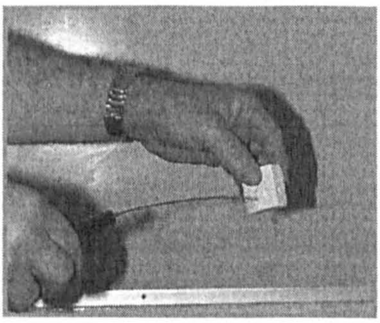

Figure 2.20: USDC safely guided by hand to drill with long, flexible drill bit [SHER 01]

The current demonstration unit weighs roughly 0.7 kg, which is sufficient to drill 12 mm holes in granite using less than 10 Watt of power. In comparison rotary drills require 20 to 30 times the force and more than three times the power of the USDC [R&D 00].

The USDC also offers an effective drilling mechanism for very hard objects from an ultra-light robot or robot arm with low axial load as shown in Figure 2.21.

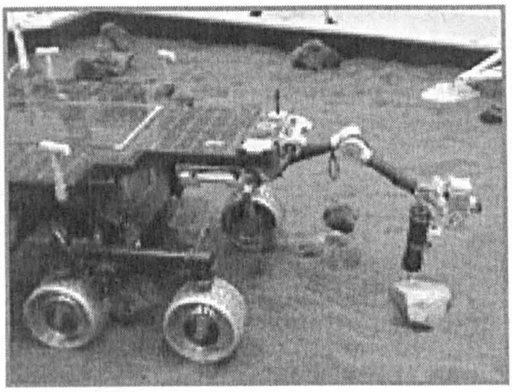

Figure 2.21: USDC operating from the Arm of the FIDO Rover [BARC 01][SHER 01]

2.6.2.2 Medical Uses of USDC

In orthopaedics the USDC would be much easier to control in bone drilling than the traditional drill and it may improve surgical outcome since it causes no heating or damage of the bone or surrounding tissue.

USDC may have other potential medical uses such as extracting pacemaker leads and the necessary drilling during skeletal diagnostic procedures. It can also be used as a minimally invasive surgical instrument and for restoring fluid flow to an implanted brain shunt [R&D 00]. The USDC can "core" holes in different cross sections such as square, round or hexagonal.

The USDC device has been further developed to make it a more intelligent (i.e. smarter tool). Figure 2.22 shows a prototype and a schematic diagram of a smart USDC with the coring bit running through the actuator. The smart USDC features the integration of onboard sensors to determine the various material properties prior or during drilling. It also features the ability of extracting dust and any volatiles through the device [SHER 01]. These features add to its advantages for the use in medical application such as orthopaedic surgery where bone fragments can be extracted and sucked out through the drill bit. It may also provide a haptic feedback regarding the type of tissue the corer head is encountering.

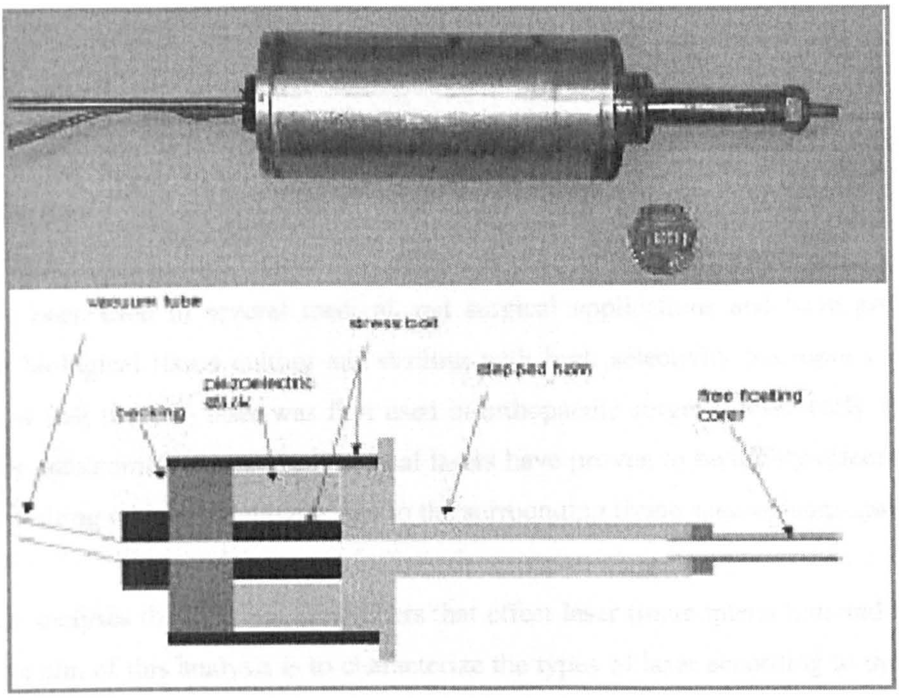

Figure 2.22: A prototype smart USDC with the capability for sample extraction through the actuator [SHER 01]

2.6.2.3 Evaluation of the USDC

In general USDC features several potential advantages over the traditionally used surgical drills. These include:

- Easy to control during bone drilling, which may lead to improved surgical outcome
- Causes no damage to the surrounding bone or tissue
- Ultra light in weight
- Can be easily adapted to computer assisted orthopaedic surgery using active robots since it causes low axial load on the robotic arm
- It can "core" holes of different cross sections and shapes
- The drill bit does not require sharpening and it self-removes debris
- Operates at low power - it requires only less than 10 Watts of power

Nevertheless, the USDC technology may suffer from some disadvantages which include:

- Tissue movement during surgery
- Physical contact with tissue may cause infection hazards
- Ultrasonic frequencies may have negative effects on patients with pacemakers or heart support devices

Chapter 3

Application of Laser in Orthopaedic Surgery

3.1 Introduction

Lasers have been used in several medical and surgical applications and have proven to be effective in biological tissue cutting and drilling with high selectivity [KIK 00][NIEM 96][SHOR2 nd]. Reports show that the CO_2 laser was first used in orthopaedic surgery in the early 1970s [FRYM 93][NIEM 96] for osteotomies. Since then medical lasers have proven to be highly effective in bone cutting and drilling with minimum damage to the surrounding tissue [NIEM 96][SHOR2 nd][STAN1 01].

This chapter analyses the different parameters that effect laser tissue interaction and hard tissue ablation. The aim of this analysis is to characterize the types of laser according to their surgical and medical application and to identify an appropriate laser and laser parameters for orthopaedic surgery. This chapter also aims to identify specific requirements for the design of a "laser End-Effector"; a new surgical tool for computer assisted orthopaedic surgery (see Chapter 5).

The study of this chapter focuses on hard tissue cutting, drilling and sculpturing with minimum invasiveness, on reducing tissue damage and on reducing surgical time. The study indicates that the Er: YAG laser is an appropriate laser for hard tissue interaction in orthopaedics and it is discussed in more detail in Chapter 4. As mentioned in Chapter 1 the intention is to show that lasers are viable replacements for the mechanical oscillating saw and pneumatic mechanical drill currently used in orthopaedic surgery.

The chapter starts by a short summary on the laser's background, a brief description of the operating principle, and basic system design. This is followed by a section on laser ablation and laser tissue interaction. The chapter then proceeds by presenting different types of laser, their medical application, laser tissue interaction mechanisms, and the different laser parameters that affect hard tissue ablation. It studies the suitability of the different lasers in medical applications with a particular focus on hard tissue ablation.

Also presented in this chapter are the different laser applications in orthopaedics and the laser selection criteria for the most appropriate laser system for such application. The chapter proceeds further by identifying the appropriate laser delivery system for the most appropriate laser. This chapter ends with a short section on laser safety and medical constraints and a summary of the set of identified requirements needed for the design of the laser End-Effector.

3.2 An Introduction to "Lasers"

"Laser" is an acronym for **L**ight **A**mplification by **S**imulated **E**mission of **R**adiation. Laser light has several features that are significantly different from regular light. Light from most sources spreads out as it travels, so that much less light hits a given area as the distance from the light source increases (Figure 3.1). Laser light, on the other hand, is collimated: its light is emitted in a very thin beam with all light rays are parallel with very little divergence (Figure 3.2) [NIEM 96][PROV nd][SHOR[1] nd].

Furthermore, laser light is monochromatic (i.e. it has a single wavelength) while regular light is a mixture of colours with each colour having a different wavelength. Laser is also coherent (i.e. laser light waves are synchronised in phase) unlike regular light where there is no definite phase relationship between light waves [O'SHE 97][SVEL 82].

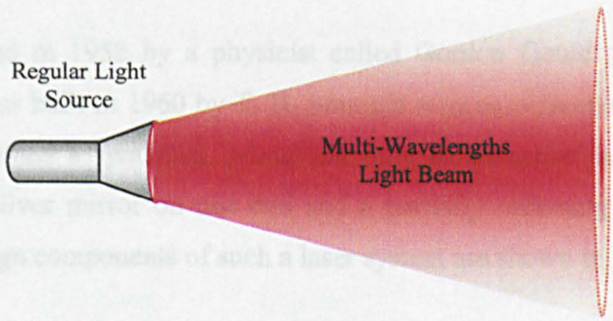

Figure 3.1: Regular light with multi-wavelengths

Figure 3.2: Collimated laser beam with light rays spreading very little with distance

3.2.1 Laser Fundamentals and operating principle

Laser systems contain five primary components regardless of their type, size and application (Figure 3.3) [NIEM 96][PROV nd][SHOR[1] nd][SREG 86]. These include

- Cavity (Chamber)
- Active medium
- Excitation energy source
- High reflectance mirror
- Partially reflective mirror

In basic laser the cavity (Figure 3.3) is designed to internally reflect light waves (IR – UV) so that they reinforce each other.

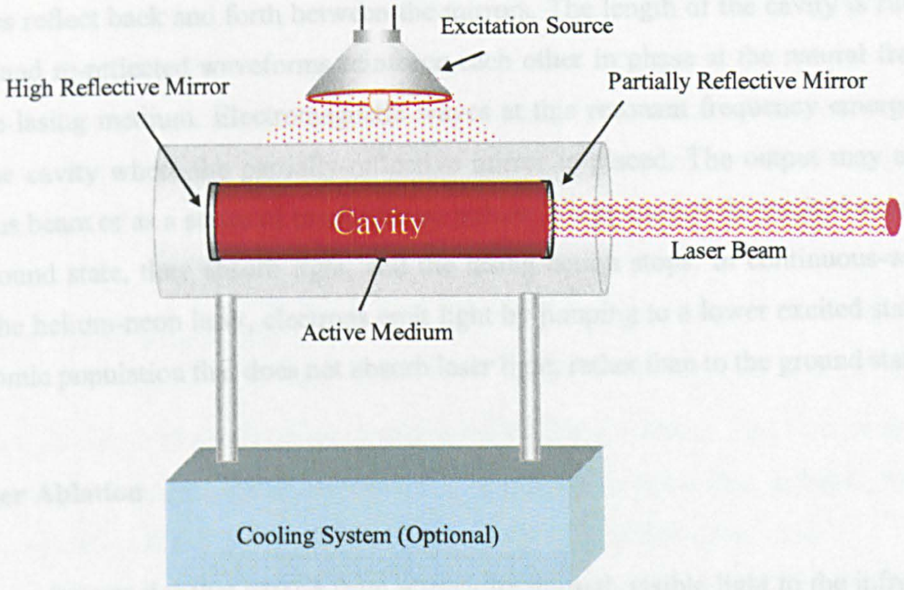

Figure 3.3: Primary laser system design components

The Laser was invented in 1958 by a physicist called Gordon Gould [NIEM 96] and the first working laser model was built in 1960 by T. H. Maiman [NIEM 96] [O'SHE 97][SVEL 82]. The cavity in this laser system contained a synthetic, cylindrical ruby as an active lasing medium with a completely reflecting silver mirror on one end and a partially reflecting silver mirror on the other. The primary design components of such a laser system are shown in Figure 3.3.

The choice of cavity material (active lasing medium) determines the wavelength of the output laser beam. The active lasing medium may be solid crystals such as ruby or Er: YAG, liquid dyes, gases like CO_2 or Helium/Neon, or semiconductor (solid state diodes) such as GaAs. Active mediums contain atoms whose electrons may be excited to a metastable energy level by an exciting energy source.

The excitation energy source pumps energy into the cavity by one or more of three basic methods; optical (Figure 3.3), electrical or chemical. As the active medium is excited electrons within the active medium atoms or molecules are pumped into a high energy level (outer orbits). When an electron drops from an outer orbit to an inner orbit (low energy level), "excess" energy is given off in the form of electromagnetic radiation such as light photons (spontaneous emission) [SREG 86][O'SHE 97][SVEL 82].

If a wave emitted by one excited atom strikes another, it stimulates the second atom to emit energy in the form of a second wave that travels parallel to and in step with the first wave. This stimulated emission results in amplification of the first wave. If the two waves strike other excited atoms, a large coherent laser beam builds up.

The waves reflect back and forth between the mirrors. The length of the cavity is such that the reflected and re-reflected waveforms reinforce each other in phase at the natural frequency of the active lasing medium. Electromagnetic waves at this resonant frequency emerge from the end of the cavity where the partially-reflective mirror is placed. The output may appear as a continuous beam or as a series of brief, intense pulses. When most of the excited atoms are back in the ground state, they absorb light, and the lasing action stops. In continuous-wave lasers, such as the helium-neon laser, electrons emit light by jumping to a lower excited state, forming a new atomic population that does not absorb laser light, rather than to the ground state [NIEM 96].

3.3 Laser Ablation

Lasers have frequencies that extend from ultraviolet through visible light to the infrared portion of the electromagnetic spectrum (Figure 3.4). These lasers can be delivered as a free beam to hand held tools via fibre optics, waveguides, or articulated arms to the patients' space [ABST2 00][NIEM 96].

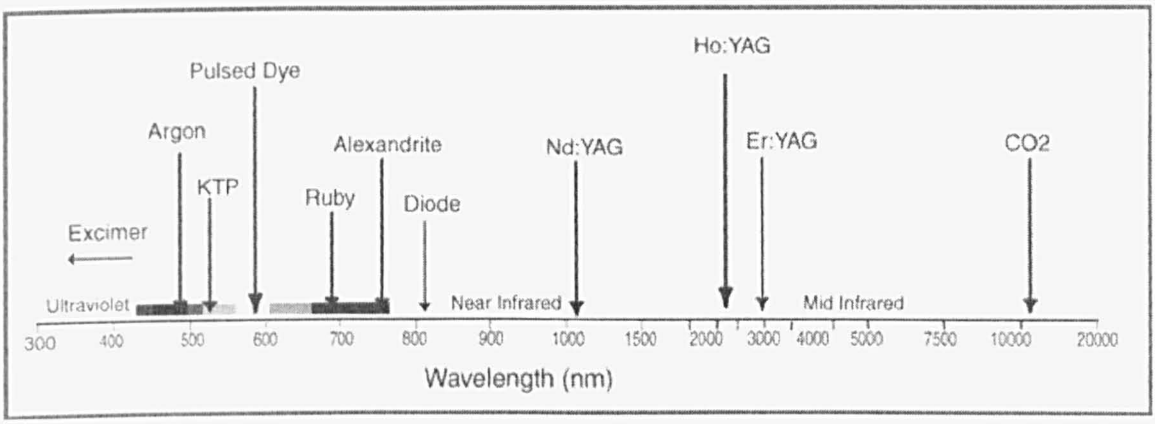

Figure 3.4: Medical Lasers Wavelengths [SHOR2 nd]

The photo-thermal effect of lasers can be used to cut, drill, coagulate, vaporize or weld tissue [NIEM 96][PROV nd]. As some lasers produce intense heat, they must be precisely localized to avoid damage to the surrounding tissue [AMER 93]. The heat produced by laser depends on several factors. These include laser wavelength, output power, spot size and application time [FRYM 93][NIEM 96]. This heat can also be affected by tissue factors such as water content, tissue colour and the surrounding medium (gas or fluid) [EVAN 93][FREN 99][NIEM 96][PROV nd].

There are many medical laser systems available and they all use the principle of getting the right amount of laser energy of the right wavelength to the right tissue to be able to selectively destroy the targeted tissue [FREN 99][NIEM 96]. Typically for these systems the surgeon can control the laser power, laser waveform (continuous or pulsed), pulse energy, pulse duration, pulse repetition time and laser spot size.

It is important to note here that pulse duration is as important as the wavelength and the power setting in medical surgery [SHOR' nd]. This is true since continuous wave lasers tend to cause temperature rise and thermal damage to the surrounding tissue [SHOR' nd] where short pulse laser tend to cause less damage [FEMT nd][LAWR nd]. In medical application the laser energy and pulse duration settings are based on the type of the laser and the specific medical application [NIEM 96].

3.3.1 Laser Tissue Interaction

Different lasers have different thermal effects on biological tissue. Laser beam absorption in biological tissue is mainly due to the presence of free water molecules, proteins, pigments and other macromolecules and this absorption is governed by Lambert's law [NIEM 96].

When the laser light energy is absorbed by tissue it is transformed into an effective thermal energy that can cut, coagulate, or ablate target tissue [NIEM 96]. The ability of laser beam to be absorbed by a tissue is determined by the wavelength of the laser beam applied and the optical properties of the target tissue. The laser wavelength and the optical property of tissue also determine the laser cutting efficiency and absorption rate.

Figure 3.5 shows the main laser absorbing components, or chromophores, of tissue [SHOR' nd]. Each type of tissue has its specific absorption characteristics depending on specific components. The main absorption components, or chromophores, of tissue are: haemoglobin, melanin and water.

Infrared light such as Er: YAG (λ= 2.94μm) and CO_2 (λ=10.6μm) laser is absorbed primarily by water, while visible light and ultraviolet light are mainly absorbed by haemoglobin and melanin, respectively. As the wavelength decreases toward the blue-violet and ultraviolet, scattering limits the depth of light penetration into tissue.

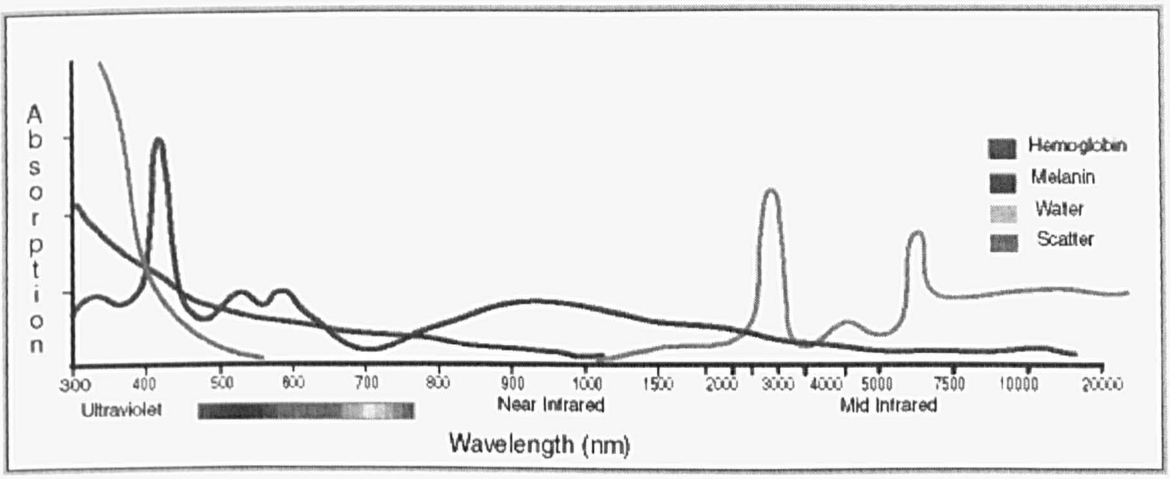

Figure 3.5: The most absorbing chromophores of tissue [SHOR' nd]

Studies on laser tissue interaction show that there are five main categories of interaction types [NIEM 96][MÜLL 91]. These are *photochemical interaction, thermal interaction, photo-ablation, plasma-induced ablation, and photodisruption.* Figure 3.6 shows the interaction types [NIEM 96][MÜLL 91] found in several experiments. All these different interaction types share a common characteristic energy density range from approximately 1 J/cm^2 to 1000 J/ cm^2 with a laser power density variation of over 15 orders of magnitude (Figure 3.6). The exposure time scale can be roughly divided into five sections: continuous wave or exposure time greater than 1 sec for photochemical interaction, from 1 sec down to 1 μs for thermal interaction, from 1 μs to 1 ns for photoablation, and less than 1 ns for plasma-induced ablation and photodisruption.

Figure 3.6 clearly shows that the reciprocal correlation between power density and exposure time. It also shows the different types of lasers and their normal type of tissue interaction.

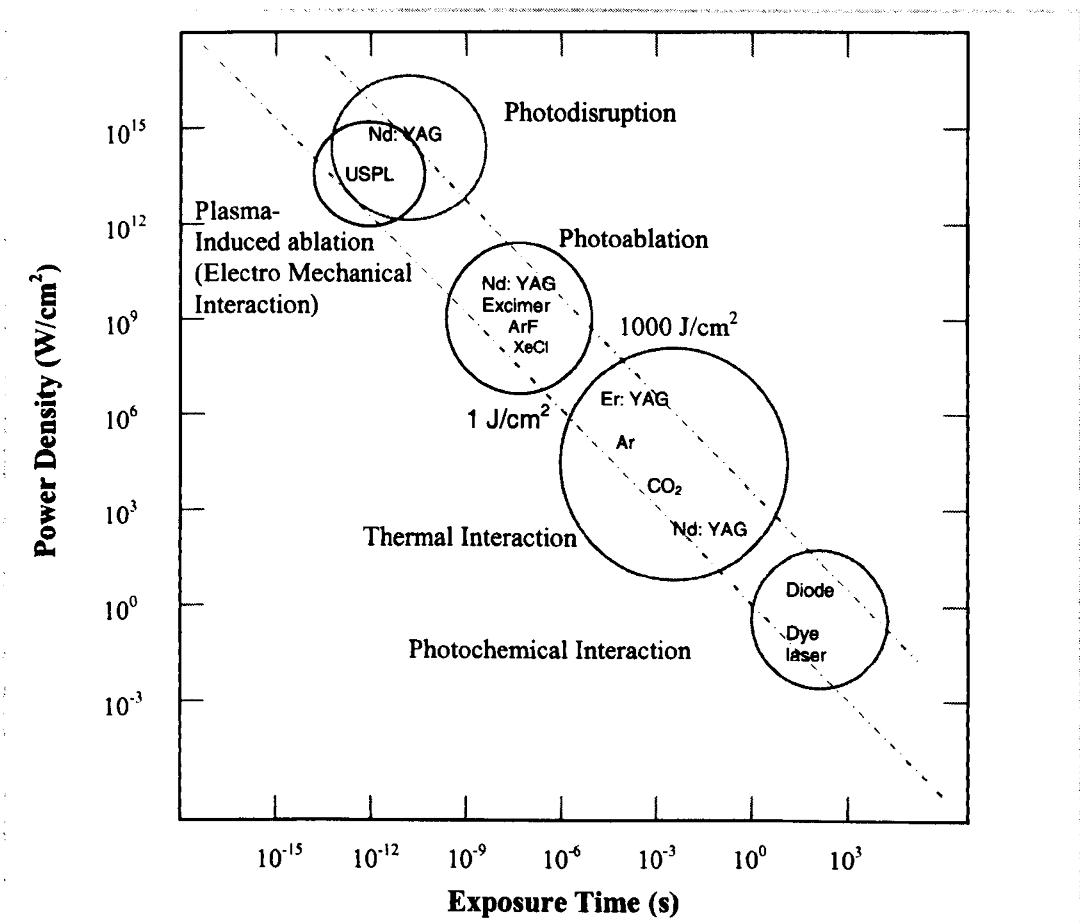

Figure 3.6: Map of Laser-Tissue Interaction [NIEM 96]

a) Thermal Interaction (Photothermal)

Thermal interaction is the heating of tissue through the conversion of the optical light energy into thermal energy when light is applied and dissipated into tissue. For Infrared (IR) lasers, absorption by water molecules plays a significant role in thermal interaction, for example

Continuous Wave (CW) CO_2 laser [EVAN 93][FREN 99][PROV nd]. Thermal interaction also occurs with long duration laser pulses in the millisecond to second range [EVAN 93].

b) Photochemical Interaction

Laser energy can initiate chemical reactions with specific molecules within tissue. In photochemical interaction laser light induces chemical effects and reactions within macromolecules or tissue [NIEM 96]. The idea of photochemical interaction is that a chromophore receptor (photosensitizer or organic dyes) acts as a catalyst. Laser irradiation puts these receptors into an excited state where they are able to store energy transferred from resonant absorption. The deactivation of these receptors causes photosensitizer oxidation leading to toxic compounds and leaves the photosensitizer in its original state.

Photochemical interaction mechanisms play a significant role during photodynamic therapy (PDT) in which a photosensitizer acts as a catalyst. For example in the case of tumour cells, a photosensitizing drug is administered which is selectively absorbed by tumour cells. When irradiated with an appropriate laser wavelength a chemical reaction takes place releasing a toxic substance that destroys the tumour. Another application of photochemical interaction is biostimulation [NIEM 96].

Photochemical interaction takes place at very low power densities (ranging from 0.01 to 50 W/cm^2) with long exposure time ranging from seconds to continuous wave. The lasers used for photochemical interaction are wavelengths in the visible range for their efficiency and their high depth of optical penetration [NIEM 96].

c) Plasma-induced Ablation (Electromechanical Interaction)

When laser power density exceeds 10^{11} W/cm^2, an optical breakdown phenomenon occurs resulting in a clearly visible bright plasma spark pointing toward the laser source [NIEM 96]. The plasma sparks (formed by ions and free electrons) creates a large *shockwave,* propagating at the speed of sound that mechanically ruptures the cells in its path [EVAN 93]. By choosing appropriate laser parameters the plasma-induce ablation, results in a very clean and well defined removal of tissue without evidence of thermal or mechanical damage. The most important parameter of plasma induced ablation is the local electric field strength E which is related to local laser power density I by the basic electrodynamic equation

Equation 3.1: Electrodynamic Equation

$$I = \tfrac{1}{2}(\varepsilon_o c E^2)$$

where ε_o is the dielectric constant, and c is the speed of light. The local electric field determines the occurrence of the optical breakdown. For optical breakdown to occur, E must exceed a certain threshold value for the ionization of atoms and molecules [NIEM 96].

Plasma-induced ablation occurs when the laser pulse duration is in the range of 100 femtosecond (fs) to 500 picoseconds (ps) and typical power densities ranging from 10^{11} to 10^{13} W/cm^2 [NIEM 96]. Ultra-Short Pulse Lasers [LAWR nd] are examples of the types of laser causing plasma-induced ablation (electromechanical interaction). Special applications of the plasma-induced ablation include refractive corneal surgery and caries therapy (minimally invasive teeth caries removal) [NIEM 96].

d) Photodisruption Interaction "cold cut"

Photodisruption interaction is also an electromechanical interaction process. It is a process that results from high energy laser pulses where fragmentation and cutting of tissue is by mechanical forces. The physical effects of photodisruption associated with optical breakdown are *plasma formation* and *shockwave* generation. In soft tissue or fluids *cavitation* and *jet formation* may also take place.

During photodisruption, while plasma-induced ablation is spatially confined to the breakdown region, shockwave and cavitation effects propagates into adjacent tissue, limiting the localizability of the interaction zone (i.e. causing damage to the surrounding tissue). The generated shockwave results in a high pressure gradient at the shock front moving at supersonic speed causing photodisruption and tissue ablation.

In cavitation a vapour inducing mechanical stress causes a successive expansion of a cavitation bubble resulting in tissue ablation [NIEM 96]. Lasers causing photodisruption include solid-state lasers, such as Nd: YAG, Nd: YLF and Ti: Sapphire, with laser pulse durations ranging from 100 fs to 100 ns and power densities in the range of 10^{11} to 10^{16} W/cm^2. The applications of photodisruption include lens fragmentation and lithotripsy [NIEM 96][HELF 01].

e) Photoablation Interaction

The main idea of photoablation interaction is the direct breaking of tissue molecular bonds by high energy UV photons. Research observations [EVAN 93][FREN 99][NIEM 96][PROV nd] showed very clean tissue removal without any appearance of thermal damage. During photoablation the resulting energy elevates the electrons of the molecules to a higher state leading to disturbance of intra-molecular bounds. The physical principles of photoablation are summarized in Table 3.1.

Table 3.1: Principle of photoablation [NIEM 96]

Absorption of high energy UV photons
⇓
Promotion to repulsive excited states
⇓
Dissociation
⇓
Ejection of fragments (no necrosis)
⇓
Ablation

The main advantages of photoablation lie in the etching precision, predictability and the lack of thermal damage to the surrounding tissue. Excimer lasers, such as (ArF, KrF, XeCl, and XeF) are typical examples of lasers that cause photoablation interaction with tissue. The typical pulse duration and power densities causing photoablation interaction are between 10 and 100 ns and 10^7 to 10^{10} W/cm respectively. One of the major applications of photoablation interaction is the refractive corneal surgery [NIEM 96].

3.3.2 Effects of focusing on laser beam interaction

When a laser beam is applied to body tissue, body fluid (water) (which forms 76% of the biological tissue) absorbs the laser beam energy and causes a localized instantaneous temperature increase in tissue. This heat energy in turn causes localized tissue destruction [PROV nd]. The resulting depth of the tissue damage or cut is highly dependent on the focusing of the laser beam. A focused laser beam will produce a deeper cut than either a pre-focused or defocused beams (Figure 3.7). A focused beam causes a narrow incision to the tissue with a relatively large depth whereas a defocused laser beam damages a wider area of tissue with a lesser distance (Figure 3.8) [PROV nd].

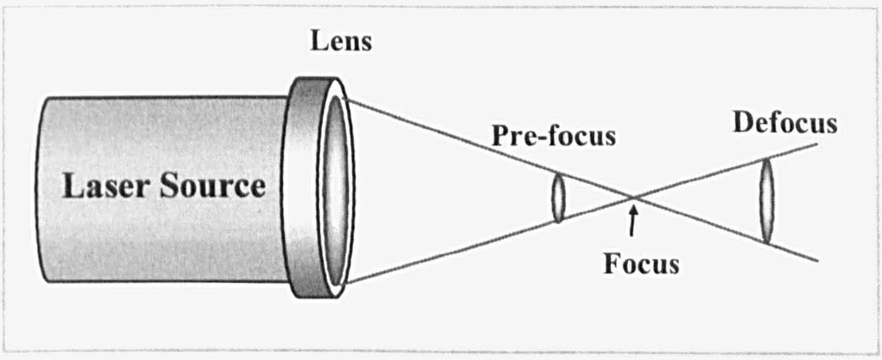

Figure 3.7: Prefocused, focused and defocused laser

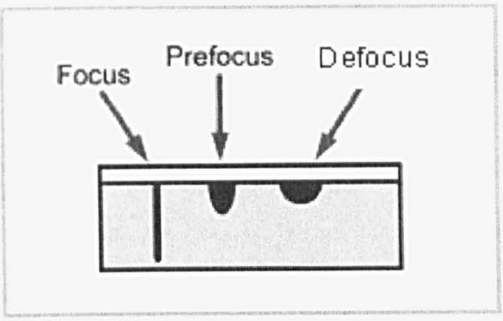

Figure 3.8: Focusing, pre-focusing & defocusing application in tissue effect [PROV nd]

For a CO_2 laser beam, for example, Photothermal interaction causes tissue fluid vaporization that leads to tissue vaporization and this tissue destruction produces a degeneration layer, a carbonisation area and ablated tissue where incision is to take place. Figure 3.9 shows the sequence of events for the affect of CO_2 on tissue.

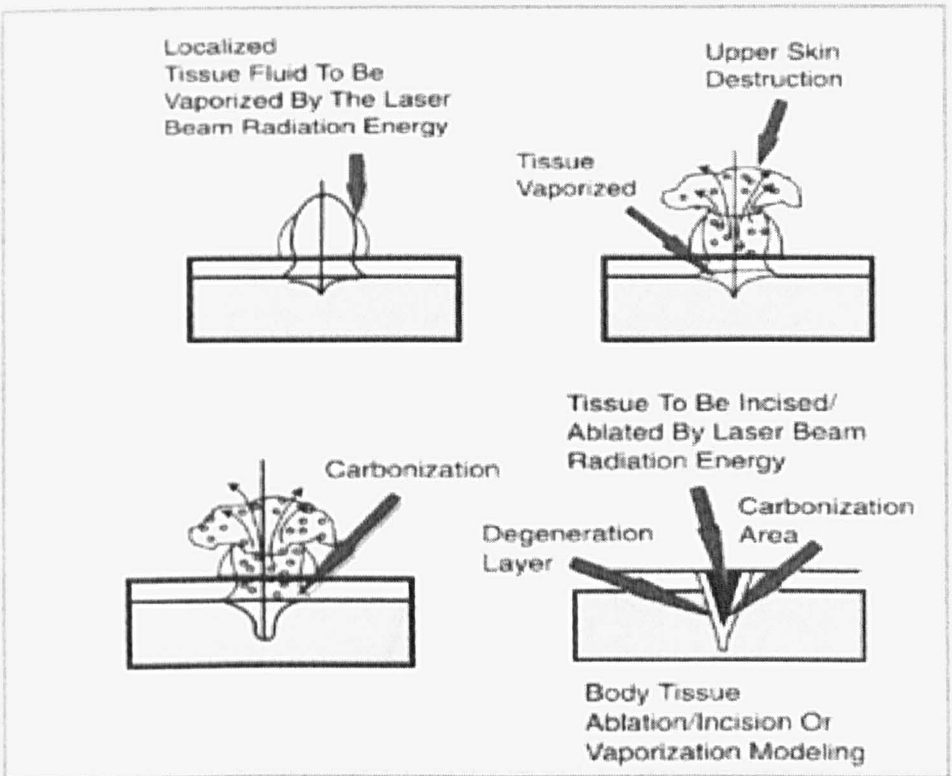

Figure 3.9: Model of CO_2 laser beam ablation of tissue [PROV nd]

The extent of the degeneration layer and carbonisation area is highly dependent on the type of laser beam, its beam parameters and type of issue. Ultra-Short Pulse Lasers (USPL), for example, creates high precision tissue cuts with minimum damage to the surrounding tissue. It produces such short bursts of laser energy that removes surface materials without any significant transfer of energy to the surrounding area.

For USPL laser pulses that are less than 10 ps, cutting occurs without any collateral damage to the surrounding tissues [NIEM 96]. The short pulse length can be advantageous in that it reduces the build up of thermal effects as the tissue has time to relax between pulses. Also the pulses can have high peak power even though the total output energy is low [NIEM 96].

3.3.3 Laser Tissue Ablation

Factors that influence tissue ablation mechanisms include laser wavelength, laser fluence (energy density), pulse duration and pulse repetition rate as well as the nature of the tissue to be ablated.

Figure 3.10 shows the typical ablation curve for a pulsed laser. The shape of this curve is independent of the laser's wavelength [NIME 9][ARCH 00]. At low energy density (fluence), there is no material removal. As fluence increases, the 'Ablation Threshold' point is reached, where material removal begins. As fluence increases further, more material is removed until the curve plateaus where the amount of material removed increases very little as the fluence increases. Hence it is not beneficial to run lasers at fluence levels beyond the operating range as they may cause secondary thermal side effects.

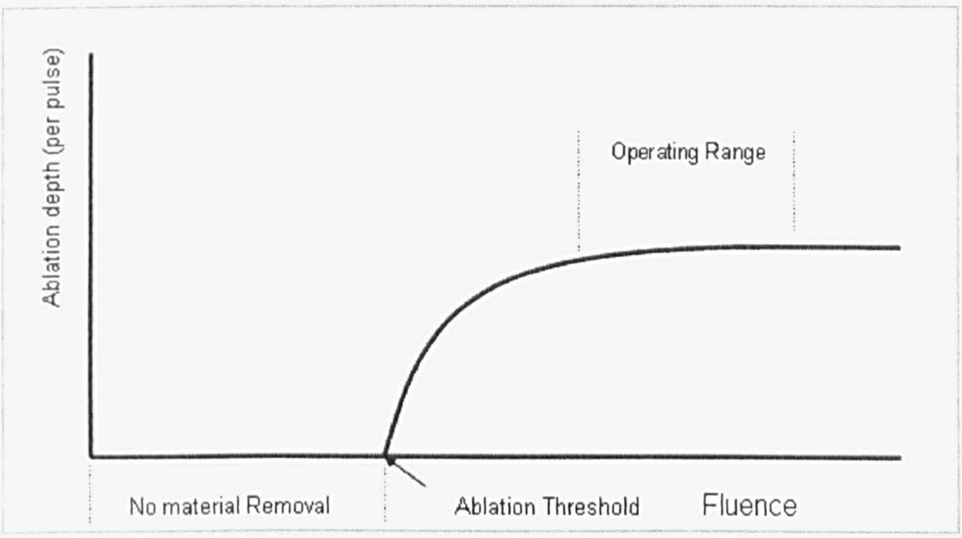

Figure 3.10: Typical ablation curve – graph of ablation rate vs. Fluence [NIME 9][ARCH 00]

3.4 Types of Lasers and their Suitability for Medical Applications

This section identifies several types of medical lasers, their properties and current medical applications. Table 3.2 classifies a number of laser systems used in medical application by their lasing medium. Later in Section 3.6 Table 3.3 provides further details of these laser systems in terms of their wavelengths, peak power, medical applications costs and other features. A scoring system is then applied to these medical lasers in order to evaluate their suitability for bone cutting in Orthopaedic surgery (Section 3.6).

Table 3.2: Laser Classification According to the Lasing Medium

Solid Lasers	Solid State Lasers	Gas Lasers	Dye and Vapour Laser
Er: YAG	Diode	Hydrogen Fluoride	Pulsed Dye
Ho: YAG		CO_2	Copper Vapour
Nd: YAG		Excimer	
KTP		Argon	
USPL			
Ruby			
Alexandrite			

3.4.1 Solid Lasers

YAG Lasers

YAG lasers use a **Y**ttrium-**A**luminium-**G**arnet crystal rod as the host medium. Dispersed in the YAG rod are rare earth elements, such as Neodymium (Nd), Erbium (Er) or Holmium (Ho), which are responsible for the different properties of each laser.

All YAG lasers may be operated in continuous wave or pulsed delivered through fibre optics and operated Q-Switched mode. The latter enables much higher peak power to be obtained for a given pump energy. In Q-Switch mode an optical shutter is placed in the cavity between the back mirror and the laser medium within the laser system [NIEM 96]. This increases the ability of the cavity to store energy between pulses over its normal value enabling very high power output [SHOR2 nd][NIEM 96].

a) Er: YAG Laser

Er: YAG laser also known as "Erbium" laser emits a mid-infrared beam at $\lambda = 2.94$ µm which coincides with the absorption peak for water (Figure 3.5) [NIEM 96][STAN1 01][HOFF 00][FARR nd]. When an Er: YAG laser beam hits a biological tissue, its wavelength dissipates heat and acoustical stress rapidly heating the localized tissue causing sudden explosive evaporation (micro-explosives) of tissue water. The resulting micro-explosives tear pieces out of the tissue and cause tissue removal [STAN1 01]. This photothermal mechanical ablation process of localized thermal decomposition of tissue [IVAN1 02][NIEM 96][STAN1 01] results in high ablation efficiency [MAJA 98] and minimal damage to the surrounding tissue. Research on Er: YAG laser has shown that at an energy density of 35 J/cm^2 using 250 µs pulses it is estimated to produce a thermal damage zone of only 12 µm is estimated [NIEM 96].

Uses of Er: YAG laser include; tissue ablation and cosmetic laser resurfacing for wrinkles. It offers the advantage of reduced redness, decreased side effects and rapid healing compared to pulsed or scanned CO_2 laser because of its limited tissue penetration. Er: YAG laser has also been used as a dental drill substitute to prepare cavities for filling [SHOR² nd][FBIH 02][IVAN 00]. In hard tissue ablation in dentistry, Er: YAG laser seems to offer the best combination of safety, efficiency and speed of other laser systems [ATTR nd]. It also offers a higher degree of surgical precision by being able to precisely cut through bone and other mineralized tissue with no or little lateral damage (Figure 3.11 & Figure 3.13) [STAN¹ 01][IVAN 00]. As an "excellent bone saw" [ABST¹ 00, STAN² 00], Er: YAG laser is highly promising laser for use in orthopaedics [ABST¹ 00][FITZ 95][JOOS 96].

In comparison to other lasers such as Ho: YAG, a lower energy density of Er: YAG laser is required to obtain a similar ablation depth in hard tissue with much less thermal damage effect (Figure 3.11) [FREN 99][NIEM 96].

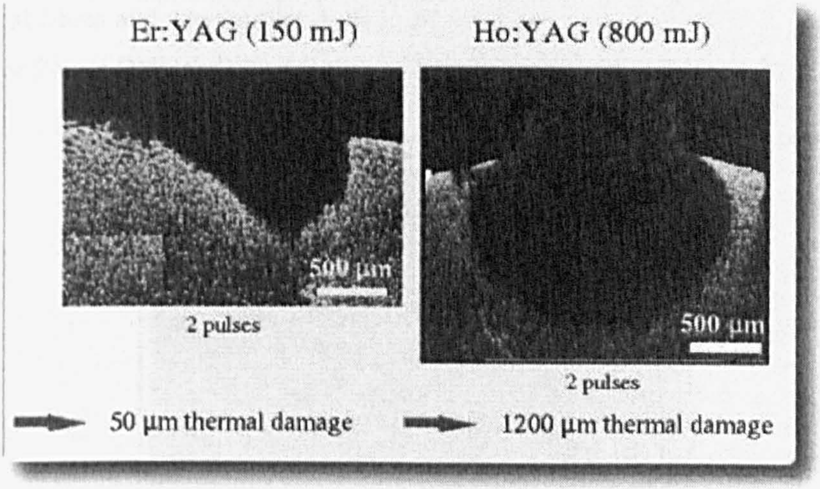

Figure 3.11: Live - dead staining of bovine cartilage after Er: YAG and Ho: YAG laser Irradiation [FREN 99]

An analysis of the Er: YAG laser cuts performance reveals that the Er: YAG laser runs in multi-transverse electromagnetic mode (TEM) profile [STAN¹ 01] (the TEM structure of a laser beam describes the power distribution across the beam (Figure 3.12) [HECH 92][KOGE 96]) resulting in an almost rectangular cut shape with very steep sides (Figure 3.13) [STAN1 01].

As a result of the multi-transverse electromagnetic mode (MTM) a negligible amount of the pulse energy is deposited in the sides allowing for deep tissue cutting. The only significant pulse energy losses are sustained as the beam passes through water spray (required for tissue cutting to prevent tissue carbonisation [IVAN 00][IVAN¹ 00][FREN 03]) and the debris cloud (Plume) [ABST¹ 00][STAN¹ 01][MAJA 98].

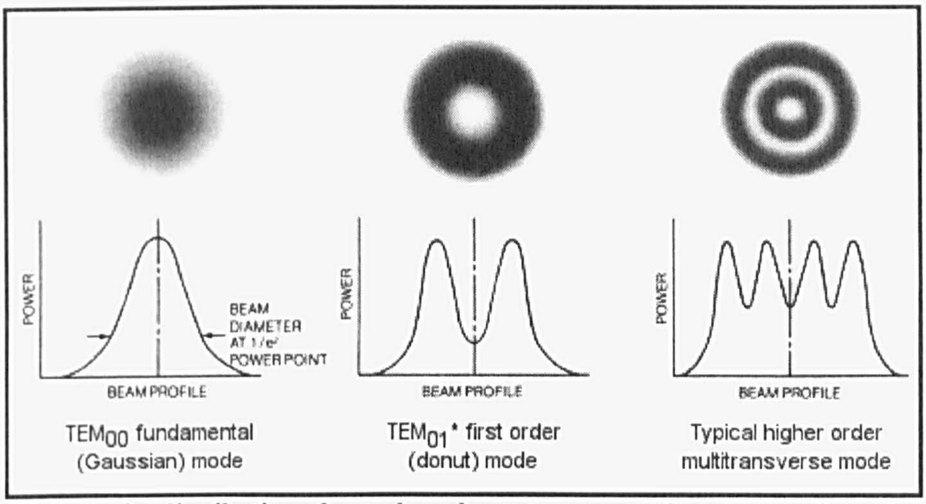

Figure 3.12: Intensity distribution of some laser beam transverse electromagnetic modes [KOGE 96]

A major negative feature of Er: YAG laser lies in its power delivery. The Er: YAG laser wavelength (λ = 2.94 µm) does not transmit through standard quartz fibres; consequently, other types of optical fibres and waveguides need to be used [ABST² 00][NIEM 96][MATS 00] (see Section 3.6: Er: YAG Laser Power Delivery).

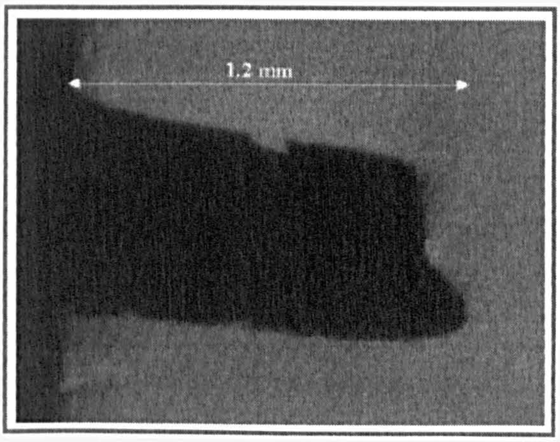

Figure 3.13: Cut through a bovine femur sample irradiated by a free running Er: YAG Laser with an energy density of 60J/cm^2 and a pulse overlap of 12 [STANI 01]

b) Ho: YAG laser

Ho: YAG laser emits a mid-infrared beam at λ = 2.1 µm. The principal use of the Ho: YAG laser is for cutting and shaping cartilaginous tissues hemostatically [ABST² 00]. It also features high fluence light that creates very clean vaporization and is effective on all cartilages regardless of their toughness [ABST² 00]. It has been used for bone ablation and many other applications including:

- Orthopaedics for arthroscopy in a fluid filled joint [ABST² 00]
- Urology for lithotripsy (Kidney stones removal)
- ENT for endoscopic sinus surgery
- Spine surgery for endoscopic disc removal

- TURP (Prostate removal) [SHOR[2] nd]

The Ho: YAG laser can be transmitted through standard quartz fibres, which is convenient for medical laser systems (tools) [ABST[2] 00].

c) Nd: YAG Laser

The Nd: YAG laser emits a near-infrared invisible light at $\lambda = 1.064$ μm that may be delivered in continuous wave (cw) mode through fibre-optics to a sapphire tip to cut tissue. It features deep penetration of tissue and it is used for direct tissue coagulation. The Q-Switched Nd: YAG is effective for removing black tattoo ink and it also has been used for hair removal.

d) KTP Laser

The KTP laser is a Nd: YAG laser with $\lambda = 1.064$ μm that passes through a Potassium-Titanyl-Phosphate (KTP) crystal to produce laser light with its wavelength λ halved to 0.532 μm (brilliant green light).

KTP can be used in CW mode to cut tissue, in pulsed mode for vascular lesions including facial and leg veins, and in Q-Switched mode for removing red/orange tattoo pigment delivered via an articulating arm. In CW and pulsed modes it can be delivered through an insulated fibre to a hand-piece, scanner, or microscope [SHOR[2] nd]. One of the major applications of KTP laser is spinal disc decompression using a silicoa optical fibre for laser delivery into the disc.

e) Ultra-Short Pulse Laser (USPL)

USPL produce low energy ultra-short pulses formed in a mode-locked Ti-sapphire laser and amplified in a regenerative amplifier where the ultra short pulses are first stretched by separating the pulses into their colour elements, amplifying the individual elements and then recombining [LAWR nd].

Ultra-Short Pulse Lasers create high precision cuts without damaging the surrounding tissue. USPL Systems are still being researched for clinical applications. Future potential uses of USPL include; heart surgery for Transmayocardial Revascularization (TMR) [LAWR nd], dentistry for teeth drilling [LAWR nd], spinal and neurosurgery for the removal of the bone impingement into openings of nerves (pinched nerve), and in bone drilling [LAWR nd]. Figure 3.14 below shows the high precision of USPL drilling on a pig myocardium.

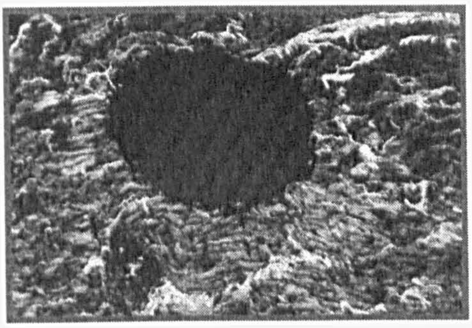

Figure 3.14: Histological section of a pig myocardium drilled by an USPL showing a smooth-sided hole free of thermal damage to surrounding tissue [LAWR nd].

In dentistry the USPL can drill teeth with minimum heat transfer and no thermal damage or cracking to tooth enamel (see Figure 3.15). Other major applications of USPL in dentistry include root sterilization and soft tissue sculpting.

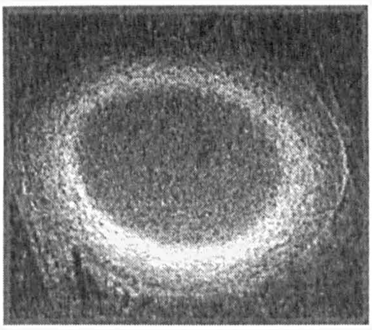

Figure 3.15: Smooth hole with no thermal damage after drilling a tooth with a USPL [LAWR nd].

f) Ruby Laser

A Ruby laser emits red light with $\lambda = 0.694$ µm. It features strong absorption by blue and black pigments and by melanin in skin and hair. Ruby laser systems are available in Q-switched mode with an articulating arm, "free running" ms range mode with fibre optic cable delivery or dual mode delivery. Current uses of the Ruby laser include tattoo removal, treatment of pigmented lesions and laser hair removal [NIEM 96].

g) Alexandrite Laser

The Alexandrite laser emits a deep red light with $\lambda = 0.750$ µm. It has similar properties to those of the Ruby laser yet it features slightly deeper skin penetration and lesser absorption by melanin. Uses of this laser include; hair and tattoo removal [NIEM 96].

h) Solid State Lasers

Solid state lasers are electro-optical devices, capable of delivering coherent radiation at very specific wavelengths, either narrow band or broad band emission. They are composed of a solid lasing media (crystal or glass) doped with ions (e.g. Nd_3^+, Cr_3^+, Er_3^+) that can emit coherent light under special physical conditions [ABST[1] 00][ABST[2] 00][NIEM 96][IVAN 97].

Solid state lasers are widely used for various medical applications including; hair removal, periodontal surgery [MORI 987][MORI 98], treatments of leg and facial veins [NIEM 96].

3.4.2 Gas lasers

Gas lasers include Hydrogen Fluoride (HF) (λ = 2.94 μm), CO_2 (λ = 9.6 and 10.6 μm), Excimer (UV) and Argon (λ = 0.488-0.514 μm).

a) Hydrogen Fluoride HF Laser

The Hydrogen Fluoride (HF) laser emits an infrared light at about 2.94 μm wavelength, a wavelength which is highly absorbed by water. Like the Er: YAG laser, the HF laser has the ability to precisely cut through bone and other mineralized tissue such as tooth enamel, which make it an excellent bone saw with minimal lateral heat damage. However this wavelength of 2.94 μm will not pass through standard quartz fibres. Other types of fibre such as single-crystal sapphire fibres and small-bore hollow waveguides could be used for HF laser delivery [ABST[2] 00].

b) CO_2 Lasers

The CO_2 laser is often referred to as the "Surgical Laser". They were the first lasers widely used by surgeons for ablation of soft biological tissues [IVAN 98][NIEM 96][SHOR[2] nd][IVAN 97]. CO_2 lasers feature strong water and bone absorption and emit either CW pulsed far infrared light at 9.6 μm and 10.6 μm wavelengths. CO_2 lasers also feature high power, high efficiency and reliability [IVAN 97]. The CO_2 lasers can be focused into a thin beam and used to cut like a scalpel, or defocused to vaporize, ablate and shave soft tissue [SHOR[2] nd]. However, the lack of a good IR fibre necessitates the use of an articulated mirror arm and long focusing optics which limits the usefulness of the CO_2 lasers [BIRM 00][IVAN 97].

CO_2 lasers can operate in several modes; quasi-CW, ultra-pulsed and Q-switched modes. Early attempts to cut bone with CW and long-pulsed CO_2 lasers caused heavy thermal damage of the bone tissue. Conversely; the application of sub-μs CO_2 laser pulses or Q-switch CO_2 lasers in combination with an air water spray to cut cortical bone lead to a minimal thermal damage of 2 – 6 μm thick at the surface of the bone [IVAN[1] 00][IVAN[2] 00]. Mechanically Q-switched CO_2 lasers can provide a lasing mode very close to TEM_{00} (a Gaussian-curve mode (Figure 3.12) that is the best collimated and produces the smallest spot size) which results in the typical cut profile shown in Figure 3.16. Uses of CO_2 lasers include:

- Removal of benign skin lesion
- As a "Laser Scalpel" in patient or body areas prone to bleeding
- No- touch tumours removal
- Laser surgery for snoring
- Dermatological applications
- Cosmetic laser resurfacing of wrinkles

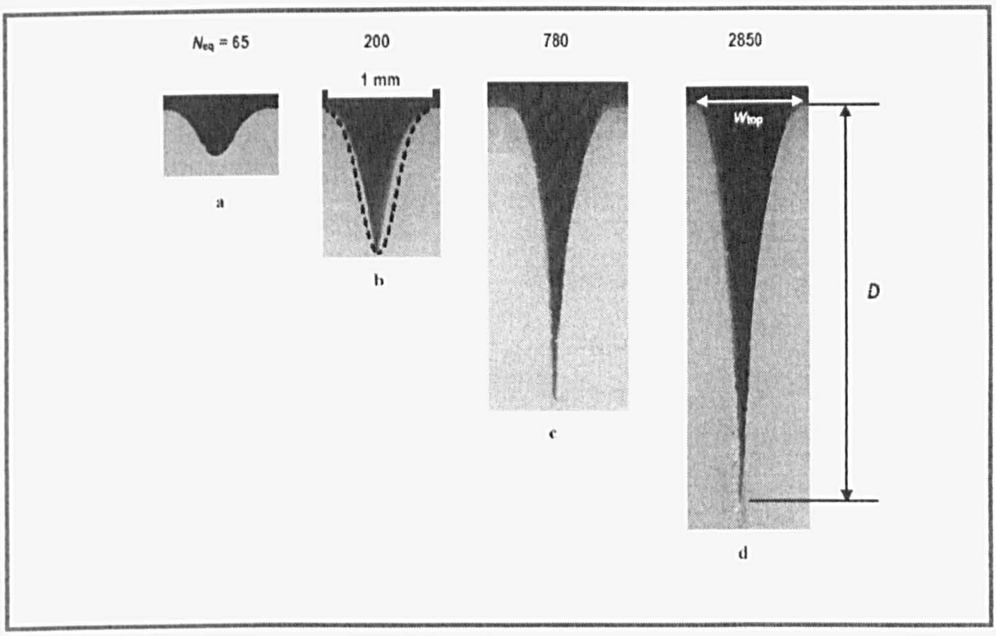

Figure 3.16: Typical cut profile in hard cortical bone with a nearly Gaussian beam of Q-switch CO_2 laser after different irradiation time. Also indicated the equivalent pulse number N_{eq} effectively acting at the same place [IVAN² 00]

c) Excimer Lasers

Excimer laser is an alternative name for "Excited Dimer laser". Excimer lasers use a gas mixture as the lasing source to emit invisible ultra-violate (UV) light. These include Argon Fluoride and Xenon Chloride lasers. In medical applications this UV light triggers a photochemical reaction in the target tissue. The very short wavelengths of Excimer lasers are capable of high resolution and microscopic surgery [SHOR² nd][NIEM 96].

The Argon Fluorine (ArF) laser at 0.193 μm is the most common excimer laser for medical applications such as vision correction. Excimer lasers can be delivered through an operating microscope integrated with the laser housing and operating table. Excimer laser radiation shows great promise for cardiac revascularization and lithotripsy, yet its use is currently limited by the lack of durable UV-capable fibre optic delivery devices [SHOR² nd][ABST¹ 00].

3.5 Lasers in Orthopaedics

Standard mechanical tools in orthopaedic surgery operate in contact mode and possibly induce severe mechanical vibration and haemorrhage. Thus it appears to be worth investigating laser beam as an alternative tool, particularly as lasers have proven to be an excellent tool in many other medical applications [LAWR nd][NIEM 96].

The hardness of the bone is due mainly to its complex structure of hydroxyapatite, water, soluble agent, collagen, and proteins. The high water content of bone makes it a strong absorber of infrared radiation, therefore CO_2, Er: YAG and Ho: YAG lasers are likely to provide an efficient mean for ablation of bone [FRYM 93].

The remainder of this section discusses the current use both clinically and in research of lasers in orthopaedics.

a) Osteotomy

Reports show that the laser was first used in orthopaedics in the early 1970s [FRYM 93] on osteotomies performed with a CO_2 laser. These reports showed delayed healing when compared with conventional osteotomies due to the thermal damage of the bone rim. XeCl lasers at 308 nm were also used to perform osteotomies, yet they too were associated with severe thermal damage as was the CO_2 laser, and again this damage was believed to have caused delayed healing [FRYM 93].

Although CW CO_2 lasers produce severe thermal side effects in bone, there is a great potential of the CO_2 laser for bone ablation with very little thermal damage by selecting carefully the laser parameters for the applied laser, i.e. wavelength (λ), pulse duration and energy density. Forrer et al. (1993) [FRYM 93] demonstrated this potential of the CO_2 laser by selecting $\lambda = 9.6\ \mu m$, a pulse duration of 1.8 μs and an energy density of 15 J/cm^2; the thermal damage zone was found to be 10-15 μm [NIEM 96]. Other research on CO_2 laser osteotomy showed thermal damage in the range of 2-6 μm [IVAN[1] 00][IVAN[2] 00]. In this case both the wavelength and the pulse duration play a significant role since bone absorption at $\lambda = 9.6\ \mu m$ is higher than that of $\lambda = 10.6\ \mu m$ and the shorter pulse duration tends to be associated with less thermal damage.

The Hydrogen Fluoride laser (HF) at $\lambda = 2.9\ \mu m$ and the Er: YAG laser at $\lambda = 2.94\ \mu m$ have shown efficient ablation of both bone and cartilage [ABST[1] 00][FRYM 93].

Another promising laser in orthopaedics is the Ho: YAG laser which emits at $\lambda = 2.1$ µm. Its major advantage is that it can be efficiently transmitted through flexible fibres. However, its thermal effects on bone are higher compared to Er: YAG at $\lambda = 2.94$ µm which are associated with very little thermal damage [FREN 99]. In comparison to the Ho: YAG laser, a lower energy density of Er: YAG laser radiation produces a similar ablation depth as with the Ho: YAG and with lesser thermal damage (see Figure 3.11).

Excimer lasers have also been proposed for the ablation of bone material due to their high precision in removing tissue. However, their efficiency is much too low to justify their clinical application [FRYM 93].

b) Arthroscopy

Arthroscopic surgery with lasers offers a number of potential advantages for their ability to cut and coagulate simultaneously. The laser allows the surgeons to access areas that are difficult to reach with standard instrumentation. The laser also allows for either precise incision of meniscal tissue or ablation of large areas of synovial tissue [FEMT nd]. Current arthroscopic surgical procedures that use lasers in the knee joint include: meniscal excision, plica resection, lateral release, excision of scar tissue and synovectomy [FEMT nd].

Laser energy can be used to ablate hypertrophic synovium, to smooth or remove fibrillated articular cartilage and resect and contour torn menisci. Also depending on the wavelength many lasers produce effective haemostasis retinacular release, bursectomy and resection of coracoacromial ligaments [AMER 93].

A major limitation for all infrared lasers in arthroscopic surgery is that the laser is delivered via flexible optical fibre cable which is regarded as a mandatory requirement for an efficient surgery procedure.

c) Lumber Spine

In the USA lasers have been used for the removal of intervertebral disc material in the lumber spine (diskectomy), yet this treatment is restricted to patients with contained disc herniations. However, large extruded or sequestered fragments of disc can not be removed safely by lasers [AMER 93].

Also with the aid of a flexible spinal endoscope through small catheters, containing an on board laser, lasers can be used for the excision of herniated fragments in the spinal canal [AMER 93].

Another major application for the laser in lumber spine surgery is using the KTP laser transmitted via silica optical fibre inserted into the disc through a needle placed into the disc at a forty five degree angle. A needle placed at this angle causes no vital danger to nerves and blood vessels within the vertebral column [AMER 93]. Laser energy transmitted to the disc causes the loss of water and some soft materials from within the disc leading to disc shrinkage by decreasing the pressure in the disc. As the disc shrinks it pulls the offending bulge off the nerve root relieving the pain totally or substantially reducing the pain.

d) Joint Revision

In total joint revision a laser has been used to vaporize polymethyl-methacrylate. However this application is limited by the toxic and flammable plume produced from the vaporization of the super heated polymethyl-methacrylate [AMER 93].

e) Other Orthopaedic uses of lasers

Lasers have been used to debride soft tissue wounds and ulcers, as well as tissue welding to repair small vessels [AMER 93]. Other orthopaedic uses of lasers include excision of musculoskeletal tumours, revision arthroplasty (cement removal), amputation, nail bed surgery and hand disorders (arthroscopic carpal tunnel release) [FEMT nd].

3.6 Selection of a Laser for Bone Cutting

Evaluation of laser types for selecting a suitable laser for further investigation is based on a scoring system developed by the author. Individual scores are given to various laser properties such as the laser delivery system, general medical application and existing applications in orthopaedics. The individual scores are then summed to give a total score. The resulting scores are shown in Table 3.4 and plotted in Figure 3.17. Lasers with higher scores are likely to be more suitable for bone cutting in orthopaedic surgery. The individual scores assigned are explained below.

a) Threshold Ablation Energy Density

A maximum score of 4 points is given to lasers with threshold ablation energy densities less than or equal to 1 J/cm^2. 3 points are assigned for lasers with thresholds ablation energy densities less than or equal to 10 J/cm^2. 2 points are assigned for lasers with thresholds ablation energy densities less than or equal to 50 J/cm^2 and 1 point is given for any value greater than 50 J/cm^2.

b) Thermal Damage

The maximum score of 4 points is given for lasers with minimum thermal (heat) damage to surrounding tissue (< 20 μm). 1 point score is given to lasers causing very large thermal damage (> 200 μm). Two other levels of scores are also given for lasers with moderate thermal damage, 3 points for ranges of 20 - 100 μm and 2 points for ranges of 100 - 200 μm.

c) Orthopaedic Application

Maximum points (4) are given for lasers used in hard and soft tissue ablation including bone cutting and drilling. Three and two points are rated based on specific surgical applications in orthopaedics such as spinal disc decompression while no points are given to lasers with no orthopaedics applications.

d) Water Absorption

Since water plays a significant role during hard tissue ablation and laser tissue interaction, scores are given to the different types of laser according to their level of water absorption. A maximum score of 4 points is given to the Er: YAG laser, which coincides with peak absorption of water. No points are given to lasers with very small water absorption coefficient < $1 cm^{-1}$. Two and three score points are given to lasers based on their level of water absorption.

e) Typical Pulse Duration

- Pulse and Q- switched mode (4 points): Q-switching produces short optical pulses with high peak power [YUSH 04][SHOR[2] nd][NIEM 96]. This provides high controllability over pulse duration and pulse rate and high pulse amplitude stability and low power consumption. Hence, allowing for high control of the ablation depth and ablation time
- Continuous and pulsed mode (3 points): less controllable and typically limited pulse durations and pulse rates
- Pulse mode only (2 points): limited pulse durations and pulse rates
- Continuous wave only (1 point): may cause energy build up which reduces the quality of the cut and the efficiency of the cutting system [NIME 96]

f) Lasing Source

The lasing source is very important in terms of environmental safety, size of the laser system, power consumption, durability and cost. Solid state lasers, for example, are given 4 points because they are environmentally safer than other solid, chemical or gas lasers, more compact in size, consume less energy, and normally low in cost.

- Solid state laser 4 points
- Solid laser 3 points
- Liquid /Chemical lasers 2 points
- Gas laser 1 point.

g) Lasing Medium Durability (life span)

- Long lasing life 4 points
- Moderate lasing life 3 points
- Short lasing life 2 points
- Very short lasing duration 1 point

h) Laser Delivery System

A maximum score of 4 is given for lasers which can be delivered using silica- based glass fibre optics for its low cost, availability, and high dexterity and flexibility. 3 points are given to lasers which require hollow waveguides since; hollow waveguides offer several advantages over many other solid core fibres. These include high power handling capabilities, durability, lack of fresnel losses and small beam divergence yet with limited flexibility and dexterity. 2 points are given for lasers that require special optical fibres (such as single–crystal sapphire fibre) for their high manufacturing cost in comparison to silica-based glass fibres or hollow waveguides. 1 point is given for lasers that require an articulator arm delivery system for lack of flexibility and bulkiness of the delivery system.

i) Surgical /Clinical

A maximum of 2 points is given for lasers which can be used surgical applications which is a basic requirement for this project. 1 point is given for lasers which offer clinical applications only.

Table 3.3: Laser classification according to the wavelength (colour),water absorption (μa cmm^{-1}), medical applications, Threshold ablation energy density $\Phi°$ peak power, Absorption length[Thermal Damage]other features [ABST2 00][IVAN 97][LAWR nd][NIEM 96][SHOR2 nd][HOFF 00]

Laser Type	Laser Wavelength (Colour)	H_2O μa cm-1	Medical Applications	Threshold ablation energy density $\Phi°$	Peak Power	Absorption length [Thermal Damage]	Other Features
Excimer **ArF** **XeCl**	0.193 μm 0.308 μm (Ultraviolet)	0.018 0.0058	Ophthalmology-Corneal reshaping Cardiovascular - angioplasty	1 J/cm^2	1.6W	6μm [10 - 50μm]	Fast Pulsed Lasers
Argon	0.488 μm & 0.514 μm (Blue and Green)	*	Ophthalmology	*	10W	*	Used in Entertainment
KTP	0.532 μm (Brilliant Green Light)	*	Laparoscopy, ENT and Dermatology	*	*	*	*
Pulsed Dye	0.517 – 0.585 μm (Yellow)	*	Dermatology – Vascular lesions & lithotripsy	*	*	*	Pulsed Laser
Copper Vapour	0.577 μm and 0.511 μm (Yellow)	*	Dermatology Pigmented lesions	*	*	*	Fast Pulsed Laser Precision
USPL	~ 0.600 μm (Yellow/Orange)	*	Medical applications	*	10kW	*	*
Ruby	0.694 μm (Red)	*	Dermatology Tattoo and Hair removal	*	100MW	*	Live holography Q- switched and Long-pulse modes
Alexandrite	0.755 μm (Deep Red)	*	Dermatology Hair removal	*	*	*	Q- switched (ns) and Long-pulsed (2-20 ms)
Diode	760 - 1060 μm (Deep Red- Near Infrared)	*	Bio-stimulation (Low Power) Dermatology for hair removal and Urology (High Power)	*	30W	*	*
Nd: YAG	1.064 μm (Near Infrared)	0.61	General laparoscopy, hysteroscopy, flexible endoscopies. Dermatology Ophthalmology	250 J/cm^2	50MW	1300μm [350μm]	Q-switched mode
Ho: YAG	2.07 μm (Med Infrared)	36	Orthopaedic Surgery Lithotripsy in URO Ophthalmology Dentistry	40 J/cm^2	10W	200μm [75-300μm]	*
Er: YAG	2.94 μm (Med Infrared)	12000	Bone cutting and drilling – dental and hard tissue. Skin resurfacing	0.2 J/cm^2	*	1μm[10-50μm]	Fine Effects
Hydrogen Fluoride (HF)	2.94 μm (Med Infrared)	12000	Investigational – Bone cutting and drilling Investigational Ophthalmology	*	50MW	1μm[10-50μm]	Excellent Effects
CO_2	9,60 μm 10.6 μm (Far Infrared)	860	Hard tissue cutting & Drilling Surgical laser, Snoring, Tumour removal Dermatology	3 J/cm^2	200W	15μm [>200μm]	Q-Switched Quasi-cw (single shot) Ultra-pulses (200Hz) Q-Switched (2kHz)

* **Insufficient Data or Not Applicable**

Table 3.4: The scores given to lasers, by the author, according to the laser orthopaedic application

Laser Type	Threshold ablation energy density Φ°	Ablation Time for Bone [CHAR 90]	Minimum Thermal Damage	Orthopaedic Application	Water Absorption coefficient	Typical Pulse Duration	Lasing Source (medium)	Lasing Medium Durability (Life span)	Laser Delivery System	Surgical / Clinical	**Total Points**
Excimer	4	0	4	0	0	3	2	1	1	2	17
Argon	0	0	1	0	0	1	2	1	4	1	10
KTP	0	0	1	2	0	4	3	3	4	2	19
Pulsed Dye	0	0	1	0	0	2	1	1	4	2	11
Copper Vapour	0	0	2	0	0	2	2	1	4	2	13
USPL	2	3	4	4	2	4	3	3	4	2	31
Ruby	0	0	2	0	0	2	3	3	4	2	16
Alexandrite	0	0	2	0	0	2	3	3	4	1	15
Diode	0	0	3	0	0	1	4	3	4	2	17
Nd: YAG	1	0	1	0	0	4	3	3	4	2	18
Ho: YAG	2	2	3	4	1	3	3	3	4	2	27
Er: YAG	4	4	4	4	4	3	3	3	3	2	34
Hydrogen Fluoride	4	4	4	4	4	3	1	1	3	2	30
CO_2	3	1	3	3	3	4	2	1	2	2	24

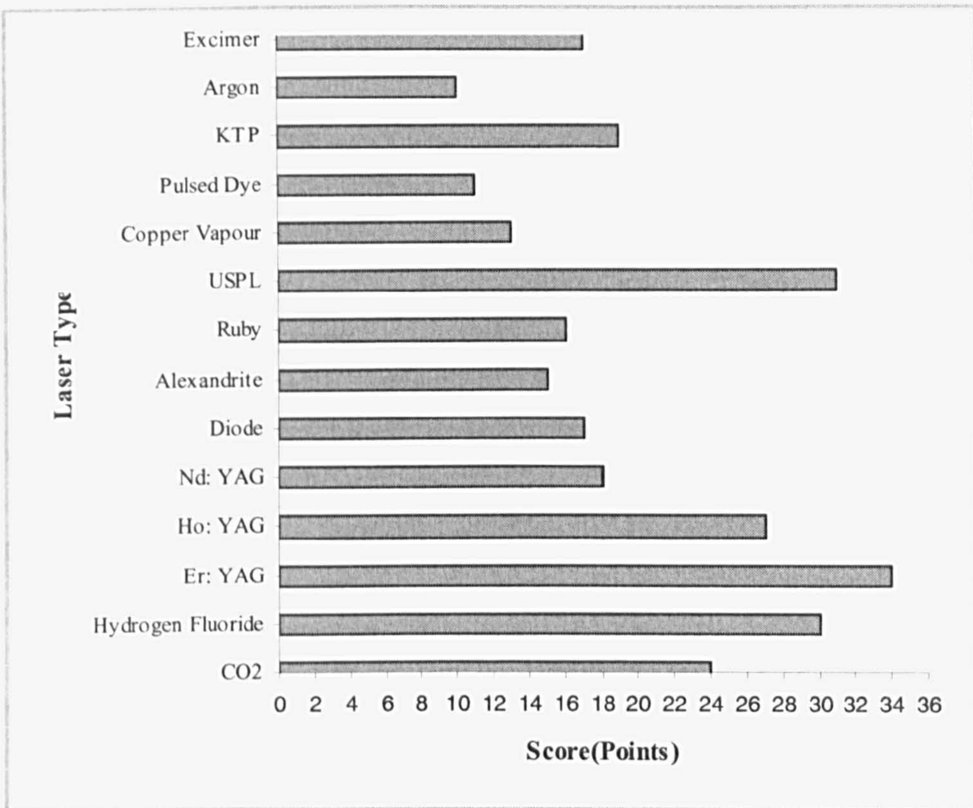

Figure 3.17: Laser types and the scores given by the author according to preference

One may conclude from the above results of Figure 3.17 that the Er: YAG is a good candidate for being a suitable laser for the application in computer assisted orthopaedic surgery. It also shows that other lasers, namely USPL, Ho: YAG and HF have good potential for being suitable for such applications as well.

3.7 Er: YAG Laser Delivery Systems

One of the major problems associated with the Er: YAG laser wavelength (2.94 μm) is that it cannot be transmitted over silica-based glass fibre due to absorption by the glass core. Much research in recent years has focused on the development of solid core optical-fibre and hollow waveguide [KOZO 96][PRYS 96][NUBL 97][WANG 97][MATS 97][RABI 99][WILK 99][SHI 01][MATS 01] delivery systems that meet the Er: YAG laser wavelength (IR laser) requirements of optical efficiency, durability and easy handling.

Solid core IR transmitting fibres have been produced from glass such as fluoride glass fibre, and crystalline materials, including heavy-metal fluorides, low-molecular-weight chalcogenides (As_2S_3), Silver halides, and Sapphire [PRYS 96][NUBL 97]. However, most of these IR transmitting solid-core fibres have significant drawbacks, such as:

- low laser damage threshold
- poor chemical and mechanical properties

- difficult and expensive fabrication

IR transmitting hollow waveguides offer several advantages and present an attractive alternative to solid-core IR fibres. Listed below and in Table 3.5 are some of the IR transmitting delivery systems available and their properties.

3.7.1 Single-Crystal Sapphire Fibre

Single-crystal sapphire fibres have proven to be an effective delivery system for the Er: YAG laser and have many physical properties that make them ideal for infrared transmission as high as ~ 3.5 μm [PRYS 96][NUBL 97]. Theoretically, sapphire fibre has an intrinsic loss of 0.13dB/m at the Er: YAG laser wavelength of 2.94 μm [NUBL 97]. Saphikon, Inc. (a commercial source of optical-quality sapphire fibres) has reported losses as low as 0.2 dB/m at 2.94 μm wavelength [PRYS 96][NUBL 97].

Sapphire is chemically inert and has a melting point in excess of 2000°C. It also has the potential of delivering very high laser energies (greater than 1 J/pulse or 10W at 10 Hz pulse rate) [PRYS 96][NUBL 97]. Furthermore, sapphire fibres are extremely durable and have a distinct advantage in medical applications because they can be safely inserted directly into the body [NUBL 97]. Sapphire fibres are fairly stiff with minimum bend radius of a 300-um-diamerter fibre ~45 mm. Conversely, sapphire fibres are very expensive and difficult to manufacture in large diameters.

3.7.2 Fluoride Glass Fibres

Fluoride glass fibres are IR transmitting fibres that are good candidates for sensory and power delivery applications. They transmit up to ~ 3.5 μm with losses below 0.05 dB/m at λ = 2.94μm. They are also quite flexible and have been used to deliver Er: YAG laser fluence as high as 200 J/cm^2.

One of these fibres is fluorozirconate (ZBLAN) which uses zirconium fluoride (ZrF_4) as the fibre material; it has an attenuation of 0.01dB/m at λ = 2.94μm [HARR 00]. However, fluoride glass fibres have major drawbacks: limited mechanical strength, low glass transition temperature (150°C), chemical reactivity with water and extremely sensitive to being damaged when contaminated at their distal ends by tissue material ejected from the operation area [NUBL 97].

3.7.3 IR Transmitting Hollow Waveguides

IR transmitting hollow waveguides are made from glass, plastic or metal tubes with highly reflective coating deposited on the inside surface. These waveguides are available with bore sizes range from 200 to 1000μm. They offer several advantages over solid-core fibres; such as high power handling capability, lack of Fresnel losses, durability, and small beam divergence.

Hollow waveguides have proven to be an excellent delivery system for Er: YAG and mid-infrared laser with very low losses (~0.1 dB/m) [KOZO 96][HARR' 00] depending on the type and the bore diameter of the hollow waveguide [KOZO 96]. The key features of hollow waveguides are their:

- ability to transmit beyond 20μm wavelengths
- inherent advantage of having an air core for high-power laser delivery
- relatively simple structure
- low cost

In general hollow waveguides have the advantage of high laser-power thresholds, low insertion loss, no end reflection, ruggedness and small beam divergence. However; their potential disadvantages include bending losses and a small NA [HARR' 00].

In 1996 Kozondoy R. et al [KOZO 96] introduced flexible hollow glass waveguides with diameters as small as 250μm capable of efficiently delivering up to 8 W of Er: YAG laser power with straight losses ranging from 0.1 to 1.73 dB/m. Wang et al (1997) [WANG 97] demonstrated that hollow waveguides as small as 320 and 200μm were fabricated for the transmission of Er: YAG laser radiation. These waveguides, with proper input coupling, are capable of efficiently delivering up to 5 W of Er: YAG laser light.

IR transmitting hollow waveguides are useful for variety of medical treatments including dentistry, orthopaedics and dermatology [WANG 97][HARR' 00][MATS 01].

Table 3.5: IR transmitting fibres and waveguides [KOZO96][NUBL 97][PRYS 96][HARR 00][MATS 01]

Delivery System	Losses (dB/m) at 2.94µm	Maximum Energy (J) [Power](W)	Maximum Fluence (J/cm^2)	Durability / Mechanical Strength	Transmission Range (µm)	Melting Point / [Transition Temperature]	Chemical Reactivity / medical safety	Flexibility
Single-crystal sapphire fibre	0.2dB/m	> 1J or [>10W @ 10 Hz]	1250 J/cm^2	Extremely durable >10000 pulses @ 400mJ	0.5 - 3.5µm	2030° C	Inert / medically safe	Fairly stiff (300µm fibre quite flexible)
Chalcogenide glass fibre As, Ge, Se, S and Te	5 dB/m			/ Weak shear strength	4 - 11µm	245° C		Fragile
Fluoride glass fibres	0.05 dB/m		200 J/cm^2	Poor / limited mechanical strength	Up to ~ 3.5µm	Low melting point / [150° C]	Reactive with Water	Quite flexible
Fluorozirconate ZBLAN (ZrF_4-BaF_2-LaF_3-AlF_3-NaF)	0.01 dB/m	300mJ at 300µm core	424J/ cm^2	Medium	0.25 - 4µm	265° C	Reactive with Water	Quite flexible
Fluoroaluminate (AlF_3-ZrF_4-BaF_2-CaF_2-YF_3)	0.1dB/m	850 mJ at 500µm core	433J/ cm^2	Excellent	0.25 - 4µm	400° C	Reactive with Water	Quite flexible
Silver halide	NA for Erbium 0.1-0.5 dB/m for CO_2	50 W (CO_2 laser)		Sensitive to Light/ Weak	4 to 20µm	415° C		
Hollow waveguides	0.1 dB/m	80 W		Sensitive bending	0.9-25µm	150° C		Size dependent flexibility

3.8 Laser Safety and Medical Constraints

No discussion on the use of laser in health care and medical surgery would be complete without considering safety aspects and the potential hazards associated with the use of the laser. Applying laser in health care and medical surgery requires very careful consideration of the potential hazards associated with lasers. Surgeons as well should be aware of the safety principles and biologic tissue effects of the specific laser wavelength chosen for use in surgery. Lasers emit beams of optical non-ionising radiation that poses ocular and skin hazards in addition to other clinical and environmental hazards.

3.8.1 Hazards

Laser hazards include ocular, skin, toxic smoke and other environmental and health hazards.

Ocular Hazards

Laser energy can be dangerous to eyes and tissue. It represents a potential for injuring several different structures of the eye, for example corneal and retinal burns. Retinal effects are possible when the laser emission wavelength is in the visible and near-infrared spectral regions (0.4 μm to 1.4 μm). Laser emissions in the ultraviolet and far-infrared outside the (0.4 μm to 1.4 μm) region however can produce ocular effects primarily at the cornea. Laser radiation at certain wavelengths can also cause damages to the lens structure [AMER 93][NIEM 96].

As a safety measure for ocular hazards, eye protection such as wavelength specific goggles for all operating personnel is suggested to prevent ocular damage.

Skin Hazards

Lasers emitting in the ultraviolet spectrum as well as high power lasers can cause skin *erythema* (sunburn), skin *cancer*, and accelerated skin *aging*. These skin effects are possible to occur while using ultraviolet lasers with wavelengths ranging from 230 nm to 380 nm, with the most severe effects occur in the UV-B (280 nm to 315 nm). Other laser wavelengths have different hazards on tissue and the most significant of all are the skin burns caused by skin exposure to lasers in the infrared range of 700nm – 1000nm [AMER 93][NIEM 96].

Hazards due to Toxic Smoke Production

As with the use of electrosurgical devices, tissue vaporisation with lasers produces a plume of steam or smoke which causes safety concerns in the operating theatre. The most significant concern is the possible spread of viral infections. Furthermore, vaporization of poly-methylmethacrylate (PMMA) results in the release of toxic gasses in the operating environment. Superheated PMMA is also flammable and may pose a risk to patients. And the exposure of such flammable material to laser beams poses a potential fire hazard [AMER 93].

As a safety measure for such hazards, products of vaporization of both tissue and PMMA must be safely evacuated from the operating theatre environment.

Other Laser Hazards

Other laser hazards include energy dissipation which may affect tissue adjacent to the immediate target.

Certain procedures using the CO_2 laser in the theatre may require positive pressure gas insufflations and this may cause tissue emphysema or gas embolus, with possible fatal results. Yet the risk of this hazard can be reduced with careful "gas bubble" or "ambient air" technique [AMER 93].

3.8.2 Laser Safety Standards and Hazard Classification

Lasers are classified based upon the hazard they presents and for each classification there is a standard set of control measures applied. The higher the classification number the greater are the potential hazards. Brief descriptions of each laser class are summariesed below [NIEM 96][DUKE 01]:

- **Class I. Lasers:**

  Class I lasers do not emit harmful levels of radiation during normal operation. They are low power lasers that are enclosed and safe to view [NIEM 96][DUKE 01].

- **Class II. Lasers:**

  Class II lasers emit visible laser light and are capable of causing eye damage through chronic exposure. The Blink reflex within 0.25 seconds provides adequate protection, it is dangerous to stare into the beam. Class II lasers have power levels less than 1 mW and are commonly found in alignment applications.

- **Class IIIa. Lasers:**

  Class IIIa lasers are medium power lasers (1- 5 mW). They are normally not hazardous when viewed momentarily by an unaided eye, however, they pose severe eye hazards when viewed through optical instruments.

- **Class IIIb. Lasers:**

  Class IIIb lasers have output power ranging from 5 -500 mW continuous wave or less than 0.03 Joule (J) for a pulsed system. These Lasers cause injury upon direct viewing of the beam and specular reflections.

- **Class IV. Lasers:**

  These lasers include all lasers with power levels greater than 500 mW CW or greater than 0.03 Joule (J) for a pulsed system. These lasers pose significant skin and ocular hazards as well as fire hazards [NIEM 96].

Certain safety consideration and measures are to be taken into account in the operating theatre and other medical applications will be discussed further in future work

3.9 Summary

The aims of this chapter to identify the most appropriate laser, laser properties and laser delivery system for computer assisted laser orthopaedic surgery have been achieved. This study shows that the Er: YAG laser is a good candidate for being the most suitable laser for such application. Although other lasers such as USPL, Ho: YAG and HF have good potential for being suitable as well. The study also identified the most suitable delivery system, namely hollow waveguides, for the selected laser type. Hollow waveguides have proven to be an excellent delivery system for Er: YAG and mid- infrared lasers with very low losses (~0.1 dB/m) [KOZO 96][HARRI 00]. They also feature some advantages over other means of laser delivery systems. These include high laser-power thresholds, low insertion loss, relatively simple structure, no end reflection, lightweight, low cost, ruggedness and small beam divergence. Although, they have the disadvantages of bending losses and a small NA [HARR' 00].

Having identified the most suitable laser, laser properties and laser delivery system, the author identifies the following requirements for the design of an overall "laser End-Effector system"; a new surgical tool for computer assisted orthopaedic surgery (discussed in Chapter 5). These requirements include:

- The laser End-Effector must be able to manipulate and position a lightweight laser waveguide and hence the laser beam within the surgical site with high accuracy and precision.
- The End-Effector's manipulation speed and time must match the Er: YAG laser properties in terms of ablation depth, ablation rate, laser spot size and ablation time.

- For environmental safety, certain measures must be taken into account. These may include:
    - The use of safety goggles by all medical staff and patients during surgery
    - Limitation imposed on the manipulation angles (laser ablation workspace) of the laser End-Effector
    - The overall system design must incorporate an air vacuum system to evacuate the toxic gases and vapours produced during the laser tissue ablation.

Chapter 4

An Investigation of how Er: YAG Laser Parameters Affect the Ablation of Biological Tissue

4.1 Introduction

Chapter 3 concluded that the Er: YAG laser appears to be a suitable laser for applications in computer assisted orthopaedic surgery. This is also confirmed by other research works [ABSTI 00][FRYM 93]. Its suitability stems from its characteristics in terms of the quality of hard tissue ablation, the cutting depth per laser pulse which provides control flexibility, and the peak absorption of water which offers efficient ablation of both bone and cartilage [ABSTI 00][FRYM 93].

This chapter first introduces the different laser parameters and the physical laws that govern their effect on biological tissue during laser tissue interaction. The chapter discusses Beer's Law and modifications to it so that it accurately estimates ablation of bone for the Er: YAG laser.

This chapter focuses on an evaluation of the Er: YAG laser parameters on ablation of biological tissue. The chapter presents predictions on the effects of varying these parameters on the depth, volume and time for ablation. These predictions are based on specific laser bone cutting and drilling techniques and a modified form of Beer's Law. The chapter also presents an experiment prepared by the author to validate these predictions and prove the modification of Beer's Law.

The chapter ends by introducing some experimental results illustrating the performance and ablation quality of the Er: YAG laser. This is followed by some concluding remarks.

4.2 Evaluation of the Effect of Laser Parameters on Tissue Ablation

The focus of this chapter is to investigate the ablation effect of the different Er: YAG laser parameters on biological tissue. These parameters include laser energy density, pulse duration, optical absorption, pulse repetition rate, beam diameter (laser spot size) and the dynamic movement of the laser beam during tissue ablation.

4.2.1 Laser Pulse duration (Er: YAG)

Studies have shown that during Continuous Wave (CW) laser cutting of biological tissue, the ablated material is vaporized and some of it is deposited onto the walls or upper surface of the cut [FEMT nd][NIEM 96]. This causes bending of the incoming laser beam and produces a rough edged cut which reduces the quality of the cut and the efficiency of the cutting system. However for pulsed lasers, a pulse deposits its energy so quickly that it does not interact with the plume of vaporized material. Here, the plasma plume leaves the surface very rapidly ensuring that it is well beyond the cut edges before the arrival of the next laser pulse thus leading to a smooth cut [FEMT nd][FBIH 02][HOFF 00].

Studies have also shown that short laser pulses help reduce the extent of damage of tissue. This is because energy deposition in the pulse is shorter relative to the thermal relaxation time (τ_{therm}). The thermal relaxation time is the rate at which a structure can conduct heat. When the laser pulse duration is shorter than this, the heat damage is confined to a limited region of the target thus reducing thermal propagation into the remaining tissue [NIEM 96][HOFF 00].

Other studies showed that for laser pulse duration $\tau < \tau_{therm}$ heat does not even diffuse beyond the distance given by the optical penetration depth L ($1/\alpha$) where α is the effective absorption coefficient. However, for $\tau > \tau_{therm}$, heat can diffuse to many times the optical penetration depth causing thermal damage to adjacent tissue.

This conduction effect imposes a limitation on the laser pulse duration for a specific laser application. In order to reduce thermal damage to the adjacent tissue, the laser pulse duration must be adjusted to minimize the thermal damage to the adjacent tissue. The scaling parameter for this time dependent problem of "*thermal relaxation time*" is obtained by the optical penetration depth (L), which equals the thermal penetration depth ($1/\alpha$), given in Equation 4.1.

Equation 4.1: Optical penetration depth

$$L = \left(\frac{1}{\alpha}\right) = \sqrt{(4\kappa\tau_{therm})}$$

where $\kappa = 0.9 \times 10^{-7}\ m^2/s$ is the thermal diffusivity of water [NIEM 96]. The shortest thermal relaxation time of approximately 1 µs occurs at the absorption peak of water around 2.94 µm (Er: YAG laser). Laser pulse durations of $\tau < 1$ µs do not normally cause thermal damage, this is known as "the 1 µs rule" [NIEM 96]. Other studies revealed that reducing the laser pulse duration to the nanoseconds region lead to an alternative laser tissue interaction namely "Laser Spallation". Here tissue removal is attributed to a fast expanding bipolar pressure wave that induces a strong mechanical tension at the tissue surface [MROC 00].

There are limitations on the laser pulse duration in the nanosecond region. These limitations include: low laser pulse amplification, and low damage threshold of commercially available optics for the 2.94 µm wavelength. Furthermore, in Q-switched mode experimental results [MROC 00] have shown high instability in tissue removal, which may stop after four laser pulses as a result of dehydration of adjacent tissue after each laser pulse. This effect leads to major technical limitations on laser pulse duration [MROC 00]. It is worth noting that some studies have showed that for a free running Er: YAG laser of 100-700 μs pulses the depth of the craters made do not depend on the pulse duration but depend only on the energy density [YOON 02].

4.2.2 The Effect of Varying the Laser Pulse Repetition Rate

To determine the effect of varying the pulse repetition rate for the Er: YAG laser, calculations of the ablation depth and time were carried out according to Beer's Law [NIEM 96][FARR nd] which relates fluence at depth ($F(x)$) to the incident fluence (F_o), the absorption coefficient (α) and the distance into the sample (x) by [FARR nd]:

Equation 4.2: Beer's Law

$$F(x)=F_o e^{-\alpha x} \Rightarrow x=\left(\frac{1}{\alpha}\right)\ln\left[\frac{F_o}{F(x)}\right]$$

The maximum etch depth (d) is reached when the optically transmitted fluence (F_o) decays to the threshold fluence for material removal (F_T) leading to:

Equation 4.3: Etch depth of laser [FARR nd]

$$d=\frac{1}{\alpha}\cdot\ln[F_o]-\frac{1}{\alpha}\cdot\ln[F_T]$$

Taking into account the plume effect on the etch rate (x) Equation 4.2 is modified such that:

Equation 4.4: New form of Beer's Law [DYER03].

$$d=\left[\frac{\mu}{\alpha\mu_P}\right]\ln\left[1+\frac{\mu_P(F_o-F_T)}{\mu F_T}\right]$$

where d is the etch depth per pulse (or etch rate), F_T is the threshold fluence required for bone removal ($F_T = 10$ J/cm^2 for a laser pulse duration of 200-250 μm [APEL 02]), and μ and μ_p are the mass absorption coefficients for the bone and plume, respectively. The etch depth d depends on whether the plume is equal ($\mu_p = \mu$), less ($\mu_p < \mu$) or more ($\mu_p > \mu$) absorbing [DYER 03] than bone.

For the Er: YAG laser, in order to take account of the micro-explosion effect that tears out pieces of the tissue during hard tissue ablation, Equation 4.1 is further modified as follow:

Equation 4.5: Modified Beer's Law

$$d=m\left[\frac{\mu}{\alpha\mu_P}\right]\ln\left[1+\frac{\mu_P(F_o-F_T)}{\mu F_T}\right]$$

where m is the scaling factor that takes account of the micro-explosion effect and is approximately 15. This modification is based on studies done by other researchers [NIEM 96][WANN 96][MAJA 98][BERG 98] on the Er: YAG laser ablation depths. This value of 15 is used throughout the laser tissue interaction analysis presented in this chapter.

Prediction times were calculated for ablating 450 mm^3 (15 x 15x 2 mm) of bone with a varying pulse rate of 1 to 23 Hz. The volume of 450 mm^3 was chosen as it represents a typical volume ablated for a bone cut for a tibial osteotomy. The results in Figure 4.1 show that ablation time decreases exponentially with the increase in pulse repetition rate. However, there are some problems associated with increasing the laser pulse repetition rate. These include a lensing effect generated within the laser system [DU 03], and the thermal damage induced within the ablated tissue.

The thermal lensing effect can cause a substantial decrease of lasing efficiency. Previous Er: YAG laser research has shown [YOON 02] that the value of the heat deposition may reach 35 – 50% of the pumping energy and about a 30% decrease of lasing efficiency is observed as the pulse repetition rate increases from 10 to 20 Hz. This is because the Er: YAG crystal is a medium with a high thermal loading factor. These effects impose some limitations on the frequency of pulse repetition rate.

The following parameters were used in the calculations:

- Laser pulse energy = 250 mJ
- Threshold fluence = 10 J/cm^2
- Beam diameter (Spot Size) = 0.5 mm
- Laser pulse duration τ = 150 μs
- Bone absorption coefficient α_{bone} =1500 cm^{-1} (Estimated for α_{H2O} = 10000 cm^{-1})
- Ablation movement speed 0.1 mm/s
- Pulse repletion rate of 1 to 23 Hz
- The volume of bone to be removed is 450 mm^3

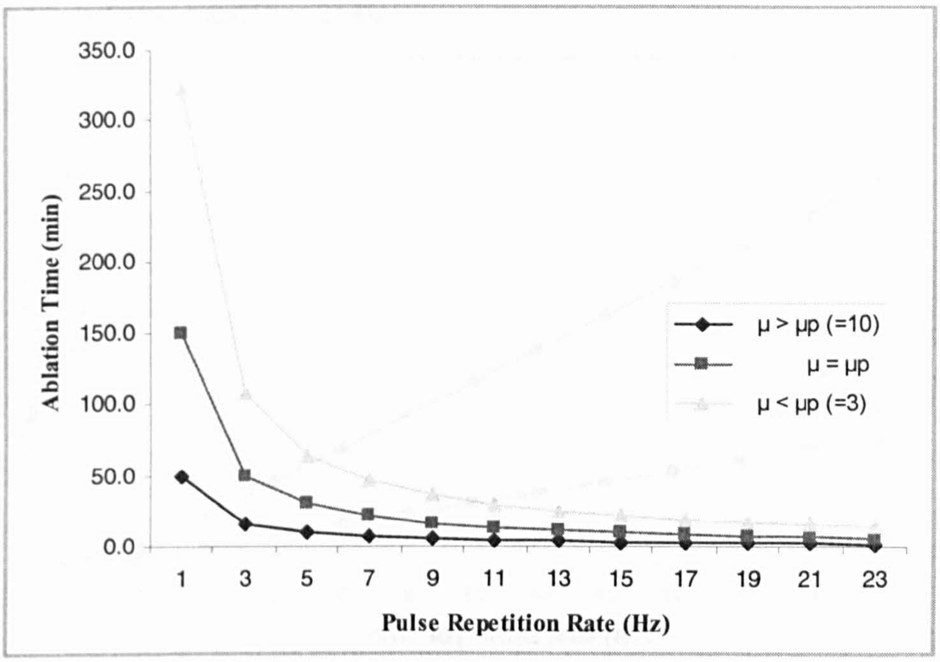

Figure 4.1: Ablation time as a function of pulse repetition rate for a bone volume of 450 mm^3

Furthermore, as mentioned in 4.2.1 an increase in pulse repetition rate may increase the interaction with the plume of vaporized material resulting in a rough edged cut. Thus sufficient time should be allowed for the plasma plume to leave the surface before applying a second pulse. This effect limits the repetition rate of the lasing pulse to a level that ensures the ejection of the plasma plume before the arrival of the next laser pulse.

In addition to the pulse repetition rate controlling the ablation time, the author suggests that it can be used to control the ablation depth during dynamic movement of the lasing system. This may be achieved by regulating the dynamic movement speed of the laser beam over the bone while varying the pulse repetition rate to control the ablation depth. Figure 4.2 shows the effect of the laser pulse repetition rate on ablation depth for a constant scanning speed of the laser beam. Figure 4.2 shows that the ablation depth increases with an increase in the pulse repetition rate and vice versa. Hence by increasing or decreasing the repetition frequency one can control the ablation depth and the level of tissue damage during tissue cutting or drilling. This effect gives the surgeon more flexibility during laser surgery and could simplify the design of a delivery system. The following parameters were used in the ablation depth calculations of Figure 4.2:

- Scanning speed = 0.1mm/s
- Beam diameter = 0.5 mm
- Pulse energy = 250 mJ
- Threshold fluence = 10 J/cm^2
- Laser pulse duration τ = 150 μs

• Pulse repletion rate of 1 to 23 Hz

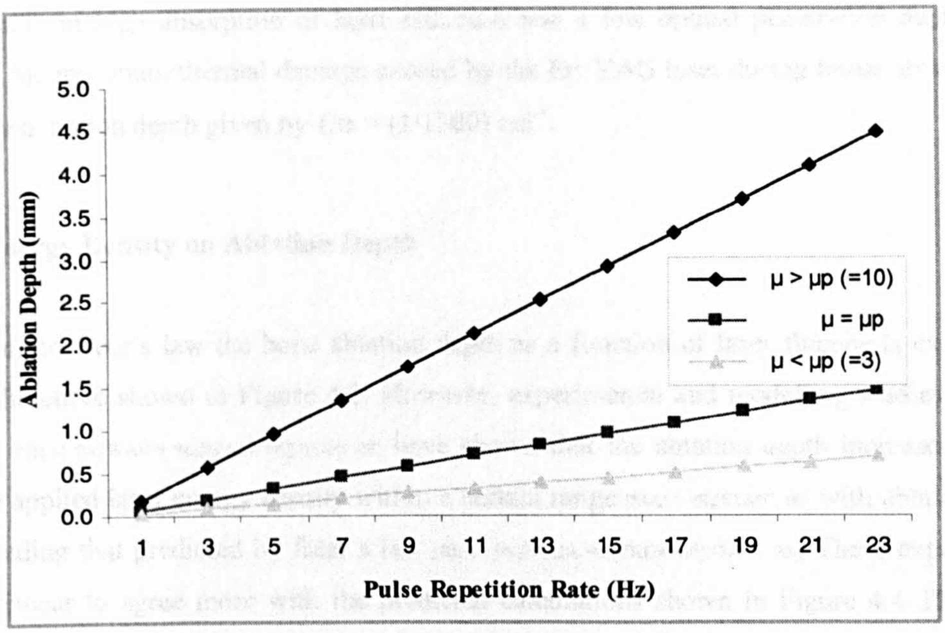

Figure 4.2: Ablation depth per pass as a function of pulse repetition rate

4.2.3 Optical Absorption Coefficient α on Tissue Ablation

This section considers the effect of the optical absorption coefficient α on laser ablation of bone. The Er: YAG laser with a wavelength (λ) of 2.94 μm coincides with the peak absorption of water ($\alpha \approx 10^4$ cm^{-1}). This explains the significance of water during Er: YAG laser tissue interaction. When the Er: YAG laser beam hits the tissue rapid heating of the localized tissue causes the intrinsic water to vaporise into steam (ablation) [NIEM 96][SHOR2 nd]. This feature makes the Er: YAG laser an excellent cutting and drilling tool in medical applications [WANN 96]. It is important to note here that the optical absorption coefficient (α) plays a significant role in determining the ablation depth of the material. Biological tissue with high water content has an optical coefficient of a relatively high value with an optical penetration depth of 1/α (the depth at which transmitted intensity has decayed to 1/e of the surface value) according to the Beer-Lambert Law [FARR nd][NIEM 96][WANN 96]

Equation 4.6: Beer Lambert law

$$I(x) = (1 - R)I_o e^{-\alpha x}$$

where I(x) = the transmitted intensity at point 'x' (W/cm^2)

Io = intensity incident at surface (W/cm^2)

R = surface reflectivity (fraction)

x = depth into tissue (cm)

α = optical absorption coefficient (cm^{-1})

Bone as a biological tissue contains 15-20 % water with α typically between 1500 -2000 cm^{-1}. This results in high absorption of laser radiation and a low optical penetration depth which explains the minimum thermal damage caused by the Er: YAG laser during tissue ablation. The optical penetration depth given by $1/\alpha = (1/1500)\ cm^{-1}$.

4.2.4 Energy Density on Ablation Depth

According to Beer's law the bone ablation depth as a function of laser fluence is expected to follow the curve shown in Figure 4.3. However, experimental and modelling studies on bone ablation [NIEM 96][WANN 96][MAJA 98][BERG 98] have shown that the ablation depth increases linearly with the applied laser energy density within a certain range [MAJA 98][STAN2 00] with ablation depth far exceeding that predicted by Beer's law [BERG 98][MAJA 98][FREN 99][STAN1 00]. These experimental results appear to agree more with the predicted calculations shown in Figure 4.4 This figure shows the Er: YAG laser bone ablation depths as predicted by the modified equation of Beer's law Equation 4.5 for three different conditions of the mass absorption coefficients μ and μ_p of the bone and the plume respectively.

The following parameters were used in the depth calculations of Figure 4.3 and Figure 4.4:

- Scanning speed = 1 mm/s
- Beam diameter = 0.5 mm
- Pulse energy of 25 to 300 mJ
- Threshold fluence = 10 J/cm2
- Laser pulse duration τ = 150 μs
- Pulse repletion rate = 10 Hz

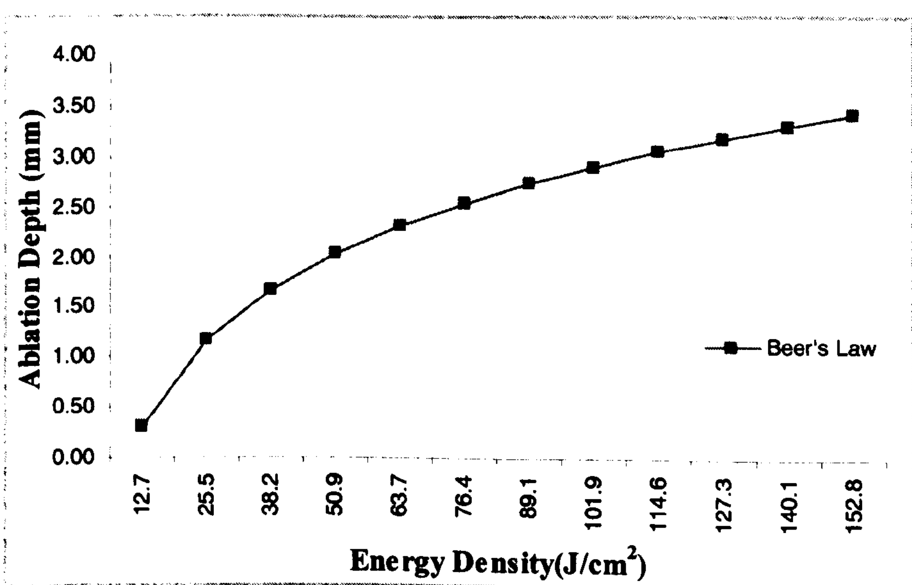

Figure 4.3: Er: YAG laser bone ablation depth as a function of energy density (Beer's law)

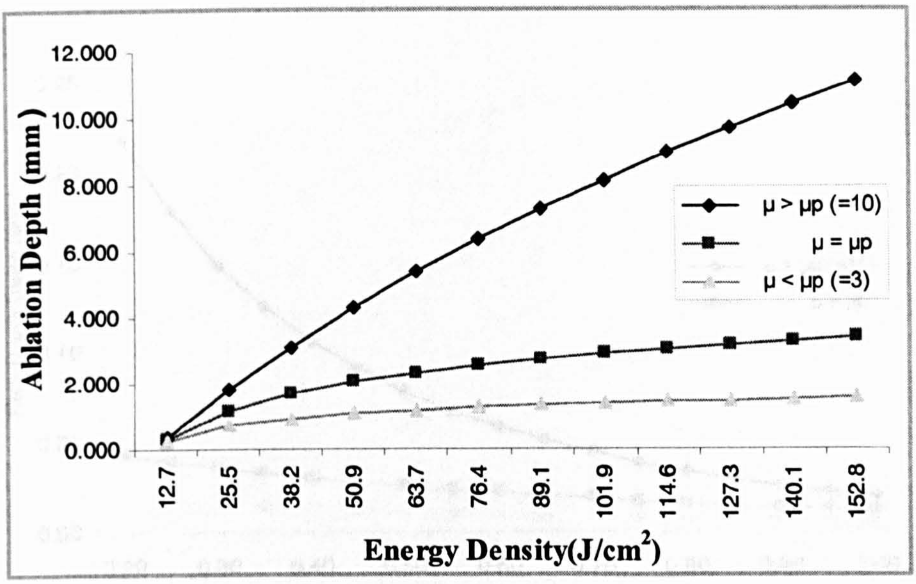

Figure 4.4: Predicted bone ablation depth according to the modified equation of Beer's law with variable energy density.

4.2.5 Effect of Laser Spot Size on Ablation Depth and Ablation Volume

Studies have shown that ablation rate is highly dependent on the laser spot size (diameter) [PROV nd][NIEM 96][FARR nd]. Laser spot size affects both laser penetration depth and ablation volume. Figure 4.5 shows predictions of the effect of laser spot size (or beam diameter) on the ablation depth. The figure shows that a well focused laser beam, where the laser spot size is very small, causes a narrow incision to the tissue with relatively large depth. However, for a larger spot size a wider area of tissue is damaged to a lesser depth. The calculations were carried out using the modified Beer's law equation (Equation 4.5) using the following parameters:

- Scanning speed = 1 mm/s
- Beam diameter ranges from 0.2 to 1 mm
- Pulse energy = 250 mJ
- Threshold fluence = 10 J/cm^2
- Laser pulse duration τ = 150 μs
- Pulse repletion rate = 10 Hz

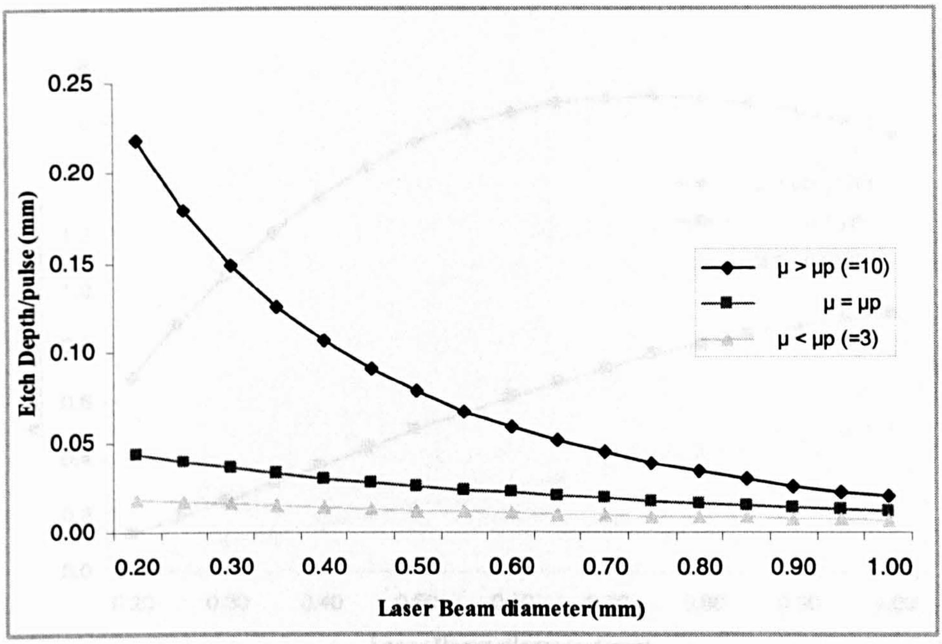

Figure 4.5: The predicted effect of the laser spot size on the ablation depth (etch depth)

On the other hand, as the spot size increases the ablation volume increases leading to reduced ablation time. These effects are illustrated in Figure 4.6 and Figure 4.7. The figures show the predicted effect of laser beam diameter on the bone ablation volume. The calculations were carried out using Equation 4.5 and the following laser parameters:

- Scanning speed = 0.1 mm/s
- Beam diameter ranges from 0.2 to 1 mm
- Pulse energy = 250 mJ
- Threshold fluence= 10 J/cm2
- Laser pulse duration τ = 150 μs
- Pulse repletion rate = 10 Hz

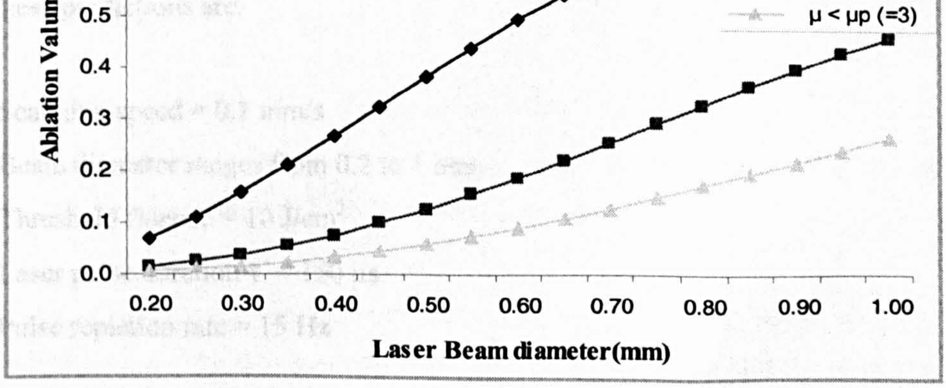

Figure 4.6: Ablation volume per laser pass as function of laser spot size

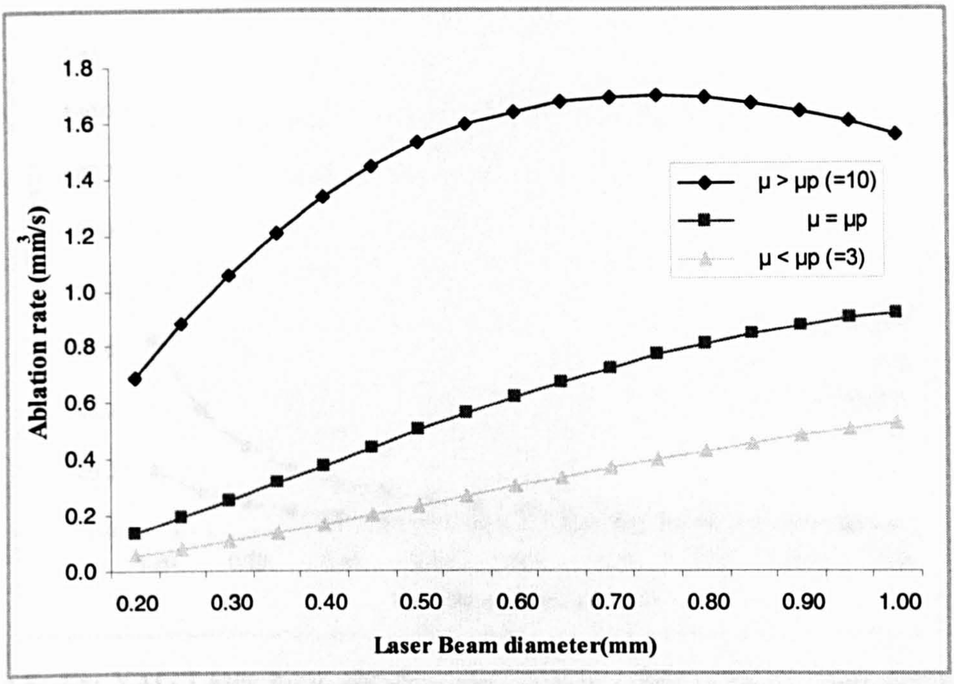

Figure 4.7: Bone ablation rate as function of laser spot size with constant pulse energy

The results gained from these analyses reveal that reduced laser ablation time per cut volume is associated with a larger spot size (Figure 4.7) though it appears that a smaller spot size can cut faster through tissue. The reason for this is that a small spot size ablates less bone volume to produce a cut of the same depth.

4.2.6 Laser Spot Size on Ablation Time

Considering, the ablation time required to cut through bone having a specific surface area will depend on the laser beam diameter. To illustrate this, Figure 4.8 and Figure 4.9 show the time required for a laser cut through bone as a function of beam diameter for cortical bone with an approximate bone volume of 450 mm^3. Figure 4.8 predicts the ablation time for a constant laser energy density (127.3 J/cm^2) and variable beam diameters. Figure 4.9 predicts the ablation time for constant laser pulse energy (250 mJ) and variable beam diameters. The other parameters used in these predictions are:

- Scanning speed = 0.1 mm/s
- Beam diameter ranges from 0.2 to 1 mm
- Threshold fluence = 10 J/cm^2
- Laser pulse duration τ = 150 μs
- Pulse repletion rate = 15 Hz

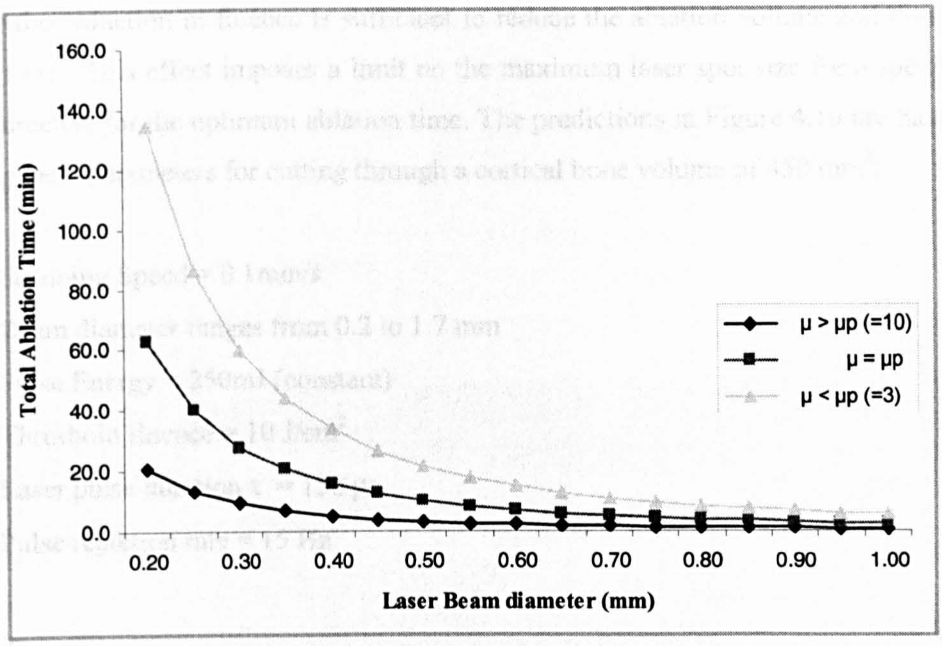

Figure 4.8: Er: YAG Laser bone ablation time as a function of laser beam diameter and constant laser beam energy density

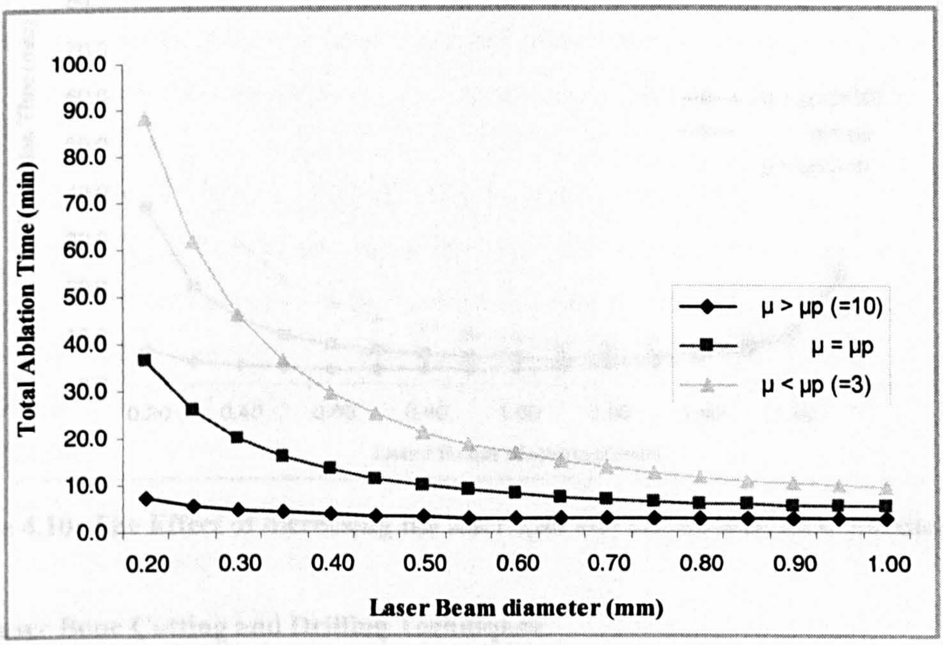

Figure 4.9: Er: YAG Laser bone ablation time as a function of laser beam diameter for constant pulse energy

For spot sizes less than about 0.50 mm, the ablation times in Figure 4.9 are less than that shown in Figure 4.8 this is because energy density values of the spot in Figure 4.9 is greater than the constant energy density value of 127.3 J/cm^2 in Figure 4.8.

There are limits imposed on the maximum laser spot size with constant pulse energy in terms of reducing ablation time. As the laser spot size initially increases, the ablation volume increases which reduces ablation time. However, beyond some threshold a further increase in the laser spot size the reduction in fluence is sufficient to reduce the ablation volume and thus increase ablation time. This effect imposes a limit on the maximum laser spot size for a specific set of laser parameters for the optimum ablation time. The predictions in Figure 4.10 are based on the following laser parameters for cutting through a cortical bone volume of 450 mm^3:

- Scanning Speed = 0.1mm/s
- Beam diameter ranges from 0.2 to 1.7 mm
- Pulse Energy = 250mJ (constant)
- Threshold fluence = 10 J/cm^2
- Laser pulse duration τ = 150 μs
- Pulse repletion rate = 15 Hz

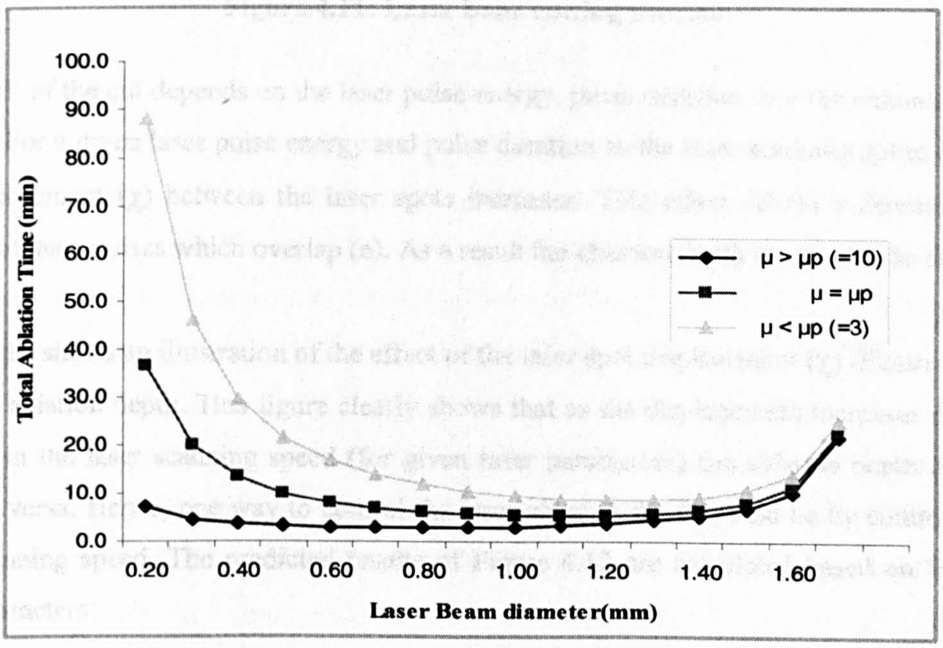

Figure 4.10: The Effect of increasing the laser spot size on the total bone ablation time

4.2.7 Laser Bone Cutting and Drilling Techniques

The analysis presented here assumes that the delivery system for the Er: YAG laser focuses the laser on the bone and that it moves in a plane either perpendicular or in an angle with the bone surface It is further assumed that the focused laser pulses scan the target at a constant speed. This causes a pulse overlap along the cutting path, and the amount of overlap (n) depends on the spot size (φ), scanning speed (v), and the laser pulse repetition rate (*f*) (see Figure 4.11).

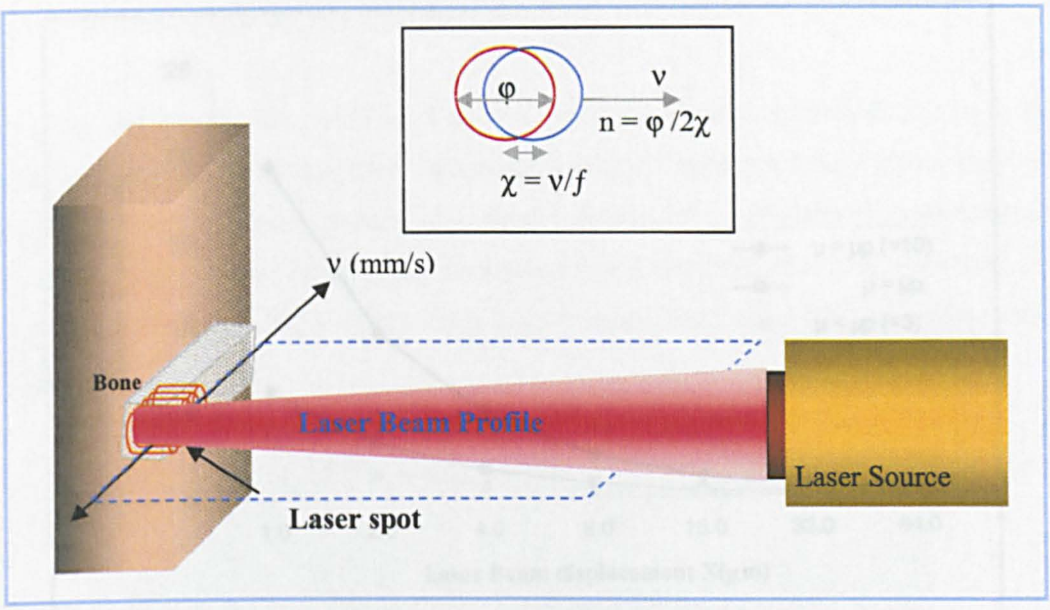

Figure 4.11: Laser bone cutting process

The depth of the cut depends on the laser pulse energy, pulse duration, and the amount of pulse overlap. For a given laser pulse energy and pulse duration as the laser scanning speed increases the displacement (χ) between the laser spots increases. This effect causes a decrease in the number of laser pulses which overlap (n). As a result the ablation depth is expected to decrease.

Figure 4.12 shows an illustration of the effect of the laser spot displacement (χ) (Figure 4.11) on the laser ablation depth. This figure clearly shows that as the displacement increases due to an increase in the laser scanning speed (for given laser parameters) the ablation depth decreases and vice versa. Hence, one way to control the laser ablation depth would be by controlling the laser scanning speed. The predicted results of Figure 4.12 are calculated based on following laser parameters:

- Scanning speed = 10 - 640 μm/s
- Laser Pulse energy = 250mJ
- Beam diameter = 0.5 mm
- Threshold fluence = 10 J/cm^2
- Laser pulse duration τ = 150 μs
- Pulse repletion rate = 10 Hz

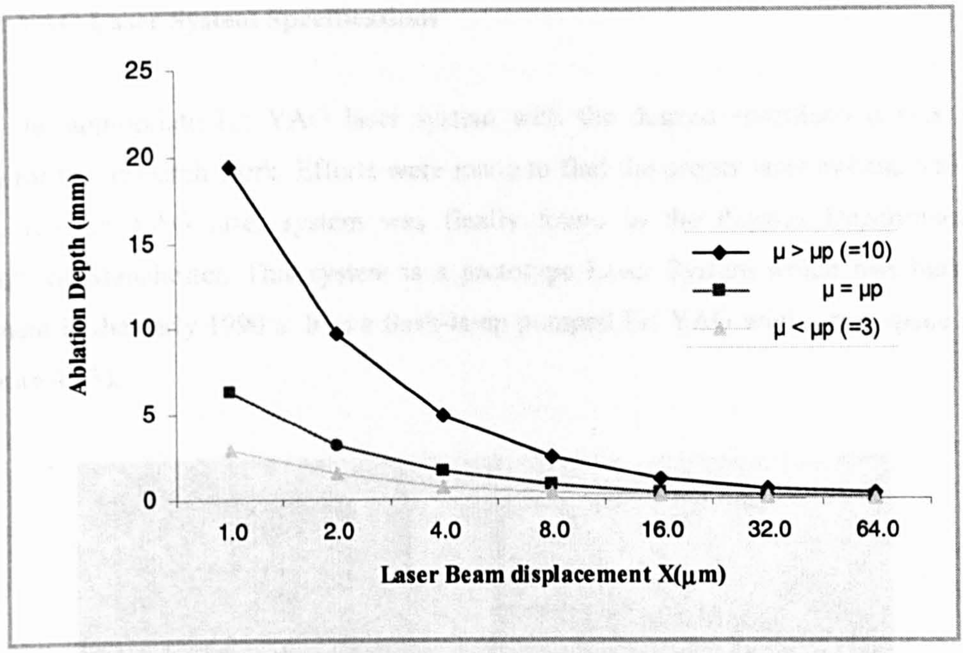

Figure 4.12: Laser ablation depths as a function of laser spot displacement (χ)

Bone cutting is a repetitive process in which the laser beam is scanned over the target until the cut is complete. After each laser cut is completed, the laser is advanced towards the target by an amount equivalent to the ablated depth of the cut so that the laser remains focused on the bone surface. In reality there may be a need for a water spray and some form of evacuation to reduce heat build-up and prevent carbonization to assist in producing a clean and smooth cut.

Laser bone drilling is a very similar process. However, bone drilling requires further mechanical control and involves more complex planning and manipulation movements. Details on the laser bone drilling technique proposed by the author are presented in Chapter 5.

In orthopaedics laser drilling for certain applications can be optimised. In the case of fractures for the femoral neck, a guide wire is normally placed in the femoral head to guide the fixation screws during the surgical procedure. Laser drilling can play a significant role in accurate placement of the guide wire. In this case a large spot size laser beam (~ 1.5 mm) with a high energy density and a high repetition rate can be used to drill through a hole (approximately 1.5 mm in diameter) to the required depth. This hole can be used as a guide for the surgeon to manually insert the 3 mm guide wire. Using computer guidance of the laser beam this leads to high accuracy in the placement of the guide wire which has the potential to improve the surgical outcome.

4.3 Er: YAG Laser System Specifications

Finding the appropriate Er: YAG laser system with the desired specification was a major concern for this research work. Efforts were made to find the proper laser system, yet with no success. An Er: YAG laser system was finally found in the Physics Department at the University of Manchester. This system is a prototype Laser System which was built by the Department in the early 1990's. It is a flash-lamp pumped Er: YAG with a free space delivery (see Figure 4.13).

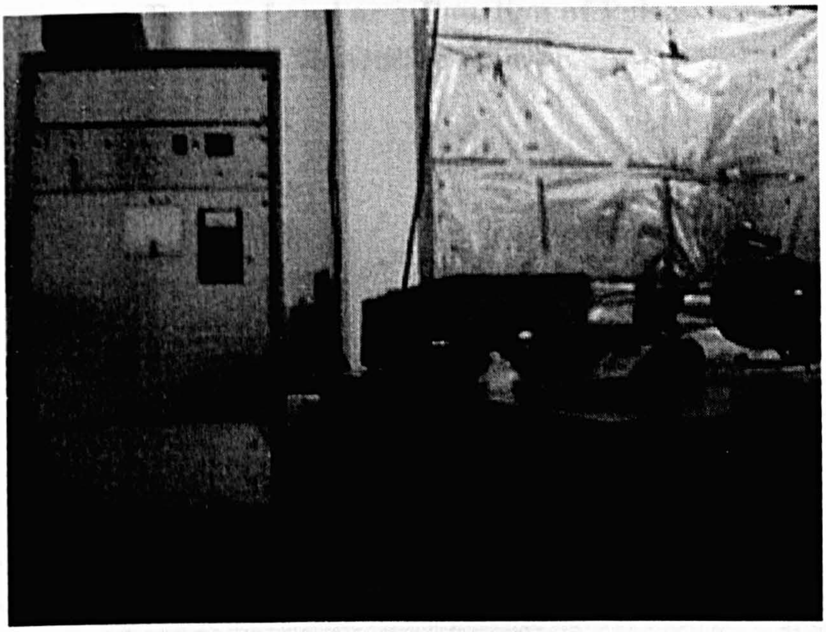

Figure 4.13: Er: YAG laser system at the University of Manchester

In this system the laser beam is directed onto the target via a focussing lens, and glass filters are used to reduce the energy level. Although, this Er: YAG laser system was assumed to have a maximum output power of 5 watts (1 J/pulse at 5 Hz pulse repetition rate (PRR)), when tested it showed much lower output levels. This drop in energy level may be due to aging, laser system misalignments, and / or changes in flash-lamps and lasing source (erbium rod) properties. A preliminary testing of the Er: YAG laser system revealed the following issues.

__Variable laser spot size and the effective focal length__: due to lensing effects within the Er: YAG laser system, the spot size and focal length were not consistent. Variation in the laser pulse repetition rate or laser output power produced changes in the laser spot size. Therefore, a change in the energy setting required new measurements to obtain the laser spot size and focal length. Setting and measuring the spot size and the effective focal length was not an easy task. It requires a highly calibrated optical microscope and several measurements of the laser spot size to find the minimum spot size relative to the focal distance. Furthermore, during the measurement time the laser spot size may change due to laser power variation.

Variable pulse energy and power levels: the pulse energy is voltage, pulse rate and time dependent with maximum laser pulse energy of 293 mJ/pulse (at 1.2 kV and 3 Hz) corresponding to an output power of 881.7 mW. A maximum output power of 1.6 W was measured at 7 Hz corresponding to a laser pulse energy of 234.9 mJ/pulse. A minor change in the applied voltage level or pulse repetition rate may result in a major change in the pulse energy (Figure 4.14) and output power levels (Figure 4.15). Time also appears to be an important factor in determining the output power levels. As time passes the pulse energy levels appeared to drop.

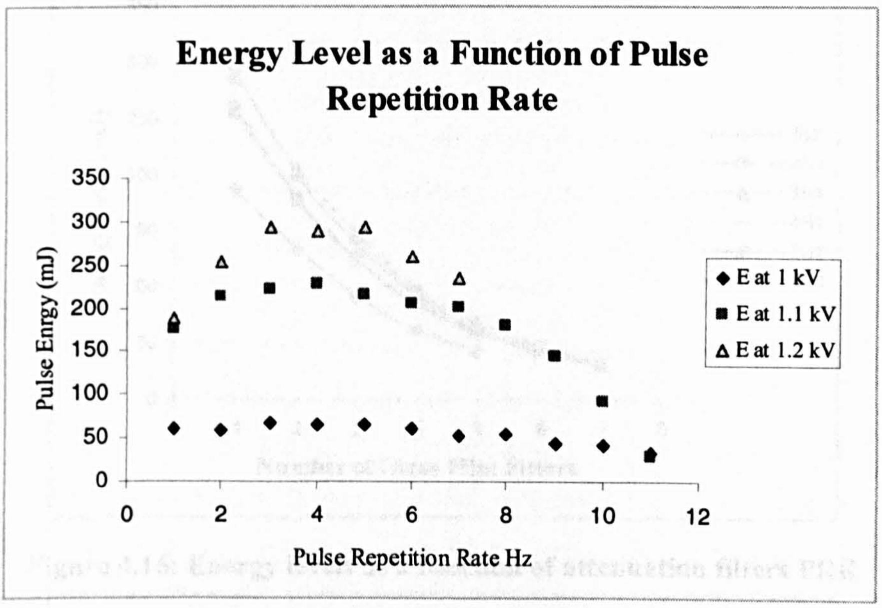

Figure 4.14: Laser pulse energy level as a function of the pulse repetition rate

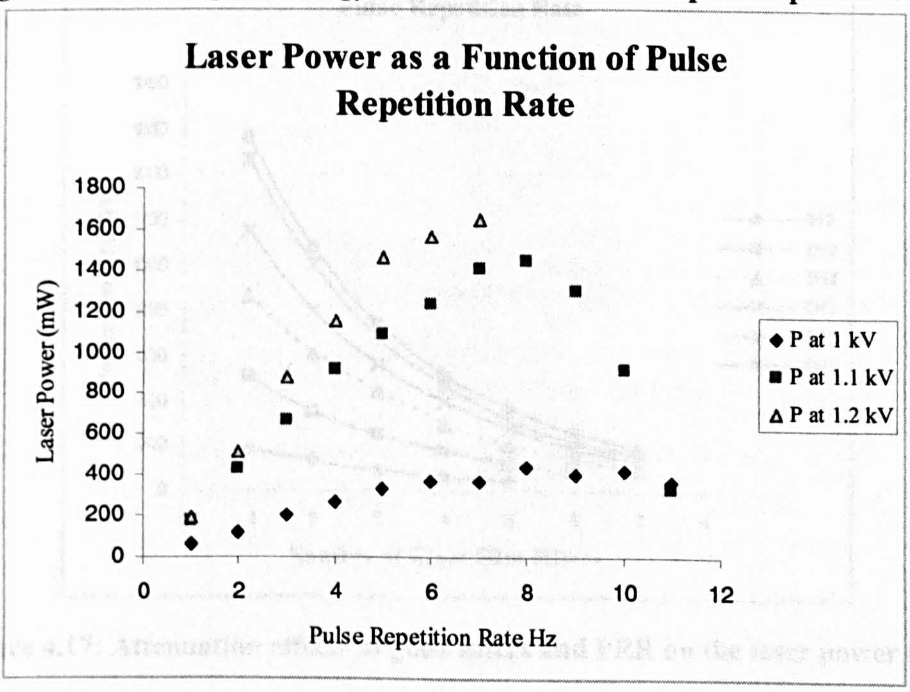

Figure 4.15: Laser output power as a function of pulse repetition rate

High attenuation effect of the glass filters: The glass filters had a very high attenuation effect on the laser energy and power levels as shown in Figure 4.16 and Figure 4.17. This was due to low initial levels of laser pulse energy where the glass filters tended to reduce the energy level below the laser bone ablation threshold. This resulted in bone necrosis (damage) rather than cutting. The figures also show the effect of the pulse repetition rate on the laser pulse energy and power levels.

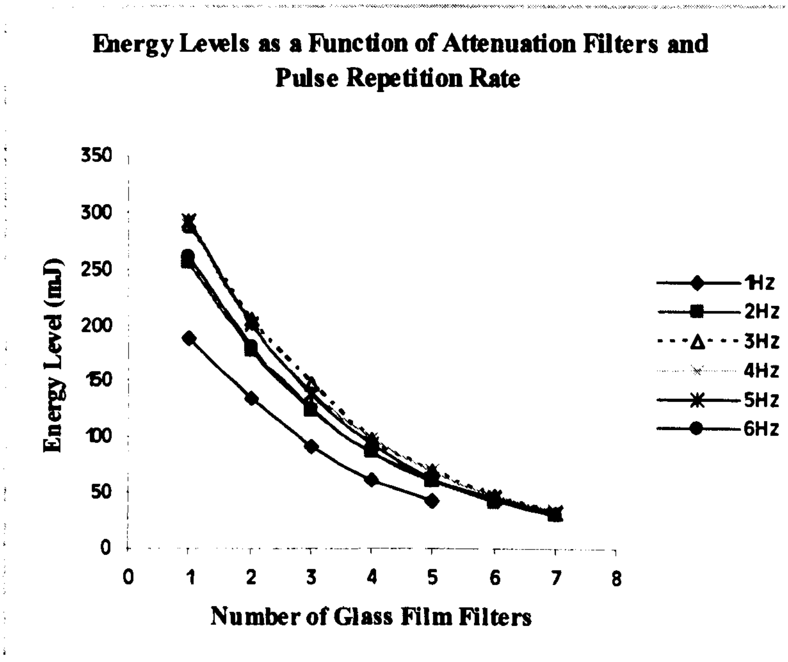

Figure 4.16: Energy levels as a function of attenuation filters PRR

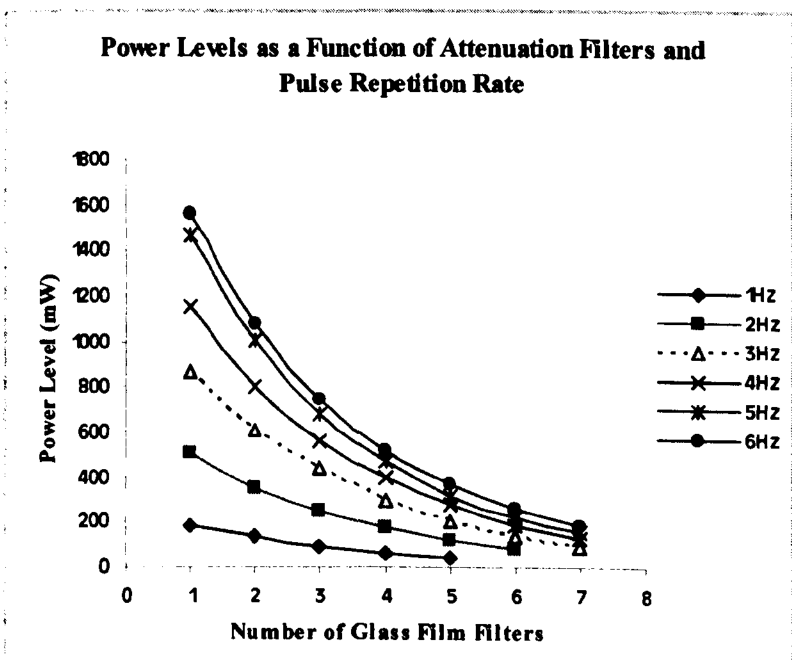

Figure 4.17: Attenuation effects of glass filters and PRR on the laser power level

Other technical problems: The laser system appeared to have some technical problems due to aging. These include; degradation in the laser rod (source) and flash-lambs, as well as problems with the water cooling system. These problems limited the operation of the system over long periods of time.

4.4 Design of the laser bone cutting experiment

The following experiment (Experiment 4.1) was prepared by the author to investigate the performance of the Er: YAG laser during laser bone cutting and drilling in terms of ablation rate, cut quality and damage to the surrounding tissue. The aim of this experiment is to study the effect of different laser parameters on laser bone cutting and drilling and to deduce the most appropriate laser parameters for such applications and thus inform the design of a computer assisted laser system for orthopaedic surgery. The experiment also aims to validate the theoretical analysis, modifications and predictions, as well as laser bone cutting and drilling techniques presented earlier in this chapter.

This experiment is designed to use a free space Er: YAG laser source (Figure 4.13) and a one degree of freedom variable speed manipulation stage (Linear Drive). In this experiment the target bone is fixed to the manipulation stage and it moves in a plane that is perpendicular to the focused laser beam (Figure 4.18). The laser beam is focused onto the surface of the bone via optical lenses with different focal spot distances and spot sizes. The manipulation stage is manually positioned with the laser source in accordance with the lens focal distance.

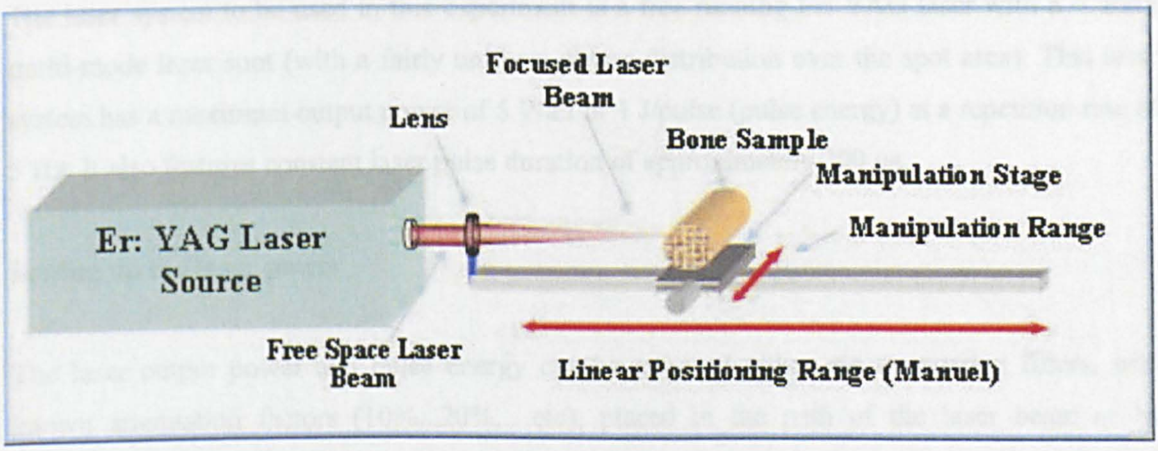

Figure 4.18: Basic laser bone cutting experiment design

4.4.1 Experiment 4.1: Laser Bone Cutting Experiment

4.4.1.1 Objective:

The aim of this experiment is to study the effect of different laser parameters on laser bone cutting and drilling, validate the theoretical analysis and predictions, and evaluate the cutting and drilling techniques. The experiment also aims to deduce the most appropriate laser parameters for such applications

4.4.1.2 Material and measuring equipments

- Er: YAG laser system (2.94 μm)
- Water spray airbrush and smoke evacuation systems
- Bone sample
- Goggles (safety glasses)
- Measuring micrometer and calliper
- Oscillator (frequency generator)
- Motor controlled positioning system (Linear or xyz translation stage)
- Computer
- Optical microscope
- Laser energy detector

4.4.1.3 Experimental Setup and procedure

The laser system to be used in this experiment is a free running Er: YAG laser with a ~ 4mm multi-mode laser spot (with a fairly uniform power distribution over the spot area). This laser system has a maximum output power of 5 Watt or 1 J/pulse (pulse energy) at a repetition rate of 5 Hz. It also features constant laser pulse duration of approximately 200 μs.

Setting up the laser power

The laser output power and pulse energy can be adjusted either via attenuation filters, with known attenuation factors (10%...20%... etc), placed in the path of the laser beam or by controlling the voltage level applied to the laser excitation lamps. However; controlling the voltage level can affect other beam parameters such as laser spot size, power distribution form (or mode), pulse energy and pulse duration. This effect may lead to an increase in the experimental time for determining the beam parameters for the different voltage settings.

Spot size setup

Controlling the laser spot size is achieved using special laser optics (elements) with different focal lengths (FL) and magnification factor M. Assuming infinite/infinite conjugates, positive and negative elements maybe utilised for such application as shown in Figure 4.19. The output laser spot size can be calculated by following equations.

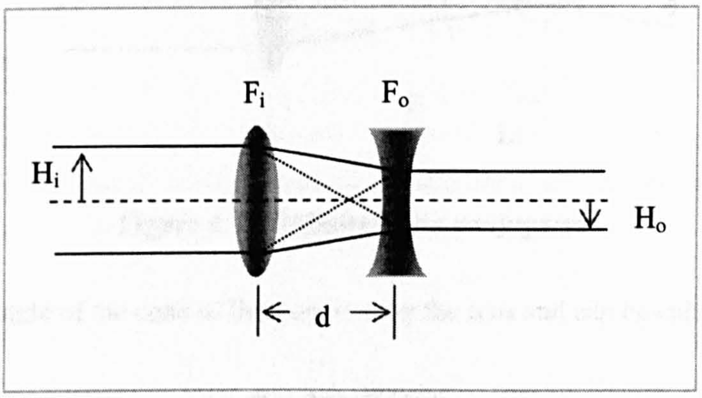

Figure 4.19: infinite/infinite conjugates

Equation 4.7: Spot Size Calculations

$$M = \frac{-F_0}{F_i} = \frac{H_i}{H_0}$$

$$d = F_0 + F_i$$

$$\text{Laser Spot size} = 2H_i$$

$$\text{Laser Spot size} = 2\left|\frac{-F_o}{F_i} H_o\right|$$

where

M: is the Magnification

Fi: is focal length of the lens closest to the image

Fo: is focal length of the lens closest to the object

Table 4.1: Input/Output Spot Size & distance d

Er: YAG Spot Size 2Ho (mm)	Input lens Fo (mm)	Output lens Fi (mm)	Lens Output Spot Size Hi (mm)	Distance between Lenses d (mm)

On the other hand, for finite output, assuming an infinite source, a one lens system can be used in which the laser spot can be found at the focal point as shown in Figure 4.20. The laser spot size is determined by the lens specific parameters such as f-number, focal length, numerical aperture (NA) and laser's wavelength.

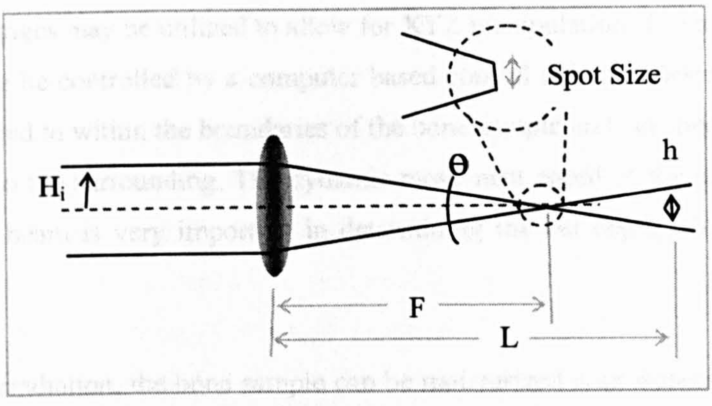

Figure 4.20: Infinite/finite conjugates

Here θ is the full angle of the cone of light emitted by the lens and can be calculated as follows:

Equation 4.8

$$\theta = 2\sin^{-1}(NA)$$

where

NA is the Numerical Aperture of the lens.

Given the value for θ, the spot size along the line passing through the focus point could be calculated at any position relative to the focus point. The spot size (spot diameter) "h" at the distance L (Figure 4.20) for example can be calculated as follows:

Equation 4.9:

$$h = (L - F)\tan(\theta) + \frac{SpotSize}{2}$$

where

SpotSize is the laser spot diameter at the focal point.

(L-F) is the distance of the spot from the focal point.

Table 4.2: Spot Size as a function of (L-F)

F (mm)	L (mm)	Spot Size @ F (μm)	θ° Degree	h (mm)

4.4.1.4 Experimental Procedure

In this experiment, it is suggested that the bone sample or the commercial hydroxyapatite (bone analogue) is fixed on a linear motorized stage facing the focused Er: YAG laser beam as shown in Figure 4.18. The motorised stage allows for the manipulation of the bone sample across the focused beam with high resolution and controllability.

Three motorised stages may be utilized to allow for XYZ manipulation. The manipulation speed and movement can be controlled by a computer based control unit. The laser irradiation of the bone must be limited to within the boundaries of the bone sample and cut specifications in order to avoid damage to the surrounding. The dynamic movement speed of the bone sample across the focused laser beam is very important in determining the cut depth, ablation volume and ablation time.

During the laser irradiation, the bone sample can be moisturized with water spray by means of an airbrush water spray system. The water layer deposited on the cut area of the bone is used to prevent bone carbonization and to assist in providing a smooth cut. At the same time a smoke evacuation system (smoke filter) must be used to filter out the smoke generated by the laser bone interaction. This smoke filter reduces the potential hazards associated with the exposure to the laser interaction procedure.

Safety glasses (goggles) must be used throughout the experiment to protect against any potential hazards due to direct or indirect exposure to the laser beam.

This experiment consists of four sections; each of these sections deals with the effect of varying a specific laser parameter during bone ablation and cutting.

<u>Section I</u>: The effect of varying laser spot size on bone ablation

In this section the laser spot size (spot diameter ϕ) will be varied from 200 μm to 1.2 mm, while all other laser parameters including laser energy density, pulse energy, pulse duration and pulse repetition rate will be kept constant throughout this section of the experiment. Similarly the dynamic movement speed of the laser beam will also be held constant.

The laser bone cutting takes place as the bone sample, placed at the focal point of the laser beam, is driven perpendicular to the focused beam at constant speed. This effect causes the laser beam to scan over the bone where the cut is to take place. The depth of the cut and the cut time is determined by the dynamic rate (speed) of the motorized stage.

The motorized stage moves the bone back and forth across the focused laser beam several times for the complete cut to take place. The number of passes over the bone depends on the cut depth per pass and the bone volume to be cut. For this experiment it is suggested that the Er: YAG laser parameters are as follow:

- Pulse repetition rate 15 Hz
- Pulse energy 250 mJ/pulse
- Pulse duration (τ) 200 μs
- Dynamic rate (speed) 100 μm /sec

Assuming that the Threshold fluence (Ft) = ~10J/cm2, Setting the above laser parameters, this experiment would be carried out by varying the spot size only while recording and calculating the etch depth/pass, ablation volume/pass and ablation time for the specific laser spot size and bone volume; reporting the optimum laser parameters for bone cutting.

Depth measurements can be attained using an optical or electron microscope. The ablation time can be calculated from the dynamic speed of the motorized stage and the number of overlap pulses. The acquired experimental data would be recorded in Table 4.3 and compared to the theoretical values plotted in Figure 4.21 and Figure 4.22.

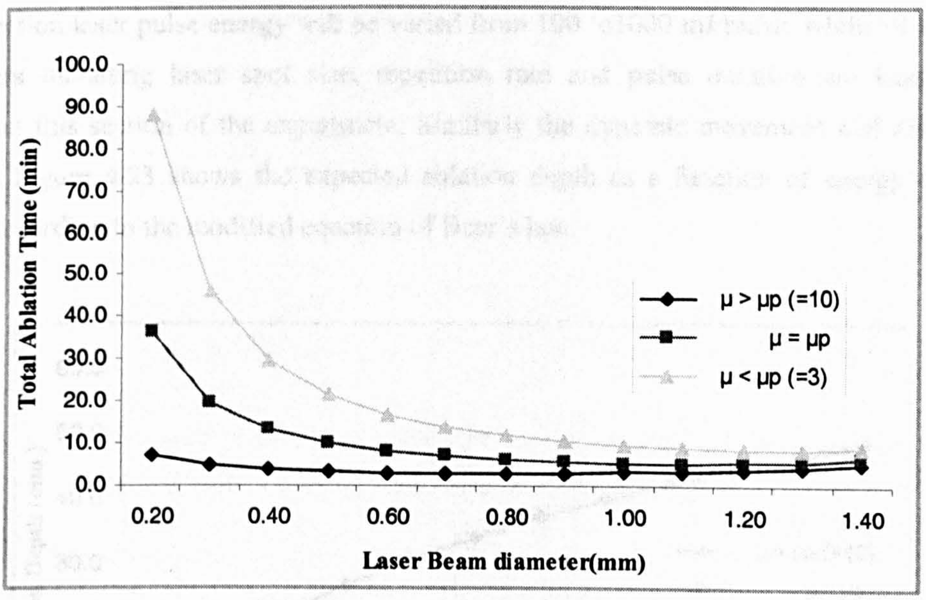

Figure 4.21: Ablation time as a function of laser beam diameter with constant energy density

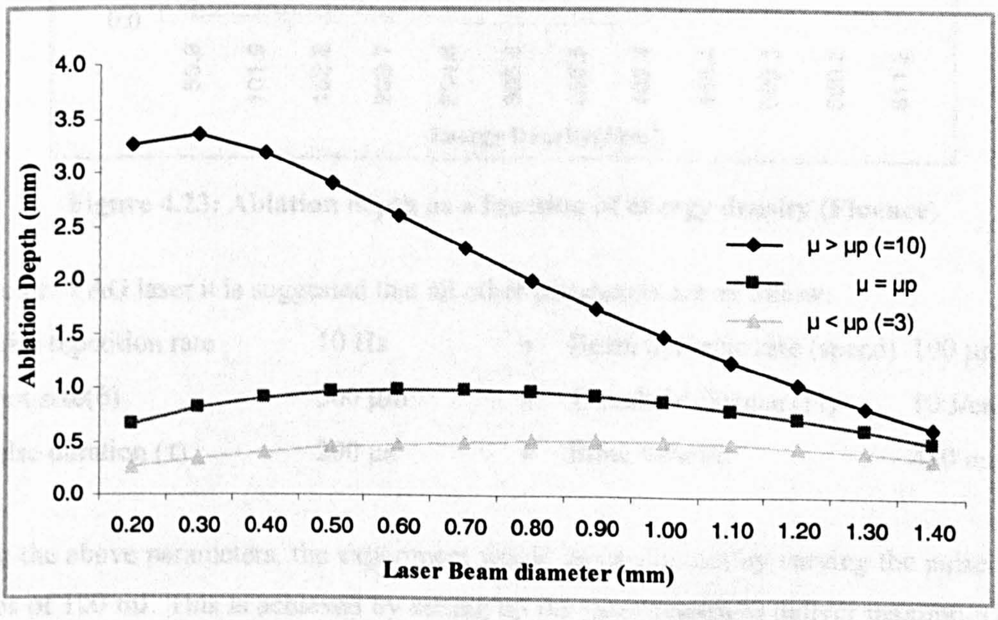

Figure 4.22: Ablation depth/pass as a function of laser beam diameter (constant energy per pulse)

Table 4.3: Study of the effect of laser spot size on the etch depth and overall cut time with constant pulse energy of 250 mJ/pulse

Laser Beam Diameter µm	Laser spot size area Cm2	Laser Energy Density J/ cm2	Bone Volume to be cut mm3	Etch Depth / Pass µm	Ablation volume / pass mm3	Over all Cutting time Sec
200	0.000314	795.77				
400	0.001257	198.94				
600	0.002827	88.42				
800	0.005027	49.74				
1000	0.007854	31.83				
1200	0.011310	22.10				

Section II: The effect of varying laser pulse energy and energy density on bone ablation

In this section laser pulse energy will be varied from 100 to1000 mJ/pulse, while all other laser parameters including laser spot size, repetition rate and pulse duration are kept constant throughout this section of the experiment. Similarly the dynamic movement will also be held constant. Figure 4.23 shows the expected ablation depth as a function of energy density or fluence according to the modified equation of Beer's law.

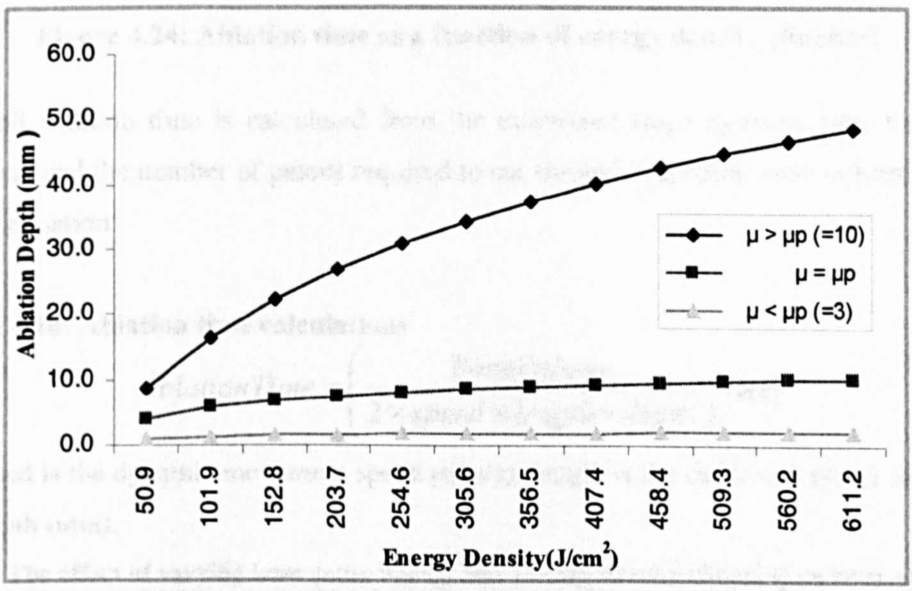

Figure 4.23: Ablation depth as a function of energy density (Fluence)

For the Er: YAG laser it is suggested that all other parameters are as follow:

- Pulse repetition rate 10 Hz
- Spot size(ϕ) 500 µm
- Pulse duration (τ) 200 µs
- Beam dynamic rate (speed) 100 µm/sec
- Threshold fluence (Ft) 10 J/cm²
- Bone volume 450 mm³

Setting the above parameters, the experiment would be carried out by varying the pulse energy in steps of 100 mJ. This is achieved by setting up the laser system to deliver maximum energy of (1 J/pulse) and using thin film attenuation filters to allow for specific energy to pass through

(10%, 20%....etc). The acquired experimental results for the specific pulse energy would be recorded in Table 4.4, plotted and compared to the theoretical values in Figure 4.23 & Figure 4.24. Measurements of the etch depth/pass, ablation volume/pass are achieved using an electron or optical microscope.

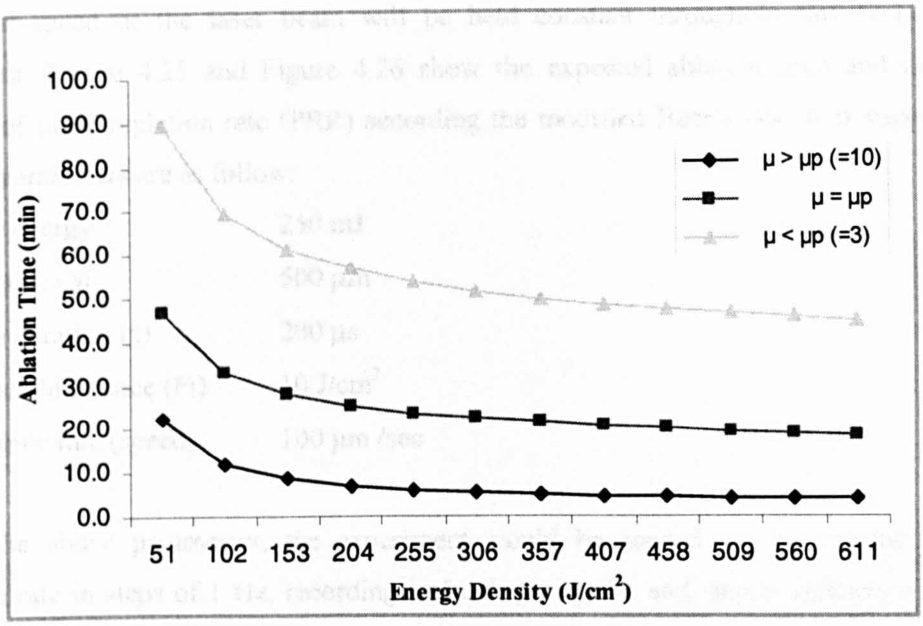

Figure 4.24: Ablation time as a function of energy density (fluence)

The overall ablation time is calculated from the motorized stage dynamic rate, the ablation volume/pass and the number of passes required to cut through a specific bone volume using the following equation:

Equation 4.10: Ablation time calculations

$$AblationTime = \left(\frac{BoneVolume}{2 \times speed \times length \times depth} \right) \textbf{(sec)}$$

where speed is the dynamic movement speed (mm/s), length is the cut length (mm) and depth is the cut depth (mm).

Table 4.4: The effect of varying laser pulse energy and energy density (fluence) on bone ablation

Laser pulse Energy mJ	Laser Energy Density (J/ cm^2)	Bone volume to cut (mm^3)	Etch Depth / Pass (μm)	Ablation volume / pass (μm^3)	Over all Cutting time (min)
100	25.45				
200	50.91				
300	76.36				
400	101.82				
500	127.27				
600	152.73				
700	178.25				
800	203.75				
900	229.18				
1000	254.65				

Section III: The effect of varying laser pulse repetition rate on bone ablation

In this section the laser pulse repetition rate (PRR) will be varied from 1 to 10 Hz, while all other laser parameters including laser spot size, pulse energy and duration as well as dynamic movement speed of the laser beam will be held constant throughout this section of the experiment. Figure 4.25 and Figure 4.26 show the expected ablation time and depth as a function of pulse repletion rate (PRR) according the modified Beer's law. It is suggested that the laser parameters are as follow:

- Pulse energy 250 mJ
- Spot size (ϕ) 500 μm
- Pulse duration (τ) 200 μs
- Threshold fluence (Ft) 10 J/cm^2
- Dynamic rate (speed) 100 μm /sec

Setting the above parameters, the experiment would be carried out by varying the pulse repetition rate in steps of 1 Hz, recording and calculating the etch depth, ablation volume and ablation time for the specific pulse energy. The acquired experimental data would be recorded in Table 4. 5 and compared to the theoretical values of (Figure 4.25 and Figure 4.26)

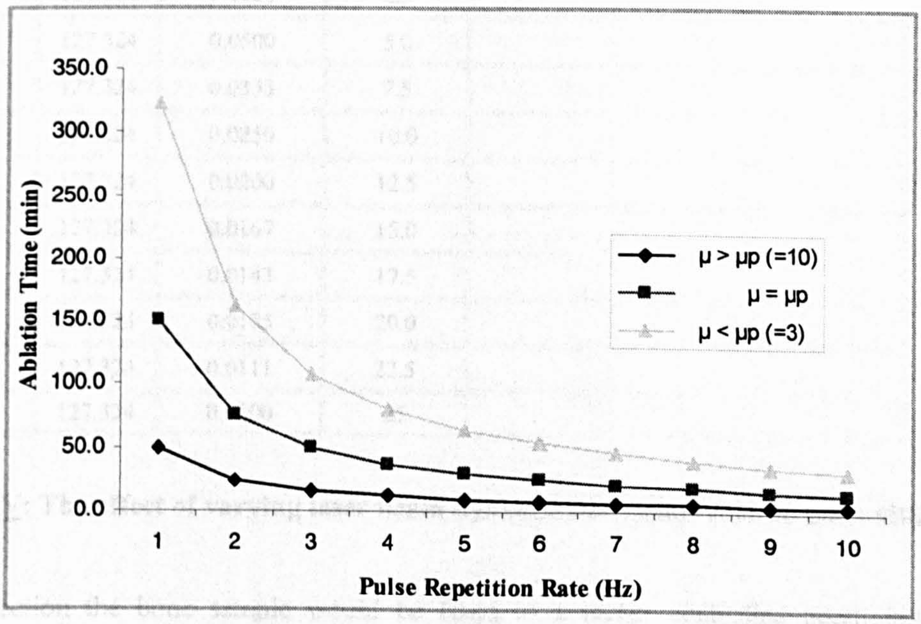

Figure 4.25: Ablation time as a function of pulse repetition rate (PRR)

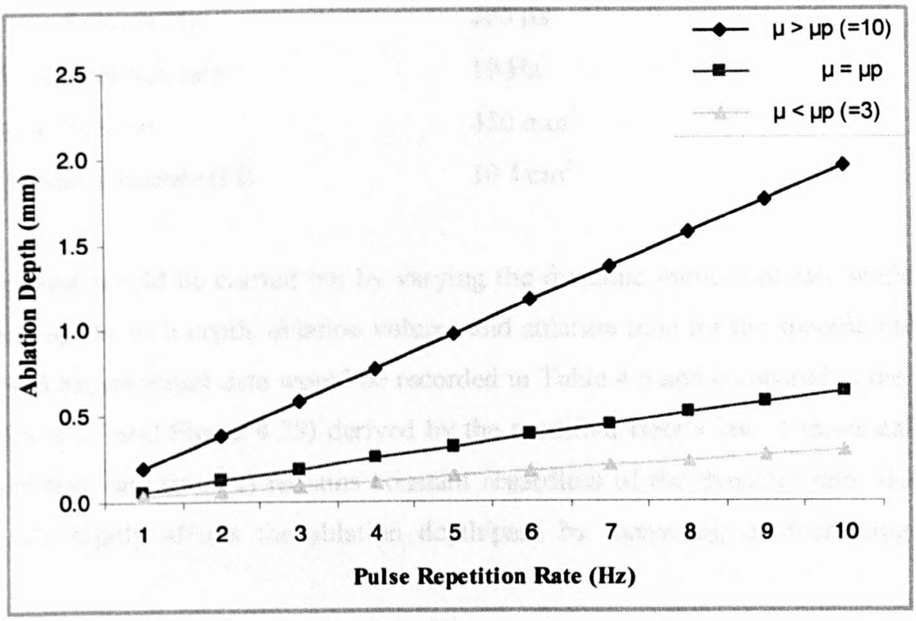

Figure 4.26: Ablation depth per pass as a function of pulse repetition rate

Table 4. 5: The effect of varying laser pulse repetition rate on bone ablation

Laser pulse repetition rate Hz	Laser Energy Density (J/ cm2)	Laser beam displacement Δx = v/f (μm)	Pulse overlap n =(ϕ/2Δx)	Bone volume to cut (mm3)	Etch Depth / Pass (μm)	Ablation volume / pass (μm 3)	Over all Cutting time (min)
1	127.324	0.1000	2.5				
2	127.324	0.0500	5.0				
3	127.324	0.0333	7.5				
4	127.324	0.0250	10.0				
5	127.324	0.0200	12.5				
6	127.324	0.0167	15.0				
7	127.324	0.0143	17.5				
8	127.324	0.0125	20.0				
9	127.324	0.0111	22.5				
10	127.324	0.0100	25				

<u>Section IV</u>: The effect of varying laser beam dynamic movement rate on bone ablation

In this section the bone sample would be fixed to a motor controlled positioning system (motorized translation stage) which can move it perpendicular to the laser beam at variable speed (dynamic rate). The speed will be varied from 1–200 μm/sec, while all other laser parameters including laser spot size, pulse energy, pulse repetition rate are held constant. It is suggested that all other laser parameters are as follows:

- Pulse energy 250 mJ
- Spot size (ϕ) 500 μm

- Pulse duration (τ) 200 μs
- Pulse repetition rate 10 Hz
- Bone Volume 450 mm^3
- Threshold fluence (Ft) 10 J/cm^2

The experiment would be carried out by varying the dynamic movement rate while recording and calculating the etch depth, ablation volume and ablation time for the specific pulse energy. The acquired experimental data would be recorded in Table 4.6 and compared to the theoretical values (Figure 27 and Figure 4.28) derived by the modified Beer's law. Theoretically one can see that ablation rate (mm^3/s) remains constant regardless of the dynamic rate. However, the dynamic rate highly affects the ablation depth/pass by increasing or decreasing the pulse overlap.

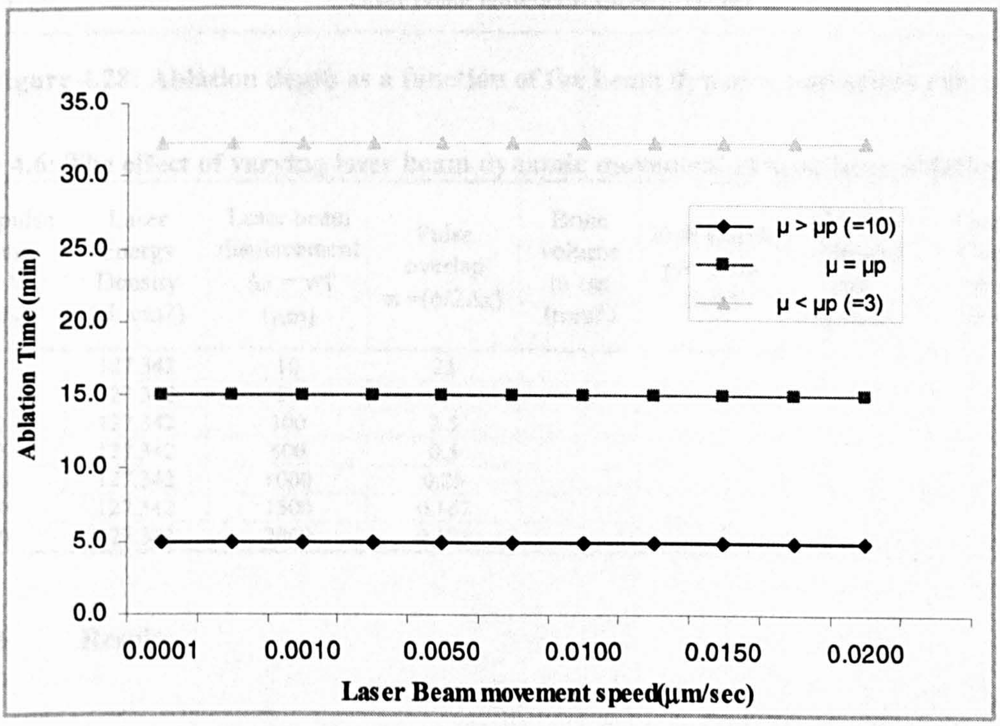

Figure 27: Ablation time as a function of dynamic movement rate (v)

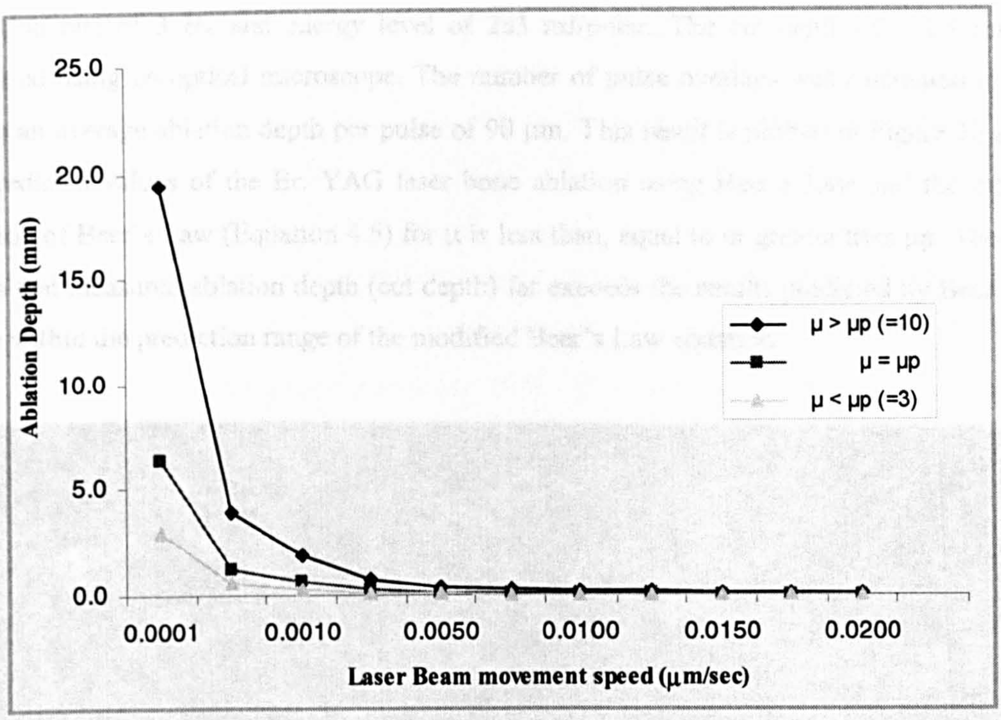

Figure 4.28: Ablation depth as a function of the beam dynamic movement rate (v)

Table 4.6: The effect of varying laser beam dynamic movement rate on bone ablation

Laser pulse dynamic rate V (μm/s)	Laser Energy Density (J/ cm2)	Laser beam displacement $\Delta x = v/f$ (μm)	Pulse overlap $n = (\phi/2\Delta x)$	Bone volume to cut (mm3)	Etch Depth per Pass (μm)	Ablation volume / pass (μm 3)	Over all Cutting time (min)
1	127.342	10	25				
5	127.342	50	5				
10	127.342	100	2.5				
50	127.342	500	0.5				
100	127.342	1000	0.25				
150	127.342	1500	0.167				
200	127.342	2000	0.125				

4.4.1.5 Results

Although this experiment was tailored to fit the assumed specifications of the available Er: YAG laser system, the author was unable to perform this experimental procedure and obtain the required measurements. This was mainly due to the limitations imposed on setting-up and adjusting the different laser parameters and other technical problems associated with the available Er: YAG laser system.

Despite these limitations, a laser bone cutting experiment was carried out using the Er: YAG laser system (Figure 4.13) which revealed some promising results. Figure 4.29 shows two images of bone cuts attained using a focused Er: YAG laser beam. The images show very clean and uniform cuts with minor damage to the surrounding tissue (less than 10μm on either side). For this experiment the laser spot size was approximately 500 μm in diameter with a laser pulse repetition rate of 3 Hz and energy level of 283 mJ/pulse. The cut depth of ~ 1.8 mm was measured using an optical microscope. The number of pulse overlaps was calculated to be 20 giving an average ablation depth per pulse of 90 μm. This result is plotted in Figure 30 against the predicted values of the Er: YAG laser bone ablation using Beer's Law and the modified equation of Beer's Law (Equation 4.5) for μ is less than, equal to or greater than μp. The figure shows that measured ablation depth (cut depth) far exceeds the results predicted by Beer's Law and is within the prediction range of the modified Beer's Law equation.

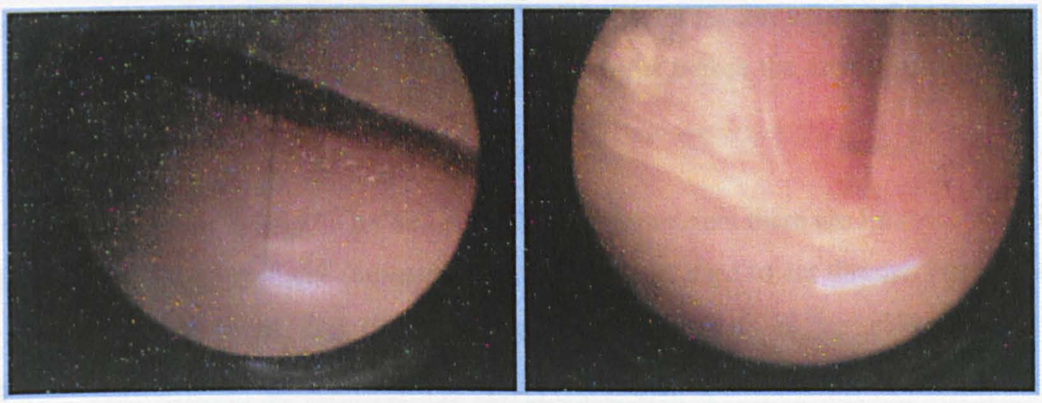

Figure 4.29: Bone cuts using Er: YAG Laser

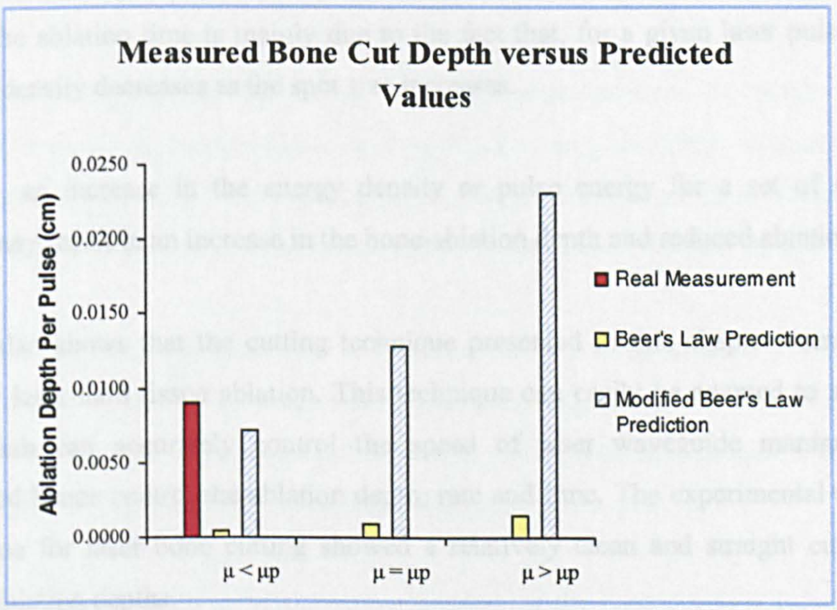

Figure 30: Measured bone cut versus the predicted values by Beer's Law and the modified Beer's Law equation (Equation 4.5) for the conditions where (μ) is less than, equal to or greater than (μ_p)

4.5 Conclusion

Different laser parameters have significant effects on ablation rate, depth, volume and time of biological tissue. These effects need to be clearly understood in designing an effective bone cutting system for orthopaedic surgery. For example, an increase in the laser pulse repetition rate speeds up the laser bone-ablation process and increases the ablation depth. However, there are limitations imposed on the pulse repetition rate. For the Er: YAG laser system the pulse repetition rate is limited to about 30 Hz. Above this limit interaction with the plume of vaporized material reduces ablation performance. This interaction could distort and bend the incoming laser beam resulting in a rough edged cut. The plume's mass absorption coefficient (μ_p) can have positive and negative effects on the laser ablation rate and ablation time. This depends mainly on the ratio between the mass absorption coefficients of the plume (μ_p) and the biological tissue (μ). Thus sufficient time should be allowed for the plasma plume to leave the surface before applying a second pulse. This effect limits the repetition rate of the lasing pulse to a level that ensures the evacuation of the plasma plume before the arrival of the next laser pulse.

On the other hand, for a specific set of Er: YAG laser parameters there are limitations imposed on the maximum laser spot size (beam diameter) that can be used to cut through bone. A small spot size (in the order of 200 μm in diameter) may result in higher ablation depths in comparison with a 1 mm spot size. However, a 1 mm spot size features a faster volume ablation rate than smaller spot sizes. This study shows that as the laser spot size gets larger (larger than 1 mm in this case) for specific laser pulse energy the laser ablation time tends to increase. This increase in the ablation time is mainly due to the fact that, for a given laser pulse energy, the laser energy density decreases as the spot size increases.

Furthermore, an increase in the energy density or pulse energy for a set of specific laser parameters may result in an increase in the bone-ablation depth and reduced ablation time.

This study also shows that the cutting technique presented in this chapter seems to be very effective for laser-hard tissue ablation. This technique can easily be adapted to a robotic end-effector which can accurately control the speed of laser waveguide manipulation (laser scanning) and hence control the ablation depth, rate and time. The experimental application of this technique for laser bone cutting showed a relatively clean and straight cut with evenly distributed ablation depths.

The experimental results also showed that the Er: YAG laser is an excellent candidate for bone ablation with an average ablation depth per pulse of 90 μm and less 10 μm damage to the surrounding tissue (for a specific set of laser parameters). They also show that Er:YAG laser can cut bone with high selectivity and it has the potential to replace the standard cutting and drilling tools currently used in orthopaedic.

Chapter 5

Robotic Delivery of Laser Radiation for Image Guided Orthopaedic Surgery

5.1 Introduction

A key aim of this research is to investigate novel robotic delivery for image guided orthopaedics surgery by introducing a new laser based surgical tool. Thus, the project involves specification and design of an active robotic end-effector suitable for a laser delivery system (i.e. a laser end-effector). In robotics, an end-effector is a device or tool connected to the end of a robot arm [FU 87].

The laser End-Effector to be designed should be capable of performing the basic tasks of bone drilling, sawing and sculpturing with high accuracy, selectivity, flexibility and dexterity [STEV 98][HOWE 99]. It should also be able to provide positioning and performance feedback. It should be designed with minimum degrees of freedom, yet, fulfilling all mandatory engineering and clinical requirements.

This chapter first identifies the end-effector's design requirements and shows the overall system design as foreseen by the author. Secondly it presents a complete design procedure and design analysis for the laser End-Effector prototype. It also presents some illustrations of the bone cutting and drilling as foreseen by the author to justify some of the overall design requirements.

The End-Effector prototype presented in this chapter is a three degrees of freedom (DOF) device, capable of robotic delivery of a laser beam to the surgical site. The mechanical design of the End-Effector is novel. It comprises of three major joints connected together with rigid links in a unique way whereby all joints manipulate about a single origin point.

The chapter ends by summarising the major features of the laser End-Effector prototype and proposes future developmental phases required to attain a clinically approved commercial laser End-Effector.

5.2 Design Requirements

The design of the End-Effector is based on various sets of requirements. These include:

- Clinical and surgical requirements

- Engineering requirements
- Surgical laser requirements (introduced in Chapter 4)

5.2.1 Clinical and Surgical Requirements

The main clinically motivated requirements that have been considered are as follows:

a) Clinical accuracy
b) Clinical and environmental safety
c) Functional scope
d) Improvement to existing surgical outcome

Under ideal conditions the End-Effector should be capable of positioning the laser spot (known as the laser front) with high accuracy (i.e. within ± 0.5 mm from the desired position [MAVR 97]) and repeatability. The End-Effector geometry and actuator control should feature fail-safe design even during power failure [HOWE 99]. It should not occupy a large area in the theatre room and it must not block the surgeon's working area. The End-Effector must have a functional scope that covers a number of orthopaedic surgical applications. However, the End-Effector's workspace should be constrained to cover just the surgical volume for a specific task. The End-Effector should be "User Friendly". It must be easily fixed and removed and it should not require an engineer as part of the medical staff present during surgery.

The End-Effector design must be clinically approved biocompatible and cause no hazards to patient, medical team nor environment. To prevent laser hazards (as mentioned in Chapter 4), debris from the laser-tissue interaction must be removed and the End-Effector speed and workspace should have a safe upper limit during surgery.

The End-Effector aims to improve the surgical outcome by providing a new surgical tool that has some of the following features: high surgical dexterity, reduces surgical invasiveness, reduces tissue damage and reduces blood losses [HOWE 99] [PROU 96][LEA 94] ,

5.2.2 Engineering Requirements

A performance goal of the designed End-Effector is to achieve an accuracy within ± 1 mm of all intended rotational and translational positioning of the laser front. The engineering requirements for the design of the laser End-Effector to achieve this goal may include:

- Minimisation of design complexity (e.g. minimum number of degrees of freedom (DOF))
- High design accuracy

- Selecting high accuracy, high repeatability, robust and reliable components
- High accuracy machining of the different End-Effector's link elements
- Precise and accurate assembly
- Safe manipulation (in terms of speed and obstacle avoidance)
- Confined functional scope
- High accuracy and resolution feedback systems
- High accuracy control system
- Complies with the surgical, clinical and environmental safety requirements

Other desirable engineering and design requirements may include:

- Auto-lock when power is off
- Low power consumption
- Ease of control
- Light in weight
- Easy to fix and remove
- Portable
- Small in size

The laser End-Effector should be capable of drilling sawing and sculpturing of bone. It should feature high flexibility and dexterity. The laser End-Effector is intended to be attached to a passive or active manipulator (Robot Arm). It should also provide automatic implementation of a surgical plan created pre-operatively or intra-operatively. Seeking to minimize the number of DOF for the End-Effector may result in increasing the DOF to the Robot Arm holding the End-Effector.

Besides the design of a robotic End-Effector and its control unit, the development of a feedback mechanism is required for controlling the laser front position within the surgical site. This is required to produce an accurate and effective laser cut. This feedback mechanism may include visual, auditory and sensory systems to provide a suitable computer based control unit with accurate positioning information, subsequently providing surgeons with a real time display of the surgical site during surgery. Techniques to provide this feedback control are discussed further in Chapter 6 Section 6.3.

The following section gives a general overview of the interaction between the major design components including the navigation, optical tracking and monitoring systems as foreseen by the author.

5.3 System Design for Laser Cutting for Computer Assisted Surgery

The system design block diagram is shown in Figure 5.1 and Table 5.1. They show the major design components that form the overall system architecture. These include the Robot Arm, the laser End-Effector, the surgical tool (laser waveguide) and all control and feedback modules associated with the positioning system. The block diagram also presents other elements which are associated with the overall design (shaded blocks) and these are outside the scope of this chapter.

This section discusses the basic operating principle of the positioning system (Robot Arm and End-Effector). It also analyses each block independently giving more details on the design and interaction of these blocks. This thesis focuses on the un-coloured blocks in Figure 5.1.

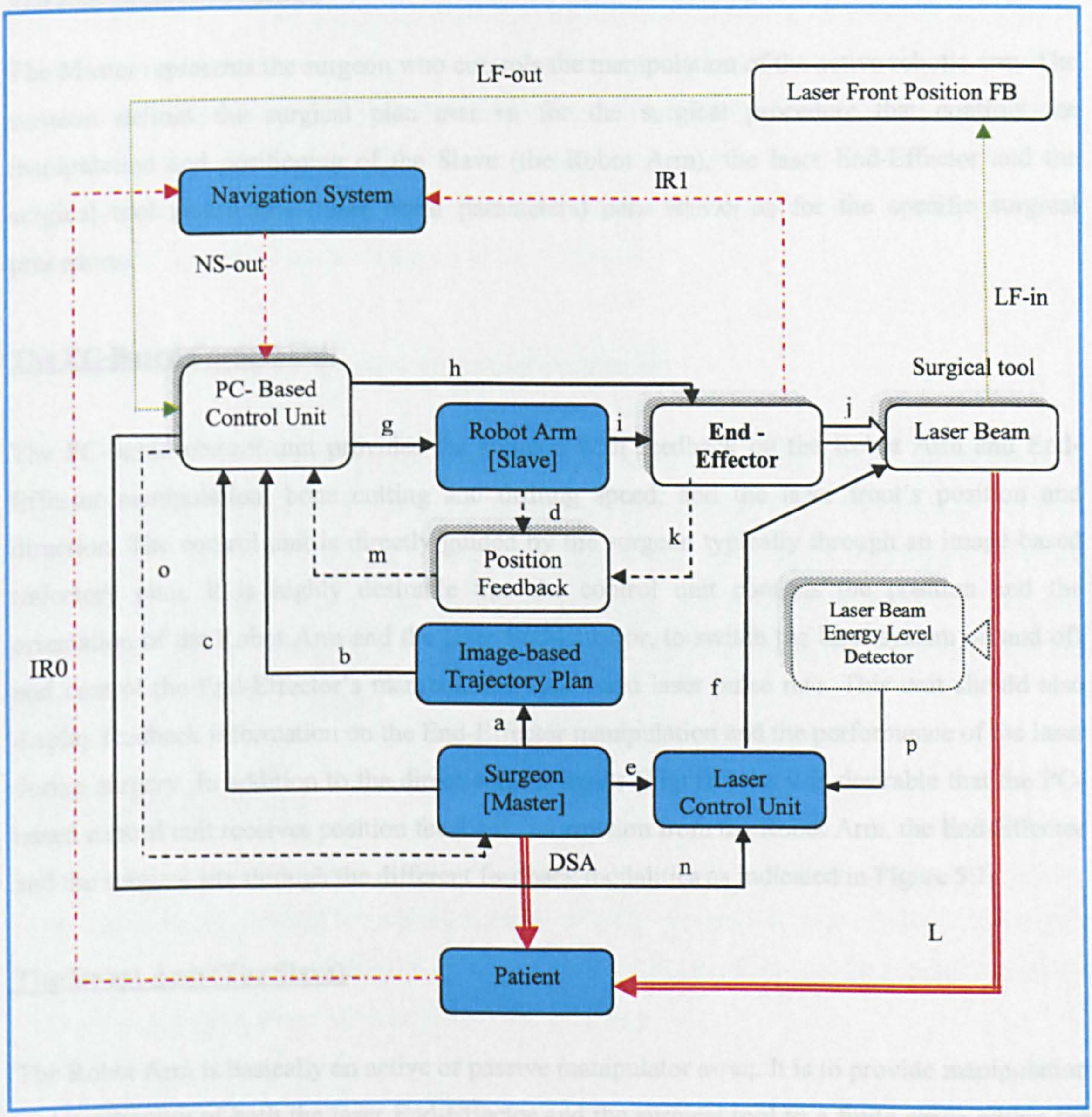

Figure 5.1: Block diagram of a robotic laser cutting system for computer assisted surgery

Table 5.1: Information flow table for the block diagram in Figure 5.1.

Label	Descriptions	Label	Descriptions
a	Setting the trajectory plan	L	Surgical laser beam
b	Trajectory plan data input	m	Position FB data(Pulses)
c	End-Effector and Robot arm initial positioning	n	Laser enable (ON/OFF) and pulse rate control
e	Setting laser parameters: pulse energy, spot size...	o	FB on manipulation speed, cut depth & position
f	Laser beam parameters	DSA	Direct surgical application /System override
g	Robot arm position control signals (output)	IR 0-1	Infrared signals for position tracking system
h	End-Effector position control signals (output)	LF-in	Reflected laser beam (from laser front position)
i	End-Effector base position	LF-out	Time of flight / laser front position
j	Laser beam position control (Front End position)	NS-out	4x4 transformation matrices on patient surgical
k	End-Effector's optical encoders output pulses		site, front End and End-Effector base
d	Robot's arm optical encoder output pulses	P	Laser energy level detection control signal

The Master (The Surgeon)

The Master represents the surgeon who controls the manipulation of the active robotic arm. The surgeon defines the surgical plan [PHIL 95] for the surgical procedure that controls the manipulation and positioning of the Slave (the Robot Arm), the laser End-Effector and the surgical tool parameters (laser beam parameters) [NIEM 96][IVAN 00] for the specific surgical procedure.

The PC-Based Control Unit

The PC-based control unit provides the surgeon with feedback on the Robot Arm and End-Effector manipulation, bone cutting and drilling speed, and the laser front's position and direction. The control unit is directly guided by the surgeon typically through an image-based trajectory plan. It is highly desirable that the control unit controls the position and the orientation of the Robot Arm and the laser End-Effector, to switch the laser system on and off and control the End-Effector's manipulation speed and laser pulse rate. This unit should also display feedback information on the End-Effector manipulation and the performance of the laser during surgery. In addition to the direct control inputs (Figure 5.1), it is desirable that the PC-based control unit receives position feedback information from the Robot Arm, the End-Effector and the surgical site through the different feedback modalities as indicated in Figure 5.1.

The Robot Arm (The Slave)

The Robot Arm is basically an active or passive manipulator [FU 87]. It is to provide manipulation and positioning of both the laser End-Effector and the surgical tool to a finite range within the surgical workspace. Passive manipulators could be positioned manually by the surgeon while its position and orientation are directly monitored by the control unit, which guides the surgeon for high positioning accuracy. On the other hand, in the case of an active manipulator, the active robot arm may get its position control commands (trajectory plan) from the Master (Surgeon) via the PC-based control unit and positions itself accordingly.

The robot arm should provide high accuracy and dexterity in manipulation, positioning and orientation. It should be designed to meet all engineering, clinical and safety requirements and cause no hazards to the patient, surgical team or environment.

The Surgical Control Unit (Laser Control)

The surgical control unit controls the activation of the surgical tool (laser beam) and sets the required laser parameters (pulse duration, pulse energy, spot size and application time) [NIME 96]. This surgical control unit gets its surgical tool performance feedback information through the PC-based control unit. This assumes direct access of the control panel of the surgical control unit by the PC-based control unit (to enable automatic control). Given the proper feedback information, it is highly desirable that the surgical control unit is capable of automatically controlling the laser output level, pulse rate, spot size and activation time during surgery. It also helps prevent accidental tissue damage and other hazards.

5.4 Bone Cutting, Drilling and Sculpturing Techniques

The following techniques are proposed by the author for bone cutting, drilling and sculpturing using the laser End-Effector. These techniques require pre-surgical 2D or 3D images of the bone at the surgical site. These images provide the surgeon with information regarding the cutting area and bone shape. During the trajectory planning, the surgeon specifies the surgical boundaries (Dashed line Figure 5.3) of the cutting area, which confines the manipulation of the surgical tool (laser End-Effector).

Bone Cutting Technique

Figure 5.2 gives an illustration of the bone preparation (cutting, drilling and sculpturing) for Total Knee Athroscopy TKA with the number of DOF required for bone cutting. This figure shows that bone cutting may require only 2 or 3 DOF. This in effect sets the number of degrees of freedom requirement for the laser End-Effector design.

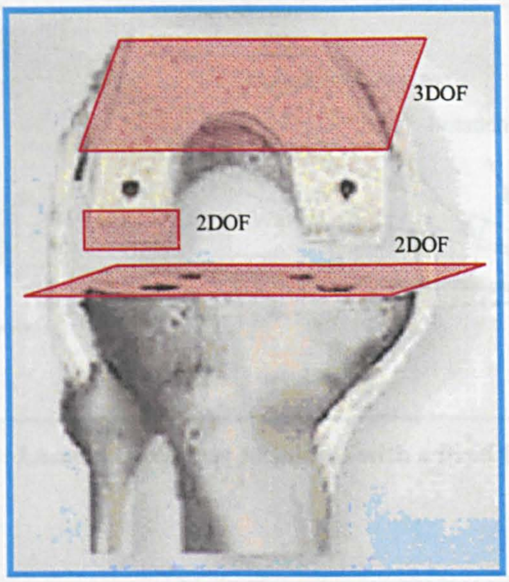

Figure 5.2: TKA bone preparation and the required DOF for bone cutting

The bone cutting technique shown in Figure 5.3 suggests that laser bone cutting requires a minimum of two degrees of freedom. These include rotational and linear movements about the origin of manipulation. The rotational movement allows the laser waveguide to swing between points on the bone boundaries (Figure 5.3) while the linear movement drives the focused laser beam into the bone.

As the focused laser beam swings over the bone at constant speed, it cuts through at a relatively constant depth in an arc form. The beam is then driven forward toward the bone for the following swing. Laser bone cutting is a repetitive process in which the laser beam swings over the target until the cut is complete.

Diagonal cutting, on the other hand, requires a minimum of 3 degrees of freedom where horizontal and vertical manipulations are required in conjunction with linear manipulation. However, limiting the End-Effector degrees of freedom would impose limitation on the different cutting angles and shapes. Hence, care must be taken during trajectory planning and End-Effector initial positioning. Laser bone cutting is highly dependent on the laser parameters, laser manipulation speed and bone characteristics. The latter plays an important role in determining the cutting rate, depth and time. Since cortical bone may require more laser irradiation time than other bone tissue, a high accuracy feedback technique may be required to determine the laser penetration depth (laser front inside tissue).

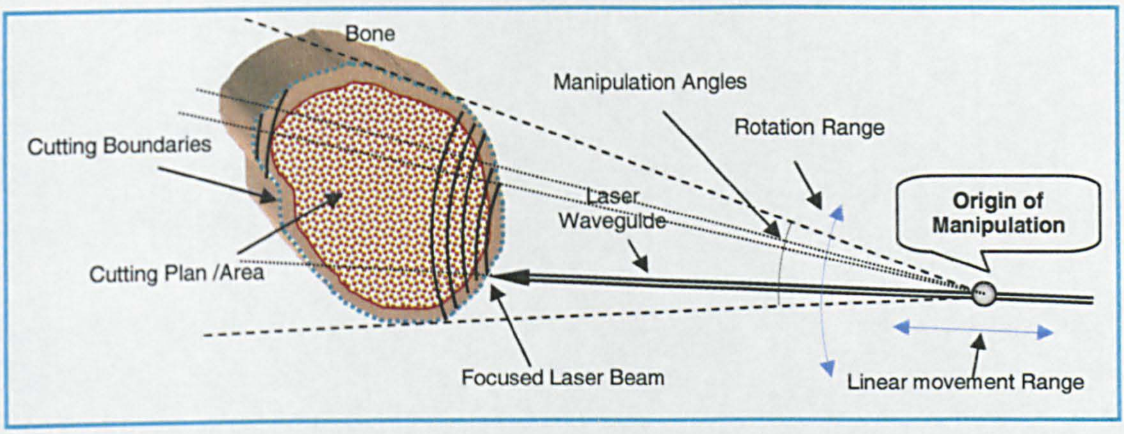

Figure 5.3: Laser bone cutting technique with a fixed focus beam

Bone Drilling

Bone drilling is another form of bone ablation. The laser beam tends to form round holes with diameters roughly equal to the beam (focal spot size) diameter near the surface [ALLM 98]. However, as the hole grows deeper it usually narrows below the surface. The reason for this phenomenon is the "channelling" of the beam by the steep wall of the hole. This channelling keeps the beam power concentrated near the axis of the hole as the ablation point advances into the bone. [ALLM 98].

Different approaches and different drilling techniques may be adopted depending on the size of the hole (i.e. diameter and depth). To drill a very fine hole less than 0.5 mm in diameter for example requires the focusing of a laser beam on the bone surface in the direction of drilling. The depth of the hole depends upon the laser pulse energy, pulse rate, spot size and irradiation time in addition to bone density [NIEM 96] [ALLM 98]. The drilling technique in this case may involve the utilization of only one degree of freedom after setting the End-Effector's initial position. In this technique a linear drive can advance the laser focal point (i.e. laser front) towards the target as the hole gets deeper inside the bone. When taking the channelling phenomenon into account then it may be possible to maintain the focal point fixed on the surface. On the other hand, to drill a large diameter hole, the technique involved may require a minimum of 3 degrees of freedom. In this technique drilling is done through a layer etching process (sculpturing). This process involves the following:

- Fixation of the target bone (relative to the laser front)
- Setting of the initial position of the laser wave guide along the axis of drilling
- Scanning (manipulation) of the focused laser beam on the surface of the bone within the hole boundaries etching through the bone.

After the initial position is set the scanning process may require all three degrees of freedom to perform the etching. This etching technique for drilling is described in Figure 5.4 and Figure 5.5. These figures show the laser drilling process assuming a laser beam drilling diameter equivalent to the laser spot size on the surface of the bone. In this technique, drilling is an iterative process in which the beam is scanned within the hole boundaries; etching bone layers.

The drilling technique shown in Figure 5.4 suggest that the End-Effector's origin of manipulation is fixed at a point along the axis line passing through the centre of the hole with its laser waveguide initially set to point towards the centre. The laser beam is then scanned within the boundaries of the hole etching through at relatively constant depth. A complete laser scan of the hole diameter results in an etched layer of bone where its depth depends on the laser parameters, manipulation speed and etched bone characteristics. The number of layers required for the laser to drill through the required depth depends upon penetration depth for each individual layer.

The drilling technique shown in Figure 5.5 suggests that the laser beam drills through the bone in an angle. To avoid drilling outside the required hole boundary, the maximum drilling and manipulation angle needs adjusting by an angle equivalent to the angular resolution of the manipulator Figure 5.5 (also see Section 5.4). The number of adjusted maximum drilling angles is independent from the number of etched layers and can be calculated as follow

$$Ndma = \left|\frac{\theta_1 - \theta_n}{\omega}\right|$$

where

$$\theta_1 = \sin^{-1}\left(\frac{\phi_h - \phi_B}{2L_1}\right)$$

$$\theta_n = \sin^{-1}\left(\frac{\phi_h - \phi_B}{2L_n}\right)$$

where

$Ndma$	is the number of maximum drilling and manipulation angles
θ_1	is the maximum angle within the hole boundary between the surface of the bone and the origin of manipulation
θ_n	is the maximum angle within the hole boundary between the deep end of the hole and the origin of manipulation
ω	is the manipulation angular resolution (the smallest manipulation angle)
ϕ_h	is the hole diameter
ϕ_B	is the laser beam diameter (spot size)
L_n	is the distance of the laser front to the origin of manipulation

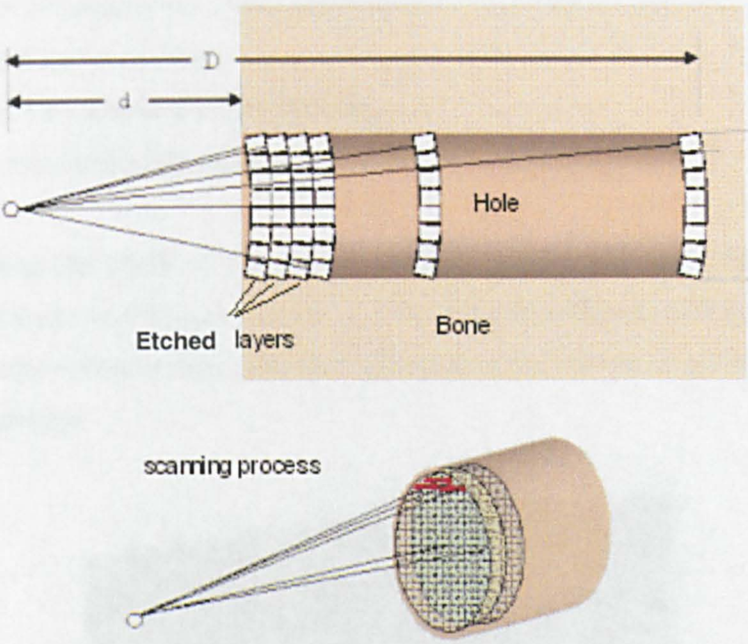

Figure 5.4: Laser scanning process

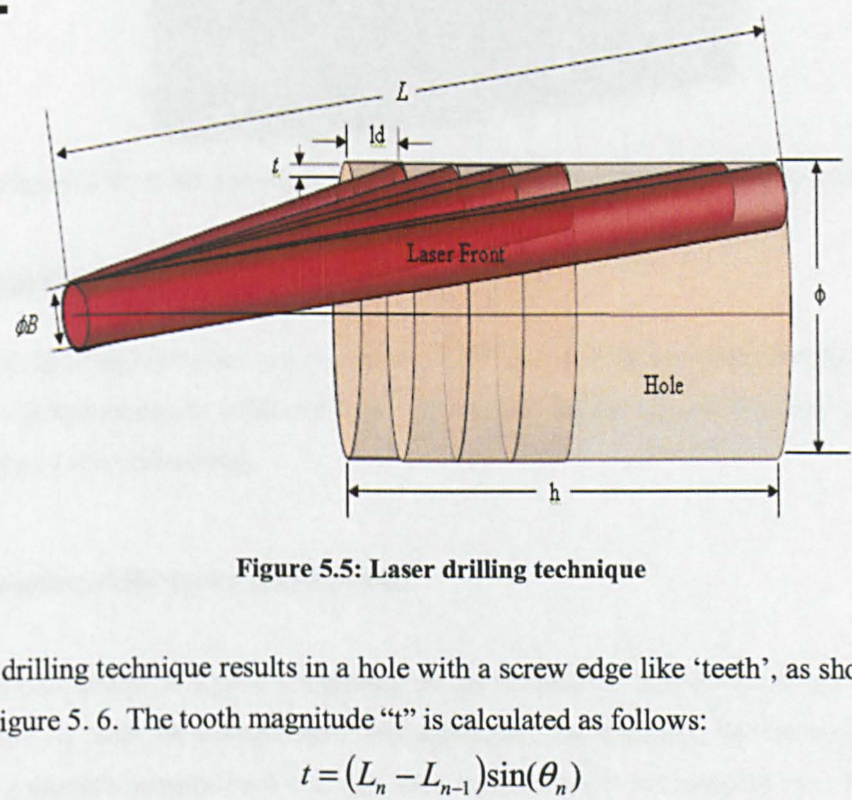

Figure 5.5: Laser drilling technique

The above drilling technique results in a hole with a screw edge like 'teeth', as shown in the 3D model of Figure 5. 6. The tooth magnitude "t" is calculated as follows:

$$t = (L_n - L_{n-1})\sin(\theta_n)$$
$$where$$
$$L_n = L_0 + D$$
$$\theta_n = \tan^{-1}\left(\frac{\phi_h / 2}{L_n}\right)$$

where

L_n is the distance from the laser front to the End-Effector origin of manipulation where L is the initial length

θ_n	is the angle of the laser beam measured with respect to the axis passing through the centre of the hole
D	is the required depth of the hole
ϕ_h	is the required hole diameter.

A 3 mm hole with the depth = 120 mm for example would have teeth magnitude ranging between 53.6-79.0 μm which represent 3.6 - 5.2 % of the hole diameter. Practical experiments are needed to confirm these results and to provide insights into the best way to refine further this laser drilling technique.

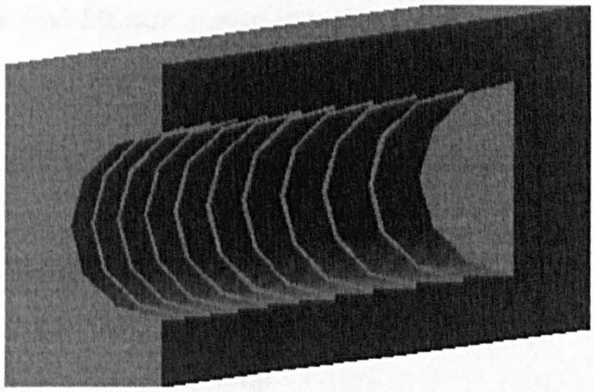

Figure 5. 6: A 3D AutoCAD [AUTO 00] model of a laser drilled hole cross section

Bone Sculpturing

The bone sculpturing technique is a combination of bone drilling and bone cutting techniques. Although sculpturing can be achieved with only 3 DOF, limitations are imposed on the shape size and type of the sculpturing.

5.5 Description of the Laser End-Effector

The laser End-Effector is a core component of the research of this thesis. It has been designed by the author to meet the manipulation and application requirements (reviewed in Section 5.2) for use of a specific surgical tool (i.e. the laser waveguide) to the surgical site. The design and calculations have been carried out using AutoCAD and MathCAD respectively, in accordance with the engineering and clinical requirements. However, the End-Effector was not implemented due to cost and other logistic issues.

The End-Effector's manipulation has been limited to three degrees of freedom due to the requirements of surgical application, i.e. bone cutting, drilling and sculpturing. It comprises of two revolute and one prismatic joint connected together with rigid links. These joints are driven by high positioning accuracy and high torque stepper motors, gearboxes and a leadscrew. The first revolute joint (Figure 5.7) has an axis of rotation parallel to the Z axis and can rotate ±30°. The second revolute joint has an axis of rotation parallel to the X axis and can rotate ±30°. The maximum travel for the third joint is 160 mm in the direction of the longitudinal Y axis. These values are selected in accordance with the orthopaedic surgical requirements. They allow for medium range functionality scope work volume and high functional flexibility for bone cutting drilling and sculpturing.

The functionality scope of the End-Effector is much less than that of the robotic arm, yet it plays the important role of fine tuning and accurate poisoning and manipulation of the surgical tool (laser waveguide). The End-Effector design incorporates stepper motors as the main driving force and high resolution optical encoders for position and orientation feedback.

Information regarding the position and orientation of the End-Effector and the laser waveguide are fed back to the control unit via the position feedback circuits, navigation system, and a laser front position feedback system. The feedback information provided would probably be in the form of pulses (pulse train), transformation matrices, and time. This information holds the position and orientation parameters of the End-Effector and the surgical tool relative to a fixed reference frame (for example the origin of the optical tracking system). This feedback to the PC-based control unit enables accurate and fine positioning of the laser waveguide within the surgical site.

The supporting structures [Appendix C: AutoCAD Blueprints] of the End-Effector are made out of aluminium to provide high strength and low weight specifications. For maximum ease in manipulation, the centre of mass for each component as well as the overall joint centre of mass were calculated and taken into account during the design process. The overall joint centre of mass was then aligned, to a specified accuracy, with the centre (origin) of manipulation. This helps reduce the effects of inertial forces and torque during manipulation. An illustration of the End-Effector's joint's movements about the centre of manipulation is presented in Figure 5.8. A description of each of the three joints of the End-Effector is given in the following sub-sections.

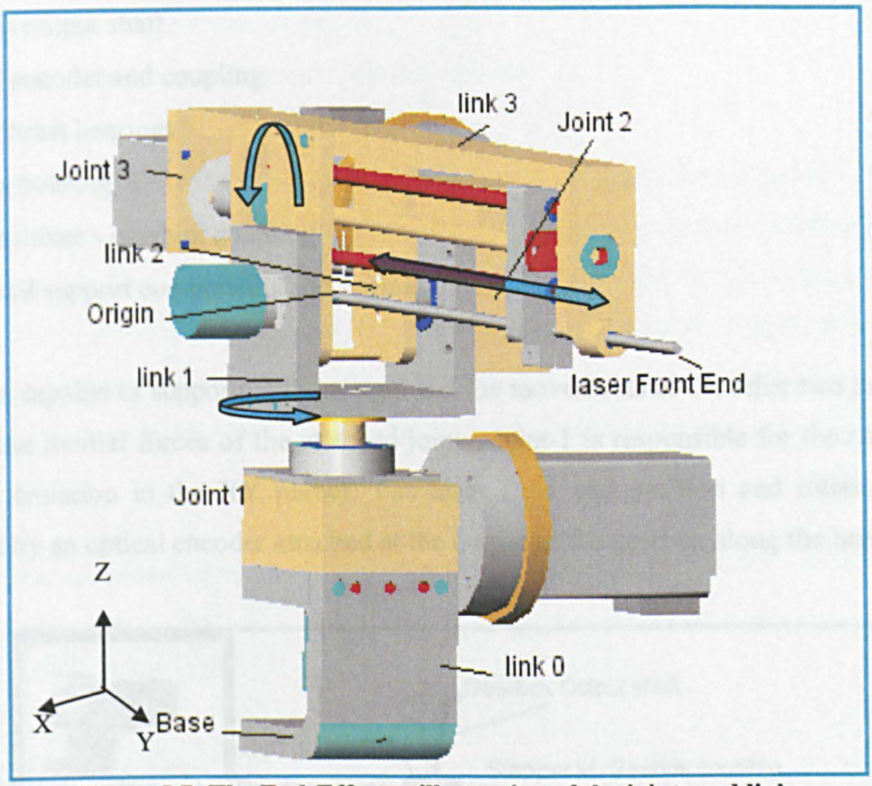

Figure 5.7: The End-Effector illustration of the joints and links

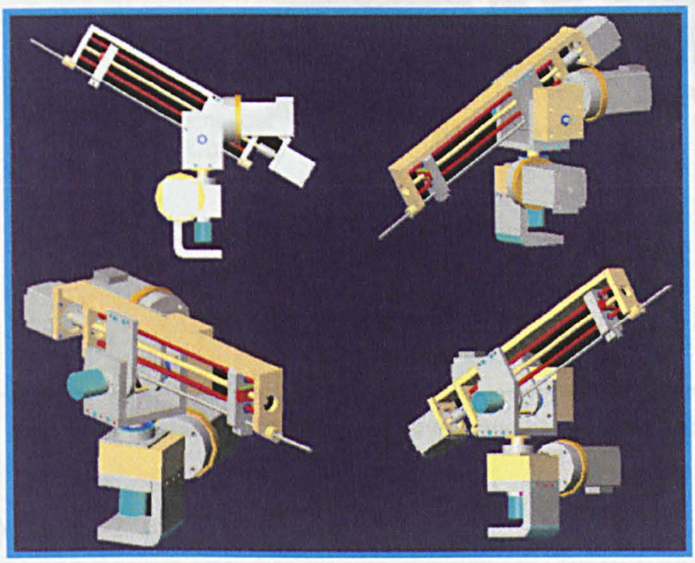

Figure 5.8: End-Effector's movements' illustration

5.5.1 End-Effector Joint-1

Joint-1 forms the "Back Bone" of the End-Effector and the link to an active or passive manipulation system [LERN 99]. It is a revolute joint which has an axis of rotation parallel to the Z axis and can rotate ±30°. It was designed to allow for fine and accurate manipulation. It comprises of (Figure 5.9): [ONDR 01][Appendix E: Data Sheets]

- Stepper motor
- Reduction gearbox

- Gearbox output shaft
- Optical encoder and coupling
- Radial thrust bearings
- Bearing housing
- Stepper motor - gearbox coupling
- Links and support components and fixtures

This joint is capable of supporting the weight and the movements of the other two joints and can overcome the inertial forces of the attached joints. Joint-1 is responsible for the rotation about the Z axis (rotation in the XY plane). The laser front end position and rotation angle are determined by an optical encoder attached at the output of the gearbox along the line of rotation.

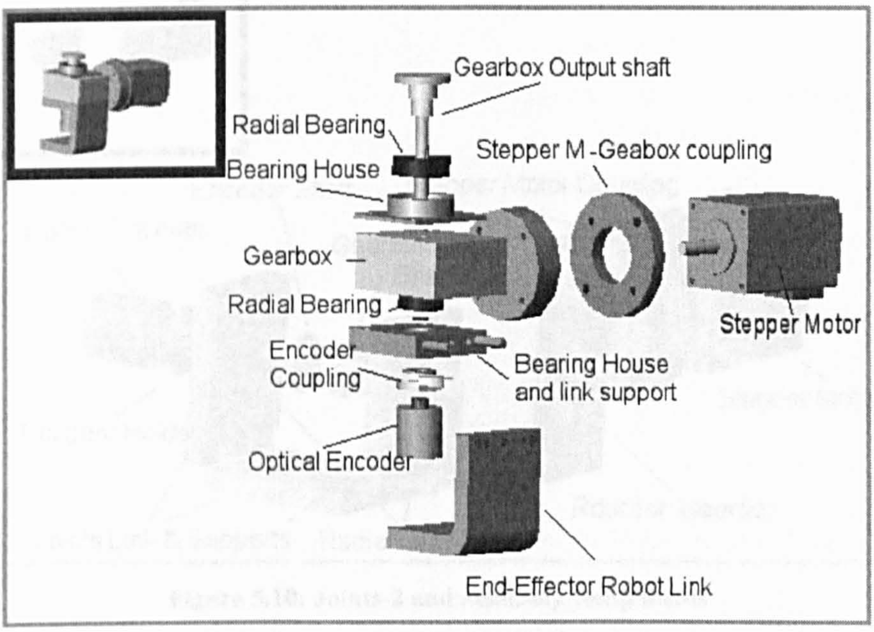

Figure 5.9: Joint 1 of the End-Effector assembly components

5.5.2 End-Effector Joint-2

Joint-2 is responsible for the vertical manipulation. It is a revolute joint [FU 87] which has an axis of rotation parallel to the X axis and can rotate ±30° for from a fixed zero point. This joint consists of:

- Stepper motor
- Reduction gearbox
- Optical encoder
- Gearbox output shaft
- Optical encoder input Shaft
- Radial thrust bearings

- Stepper motor - gearbox coupling
- Joint links and support components and fixtures

This joint forms the link between joint 1 and joint 3 and it supports the weight and movement of the components in joint 3. It is also responsible for the vertical manipulation of the laser waveguide [KOZO 96][WANG 97][MATS 00] by rotating about the X axis Figure 5.10. The optical encoder in joint-2 is connected along the line passing through the gearbox output shaft to directly measure the rotating angle and hence determine the laser front end position. The positioning of the encoder at the gearbox output allows for high resolution measurements thus reducing the positioning error.

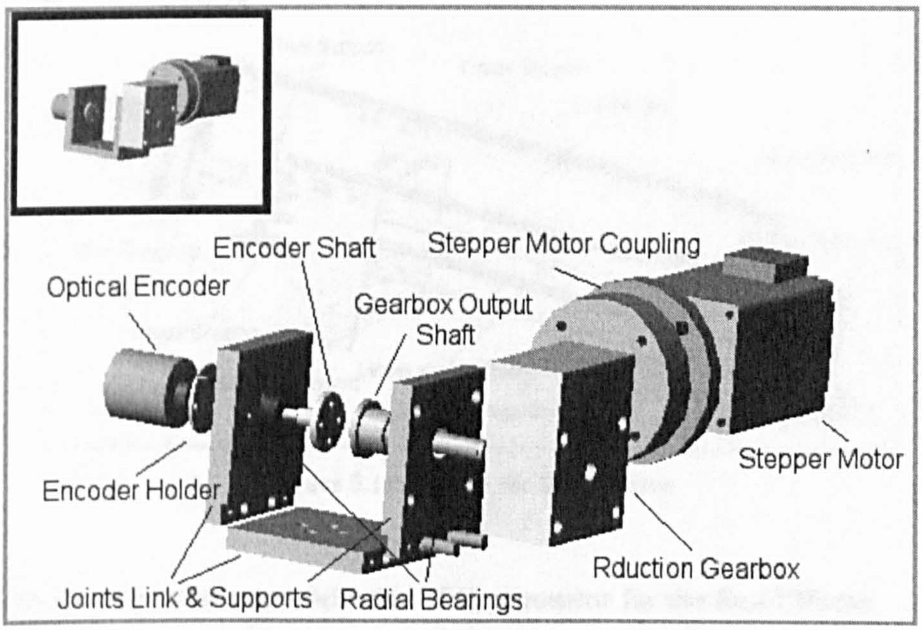

Figure 5.10: Joints-2 and assembly components

5.5.3 End-Effector Joint 3

The third joint is a prismatic one [FU 87]. It forms the third degree of freedom. This joint is mainly responsible for the linear manipulation and positioning of the laser waveguide in the Y axis direction during the surgical application. In this joint the power is transmitted by a stepper motor driven leadscrew [Appendix E: Data Sheets] forming a linear drive. This joint consists of (Figure 5.11):

- Stepper motor
- Anti-backlash Miniature leadscrew and nut combination
- Radial thrust bearings
- Bearing support housing
- Linear shaft-guides
- Linear bearings

- Laser waveguide
- Laser waveguide holder/driver unit
- Links and support components

Other supporting components include: laser waveguide and waveguide holders. Positioning in this joint is controlled by the number of pulses applied to the stepper motor; however, an additional linear encoder [Appendix E: Data Sheets] may be built into the design to give a more accurate linear position measurement.

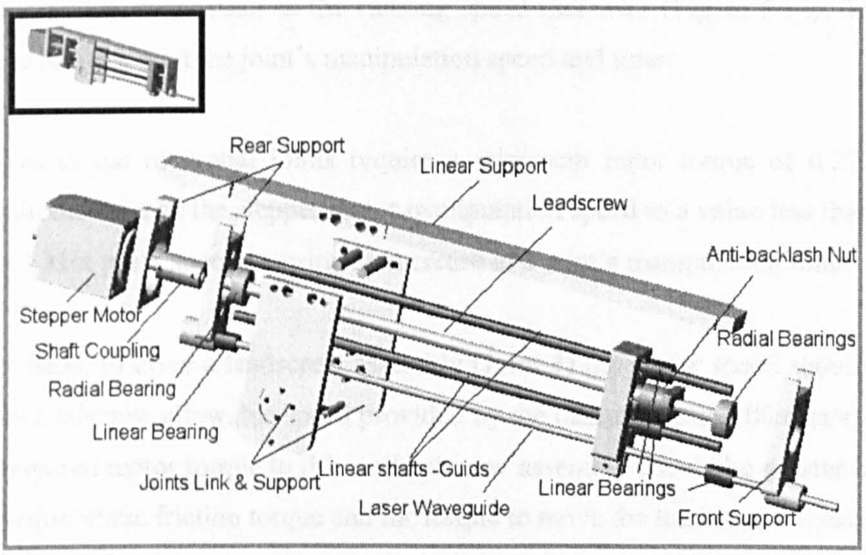

Figure 5.11: Joint 3 the linear drive

5.6 Design Considerations and Selection of Components for the End-Effector

All design components and parts were selected and designed according to the engineering requirements. Summarized below are some of the components applications, specifications and features.

5.6.1 The Stepper Motors

The stepper motors used in the design were selected to fulfil the engineering design requirements. They provide high output torque and accurate positioning with low power consumption. They were selected to provide the required power for the attached components and overcome their inertial forces and input torque. They also feature: [Appendix E: Data Sheets]

- Compact and low weight
- Step angle =1.8° per steps (200 steps / revolution)

- Excellent speed torque relation (to allow rotation at high speed while maintaining high output torque Figure 5.12)
- High torque per volume
- In addition to other control parameters such as rated voltage and current, and maximum control pulse frequency (15 kHz)

Motor Speed and Manipulation Time Limitations

The data provided by the stepper motor manufacturer, indicates a decrease in the motor's pullout torque [Appendix E: Data Sheets] as the running speed increases (Figure 5.12). This in effect imposes some limitation on the joint's manipulation speed and time.

The gearboxes at the rotational joints require a minimum input torque of 0.271 Nm. This gearbox requirement limits the stepper motor manipulation speed to a value less than or equal to 300 Rpm (or 1 kHz pulse speed) causing an increase in a joint's manipulation time.

On the other hand, to drive a leadscrew assembly (Joint 3) the motor speed should not exceed the maximum leadscrew allowable speed provided by the manufacturer (100 mm/s) [RELI 00][DAVA n.d.]. As the required motor torque to drive a leadscrew assembly should be greater than the sum of: inertial torque, static friction torque and the torque to move the load [Appendix E: Data Sheets] [RELI 00]. This is in addition to the torque values associated with the driving and supporting components such as the radial and linear bearings, and the coupling components. The calculations for the various torques of the leadscrew are as follows:

The leadscrew inertial torque (T_i)

$$T_i = I\alpha$$

where

I = inertia of the leadscrew (8.34×10^{-7} kgm^2)

α = Angular acceleration (rad/s^2) ($\alpha = 0$ for constant angular velocity (ω))

Leadscrew static friction torque (T_f)

According to manufacturer information [RELI 00], the miniature leadscrew used in the design have a typical static friction torque < 0.007Nm

Torque to move the load (T_l)

The torque to move a certain load is a function of the lead and the efficiency of the leadscrew assembly.

$$T_l = \frac{Load \times Lead}{2\pi \times Efficiency} Nm$$

where the lead for the selected leadscrew is 10.85 mm and the efficiency = 84%

For a given load of 1 N, T_l is approximately 0.002 Nm. Thus the overall leadscrew drive torque would be (0.009 Nm). Taking the above data and calculations into account while selecting the leadscrew assembly driving motor, one can see that the selected motor specifications fit the design requirements.

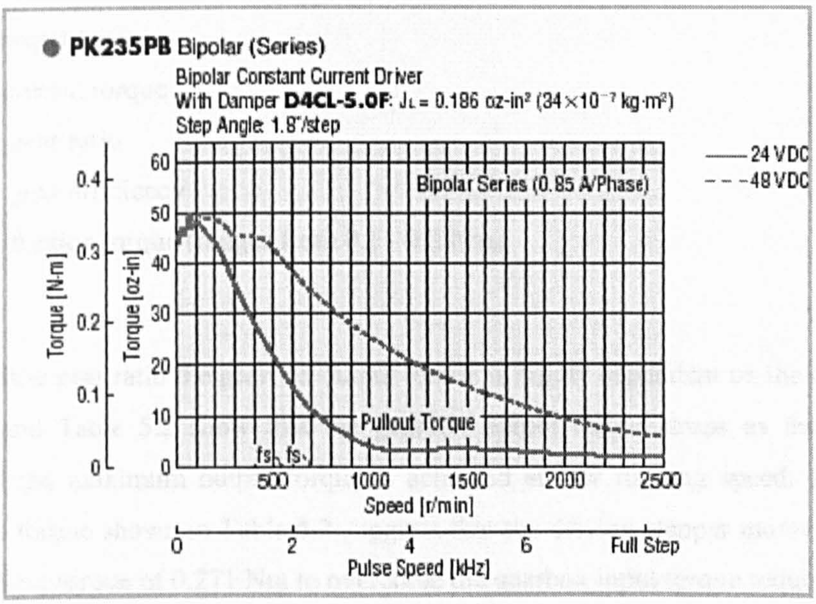

Figure 5.12: Stepper motor torque characteristics [Appendix E: Data Sheets]

5.6.2 The Reduction Gearbox

The selected reduction gearboxes [ONDR 01] provide high position accuracy of the End-Effector front end, and it magnifies the output torque of the attached stepper motors. It transmits the stepper motor output power to the moving parts at reduced speed and magnified torque [MERI 93]. The selected high gear ratio (120:1) allows for fine output resolution and precise manipulation. These gearboxes feature

- Compact and lightweight
- Low backlash value (8')
- High output torque
- High input speed
- Low cost

The net effect of backlash [ONDR 01][RELI 00][DAVA n.d.] on the front end of the cutting tool ranges from (0.29 - 0.75 mm) depending on the length of the laser waveguide. This effect may be eliminated by selecting an anti-backlash gearbox. The gearbox output power and torque parameters were selected based on inertial [MERI 93] and torque calculations for the moving parts of the End-Effector.

The Gearbox Input Torque Requirements

According to data provided by the gearbox manufacturer [ONDR 01], the required input torque can be calculated by the following equation:

$$T_{in} = \frac{T_{out}}{G_R \times G_E} + T_{Fr}$$

where

T_{in} is the input torque

T_{out} is the output torque

G_R is the gear ratio

G_E is the gear efficiency

T_{Fr} is the friction torque (ranges from 0.1 - 0.2 Nm)

In addition to the gear ratio the gearbox output torque is highly dependent on the running speed. Figure 5.10 and Table 5.2 show that the gearbox output torque drops as the motor speed increases and the maximum output torque is achieved at low running speed. The calculated gearbox input torque shown in Table 5.2 suggests that the driving stepper motor should have a minimum pullout torque of 0.271 Nm to overcome the gearbox input torque requirements.

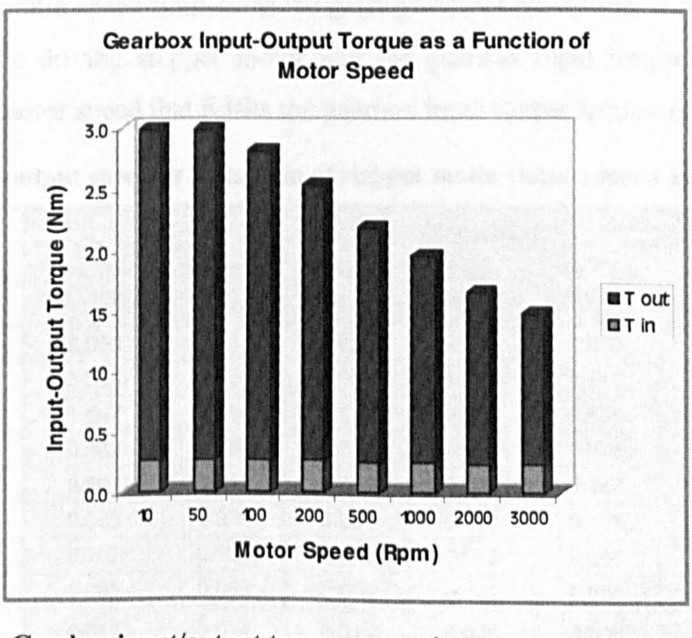

Figure 5.13: Gearbox input/output torque versus input speed at 120:1 gearbox ratio

Figure 5.13 shows that the gear box output torque drops as the motor speed increases, however, this torque decrease is not very significant within the range of operation.

Table 5.2: Gearbox Output Torque Nm [ONDR 01]

	Output Torque							Input Torque for Gear ratio =120:1			
Ratio / Rpm Input	" 10:1"	" 12:1"	"15:1"	"20:1"	"30:1"	"60:1"	"120:1"	Gear Efficiency	Gear Ratio	Friction Torque	Input Torque Max
3000	1.4	1.5	1.6	1.7	1.9	2.1	**1.25**	0.32	120	0.2	**0.233**
2000	1.7	1.7	1.8	1.8	2.1	2.4	**1.42**	0.32	120	0.2	**0.237**
1000	2.1	2.3	2.3	2.5	2.7	2.9	**1.7**	0.32	120	0.2	**0.244**
500	2.7	2.7	2.8	2.9	3.2	3.5	**1.94**	0.32	120	0.2	**0.251**
200	3.4	3.5	3.5	3.7	3.9	4.1	**2.27**	0.32	120	0.2	**0.259**
100	3.9	3.9	4.1	4.2	4.3	4.5	**2.55**	0.32	120	0.2	**0.266**
50	4.4	4.5	4.5	4.6	4.7	4.8	**2.72**	0.32	120	0.2	**0.271**
10	4.8	4.8	4.9	4.9	5	5	**2.72**	0.32	120	0.2	**0.271**

The Impact of Gearbox Ratio on Speed, Time and Resolution

The gearbox ratio has a very significant influence on the manipulation and positioning speed, time and resolution. As the gearbox ratio increases the output manipulation speed decreases causing an increase in positioning time. However, the best resolution can only be achieved by high gearbox ratio. Therefore, to select the proper gearbox one has to compromise for the positioning time to achieve best output resolution.

Gearbox Output Speed

The impact of gearbox ratio on the output speed is shown in Figure 5.14 and Table 5.3. In addition to the gear ratio speed limitations the gearbox output manipulation speed is also limited by the speed of the driving stepper motor and the gearbox input torque requirements. The maximum stepper motor speed that fulfils the gearbox input torque requirements is 300 Rpm.

Table 5.3: Gearbox output speed as a function of stepper motor (input) speed and gear ratio

Input Stepper Motor Speed (Rpm)	Output Speed						
	Rev/sec ratio = 10:1	Rev/sec ratio=12:1	Rev/sec ratio=15:1	Rev/sec ratio=20:1	Rev/sec ratio=30:1	Rev/sec ratio=60:1	Rev/sec ratio=120:1
3000	6.000	4.167	3.333	2.500	1.667	0.833	0.417
2000	3.333	2.778	2.222	1.667	1.111	0.556	0.278
1000	1.667	1.389	1.111	0.833	0.556	0.278	0.139
500	0.833	0.694	0.556	0.417	0.278	0.139	0.069
300*	**0.500**	**0.417**	**0.333**	**0.250**	**0.167**	**0.083**	**0.042**
200	0.333	0.278	0.222	0.167	0.111	0.056	0.028
100	0.167	0.139	0.111	0.083	0.056	0.028	0.014
50	0.083	0.069	0.056	0.042	0.028	0.014	0.007
10	0.017	0.014	0.011	0.008	0.006	0.003	0.001

* Maximum running speed

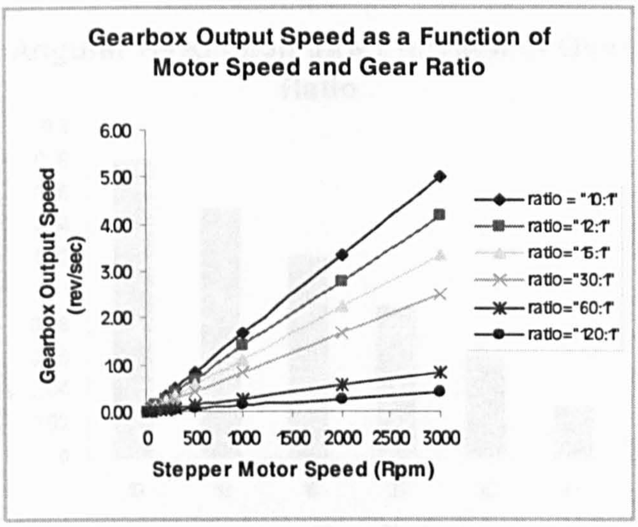

Figure 5.14: The impact of gear ratio on the gearbox output manipulation speed

Gearbox Positioning Resolution

The gearbox positioning resolution is highly affected by the gear ratio and the linear positioning distance from the origin of manipulation. Table 5.4 shows that high gear ratio feature small angular resolution per step which indicates a fine positioning resolution. The gearbox positioning resolution is also controlled by the distance of the laser front end to the origin of manipulation as shown in Figure 5.16. The figure shows that the best resolutions are achieved at high gear ratio and smaller positioning distance.

Table 5.4: Gearbox angular and positioning resolution

	Input	Output						
Gear Ratio : 1		10	12	15	20	30	60	120
Step Angle (θ °)	1.8	0.18	0.15	0.120	0.090	0.060	0.030	0.015
Step Angle ((θ rad)	0.031416	0.00314	0.00262	0.00209	0.00157	0.00105	0.00052	0.00026
	Distance [r]	Positioning Resolution= 2rsin((θ/2) mm						
	200 mm	0.628	0.524	0.419	0.314	0.209	0.105	0.052
	240 mm	0.754	0.628	0.503	0.377	0.251	0.126	0.063
	280 mm	0.880	0.733	0.586	0.440	0.293	0.147	0.073
	320 mm	1.005	0.838	0.670	0.503	0.335	0.168	0.084
	360 mm	1.131	0.942	0.754	0.565	0.377	0.188	0.094

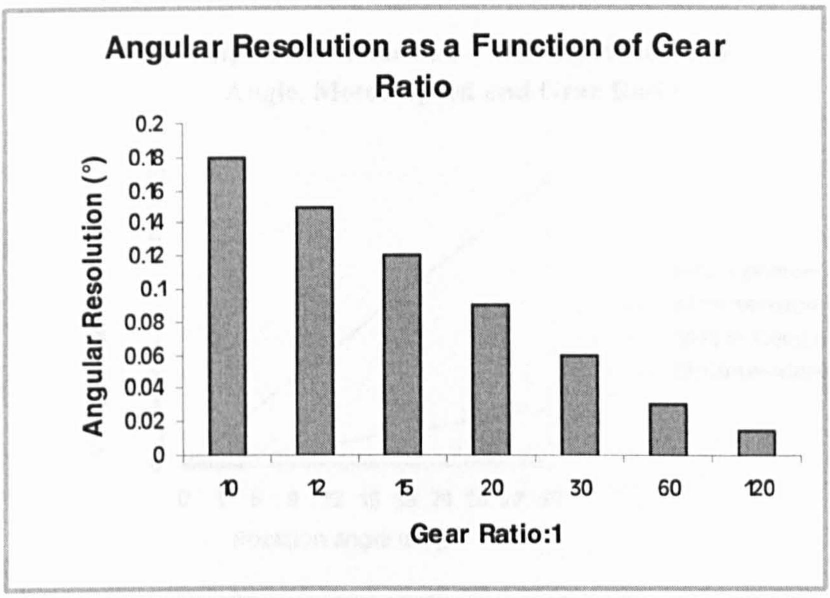

Figure 5.15: Angular resolution (Step Angle) as a function of gear ratio

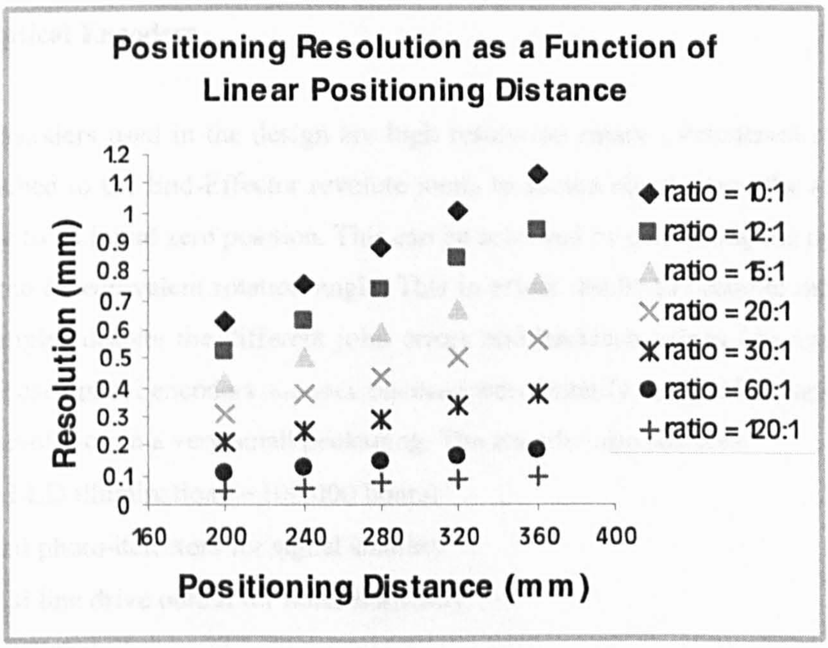

Figure 5.16: Gearbox positioning resolution as a function of gear ratio and linear positioning distance

<u>Gearbox Positioning Time</u>

The gearbox positioning time is a function of gearbox ratio, stepper motor speed and the manipulation angle. As the gearbox ratio increases its output speed deceases causing an increase in positioning time (Figure 5.17). Similarly an increase in manipulation angle results in an increase in positioning time. Figure 5.17 shows the effect of gear ratio on the manipulation time. Figure 5.17 shows that better (shorter) manipulation time can be achieved at a low gear ratio, however, a lower gear ratio results in a larger positioning resolution Figure 5.16.

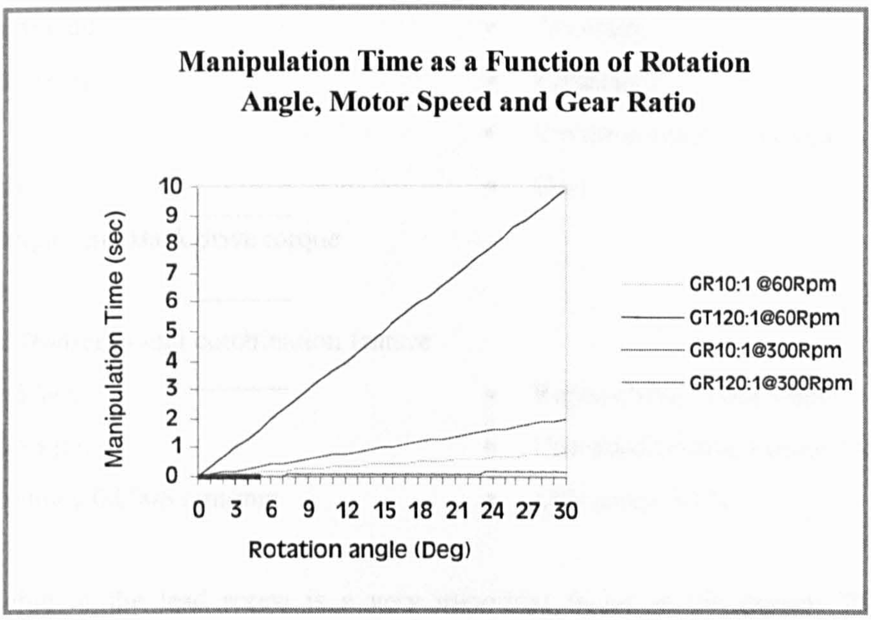

Figure 5.17: Manipulation time as a function of gear ration manipulation speed and rotation angle

5.6.3 The Optical Encoders

The optical encoders used in the design are high resolution rotary incremental mini-encoders. They are attached to the End-Effector revolute joints to accurately measure the joint's rotation angles relative to an initial zero position. This can be achieved by converting the optical encoder output data into an equivalent rotation angle. This in effect results in accurate measurement of the rotation angles despite the different joint errors and backlash values (discussed further in Chapter 7). These optical encoders [Appendix E: Data Sheets] were initially designed for applications that require high resolution in a very small packaging. The encoder also features:

- Long life LED illumination (> 100,000 hours)
- Differential photo-detectors for signal stability
- Differential line drive output for noise immunity
- Zero index signal
- Monolithic integrated ASIC for internally interpolated resolution up to 10,240 cycles /rev (40,960 counts /rev)

The optical encoders play important roles in measuring the positioning and orientation of the laser front end by sending real time data to the PC-based control unit.

5.6.4 Miniature Anti-backlash Leadscrew-Nut Combination (Joint 3)

Many factors contributed to the selection of the leadscrew – nut combination used in the design of Joint 3 (the linear drive). These factors include: [ONDR 01][RELI 00]

- Maximum load
- Traverse speed
- Lead
- Backlash
- Drive torque and Back drive torque
- Accuracy
- Efficiency
- Environmental constraints
- Cost

The selected leadscrew-nut combination feature

- Zero backlash
- Lead 10.85 mm
- Lead accuracy 0.0006 mm/mm
- Repeatability 0.0015 mm
- Unloaded friction torque < 0.007 Nm
- Efficiency 84 %

The lead value of the lead screw is a very important factor in the design. This value in combination with the stepper motor specification can determine the maximum resolution and the positioning time as follows:

Linear Positioning Resolution (*R*)

$$R = \frac{Lead(mm/rev)}{Steps/rev} \quad \text{mm/step}$$

Linear Positioning Time (*PT*)

$$PT = \frac{D(mm)}{LPS(mm/\sec)} \qquad \text{sec}$$

where

D is the leadscrew distance of travel from the origin of rotation

LPS is the linear drive positioning speed which can be calculated as follow

Linear Positioning Speed (*LPS*)

$$LPS = MotorSpeed(rev/\min) \times \frac{Lead(mm/rev)}{60(\sec/\min)} \qquad \text{mm/sec}$$

The data provided by the leadscrew manufacturer [RELI 00] suggests that the maximum allowable linear traverse speed is 100 mm/sec. However, the drive torque requirements for the leadscrew assembly limit the traverse speed to a much lower value.

The maximum linear traverse speed is controlled by the stepper motor speed and the leadscrew lead value. The figures in Table 5.5 show the effect of the lead value on the manipulation and positioning speed, the positioning time, and the linear positioning resolution. These figures show that a larger lead value allows for faster manipulation and less positioning time; yet they provide a larger positioning resolution. Thus, while choosing the specific leadscrew for the design, the speed, time and resolution requirements were taken into account.

Table 5.5: The affect of the leadscrew lead value on the linear positioning resolution manipulation speed and positioning time

Lead = 0.5 mm/rev Linear Positioning Resolution = 2.5 μm Maximum Linear Traverse Speed =100mm/s or 12000 rev/min Max. Travel Distance = 160 mm (200-360mm)	Lead = 10.85 mm/rev Linear Positioning Resolution = 54.25 μm Maximum Linear Traverse Speed =100mm/s or 553 rev/min Max. Travel Distance = 160 mm (200-360mm)
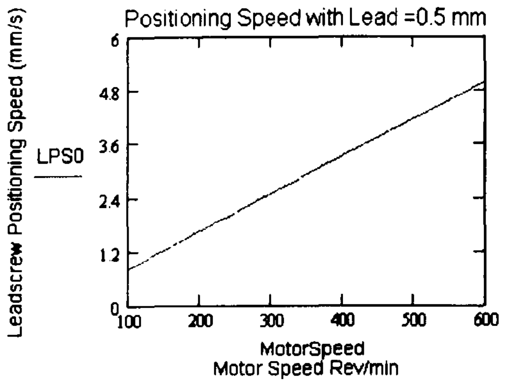 **Figure 5.18: Positioning speed as a function of stepper motor speed with Lead = 0.5 mm**	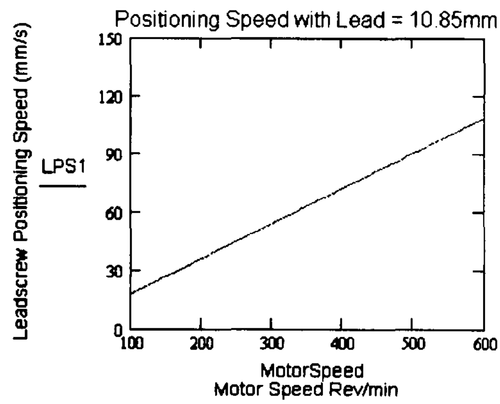 **Figure 5.19: Positioning speed as a function of stepper motor speed with Lead = 10.85 mm**
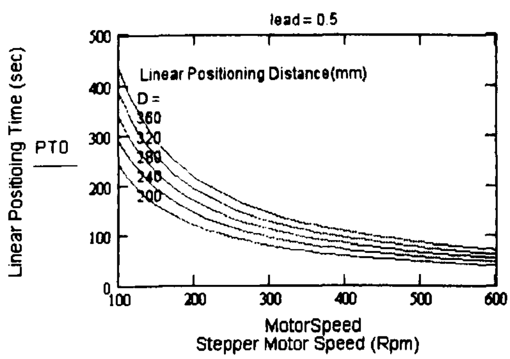 **Figure 5.20: Linear drive positioning time as a function of stepper motor speed and linear positioning distance (D) with Lead = 0.5 mm**	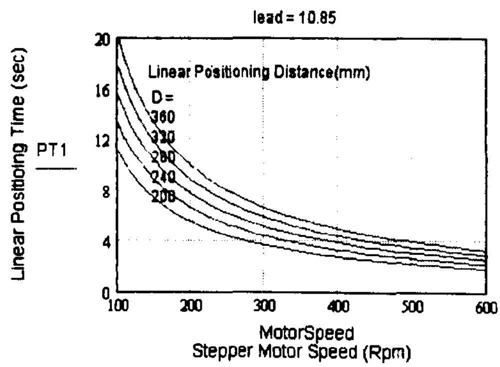 **Figure 5.21: Linear drive positioning time as a function of stepper motor speed and linear positioning distance (D) with Lead = 10.85 mm**

The above specifications suggest that the leadscrew assembly can provide laser front end positioning at high speed and accuracy with a maximum resolution of ~54 μm.

5.6.5 Design Considerations between the Gearbox, Stepper Motor and Leadscrew

Together the gearbox, stepper motor and leadscrew combination set up the final resolution and accuracy of the End-Effector laser front end.

The uniqueness of the design is that the axes extensions of all the joints meet in a single point namely the "Origin" of manipulation (Figure 5.22). This in affect governs the manipulation of the End-Effector and limits its workspace to a spherical movement. This spherical movement may have many inherent advantages

- End-Effector movement can be broken-down into easily quantified and defined individual movements
- Reduced positioning error since multi-axis movements are not required for positioning

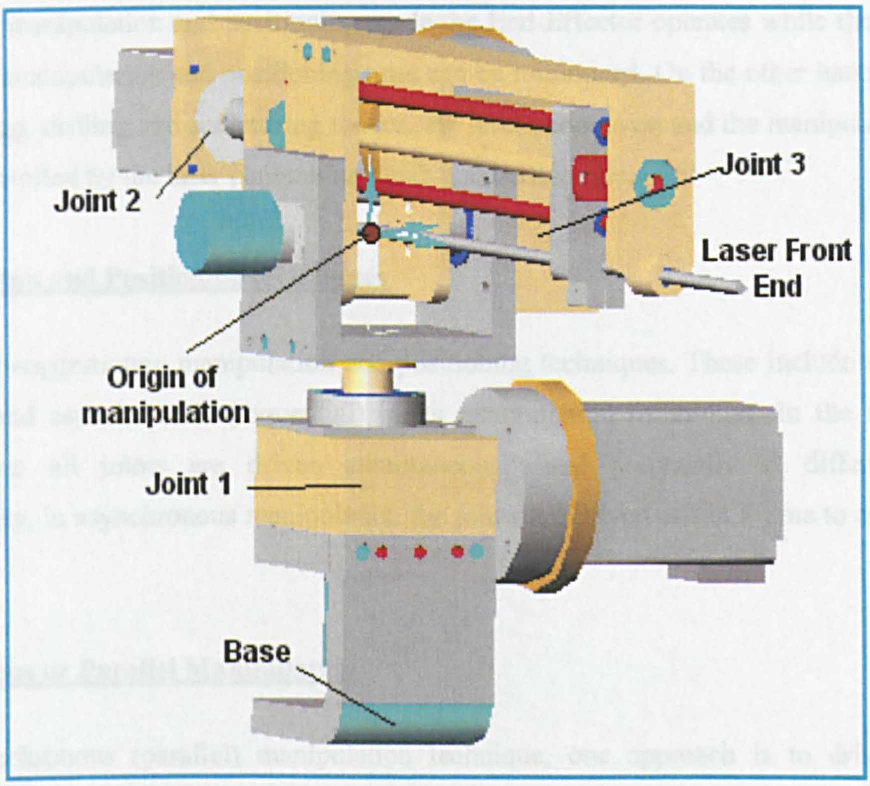

Figure 5.22: This Figure shows that the axes extensions of all three joints meet in a single Origin

The stepper motors can be driven either independently or together with the other motors depending on the specific application.

5.6.5.1 The Total Manipulation and Positioning Time

There are many factors involved in the total manipulation and positioning time of the laser End-Effector. These include the rotation angles, linear positioning displacement, gearbox gear ratio, leadscew specifications, and stepper motor's running speed. Another major factor that affects the total manipulation time is the laser cutting or drilling rate. This may involve laser pulse rate (f), spot size (ϕ), power (W) and the amount of pulse overlap (n) and this was discussed in

Chapter 4. The total manipulation and positioning time while the laser is off is expected to be much less than the surgical application time while the laser is on because laser front manipulation is more or less continuous during bone. The laser End-Effector can operate in four different modes. These include:

- Manipulation and positioning mode
- Tissue cutting mode
- Tissue drilling mode
- Sculpturing mode

During the manipulation and positioning mode the End-Effector operates while the laser beam is off, thus manipulation and positioning time can be minimised. On the other hand, during the tissue cutting, drilling and sculpturing modes, the laser beam is on and the manipulation time is mainly controlled by the laser penetration depth and cutting rate.

Manipulation and Positioning techniques

The author suggests two manipulation and positioning techniques. These include synchronous (parallel) and asynchronous (sequential) joints manipulation techniques. In the synchronous manipulation all joints are driven simultaneously and potentially at different speeds. Alternatively, in asynchronous manipulation the joints are driven one at a time to reach the end position.

Synchronous or Parallel Manipulation

In the synchronous (parallel) manipulation technique, one approach is to drive all joints concurrently so that they all reach the end target position at the same time. This implies that the time required for the laser front end to move from one point to another is equal to the manipulation time of a single joint only.

$$T_{\mathrm{Sync}} = T_{\mathrm{joint1}} = T_{\mathrm{joint2}} = T_{\mathrm{joint3}}$$

where

T_{Sync} is the total synchronous manipulation time

T_{joint1} is Joint 1 manipulation time

T_{joint2} is Joint 2 manipulation time

T_{joint3} is Joint 3 manipulation Time

This parallel technique suggests that the θ rotation at Joint 1, α rotation at Joint 2 and LD displacement at Joint 3 take place simultaneously in a minimum possible time T_{Sync}. The manipulation time is controlled by the motors speed, rotation angles and/or the linear displacement distance as well as the End-Effector components specifications [Appendix E: Data Sheets]. The joints' manipulation time can be calculated as follows assuming maximum manipulation stepper motor speed equal to 1000 P/sec or 300 Rpm:

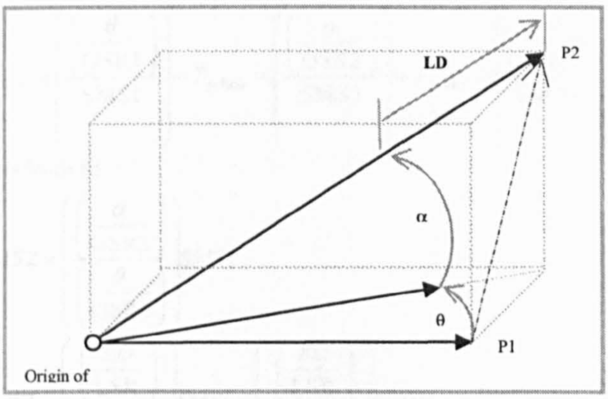

Figure 5.23: End-Effector manipulation from position P1 to P2

$$T_{joint1} = \left(\frac{\left(\dfrac{\theta}{\text{Gearbox Step Resolution}} \right)}{\text{Stepper Motor Speed (P/sec)}} \right) \text{(sec)}$$

$$T_{joint2} = \left(\frac{\left(\dfrac{\alpha}{\text{Gearbox Step Resolution}} \right)}{\text{Stepper Motor Speed (P/sec)}} \right) \text{(sec)}$$

$$T_{joint3} = \left(\frac{\left(\dfrac{LD}{\text{Leadscew Step Resolution}} \right)}{\text{Stepper Motor Speed (P/sec)}} \right) \text{(sec)}$$

An alternative approach for synchronous mode, is to drive the stepper motors at a fixed speed. Thus the total manipulation time will be equal to the maximum manipulation time of the single joints (i.e $T_{Sync} = \mathbf{Max}(T_{joint1}, T_{joint2}, T_{joint3})$). This is illustrated in Table 5.6.

Table 5.6: The manipulation time as all joints runs at the same speed (Laser off)

Variables GOS =Gearbox output Speed			M Speed R/m	M Pulse Rate	GOS R/s	Tj1 (s)	Tj2 (s)	Tj3(L2) (s)	Tj3(L1) (s)	SynchL2. Time (s)	Asynch. Time(s)
Lead1 (mm)	**L1**	**0.5**	30	100	0.00417	20.00	20.00	29.49	640.00	**29.49**	**69.49**
Lead2 (mm)	**L2**	**10.9**	60	200	0.00833	10.00	10.00	14.75	320.00	**14.75**	**34.75**
Gear Ratio		**120:1**	90	300	0.01250	6.67	6.67	9.83	213.33	**9.83**	**23.16**
Gearbox resolution(°)		**0.015**	120	400	0.01667	6.00	6.00	7.37	160.00	**7.37**	**17.37**
Rotation about Z (θ°)		**30**	150	500	0.02083	4.00	4.00	6.90	128.00	**6.90**	**13.90**
Rotation about X (α°)		**30**	180	600	0.02500	3.33	3.33	4.92	106.67	**4.92**	**11.58**
Linear distance (mm)		**160**	210	700	0.02917	2.86	2.86	4.21	91.43	**4.21**	**9.93**
Length of laser waveguide Min.		200	240	800	0.03333	2.50	2.50	3.69	80.00	**3.69**	**8.69**
Length of laser waveguide Max.		360	270	900	0.03750	2.22	2.22	3.28	71.11	**3.28**	**7.72**
Leadscrew Resolution (mm)		**0.0543**	300	1000	0.04167	2.00	2.00	2.95	64.00	**2.95**	**6.95**

For the manipulation time to be identical in all joints, the actuators attached to the joints may have to be driven at different speed. The speed relation between the joints can be found from the following equations.

$$T_{joint1} = \left(\frac{\left(\frac{\theta}{\mathrm{GSR1}} \right)}{\mathrm{SMS1}} \right) = T_{joint2} = \left(\frac{\left(\frac{\alpha}{\mathrm{GSR2}} \right)}{\mathrm{SMS2}} \right) = T_{joint3} = \left(\frac{\left(\frac{LD}{\mathrm{LSR}} \right)}{\mathrm{SMS3}} \right)$$

This leads to

$$SMS2 = \left(\frac{\left(\frac{\alpha}{\mathrm{GSR2}} \right)}{\left(\frac{\theta}{\mathrm{GSR1}} \right)} \right) SMS1$$

$$SMS3 = \left(\frac{\left(\frac{LD}{\mathrm{LSR}} \right)}{\left(\frac{\theta}{\mathrm{GSR1}} \right)} \right) SMS1 = \left(\frac{\left(\frac{LD}{\mathrm{LSR}} \right)}{\left(\frac{\alpha}{\mathrm{GSR2}} \right)} \right) SMS2$$

$$SMS2 = \left(\frac{\frac{\alpha}{0.015}}{\frac{\theta}{0.015}} \right) SMS1 = \left(\frac{\alpha}{\theta} \right) SMS1$$

$$SMS3 = \left(\frac{\frac{LD}{0.054}}{\frac{\theta}{0.015}} \right) SMS1 = \left(\frac{LD/3.617}{\theta} \right) SMS1 = \left(\frac{LD/3.617}{\alpha} \right) SMS2$$

where GSR is the gearbox step resolution and SMS is the stepper motor speed.

For parallel manipulation where all joints operate and stop simultaneously, the above speed relation must be taken into account during calculating the motors running speeds. However, one must take into consideration that the maximum manipulation speed must not exceed the maximum design requirements (300 Rpm or 1000 P/s). In this case the manipulation time would be $T_{Sync} = T_{joint1} = T_{joint2} = T_{joint3}$ as shown in Table 5.7

Table 5.7: Manipulation time and joints motor speed relations for maximum manipulation

Variables			SMS1 P/s	SMS2 P/s	SMS3 P/s	Tj1 sec	Tj2 sec	Tj3(lead2) Sec	SynchL2. Time (sec)	Asynch. Time(sec)
Lead (mm)	L1	0.5	67.82	67.82	100	29.49	29.49	29.49	**29.49**	**88.47**
	L2	**10.85**	136.64	136.64	200	14.74	14.74	14.75	**14.75**	**44.24**
Gear Ratio		**120:1**	203.46	203.46	300	9.83	9.83	9.83	**9.83**	**29.49**
Gearbox resolution(°)		**0.015**	271.28	271.28	400	7.37	7.37	7.37	**7.37**	**22.12**
Rotation about Z (θ°)	**MAX**	**30**	339.09	339.09	500	6.90	6.90	6.90	**6.90**	**17.69**
Rotation about X (α°)	**MAX**	**30**	406.91	406.91	600	4.92	4.92	4.92	**4.92**	**14.75**
Linear distance (mm)	**MAX**	**160**	474.73	474.73	700	4.21	4.21	4.21	**4.21**	**12.64**
Min laser waveguide length (mm).		200	542.55	542.55	800	3.69	3.69	3.69	**3.69**	**11.06**
Max laser waveguide length (mm).		360	610.37	610.37	900	3.28	3.28	3.28	**3.28**	**9.83**
Leadscrew resolution		**0.0543**	678.19	678.19	1000	2.95	2.95	2.95	**2.95**	**8.85**

Asynchronous or sequential manipulation mode

In the asynchronous (sequential) mode, the total manipulation time is equal to the overall sum of the time required for individual joint's manipulation. This is illustrated by the equation below which assumes no switching time delay between joint movements.

$$T_{\text{Async}} = T_{\text{joint1}} + T_{\text{joint2}} + T_{\text{joint3}}$$

where T_{Async} is the total asynchronous (sequential) manipulation time

The above equation indicates that the total manipulation time is the maximum during the asynchronous manipulation technique Table 5.6 and Table 5.7. Depending on the application and the operation mode, one may choose either of the above techniques.

5.7 Kinematics

The laser End-Effector can be modelled as an open loop system with 3 degrees of freedom. These degrees of freedom are generated by 2 revolute joints and one linear joint connected together with rigid links and driven by stepper motors. One end of the End-Effector is connected to a supporting base with the other end having a laser waveguide. The relative motion of the joints results in the positioning of the "Front End" of the laser waveguide in a desired location and orientation. This section addresses the analytical description of the spatial displacement of the laser End-Effector as a function of time, joint space and the Front End position and orientation. It also addresses the forward and inverse kinematics problems of the End-Effector (Figure 5.24).

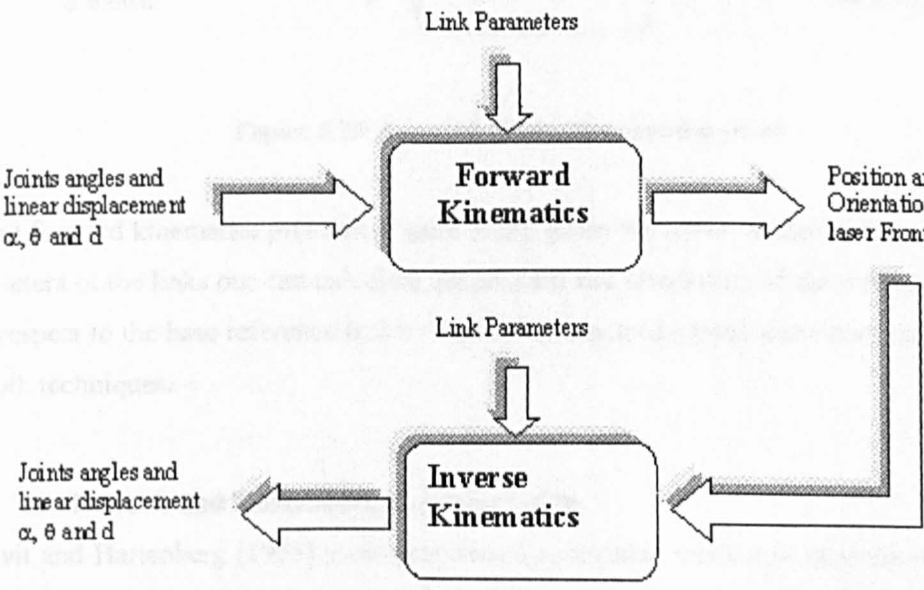

Figure 5.24: The forward and inverse kinematics problems of the End-Effector [FU 87]

5.7.1 The Forward Kinematics

Since the links of the End-Effector may rotate /or translate with respect to a base reference coordinate system of the End-Effector, the total spatial displacement of the laser front end is due to the angular rotations and linear translation of the links. This section presents two techniques to describe and represent the spatial geometry of the links within the End-Effector with respect to a fixed reference frame.

The first technique is the standard Denavit and Hartenberg [FU 87][BALA n.d.] representation. This technique is a systematic and generalized approach that uses matrix algebra to describe and represent the spatial geometry of the robotic links.

The second technique is an intuitive geometric approach which takes advantage of the fact that the three joints share the same origin for manipulation. This technique was derived by the author to represent the spatial geometry of the End-Effector links and joints with respect to a fixed reference frame (the base coordinate system). This is a more straightforward approach than the Denavit and Hartenberg approach but it gives similar results. Hence, this second technique is used more during the analysis presented in this thesis.

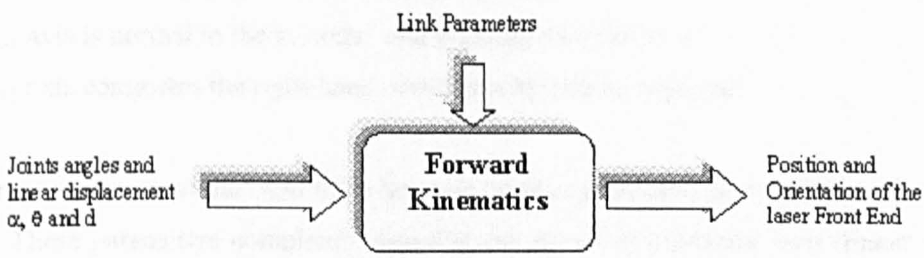

Figure 5.25: Forward kinematics problem [FU 87]

For the forward kinematics problem (Figure 5.25), given the joints' angles and linear translation parameters of the links one can calculate the position and orientation of the waveguide front end with respect to the base reference frame. This following subsections show how this can be done for both techniques.

5.7.2 The Denavit and Hartenberg Representation

Denavit and Hartenberg [1955] [FU 87] proposed a systematic method to describe the translation and rotation relationships between adjacent links within a kinematic chain with respect to a fixed reference frame. This method uses homogenous transformation matrices to describe the spatial relationships. In the forward kinematics the Denavit and Hartenberg (D-H) representation results in a 4×4 homogeneous transformation matrix representing each link's coordinate system at the joint with respect to the previous link's coordinate system. Using this method the forward kinematics problem of the End-Effector is simplified through sequential transformation to a 4×4 homogeneous transformation matrix [FU 87][BALA n.d.]. This matrix describes the relation between the Front End of the laser waveguide and the Base coordinate system of the End-Effector [FU87].

In the D-H representation an orthonormal Cartesian coordinate system ($\mathbf{x}_i$, $\mathbf{y}_i$, $\mathbf{z}_i$) can be established for each link at its joint axis where i =1,2,3….n (n=number of degrees of freedom plus the base coordinate frame). The Base coordinates of the End-Effector are defined as the 0th coordinate frame ($\mathbf{x}_0$, $\mathbf{y}_0$, $\mathbf{z}_0$) which is also the inertial coordinate frame of the End-Effector. The spatial description of the Front End of the laser waveguide relative to the fixed Base coordinate system is shown in Figure 5.26. This spatial description may indicate that the End-Effector has more than 3 Degrees of freedom, However, since the extension of all joints meet at the single point namely the Origin, the End-Effector is limited only to 3 degrees of freedom with 3 joints and 3 links.

In the D-H representation every coordinate frame is determined and established on the basis of three rules [FU 87]:

1. The z_{i-1} axis lies along the axis of motion of the *i*th joint
2. The x_{i-1} axis is normal to the z_{i-1} axis, and pointing away from it
3. The y_{i-1} axis completes the right-hand coordinate system as required

The D-H representation of the rigid links depends on four geometric parameters associated with each link. These parameters completely describe any revolt or prismatic joint (linear joint) [FU 87][BALA n.d.].

θ_i is the joint angle from the x_{i-1} axis to the x_i axis about the z_{i-1}axis (using the right hand rule.

d_i is the distance from the origin of the $(i\text{-}1)^{th}$ coordinate frame to the intersection of the z_{i-1}axis with the x_i axis along the z_{i-1} axis

a_i is the offset distance from the intersection of the z_{i-1}axis with the xi axis to the origin of the i^{th} frame along the x_i (or the shortest distance between the z_{i-1} and the z_i axes)

α_i is the offset angle from the z_{i-1}axis to the z_i axis about the x_i axis (using the right hand rule.

Once the D-H coordinate system has been established for each link and the joints and link parameters are found, the homogenous transformation matrix can be developed to relate the i^{th}

coordinate frame to the (i-1)th coordinate frame. The resulting homogenous transformation matrix (${}^{i-1}A_i$) is a composite of four basic rotation-translation matrices and can be determined as follow:

$$^{i-1}A_i = T_{z,d}T_{z,\theta}T_{x,a}T_{x,\alpha}$$

where

$T_{z,d}$ is the translation along the z_{i-1} axis a distance of d_i to bring the x_{i-1} and x_i axes in coincidence.

$T_{z,\theta}$ is the rotation about the z_{i-1} axis an angle of θ_i to align the x_{i-1} axis with the x_i axis

$T_{z,a}$ is the translation along the x_i axis a distance of a_i to bring the two origins as well as the x axis into coincidence.

$T_{x,\alpha}$ is the rotation about the x_i axis and the angle of α_i to bring the two coordinate systems into coincidence.

$$^{i-1}A_i = T_{z,d}T_{z,\theta}T_{x,a}T_{x,\alpha}$$

$$^{i-1}A_i = \begin{bmatrix} 1 & 0 & 0 & 0 \\ 0 & 1 & 0 & 0 \\ 0 & 0 & 1 & d_i \\ 0 & 0 & 0 & 1 \end{bmatrix} \begin{bmatrix} \cos\theta_i & -\sin\theta_i & 0 & 0 \\ \sin\theta_i & \cos\theta_i & 0 & 0 \\ 0 & 0 & 1 & 0 \\ 0 & 0 & 0 & 1 \end{bmatrix} \begin{bmatrix} 1 & 0 & 0 & a_i \\ 0 & 1 & 0 & 0 \\ 0 & 0 & 1 & 0 \\ 0 & 0 & 0 & 1 \end{bmatrix} \begin{bmatrix} 1 & 0 & 0 & 0 \\ 0 & \cos\alpha_i & -\sin\alpha_i & 0 \\ 0 & \sin\alpha_i & \cos\alpha_i & 0 \\ 0 & 0 & 0 & 1 \end{bmatrix}$$

Thus

$$^{i-1}A_i = \begin{bmatrix} \cos\theta_i & -\cos\alpha_i \sin\theta_i & \sin\alpha_i \sin\theta_i & a_i \cos\theta_i \\ \sin\theta_i & \cos\alpha_i \sin\theta_i & -\sin\alpha_i \cos\theta_i & a_i \sin\theta_i \\ 0 & \sin\alpha_i & \cos\alpha_i & d_i \\ 0 & 0 & 0 & 1 \end{bmatrix}$$

Where $\alpha_i, \theta_i, a_i,$ *and* d_i are the joints parameters of the End-Effector. For the rotary joints1 and 2 of the End-Effector the joint parameters $\alpha_i, a_i,$ *and* d_i remain constant while θ_i is the joint variable that changes when the link *i* moves with respect to link *i*-1. However, for the linear or prismatic joint (joint 3), the joint parameters $\alpha_i, \theta_i,$ *and* a_i remain constant while d_i is the joint variable.

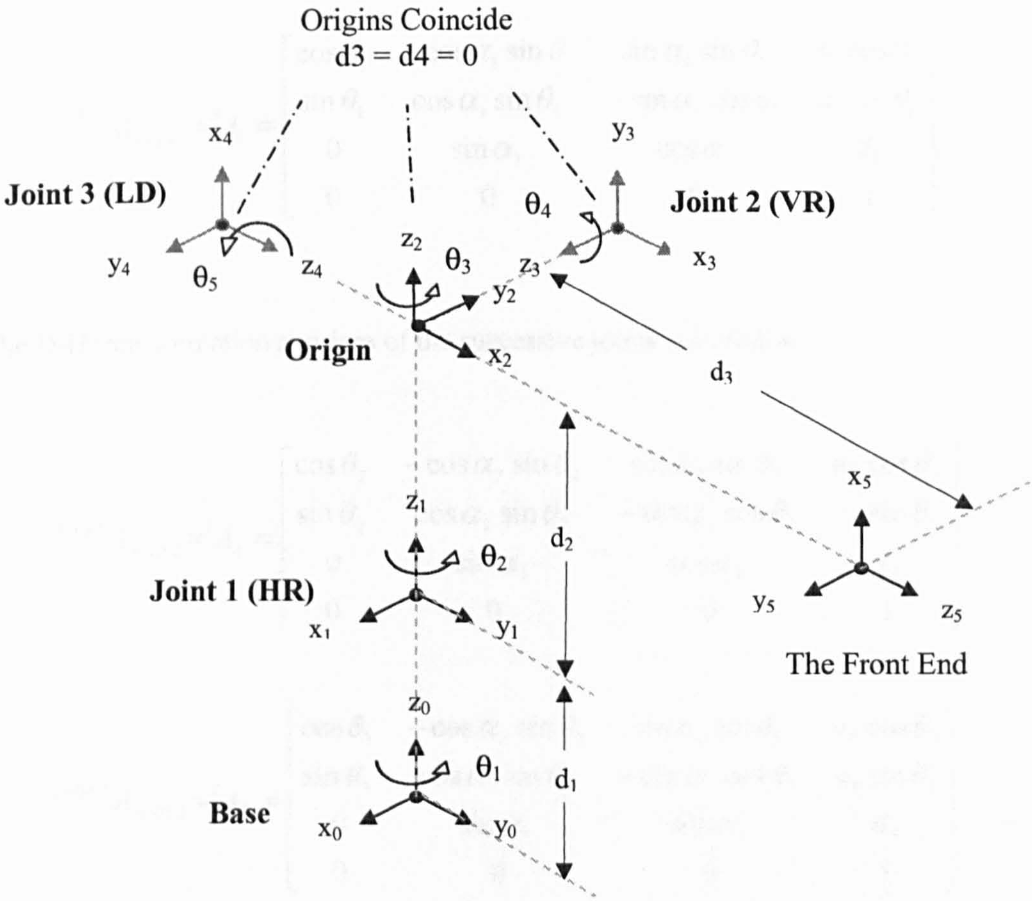

Figure 5.26: The spatial description of the Front End of the laser waveguide with respect to the Base coordinate system

For the forward kinematic problem of the End-Effector the D-H transformation matrices can be applied to relate the Front End of the laser waveguide to the Base coordinate frame of the End-Effector. This can be done by establishing the link coordinate system of the End-Effector, and finding the joint coordinate parameters Figure 5.26 and Figure 5.27.

End-Effector link parameters				
Joint i	**θ_i *rad***	**α_I *rad***	**a_i *(mm)***	***i (mm)***
1	0	0	0	59
2	$\pi/2$	0	0	57.25
3	0	$\pi/2$	0	0
4	$\pi/2$	$\pi/2$	0	0
5	0	0	0	D5

Figure 5.27: Establishing link coordinate system of the laser End-Effector

Assuming the Base coordinate system is established at point (0, 0, 0), the D-H transformation matrix for joint 1 coordinate frame and the Base coordinate frame (${}^{Base}A_{joint1}$) can be found as follow [Appendix B: MathCAD Work].

$$
{}^{Base}A_{joint\,1} = {}^{0}A_{1} = \begin{bmatrix} \cos\theta_1 & -\cos\alpha_1 \sin\theta_1 & \sin\alpha_1 \sin\theta_1 & a_1 \cos\theta_1 \\ \sin\theta_1 & \cos\alpha_1 \sin\theta_1 & -\sin\alpha_1 \cos\theta_1 & a_1 \sin\theta_1 \\ 0 & \sin\alpha_1 & \cos\alpha_1 & d_1 \\ 0 & 0 & 0 & 1 \end{bmatrix}
$$

And the D-H transformation matrices of the successive joints is as follow

$$
{}^{joint\,1}A_{joint\,2} = {}^{1}A_{2} = \begin{bmatrix} \cos\theta_2 & -\cos\alpha_2 \sin\theta_2 & \sin\alpha_2 \sin\theta_2 & a_2 \cos\theta_2 \\ \sin\theta_2 & \cos\alpha_2 \sin\theta_2 & -\sin\alpha_2 \cos\theta_2 & a_2 \sin\theta_2 \\ 0 & \sin\alpha_2 & \cos\alpha_2 & d_2 \\ 0 & 0 & 0 & 1 \end{bmatrix}
$$

$$
{}^{joint\,2}A_{joint\,3} = {}^{2}A_{3} = \begin{bmatrix} \cos\theta_3 & -\cos\alpha_3 \sin\theta_3 & \sin\alpha_3 \sin\theta_3 & a_3 \cos\theta_3 \\ \sin\theta_3 & \cos\alpha_3 \sin\theta_3 & -\sin\alpha_3 \cos\theta_3 & a_3 \sin\theta_3 \\ 0 & \sin\alpha_3 & \cos\alpha_3 & d_3 \\ 0 & 0 & 0 & 1 \end{bmatrix}
$$

$$
{}^{joint\,3}A_{joint\,4} = {}^{3}A_{4} = \begin{bmatrix} \cos\theta_4 & -\cos\alpha_4 \sin\theta_4 & \sin\alpha_4 \sin\theta_4 & a_4 \cos\theta_4 \\ \sin\theta_4 & \cos\alpha_4 \sin\theta_4 & -\sin\alpha_4 \cos\theta_4 & a_4 \sin\theta_4 \\ 0 & \sin\alpha_4 & \cos\alpha_4 & d_4 \\ 0 & 0 & 0 & 1 \end{bmatrix}
$$

$$
{}^{joint\,4}A_{joint\,5} = {}^{4}A_{5} = \begin{bmatrix} \cos\theta_5 & -\cos\alpha_5 \sin\theta_5 & \sin\alpha_5 \sin\theta_5 & a_5 \cos\theta_5 \\ \sin\theta_5 & \cos\alpha_5 \sin\theta_5 & -\sin\alpha_5 \cos\theta_5 & a_5 \sin\theta_5 \\ 0 & \sin\alpha_5 & \cos\alpha_5 & d_5 \\ 0 & 0 & 0 & 1 \end{bmatrix}
$$

5.7.2.1 Kinematic Equations for the End-Effector Manipulation

According to the D-H representation, the homogenous transformation matrix (${}^{Base}\boldsymbol{T}_{FrontEnd}$) which specifies the location of the laser waveguide Front End coordinate frame with respect to the Base coordinate system is the chain product of successive coordinate transformation matrices of (${}^{i-1}\boldsymbol{A}_i$) and expressed as

$$^{Base}T_{FrontEnd} = {}^{Base}A_{joint1}\,{}^{joint1}A_{joint2}\,{}^{joint2}A_{joint3}\,{}^{joint3}A_{joint4}\,{}^{joint4}A_{FrontEnd}$$

or

$${}^{0}T_5 = {}^{0}A_1\,{}^{1}A_2\,{}^{2}A_3\,{}^{3}A_4\,{}^{4}A_5$$

$${}^{0}T_5 = \begin{bmatrix} \vec{x}_5 & \vec{y}_5 & \vec{z}_5 & \vec{p}_5 \\ 0 & 0 & 0 & 1 \end{bmatrix} = \begin{bmatrix} {}^{0}R_5 & {}^{0}p_5 \\ 0 & 1 \end{bmatrix}$$

where

$[\vec{x}_5 \quad \vec{y}_5 \quad \vec{z}_5]$ is the orientation transformation matrix of the Front End coordinate frame with respect to the Base coordinate system. It is the upper left 3×3 partitioned matrix of the $^{0}\boldsymbol{T}_5$.

$^{0}\boldsymbol{p}_5$ is the position vector which points from the origin of the Base coordinate system. It is the upper right 3×1 partitioned matrix of the $^{0}\boldsymbol{T}_5$.

$^{0}\boldsymbol{R}_5$ is the orientation transformation matrix of the Front End coordinate frame with respect to the Base coordinate system. It is the upper left 3×3 partitioned matrix of the $^{0}\boldsymbol{T}_5$.

The direct (forward) kinematics solution of the End-Effector is simply a matter of calculating the homogenous transformation matrix $^{Base}\boldsymbol{T}_{FrontEnd}$ by the chain multiplying the five $^{i-1}\boldsymbol{A}_i$ matrices and evaluating each element in the $\boldsymbol{T}$ matrix ($^{Base}\boldsymbol{T}_{FrontEnd}$). Note that the forward kinematics solution yield a unique $\boldsymbol{T}$ matrix for a given $\boldsymbol{q}=(q_1\ q_2 \ldots q_5)$T and given a set of coordinate systems, where $q_i = \theta_i$ for the rotary joints 1 and 2 and $q_i=d_i$ for the linear joint 3. The only constraints are the physical bounds of θ_i (± 30°) and d_i (200-360mm) for each joint of the End-Effector.

Having obtained all the coordinate transformation matrices $^{i-1}\boldsymbol{A}_i$ for the End-Effector, the next task is to find an efficient method for computing the $\boldsymbol{T}$ matrix on a general purpose computer. The most efficient method is by multiplying all five $^{i-1}\boldsymbol{A}_i$ matrices together manually and evaluating the elements of the $\boldsymbol{T}$ matrix out explicitly on a computer program. However, this approach is difficult, time consuming and lacks flexibility.

An alternative approach is to "hand" multiply the first three $^{i-1}\boldsymbol{A}_i$ matrices together to form $\boldsymbol{T}_1= {}^{0}\boldsymbol{A}_1\,{}^{1}\boldsymbol{A}_2\,{}^{2}\boldsymbol{A}_3$ and also the last two $^{i-1}\boldsymbol{A}_i$ matrices together to form $\boldsymbol{T}_2= {}^{3}\boldsymbol{A}_4\,{}^{4}\boldsymbol{A}_5$ Then we express the elements of the $\boldsymbol{T}_1$ and $\boldsymbol{T}_2$ out in a computer program explicitly and let the computer multiply them together to form the resultant End-Effector homogenous transformation matrix $\boldsymbol{T}$ ($^{Base}\boldsymbol{T}_{FrontEnd}$). This method has both fast computation and flexibility. For the laser End-Effector $\boldsymbol{T}_1= {}^{0}\boldsymbol{A}_1\,{}^{1}\boldsymbol{A}_2\,{}^{2}\boldsymbol{A}_3$ was found to be

$$T_1 = \begin{bmatrix} [C_3(C_1C_2 - S_1S_2)] - S_3(C_1S_2 + S_1C_2) & 0 & S_3(C_1C_2 - S_1S_2) + C_3(C_1S_2 - S_1C_2) & 0 \\ C_3(S_1C_2 + C_1S_2) - S_1S_2S_3 - C_1C_2S_3 & 0 & S_3(S_1C_2 + C_1S_2) + C_3(S_1S_2 - C_1C_2) & 0 \\ 0 & 1 & 0 & 116.25 \\ 0 & 0 & 0 & 1 \end{bmatrix}$$

where

$C_i = \cos\,\theta_i$ *and* $S_i = \sin\,\theta_i$

and $\boldsymbol{T}_2 = {}^3\boldsymbol{A}_4\,{}^4\boldsymbol{A}_5$ was found to be

$$T_2 = \begin{bmatrix} C_4C_5 & -C_4S_5 & S_4 & d_5S_4 \\ S_4C_5 & -S_4S_5 & -C_4 & -d_5C_4 \\ S_5 & C_5 & 0 & 0 \\ 0 & 0 & 0 & 1 \end{bmatrix}$$

Hence the End-Effector homogenous transformation matrix $\boldsymbol{T}$ (${}^{Base}\boldsymbol{T}_{FrontEnd}$) can be found by multiplying $\boldsymbol{T}_1$ by $\boldsymbol{T}_2$ and substituting for the values of the link parameters α_i, θ_i, a_i, and d_i given above in Figure 5.27.

$$^{Base}\boldsymbol{T}_{FrontEnd} = \boldsymbol{T} = \boldsymbol{T}_1\ \boldsymbol{T}_2 = {}^0\boldsymbol{A}_1\,{}^1\boldsymbol{A}_2\,{}^2\boldsymbol{A}_3\,{}^3\boldsymbol{A}_4\,{}^4\boldsymbol{A}_5$$

and

$$^{Front\ End}\boldsymbol{T}_{Base} = ({}^{Base}\boldsymbol{T}_{FrontEnd})^{-1}$$

$$T = \begin{bmatrix} x_5 & y_5 & z_5 & p_5 \\ 0 & 0 & 0 & 1 \end{bmatrix} = \begin{bmatrix} {}^0R_5 & {}^0p_5 \\ 0 & 1 \end{bmatrix} = \begin{bmatrix} \vec{n} & \vec{s} & \vec{a} & \vec{p} \\ 0 & 0 & 0 & 1 \end{bmatrix}$$

$$T = \begin{bmatrix} n_x & s_x & a_x & p_x \\ n_y & s_y & a_y & p_y \\ n_z & s_z & a_z & p_z \\ 0 & 0 & 0 & 1 \end{bmatrix} = \begin{bmatrix} \cos\theta_2\cos\theta_4 & \sin\theta_2 & \cos\theta_2\sin\theta_4 & d_5\cos\theta_2\sin\theta_4 \\ \sin\theta_2\cos\theta_4 & -\cos\theta_2 & \sin\theta_2\sin\theta_4 & d_5\sin\theta_2\sin\theta_4 \\ \sin\theta_4 & 0 & -\cos\theta_4 & -d_5\cos\theta_4 + 116.25 \\ 0 & 0 & 0 & 1 \end{bmatrix}$$

where

$$\vec{n} = \begin{bmatrix} n_x & n_y & n_z \end{bmatrix}^T \qquad \vec{s} = \begin{bmatrix} s_x & s_y & s_z \end{bmatrix}^T \qquad \vec{a} = \begin{bmatrix} a_x & a_y & a_z \end{bmatrix}^T$$

$$, \quad {}^0R_5 = \begin{bmatrix} n_x & s_x & a_x \\ n_y & s_y & a_y \\ n_z & s_z & a_z \end{bmatrix} \quad \text{and} \quad {}^0p_5 = \begin{bmatrix} p_x \\ p_y \\ p_z \end{bmatrix}$$

It is worth noting here that the End-Effector homogenous transformation matrix depends only on the joint rotation angles θ_2 and θ_4, and the linear translation d_6. These results were expected because the rotation angles θ_2 and θ_4 are responsible for the horizontal and vertical rotation respectively. And d_5 represents the linear translation of the laser waveguide along the direction of application.

5.7.2.2 End-Effector Work-Space

Using the above equations of the D-H representation one can easily derive the End-Effector's work space. Figure 5.28 shows a MathCAD 3D model [MATH 95] of the End-Effector workspace based on the D-H representation [Appendix B: MathCAD Work].

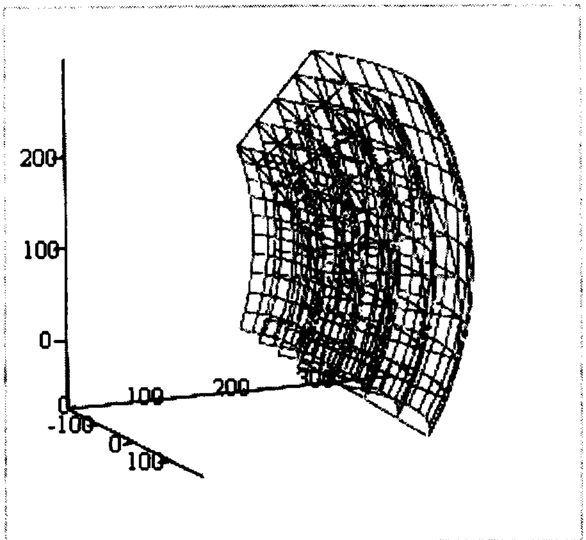

Figure 5.28: End-Effector workspace using D&H representation (Units are in mm)

One of the major requirements of the End-Effector applications is that, the surgical site should be within the reachability or the workspace of the laser End-Effector which is limited in the angular and displacement movements and the number of degrees of freedom.

The workspace reachable by the End-Effector is shown in Figure 5.28. The boundaries of the workspace are limited by the maximum and minimum lengths of the laser waveguide and the preset maximum rotation angles. As shown in the figure the workspace is bounded by two spherical shapes representing the maximum and minimum reachable area of application.

5.7.3 The Geometric Approach for Solving the Forward Kinematics

This approach was developed by the author to represent the spatial geometry of the End-Effector links and joints with respect to a fixed reference frame (the Base coordinate system). This approach considers an End-Effector with a single joint and two links as shown in Figure 5.29. This joint is at the origin of rotation and featuring three degrees of freedom; two rotational and one linear. The origin of rotation is connected through links to the laser Front End from one side and to the Base from the other side. The origin of rotation is positioned at a fixed distance from the Base coordinate system with its coordinate system parallel to that of the base. The range of movement of the laser front End is limited by $\pm$ 30° of rotation about the z and x axes and 160 mm of linear movement of the laser waveguide in the direction of application (y axis) (between 200 – 360 mm from the origin).

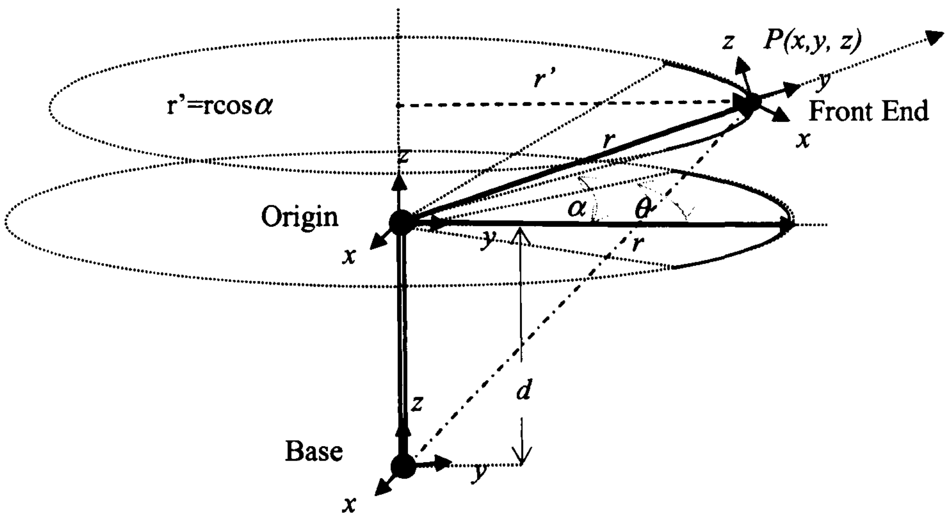

Figure 5.29: Geometric approach joints and links model

The geometric approach states that as the laser waveguide rotates about the z or x axes it forms an arc of a circle with its radius (r) equal to the length of the laser waveguide. The position of the Font End of the laser waveguide could be at any point within this arc.

A rotation of α about the x axis for example followed by a rotation of θ about the z axis while keeping the length of the laser waveguide constant (r) results in a Front End position within an arc whose radius (r'= r cos (α)). In general the position and orientation coordinates of the laser waveguide Front End can be calculated as follow:

The Front End position $P_{FrontEnd}$ $(p_x \;\; p_y \;\; p_z)$ and the orientation of the laser waveguide with respect to the Base position $(B_x \;\; B_y \;\; B_z)$ are

Position **Direction**

$$p_z = r\sin(\alpha) + B_z$$
$$p_y = r\cos(\alpha)\cos(\theta) + B_y$$
$$px = -r\cos(\alpha)\sin(\theta) + B_z$$

$$Y_{FrontEnd} = \begin{bmatrix} -\cos(\alpha)\sin(\theta) \\ \cos(\alpha)\cos(\theta) \\ \sin(\alpha) \end{bmatrix}$$

As shown in Figure 5.29 above the orientation of the laser waveguide Front End is in the direction of its y coordinate. In general position and orientation of the transformation matrix *TG* based on the geometric approach is given by

$$T_{geo} = \begin{bmatrix} \cos(\theta) & -\cos(\alpha)\sin(\theta) & \sin(\alpha)\cos(\theta) & -r\cos(\alpha)\sin(\theta)+B_x \\ \sin(\theta) & \cos(\alpha)\cos(\theta) & -\sin(\alpha)\sin(\theta) & r\cos(\alpha)\cos(\theta)+B_y \\ 0 & \sin(\alpha) & \cos(\alpha) & r\sin(\alpha)+B_z \\ 0 & 0 & 0 & 1 \end{bmatrix}$$

where the upper left 3×3 partitioned matrix represents the orientation transformation (rotation matrix) of the laser Front End coordinate system and upper right 3×1 partitioned matrix of *TG* is the position vector of the laser Font End which points from the origin of the Base coordinate system. Calculating the work space using the geometric approach results in very similar workspace derived by the H-D representation stated above.

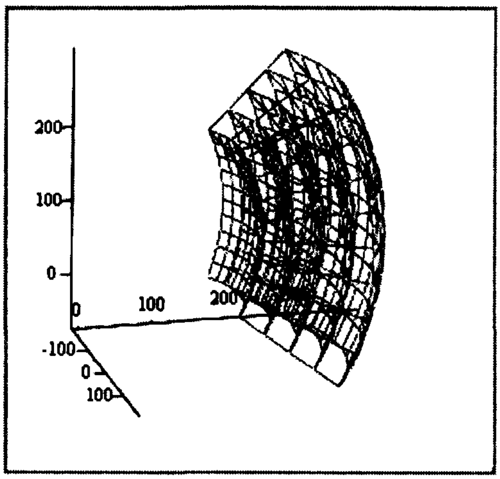

Figure 5.30: End-Effector workspace plot using the geometric representation (Units are in mm)

5.7.4 The Inverse Kinematics

In general the Inverse kinematics problem can be solved by several techniques such as matrix algebra, iteration and the geometric approach. A solution for the inverse kinematics problem can be easily achieved using the geometric approach derived by the author. With this approach, given any point in space (Px, Py, Pz) within the reachability of the End-Effector, all angular and translation parameters required for manipulation (θ, α and d) can be calculated using the following equation

$$\theta = \tan^{-1}\left[-\frac{(p_x - B_x)}{(p_y - B_y)}\right] \qquad \alpha = \tan^{-1}\left[\left[\frac{p_z - B_z}{p_y - B_y}\right]\cos\left[\tan^{-1}\left[-\frac{p_x - B_x}{p_y - B_y}\right]\right]\right]$$

$$d = \frac{p_y - B_y}{\cos(\alpha)\cos(\theta)}$$

where

θ: is the angular rotation about the Z axis at the origin of manipulation

α is the angular rotation about the X axis at the origin of manipulation

d is the displacement of the laser waveguide in the direction of application

B_x, B_x, B_x are (x y z) Base coordinate system parameters.

5.8 Summary and Proposed Phases of Future Development

The laser End-Effector prototype presented in this chapter is a 3 DOF robotic delivery system that is capable of delivering a laser surgical tool for image guided orthopaedic surgery. It is a three degrees of freedom device with a novel design. It comprises of three major joints connected together with rigid links in a unique way; where all joints manipulate about a single origin point. The laser End-Effector design is based on a set of requirements that govern its functionalities, capabilities and performance. These requirements impose certain limitations on the End-Effector's dexterity, flexibility and workspace. However, these limitations will have very little effect when taking into considerations that the laser End-Effector is to be attached to a passive or active manipulator. Since the latter contributes to the number of degrees of freedom and the manipulation dexterity and flexibility.

The End-Effector prototype features several advantages and disadvantages. The advantages are associated with the

- Design simplicity
- Ease of control and manipulation
- Simple solution for the forward and inverse kinematics
- Fast manipulation time
- Ability of sequential time and parallel time manipulation

The disadvantages, however, are linked to the manipulation technique which limits the functionality scope and workspace. These include:

- The bone fixation requirement
- Limited degrees of freedom
- The selected components

Future phases of development

The second development phase of the laser End-Effector would be to design and implement a complete laboratory End-Effector prototype. The new prototype should fulfil all mandatory and desirable requirements taking into account all the problems associated with the first laser End-

Effector prototype. It may incorporate more sensory feedback elements including visual and auditory sensing devices [KIRK 00]. It may also feature higher degrees of freedom to enhance the basic end-effector performance capabilities allowing for performing new tasks such as bone sculpturing with improved dexterity and accuracy. The new prototype would be utilized to perform in-vitro experiments on real bone. The overall new prototype system may incorporate a water spray system [IVAN 00] and a debris removal suction device [Chapter 4] during the laser bone cutting process to insure safe and clean cutting.

The third development phase may involve the design and development of a fully functional clinically approved End-Effector system (i.e. a clinical prototype) which can be used in the operating theatre for in-vivo orthopaedics surgery. The design must fulfil all engineering, clinical and safety requirements. This clinical prototype may feature six or more degrees of freedom, additional means of control modalities and feedback mechanism [STON n.d.][ADAM 98]. It may also feature more control flexibility, portability and lightweight. The design modification may include an adaptive automatic control system to adapt for patient movements. End-effector of the clinical prototype may also introduce new surgical techniques for orthopaedics.

The fourth development phase may involve the design and development of a clinically approved commercial End-Effector system which can be manufactured to fit the needs of different orthopaedics applications.

Chapter 6

Feedback Techniques for Laser Tissue Interaction

6.1 Introduction

The design and development of a computer assisted laser End-Effector for orthopaedic surgery requires a feedback system. This system must consider all mechanical movements and positions. It must also consider the position of the patient's anatomy, the laser End-Effector and other monitoring devices relative to each other. Most importantly this feedback system must determine the laser-front position during laser bone interaction and give accurate measurements for the laser ablation depth and ablation rate in real time.

Although, laser feedback systems exist in a variety of applications, very few are available for medical applications. This chapter presents two innovative laser feedback techniques developed by the author to measure the ablation depth and ablation rate during laser bone interaction. The aim of these techniques is to develop a real time feedback system to control the depth of the laser cut into bone suitable for use in computer assisted orthopaedic surgery. This feedback system must give sufficient information about the overall surgical performance for both the computer based control system as well as the surgical team. This information also allows for automatic manipulation control of the laser delivery system as well as control of the laser parameters and for switching on and off the laser beam.

This chapter specifies first the basic feedback and control requirements for the design of the laser End-Effector control unit: these include all surgical (clinical) and functional requirements. Then it discusses the laser feedback techniques developed by the author followed by alternative laser feedback techniques.

6.2 Basic Feedback and Control Requirements

Certain requirements must be met by the design and implementation of the laser control system. These include surgical and functional requirements. The surgical requirements include: registration, trajectory planning, surgical navigation and treatments (laser bone ablation). The functional requirements include:

- Safe and accurate manipulation control of the laser End-Effector

- Accurate and precise positioning control of the laser front
- Accurate implementation of the End-Effector's equation of motion
- Accurate feedback and navigation measurements
- Confine the operation of the laser bone ablation to within the workspace boundaries specified by the preset trajectory plan
- Accurate estimation of the laser ablation depth per pulse at any given moment in time.

Other requirements related to the design and implementation of the control unit are presented and discussed within this chapter.

6.3 Feedback

Feedback is a key requirement in computer assisted surgery. It can provide information about surgical tool performance, the property of the tissue undergoing surgery and the overall surgical application. It contributes to safe and accurate manipulation of the laser End-Effector as well as the accurate positioning of the laser front. It also aids in pinpointing the position and orientation of the surgical tool relative to the patient's anatomy, and in regulating the output level of the surgical tool (laser). Feedback systems in computer assisted surgery may include (Figure 5.1):

- Visual or imaging feedback
- Optical tracking of instruments, implants or anatomy
- Mechanical feedback
- Sensory feedback devices related to the surgical tool and patient anatomy

Feedback is considered it two parts. Firstly, feedback is required to determine the position of the laser End-Effector so as to correct for errors in manipulation due to estimates in driving motors, small errors in limb lengths, backlash in joints, etc. This is described in 6.3.1. Secondly, feedback is required to monitor the progress of the laser cut, i.e. localisation of the laser cut, and to modify the laser parameters and movement of the End-Effector laser waveguide. Solution to this problem is the main focus of this chapter and this is discussed in 6.4 onwards.

6.3.1 Position tracking and feedback devices for the laser End-Effector

The type of feedback for computer assisted surgery feedback depends upon the type of surgery and the surgical tool involved. This section presents two different feedback techniques proposed by the author for manipulation of the laser End-Effector, namely: absolute optical encoders and optical tracking systems.

Absolute optical encoders are position verification feedback devices that provide unique shaft position information with very high resolution and accuracy [PARK nd]. They feature the capability of reading actual shaft position without loss of position information during power failure. As feedback devices the absolute optical encoders are connected directly to the outputs of the End-Effector's joints (the gearbox shaft) to measure the exact manipulation angles or displacement at the joints. These angles allow calculation of the position and orientation of the laser waveguide Front End relative to the End-Effector's base coordinate system.

Optical tracking is used widely for registration and navigation in computer assisted surgery. It can provide the necessary information needed to perform pre-surgical and intra-surgical registration, planning and navigation [LEA 94][LEA 98]. Optical trackers such as NDI Polaris (by Northern Digital Inc) [BRUC 02][WILE 04][RIBO 01][FRAN 04] are Infrared-based navigation systems. For this project it is proposed to use optical tracking of the position and orientation of the End-Effector, the laser waveguide Front End and the surgical object (SO) [BRUC 02][LEA 94][LEA' 95].

Optical tracking systems support real-time tracking. This feature together with tracking information about the location and orientation of equipment and anatomy provides a basis for a computer based control unit to control precisely the manipulation of the laser End-Effector and adapt for any bone movement during surgery.

It is envisaged that the optical tracker would be placed in the surgical room in a position where it can monitor the laser End-Effector and the surgical object (SO) with no obstacles. Figure 6.1 shows a block diagram of a proposed registration and navigation technique for laser bone cutting.

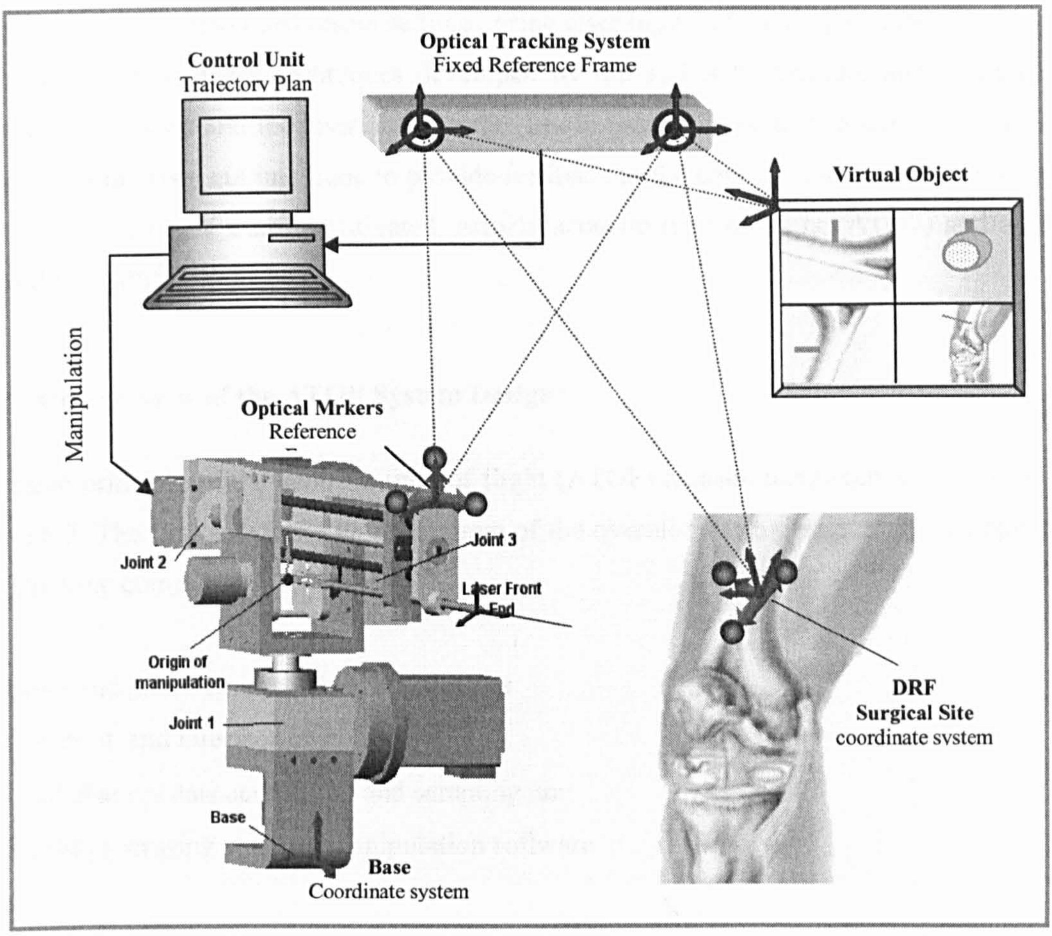

Figure 6.1: Registration and surgical navigation technique

6.4 Localisation of the laser cut

Research on the laser tissue interaction showed that laser pulses (such as Er: YAG, Ho: YAG and CO_2) striking biological tissue produce loud photo-acoustic effects [KIRK 00] [KU 00][HARR 00][IVAN 02]. These effects are caused by the rapid expansion of water molecules and localised water-microexplosions inside the tissue [IVAN 02] [NICO 02] [ZHIG 99] [KODA 99]. These effects feature a wide range of audio frequencies ranging from sonic to ultrasound that depends on the ablated material and the ablation process.

Photo-acoustic effects are depth related [HARR 00] and therefore they can be utilised for depth measurements and localisation of the laser front position inside tissue. The magnitude and duration of the photo-acoustic waves are directly related to the laser energy density, laser pulse duration and depth inside tissue. However, the photo-acoustic response time is affected by other factors such as the speed of sound (temperature and humidity dependent), the level of laser induced pressure, velocity of ejected molecules during laser ablation [ZHIG 97], and tissue type (in terms of water contents).

The photo-acoustic effect and response time during laser tissue interaction provide a basis for an innovative laser feedback techniques developed by the author to measure and calculate the Laser Front position and the laser ablation rate inside tissue. These techniques aim to measure the depth of the laser cut into bone to provide feedback to the control system for the laser front. Two main techniques were investigated, namely acoustic time of flight (ATOF) and acoustic phase shift (APS).

6.5 An Overview of the ATOF System Design

The basic principle of the acoustic time of flight (ATOF) measurement technique is shown in Figure 6.2. The figure shows a block diagram of the overall system design which comprises of the following components:

- Laser and photo-acoustic detection devices
- Detection and interface circuit
- Dual channel data acquisition and sampling unit
- Signal processing and data manipulation software

The output of this feedback system includes information about the ATOF, the position of the laser front inside bone and the bone ablation rate.

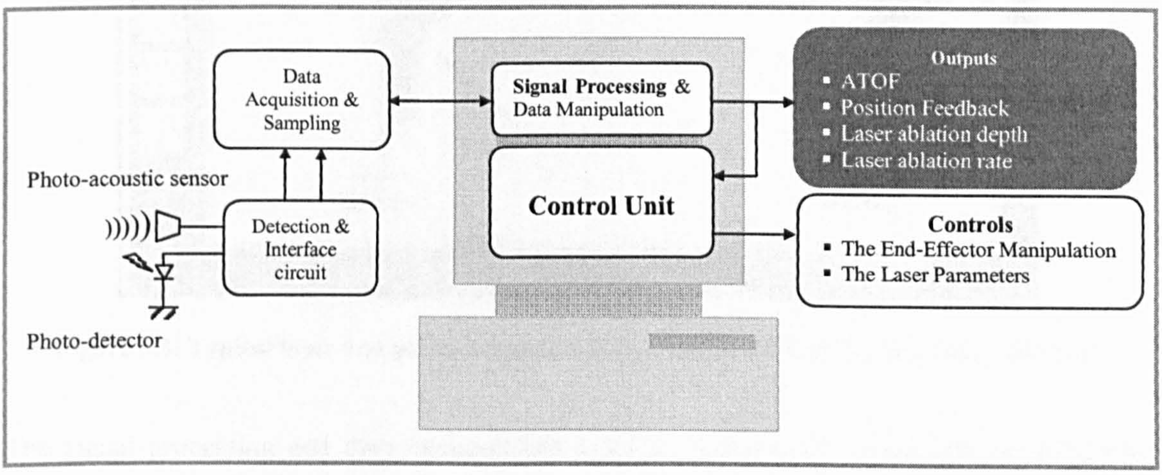

Figure 6.2: A block diagram of the ATOF feedback and control system design

The detection and interface circuit involves the detection of the reflected laser ablation beam (interaction induced light) and the induced photo-acoustic waves. The induced light is detected using a narrow band photo-detector (matches the ablating laser wavelength) with a high gain, high signal to noise ratio (S/N) amplifier circuit. The induced photo-acoustic waves, on the other hand, are detected using a low cost (41 kHz) ultrasound transducer with fast response time and a high signal to noise ratio (S/N). These photo-acoustic waves are amplified using a wideband (up to 200 KHz) acoustic amplifier circuit with high gain and automatic gain control.

This detection and interface circuit have two outputs. The first output carries an amplified analogue pulse that corresponds to the laser ablation pulse in terms of starting time and pulse duration. The second output carries the amplified photo-acoustic waves. These outputs are directly connected to the data acquisition and sampling circuit.

The data acquisition and sampling circuit acquires the amplified laser pulse and photo-acoustic waves (Figure 6.3) and samples them in real time. The sampled results (data) are stored in direct access memory locations. This data contains time and magnitude information for both signals that can be accessed in real time by a signal processing software for further data manipulation.

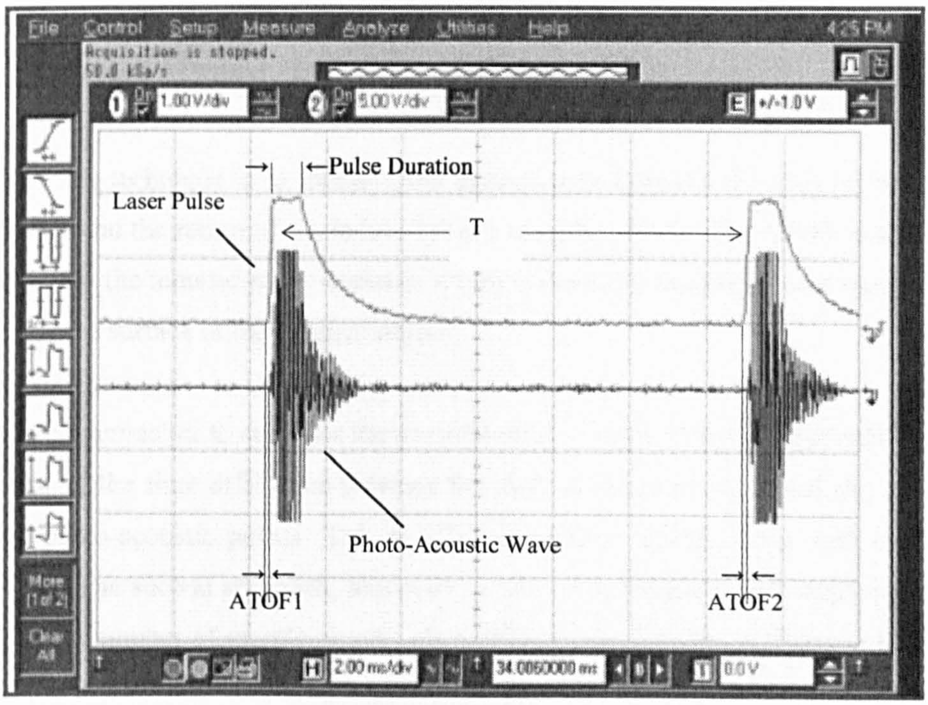

Figure 6.3: Typical laser and photo-acoustic waves detected during CO_2 laser bone ablation

The signal processing and data manipulation software is designed to perform the following signal processing tasks:

- DC offset nulling (setting the signals baseline to zero for both signals)
- Photo-acoustic waves rectification (inverting the negative side of the photo-acoustic waves)
- Envelope detection of the rectified photo-acoustic waves
- Setting threshold levels for the laser pulses and photo-acoustic waves' envelopes. Variable threshold levels may be used for the photo-acoustic waves' envelopes to

compensate for the effect of speed of sound variation and response time for the photo-acoustic sensor.

- Finally, pulse shaping (converting the analogue signals into pulses). The analogue representation of the laser pulse and the envelope of the photo-acoustic wave are converted into pulses as soon as the signals pass the preset threshold levels. This in effect results in a single laser pulse and a train of overlapped photo-acoustic pulses as shown in the illustrations (Figure 6.4). This pulse overlap is due to the variable threshold levels.

Once the signal processing is completed the software calculates for ATOF, ablation depth (i.e. the laser front position) and the ablation rate. This information is then fed back to the control unit to adjust the End-Effector's manipulation speed and to control the different laser parameter including switching the laser beam on / off.

6.6 Acoustic Time of Flight (ATOF) Measurement and Calculation Techniques

The basis of this technique is to measure the elapsed time between the start of the laser bone ablation pulses and the return of the induced photo acoustic effects. The ATOF is defined as the time required for the induced photo-acoustic waves to reach an acoustic sensor placed at a fixed distance from the surface of the surgical object.

There are two approaches to calculate the acoustic time of flight. The first approach is the direct measurement of the time difference between the start of the laser pulse and the average start time of the photo-acoustic pulses This in effect requires a timing circuit with start and stop control inputs. The second approach, however, is a novel technique which employs a sampling frequency and a number of sample points calculated between the start of the laser pulse and the start of the photo-acoustic wave. This approach removes the need for a timing circuit.

6.6.1 Calculating Laser Ablation Depth and Ablation Rate

Given the speed of sound at the time of the laser tissue interaction, the acoustic time of flight can be used to calculate the laser ablation depth per laser pulse as follows (Equation 6.1):

Equation 6.1: Calculating the ATOF and ablation depth

$$ATOF = T_{start} - T_{stop}$$
$$D = v \cdot ATOF$$
$$d = D - D_{fixed}$$

where

T_{start}	is the start time of the laser ablation pulse
T_{stop}	is the arrival time of the induced photo-acoustic wave
$ATOF$	is the acoustic time of flight
D	is the measured distance between the acoustic sensor and the laser ablation Front
v	is the speed of sound
D_{fixed}	is the distance between the acoustic sensor and the surface of the surgical object
d	is the laser ablation depth

Alternatively, the ablation depth per pulse can be calculated from the difference in time between two consecutive ATOF (ATOF1, ATOF2) values (Figure 6.3) multiplied by the speed of sound (Equation 6.2). Given the laser pulse repetition rate (PRR), the laser ablation rate can be calculated as follow:

Equation 6.2: Calculating the ablation depth per pulse and the ablation rate

$$d_{pp} = (ATOF2 - ATOF1) \times v$$
$$AR = d_{pp} \times PRR$$

where

d_{pp}	is the ablation depth per laser pulse
$ATOF1$	is the time of Flight for the first laser pulse
$ATOF2$	is the time of Flight for the second laser pulse
v	is the speed of sound
AR	is the laser ablation rate
PRR	is the laser pulse repetition rate

A summary of the ATOF measuring and feedback technique is presented in Figure 6.4. The block diagram in this figure shows chronologically the steps of this technique. It starts by detecting and processing of the induced interaction light (laser beam) and photo-acoustic waves and ends with the ATOF value and the laser ablation depth. The illustrations on the right side of the figure show the progression of the waves processing for evaluating the ATOF. Further detail of the block diagram of Figure 6.4 is shown in the ATOF example presented later in this chapter (Section 6.6.3). This example shows an illustration of ATOF calculations for real data acquired during a laser bone ablation feedback experiment.

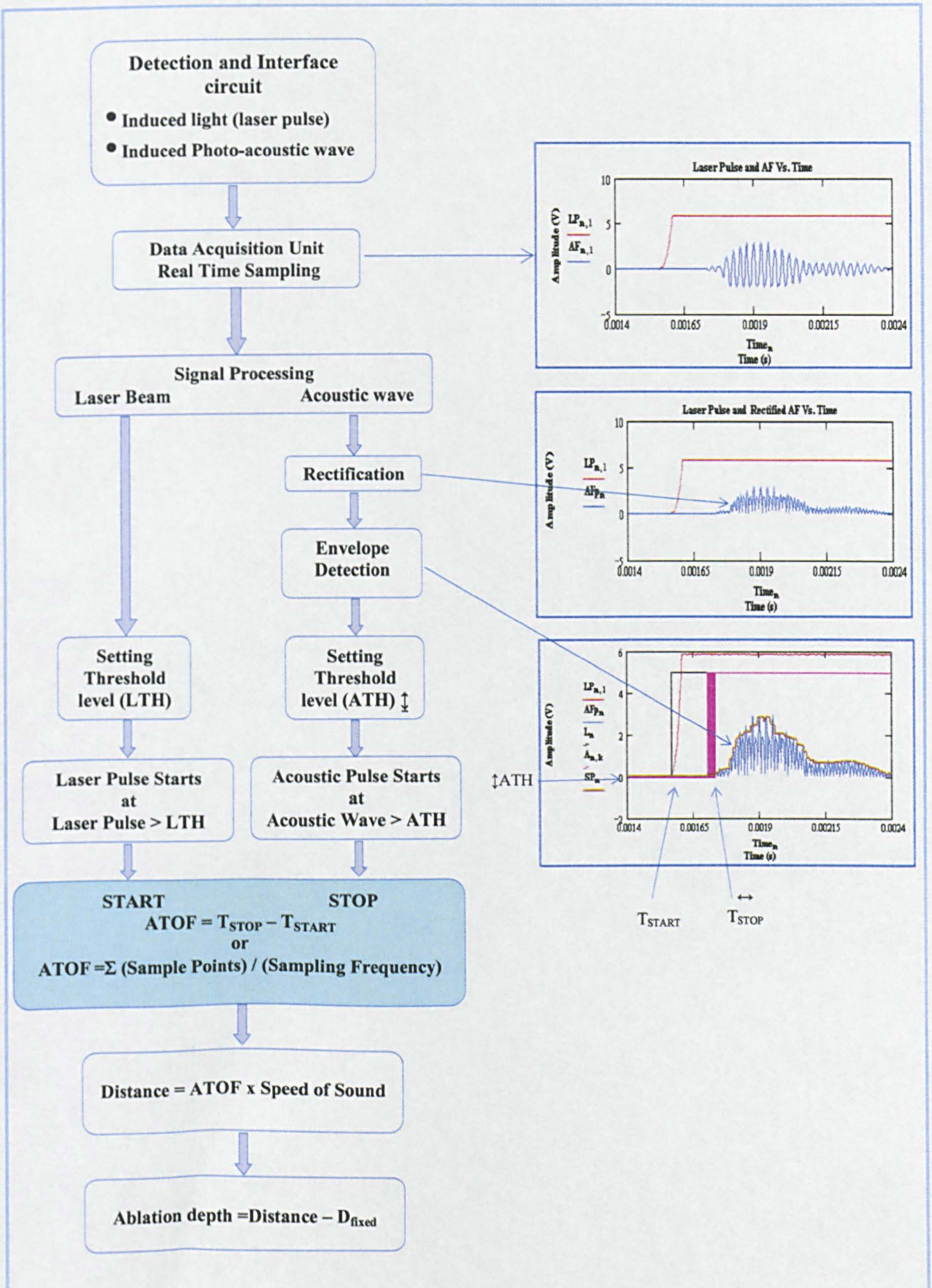

Figure 6.4: Acoustic Time of Flight measurement technique

6.6.2 Laser Bone Ablation Feedback Experiment

This section presents the experiment conducted to investigate the feedback technique presented in 6.6.1 for determining the laser front position during laser bone-interaction in real time. The apparatus used for this experiment included:

- A laser source (CO_2)
- Fresh bone samples
- Digital Storage Oscilloscope
- A photo-acoustic sensor (41 kHz Piezoelectric Ultrasound Transducer)
- A photo-detector (light detector)
- An interface circuit
- An optical rail

This experiment was initially designed to be carried out using an Er: YAG laser system for bone cutting. However, due to the unavailability of an Er: YAG laser system at the University of Hull a decision was made to use a surgical CO_2 laser system in place. This could have a negative impact on the results due to the following factors:

a) The Er: YAG laser causes a slight rise in temperature to the surrounding tissue [KIRK 00][NIEM 96] and there is less heat build-up than for a CO_2 laser. This is because the ablation time for Er: YAG laser is almost equal to the thermal relaxation time (i.e. $T_{ab} \cong \tau_r \approx 3\mu s$) whereas, a CO_2 laser $T_{ab} >> \tau_r$ (T_{ab}= 6000μs and τ_r = 500μs) causes a gradual heating around the area of interaction [KIRK 00]. This heat build-up may alter the speed of sound causing uncertainty in the measurements.

b) The Er: YAG laser features a high induced photo-acoustic levels (measured 99 dB for 2mm spot size at 1.5J for skin ablation [KIRK 00]) compared with CO_2.

c) Er: YAG laser systems use a lower pulse repetition rate (≤30 Hz) than CO_2 laser [NIEM 96][KIRK 00] which can be in the kHz range. Thus for an Er: YAG laser, this allows for total decay of the tissue heating effect of the previous Er:YAG laser pulse before the next pulse arrives which is not the case for CO_2 laser especially at high pulse repetition rates.

In this experiment, the bone sample is placed on an optical rail at a specified distance from the front-end of the laser source (Figure 6.5) and facing the laser beam. The photo-acoustic sensor and photo-detector are also placed at specified distance from the laser-bone interaction point.

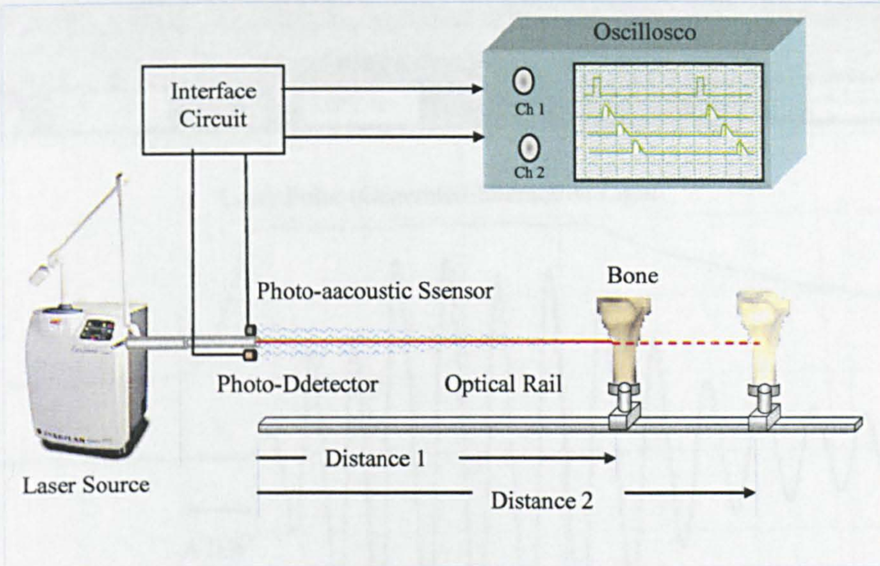

Figure 6.5: Laser feedback experimental setup

As the laser pulses hit the bone they cause bone ablations which generate bright visible light waves and photo-acoustic waves. The induced bright light wave represents the laser ablation pulse while the photo-acoustic wave represents the sound generated during the laser bone-interaction. These induced light and photo-acoustic waves are detected, amplified by the interface circuit, recorded and sampled by the digital storage oscilloscope. The sampled waves (Figure 6.6) are then imported by the MathCAD software and processed to provide measurements for the bone-ablation ablation depth and laser ablation rate.

Obviously a feedback system for the proposed laser cutting surgery system would require measurements and calculations in real time. In this case the digital storage oscilloscope and the MathCAD software may be replaced by multi-channel data acquisition card, digital signal processing circuits and software and software for the mathematical manipulations.

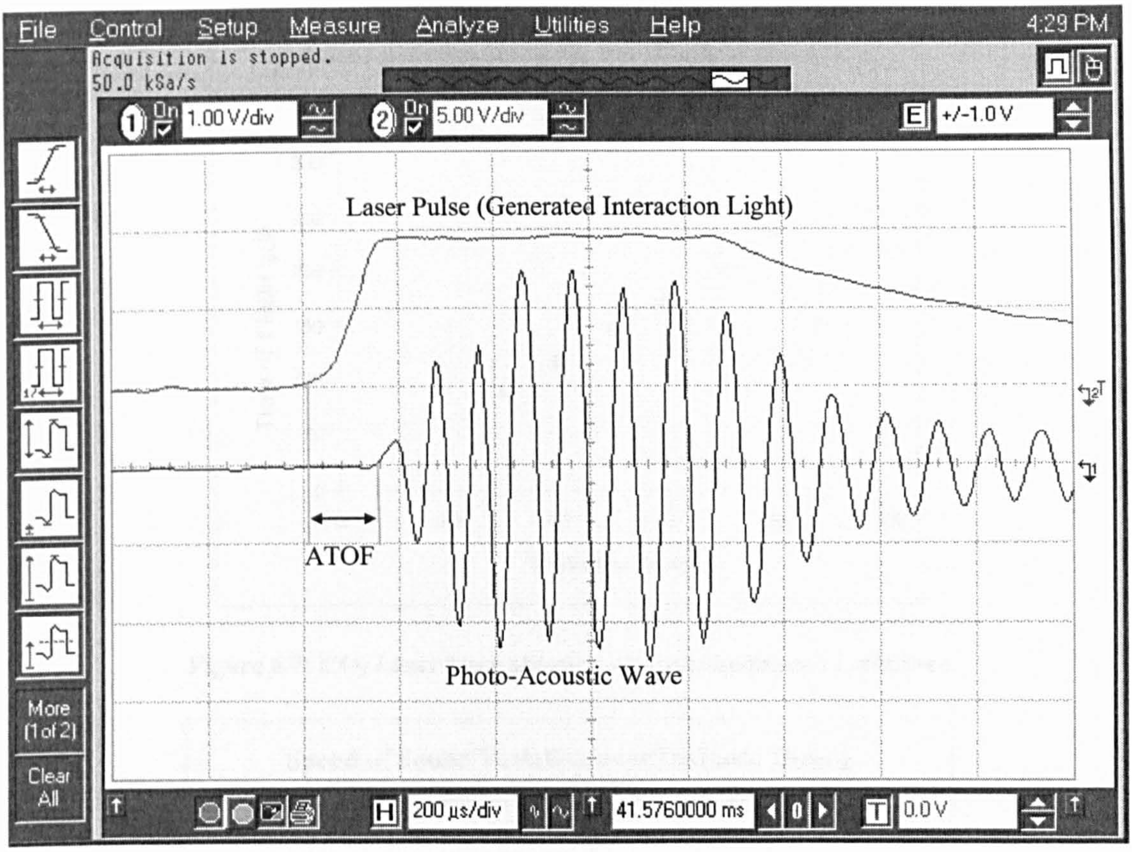

Figure 6.6: A digital storage oscilloscope plots of the generated light and photo-acoustic waves recorded for a single laser pulse during a laser bone ablation experiment. The plots show the time difference (ATOF) between the start of the laser pulse and the arrival of the photo-acoustic wave.

Experimental results on the photo-acoustic feedback for CO_2 laser bone ablation showed a linear correlation between the laser front position on the tissue surface and the acoustic feedback time of flight - ATOF (Figure 6.7). The accuracy of this technique however, is highly dependent on the accurate evaluation of the speed of sound during the laser tissue interaction and the specifications of the photo-acoustic sensor. Hence accurate measurements may require real time speed of sound measurement.

The inaccuracies in the measurements were mainly due to variation in the speed of sound, the acoustic response time of the photo-acoustic sensor and the environmental noise. Figure 6.8 clearly shows higher speed of sound values at close ranges to the ablation site than those at further distances. This is due mainly to the heat propagation and heat buildup during laser tissue interaction, and other environmental factors such as humidity (water vapor), ablation debris and pressure buildup close to the laser bone ablation point.

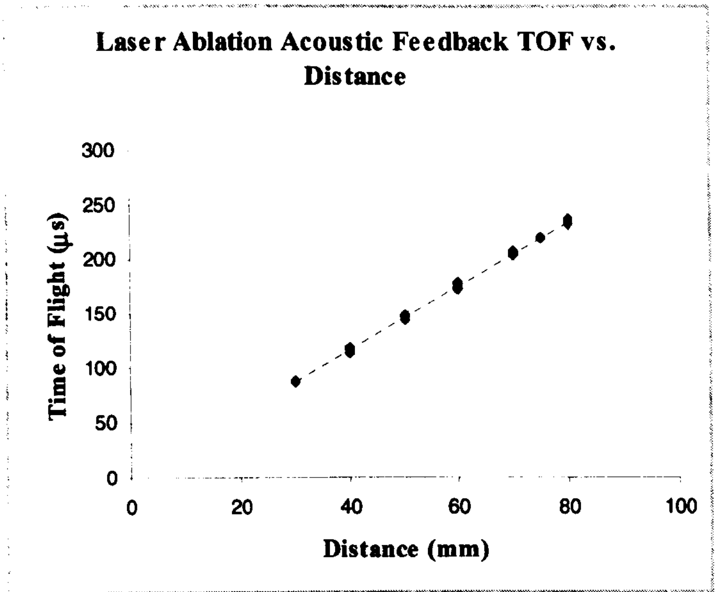

Figure 6.7: CO_2 Laser bone ablation acoustic feedback vs. distance

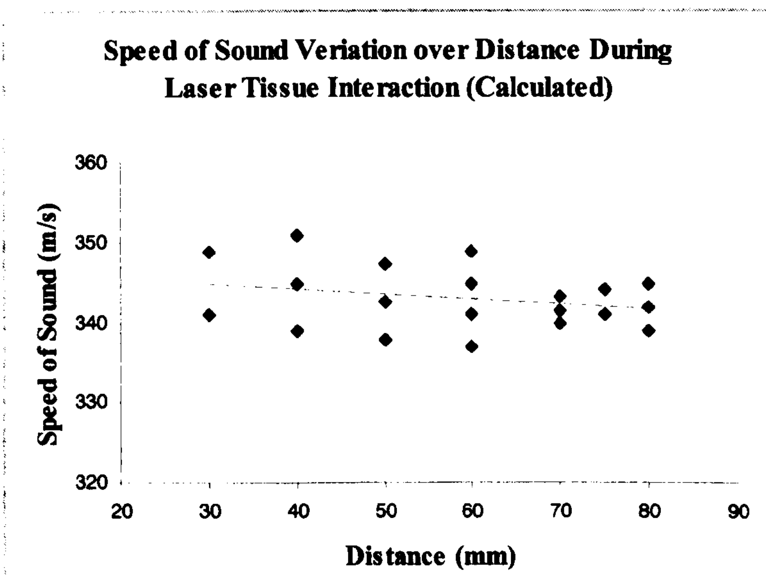

Figure 6.8: Calculated values for speed of sound over distance during CO_2 laser bone ablation

6.6.3 ATOF Calculation Results

This example calculates the acoustic time of flight ATOF using MathCAD. This section presents data and results for measuring ablation during using the experimental set up as presented in the previous section (6.6.2) In this experiment the distance between the photo-acoustic sensor and bone surface at the ablation site was measured to be 50 mm.

The tables below present the data acquired for the induced light (reflected laser beam) (LP) and the photo-acoustic waves (AFB) during a laser bone ablation experiment with a sampling frequency of 500 k Samples /sec. These data are then plotted against time in Figure 6.9. The figure clearly shows the time difference between the reflected laser beam at the time of ablation and the start of the induced photo-acoustic waves.

$\mathbf{n} := 700..\ 1200$

LP :=

	0	1
0	-0.04168	-1.69
1	-0.04167	-1.7
2	-0.04167	-1.71

AFB :=

	0	1
0	-0.04168	-0.03
1	-0.04167	-0.02
2	-0.04167	0

$\mathbf{LPI_{n,0} := LP_{n,0} - LP_{0,0}}$

$\mathbf{Time_n := LPI_{n,0}}$

LP is the Laser Pulse
AFB is the acoustic Feedback
column (0) represent the time

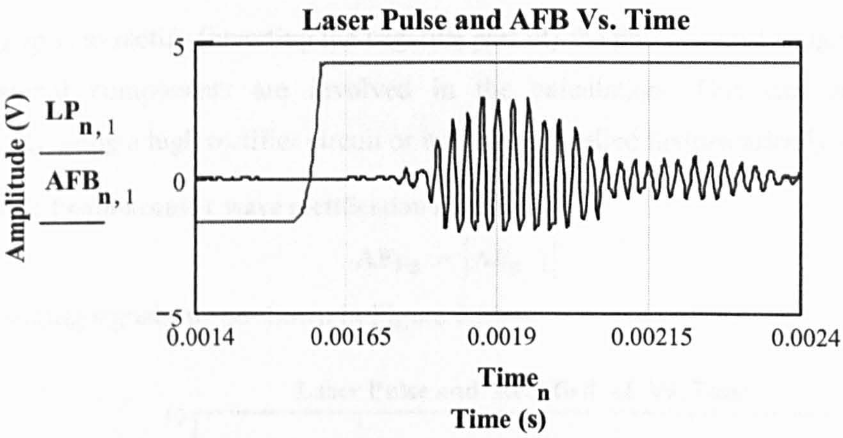

Figure 6.9: Reflected laser beam and generated photo-acoustic waves as a function of time

To calculate the time difference between the two signals (LP and AFB) both signals must be set to the zero baseline (i.e. DC offset null). This can be achieved by filtering out the DC offset components of the two signals leaving the AC components unchanged. This can be done physically using a high pass (AC) filter circuit, or mathematically using Equation 6.3 and Equation 6.4. These equations calculate the average baseline value for each of the acquired signals and subtract the average value from the original signal over the entire time span. The resulting signals with a single base line at the zero DC level as shown in Figure 10.

Equation 6.3: DC offset null of the photo-acoustic wave

$$\mathbf{AFbase := mean\left(AFB_{600,1}, AFB_{550,1}, AFB_{500,1}, AFB_{450,1}, AFB_{400,1}, AFB_{350,1}\right)}$$

$$\mathbf{AF_{n,1} := AFB_{n,1} - AFbase}$$

Equation 6.4: DC offset null of the reflected laser beam

$$\mathbf{LPbase := mean\left(LP_{600,1}, LP_{550,1}, LP_{500,1}, LP_{450,1}, LP_{400,1}, LP_{350,1}\right)}$$

$$\mathbf{LP_{n,1} := LP_{n,1} - LPbase}$$

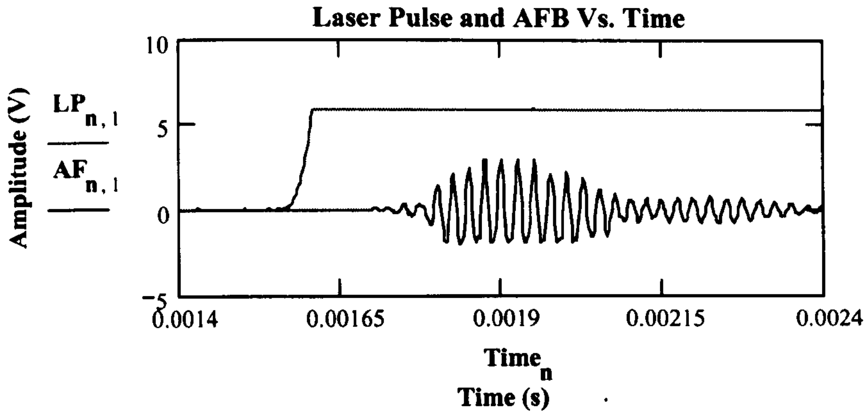

Figure 10: The acquired laser beam and photo-acoustic waves set at the zero base line

The next step is to rectify (inverting the negative part of) the photo-acoustic signal to insure that all AC signal components are involved in the calculation. This can be implemented electronically using a high rectifier circuit or it can be modelled mathematically as follow:

Equation 6.5: Photo-acoustic wave rectification model

$$\mathbf{AFp_n := \left|AF_{n,1}\right|}$$

and the resulting signals are as shown in Figure 6.11

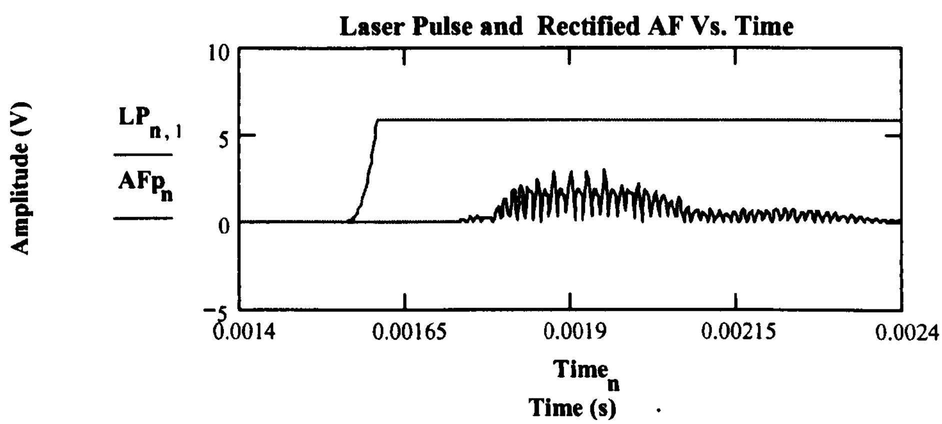

Figure 6.11: Reflected laser beam and rectified photo-acoustic wave as a function of time.

The next step is to generate an envelope for the resonated acoustic wave. This is important for determining the state of the detected photo-acoustic wave. Electronically this can be achieved using an envelope detection circuit. Alternatively, a mathematical model for envelope detection was provided in MathCAD. In this model Equation 6.6 calculates the peaks (Figure 6.12) of the photo-acoustic wave while Equation 6.7 smoothes the curve that forms the envelope (Figure 6.13).

Equation 6.6: Calculation f the photo-acoustic wave envelope (Peak-Detection)

$$\mathbf{Peak_n :=} \left| \begin{array}{l} \mathbf{AFp_n \text{ if } AFp_n > \max\left(AFp_{n-1}, AFp_{n-2}, AFp_{n-3}, AFp_{n-4}, AFp_{n-5}, AFp_{n-6}\right)} \\ \mathbf{\max\left(AFp_{n-1}, AFp_{n-2}, AFp_{n-3}, AFp_{n-4}, AFp_{n-5}, AFp_{n-6}\right) \text{ otherwise}} \end{array} \right.$$

Equation 6.7: Curve smoothing

$$\mathbf{SP} := \mathbf{medsmooth}\,(\mathbf{Peak}\,, 25)$$

where

SP: smoothed curve (envelope) of the photo-acoustic wave

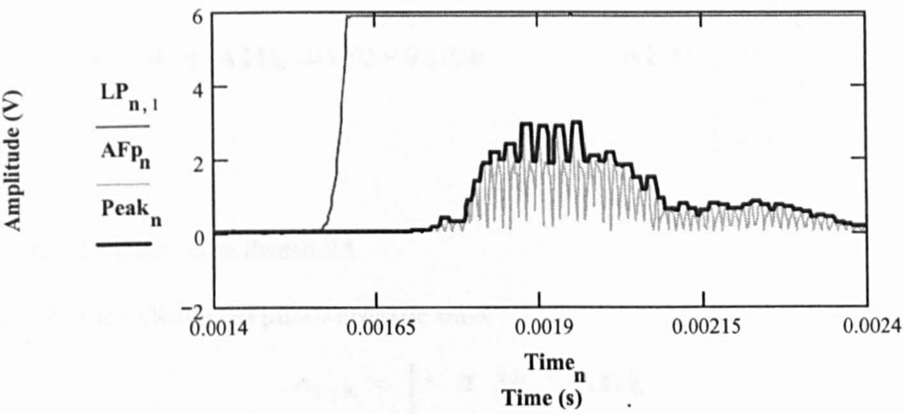

Figure 6.12: The calculated peaks envelope of the photo-acoustic wave

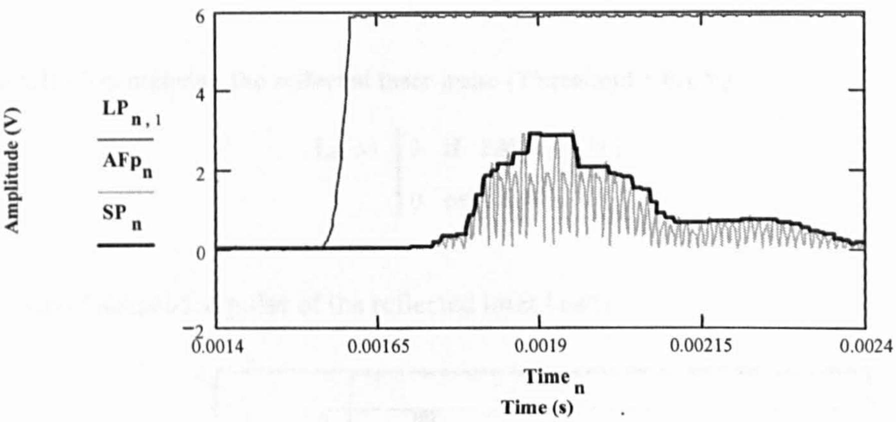

Figure 6.13: Smoothing of the photo-acoustic wave envelope

The next step is to normalize (convert into step pulses) the reflected laser beam pulse and the envelope of the photo-acoustic wave (Figure 6.14). This can be achieved by setting threshold levels for both signals. These threshold levels are normally less than or equal (0.1 V) and used to determine the start points of the reflected laser beam and the photo-acoustic wave. A high value (5V) is assigned if the signal is above the threshold level otherwise a low value (0V) is assigned (Equation 6.9 and Equation 6.10). Different threshold levels may be set for both signals depending on the baseline signal to noise ratio. Furthermore, to eliminate the ambiguity in determining the exact start point of the photo-acoustic wave several threshold levels may be used and the average TOF used. This helps reduce early detection due to noise, however rather than using the average TOF the TOF values could be analysed to provide a better TOF estimate. The lower and upper threshold level limits in this example have been carefully selected after performing a large number of TOF experiments. Although a better TOF estimate may be attained by increasing the number of threshold levels within these limits.

Equation 6.8: Calculating the photo-acoustic threshold values

$$k := 0..4 \quad ATH_k := 0.03 + 0.010 \cdot k \qquad ATH = \begin{pmatrix} 0.03 \\ 0.04 \\ 0.05 \\ 0.06 \\ 0.07 \end{pmatrix} \text{V}$$

where

ATH: is the photo-acoustic threshold

Equation 6.9: Normalising the photo-acoustic wave

$$A_{n,k} := \begin{vmatrix} 5 & \text{if } SP_n > ATH_k \\ 0 & \text{otherwise} \end{vmatrix}$$

where

A: is the Normalised pulse of the photo-acoustic wave

Equation 6.10: Normalising the reflected laser pulse (Threshold = 0.1 V)

$$L_n := \begin{vmatrix} 5 & \text{if } LP_{n,1} > 0.1 \\ 0 & \text{otherwise} \end{vmatrix}$$

where

L: is the Normalised pulse of the reflected laser beam

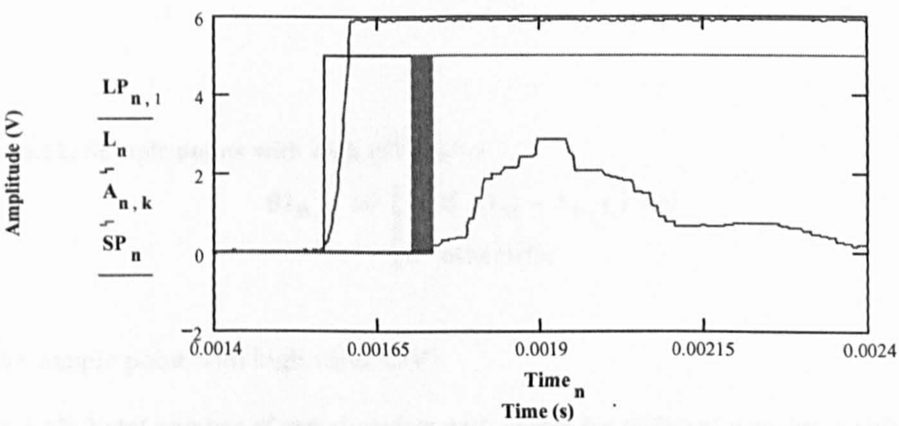

Figure 6.14: Normalised reflected laser beam pulse and photo-acoustic wave envelope

The time delay between the reflected laser pulse and the pulse that represents the arrival of the photo-acoustic wave is calculated by counting the number of sample point between the pulses (i.e. total number High level sample points (Figure 6.15)).

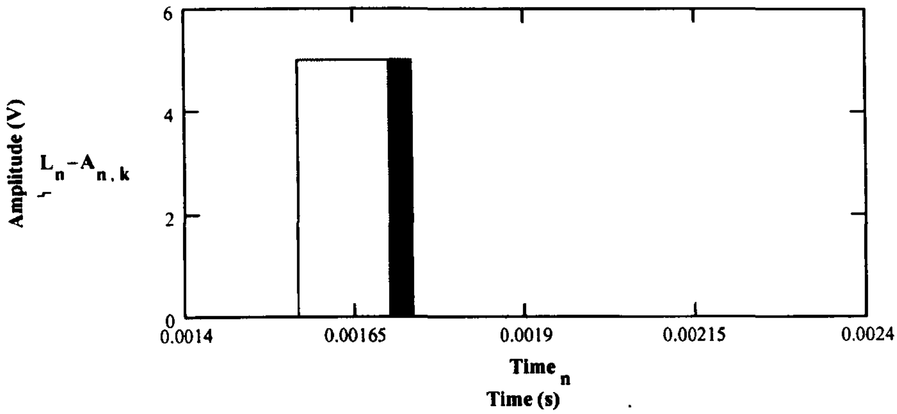

Figure 6.15: The difference in samples point and time between the detection of the laser pulse and the photo-acoustic wave

According to this technique for the given sampling rate (SR =500 K Samples /sec), the time delay (TOF) can be calculated as follows

Equation 6.11: General form of time delay calculation

$$\mathbf{SR} := 500 \cdot 10^3 \qquad \lambda := \frac{1}{\mathbf{SR}} \qquad \mathbf{TOF} := \mathbf{S} \cdot \lambda$$

where

SR: is the sample rate (Sa/sec)

λ: is time duration per sample pulse

S: is the total number of samples with high values that form the difference between the start of the reflected laser pulse and the start of the photo-acoustic wave. This can be calculated as follows:

Equation 6.12: Sample points with high (5V) value

$$\theta 1_{n,k} := \left| \begin{array}{l} 1 \ \text{if} \ (L_n - A_{n,k}) > 0 \\ 0 \ \text{otherwise} \end{array} \right.$$

where

$\theta 1$: is the sample point with high value (5V)

Equation 6.13: Total number of sample points with values for different acoustic threshold levels

$$S_k := \sum_n \theta 1_{n,k} \qquad S = \begin{pmatrix} 68 \\ 68 \\ 70 \\ 79 \\ 84 \end{pmatrix}$$

Hence the time delay (TOF) for the different photo-acoustic threshold levels is:

$$\mathbf{TOF} = \begin{pmatrix} 1.36\times 10^{-4} \\ 1.36\times 10^{-4} \\ 1.4\times 10^{-4} \\ 1.58\times 10^{-4} \\ 1.68\times 10^{-4} \end{pmatrix} \quad \mathbf{sec}$$

For the given distance of **50 mm** between the photo-acoustic sensor and the bone ablation site and a speed of sound = **340 m/s**. The measured distance using this technique is estimated as the average distance calculated for the different photo-acoustic threshold levels as shown below:

Equation 6.14: Calculated distance for the different photo-acoustic threshold levels

$$\text{For} \quad v := 340 \quad \text{m/s}$$

$$\mathbf{D} := v \cdot \mathbf{TOF} \quad \text{m} \qquad \mathbf{D} = \begin{pmatrix} 46.24\times 10^{-3} \\ 46.24\times 10^{-3} \\ 47.6\times 10^{-3} \\ 53.72\times 10^{-3} \\ 57.12\times 10^{-3} \end{pmatrix} \quad \text{m}$$

And the average calculated distance is

$$\mathbf{Distance} := \mathbf{mean}(\mathbf{D}) \quad \text{m} \qquad \mathbf{Distance} = 50.18\times 10^{-3} \quad \text{m}$$

The median and standard deviation of the calculated distance are:

$$\mathbf{median}(\mathbf{D}) = 47.6\times 10^{-3} \quad \text{m}$$

$$\sigma := \mathbf{stdev}(\mathbf{D}) \qquad \sigma = 4.436\times 10^{-3} \quad \text{m}$$

This ATOF technique shows an average calculated distance of 50.18 mm with a standard deviation of ~ 4.4 mm. This stand deviation value is highly dependent on the preset Acoustic Threshold (ATH) levels. As the difference between the acoustic thresholds levels decreases, the standard deviation decreases and vice versa. These ATH levels may also affect the average measured distance hence the initial threshold level must be carefully set to avoid noise detection yet to be small enough to detect the start of the rising edge of the induced photo-acoustic wave.

Although the standard deviation value seems large, the average measured distance (50.18 mm) using the ATOF appears to agree with the preset distance (50 mm) between the photo-acoustic sensor and bone surface at the ablation site. The ATOF's average measured distance of 50.18 mm represents the position of the Laser Front at the ablation site relative to a fixed reference point (the position of the photo-acoustic sensor). Errors in the measurement are possibly due to:

- measurement error in the preset distance between the photo-acoustic sensor and bone surface at the ablation site

- the Laser Front propagation into bone during the laser ablation
- the response time for the photo-acoustic sensor
- the assumed value of the speed of sound (340 m/s) used in this calculation. Ideally due to environmental factors [Appendix F], the speed of sound may fluctuate. Therefore, for higher accuracy measurements, an adaptive calibration circuit may be required to adjust the value of the speed of sound in real time.

Despite the large standard deviation value and the ATOF measurement error, this result shows that with the proper detection components this technique may be effective in accurately determining the position of the Laser Front inside tissue during the laser tissue interaction.

6.7 Acoustic Phase Shift Technique

This second technique developed aimed to measure the average ablation depth per laser pulse in real time during laser tissue interaction. It measures the phase shift between "non-uniform" irregular waveforms sharing similar characteristic in terms of their frequency and waveform and calculates the average ablation depth per pulse and the ablation rate. Figure 6.16 shows the phase shift between two subsequent induced photo-acoustic waves, achieved by synchronising the corresponding ablation laser pulses.

This phase shift technique features time independent measurements which have high immunity to amplitude noise. It measures the phase shifts over a number of photo-acoustic cycles by means of a sampling frequency and the number of sample points involved. Section 6.7.1 explains steps of the phase shift technique. Section 6.7.2 then verifies the technique using a mathematical model that provides idealised waveforms. Finally, Section 6.7.3 validates the technique using real data measurements for waveforms acquired during CO_2 laser bone ablation.

This technique is frequency dependent and can measure depths ranging from 0 to λ mm (the wavelength of the acquired photo-acoustic wave) corresponding to 0 to 2π radians of a phase shift. Therefore, the maximum measurable depth is limited by the frequency of the acquired photo-acoustic waves and the speed of sound. For example, a 40 kHz photo-acoustic wave at a speed of sound of 340 m/s limits the maximum depth measurement to about 8.5 mm; at 100 kHz the depth measured is limited to 3.4 mm.

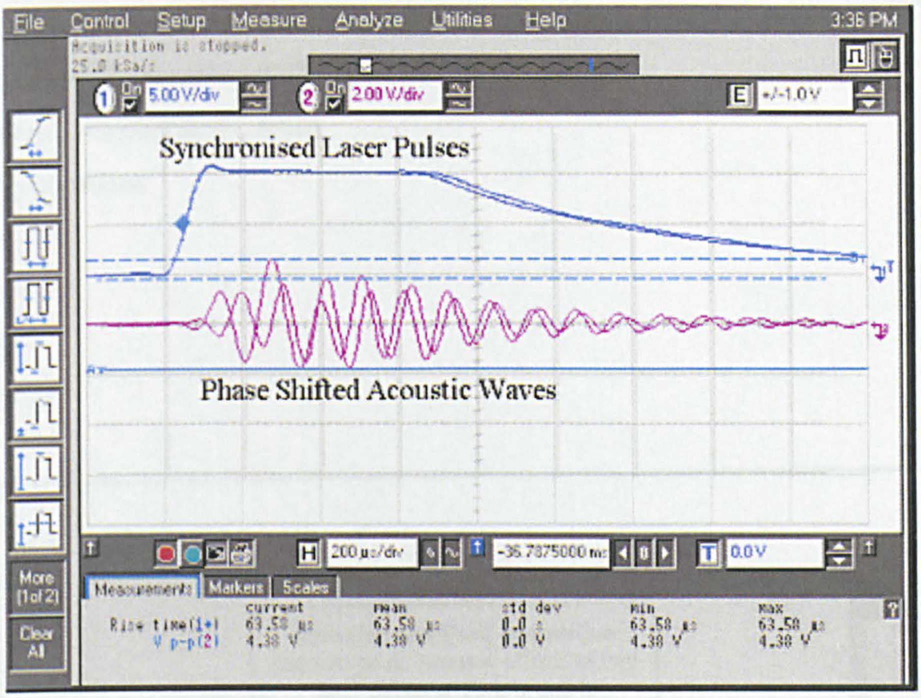

Figure 6.16: Phase shift of two sequential acoustic waves with synchronized laser pulses

6.7.1 Phase Shift Measurement and Feedback Technique

The phase shift measurement and feedback technique consists of the following major design components:

- Laser and photo-acoustic detection devices
- Detection and interface circuit
- Dual channel data acquisition and sampling unit
- Signal processing and data manipulation software

The output of this technique contains information about the average phase shift between the induced photo-acoustic waves (could be more than two waves: Group Phase Shift). This phase shift in time corresponds to the bone ablation depth per pulse or number of pulses. The output may also contain information about the ablation rate.

Figure 6.17 shows a block diagram of the operation principle of this phase shift measurement and the feedback technique with step by step illustrations of the signal processing and data manipulation. The phase measurement system can either be implemented by software or hardware and the major implementation components as shown in the circuit design in Figure 6.18 include:

- AC coupled analogue switch (tri-state analogue buffer)

- Synchronisation window generator circuit (analogue switch control circuit) with TTL input
- Sampling circuit (Sample and Hold)
- Comparator (normalising circuit)
- Memory locations
- XOR Gate
- Up-Counter
- Divider
- Multiplier

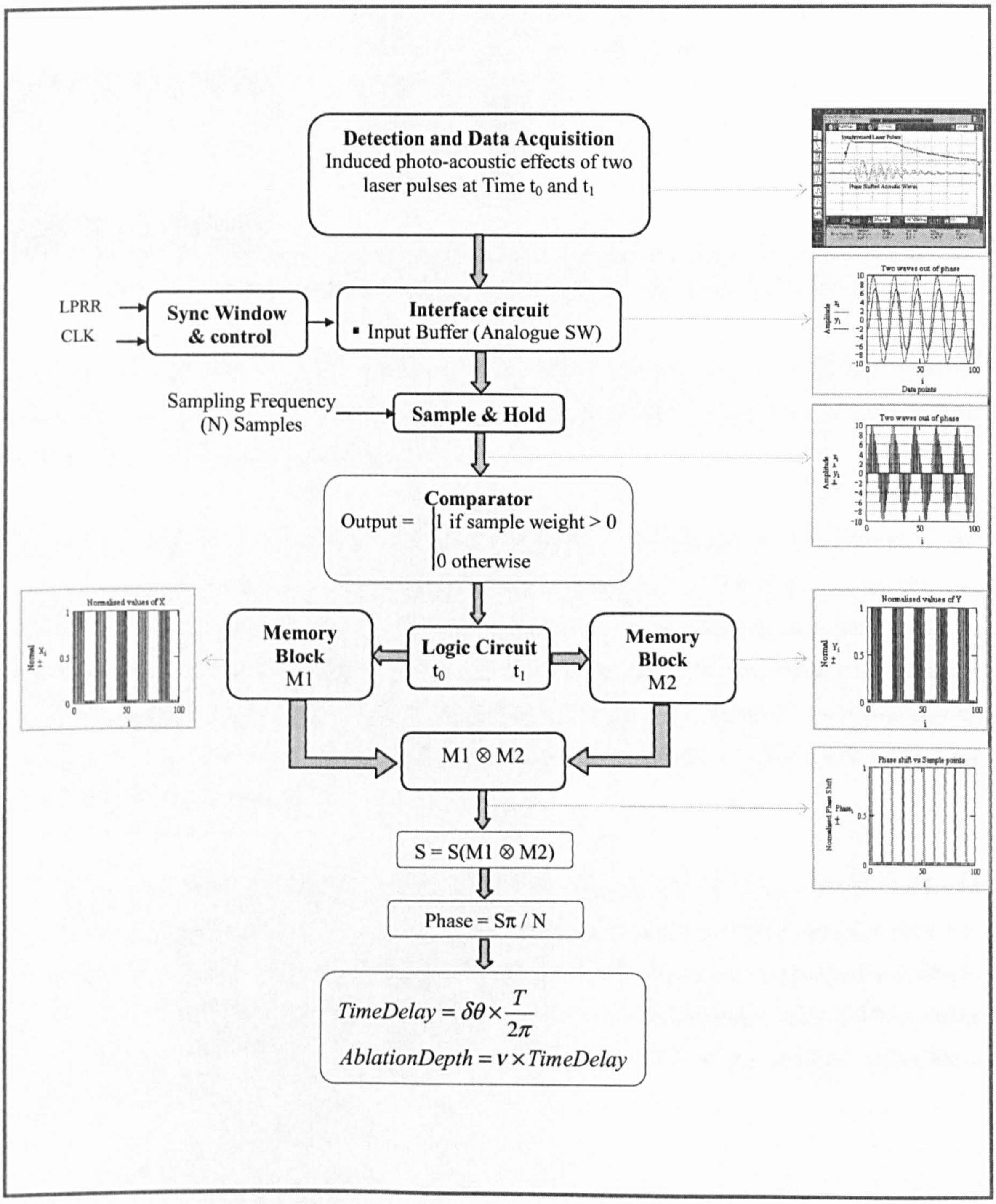

Figure 6.17: A block diagram of the phase shift measurement technique operation principle

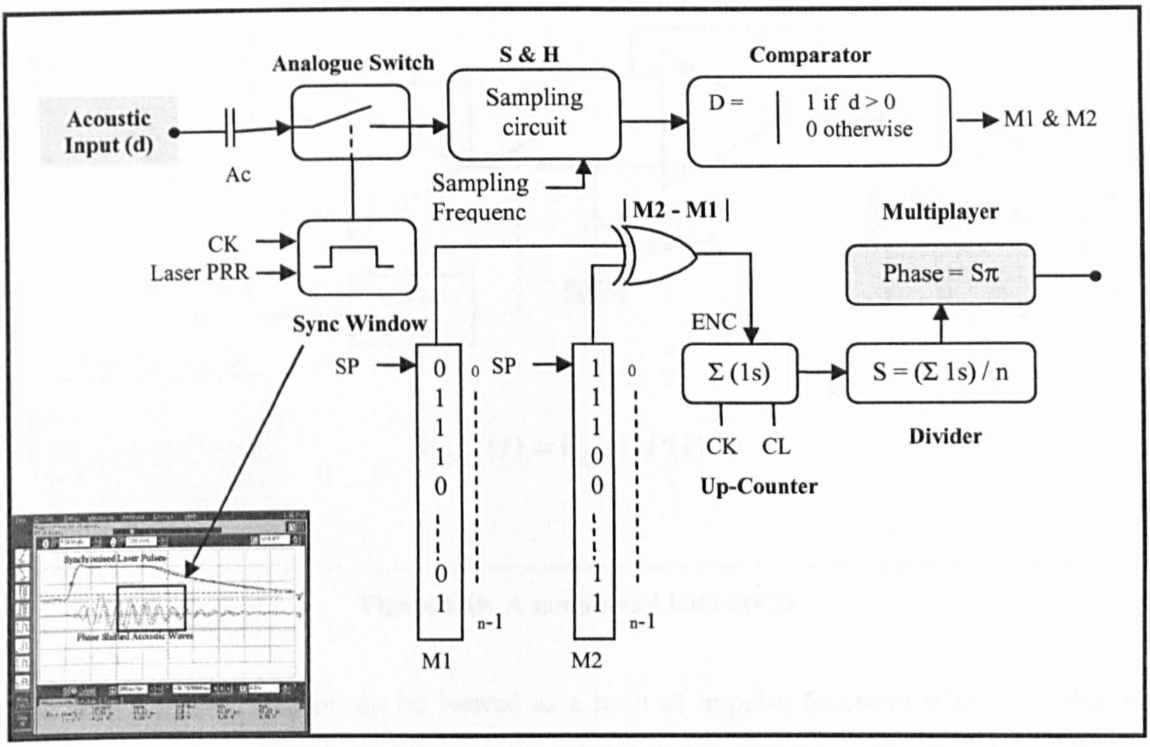

Figure 6.18: A block diagram of the phase shift measurement technique circuit design

The AC coupled analogue switch (Figure 6.18) controls the acquisition of the laser induced photo-acoustic waves by allowing only a limited number of acoustic cycles to pass through to the sampling circuit (Sample and Hold).

The Synchronisation window generator circuit is basically an analogue switch control circuit. This circuit synchronises the acquisition of the photo-acoustic waves with respect to the ablation laser pulses. This circuit is triggered by TTL input pulses representing the laser and generates delayed output pulses with a pulse repetition equivalent to that of the laser, and pulse duration much larger than that of a single acoustic wave. The pulse delay is required in order to avoid the acquisition of the early acoustic response cycles. However, this delay should not affect the pulse repetition rate by any means.

The sampling (Sample & Hold) circuit is a device for analogue signal conversion into a train of amplitude modulated pulses [GOPA 88]. The actual design of a sample and hold circuit is shown in Figure 6.19. It typically consists of a capacitor, an electronic switch and operational amplifiers. The operational amplifiers are needed for isolation, to reduce the capacitor loading effect on the analogue signals. The capacitor (Hold Device) holds the value of the sampled pulse for a prescribed time duration.

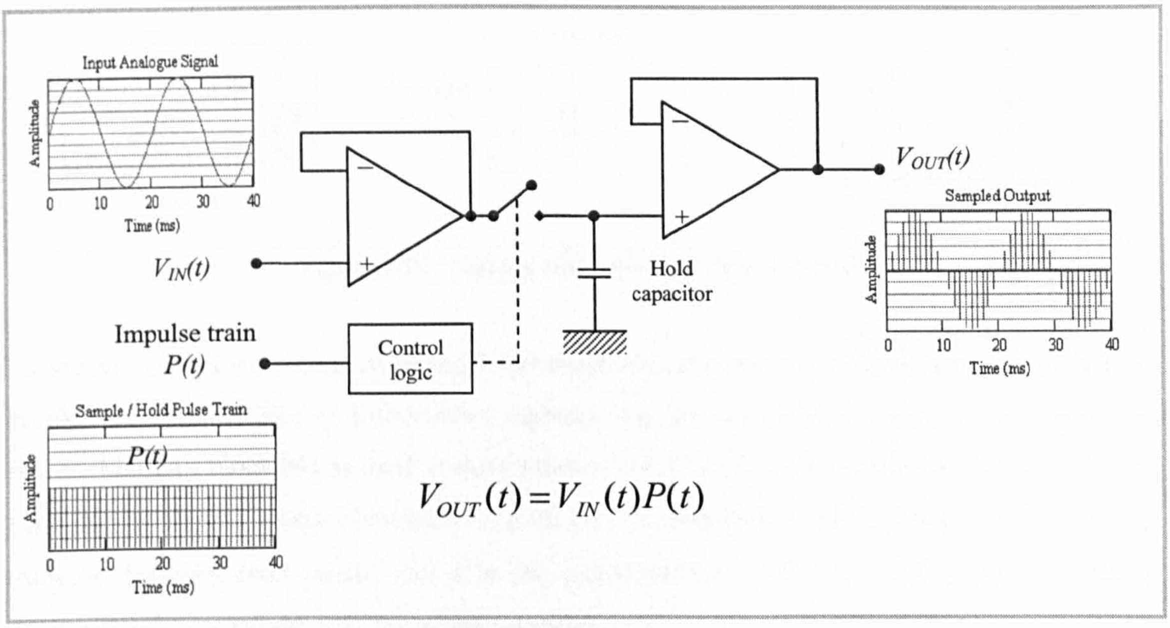

Figure 6.19: A sample and hold device

The output of the sampler can be viewed as a train of impulse functions whose weights are equal to the values of the continuous input signal at the instants of the sampling (impulse modulation). It is important to note here that sampling frequency should be at least twice the input frequency to avoid aliasing [GOPA 88] [HAYK 99]. For high sampling resolution the sampling frequency must be much larger than the input frequency. Mathematically the sampled signal $V_{OUT}(t)$ of an ideal sampler is represented as the product of the original input continuous-time $V_{IN}(t)$ signal and an impulse train $P(t)$ [GOPA 88] [HAYK 99], (Equation 6.15).

Equation 6.15

$$V_{OUT}(t) = V_{IN}(t)P(t)$$

where

$$P(t) = \sum_{0}^{n-1} \delta(t - nT)$$

and T is the sampling interval with a sampling frequency f_s equals $1/T$, and n is the number of sample points.

The main function of the comparator circuit is to compare the weights of the sampled signal's impulse functions with zero and generate a binary output accordingly. A (1) value is given for all sample data points whose weights are greater than zero and (0) otherwise (Figure 6.20). These binary outputs are then stored in pre-specified memory locations.

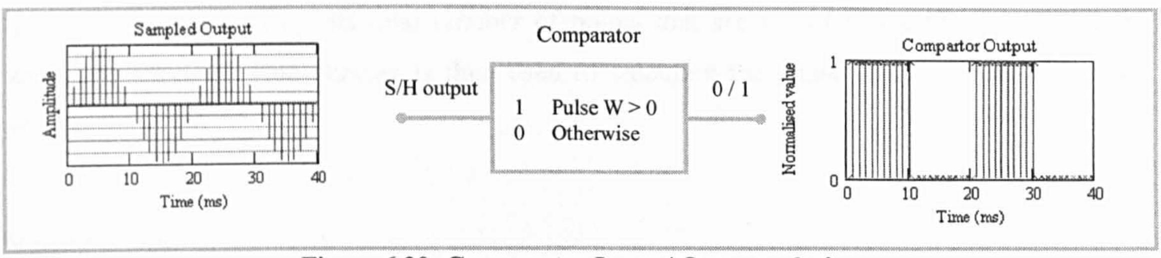

Figure 6.20: Comparator Input / Output relation

As shown in Figure 6.17, the phase shift technique requires two memory blocks. These memory blocks are to store binary information representing the normalised values of the sampling points. Memory block M1 is used to store information from the initial photo-acoustic waves (at time $[t_0]$) while M2 stores information for all other subsequent waves $[t_0 + \tau\kappa]$; where τ is the duration between laser pulses and κ is the pulse number. The size of the memory blocks determines the maximum number of data samples (n).

The X-OR gate calculates the absolute difference between data stored in M1 and M2. The X-OR gate output will be (1) if and only if the absolute difference between data stored in M1 and M2 at address x, equals (1) (i.e. $|M1\text{-}M2| = 1$). This output increments an up-counter every time the output is a (1). The (1s) here represent the sample points that are out of phase.

An alternative to the X-OR would be a comparator circuit that compares the data points in M1 and M2 generating a (1) output if and only if M1>M2 and (0) otherwise. Figure 6.21 shows the expected outputs of the both the X-OR circuit and comparator circuit for two signals out of phase.

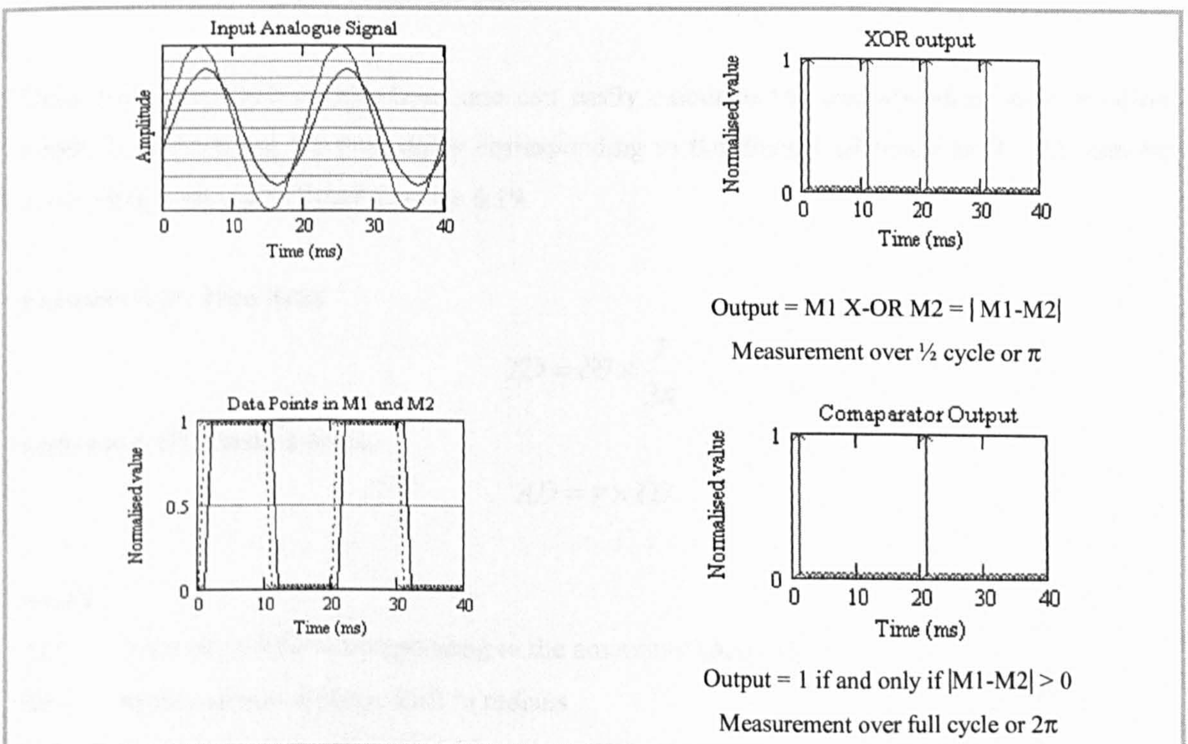

Figure 6.21: The expected X-OR and Comparator outputs for the same analogue signals

The up-counter sums up the total number of points that are out of phase (S) over the entire sampling window. This number is then used to calculate the phase shift between two wave forms.

Equation 6.16

$$S_{XOR} = \sum_{0}^{n-1} |M1 - M2| \qquad \text{or} \qquad S_{comp} = \sum_{0}^{n-1} [(M1 - M2) > 0]$$

The Divider and Multiplier can be implemented by software to calculate the phase shift between two consecutive signals. The phase shift equals to the total number of (1s) over the total number of samples multiplied by π for the X-OR implementation or 2π for the comparator one Equation 6.16. This gives the phase shift value in radians which can then be converted to time and distance as shown in Equation 6.17 below. The phase shift technique presented is immune to amplitude noise and can be applied to real time or streaming signals with high accuracy.

Equation 6.17

$$\delta\theta = S_{XOR} \frac{\pi}{n} \qquad \text{or} \qquad \delta\theta = S_{comp} \frac{2\pi}{n}$$

where

δθ	is the calculated phase shift in radians
S	is the total number of (1s) for either the X-OR and comparator implementations
n	is the total number of sample points

Once the phase shift is calculated one can easily calculate the corresponding laser ablation depth, by calculating the time delay corresponding to the amount of phase shift. This can be done using Equation 6.18 and Equation 6.19.

Equation 6.18: Time delay

$$TD = \delta\theta \times \frac{T}{2\pi}$$

Equation 6.19: Ablation depth

$$AD = v \times TD$$

where

TD	is the time delay corresponding to the amount of phase shift
δθ	is the calculated phase shift in radians
T	is the period (in radians) of the given signal (photo-acoustic wave)

v	is the speed of sound
AD	is the laser ablation depth

The following section presents a mathematical model of the phase shift measurement technique followed by an example on real data acquired during laser bone ablation.

6.7.2 Mathematical Verification of the Acoustic Phase Shift Measurements Technique

This section uses a mathematical model implemented in MathCAD to verify the phase shift measurements technique. This model also demonstrates the efficiency of the technique that calculates the phase shift between two waves which have similar properties in terms of wavelengths and wave shape. The waves (**x** and **y**) presented in this model are computer generated waves with differences in magnitudes and a pre specified phase shift (**Δθ**). As discussed in the previous section this model uses sampling to calculate the phase shift between waves. The model involves a number of steps.

Step1: Creating the Waveforms

Let (**i**) be the number of sample points. **x** and **y** (Figure 6.22) are the two waves that shifted in phase by **Δθ**

$$i := 1 .. 100 \qquad \theta_i := i \cdot \frac{\pi}{10} \qquad \Delta\theta := \frac{\pi}{5} \qquad \Delta\theta = 0.628$$

$$x_i := 10\sin(\theta_i) \qquad y_i := 5\sin(\theta_i - \Delta\theta)$$

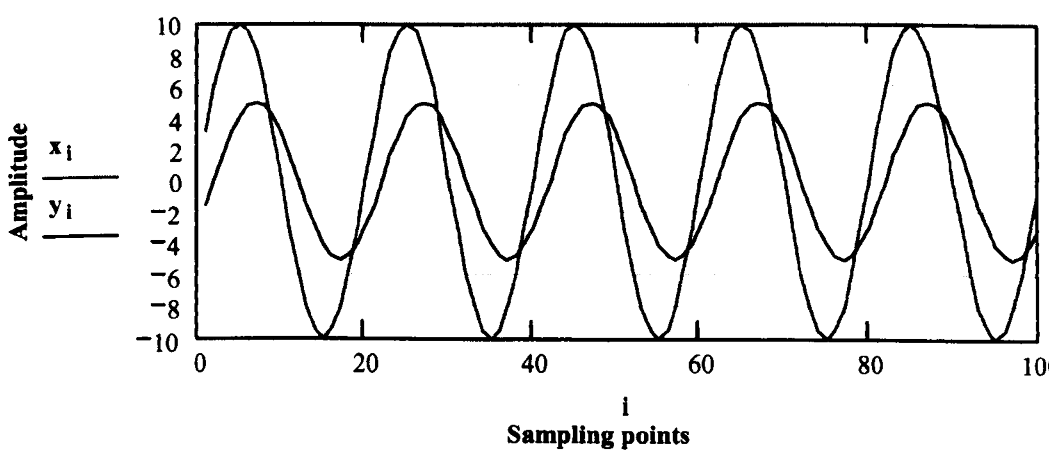

Figure 6.22: Two waves x and y that are out of phase

Step 2: Wave Normalising

A value [1] is assigned for all points greater than 0 and [0] otherwise.

Equation 6.20: Wave Normalising equations

$$X_i := \begin{cases} 1 & \text{if } x_i > 0 \\ 0 & \text{otherwise} \end{cases} \qquad Y_i := \begin{cases} 1 & \text{if } y_i > 0 \\ 0 & \text{otherwise} \end{cases}$$

where

X and Y: are the normalised values for the **x** and y waves respectively

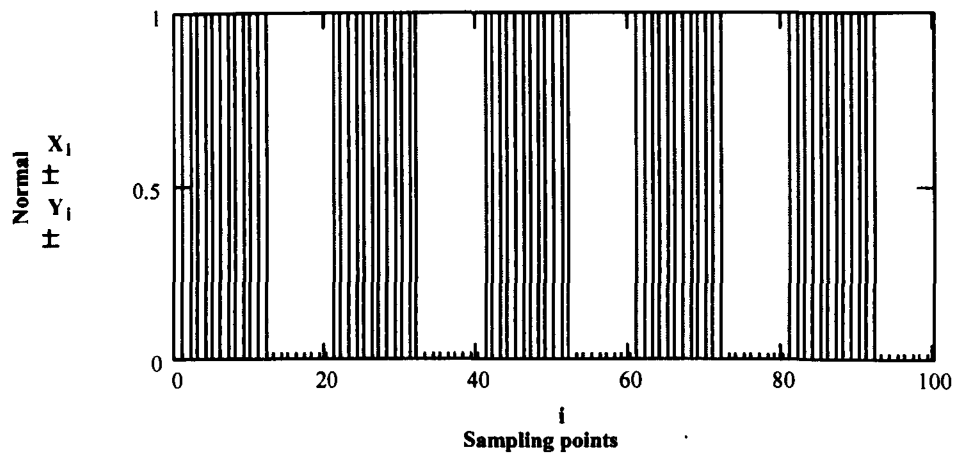

Figure 6.23: Normalised values of the x and y waves

Step 3: Calculating the Phase Shift

To calculate the phase shift one must calculate the number of Normalised sample points that are out of phase. These points are equal to the absolute difference between the normalised values of x and y (Equation 6.21)

Equation 6.21: Phase shift calculations

$$\mathbf{PSpoints}_i := \left| X_i - Y_i \right|$$

where

PSpoints: are the out of phase sample points

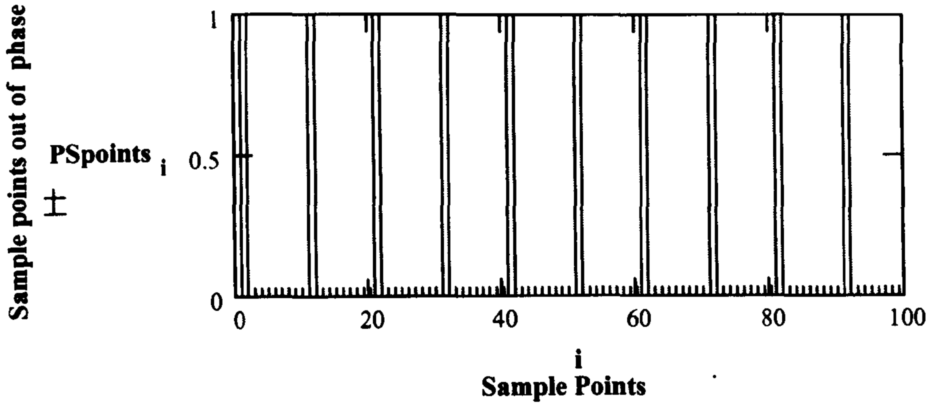

Figure 6.24: Sample points that are out of phase

Equation 22: Total number of points that are out of phase

$$S := \sum_i PSpoints_i \qquad S = 20$$

where

S is the total number of points that are equal [1] value.

Equation 6.23: Phase shift

$$PHASE := \frac{S\pi}{100} \ \text{rad} \qquad PHASE = 0.628 \ \text{rad}$$

where

PHASE: is the phase shift value and (100) is the number of sampling points

The phase shift calculation results using this APS model show that the calculated phase value (PHASE) is 0.628 radians which is identical to the preset phase shift value ($\Delta\theta$). This verifies the phase shift technique is accurate and indicates that it has the potential to provide an accurate phase shift measurement values. More supporting examples are presented in Appendix A: Feedback Techniques.

6.7.3 Experimental Evaluation of the Acoustic Phase Shift Measurements Technique (APS)

The acoustic phase shift technique is applicable to real time or (streaming) waves. Thus it provides a means to calculate the bone ablation depth per pulse by measuring the phase shift between the induced photo-acoustic waves. As mentioned previously the measured bone depth is limited to the acoustic wavelength and the laser bone ablation rate is easily calculated from the ablation depth. In order to apply this technique for laser bone ablation measurements, the following is required:

- The laser pulse repetition rate
- The period between laser pulses
- A limited number of photo-acoustic waves cycles (window)
- The exact frequency of the acquired photo-acoustic waves
- An accurate evaluation of the speed of sound at the time of laser tissue interaction

In this technique the laser pulse repetition rate is mainly required for photo-acoustic waves' synchronisation as shown in the following example:

Data and results are given below from an experiment conducted to calculate the phase shift between two induced photo-acoustic waves acquired during CO_2 laser bone ablation. These waves are acquired for two sequential laser pulses (Figure 6.25). The acquired data as stated in Section 6.7.1 are captured via a digital storage oscilloscope and exported to MathCAD for further calculations and analysis. Samples of the acquired data are presented in the following tables:

$\mathbf{n} := 100..\,9000$

LP :=

	0	1
0	-0.05154	-1.78
1	-0.05154	-1.77
2	-0.05153	-1.76

AFB :=

	0	1
0	-0.05154	0
1	-0.05154	0
2	-0.05153	-0.01

$\mathbf{LPI_{n,0}} := \mathbf{LP_{n,0}} - \mathbf{LP_{0,0}}$

$\mathbf{Time_n} := \mathbf{LPI_{n,0}}$

LP is the Laser Pulse
AFB is the acoustic Feedback

column (0) represent the time

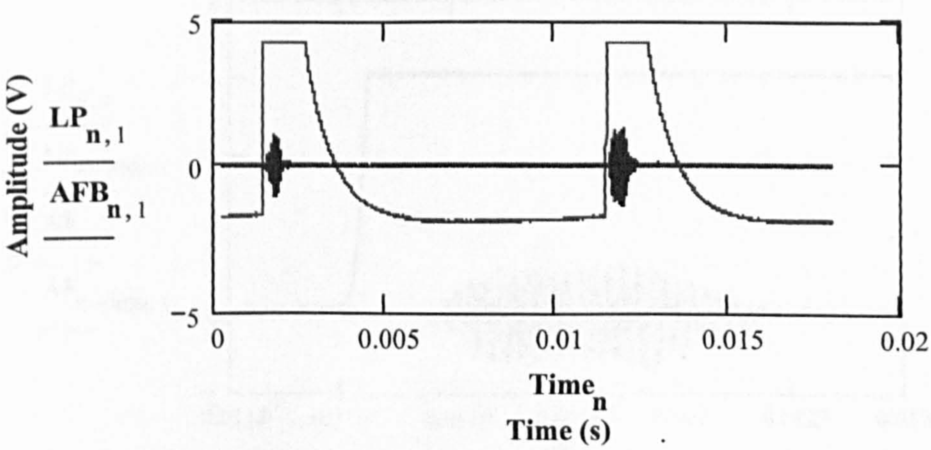

Figure 6.25: Acquired induced light and photo-acoustic waves plotted as a function of time

The acquired waves undergo the following signal processing procedure and mathematical manipulation in order to calculate the acoustic phase shift. The first step was to remove the DC component of both signals and set the zero baselines for each of the induced light (laser beam) and photo-acoustic waves (DC offset null). Due to possible variation in DC levels for each induced wave, the zero baseline for each signal should be set independently (Equation 6.24 and Equation 6.25)

Equation 6.24: Setting the photo-acoustic zero baseline

$$\mathbf{AFbase1} := \mathbf{mean}\left(\mathbf{AFB}_{500,1}, \mathbf{AFB}_{450,1}, \mathbf{AFB}_{400,1}, \mathbf{AFB}_{350,1}, \mathbf{AFB}_{300,1}, \mathbf{AFB}_{250,1}\right)$$

$$\mathbf{AF}_{n,1} := \mathbf{AFB}_{n,1} - \mathbf{AFbase1}$$

$$\mathbf{AFbase2} := \mathbf{mean}\left(\mathbf{AFB}_{5500,1}, \mathbf{AFB}_{5450,1}, \mathbf{AFB}_{5400,1}, \mathbf{AFB}_{5350,1}, \mathbf{AFB}_{5300,1}, \mathbf{AFB}_{5250,1}\right)$$

$$\mathbf{AF}_{n+5000,1} := \mathbf{AFB}_{n,1} - \mathbf{AFbase2}$$

Equation 6.25: Setting the laser pulse zero baseline

$$\mathbf{LPbase1} := \mathbf{mean}\left(\mathbf{LP}_{500,1}, \mathbf{LP}_{450,1}, \mathbf{LP}_{400,1}, \mathbf{LP}_{350,1}, \mathbf{LP}_{300,1}, \mathbf{LP}_{250,1}\right)$$

$$\mathbf{LP}_{n,1} := \mathbf{LP}_{n,1} - \mathbf{LPbase1}$$

$$\mathbf{LPbase2} := \mathbf{mean}\left(\mathbf{LP}_{5500,1}, \mathbf{LP}_{5450,1}, \mathbf{LP}_{5400,1}, \mathbf{LP}_{5350,1}, \mathbf{LP}_{5300,1}, \mathbf{LP}_{5250,1}\right)$$

$$\mathbf{LP}_{n+5000,1} := \mathbf{LP}_{n,1} - \mathbf{LPbase2}$$

The next step is to synchronise the induced light waves (laser pulses) by overlapping the two laser pulses with 0 phase shift. This in effect results in overlapping the induced photo-acoustic waves (Figure 6.26). However, due to the time difference between laser pulses the photo-acoustic wave will be out of phase.

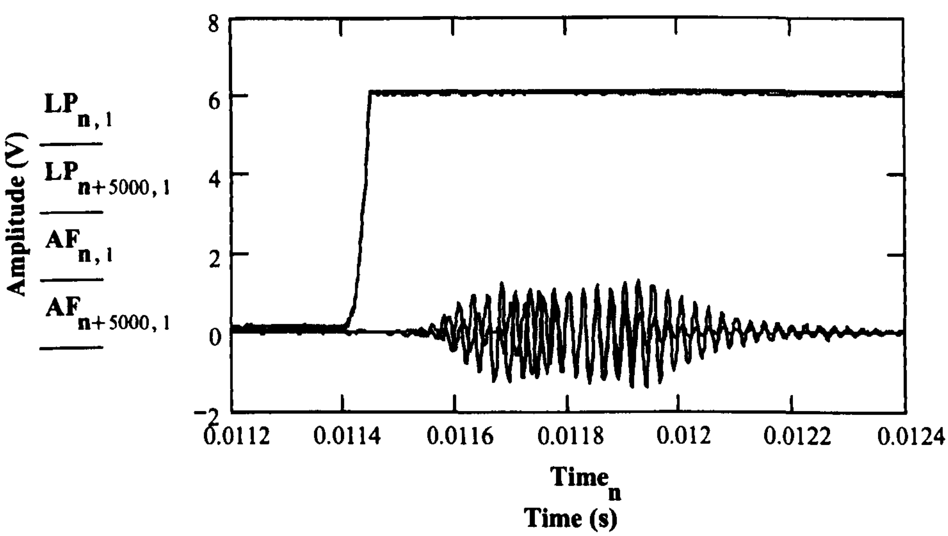

Figure 6.26: Synchronized laser pulses and phase shifted induced photo-acoustic waves plotted as a function of time

Next a window of a number of sample points is set up for calculating the average phase shift between the two photo-acoustic waves over a number of wave cycles (Figure 6.27).

$w := 200$ $n := 5850 .. 6150$

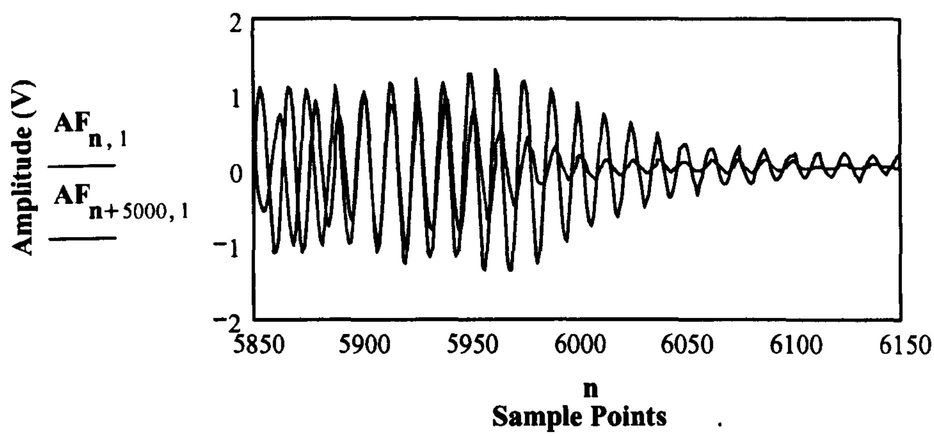

Figure 6.27: A window of 200 points for the overlapped photo-acoustic waves

The next step would be wave normalising; where logic [1] value is assigned for all points greater than 0 and [0] otherwise.

Equation 6.26: Normalising the induced photo-acoustic waves

$$U0_n := \begin{cases} 1 & \text{if } AF_{n,1} > 0 \\ 0 & \text{otherwise} \end{cases} \qquad U1_n := \begin{cases} 1 & \text{if } AF_{n+5000,1} > 0 \\ 0 & \text{otherwise} \end{cases}$$

where

U0 and U1: are the Normalised sample values for the photo-acoustics waves

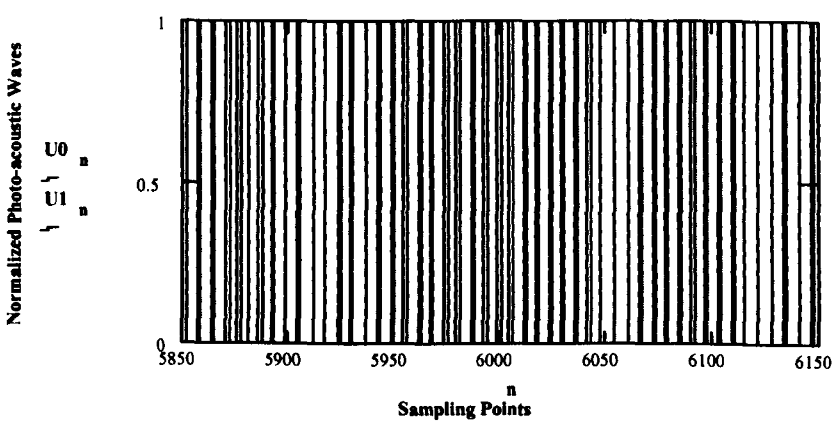

Figure 6.28: Plot of the normalised sample values of the photo-acoustic waves as a function of sampling points.

Once the normalising is completed the phase shift can be calculated. As explained in 6.7.1 the phase shift is calculated using the number samples that are out of phase. This can be done as follows:

Equation 6.27: Points out of phase

$$\mathbf{POP_n := |U0_n - U1_n|}$$

where

POP: represents the points that are out of phase

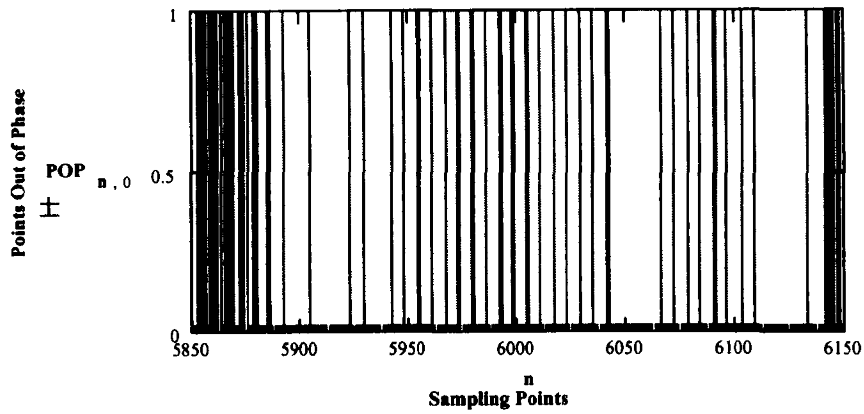

Figure 6.29: The Normalised out of phase points for the photo-acoustic waves

Equation 6.28: Total number of points that are out of phase

$$\mathbf{SReal} := \sum_{\mathbf{n}} \mathbf{POP_{n,0}} \qquad \mathbf{SReal} = 71$$

where
SReal: is the total number of points that are out of phase

Equation 6.29: Phase shift calculation

$$\mathbf{PHASE} := \frac{\mathbf{SReal}\pi}{\mathbf{w}} \qquad \mathbf{PHASE} = 1.115 \quad \mathbf{rad}$$

where
PHASE: is the phase shift in radians

Equation 6.30: The Phase shift value in degrees

$$\mathbf{PHASE\_deg} := \mathbf{SReal} \cdot \frac{180}{\mathbf{w}} \qquad \mathbf{PHASE\_deg} = 63.9 \quad \mathbf{Deg.}$$

where
PHASE_deg: is the Phase shift in degrees

To calculate the laser ablation depth one must first calculate the phase shift in time (the Time Delay). This can be achieved using Equation 6.31 which involves the frequency and wavelength of induced photo-acoustic waves. For this example the frequency of the photo-acoustic waves is 36.03 KHz and wavelength T is 27.75 μs. Thus time delay can be calculated as follows:

Equation 6.31: Time Delay (TD) Calculation

$$\mathbf{TD} := \mathbf{PHASE\_deg}\cdot\frac{\mathbf{T}}{360} \qquad \mathbf{TD} = 4.926\times 10^{-6} \quad \mathbf{sec}$$

and the corresponding ablation depth is:

Equation 6.32: Laser Ablation Depth

$$\mathbf{Depth} := 345\cdot\mathbf{TD} \qquad \mathbf{Depth} = 1.699\times 10^{-3} \quad \mathbf{m}$$

This yields the CO_2 laser bone ablation depth per pulse For the purpose of comparison the following section calculates the ablation depth using the new form of Beer's Law equation (Equation 6.33) for the given laser and bone parameters used in the actual experiment.

Equation 6.33: New Form of Beers Law

$$\mathbf{x} := \left(\frac{\mu}{\alpha\mu_{\mathbf{p}}}\right)\cdot\mathbf{ln}\left[1+\mu_{\mathbf{p}}\frac{(\mathbf{F}-\mathbf{Fth})}{\mu\mathbf{Fth}}\right]$$

where

- **x** is the ablation depth
- μ is the mass absorption coefficients for the bone
- $\mu_{\mathbf{p}}$ is the mass absorption coefficients for the plume
- α is the absorption coefficients
- **F** is the incident Fluence J/cm^2
- **Fth** is the threshold Fluence 1.4 J/cm^2 [IVAN 98]

Given the following parameters:

Spot Size = 52 μm $\alpha = 875$ cm^{-1} **Fth** =1.4 J/cm^2 F = 47.087 J/cm^2

For $\mu = \mu_p$

$$\mathbf{x} := \left(\frac{1}{\alpha}\right)\cdot\mathbf{ln}\left[1+\frac{(\mathbf{F}-\mathbf{Fth})}{\mathbf{Fth}}\right] \qquad \mathbf{x} = 4.018\times 10^{-3}$$

For $\mu > \mu_p$ (μ_p=0.33μ)

$$\mathbf{x} := \left(\frac{3}{\alpha}\right)\cdot\mathbf{ln}\left[1+\frac{(\mathbf{F}-\mathbf{Fth})\cdot 0.33}{\mathbf{Fth}}\right] \qquad \mathbf{x} = 8.453\times 10^{-3}$$

For $\mu < \mu_p$ (μ_p=3μ)

$$\mathbf{x} := \left(\frac{0.33}{\alpha}\right)\cdot\mathbf{ln}\left[1+\frac{(\mathbf{F}-\mathbf{Fth})\cdot 3}{\mathbf{Fth}}\right] \qquad \mathbf{x} = 1.733\times 10^{-3}$$

Comparing the above results with the laser ablation depth results obtained using the acoustic phase shift technique (APS); one can see that the APS technique shows an ablation depth per pulse, for the given set of laser parameters and a speed of sound = 345 m/s, approximately equal 1.7 mm. However, the ablation depth per pulse as predicted by the new form of Beer's Law is highly dependent on the mass absorption coefficients of the bone and the plume. For $\mu = \mu_P$ for example the ablation depth per pulse is predicted to be ~4 mm and for $\mu = 10\mu_P$ the ablation depth per pulse is predicted to be ~8.5 mm.

On the other hand, for $\mu_P = 3\mu$ (i.e the mass absorption coefficients for the plume is three times that of the bone) the ablation depth per pulse is predicted to be approximately equal to 1.7 mm which is similar to the acoustic phase shift calculations results. However; further investigation may be required in the future in order to validate these results. This may include: accurate evaluation of the speed of sound and the mass absorption coefficients during the laser bone interaction, and the direct measurements of the ablated craters (Microscopic Measurements). This also may include: the use of a spectrum analyser to investigating the exact frequency of the induced photo-acoustic waves. This in effect helps in selecting the most appropriate photo-acoustic feedback sensor (narrow band), that matches the frequency of the induced photo-acoustic waves. This may insure the detection of similar photo-acoustic waveforms and eliminate the ambiguity in identifying the depolarisation start points of the photo-acoustic waves. This may also insure no random phase shift between two consecutive pulses.

6.7.4 Potential Sources of Errors in the Measurements

The potential sources of errors associated with the photo-acoustic time of flight and phase shift measurements are mainly due to the following factors:

- Speed of sound variation due to environmental factors (Appendix F)
- Environmental noise
- Response time of the photo-acoustic transducer and Photo-detector
- The mass absorption coefficient of the plume relative to that of the bone
- Factor associated with the steps of the technique. These include: zero offset nulling, threshold level setting and accurate envelope evaluation (ATOF)

Over time bone loses some of its fluid due to dehydration. This in affect may cause an initial rise in temperature at the ablation site leading to an increase in the speed of sound. This may help explain the variation of the speed of sound through out the experiment.

6.8 Alternative Techniques for Measuring the Laser Front Position

Due to the environmental affects on the speed of sound and affects on the photo-acoustic measurements the author suggests the use of non-contact laser feedback ranging techniques as alternatives to photo-acoustic waves. These techniques include laser time of flight (TOF) and laser phase shift (PS) measurements.

Several other techniques have been developed elsewhere for laser range finding and distance measurements each of which is suitable for different application and measuring ranges. Some of these techniques may be applicable for laser orthopaedic surgery to determine the laser front position inside tissue. This section discusses three techniques worthy of further investigation but are beyond the scope of this project.

6.8.1 Laser Time of Flight (TOF) Measurement

This technique would measure time of flight of a laser thus it would remove the speed of sound variation problem the acoustic time of flight method presented earlier

Photons require a certain period of time to cover a distance from the sensor (Tx / Rx) to the target and back. In the laser TOF measurement system a short laser pulse is sent out toward a target and the time Δt required for the laser pulse to return is measured. This time is directly proportional to the distance travelled; taking into account the velocity of light in the medium involved it can be calculated as follows

$$d = \frac{c\Delta t}{2}$$

where

d is the travelled distance

c is the speed of light ($3\text{x}10^8$ m/s)

Δt is the time required for the round trip of the laser pulse

The TOF measuring technique may be applied during Er: YAG laser tissue interaction to measure the ablation depth and the position of laser front inside tissue. However; it may only be operational during the relaxation time between the ablation laser pulses. Given that the Er: YAG a laser pulse repetition rate of 1-30 Hz and a pulse duration of approximately 200 μs, the relaxation time would be in the range of 33.3328 -999.8 ms (~ 33 -1000 ms).

For high accuracy and precise measurements the TOF technique can be applied several times during the time interval between the laser ablation pulses. Figure 6.30 shows the operation principle and implementation of the TOF technique. This technique suggests repeated TOF measurements for a single position where the actual TOF is the average. Repeated TOF measurements may improve the signal-to-noise ratio and result in higher accuracies. The Advantages of the laser TOF over the acoustic TOF (ATOF) are as follow:

- Straight line active sensing (The transmitted and received laser pulses follow the same bath (Figure 6.30)
- The absolute range to the observed point is readily available with no complicated analysis ($d = c\Delta t/2$) and no assumptions and no environmental affects on the speed of light
- Accuracy is independent of the range in the laser TOF whereas in the ATOF accuracy is highly dependent on the magnitude of the induced photo-acoustic wave.
- Repeated TOF measurement for the laser type to improve accuracy while only one photo-acoustic measurement may be taken per laser pulse.

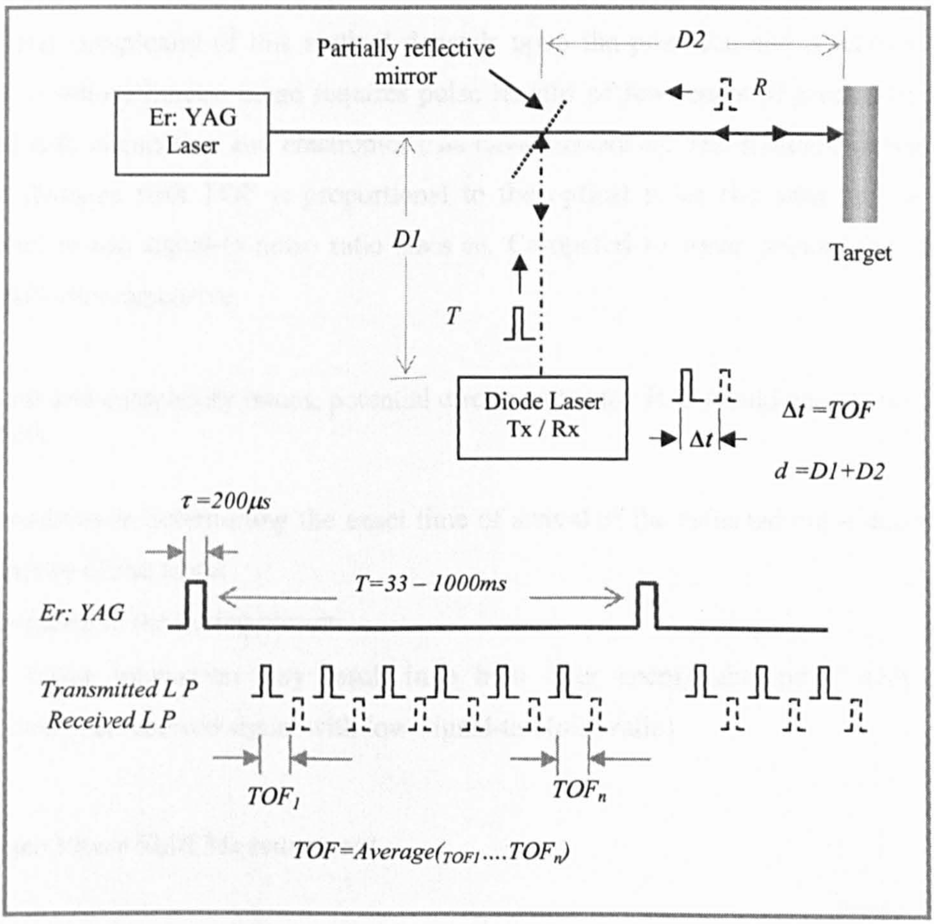

Figure 6.30: TOF laser ranging system during laser tissue ablation

The TOF technique must meet certain requirements. These include:

- Laser diode source (Class -1 eye safe) with a high sensitivity photodiode detector
- Short laser pulse durations.

- Non or minimal interaction with tissue (very low tissue interaction coefficient)
- High reflectivity (high tissue reflective or scatter coefficient)
- Safe to patient, medical staff and environment (cause no hazards)
- Accurate alignment and positioning relative to the laser line of interaction
- Must be fixed to the laser End-Effector and cause no constraints on laser manipulation
- High speed measurements (much higher than 30 Hz)
- Laser frequency response other than that of the Er: YAG (ablation) laser.
- The partially reflective mirror must cause no affect on the Er: YAG laser while causing total reflection of the diode laser
- Diode laser spot size must be much less than that of the ablation laser to allow for measurements inside holes.
- Ideally low cost
- Lightweight

The cost and complexity of this method depends upon the precision and resolution required. Precision in sub-millimetre range requires pulse lengths of few tenths of picoseconds and the associated data acquisition and electronics [Laser Components][ABOS 03]. The standard deviation in the measured distance with TOF is proportional to the optical pulse rise time and is inversely proportional to the signal-to-noise ratio [ABOS 03]. Compared to sonar sensors the laser range finder is still very expensive.

Besides cost and complexity issues, potential error sources for TOF would need to be investigated:

- Uncertainties in determining the exact time of arrival of the reflected pulse due to varying reflectivity of the target
- Inaccuracies in the timing circuit
- Laser tissue interaction may result in a high laser energy absorption with minimum reflection (i.e. received signal with low Signal-to-Noise ratio)

6.8.2 Laser Phase Shift Measurement

This method effectively measures the "echo" of a modulated continuous wave (CW) laser beam (Figure 6.31). The phase shift between the emitted and received signal is proportional to the distance travelled which can easily be calculated. With this method the maximum useful measurable distance is half of the distance travelled by light during one period, because for phase shift of over 360° (2π radians) the determination of measuring the distance travelled is not trivial. This method is typically used for measuring distances of a few tens of metres and can be extended by using modulation with variable frequencies or at more than one frequency simultaneously [ABOS 03]. This technique when implemented can make use of the phase shift model presented in Section 6.7.

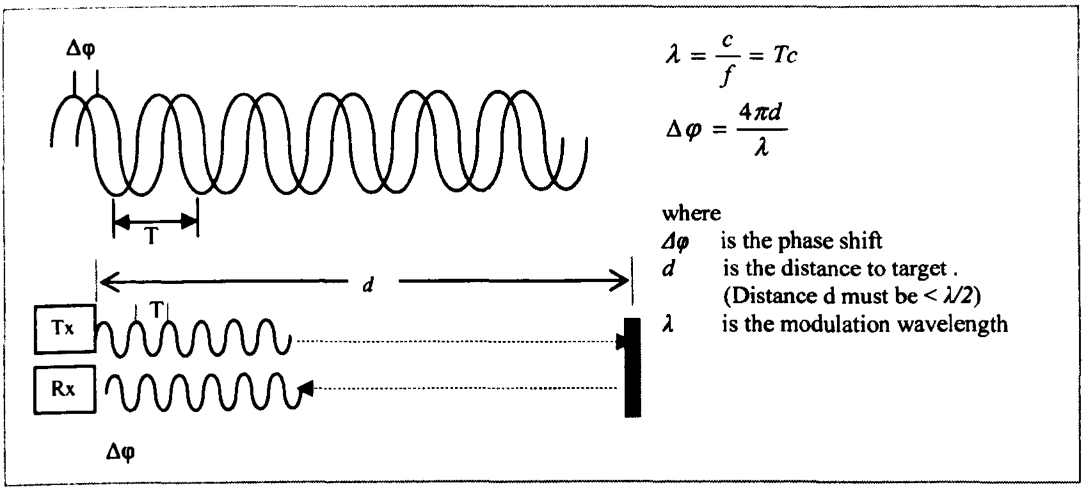

Figure 6.31: Laser phase shift measurement technique

6.8.3 Laser Absolute Interferometry

Absolute distance Interferometry (ADI) has been developed for high precision simultaneous absolute distance measurements [COE 02][KIND 02]. It is a general technique for measuring an interferometer of unknown length by comparing with a reference interferometer [DUNN 96] [COE 02]. The absolute distance interferometry allows for an unambiguous measurement of unknown length interferometry. It compares the distance to be measured with the wavelength of a known frequency of light.

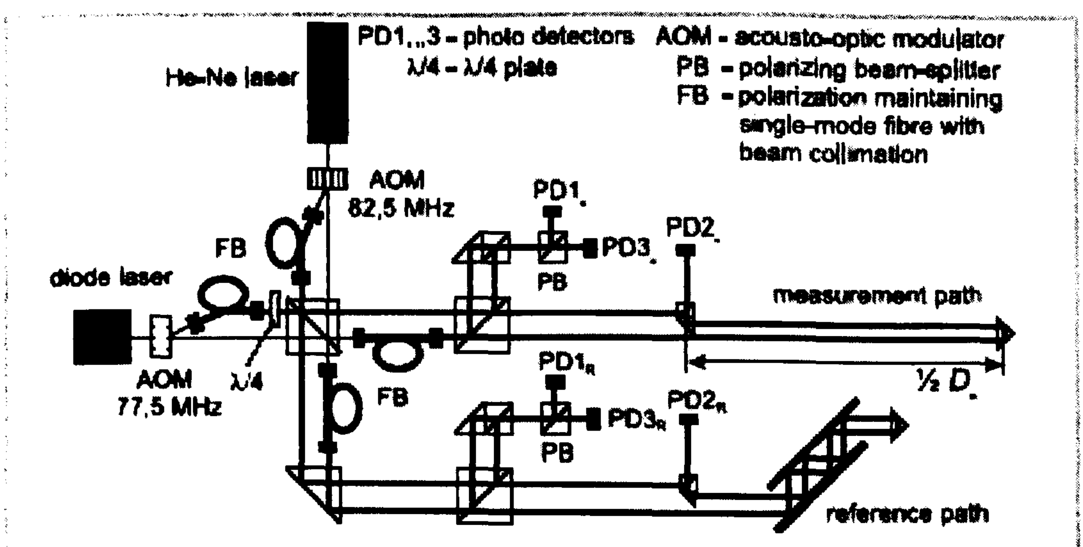

Figure 6.32: A schematic diagram of an absolute distance interferometer (ADI) [KIND 02]

The measurement principle of absolute distance interferometry is shown in Figure 6.32. A certain number of light waves (of wavelength λ_1) correspond to distance L. If this wavelength is continuously tuned (stretched) to λ_2, the number of wave forms corresponding to distance L will change. This number can be determined using an interferometer. The measurable phase difference resulting from this wavelength stretching is $\Delta\phi$, where [ABOS 03]:

$$L = \Delta\phi \frac{\lambda_1 \cdot \lambda_2}{2|\lambda_1 - \lambda_2|}$$

The phase change during the wavelength change from λ_1 to λ_2 can be measured using an interferometer. During the continuous laser tuning from λ_1 to λ_2 a second reference interferometer is used to simultaneously monitor a well-defined reference path, since the wavelength change of the diode laser is difficult to reproduce exactly [ABOS 03] [COE 02]. Because the phase change in the interferometer is proportional to its length, the ratio of phase change in the measurement interferometer ($\Delta\phi$) to the phase change in the reference interferometer ($\Delta\phi_{ref}$) is just equal to the ratio of the unknown measurement length (L) to the known length of the reference interferometer (L_{ref}) [STON 99][ABOS 03]. This gives

$$L = L_{ref} \frac{\Delta\phi}{\Delta\phi_{ref}}$$

The reference interferometer, on the other hand, may be replaced by a regulating interferometer which changes a defined λ_1 by a known increment $\Delta\lambda$ [ABOS 03].

The accuracy of this technique depends on the laser diode tuning range: the wider the continuous tuning (wavelength stretching) range of the laser, the higher the phase resolution and therefore the accuracy [ABOS 03].

Certain system requirements must be met before using absolute distance interferometry (ADI) as feedback system in the medical field during laser surgery; these include:

- The ADI laser source wavelengths must be safe and cause no tissue interaction or environmental hazards
- The ADI detectors must not react to reflected laser ablation beam wavelength
- The ADI must be compact and cause no constraints to other systems during surgical application

The major disadvantage of the variable-wavelengths ADI system is its high sensitivity to all error sources that affect the phase of the interferometer signals [KIND 02]. These sources may include analogue electronic circuits (amplifiers, band-pass filters and so on) that cause electronic phase shift. Large errors can occur if the distance being measured changes during the laser frequency sweep [KIND 02].

6.9 Summary

With the development of two innovative photo-acoustic feedback techniques presented in this chapter it appears possible to implement a closed loop control system for computer assisted laser bone surgery. These techniques determine the position of the laser front inside bone during laser bone interaction.

The acoustic time of flight technique (ATOF) can be used to measure the distance between the Laser Front position inside tissue and the photo-acoustic sensor placed inline with the laser beam at a fixed position from the tissue surface ($D_{measured}$). Hence, given the distance (D) between the acoustic sensor and the tissue surface, the depth of the laser front inside tissue can be calculated from the difference between $D_{measured}$ and D. The ATOF can also be used to measure the laser ablation rate and the laser ablation rate per pulse.

The alternative acoustic phase shift (APS) technique also measures the laser ablation depth and ablation rate. However this technique is limited in measurement to a maximum depth of one photo-acoustic wavelength for the ablation caused by a single pulse. An advantage of this technique over the ATOF is that it does not depend on the position of the photo-acoustic sensor relative to the ablation site. It only requires information about the start of the laser ablation pulse and the pulse repetition rate. This technique showed 100% accuracy for measuring the phase shift between well defined waves. This technique can also be used to measure group delay (phase shift) between a number of waves at one time for condition that the maximum delay is less than or equal to one acoustic wave length.

Although these two techniques offer the potential of being effective in determining the laser front position inside tissue, both are very sensitive to variations in the speed of sound which can be affected by environmental factors such as temperature, humidity and pressure. Therefore further investigation of the practical realisation of these techniques is required and alternative laser ranging techniques based on the sampling points principle should also be considered.

Chapter 7

Error Analysis and Evaluation of the End-Effector

7.1 Introduction

In computer assisted laser bone surgery sufficiently accurate position of the Front End of the laser waveguide is a mandatory requirement. A positioning or orientation error beyond the specified error tolerance can have dangerous and costly consequences.

This chapter aims to analyse the errors that might occur, and quantify them during the positioning of the laser waveguide. It also aims to pinpoint potential sources of errors that are associated with the design components, feedback measurements and control mechanisms.

Positioning inaccuracies within the laser End-Effector system can stem from a number of sources. These include:

- End-Effector's structural errors
- End-Effector base positioning and orientation errors
- Measurements and registration errors
- Controller errors

End-Effector error analysis is an important aspect of design that ensures the overall performance requirements are met and optimised for positioning accuracy. Kinematic error analysis is an essential step during the design phase in order to verify whether or not a proposed end-effector design meets the accuracy requirements. It is also important during the End-Effector implementation and calibration phase. Hence, correct identification of the laser End-Effector's kinematic errors can serve to increase the effectiveness of the calibration process and thereby improve the End-Effector's positioning accuracy.

A considerable amount of research work has been conducted in the area of kinematic error analysis and calibration of robotic manipulators [MAVR 97][MOON 01][FU 87][RIVA 04]. Mathematical models of kinematic errors have been developed based on screw theory [MOON 01], Jacobian matrices [FU 87][RIVA 04], homogeneous matrices, and Denavit and Hartenberg representation [FU 87]. Some of the conducted research work has considered the effect of manipulation joint errors [BENH 87][WALD 79] while other has focused on the effect of dimensional errors of the links [FERR 86][VAIC 87].

The error analysis model for the laser End-Effector presented in Chapter 5 is based on the geometric approach for solving the forward kinematic model (Section 5.7.3). This model can be used to perform worst case accuracy evaluation and it can help to set the requirements for the calibration process. It can also analyse the effect of physical error sources that may exist within the laser End-Effector. The error analysis model presented in this chapter was implemented using MathCAD and tested over a range of different error sources to study their overall effect on the laser delivery and positioning.

In addition to the physical errors, this chapter also presents other sources of errors that may have an effect on the performance and positioning accuracy of laser delivery during laser bone cutting and drilling applications. These include: error related to the mechanical structure of the End-Effector, mechanical feedback errors, Laser Front position feedback errors, and controller errors.

7.2 End-Effector Structural Error

Errors within the laser End-Effector structure can be classified according to their source, type and their overall effect on the manipulation and positioning of the laser. There are many possible sources of errors in the laser End-Effector system. These errors are referred to as physical errors.

The two types of physical errors that may occur within the End-Effector structure are linear and rotational errors. Linear errors are defined as errors that can cause translations in the positions of the coordinate frames (systems) without affecting their orientations. Rotational errors on the other hand affect both the positions and orientations of the coordinate frames.

7.2.1 Physical Errors

Physical errors within the basic structure of the End-Effector system can be caused by several factors. The main sources of these physical errors include:

- Machining errors
- Components errors
- Assembly errors
- Deflection errors
- Clearance

Machining errors result from machining tolerances of the individual mechanical and support components of the laser End-Effector. These errors can cause a shift in the origin of manipulation of the laser End-Effector.

Components errors are associated with components accuracy and resolutions as specified by the manufacturers. They may also include bearing run-out errors in the rotating joints and leadscrew curvature (deformation) in the linear drive. The resolution of the stepper motors, gearboxes and leadscrew are examples of this type of errors.

Assembly errors can include both linear and angular errors [MARV 97] that may be produced during the assembly of the various End-Effector mechanical and support components. These errors can result in a shift or rotation in the centre of manipulation (manipulation origin) of the Laser End-Effector. They can also result in multiple origins of manipulation. This can cause large errors at the point of laser delivery.

Deflection errors may occur within the linear drive and the laser waveguide of the End-Effector. This may be due to the light weight requirement of the structural components. This light weight requirement suggests a high possibility of structural deformation [MEGG 98] which can cause deflection errors.

Furthermore, the flexibility of the laser waveguide attached to the linear drive can be a major source of deflection errors. This is due to the unsupported structure of the laser waveguide Front End. Local material deformation within other parts of the laser End Effector can also form a source of deflection errors [MAVR 97] which can affect both the positioning and manipulation. In most cases, these deflection errors can cause very large Front End positioning errors [MEGG 98][MAVR 97] and limit the absolute positioning accuracy [MEGG 99] of the End-Effector especially at the maximum extension of the laser waveguide.

Joint clearances due to manufacturing tolerances and wear can seriously affect the dynamic response of the End-Effector mechanical performance and positioning [GOSS 02][SCHW 02]. It is considered one of the most important factors affecting the relative and absolute positioning accuracy [BODU 88] [KAKI 93] [WANG 88].

Joint clearance may be inherent within gearboxes or stepper motors and is referred to as backlash. Backlash can cause rotational errors at the joints of the End- Effector. These errors can be amplified by the End-Effector structure to cause larger errors at the laser waveguide Front End. Therefore, it is important to quantify the effects of joint clearance on the End-Effector positioning accuracy in order to define the minimum level of suitable tolerances that achieves the required performance.

In general the physical errors discussed above are expected to be very small during the implementation of the laser End-Effector. However, these small errors can cause large positioning accuracy errors at the Front End of the laser waveguide. Therefore, it is important to identify such errors which can highly influence the End-Effector positioning and orientation accuracy during the design and calibration stages.

7.2.2 Other Errors Affecting End-Effector Positioning

Unlike the End-Effector's structure errors, the base positioning and orientation errors are mainly caused by external factors, yet they can produce similar effects on the overall End-Effector performance. These errors can be produced by the End-Effector delivery and positioning system such as a passive or an active robot arm. Base positioning can also be influenced by measurement, registration and navigation errors. These errors can lead to an inaccurate positioning and orientation of the End-Effector relative to the laser ablation site (surgical site).

Errors associated with the measurements and navigational systems, optical encoders, and optical tracking devices can cause inaccuracies in the positioning and manipulation of the laser End-Effector prior or during the bone cutting or drilling process. They can indirectly cause deviations from the required bone ablation sites resulting in damage to the surrounding tissue.

Inaccuracies in the feedback systems and devices can have a high impact on the overall performance of the laser End-Effector. A low resolution optical encoder for a joint, for example, can cause an error in determining the actual position and orientation of that joint, resulting in a large Front End positioning error. Therefore, selecting high resolution components on feedback systems plays a great role in reducing the effects of feedback errors.

Errors within the control system or the actuators (stepper motors) can also cause Front End positioning and orientation errors. The magnitudes of these errors are highly dependent on the resolutions of these devices and systems, and the error type (linear or rotational). Perhaps, high resolution components and devices can also overcome this problem.

7.3 Kinematic Model without Errors

The geometric kinematic model for the laser End-Effector manipulation (Chapter 5) gives the relation between the laser waveguide Front End position (P_x,P_y,P_z) (Figure 7.1), the origin of manipulation (O_x,O_y,O_z) and the End-Effectors base coordinate system (B_x,B_y,B_z) as shown below (Equation 7.1 and Equation 7.2).

The origin of manipulation where the two axis of the revolve joints and the axis of the linear joint intersect is located along the z-axis base coordinate system at a distance of 116.25 mm from the base. Its coordinates relative to the base can be calculated as follow:

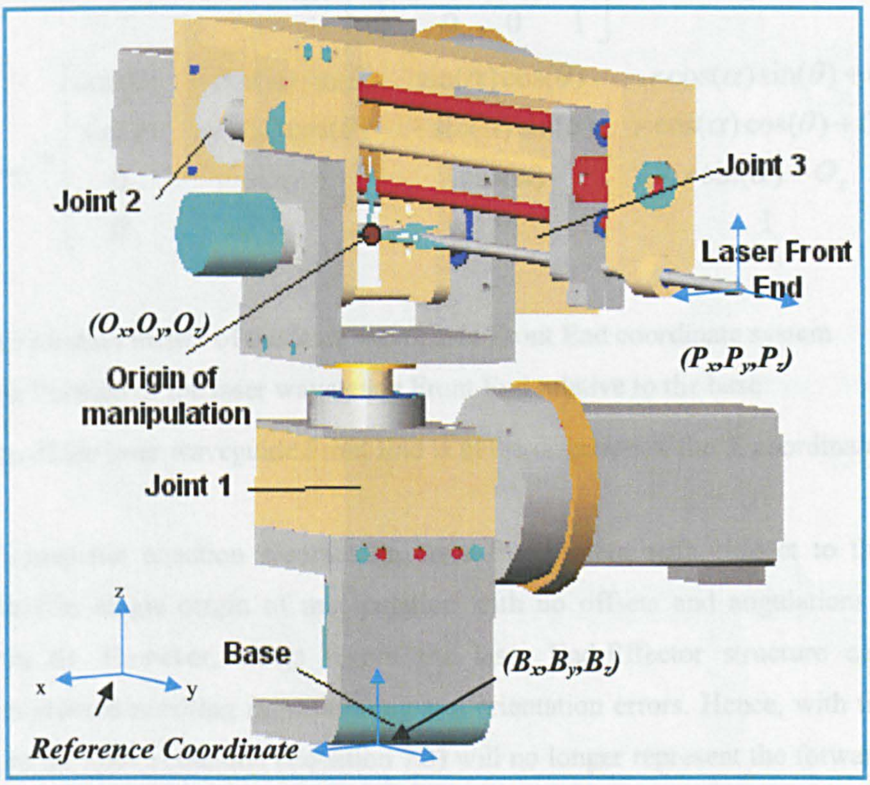

Figure 7.1: The End-Effector's coordinate system

Equation 7.1: The Origin of Manipulation

$$O_x = 0 + B_x$$
$$O_y = 0 + B_y$$
$$O_z = 116.25 + B_z$$

The position of the laser waveguide Front End (P_x,P_y,P_z) relative to the base coordinate system can be calculated using the geometric approach for solving the kinematic problem for the laser End-Effector (Equation 7.2):

Equation 7.2: The Front End Position

$$P_x = -r\cos(\alpha)\sin(\theta) + O_x = -r\cos(\alpha)\sin(\theta) + B_x$$
$$Py = r\cos(\alpha)\cos(\theta) + O_y = r\cos(\alpha)\cos(\theta) + B_y$$
$$Pz = r\sin(\alpha) + O_z = 116.25 + r\sin(\alpha) + B_z$$

where

α is the rotation angle about the X-axis of the origin of manipulation

θ is the rotation angle about the Z-axis of the origin of manipulation

The orientation of the coordinate system of the laser waveguide Front End relative to the base coordinate system is governed by the following relation:

Equation 7.3: Transformation Matrix

$$^{FE}T_{Base} = \begin{bmatrix} ^{FE}R_{Base} & ^{FE}P_{Base} \\ 0 & 1 \end{bmatrix} = \begin{bmatrix} X_x & Y_x & Z_x & P_x \\ X_y & Y_y & Z_y & P_y \\ X_x & Y_z & Z_z & P_z \\ 0 & 0 & 0 & 1 \end{bmatrix}$$

$$^{FE}T_{Base} = \begin{bmatrix} \cos(\theta) & -\cos(a)\sin(\theta) & \sin(\alpha)\cos(\theta) & -r\cos(\alpha)\sin(\theta)+O_x \\ \sin(\theta) & \cos(a)\cos(\theta) & -\sin(\alpha)\sin(\theta) & r\cos(\alpha)\cos(\theta)+O_y \\ 0 & \sin(\alpha) & \cos(\alpha) & r\sin(\alpha)+O_z \\ 0 & 0 & 0 & 1 \end{bmatrix}$$

where

$^{FE}R_{Base}$ is the rotation matrix of the laser waveguide Front End coordinate system

$^{FE}P_{Base}$ is the Position of the laser waveguide Front End relative to the base

The direction of the laser waveguide Front End is in the direction of the $\vec{Y}$ coordinate vector.

The above kinematic equation assumes an error free system with respect to the origin of manipulation (i.e. single origin of manipulation with no offsets and angulations (rotational) errors within it). However, errors within the laser End-Effector structure can alter the manipulation scheme resulting in positioning and orientation errors. Hence, with the existence of such errors the above equation (Equation 7.3) will no longer represent the forward kinematic problem. In this case Equation 7.3 must be modified to account for assembly errors that may alter the origin of manipulation resulting in multiple origin points or other manipulation errors as illustrated in Figure 7.2. The figure gives an illustration of the ideal condition (Figure 7.2A) which can be represented by Equation 7.3 in comparison with five other cases containing offset or rotational errors. As shown by the figure a single offset assembly error (Figure 7.2B) may result in two origins of manipulations. A combination of offset and rotational assembly errors or multiple offset errors, on the other hand, may result in multiple origins of manipulations as illustrated in Figure 7.2C and Figure 7.2D respectively. Furthermore, assembly rotational errors can still exist within a single origin of manipulation (Figure 7.2E and Figure 7.2F). Such errors may have "static" effect on the manipulation and positioning (i.e. these error would not effect the positioning and orientation repeatability).

The mathematical analysis of these errors is out of the scope of this research work. However, the effects of some of these errors on manipulation, positioning and the End-Effector's workspace are briefly discussed later in this chapter.

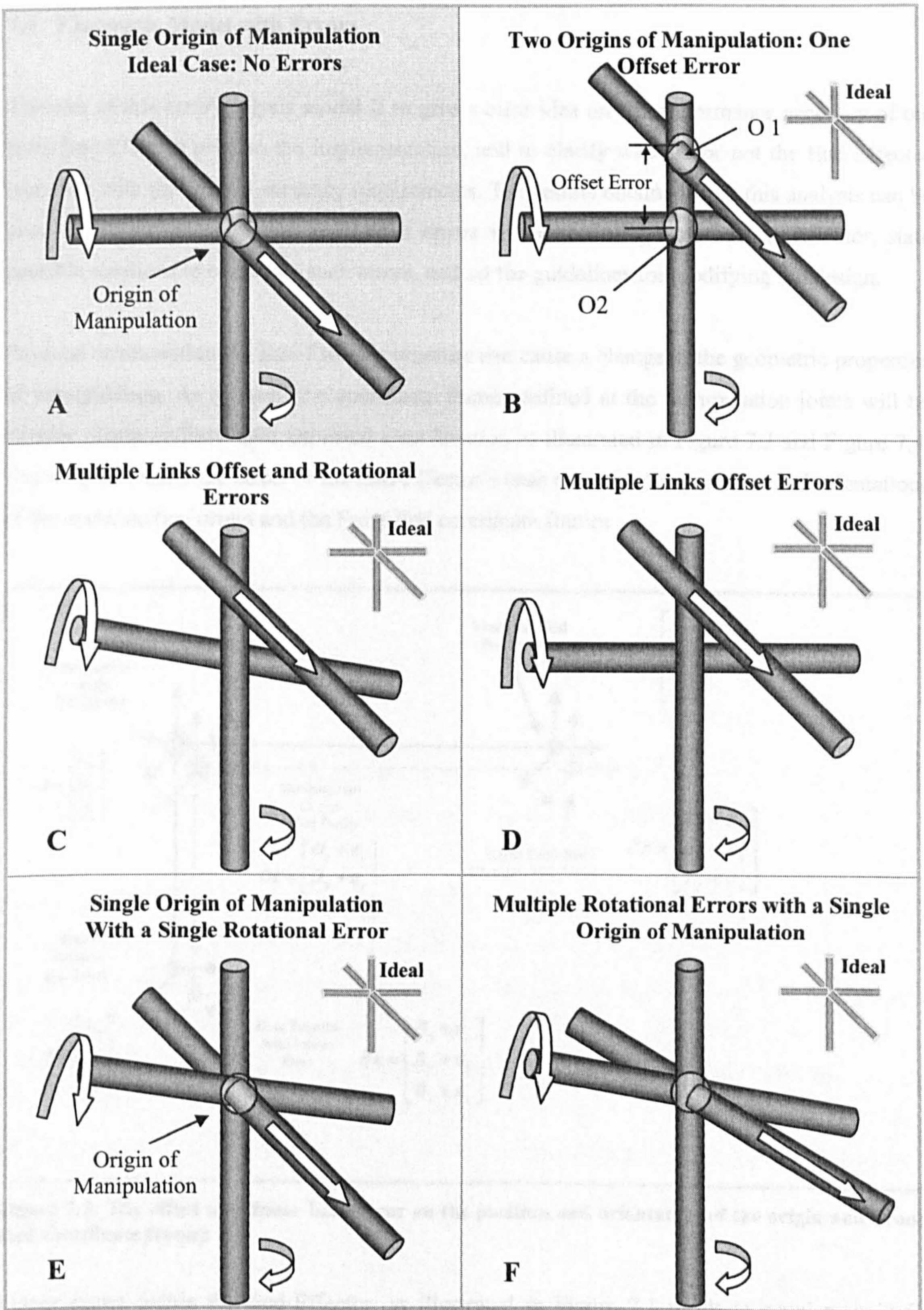

Figure 7.2: Possible offset (linear) and rotational origin of manipulation assembly errors

The following section studies the effect of different types of errors on the End-Effector manipulation and positioning. It also introduces equations which are formulated to accurately represent the forward kinematic problem based on the ideal case condition where the origin of manipulation is error free.

7.4 Kinematic Model with Errors

The aim of this error analysis model is to give a clear idea on the performance accuracy of the laser End-Effector prior to the implementation, and to clarify whether or not the End-Effector complies with the clinical accuracy requirements. The results obtained from this analysis can be used to identify the potential sources of errors within the design of the End-Effector, state possible solutions to overcome such errors, and set the guidelines for modifying the design.

Physical errors within the End-Effector structure can cause a change in the geometric properties of manipulation. As a result, the coordinate frames defined at the manipulation joints will be slightly displaced from their expected ideal location as illustrated in Figure 7.3 and Figure 7.4. These figures show the effect of the End-Effector's base errors on the positions and orientations of the manipulation origin and the Front End coordinate frames

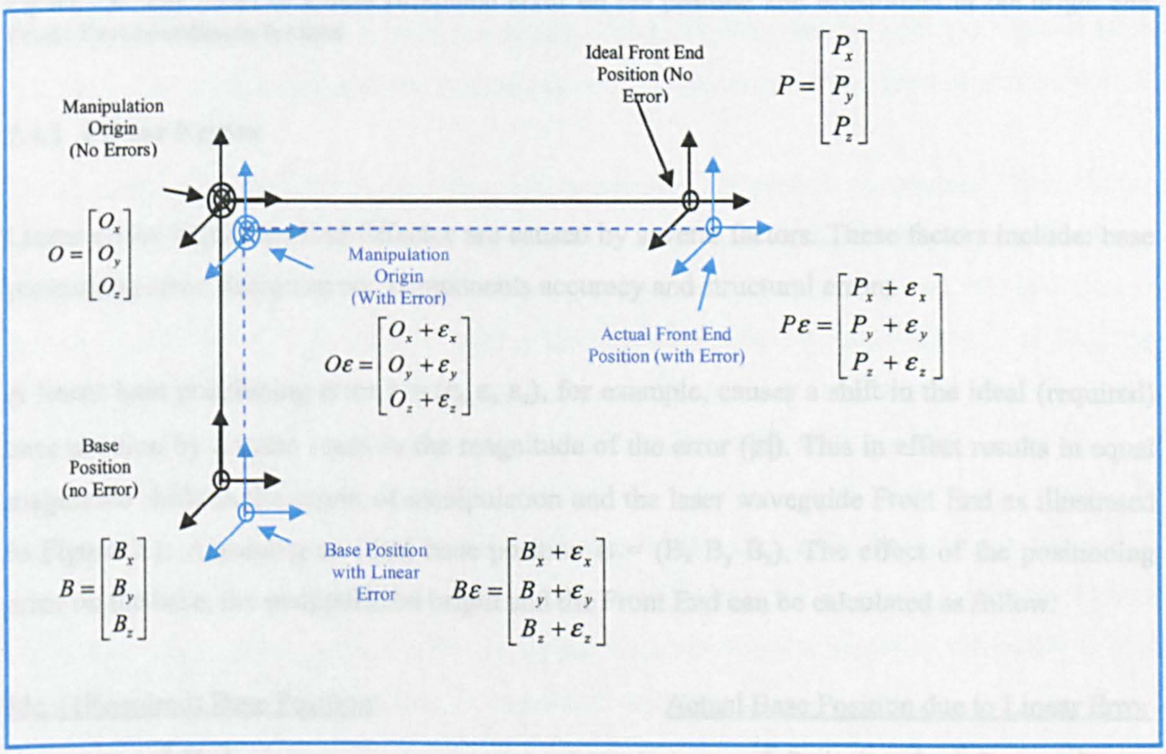

Figure 7.3: The effect of a linear base error on the position and orientation of the origin and Front End coordinate frames

Linear errors within the End-Effector, as illustrated in Figure 7.3 result in equal magnitude errors at the laser waveguide Front End. The magnitude of rotational errors Figure 7.4 on the other hand, is dependent on the distance between the manipulation origin and the Front End (i.e. the length of the laser waveguide).

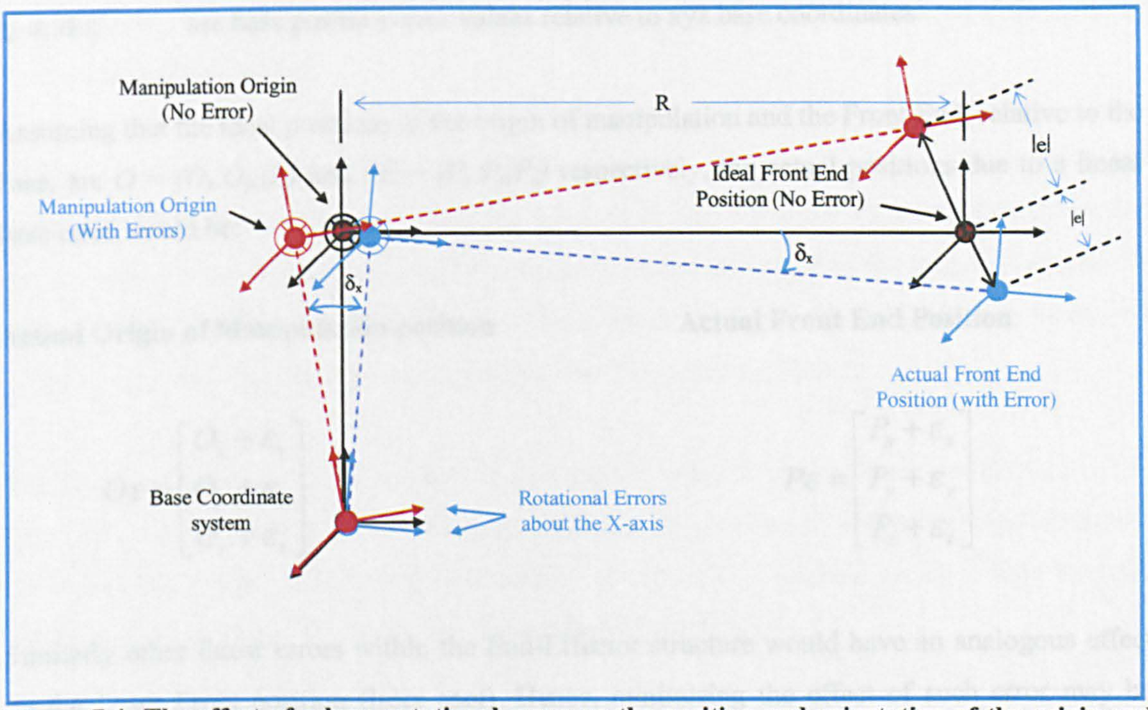

Figure 7.4: The effect of a base rotational error on the position and orientation of the origin and Front End coordinate frames

7.4.1 Linear Errors

Linear errors within the End-Effector are caused by several factors. These factors include: base positioning error, design errors, components accuracy and structural errors.

A linear base positioning error $\varepsilon = (\varepsilon_x\ \varepsilon_y\ \varepsilon_z)$, for example, causes a shift in the ideal (required) base position by a value equal to the magnitude of the error ($|\varepsilon|$). This in effect results in equal magnitude shifts in the origin of manipulation and the laser waveguide Front End as illustrated in Figure 7.1. Assuming an ideal base position $B = (B_x\ B_y\ B_z)$, The effect of the positioning error on the base, the manipulation origin and the Front End can be calculated as follow:

<u>Ideal (Required) Base Position</u> <u>Actual Base Position due to Linear Error</u>

$$B = \begin{bmatrix} B_x \\ B_y \\ B_z \end{bmatrix} \qquad B\varepsilon = \begin{bmatrix} B_x \\ B_y \\ B_z \end{bmatrix} + \begin{bmatrix} \varepsilon_x \\ \varepsilon_y \\ \varepsilon_z \end{bmatrix} = \begin{bmatrix} B_x + \varepsilon_x \\ B_y + \varepsilon_y \\ B_z + \varepsilon_z \end{bmatrix}$$

<u>The Magnitude of the Linear Base Error</u>

$$|\varepsilon| = \sqrt{(\varepsilon_x)^2 + (\varepsilon_y)^2 + (\varepsilon_z)^2}$$

where

B is the required base position

B_ε is the actual base position due to a linear error

$\varepsilon_x, \varepsilon_x \& \varepsilon_y$ are base position error values relative to xyz base coordinates

Assuming that the ideal positions of the origin of manipulation and the Front End, relative to the base, are $O = (O_x, O_y, O_z)$ and $FE = (P_x, P_y, P_z)$ respectively, the actual positions due to a linear base error would be:

Actual Origin of Manipulation position **Actual Front End Position**

$$O\varepsilon = \begin{bmatrix} O_x + \varepsilon_x \\ O_y + \varepsilon_y \\ O_z + \varepsilon_z \end{bmatrix} \qquad P\varepsilon = \begin{bmatrix} P_x + \varepsilon_x \\ P_y + \varepsilon_y \\ P_z + \varepsilon_z \end{bmatrix}$$

Similarly other linear errors within the End-Effector structure would have an analogous effect on the Laser Front position (laser spot). Hence, minimising the effect of such error may be achieved by minimizing the error at the source. Therefore, accurate base positioning and End-Effector structural implementation are essential to effectively reduce the effect of such errors.

Errors within the End-Effector structure could be classified as "static" or "random". Static linear errors within the physical structure of the End-Effector may result from assembly misalignment or design errors. The effect of static errors on the overall positioning and manipulation is repeatable and can be accounted for during the calibration process. Minimizing or eliminating the effect of such errors can be easily achieved via accurate and precise End-Effector's structural adjustments or modification of the End-Effector manipulation equation.

Random errors, on the other hand, are not easy to predict and must be dealt with as they occur. An example of random linear error is the error that may occur within the End-Effector's linear drive due to the clearance (backlash) within the leadscrew system assembly. Minimising such error could be achieved by selecting zero backlash components.

7.4.2 Rotational Errors

Rotational errors within the End-Effector structure could also be related to the same factors that cause the linear errors. However; these errors can have more effect on the manipulation and positioning of the laser waveguide Front End and the Laser Front. They can affect both the position and orientation of the coordinate systems within the End-Effector structure leading to large positioning errors at the laser waveguide Front End and the Laser Front. The magnitudes of such errors are dependent on the error sources, positions in space relative to the origin of manipulation, and the length of the laser waveguide (the distance (R) between the origin and the laser waveguide Front End).

Figure 7.4 shows the effect of the End-Effector's base rotational error on the position and orientation of the manipulation origin, the Front End, and the Laser Front. It also shows the direct relation between the Front End error magnitude and the length of the laser waveguide. To calculate the effect of the End-Effector rotational errors on the manipulation and the Front End position, the following rotational error matrix was derived by the author.

The rotational error matrix (Equation 7.4) was derived using the *basic rotation matrices* [FU 87] to represent a general form for the rotational errors that may occur within the End-Effector's structure. This matrix can be used to calculate the effect of rotational errors within the End-Effector on the origin of manipulation and the Front End position.

Equation 7.4: Rotational error matrix

$$RE = \begin{bmatrix} \cos(\delta_z)\cos(\delta_y) & -\sin(\delta_z)\cos(\delta_x)+\cos(\delta_z)\sin(\delta_y)\sin(\delta_x) & \sin(\delta_z)\sin(\delta_x)+\cos(\delta_z)\sin(\delta_y)\cos(\delta_x) \\ \sin(\delta_z)\cos(\delta_y) & \cos(\delta_z)\cos(\delta_x)+\sin(\delta_z)\sin(\delta_y)\sin(\delta_x) & -\cos(\delta_z)\sin(\delta_x)+\sin(\delta_z)\sin(\delta_y)\cos(\delta_x) \\ -\sin(\delta_y) & \cos(\delta_y)\sin(\delta_x) & \cos(\delta_y)\cos(\delta_x) \end{bmatrix}$$

where

RE represents the rotational error matrix

δ represents the actual rotation error and the subscript donates the rotation axis

Rotational errors within the End-Effector can cause a shift in the position of the manipulation origin in addition to the orientation effects. The amount of this position shift is dependent on the distance between the origin and the error source. The orientation effect is equivalent to the error orientation angle. The shift in the origin position can be calculated as follow:

Equation 7.5: Shift on the origin position

$$OPshift = \left\| \left(RE \cdot \begin{bmatrix} O_x - E_x \\ O_y - E_y \\ O_z - E_z \end{bmatrix} \right) - \begin{bmatrix} O_x \\ O_y \\ O_z \end{bmatrix} \right\|$$

where

OPshift is the origin position shift magnitude

E_x E_y E_z are the xyz coordinates of the error position

A rotational error at the base for example can cause a shift in the origin of manipulation resulting in a new origin position (NOP). Using the rotational error matrix the NOP can simply be calculated as follow:

Equation 6: New origin position due to a base rotational error

$$NOP = RE \times \begin{bmatrix} O_x - B_x \\ O_y - B_y \\ O_z - B_z \end{bmatrix}$$

where

NOP is the new origin position due to a base rotational error

This shift in the origin position can affect the overall End-Effector performance causing a large error at the laser waveguide Front End as illustrated in Figure 7.4. This figure shows the effect of base rotational error, on the position and orientation of the origin of manipulation and the laser waveguide Front End. It also shows that the magnitude of the Front End error ($|e|$) is directly related to the rotational error (δ_x). Therefore, minimizing the magnitude of the Front End error can be achieved by reducing the size of the rotational error. This can be done by accurate positioning and orientation, accurate calibration, and accurate machining and assembly.

7.5 Generalized Error Model

Combining the physical error models stated above, results in a generalized error model which can be applied to study the effect all physical errors within the End-Effector structure. This model can be presented in a homogeneous transformation matrix form as shown in Equation 7.7 and can be used to calculate the actual laser waveguide Front End position and orientation relative to the ideal one.

Equation 7.7: Generalized Error Model

$$GE = \begin{bmatrix} R_{3\times3} & P_{3\times1} \\ f_{1\times3} & S_{1\times1} \end{bmatrix} = \begin{bmatrix} \begin{matrix} Rotation \\ Error_{3\times3} \end{matrix} & \begin{matrix} LinearPosition + \\ Error_{3\times1} \end{matrix} \\ \begin{matrix} Perospective \\ Traansformation_{1\times3} \end{matrix} & Scaling_{1\times1} \end{bmatrix}$$

$$GE = \begin{bmatrix} \cos(\delta_z)\cos(\delta_y) & -\sin(\delta_z)\cos(\delta_x) + \cos(\delta_z)\sin(\delta_y)\sin(\delta_x) & \sin(\delta_z)\sin(\delta_x) + \cos(\delta_z)\sin(\delta_y)\cos(\delta_x) & X_e + \varepsilon_x \\ \sin(\delta_z)\cos(\delta_y) & \cos(\delta_z)\cos(\delta_x) + \sin(\delta_z)\sin(\delta_y)\sin(\delta_x) & -\cos(\delta_z)\sin(\delta_x) + \sin(\delta_z)\sin(\delta_y)\cos(\delta_x) & Y_e + \varepsilon_y \\ -\sin(\delta_y) & \cos(\delta_y)\sin(\delta_x) & \cos(\delta_y)\cos(\delta_x) & Z_e + \varepsilon_z \\ 0 & 0 & 0 & 1 \end{bmatrix}$$

where

GE is the generalized error matrix

R_{3x3} represents the 3x3 rotational error matrix

P_{3x1} represents the linear position vector including error $(X_e+\varepsilon_x \ Y_e+\varepsilon_y \ Z_e+\varepsilon_z)^T$

f_{1x3} represents the *Perspective Transformation* [(0 0 0) for robotics] [FU 87]

S_{1x1} is the global *Scaling* factor which is equal to 1 in robotics [FU 87]

$X_e\ Y_e\ Z_e$ are the coordinates of the error source position relative to the fixed reference

$\delta_x\ \delta_y\ \delta_z$ are x y z rotational error parameters

$\varepsilon_x\ \varepsilon_y\ \varepsilon_z$ are the x y z linear error parameters

The above generalized error model can be applied to calculate the effects of different errors that may occur within the End-Effector system including those caused by external factors. The following example (Example 7.1) gives an illustration of the use of the generalized error model for determining the effect of base rotational errors on the Front End positioning and orientation.

Example 7.1: To determine the effect of base positioning error on the positioning and orientation of the laser waveguide Front End and the Laser Front.

The aim of this example is to study the effect of a base positioning error on the position and orientation of the laser waveguide Front End and to identify the maximum tolerable base error that achieves the required performance.

Assuming a rotational base error of 1 degree about the x-axis

$$\delta x := \frac{1\pi}{180} \qquad \delta y := \frac{0\pi}{180} \qquad \delta z := \frac{0\pi}{180} \qquad \varepsilon x := 0 \qquad \varepsilon y := 0 \qquad \varepsilon z := 0$$

$$Xe := Bx \qquad Ye := By \qquad Ze := Bz$$

Using the generalised error model in Equation 7.7 one can calculate the effect of the base error on the laser waveguide Front End as follow:

Equation 7.8: General model of the base error affect on the Front End position and orientation

$$GBE := \begin{pmatrix} \cos(\delta z)\cdot\cos(\delta y) & -\sin(\delta z)\cdot\cos(\delta x) + \cos(\delta z)\cdot\sin(\delta y)\cdot\sin(\delta x) & \sin(\delta z)\cdot\sin(\delta x) + \cos(\delta z)\cdot\sin(\delta y)\cdot\cos(\delta x) & Xe + \varepsilon x \\ \sin(\delta z)\cdot\cos(\delta y) & \cos(\delta z)\cdot\cos(\delta x) + \sin(\delta z)\cdot\sin(\delta y)\cdot\sin(\delta x) & -\cos(\delta z)\cdot\sin(\delta x) + \sin(\delta z)\cdot\sin(\delta y)\cdot\cos(\delta x) & Ye + \varepsilon y \\ -\sin(\delta y) & \cos(\delta y)\cdot\sin(\delta x) & \cos(\delta y)\cdot\cos(\delta x) & Ze + \varepsilon z \\ 0 & 0 & 0 & 1 \end{pmatrix}$$

Equation 7.9: The actual Front End position, error magnitude and orientation due to a 1° rotational base positioning error (about the X-axis)

New Front End Position

$$NewFE_{m,n} := (GBE)\cdot\begin{pmatrix} Px_{m,n} - Bx \\ Py_{m,n} - By \\ Pz_{m,n} - Bz \\ 1 \end{pmatrix} \qquad \begin{pmatrix} BEPx_{m,n} \\ BEPy_{m,n} \\ BEPz_{m,n} \\ S \end{pmatrix} := NewFE_{m,n} \qquad BEFE_{m,n} := \begin{pmatrix} BEPx_{m,n} \\ BEPy_{m,n} \\ BEPz_{m,n} \end{pmatrix}$$

Error magnitude

$$MagFEerror1_{m,n} := \left|BEFE_{m,n} - FE_{m,n}\right|$$

$Max1 := \max(MagFEerror1)$ $\quad Max1 = 7.506$ mm

$Min1 := \min(MagFEerror1)$ $\quad Min1 = 4.842$ mm

Orientation Relative to Ideal

$$RBTM := \begin{pmatrix} GBE_{0,0} & GBE_{0,1} & GBE_{0,2} \\ GBE_{1,0} & GBE_{1,1} & GBE_{1,2} \\ GBE_{2,0} & GBE_{2,1} & GBE_{2,2} \end{pmatrix}$$

$$RBTM = \begin{pmatrix} 1 & 0 & 0 \\ 0 & 1 & -0.017 \\ 0 & 0.017 & 1 \end{pmatrix}$$

where

GBE	is the generalised base error model
NewFE	is the new Front End position including scalar factor 1
BEFE	is the co-ordinates of the Front End position
MagFEerror1	is the magnitude of the Front End Positioning Error.
Max	is the maximum Front End error magnitude (R =360 mm)
Min	is the minimum Front End error magnitude (R =200 mm)
RBTM	is the rotational error effect on the ideal orientation of the Front End

Similarly 0.5° and 0.1° rotational errors about the x-axis can cause Front End positioning and orientation errors with the following magnitudes when compared to the ideal or desired positions.

The Max & Min Front End error magnitudes and orientation due to a 0.5° rotational base error about the x-axis

$$\delta x := \frac{0.5\pi}{180} \qquad \delta y := \frac{0\pi}{180} \qquad \delta z := \frac{0\pi}{180} \qquad \varepsilon x := 0 \qquad \varepsilon y := 0 \qquad \varepsilon z := 0$$

Error Magnitude

$$MagFEerror05_{m,n} := \left|BEFE_{m,n} - FE_{m,n}\right|$$

$Max05 := \max(MagFEerror05)$ $\quad Max05 = 3.753$ mm

$Min05 := \min(MagFEerror05)$ $\quad Min05 = 2.421$ mm

Orientation Relative to Ideal

$$RBTM05 := \begin{pmatrix} GBE_{0,0} & GBE_{0,1} & GBE_{0,2} \\ GBE_{1,0} & GBE_{1,1} & GBE_{1,2} \\ GBE_{2,0} & GBE_{2,1} & GBE_{2,2} \end{pmatrix}$$

$$RBTM05 = \begin{pmatrix} 1 & 0 & 0 \\ 0 & 1 & -8.727\times 10^{-3} \\ 0 & 8.727\times 10^{-3} & 1 \end{pmatrix}$$

The Max & Min Front End error magnitudes and orientation due to a 0.1° rotational base error about the x-axis

$$\delta x := \frac{0.1\pi}{180} \qquad \delta y := \frac{0\pi}{180} \qquad \delta z := \frac{0\pi}{180} \qquad \varepsilon x := 0 \qquad \varepsilon y := 0 \qquad \varepsilon z := 0$$

Error Magnitude

$$MagFEerror01_{m,n} := \left|BEFE_{m,n} - FE_{m,n}\right|$$

$Max01 := max(MagFEerror01)$ $\quad Max01 = 0.751$ mm

$Min01 := min(MagFEerror01)$ $\quad Min01 = 0.484$ mm

Orientation Relative to Ideal

$$RBTM01 := \begin{pmatrix} GBE_{0,0} & GBE_{0,1} & GBE_{0,2} \\ GBE_{1,0} & GBE_{1,1} & GBE_{1,2} \\ GBE_{2,0} & GBE_{2,1} & GBE_{2,2} \end{pmatrix}$$

$$RBTM01 = \begin{pmatrix} 1 & 0 & 0 \\ 0 & 1 & -1.745\times 10^{-3} \\ 0 & 1.745\times 10^{-3} & 1 \end{pmatrix}$$

Plotting the magnitude of Front End positioning error against the rotational base errors shows a linear correlation between them as shown in Figure 7.5. This is also clearly illustrated by the 3D plots shown in Figure 7.6. This figure shows 3D plots relating the Front End error magnitude as a function of the rotational base error and the End-Effector's manipulation angles.

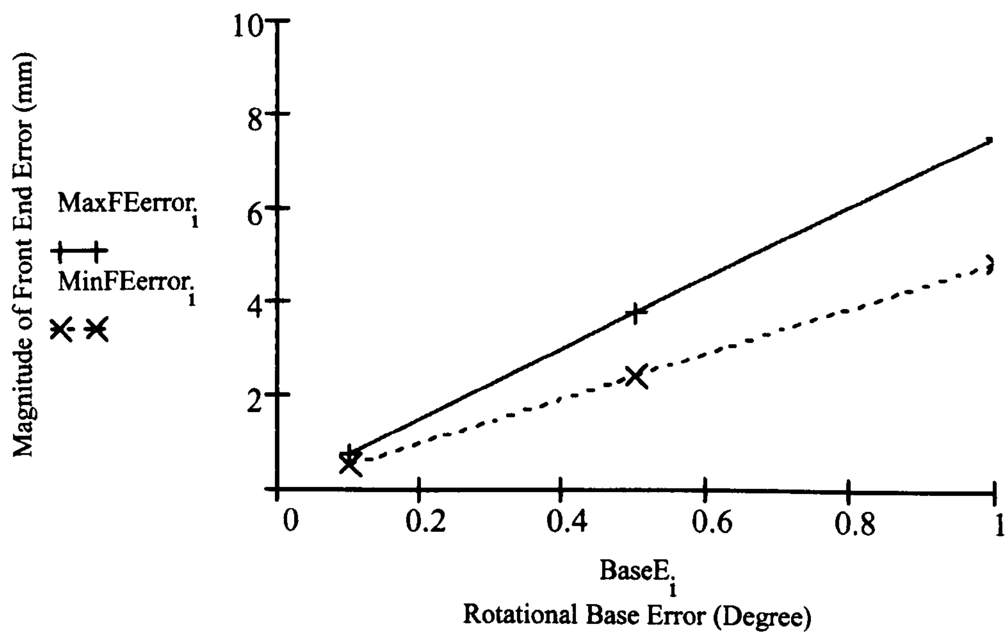

Figure 7.5: The magnitude of the Front End positioning error as a function of rotational base error

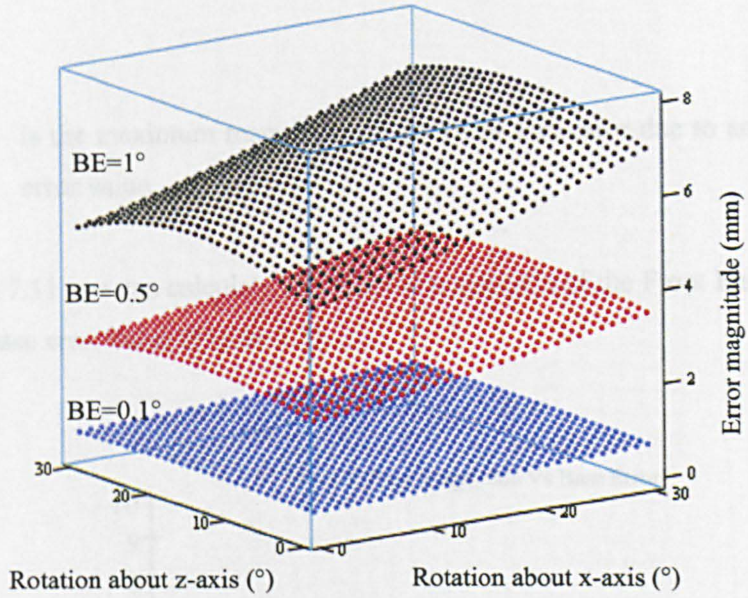

Figure 7.6: 3D plot of the magnitude of the Front End errors relative to 1°, 0.5° and 0.1° rotational base errors about the x-axis and the End-Effector manipulation angles α and θ

Calculating the slopes of the lines in Figure 7.5 one can derive the line equation which can be used to predict the magnitude of the Front End positioning error for any given value of the rotational base error. Hence, given the maximum tolerable magnitude of the Front End positioning error, using the derived line equation, one can calculate the maximum allowable rotational base error. This correlation can be very beneficial during the design components selection and the calibration process of the delivery system which puts the laser End-Effector in the desired position relative to the surgical site and the fixed reference frame.

Equation 7.10: Line Slope Calculation

$$\text{Maxslope} := \left[\frac{(\text{Max1} - \text{Max05})}{\left(\text{BaseE}_2 - \text{BaseE}_1\right)}\right] \qquad \text{Maxslope} = 7.506$$

$$\text{Minslope} := \left[\frac{(\text{Min1} - \text{Min05})}{\left(\text{BaseE}_2 - \text{BaseE}_1\right)}\right] \qquad \text{Minslope} = 4.842$$

where

BaseE	is the rotational base error of the End Effector
MaxSlope	is the slope of the line linking the base errors to the maximum magnitudes of the Front End error
MinSlope	is the slope of the line linking the base errors to the minimum magnitudes of the Front End error

Equation 7.11: The maximum magnitude of the Front End error line equation

$$MagFEPerror := (Maxslope) \cdot (BaseE)$$

where

MagFEPerror is the maximum magnitude of the Front End error due to any rotational base error value.

Using Equation 7.11 one can calculate and plot the magnitude of the Front End error relative to any rotational base error value (Figure 7.7).

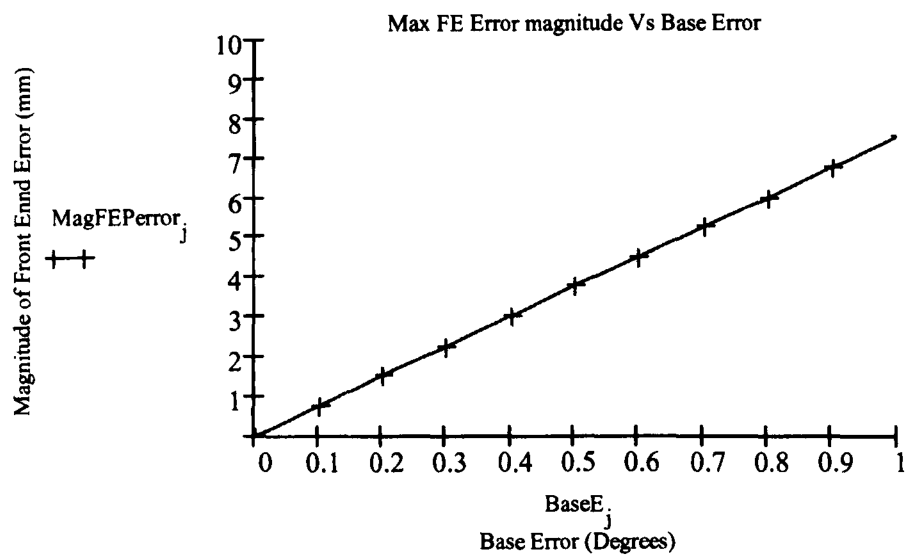

Figure 7.7: The maximum magnitude of the Front End errors relative to rotational base errors

The base rotation error about the Y or Z axes showed similar results, however, the magnitude and direction of the error appear to vary depending on the errors' positions within the workspace of the laser End-Effector. Figure 7.8 and Figure 7.9 give an illustration on the effect of a (1°) base rotation error about the Y-axis. Figure 7.8 shows the End-Effector workspace assuming maximum extension of the laser waveguide and a laser focal point of 50 mm (i.e. the Laser Front is at 410 mm linear distance from the End-Effector's origin of manipulation).

Figure 7.9 on the other hand shows the magnitudes and orientations of Laser Front positioning errors. These magnitude variations depend on the laser Front error position with respect to the base coordinates. The Laser Front (laser spot) error magnitude for the given (1°) base rotation angle varied from (0.198 to 7.98) mm. It is worth noting here that such base rotation error may have different effects on the position of the error magnitude and orientation at the Laser Front depending on the rotation axis.

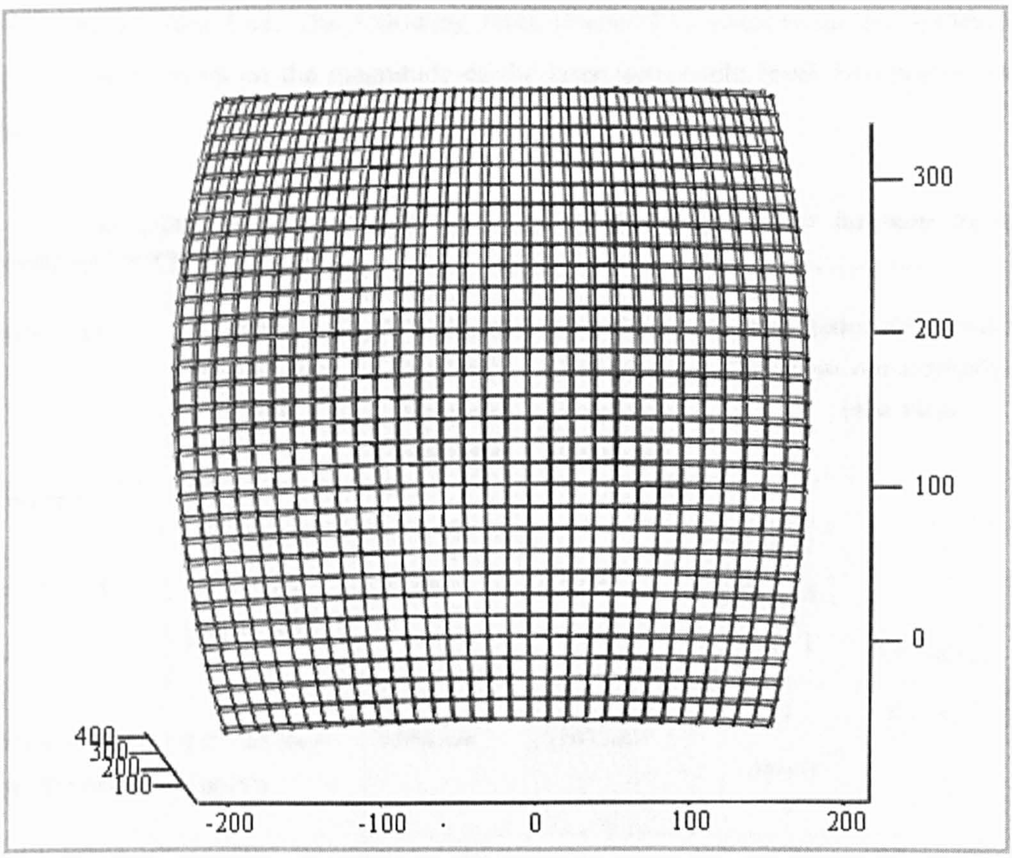

Figure 7.8: The effect or (1°) base rotational error about the Y-axis on the End-Effector's workspace

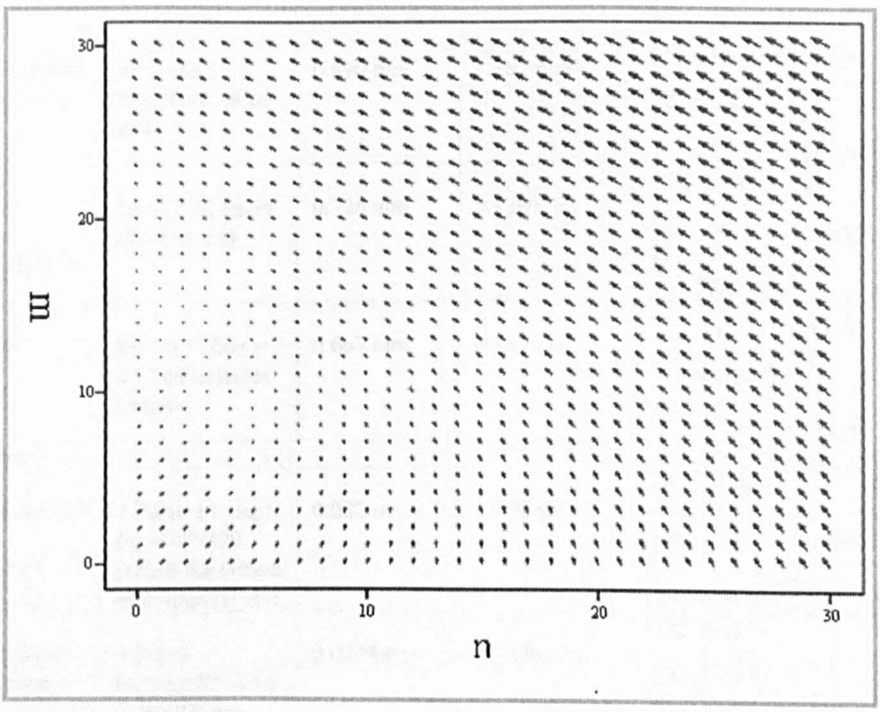

Figure 7.9: Laser Front position errors (magnitude and orientation) due to a (1°) base rotational error about the Y-axis

The same techniques can be applied to quantify the effects of other types of errors on the Front End and Laser Front positions. The Laser Front is in line with Front End of the laser End-Effector with a distance equal to the focal length of the focusing lens placed at the tip of the laser waveguide Front End. The following table (Table 7.1) summarises the effects of the different types of errors on the magnitude of the laser waveguide Front End positioning and orientation.

Table 7.1: The affect of different types of errors on the magnitude of the laser Front End positioning and orientation errors

Error Type	Error Magnitude & Type	Min. Front-End Error Magnitude R=200 mm	Max. Front-End Error Magnitude R=360 mm	Orientation of the Front End Coordinate system Relative to the Ideal Value
Physical Errors				
Linear Machining error	$\varepsilon y = 0.1$ mm (Origin shift)	0.1 mm	0.1 mm	$\begin{pmatrix} 1 & 0 & 0 \\ 0 & 1 & 0 \\ 0 & 0 & 1 \end{pmatrix}$ No Rotation
Stepper motor error (0.5 Step) Rotational*	0.9°/120 (δoz = 0.0075°)	0.050 mm	0.067 mm	$\begin{pmatrix} 1 & -1.309\times 10^{-4} & 0 \\ 1.309\times 10^{-4} & 1 & 0 \\ 0 & 0 & 1 \end{pmatrix}$
Assembly error (Rotational about the z-axis)	$\delta z = 0.1°$ at the Origin	0.544 mm	0.628 mm	$\begin{pmatrix} 1 & -1.745\times 10^{-3} & 0 \\ 1.745\times 10^{-3} & 1 & 0 \\ 0 & 0 & 1 \end{pmatrix}$
Clearance error (Dual Joints) GearBox-Backlash*	$\delta x = \delta oz$ = 2.327E-3° (8'of arc)	0.890 mm	1.185 mm	$\begin{pmatrix} 1 & -2.327\times 10^{-3} & 5.415\times 10^{-6} \\ 2.327\times 10^{-3} & 1 & -2.327\times 10^{-3} \\ 0 & 2.327\times 10^{-3} & 1 \end{pmatrix}$
Clearance error (Single Joint) GearBox-Backlash *	δx = (2.327E-3)° (8'of an arc)	0.726 mm	0.838 mm	$\begin{pmatrix} 1 & 0 & 0 \\ 0 & 1 & -2.327\times 10^{-3} \\ 0 & 2.327\times 10^{-3} & 1 \end{pmatrix}$
Deflection error	$\delta x = 0.1°$ $\delta oz = -0.1°$ reflected at Origin	0.667 mm	0.889 mm	$\begin{pmatrix} 1 & 1.745\times 10^{-3} & -3.046\times 10^{-6} \\ -1.745\times 10^{-3} & 1 & -1.745\times 10^{-3} \\ 0 & 1.745\times 10^{-3} & 1 \end{pmatrix}$
Control Errors				
Stepper motor drive pulse error (Rotational Joint)	1 Pulse (1 step) δx =1.8°/120 (about the Origin of manipulation)	0.082 mm	0.094 mm	$\begin{pmatrix} 1 & 0 & 0 \\ 0 & 1 & -2.618\times 10^{-4} \\ 0 & 2.618\times 10^{-4} & 1 \end{pmatrix}$
Stepper motor drive pulse error (Linear Drive)	1 Pulse $\delta y = \pm 1.8° \rightarrow \varepsilon y = \pm 0.054$ mm	0.0534 mm	0.0546 mm	$\begin{pmatrix} 1 & 0 & 0 \\ 0 & 1 & 0 \\ 0 & 0 & 1 \end{pmatrix}$ No Rotation
Feedback Errors				
Optical Encoder (x-axis)	1 count (1 pulse) $\rightarrow$ $\delta x = \pm(8.789\text{E-}3)°$	0.048 mm	0.055 mm	$\begin{pmatrix} 1 & 0 & 0 \\ 0 & 1 & -1.534\times 10^{-4} \\ 0 & 1.534\times 10^{-4} & 1 \end{pmatrix}$
* Errors that are inherent within the system (worst condition error values)				

The table shows large affects on the magnitude of the Front End positioning error with slight change in the orientation. It also shows that certain errors such as backlash and deflection errors can greatly affect the laser waveguide Front End positioning accuracy and repeatability. Therefore; these error sources need to be consided when designing and implementing future versions of the End-Effector (future work).

Studying the effect of some of the errors labelled with "*" (Table 7.1) on the overall positioning accuracy of the End-Effector, one can see that some Front End positioning accuracy values are greater than the maximum allowable (±0.5 mm). Assuming the linear combination of all of the errors presented in Table 7.1 The total Front End positioning error would be approximately three times greater than the allowable maximum value. However, some of these errors are random in nature and can have error values in different directions (thus they may cancel each other out) and result in the error being a lot less than the maximum quoted value. An example of total positioning error reduction due to the error's orientation is presented in Table 7.1 (Gearbox Backlash errors). The example shows that for a single Joint backlash error the maximum Front End positioning error is 0.889 mm while it is 1.185 mm for dual Joints backlash. The reason for the reduction in the total error magnitude is related to the difference in the orientations of the backlash errors.

Therefore, to calculate the total Front End or Laser Front positioning error one must know the direction and the magnitude of each error. In this case the total positioning error could have a smaller magnitude than the above prediction.

A solution to the total positioning error problem would be selecting components with better design specifications in terms of accuracy, resolution and repeatability to replace some of the existing End-Effector's components.

The error values presented in Table 7.1 do not account for other physical or external errors that may arise during the initial positioning of the End-Effector. Therefore, it is not possible to predict the overall accuracy of the system unless it is implemented and tested. However, as the overall accuracy of the End-Effector is governed by all physical and external errors, its value would be related to the total positioning error at the laser Front (Spot) which can be calculated as follow (Equation 12):

Equation 12:Total Laser Front Error Calculations

$$TLFPerror = \max(\sum |LFerror\_due\_to\_Physical\_Errors|) + \max(\sum |LFerror\_due\_to\_External\_Errors|)$$

where

The equation assumes vector summation

TLFPerror	is the total Laser Front positioning error
LFerror	is the Laser Front End Error

7.6 Error Compensation

Provided having a stable feedback and control system many of these errors can be compensated for since the optical tracking (Chapter 5) can verify the end position of the laser Front End relative to the surgical site. These errors may include linear static errors that can affect the position of Laser Front without altering the Front End orientation and the positioning repeatability. They may also include other structural errors which may have similar effects to linear static errors and cause no alteration to the End-Effector's workspace.

7.7 End-Effector Performance and Accuracy Evaluation

A large set of potential physical errors has been identified for the End-Effector system. The effects of these errors were modelled mathematically and some of the results were presented in Example 7.1 and Table 7.1

The overall accuracy of the laser End-Effector system is determined by all factors that influence its performance. Under ideal conditions the End-Effector should be capable of positioning the laser waveguide Front End with high accuracy (to within ± 0.5 mm from the desired position), resolution, and repeatability. However; this can only be achieved by minimizing or eliminating the effect of all error sources, for example by selecting the appropriate system components and devices that guarantee that.

In addition to the external error sources the overall system accuracy, resolution and repeatability are influenced by the individual components' properties. Accuracy, cost and speed were the top priority factors during the design phase of the initial laser End-Effector. This resulted in selecting design components with lower specifications than intended. These components include; gearboxes with (1:120) 8' of an arc backlash, high lead value leadscrew (10.85 mm), incremental optical encoders (40,960 counts) and relatively low step per revolution high torque stepper motor (200 steps/rev). The components' specifications can have major impact on the overall accuracy and resolution of the laser End-Effector when the system is implemented.

Studying the worst case scenario for the effect of the above components' resolution on the overall Front End positioning resolution shows that:

- The stepper-motor-gearbox combination would have an angular positioning resolution ranging from 52 to 94 μm in the XZ plane
- The stepper-motor-leadscrew combination within the linear drive would have a linear positioning resolution along the Y-axis that is equal to 54.25μm

These values tend to have negative effect on the laser cutting and drilling speed due the fact that they impose some limitations on the number of laser spot overlap.

7.8 Conclusion

This chapter fulfils the goal of evaluating the overall system performance as foreseen by the author due to the fact that the system was never implemented and tested physically. The chapter introduced an error analysis model to quantify the effect of the potential sources of errors within the End-Effector and its impact on the Front End and Laser Front position and orientation.

This chapter also identifies potential sources of errors that are associated with the design components, feedback measurements and control mechanisms. It also gives some suggestions for error reduction or elimination

The error analysis model presented in this chapter appears to be effective in determining the Laser Front positioning error at any point within the End-Effector work space. This model as indicated earlier is based on an ideal condition and may need further modifications to account for assembly error that affect the origin of manipulation. However, this model can still be applied to specify the maximum tolerable errors that will allow for End-Effector positioning accuracy of ± 0.5 mm.

The major sources of origin of manipulation offset errors as foreseen by the author may be due to machining and assembly problems. Therefore, care must be taken during the machining process of the End-Effector's supporting components to avoid such conditions. Also during the assembly process some form of calibration technique must be implemented to insure accurate and precise components of the laser End-Effector

For the future work the author suggests modification of the error model and the manipulation equation to account for any offsets in the origin of manipulation. Furthermore, the next version of the End-Effector prototype-2 should take into account all sources of errors that exist within the proposed End-Effector and minimize them.

Chapter 8

Conclusion

8.1 Introduction

The aim of this project is to investigate the design of a new orthopaedic surgical tool capable of sawing, drilling and sculpturing of bone in support of image guided surgery. The research of this thesis involved the design of an active positioning system (i.e. a robotic End-Effector) that uses laser technology that potentially may replace some of the current orthopaedic surgical tools. This End-Effector aims to introduce new surgical techniques that can augment the human surgeon capabilities which can reduce invasiveness, blood loss and exposure to X- radiation. It may also reduce the surgical and post hospitalisation time. This End-Effector provides the physical link between a computer based preoperative or intra-operative surgical plan and the patient anatomy. It also provides accurate laser beam guidance for precise surgical performance.

At the early stages of this research the author investigated the different computer assisted surgical systems currently available (Chapter 2). The investigation also included some of the newly emerging technologies (namely water-jet, ultrasound and laser) and the possibility of integrating such technologies with an active positioning system. These investigations aimed to define a set of requirements for the design of the new surgical tool and identify the type of technology that can potentially improve on current orthopaedic surgical tools.

The investigations led to the selection of the laser, as the new surgical tool. The design of the laser End-Effector prototype was provided in Chapter 5 Section 5.5. This design was based on several factors including; system's flexibility, dexterity, precision, reliability, and ease of control. This is in addition to some other medical related factors such as, surgical time, invasiveness, blood loss, and most importantly environment, staff and patient's safety.

This thesis identifies the basic principles and design requirements of the robotic laser delivery system (the laser End-Effector). It identifies the most appropriate type of laser and laser delivery system. It also introduces the mechanical design of a laser End-Effector prototype with its feedback and control mechanism (Chapter 6). The thesis also presents an overall mechanical system and error analysis models (Chapters 5 and 7).

8.2 Laser Selection and Beer's Law Modification

The thesis investigates the different types of laser currently available and studies their suitability for hard tissue ablation. Moreover, it presents the selection criteria for identifying the most appropriate medical laser (Er: YAG) and laser delivery (laser waveguide) system (Chapter 3) for applications in orthopaedic surgery. These laser selection criteria were based on several factors including: the type of laser tissue interaction, the damage to the surrounding tissue, water absorption, ablation rate and other factors.

Furthermore, the thesis introduces an in depth analysis on the predicted effect of the different Er: YAG laser parameters on biological tissue (Chapter 4) as foreseen by the author. This analysis was founded on the modified Beer's law equation (Section 4.2.2) in accordance with the laser cutting and drilling techniques presented in Section 4.2.7 and Section 5.4. This modification of Beer's law is based on different studies obtained by other researchers on the behaviour of the Er: YAG laser during hard-tissue interaction. These studies showed that the Er: YAG laser does not directly follow Beer's law for laser tissue ablation depth. In fact, due to the microexplosion effects of the Er: YAG laser during laser tissue interaction, the laser ablation depth is much higher than that predicted by Beer's law. This in effect justifies the equation's modification.

To validate the modification of Beer's law equation the author prepared a set of experiments (Chapter 4) to study the affect of varying the different laser parameter on bone ablation. However, the lack of flexibility in the available Er: YAG laser system prevented the author from fulfilling this goal.

8.3 The laser End-Effector

The development of a fully functional, theatre ready laser End-Effector system necessitates the design and development of an experimental prototype which can be tested on real bone (in-vitro). Once the performance of this prototype is validated, the system can be further modified to become a complete laboratory prototype then a fully functional clinical system which can be developed further to be a theatre ready system. The End-Effector prototype presented in Chapter 5 features a unique design which allows for a 3 DOF manipulation about a single manipulation point (origin). This design was based on a number of predefined requirements. These include: design simplicity, low cost, limited functional scope, safety (environmental, staff, and patient safety) and minimum degrees of freedom. These are in addition to other medical, laser, and functional requirements. By itself, the End-Effector's dexterity, flexibility and workspace is limited and do not satisfy all the clinical functional requirements. However, these limitations are removed as the laser End-Effector would be attached to a passive or active manipulator which increases the number of degrees of freedom and the working volume of the full system.

The detailed End-Effector's design is presented in Chapter 5 and the AutoCAD blue prints for some of the supporting elements and the design components' data sheets are presented in Appendices C and E respectively.

Chapter 5 also presents two approaches for the complete kinematic analysis of the laser End-Effector. The first approach is based on the Denavit-Hartenberg representation (Section 5.7.2) and the second is a geometric approach developed by the author (Section 5.7.3).

With the limited degrees of freedom the laser End-Effector is expected to fulfil the requirements for an experimental laser active delivery system. The kinematic models showed that with accurate design implementation, the End-Effector can reach any point within its workspace with high accuracy. Assuming an error free system, the End-Effector can have a linear positioning resolution as low as 2.5 μm and a rotational resolution of 54 μm. However, these values can be affected by physical and structural errors (Section 7.2) which may arise during the implementation and manipulation.

Guided by a preset trajectory plan and controlled by a PC based control unit with multiple feedback modalities, the laser End-Effector is expected to feature high performance accuracy. The control and feedback modalities aim to provide accurate manipulation of the laser End-Effector during the implementation of the trajectory plans.

8.4 Current Status of the Laser End-Effector

Unfortunately, due to some logistic problems including cost of components, manpower construction costs, etc. it was not feasible to construct the laser End-Effector within the budget constraints of the project, even though this was an early goal of the project. However, a single stage linear drive was used (as shown in Figure 4.18) to investigate the laser cutting and drilling techniques presented by the author in Section 4.2.7 and Section 5.4.

8.5 Feedback Techniques and Mechanisms

The design and development of a computer assisted laser End-Effector requires a feedback that can provide information about the laser ablation rate and ablation depth. The feedback modalities presented in this thesis include: real time mechanical, position and orientation tracking, and laser tissue interaction feedback. The mechanical feedback is achieved via optical encoders linked to the individual End-Effector's joint to determine the joints' rotational angles or linear displacement with respect to predefined initial values. The position and orientation tracking feedback, on the other hand, is achieved by an optical tracking system which monitors the position and orientation of the Front End of the laser End-Effector relative to a fixed reference frame and to the surgical site. Finally, for the laser tissue interaction feedback techniques, two innovative techniques were developed by the author to measure the laser ablation depth and ablation rate during laser tissue interaction (Section 6.6). These feedback techniques give feedback information about the overall surgical performance in terms of bone ablation depth and ablation rate for both the computer based control unit and the surgical team. These techniques are based on the photo-acoustic effects produced by the rapid expansion of water molecules and the localized water microexplosions inside tissue during laser tissue-interaction.

These laser feedback techniques measure the ablation depth and ablation rate by means of measuring the photo-acoustic time of flight (ATOF) and the acoustic phase shift (APS) of the laser induced photo-acoustic waves. The techniques were tested on real data gathered during laser bone ablation using a CO_2 laser. For a preset distance of 50 mm, the ATOF results showed an averaged measured distance of 50.18 mm with a standard deviation of ~4.4 mm for a given set of acoustic threshold levels (ATH). However, these results could be improved by selecting higher quality photo-acoustic detection devices, refining the acoustic threshold levels and accurately measuring the speed of sound in the air at the vicinity of the laser tissue interaction. Similarly the APS technique showed 100% accuracy when applied to well-defined waveforms sharing similar characteristics in terms of frequency and wave-shape. It even showed high immunity to amplitude noise as shown in the examples presented in Appendix A. The APS technique can also be used to measure group delay (phase shift) between a number of waves at one time for the condition that the maximum delay is less than or equal to one wavelength.

Although the ATOF and APS techniques offer the potential of being effective in determining the laser front position inside tissue, both are very sensitive to variations in the speed of sound which can be affected by environmental factors such as temperature, humidity and pressure. Therefore further investigation of the practical realisation of these techniques is required and alternative laser ranging techniques based on the innovative sampling points principle warrant further consideration.

8.6 Overall System Evaluation

This research study showed that the laser cutting technique presented in Chapter 4 seems to be very effective for laser-hard tissue ablation. This technique can easily be adapted to a robotic end-effector which can accurately control the laser waveguide manipulation speed (laser scanning speed) and hence control the ablation depth, rate and time. The experimental application of this technique for laser bone cutting showed relatively clean and straight cuts with evenly distributed ablation depths (Figure 4.29).

The experimental results also showed that the Er: YAG laser is an excellent candidate for bone ablation with an average ablation depth per pulse of 90 μm and less than 10 μm damage to the surrounding tissue (for a specific set of laser parameters) (Figure 4.29). They also show that Er:YAG laser can cut bone with high selectivity and it has the potential to improve on the standard cutting and drilling tools currently used in orthopaedic surgery.

The laser End-Effector prototype presented in this thesis appears to be an excellent surgical tool with a unique design; however, care must be taken during the structural implementation and development of this tool. An implementation error for example can result in large Laser Front positioning and orientation errors. To study the effect of these errors on the manipulation and positioning process of the Laser Front an error analysis model was developed by the author (Section 7.4). This error analysis model quantifies the effect of the potential sources of errors within the End-Effector and its impact on the Front End and Laser Front position and orientation. In addition to this error analysis model, Chapter 7 identifies the potential sources of errors that are associated with the design components, feedback measurements and control mechanisms and gives some suggestions for error reduction or elimination.

The error analysis model presented in this thesis was tested on several errors examples (Table 7.1) and appears to be effective in determining the Laser Front positioning error at any point within the End-Effector's workspace. Further, this model can also be applied to specify the maximum tolerable errors that will allow for total End-Effector positioning accuracy of ± 0.5 mm.

8.7 Achievements

The following is a list of achievements that were successfully completed by the author during this PhD research work:

- The selection of the most appropriate medical laser and laser delivery system
- The suggested modification of Beer's Law equation for bone ablation depth
- The preparation of laser experiments to validate the modification of the Beer's Law equation
- The design of a unique laser End-Effector prototype

- The development of two kinematics analysis models for the laser End-Effector
- The development of an error analysis model which can determine the effects of most mechanical, structural and control errors on the positioning, workspace, functionality and overall manipulation performance of the laser End-effector
- The development and implementation of two innovative laser front feedback techniques
- The preparation and carrying out experiments to measure the laser ablation depth and ablation rate using the laser feedback techniques

8.8 Contributions

This thesis has proposed a new surgical tool that could be an orthopaedic surgical tool of the future. Such a tool could revolutionise the future of orthopaedic surgery and contributes to the development of new surgical techniques that are safe (in terms of the amount of X-Ray radiation) less invasive, and may result in faster post-surgical recovery time. Furthermore, the design of such tools for computer assisted image guided surgery may set the platform for the design and development of specific purpose small surgical robotic arms for the operating theatre.

Moreover, the development of the photo-acoustic laser feedback techniques appears to be a step forward towards the development of a closed loop control system for laser surgery. In addition the methodology used in these techniques could have many other applications, these include: medical imaging and diagnostic systems, communication and radar systems and digital signal processing in general.

8.9 Future work

The author suggests further investigations of the Er:YAG laser bone cutting and drilling techniques in order to validate the suggested modification of Beer's Law. This may be achieved by performing the laser cutting and drilling experiments prepared by the author and comparing the results with pre-predicted values.

The author also suggests the modification of the laser End-Effector by increasing the number of degrees of freedom to accommodate for higher manipulation dexterity and flexibility. This may also include the modification of the kinematics and error analysis models.

References

[ABDE 97] Abdel-Malek, K. et al. 1997. Bone Registration Method for Robot-Assisted Surgery: Pedicle Screw Insertion. *IMechE Journal of Engineering in Medicine*, 211(H). pp.221-233.

[ABOS 03] Aboshosha A. 2003. *An Introduction to Robot Distributed Sensors Part1*. Computer Science Department, WSI. University of Tübingen.

[ABST 99] Absten G.T.1999. The language of lasers. *An Encyclopedic Glossary of Laser Terms*.The Laser Training Institute.

[ABST1 00] Absten, G.T. [Editor].2000. *Laser / Tissue Interaction.* [Online]. Professional Medical Education Association, Inc. Available: http://www.lasertraining.org/Biophysics.PDF. [Accessed 24 August 2001].

[ABST2 00] Absten, G.T. [Editor].2000. *Laser Medicine and Surgery: Fundamentals for the Operating Room & Clinics.* [Online]. Professional Medical Education Association, Inc. Available: http://www.lasertraining.org/Biophysics.PDF . [Accessed 24 August 2001].

[ADAM 98] Adams, R. J. and Hannaford, B. 1998. A two-port Framework for the design of Unconditionally stable haptic interfaces. *Proceeding of the 1998 IEEE/RSJ International Conference on Intelligent Robots and Systems*. pp 1254 – 1259.

[ADAM 98] Adams, M. D. 1998. Adaptive Motor control to Aid Mobile Robot Trajectory Execution in the Presence of Changing System Parameters. *IEEE Transaction on Robotics and Automation*, 14(6).pp 894-901.

[ALLM 98] Allamen, M. and Blatter, A. 1998. *Laser-Beam Interactions with Materials: Physical Principles and Applications*. 2nd ed. New York: Springer-Verlag Berlin Heidelberg.

[AMER 93] American Association of Orthopaedic Surgeons. 1993. *Advisory Statement: Use of Laser in Orthopaedic Surgery.* [Online]. Available: http://www.aaos.org/wordhtml/papers/advistmt/laser.htm [Accessed 05 Feb 2001].

[AMIO 00] Amiot, L.-P. et al. 2000. Comparative Results Between Conventional and Computer-Assisted Pedicle Screw Installation in the Thoracic. *Lumbar and Sacral Spine, Spine* ,25(5). pp. 606-614.

[APEL 02] Apel C. et al. 2002. *Influence of the Pulse length of an Erbium YAG Laser system on the Ablation Threshold of Human Dental Enamel.* Laser Med Sci, 17(2002). pp 137. 11th International Congress German Society for Lasers in Dentistry -25 -27 January 2002, Berlin. [Online]. Available: http://link.springer.de/link/service/jounals/10103/papers/2017002/20170137.pdf . [Accessed 14 July 2002].

[ARCH 00] **Archives** *A closer look at laser ablation*, September 2000. [Online]. Available: http://www.ilr.com.archive/2000/09/0900fea3.html. [Accessed 20 February 2001].

[ATTR 00] Attrill D.C. et al .2000. *Er: YAG (λ=2.94μm) Laser Etching of Dental Enamel as an Alternative to Acid Etching.* Laser Med Sci, 15. Pp 154-161. [Online] Available: http://link.springer.de/seaech.htm [Accessed 5 June 2002].

[ATTR nd] Attrill D. n.d. *Evaluation of Erbium: YAG and Holmium: YAG laser radiation on Denta Hard Tissue.* [Online]. Available; http://www.lpg.man.ac.uk/web_page/Theses_abstracts/DAttrill/DAttrillabstract.htm [Accessed 17 July 2002].

[BALA n.d.] Balasubramanian, R. n.d. *The Denavit Hartenberg Convention.* [Online]. Carnegie Mellon University. Available: http://www-2.cs.cmu.edu/afs/cs/academic/class/15384/web/DenavitHartenberg.pdf [Accessed 12 Dec. 2002].

[BARC 01] Bar-Cohen, Y., et al. 2001. Ultrasonic/sonic drilling /coring (USDC) for planetary applications. *Proceeding of SPIE's 8th Annual International Symposium on Smart Structures and Materials,* Newport, CA. 5-8 March 2001. Paper No. 4327-4355.

[BAST 00] Basting, R. F. 2000. New Techniques - Use of Water Jet Resection in Renal Surgery: Early Clinical Experiences. *European Urology*, 38(1). pp.104-107.

[BENH 87] Benhabib, B., Fenton, R. and Goldenberg, A. 1987.Computer-Aided Joint Error Analysis of Robots. *IEEE Journal of Robotics and Automation,* RA-3(4). pp. 317-322.

[BERG 98] Berger J. W. 1998. Er: YAG Laser Ablation: The Myth of 1- μm Penetration. *ARCH OPHTHALMOL*, 116 (June 98). [Online]. Available: http://archopht.ama-assn.org/issues/v116n6/fpdf/elt0698.pdf . [Accessed 3 June 2001].

[BIRM 00] Birnbaum k. et al. 2000. *Experimental Study of Different Laser Systems for PMMA Extraction Within the Scope of Revision Hip Arthroplasty.* Laser Med Sci, 15(2000). Pp 246 251. [Online]. Available: http://link.springer.de/search.htm [Accessed 15 June 2002].

[BLAK 98] Blackwell, M., Morgan, F. and DiGioia, A. M. 1998. Augmented reality and its future in orthopaedics. *Clin Orthop*, 354(1998). pp. 111-22.

[BOHN 88] Bohn, D. A. 1988. Environmental Effects on the Speed of Sound. *J. Audio Eng. Soc.*,36(4). Pp. 2735-2739.

[BRUC 02] Bruckner, S., Seemann, R., and Elmenreich, W. 2002. *Applying a Real Time Interface to an Optical Tracking System.* [Online]. Available: http://www.vmars.tuwien.ac.at/~wilfried/papers/rr-24-2002.pdf. [Accessed 20 July 2004].

[BRYA nd] Bryan, C. n.d. Robotics in Surgery. [Online] Available: http://mechsys4.me.udel.edu/MEEG667/surgicalrobots.doc [Accessed 20 May 2002].

[BZOS 00] Bzostek, A., et al. 2000. *Distributed modular computer-integrated surgical robotic system: Implementation using modular software and networked systems.* [Online]. Johns Hopkins University, USA. Available: http://cisstweb.cs.jhu.edu/resources/publications/download/bzostek-etal-miccai-2000.pdf [Accessed 15 November 2001].

[CARR 86] Carruth, J. A. S. and Mckenzie, A. L. 1986. *Medical lasers: science and clinical practice. England*: Adam Hilger Ltd.

[CARR 97] Carretero, J. A., et al. 1997. *Kinematic analysis of a three-DOF parallel mechanism for telescope applications.* [Online]. Available: http://subspace.me.uvic.ca/~jcarrete/work/papers/detc97/detc97.html [Accessed 30 November 2001].

[CARR[1] 00] Carretero, J. A., Poldhorodeski, R. P. & Nahon M. A. 2000. *Kinematic analysis and optimization of new three degree-of-freedom spatial parallel manipulator.* [Online]. University of Victoria, Canada. Available: http://subspace.me.uvic.ca/~jcarrete/work/papers/jmd-march-2000/ca-po-na-go-jmd-march-2000.pdf [Accessed 30 November 2001].

[CARR[2] 00] Carretero, J. A., Nahon M. A. & Poldhorodeski, R. P. 2000. *Workspace analysis and optimizationof a novel 3-DOF parallel Manipulator.* [Online]. University of Victoria, Canada. Available: http://subspace.me.uvic.ca/~jcarrete/work/papers/ijra-dec-2000/ca-na-po-ijra-2000.pdf [Accessed 30 November 2001].

[CASA nd] Casadei, C., et al. n.d. *A PC-based work station for robotic discectomy.* [Online]. Available: http://robotics.jpl.nasa.gov/people/fiorini/papers/pub.ps. [Accessed 2 January 2003].

[CAST 97] Castro-Linares, R., Alvarez-Gallegos, Jm., and Vásquez-López, V. 1997. *Position Control of a Stepper Motor Via a Reduced Order Nonlinear Controller-Observer Scheme.* [Online]. Available: http://www.cds.caltech.edu/conferences/related/ECC97/proceeds/1_250/ECC209.PDF. [Accessed 14 July 2004].

[CHAR 90] Charlton, A. et al. 1990. Erbium-YAG and Holmium-YAG Laser Ablation of Bone. *Lasers in Medical Science*, 5. p. 365.

[DAVA n.d.] DAVALL Stock Gears. n.d. *Handbook of METRIC Drive Components.* DAVALL Stock Gears. England.

[DEKA nd] Deka M. n. d. *Laser Tissue Interaction. Medical Laser.* [Online]. Available: http://www.dekamela.com/laser-tissue.htm. [Accessed 29 July 2002].

[DIGI nd] Di Gioia, A. n.d. *Knee Navigation System (KneeNav TKR/ACL)*. The Robotic Institute. [Online]. Available: http://www.ri.cmu.edu/projects/project_426.html. [Accessed 29 Jan 2005].

[DIGI⁰ 98] Di Gioia, A.M. 1998. Symposium: Computer assisted orthopaedic surgery: Medical Robotics and Image Guided Surgery. *Clinical Orthopaedics and Related Research*, 354. pp 2-4

[DIGI¹ 98] Di Gioia, A.M., Jaramaz, B. and Colgan, B.D. 1998. Computer assisted orthopaedic surgery. Image guided and robotic assistive technologies. *Clinical Orthopaedics and Related Research*, 354. pp 8-16

[DIGI² 98] Di Gioia, A. et al. 1998. An image guided navigation system to measure intraoperatively acetabular implant alignment. *Clinical Orthopaedics and Related Research*, 354. pp 8-22

[DOME 00] Domergur, G. and Viant, W. J. 2000. *3D Registration through Pseudo X-ray Image Generation*. Department of Computer Science University of Hull, Hull, UK

[DU 03] Du, K. etal. 2003. Electro-optically *Q*-switched Nd:YVO4 slab laser with a high repetition rate and a short pulse width. *Optical Letters,* 28(2). pp. 87-89.

[DUKE 01] Duke University. 2001. *Laser safety Policy*. Duke University Medical Center.

[DYER 03] Dyer, P. E. 2003. Excimer laser polymer ablation: twenty years on. *Applied Physics A*, 77. pp. 167-173.

[EBIH 02] Ebihara A. et al. 2002. *Er: YAG Laser Modification of root Canal Dentine: Influence of Pulse Duration, Repetitive Irradiation and Water Spray*. Laser Med Sci, 17 (2002). Pp 198 207. [Online]. Available: http://link.springer.de/link/service/jounals/10103/papers/2017003/20170198.pdf . [Accessed 15 July 2002]

[ERYA nd] Er: YAG Laser.[Online]. Available: http://www.fotona.si/lasers/twinapp.html . [Accessed 11 June 2001].

[EULE 03] Euler, E. et al. 2003. C-arm-based three-dimensional navigation: a preliminary feasibility study. *Computer Aided Surgery*, 8. pp 35-41

[EVAN 93] Evans, G. 1993. *Studying Laser/Tissue Interaction – Excimer Laser Coronary Angioplasty.* [Online]. Available: http://www.ece.orst.edu/~ece482/lasers/ee488prev/gevans/gevans.htm [Accessed 30 July 2001].

[FADD 94] Fadda M. et al. 1994 *Computer-Assisted Knee arthroplasty at Rizzoli Institutes.* Proceeding of the First International Symposium on Medical Robotics and Computer Assisted Surgery, 1. pp. 26-30.

[FARR nd] Farrar S. n.d. *Background: Why use lasers for medical applications?.* Physics Department, The University of Hull, Hull UK.

[FEMT nd] FEMTO GROUP *Femtosecond Lasers and Applications.* Institute of Applied Physics University of Heidelberg, Germany.

[FERR 86] Ferrreira, P.M. and Liu, C. R. 1986. An analytical Quadratic Model for the Geometric Error of a Machine Tool. *Journal of Manufacturing Systems*, 5(1). pp. 51-60.

[FITZ 01] Fitzpatrick, J. M. and Galloway, R. L. 2001. The use of fiducials in the registration of 3D images. *Automedica: Special Issue: Engineering Approaches to Neurological Surgery* 20 (Jun)

[FITZ 95] Fitzgibbon, J. et al. 1995. Sapphire Optical Fibers for the Delivery of Erbium: YAG laser energy. *Biomedical Optoelectronic Instrumentation.* [Online]. Available: http://www.saphikon.com/yagwhit.htm. [Accessed 11 June 2001].

[FORR 92] Forrer, M. et al. 1992. Bone-Ablation Mechanism Using CO_2 Lasers of Different Pulse Duration and Wavelength. *Applied Physics B,* 56. pp.104-112.

[FRAN 04] Frantz, D., Kirsch, S. and Wiles, A. 2004. *Specifying 3D Tracking System Accuracy One Manufacturer's Views.* [Online]. Available: http://www.ndigital.com/markets/respapers/bvm2004.pdf. [Accessed 14 July 2004].

[FREN 99] Frenz M., et al. 1999. *Annual Report 1998/1999 Laser Surgery.* [Online]. Available: http://ubecx01.unibe.ch:8081/AnnualReport/1999/research/LA/frenz.html. [Accessed 7 February 2001].

[FRYM 93] Frymoyer, J.W. (Editer).1993. Laser in Orthopaedics. In: *Orthopaedic Knowledge Update 4.* Rosemont, IL: American Academy of Orthopaedic Surgeons. pp.227-231.

[FU 87] Fu K. S., Gonzalez R.C. & Lee C.S. G., 1987. *ROBOTICS Control, Sensing, Vision, and Intelligence.* McGraw-Hill International Edition.

[FUKA 00] Fukao, T., Nakagawa, H. and Adachi, N. 2000. Adaptive Tracking Control of a Nonholonomic Mobile Robnot. *IEEE Transaction on Robotics and Automation*, 16(5). pp 609-615.

[GLOS 99] Glossop, N. et al. 1999. Registration Methods for Percutaneous Image Guided Spine Surgery. *Computer Assisted Radiology and Surgery*, proceedings of the 13th international congress and exhibition, Paris, France, June 23-26, 1999 pp. 746-755.

[GLOZ 01] Glozman, D., Shoham, M. and Fischer, A. 2001. A Surface-Matching Technique for Robot-Assisted Registration. *Computer Aided Surgery,* 6. pp. 259–269.

[GOBA 88] Gopal, M. 1988. *Digital Control Engineering*. New Delhi: Wiley Eastern Limited.

[GRIF nd] Griffiths, J. G., Phillips, R. and Viant, W. J. n.d. *Computer assisted Orthopaedic Surgery.* Department of Computer Science, University of Hull. Hull, UK.

[GRIG 95] Grigorjeva, L. G. et al. 1995.Optical properties of silver halide fibres: ageing effects. *J. Phys. D: Appl. Phys.*, 29. pp. 578-583.

[GüLS 01] Gülsoy M. et al. 2001. Er: YAG laser Ablation of Cerebellar and Cerebral tissue. Lasers Med Sci, 16. pp 40 -43. [Online] Available: http://link.springer.de/search.htm. [Accessed 1 June 2002].

[HAFE nd] Hafez, M. A., et al. n.d. *Computer-Assisted Fixation of Proximal femoral Fracture*. Orthopaedic Department, Hull royal Infirmary and Castle Hill Hospital, Department of Computer Science, University of Hull. Hull, UK.

[HANS nd] Hansen, S. C. and Todd, R. H. nd. *Design Parameters for Removing Tooth Decay Using a Water Jet Stream*. [Online] Available: http://marketing.byu.edu/htmlpages/student_projects/p61/paper.htm. [Accessed 15 February 2001]

[HARR 00] Harrington, J. A. 2000. A review of IR Transmitting, Hollow Waveguides. *Fibre and Integrated Optics*, 19. pp. 211-217.

[HARR nd] Harrington, J. A. n.d. *Infrared Fiber Optics*. [Online]. Rutgers University at NJ, USA. Available: http://irfibres.rutgers.edu/pdf_files/ir_fiber_review.pdf [Accessed 20 June 2003].

[HATA 94] Hata, Y. et al. 1994. Liver resection in children, using a water-jet. *Pediatr Surg*, 29. pp 648-650.

[HAYK 99] Haykin, S. & Veen, B. V. 1999. *Signals and Systems*. New York: John Wiley & Sons, Inc.

[HAZA 03] Hazan, E.J. and Joskowicz, L. 2003.Computer-Assisted Image-Guided Intramedullary Nailing of Femoral Shaft Fractures. *Techniques in Orthopaedics®*, 18(2). pp. 1-10.

[HECH 92] Hecht, J. *The laser guidebook*, McGraw-Hill, pp 32-37

[HEFT 98] Hefti, J. L., et al. 1998. Biomedical paper: Robotic three-dimensional positioning of a stimulation electrode in the brain. *Computer aided surgery*, 3(March). pp.1-10.

[HELF 01] Helfmann J. and Müller G. 2001. Laser Lithotripsy: Process and Overview. *Medical Laser Application*, 16(1). pp. 30-37

[HICK 98] Hicks, B. 1998. Invest in the ground floor of future surgeries-robotic doctors! [Online]. Available: http://taipanonline.com/archive/0998/0998microcaps.html [Accessed 5 February 2001].

[HOFF 00] Hoffman H. J. and Telfair W. B. 2000. *Photospallation: A New Theory and Mechanism for Mid-infrared Corneal Ablations*. Journal of Refractive Surgery, 16 (2000). Pp. 90 – 94. [Online]. Available: http://jrs.slackinc.com/vol161/hoff.pdf. [Accessed 14 July 2002].

[HOFS 00] Hofstetter, R. et al. 2000. Computer-Assisted Fluoroscopy-Based Reduction of Femoral Fractures and Antetorsion Correction. *Computer Aided Surgery* . 5(2000). pp.311–325.

[HOFS 99] Hofstetter, R. et al. 1999. Fluoroscopy as an Imaging Means for Computer-Assisted Surgical Navigation. *Computer Aided Surgery,* 4(1999). pp. 65–76.

[HONL 99] Honl, M. et al.1999.*Water Jet cutting of bone and bone cement for prosthesis revision surgery.*[Online].Available: http://www.tu-harburg.de/bim/ep9899/cop9899.htm. [Accessed 20 February 2001].

[HONL nd] Honl, M. et al, *Jet Cutting – the water jet as a new therapeutic instrument for orthopaedic diseases*. [Online] Available: http://www.bioeng.de/pool/sektion_4e.htm. [Accessed 20 February 2001].

[HOWE 99] Howe R. D. & Matsuoka Yoky. 1999. Robotics for surgery. *Annual Review of Biomedical Engineering*, 1, pp. 211 - 240.

[HUMM 02] Hummel, J. et al. 2002. Evaluation of a Miniature Electromagnetic Position Tracker. *Medical Physics*, 29(10). pp. 2205-2212.

[IVAN 02] Ivanenko, M. M. et al. 2002. Bone Tissue Ablation with sub-μs Pulses of a Q-switched CO_2 Laser: Histological Examination of Thermal Side Effects. Laser Med. Sci., 17. pp 258-264

[IVAN 97] Ivanenko M.M. et al. 1997. Transmyocardial laser revascularization: Are new approaches with new lasers possible? *TMLR: Management of Coronary Artery Diseases*, pp. 153-164, Springre,1997.

[IVAN 98] Ivanenko, M. M. and Hering, P. 1998. Wet bone ablation with mechanically Q-switched high-repetition-rate CO_2 laser. *Applied Physics B*, 67. pp. 395-397.

[IVAN[1] 00] Ivanenko, M. M. et al. 2000. In vitro incision of bone tissue with a Q-switch CO_2 laser. Histological examination. *Lasers in the Life Sciences*, 9. pp. 171-179.

[IVAN[1] 02] Ivanenko, M. M. et al. 2002. Bone Tissue Ablation with sub-µs Pulses of a Q-switch CO_2 laser: Histological Examination of Thermal Side Effects. *Laser in Medical Sciences*, 17. pp. 258-264.

[IVAN[2] 00] Ivanenko, M. M., Mitra T. & Hering P. 2000. *Hard tissue ablation with sub-µs CO_2 laser pulses with the use of an air-water spray*. [Online]. Available: http://www.caesar.de/english/dounload/2000_SPIE.pdf [Accessed 23 August 2002].

[IVAN[2] 00] Ivanenko, M. M., Mitra, T. and Hering, P. 2000. Hard tissue ablation with sub-µs CO_2 laser pulses with the use of an air-water spray. *SPIE Proc. Optical Biopsy and Tissue Optics*, 4161(08). pp.46-51.

[IVAN2 02] Ivanov B. et al. 2002. *Bone ablation at 2.94µm Using the Free- Electron Laser and Er: YAG Laser.* [Online]. Available: http://www.eps.org/aps/meet/MAR02/baps/abs/S4735114.html [Accessed 17 July 2002].

[JELE 02] Jelenkovic, L. & Budin, L. 2002. *Error analysis of Stewart platform based manipulators*. [Online]. Available: http://www.zemris.fer.hr/~leonj/unofficial/radovi/ines2002.pdf . [Accessed 1 June 2003]

[JOHN 01] John, N. W., et al. 2001. *An Integrated Simulator for Surgery of the Petrous Bone*. [Online]. University of Manchester, UK. Available: http://www.crs4.it/vvr/bib/papers/mmvr-2001-ierapsr.pdf. [Accessed 15 July 2002]

[JOOS 96] Joos, K. 1996. Micro Erbium Laser Intraocular Cutting Probe. *Biomedical Engineering*. [Online]. Available: http://wf66.whitaker.org/abstracts/mar96/joos.html. [Accessed 3 January 2001].

[JOSK 00] Joskowicz, L. 2000. *Fluoroscopy-Based Navigation In Computer-Aided Orthopaedic Surgery.* [Online]. The Hebrew University of Jerusalem. Available: http://www.cs.huji.ac.il/~josko. [Accessed 10 August 2001]

[KAMP 99] Kampmeier J. et al. 1999. *Comparison of Free-running vs. Q-switched Er: YAG Laser Photorerfratctive Keratectomy (Scanning Mode) in Swine Eyes.* Journal of Refractive Surgery, 15. 1999 [Online]. Available: http://jrs.Slackkine.com/vol155/kamp.pdf [Accessed 1 August 2002].

[KIM 00] Kim, H. S. & Choi, Y. J. 2000. The kinematic error bound analysis of the stewart platform. *Journal of robotic system*, 17(1).pp.63-73.

[KIMI 00] Kimia, B. and Bullitt, E. 2000.Chapter 5 at a Glance: Registration and Segmentation. *Technical Requirements of Image-Guided Spine Procedures.* ISIS, Washington, pp. 24-31.

[KIND 02] Kinder, T. & Salewski, K-D. 2002. Absolute distance interferometer with grating-stabilized tunable diode laser at 633nm. Journal of Optics A: Pure and Applied Optics, 4(Nov.). pp S364-S368.

[KIRK 00] Kirkpatrick, J. J. R. and Mackay, I. R. 2000.Sound levels produced by erbium YAG lasers: Health and Safety issues. *Lasers Med Sci.* 15. pp 263 -265.

[KODA 99] Kodali, P. B. S., Zhigilei, L. V. & Garrison, B. J. 1999. Phase transition at low fluences in laser desorption of organic solids: a molecular dynamics study. *Nuclear Instruments and Methods in Physics Research B*, 153(1999). pp 167-171.

[KOGE 66] Kogelnik, H. and Li, T. 1966. Laser Beams and Resonators, *Applied Optics*, 5. pp 1550 -1567.

[KOSE 98] Koseki, Y., et al. 1998. *Design and accuracy evaluation of high speed and high precision parallel mechanism.* [Online]. Available: http://staff.aist.go.jp/koseki-y/publications/pdf/icra1998.pdf. [Accessed 20 May 2000].

[KOTA 01] Kotan, C. et al. 2001. Diameter and Pressure of the Water-Jet for Live Resection. *Eastern Journal of Medicine*, 6(2). pp 43-47.

[KOZO 96] Kozodoy, R., Pagkalinawan, A. T. and Harrington, J. 1996. Small-bore hollow waveguides for dlivery of 3-μm **laser radiation.** *Applied Optics*, 35(7). pp. 1077 - 1082.

[KUMA 04] Kumar T. Rajamania, K. T. et al. 2004. *Bone Morphing with statistical shape models for enhanced visualization.* [Online]. Available: http://cranium.unibe.ch/users/mstyner/docs/SPIE04_BoneMorph_2004.pdf. [Accessed 08 September 2004].

[LAHM 99] Lahmer, A., Wiesel, U. and Borner, M.1999. Experience in using the ROBODOC system without pins. *Computer Aided Surgery*, 4(3). pp.160

[LAIB 00] Laib, A. 2000. Adaptive Output Regulation of Robot Manipulators Under Actuator Constraints. *IEEE Transaction on Robotics and Automation*, 16(1). pp 29-35.

[LAVA 94] Lavallže S. et al. 1994 *Computer Assisted Spine Surgery: A Technique for Accurate Transpedicular Screw Fixation using Ct Data and a 3D Optical Localizer.* Proceeding of the First International Symposium on Medical Robotics and computer Assisted Surgery, 2. pp. 315-322.

[LAVA 95] Lavallže, S. 1995.Registration for computer-integrated surgery: Methodology, state of the art. In Taylor, et al., editors. 1995. *Computer-Integrated Surgery*, chapter 5. pp. 77–97.

[LAWR nd] Lawrence Livermore National Laboratory. n. d. *Ultra-Short Pulse Laser Surgery.* [Online]. Medical Technology Program. Available: http://www-laser.llnl.gov/lasers/mtp/ultra.html. [Accessed 6 February 2001].

[LEA 94] Lea J. T. et al. 1994. *Registration and Immobilization in Robot-Assisted Surgery.* [Online]. Available: http://othello.mech.nwu.edu/~peshkin/pubs/1995_RegistrationImmobilization.pdf. Accessed [22 June 2004].

[LEA 98] Lea, J. T. 1998. *Registration Graphs: A language for Modeling and Analyzing Registration in Image-Guided Surgery.* Ph.D. diss, Northwestern University.

[LEA[1] 95] Lea J. T. et al. 1995. Registration and Immobilization in Robot-Assisted Surgery. *Jurnal of Image Guided Surgery*, 1(2). pp. 80-87.

[LEA[2] 95] Lea J.T., Santos-Munné, J. J. and Pishkin, M. A. 1995.Diagramming Registration Connectivity and Structure. *Medicine Meets Virtual Reality III.* San Diego, CA. pp.1-10

[LERN 99] Lerner, A. G. et al. 1999. A passive positioning and supporting device for surgical robots and instrumentation. [Online]. Johns Hopkins University, USA. Available: http://robotics.me.jhu.edu/%7Ellw/ps/miccai99_grey_preprint.pdf [Accessed 12 Feb. 2001]

[LI 92] LI, Z. et al. 1992. Bone Ablation with Er: YAG and CO_2 lasers: Study of thermal and Acoustic Effects. *Lases Surgery and Medicine*, 12. pp. 79-85.

[LIAO 04] Liao, H. et al. 2004. Surgical Navigation by Autostereoscopic Image Overlay of Integral Videography. *IEEE Transaction on Information Technology in Biomedicine*, 8(2), pp.114-121.

[MAI 00] Mai, S., Lörke, C. and Siebert W. 2000. Implantation of Knee Endoprostheses with the New CASPAR robotic Operation System. *Orthopadische Praxis* 36, 12(2000). pp. 792-800.

[MAJA 98] Majaron B. et al. 1998. Heat Diffusion and Debris Screening in Er: YAG Laser Ablation of Hard Biological Tissues. *Appl. Phys. B, 66(1998)*. Pp 479-487.

[MARC 96] The Center for MRCAS. 1996. HipNav Overview. *Medical robotics and computer assisted surgery*.[Online]. Available: http://www.mrcas.ri.cmu.edu/projects/hipnav/overview.html. [Accessed 6 September 2001]

[MARS 01] Matsuura Y. et al. 2001. Infrared-Laser delivery system based on polymer-coated hollow fibers. *Optics & Laser Technology*, 33(2001). Pp 279-283.

[MATH 95] MathSoft, Inc. 1995. *Mathcad User's Guide*. MathSoft Inc. USA

[MATS 01] Matsuura, Y. et al. 2001. Infrared-laser delivery system based on polymer-coated hollow fibres. *Optics and Laser Technology*, 33. pp. 279-283.

[MATS 95] Matsuura, Y., Abel, T. and Harrington, J. 1995. Optical property of small-bore hollow glass waveguides. *Applied Optics*, 34(30). pp. 6842-6847.

[MATS 97] Matsuura, Y. and Harrington, J. 1997. Hollow glass waveguides with three-layer dielectric coating fabricated by chemical vapour deposition. *Optical Society of America*, 14(6). pp. 1255-1259.

[MAVR 97] Mavroidis, C. et al. 1997. A Systematic Error Analysis of Robotic Manipulators: Application to a High Performance Medical Robot. *Proceedings of the 1997 International Conference in Robotics and Automation Albuquerque, NM*, April, 1997.

[MAVR 98] Mavroidis, C., et al. 1998. High performance medical robot requirements and accuracy analysis. *Robotics and Computer Integrated Manufacturing*. 14(5). pp. 329-338.

[MCGU 66] McGuff P. 1966. *Surgical Application of Laser.*

[MCKE 01] McKenzie G. et al. 2001. *Electrophoresis as a technique for direct analysis of the laser-tissue ablation products.* Micropathology Ltd, University of Warwick Science Park, Coventry, UK. [Online]. Available: http://www.eng.warwick.ac.uk/~espbc/papers/2001/4707-20.pdf [Accessed 1 August 2002].

[MCLA 96] McLachlan, D. S. 1996. *Novel robot design for complex intra-cranial neurosurgery.* [Online]. University of Teesside, UK. Available: http://sst.tees.ac.uk/external/u0000981/research/papers/IMC13/IMC13_3P.PDF [Accessed 10 January 2000]

[MERI 93] Meriam J. L. & Kraige L. G. 1993. *Engineering Mechanics.* Volume two. 3rd ed., John Wiley & Sons, Inc. New York

[MITT 94] Mittelstadt, B. D. et al. 1994. *The Evolution of a Surgical Robot from Prototype to Human Clinical Use.* In First International Symposium on Medical Robotics and Computer Assisted Surgery (MRCAS'94), 1(Septemper). pp. 36-41.

[MOHN 95] Mohsen, A., et al. 1995. End User Issues for Computer Assisted Surgical Systems. *Transaction of the institute of Measurement and Control*. 17(5). pp. 265-27.

[MORI 97] Moritz, A. et al. 1997.Bacterial reduction in periodontal pockets through irradiation with a diode laser: A pilot study. *J Clin Laser Med Surg,* 15. pp. 33-37.

[MORI 98] Moritz, A. et al. 1998.Treatment of periodontal pockets with a diode laser. *Lasers Surg Med,* 22. pp. 302-311.

[MOON 01] Moon, S-K., Moon, Y-M. and Kota, S. 2001. Screw Theory Based Metrology for Design and Error Compensation of Machine Tools. *Proceedings of DETC'01: ASME 2001 Design Engineering Technical Conferences Pittsburgh, Pennsylvania*, September 9-12, 2001.

[MROC 00] Mrochen M. et al. 2000. Limitations of Erbium: YAG Laser Photorefractive Keratectomy. *Journal of Refractive Surgery*, 16 (Jan/Feb). pp 51-59.

[MüLL 91] Müller A. G. 1991. State-of-the-Art of Safety Technology in Medical Uses of Lasers. [Online]. Available: http://www.tuwien.ac.at/islt/tmp/refs/albre91.htm. [Accessed 8 March 2001].

[MURP 02] Murphy, S. and Gobezie, R. 2002. *Image-guided surgical navigation: basic principles and applications to reconstructive surgery*. [Online]. Available: http://www.orthojournalhms.org/ojhms2002/pdfs/manuscript-02.pdf. [Accessed 22 July 2004].

[NAHE 99] Nahen K. and Vogel A. 1999. Investigation on acoustic on-line monitoring of IR laser ablation of burned skin. *Lasers Surg. Med.*, 25(1). pp. 69-78.

[NASS 98] Nasser, J. A. et al. 1998. Preliminary Results in Surgery of Parkinson's Disease. *Arq Neuropsiquiatr,* 56(3-B). pp.533-539.

[NELS 88] Nelson, J. S. et al. 1988. Ablation of Bone Methacrylate by a Prototype Mid-Infrared Erbium: YAG Laser. *Lasers in Surgery and Medicine*, 8. pp. 494-500.

[NICO 02] Nicola, J. H. et al. 2002.Speed of particles ejected from animal skin by CO_2 laser pulses, measured by laser Doppler velocimetry. *Phys. Med. Biol.*, 47(2002). pp 847-856.

[NIEM 96] Niemz, M. H. (1996) *Laser-Tissue Interaction Fundamental and Applications*, Springer ISBN 3-540-60363-8.

[NISH 03] Nishihara, S. et al. 2003. Accuracy evaluation of a shape-based registration method for a computer navigation system for total knee arthroplasty. *J Knee Surg*, 16(2). pp. 98-105.

[NOBU 00] Nobuhiko Sugano, N. and Ochi, T. 2000. Medical Robotics and Computer-Assisted Surgery in the Surgical Treatment of Patients with Rheumatic Diseases. *Cutting Edge Report.* [Online]. Available: http://www.rheuma21st.com/downloads/cutting_edge_Robotics_Japan.pdf[Accessed 08 September 2004]

[NOLT 02] Nolte, L.P. et al. 2002. A novel mobile C-arm system for use in image guided surgery-a feasibility study. *Proceeding CAOS.*

[NOLT 04] Nolte, L.P. and Beutler, T. 2004. Basic principles of CAOS. *Injury, Int. J. Care Injured*, 35(June), S-A6 - S-A16.

[NUBL 96] Nubling, R. K. and Harrington, J. 1996. Hollow-waveguide delivery systems for high-power, industrial CO_2 lasers. *Applied Optics*, 34(3). pp. 372-380.

[NUBL 97] Nubling, R. K. and Harrington, J. 1997. Optical properties of single-crystal sapphire fibers. *Applied Optics*, 36(24). pp. 5934-5935.

[NUSS 88] Nuss, R. C. et al. 1988. Infrared Laser Bone Ablation. *Lasers in Surgery and Medicine*, 8. pp.381-391.

[OBOE 98] Oboe, R. & Fiorini, P. 1998. A design of control environment for internet-based telerobotics. *The international journal of robotics research*, 17(4). pp.433-449.

[ONDR 01] ONDRIVES LIMITED. 2001. *Mechanical drive components*. Ondrives limited, England.

[ORTH 99] ORTHO*soft* Inc. 1999. Navitrack System receives FDA clearance in the USA August 23rd 2000. *Orthopaedics Today September 99*. [Online]. Available: http://www.orthsoft.ca/navitrack%20%in20US.htm. [Accessed 6 September 2001]

[OZAN 98] Ozanian, T. O., et al. 1998. *Image Analysis for Computer-Assisted Surgery of Hip Fractures*. Department of computer Science, University of Hull, Hull, UK

[PAPA 82] Papachristou, D.N. and Barters, R. 1982. Resection of the liver with a water jet. *Br J Surg*. 69(2). pp 93-94.

[PARK nd] PARKER Motion & Control. n.d. Feedback Devices. *Engineering Reference A*. [Online]. Available: http://www.compumotor.com/catalog/cataloga/A39-A44.pdf. [Accessed 1 May 2001]

[PETE 00] Petermann, J., et al. 2000. Computer Assisted Planning and Robot Assisted Surgery in the Reconstruction of the Anterior Cruciate Ligament Reconstruction. *Operative Techniques in Orthopaedic,* 10. pp. 50-55.

[PHIL 95] Phillips, R., et al. 95. *Accuracy Analysis of an Image Guided Orthopaedic System.* Department of Computer Science, University of Hull, Hull,UK.

[PHIL1 00] Phillips, R., et al. 2000. *Development of the Hull Computer Assisted Orthopaedic Surgery System (CAOSS) Projects. Department of Computer Science*, University of Hull, Hull, UK.

[PHIL1 02] Phillips, R. et al. 2002. *A Virtual Fluoroscopy System based on a Small and Unobtrusive Registration / Calibration Phantom*. Proceedings of Computer Assisted Radiology and Surgery, CARS 2002, pp. 275-280.

[PHIL1 95] Phillips, R., et al. 1995. Image Guided Orthopaedic Surgery Design and Analysis. *Transaction of the institute of Measurement and Control*. 17(5). pp. 251-264.

[PHIL2 00] Phillips, R., et al. 2000. Development of the Hull Computer Assisted Orthopaedic Surgery System (CAOSS) Projects. *Department of Computer Science*, University of Hull. Hull, UK.

[PHIL[2] 02] Phillips, R. et al. 2002. A Virtual Fluoroscopy System and its use for Image Guidance in Unicomparmental Knee Surgery. *Proceeding of Medicine Meets Virtual Reality*, pp. 341-347.

[PHIL[3] 00] Phillips, R., et al. 2000. Hip Trauma In: DiGioia, A. M., et al. ed. Hip and Knee Surgery-Navigation, Robotics and Computer Assisted Surgical Tools. *Department of Computer Science*, University of Hull. Hull, UK.

[PIEP 97] Pieper, S., Weidenbach, M. and Berlage, T. 1997. Registration of £D Ultrasound Images to Surface Model of the Heart. *Proceedings of the Interface to Real & Virtual Worlds -Montpellier, France*, May 28-30, 1997.

[PROV nd] PROVIEW. *About Laser Surgery.* [Online] Available: http://proview.com.tw/laser/about.html. [Accessed 5 February 2001].

[PRYS 96] Pryshlak, A. P. et al. 1996. Advancements in sapphire optical fibers for the delivery of Erbium laser energy and IR sensor applications. *Biomedical Fiber Optics*, 2677(January). [Online]. Available: http://www.saphikon.com/fiberwht.htm. [Accessed 13 July 2003].

[R&D 00] R&D Research and Development. 2000. *Sonic Drill Could Go into Space.* [Online]. Available: http://ndeaa.jpl.nasa.gov/nasa-nde/nde-aa-l/PressRelease/RandDSonicDrill.pdf .[Accessed 15 February 2001]

[RABI 99] Rabii, C. D. and Harrington, J. 1999. Mechanical properties of hollow glass waveguides. *Opt. Eng.*, 38(9). pp. 1490-1499.

[REIS 01] Reiss, S. M. 2001. Unlocking the Mysteries of Laser-Tissue Interaction. *BIOPHOTANIC INTERNATIONAL.* (July/August 2001). pp. 40-45.

[RIBO 01] Ribo, M., Pinz, A. and Fuhrmann, A. 2001. Anew Optical tracking system for Virtual and Augmented Reality Applications. *IEEE Instrumentation and Measurements Technology Conference*, Budapest, Hungary, May 21-23, 2001.

[RITT 02] Ritter, D., Mitschke, M. and Graumann, R. 2002. Markerless Navigation with the Intra-OperativeImaging Modality SIREMOBIL Iso-C3D. *Electromedica*, 70 (1). pp. 31-36.

[RIVA 04] Rivals, I. and Personnaz, L. 2004. Jacobian conditioning analysis for model validation. *Neural Computation,* 16(2004). pp. 401-418.

[RODR 01] Rodreiguez G. P. et al. 2001. Measurement of Thermal Diffusivity of Bone, Hydroxyapatite and Metals for Biomedical Application. *Analytical Science,* 17 (April). s357-s360.

[SALB 01] Salb, T. et al. 2001. Comparison of Tracking Techniques for Intra- operative presentation of Medical Data using a See-Through Head-Mounted Display. Stud Health Technol Inform, 81. pp. 443-445.

[SAPH 98] SAPHIR MEDICAL PRODUCTS. 1998. *Water Jet Technology For Medical Use*. [Online]. Available: http://www.saphir-medical.com/products/index.html. [Accessed 20 February 2001]

[SCHL 02] Schlaier, J., Warnat, J. & Brawanski, A. 2002. Clinical paper: Registration accuracy and practicability of laser-directed surface matching. *Computer aided surgery*, 7(October). pp. 284-290.

[SCHW 02] Schwab, A.L., Meijaard, J.P. and Meijers, P. 2002. A comparison of revolute joint clearance models in the dynamic analysis of rigid and elastic mechanical systems. *Mechanism and Machine Theory*, 37 (2002). pp. 895–913.

[SHER 01] Sherrit, S. et al.2001. Sample Acquisition and In-Situ Analysis Using the Ultrasonic/Sonic Driller/Corer (USDC) and Robotic Platforms. *The 6th International Symposium on Artificial Intelligence, Robotics and Automation in Space (i-SAIRAS-01),* Montreal, Canada, June 18-21, 2001. [Online]. Available: http://ndeaa.jpl.nasa.gov/ndeaa-pub/Canada/paper_am006.pdf. [Accessed 29 August 2001]

[SHI 01] Shi, Y. et al. 2001. Properties of hollow bent output tips in CO_2 laser light delivery system. *Optics & Laser Technology*, 33. pp. 225-230.

[SHOR1 nd] ShoreLaser Center, *More About Laser*. [Online] Available: http://www.shorelaser.com/AboutLasersDet.html. [Accessed 22 January 2001]

[SHOR2 nd] ShoreLaser Center. n. d. *Medical Laser*. [Online]. Available: http://www.shorelaser.com/AboutLaserMed.html. [Accessed 22 January 2001].

[SIMO 97] Simon, D. A. 1997. What is "Registration" and Why is it so Important in CAOS?. *Center for Orthopaedic Research, Shadyside Hospital*, Pittsburgh, PA, USA.

[SIMO 98] Simon, D.A. and Lavallée, S. 1998. Medical imaging and registration in computer assisted surgery. *Clinical Orthopaedics and Related Research*, 354. pp. 17-27.

[SPRE 97] Sprenger, B. & Siegwert, R. 1997. *Novel high speed 3 DOF linear direct drive operating with submicron precision.* [Online]. Available: http://www.ifr.mavt.ethz.ch/publications/sprenger97c.pdf. [Accessed 20 may 2000].

[STAN 01] Stanislawki M. et al. 2001. Hard tissue ablation with a free running Er: YAG and a Q-switched CO_2 Laser: a Comparative Study. *Applied Physics B*, 72 (1), pp. 115-120.

[STON 99] Stone, J. A., Stejskal, A. & Howard, L. 1999. *Diode Lasers in Length Metrology Application to Absolute Distance Interferometry*. Cal. Lab., Nov. /Dec. [Online]. Available: http://www.callabmag.com/artstoneja.pdf [Accessed 19 November 2001]

[STON n.d.] Stone, R. J. n.d. *Haptic feedback: A Potted history, from telepresence to virtual reality*. [Online]. Available: http://www.dcs.gla.ac.uk/~stephen/workshops/haptic/papers/stone.pdf. [Accessed 19 November 2001]

[STRO 04] Stronger, D. and Stone, P., 2004. A Model-Based Approach to Robt joint Control. *RoboCup-2004. Robot Soccer World Cup VIII*, pp. 297-309, Lisbon, Portugal.

[STUL 00] Stulberg, D. 2000. Robot-Assisted Hip Surgery. [Online]. Available: http://www.orthopaedics.nwu.edu/orthopaedics/research/robodoc.htm [Accessed 5 April 2001].

[SUGA 00] Sugano, N. and Ochi, T. 2000. *Medical Robotics and Computer-Assisted Surgery in the Surgical Treatment of Patients with Rheumatic Diseases*. Cutting Edge Reports. [Online]. Available: http://www.rheuma21st.com/cutting_index.html. [Accessed 20 August 2001]

[SULZ[1] nd] SULZER*MEDICA*. n.d. *Navitrack Total Knee Application*. [Online]. Available: http://www.sulzerorthoeu.com/asp/article.asp?ArtID=98. [Accessed: 6 September 2001].

[SULZ[2] nd] SULZER*MEDICA*. n.d. *Versatility in Computer Assisted Surgery*. [Online]. Available: http://www.sulzerorthoeu.com/asp/article.asp?ArtID=58. [Accessed: 6 September 2001].

[TAYL 94] Taylor RH, Mittelstadt BD, Paul HA, et al. An image-directed robotic system for precise orthopaedic surgery. *IEEE Trans. Robotics and Automation*, 10. pp. 261-275.

[TAYL 99] Taylor, R., et al. 1999. A steady –hand robotic system for microsurgical augmentation. [Online] The John Hopkins University, USA. Available: http://robotics.me.jhu.edu/~llw/ps/IJRR99_preprint.pdf [Accessed 5 May 2001].

[TALY 03] Taylor, R. H. 2003. Medical Robotics in Computer-Integrated Surgery. *IEEE Transaction on robotics and Automation, 19(5).* pp. 765-781.

[TOWN 99] Townsend, W. T. and Guertin, J. A. 1999. Tutorial: Teleoperator slave-WAM design methodology. *Industrial Robot.* 26(3). pp 167-177

[TRAX 01] Traxtal Technologies. 2001. *Registration 101: An Introduction to the Most Fundamental Technical aspect of CAS.* [Online]. Available: http://www.traxtal.com/registration.htm [Accessed 10 September 2001].

[UNIV[1] nd] Universal Robot Systems (URS).n.d. CASPAR General Information: Precision Work for Joint Surgeries Using Computer-Supported Medical Technology. [Online]. Available: http://www.ortomaquet.com/eseiten/index.htm [Accessed 12 September 2001].

[UNIV² nd] Universal Robot Systems (URS).n.d. The CASPAR Orthopaedics System.[Online]. Available:http://www.ortomaquet.com/eseiten/index.htm [Accessed 11 September 2001].

[VAIC 87] Vaichav, R. and Magrab, E. 1987. A General Procedure to Evaluate Robot Positioning Errors. *The International Journal of Robotics Research*, 6(1). pp. 59-74.

[VERS 00] Versweyveld, L. 2000. CASPAR robot to replace knee joints without effort at Pellenberg Hospital. *Virtual Medical Words*. [Online]. Available: http://www.hoise.com/vmw/00/articles/vmw/LV-VM-10-00-16.html [Accessed 6 September 2001].

[VIAN 00] Viant, W. J. and Barnel, F. 2000. *3D Registration through Pseudo X-ray Image Generation*. Department of Computer Science University of Hull, Hull, UK

[VIAN 95] Viant, W. J. et al. 1995. *A Safe, Accurate and Sterilisable Intelligent Orthopaedic Drill guide*. Proc. of the International Advanced Robotic and Intelligent Machines Workshop, Salford, April 1995.

[VIAN 97] Viant, W. J., et al. 1997. A computer assisted orthopaedic Surgical System for Distal Locking of intramedullary nails. *Proc. Instn. Mech. Engrs*. 211(H). pp. 293-300.

[VIJA nd] Vijay, M. M. and Brierley, W. H.n.d. *Cutting Cleaning And Fragmentation Of Material With High Pressure Liquid Jets.* Gas Dynamic Laboratory, Division of Mechanical Engineering, National Research Council of Canada.[Online]. Available: http://www.wjta.org/Book%201/5_4a_Vijay_&_Brierley.pdf. Accessed [12 January 2003].

[VISA 97] Visarius, H., et al. 1997. Biomedical paper: Man-machine interfaces in computer assisted surgery. *Computer aided surgery*, 2(February). pp.102-107.

[WALD 79] Waldron, K. and Kumar, V. 1979. Development of a Theory of Errors for Manipulators. *Proceedings of the Fifth World Congress on the Theory of Machines and Mechanisms*. pp. 821-82.

[WANG 97] Wang, Y. et al. 1997. Small-bore fluorocarbon polymer-coated silver hollow glass waveguides for Er: YAG laser light. *Optics & Laser Technology*. 29(8). pp. 455-461.

[WANN 96] Wannop N. M. et al. 1996. Ablation Studies of Erbium: YAG Laser Radiation with Pellethane. *J.Phys. D: Appl. Phys*, 29 (1996). Pp 2735-2739.

[WEGN 98] Wegner, K. 1998.Surgical Navigation System and Method Using Audio Feedback. [Online]. Available: http://www.icad.org/websiteV2.0/Conferences/ICAD98/papers/WEGNER.PDF [Accessed 12 June 2002].

[WEST 01] West, J.B. et al. 2001. Fiducial Point Placement and the Accuracy of Point-based, Rigid Body Registration, *Neurosurgery*.Vol. 48 (4). pp. 810-817.

[WHIT 97] Whitcomb, L. et al. 1997. Adaptive Model-Based Hybrid Control of Geometrically Constrained Robot Arms. *IEEE Transaction on Robotics and Automation*, 13(1). pp 105-116.

[WIEB 97] Wiebusch Bruce. 1997. *Laser Gets First-ever FDA Clearance for Hard-tissue Dental Applications*. [Online]. Available: http://www.manufacturingcenter.com/med/archives/1197/11971g.html [Accessed 5 May 2001].

[WILE1 04] Wiles, A., Thompson, D. and Frantz, D. 2004. *Accuracy assessment and interpretation for optical tracking systems*. [Online]. Available: http://www.ndigital.com/products/polaris/documents/SPIE_5367-47.pdf. [Accessed 14 July 2004].

[WILE2 04] Wiles, A., Vanderkooy, G. and Frantz, D. 2004. In Field Accuracy Assessment for Optical Position Sensors. [Online]. Available: http://www.ndigital.com/products/polaris/documents/In-FieldAccuracyAssessmentforOptialPositonSensors.pdf. [Accessed 14 July 2004].

[WILK 99] Wilkens, V. et al. 1999. Fibre-Optic dielectric multilayer temperataure sensor: in situ measurement in vitreous during Er: YAG laser irradiation. *Optics & Laser Technology*, 31.pp.593-599.

[WOLF 04] A. Wolf, B. Jaramaz, A. Mor, and A.M. Di Gioia, III, MD. 2004. Computer-Guided Total Knee Arthroplasty. *Manual of MIS Techniques in Orthopedics*, Springer-Verlag, 2004.

[WONG 00] Wong B. J. F. et al. 2000. *Measurement of Acoustic Transients During Pulsed Holmium: YAG laser Ablation of Cadaveric Human temporal Bone*. Laser Med Sci, 15. pp 2 – 5. [Online]. Available: http://link.springer.de/link/service/journals/1010/papers/0015001/00150002.pdf [Accessed 1 August 2002].

[WU 99] Wu, P. et al. 1999. A model-based fuzzy ultrasound signal processing system for determining coagulation front in laser irradiated tissues. *International Journal of Fuzzy Systems.* 1(2). pp 120-128.

[YANI 00] Yaniv, Z., Sandowsky, O. and Joskowicz, L. 2000. In-vitro Accuracy study of contact and image-based registration: Materials, Methods and Experimental Results. [Online]. Available: http://www.cs.huji.ac.il/~josko/abst/cars2000-reg.html [Accessed 10 September 2001].

[YOON 02] Yoon G. et al. 2002. A Compact 1.06/1.32/2.94 μm pulsed laser for dentistry. *Optical & Laser Technology*, 34. pp.213-217.

[YUSH 04] Kaneda Y. et al. 2004. Single-frequency, all-fiber Q-switched laser at 1550-nm. [Online]. Available: http://www.npphotonics.com/files/article/Kaneda_ASSP2004_PD5.pdf. [Accessed 13 Jan 2005].

[ZHIG 97] Zhigilei, L.V. & Garrison, B. J.1997. Velocity distributions of molecules ejected in laser ablation. Appl. Phys. Left., 71(4). pp 551-553.

[ZHIG 99] Zhigilei, L.V. & Garrison, B. J.1999. Mechanisms of laser ablation from molecular dynamics simulations: dependence on the initial temperature and pulse duration. *Applied Physics A*. 69 [Suppl.]. s75-s80.

Appendix A

Laser Feedback Techniques

Acoustic Feedback for Laser Tissue Interaction

Ahwal, F. & Phillips, R.
Department of Computer Science
University of Hull

ABSTRACT

Research on laser tissue interaction showed that as laser pulses strike biological tissue they produce a loud Photo-acoustic effect [KIRK 00] [HARR 00]. This photo-acoustic effect is due to the laser-induced pressure on tissue and the rapid expansion of water molecules resulting in steam (ejected molecules), localised water-microexplosions and tissue ablation [IVAN 02]. The magnitude, duration and response time of the photo-acoustic effect, depend on the laser energy density, pulse duration and ablation depth. Other factors effect the photo-acoustic response time include the speed of sound, the magnitude of laser-induced pressure, the velocity of ejected molecules during laser ablation, and the biological tissue type.

The aim of our research is to develop a feedback mechanism for laser ablation depth and the depth of laser front inside tissue based on the photo-acoustic response time. Our poster session presents two-feedback techniques developed for laser front detection and laser ablation depth. These techniques are the acoustic time of flight (ATOF) and the acoustic phase-shift measurements.

The ATOF technique measures the elapse time between the start of laser ablation pulse and the arrival of the photo-acoustic wave. This technique requires the detection of the reflected laser beam and the photo-acoustic wave during ablation. Measurements are in real time and give the position of the laser front inside tissue relative to a fixed reference (photo-acoustic sensor position). The accuracy of the measurement, however, is highly affected by the speed of sound (temperature and humidity dependent), and the response time of the acoustic sensor. To compensate for the acoustic sensor response time, a multi threshold measurement levels are considered to give an average ATOF measurement.

The acoustic phase-shift measurement technique, on the other hand, is time independent and can measure the laser ablation depth per pulse with a maximum depth of one acoustic cycle (frequency dependent). However, given the number of laser pulses and the average ablation depth per pulse one can calculate the position of the laser front inside tissue regardless of the depth. This technique uses the sampling frequency and the number of sample points to calculate the phase shift measurements with high accuracy.

The above techniques were tested on real data during CO_2 laser bone drilling. And the experimental results showed that the ablation depth is linearly related to the photo-acoustic phase shift and time of flight. They also showed that the phase shift technique is immune to amplitude noise and can be applied in real time to measure the phase with high accuracy. For real time acoustic feedback measurement, however, a highly controlled environment is recommended for accurate speed of sound evaluation.

References

[IVAN 02] Ivanenko, M. M. et al. 2002. Bone Tissue Ablation with sub-µs Pulses of a Q-switched CO_2 Laser: Histological Examination of Thermal Side Effects. *Laser Med. Sci.*, *17*. pp 258-264

[KIRK 00] Kirkpatrick, J. J. R. and Mackay, I. R. 2000. SHORT REPORT Sound Levels Produced by Erbium YAG Lasers: Health and Safety Issue. *Laser Med. Sci.* 15. pp 263-265

[HARR 00] Harris, D. M. and Fried, D. 2000. Pulsed Nd: YAG laser selective ablation of surface enamel caries: I. Photoacoustic response and FTIR spectroscopy. *SPIE BIO.*, S2000. MS# 3910-25

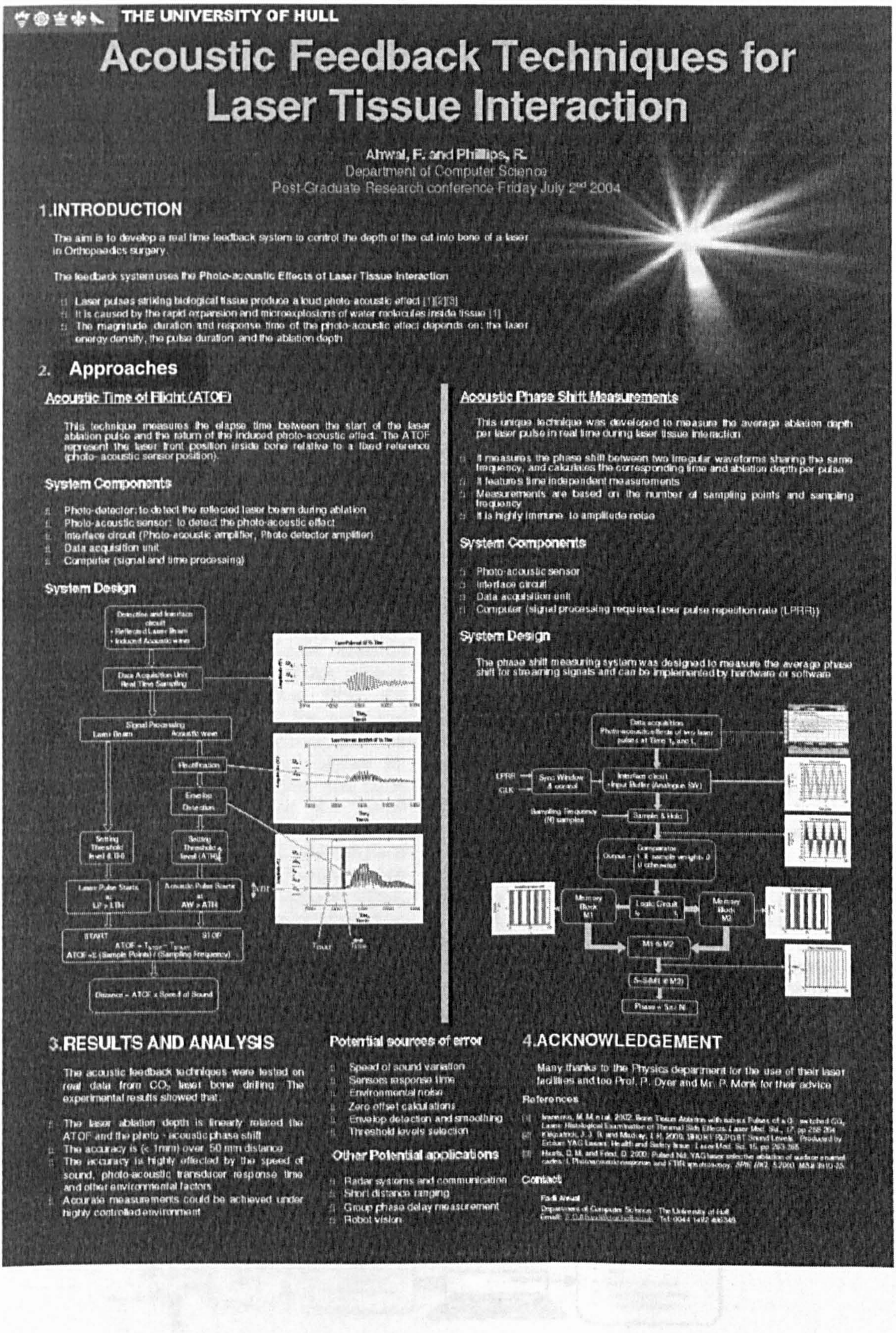
THE UNIVERSITY OF HULL
Acoustic Feedback Techniques for Laser Tissue Interaction
Ahwal, F. and Phillips, R.
Department of Computer Science
Post-Graduate Research conference Friday July 2nd 2004
1.INTRODUCTION
The aim is to develop a real time feedback system to control the depth of the cut into bone of a laser in Orthopaedics surgery.
The feedback system uses the Photo-acoustic Effects of Laser Tissue Interaction
Laser pulses striking biological tissue produce a loud photo-acoustic effect [1][2][3]
It is caused by the rapid expansion and microexplosions of water molecules inside tissue [1]
The magnitude duration and response time of the photo-acoustic affect depends on: the laser energy density, the pulse duration and the ablation depth
2. Approaches
Acoustic Time of Flight (ATOF)
This technique measures the elapse time between the start of the laser ablation pulse and the return of the induced photo-acoustic effect. The ATOF represent the laser front position inside bone relative to a fixed reference (photo- acoustic sensor position).
System Components
Photo-detector: to detect the reflected laser beam during ablation
Photo-acoustic sensor: to detect the photo-acoustic effect
Interface circuit (Photo-acoustic amplifier, Photo detector amplifier)
Data acquisition unit
Computer (signal and time processing)
System Design
Data Acquisition Unit Real Time Sampling
Signal Processing
Laser Beam
Acoustic wave
Rectification
START
STOP
ATOF = Σ (Sample Points) / (Sampling Frequency)
Distance = ATOF x Speed of Sound
Acoustic Phase Shift Measurements
This unique technique was developed to measure the average ablation depth per laser pulse in real time during laser tissue interaction.
It measures the phase shift between two irregular waveforms sharing the same frequency, and calculates the corresponding time and ablation depth per pulse
It features time independent measurements
Measurements are based on the number of sampling points and sampling frequency
It is highly immune to amplitude noise
System Components
Photo-acoustic sensor
Interface circuit
Data acquisition unit
Computer (signal processing requires laser pulse repetition rate (LPRR))
System Design
The phase shift measuring system was designed to measure the average phase shift for streaming signals and can be implemented by hardware or software
LPRR
CLK
Sync Window
Sample & Hold
M1 & M2
3.RESULTS AND ANALYSIS
The acoustic feedback techniques were tested on real data from CO2 laser bone drilling. The experimental results showed that:
The laser ablation depth is linearly related the ATOF and the photo - acoustic phase shift
The accuracy is (< 1mm) over 50 mm distance
The accuracy is highly effected by the speed of sound, photo-acoustic transducer response time and other environmental factors
Accurate measurements could be achieved under highly controlled environment
Potential sources of error
Speed of sound variation
Sensors response time
Environmental noise
Zero offset calculations
Envelop detection and smoothing
Threshold levels selection
Other Potential applications
Radar systems and communication
Short distance ranging
Group phase delay measurement
Robot vision
4.ACKNOWLEDGEMENT
Many thanks to the Physics department for the use of their laser facilities and too Prof. P. Dyer and Mr. P. Monk for their advice
References
Contact

Photo-Acoustic Feedback Techniques for Laser Tissue Interaction

Ahwal F. and Phillips R, Department of Computer Science

Introduction

The design and development of a computer assisted laser delivery system for orthopaedic surgery (laser End-Effector) necessitate the presence of an adequate feedback system. This system must consider all mechanical movements and positions. It must also consider the positions of patient anatomy, the laser End-Effector and other monitoring devices relative to each other and to a fixed reference point. Most importantly this feedback system must resolve the laser-front position inside tissue during laser tissue interaction and give accurate measurements for the laser ablation depth and ablation rate in real time.

Although, there are various laser feedback systems, very few are available for medical applications. This paper presents innovative laser feedback techniques to measure the ablation depth and ablation rate during laser tissue interaction. The aim of these techniques is to develop a real time feedback system to control the depth of the laser cut into bone in computer assisted orthopaedic surgery. This feedback system must give sufficient information about the overall surgical performance for both the computer based control system and the surgical team. This information allows for automatic manipulation control of the laser delivery system as well as the on/off switching of the laser system.

Research on laser tissue interaction showed that laser pulses striking biological tissue produce loud photo-acoustic effects [1][2][3]. These photo-acoustic effects are caused by the rapid expansion of water molecules and localised micro-explosions inside the tissue [2] [4] [5]. The photo-acoustic effects are depth related [3] and therefore they can be utilised for depth measurements and localisation of the laser front position inside tissue. The magnitude and duration of the photo-acoustic waves are directly proportional to the laser energy density, laser pulse duration and depth inside tissue. However, the photo-acoustic response time is affected by other factors such as the speed of sound (temperature and humidity dependent), the level of laser induced pressure, velocity of ejected molecules during laser ablation [5], and tissue type (in terms of water contents).

The photo-acoustic effect and response time during laser tissue interaction are the bases of the innovative laser feedback techniques presented in this paper. An advantage of these techniques is that they are applicable in many disciplines besides medicine.

Method

The method used is described in Figure 1 where a photo-detector and acoustic sensor are used to detect the reflected laser beam and the induced acoustic respectively. The acquired signals are then processed to calculate acoustic time of flight (ATOF) and phase shift (APS) which can reveal the laser-front position, ablation rate and ablation depth. The approaches used by the feedback system to measure acoustic time of flight (ATOF) and acoustic phase shift (APS) are as follows:

1. The Acoustic Time of Flight

This technique measures the elapsed time between the start of the reflected laser beam and the induced photo-acoustic waves.

This elapsed time is directly related to the laser front position inside tissue relative to a fixed reference (photo-acoustic sensors position).

Figure 2 presents a block diagram of ATOF starting from data acquisition and signal conditioning then time evaluation. The signal processing and conditioning involves: null offsetting of the acquired signals (i.e. signals must be centred about zero dc line), photo-acoustic wave rectification and envelope detection. The next step is to compare the two signals with a preset threshold to determine the start points of each signal with no noise effect. From this the time difference represents the ATOF. This ATOF is then be used to calculate the ablation depth.

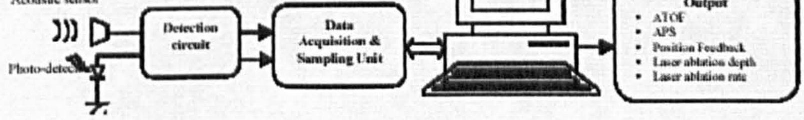

Figure 1: A block diagram of the feedback methodology

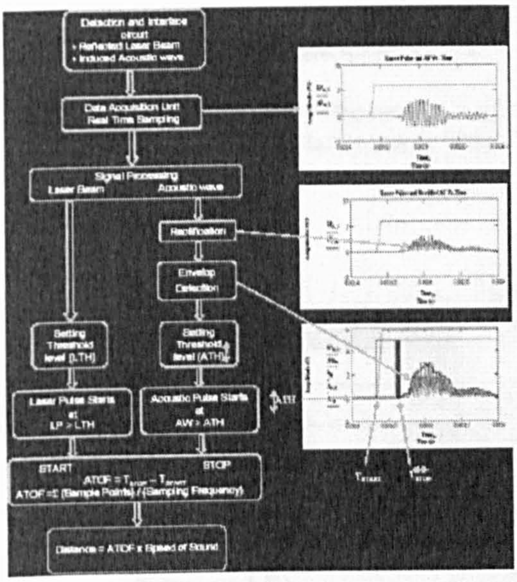

Figure 2: ATOF measurement approach

2. The Acoustic Phase Shift

This innovative technique was developed to measure ablation depth per laser pulse in real time during laser tissue interaction. It measures the phase shift between two or more photo-acoustic waves sharing similar characteristics in terms of frequency and waveform. The measurement technique involves: data acquisition and sampling, zero comparison and normalising, real time data storage and logic manipulation to calculate the phase shift between the acquired photo-acoustic waves. The phase shift will then be used to calculate the ablation rate and ablation depth per pulse. This technique features time independent measurements and high immunity to amplitude noise.

Results and Discussion

Experimental results on photo-acoustic feedback of CO_2 laser bone ablation showed a linear correlation between the laser front position on the tissue surface and the acoustic time of flight (ATOF). In these experiments the feedback system showed that measurements were accurate to within 1mm over a 50 mm distance. The accuracy of the measurements, however, was highly affected by the speed of sound which may vary during the experiment. It can also depend on the photo-acoustic transducer response time and other environmental factors such as humidity and temperature. Thus, higher accuracies may be achieved with accuracy detection devices and highly controlled environment. The phase shift measurement technique, on the other hand, showed high immunity to amplitude noise and high measurement accuracy with 0% error on well defied waveforms. It also showed high measurement accuracy with real time photo-acoustic data.

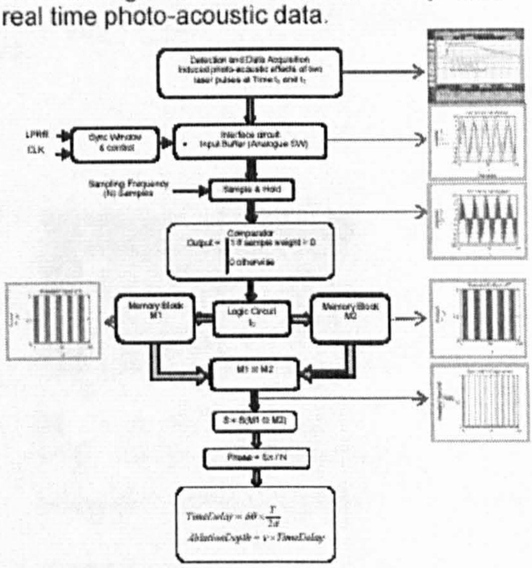

Figure 3: APS measurement approach

Conclusion

The feedback techniques presented are highly effective in computer assisted laser surgery. They proved to provide real time feedback information on the position of the laser front inside tissue with relatively high accuracy under controlled environment. Although these techniques were specifically developed, they can have high potential application in short distance ranging, acoustics, radar communication, robot vision and group phase delay measurements.

References

[1] Kirkpatrick, J. J. R. and Mackay, I. R. 2000. SHORT REPORT Sound Levels Produced by Erbium YAG Lasers: Health and Safety Issue. *Laser Med. Sci.* 15. pp 263-265.

[2] Ivanenko MM et al, 2002. Bone Tissue Ablation with sub-µs Pulses of a Q-switched CO_2 Laser: Histological Examination of Thermal Side Effects. *Laser Med. Sci., 17.* pp 258-264.

[3] Harris, D. M. and Fried, D. 2000. Pulsed Nd: YAG laser selective ablation of surface enamel caries: I. Photoacoustic response and FTIR spectroscopy. *SPIE BIO.*, S2000. MS# 3910-25

[4] Kodali, P. B. S., Zhigilei, L. V. & Garrison, B. J. 1999. Phase transition at low fluences in laser desorption of organic solids: a mol%cular dynamics study. *Nuclear Instruments and Methods in Physics Research B*, 153(1999). pp 167-171.

[5] Zhigilei, L.V. & Garrison, B. J.1997. Velocity distributions of molecules ejected in laser ablation. *Appl. Phys. Left.*, 71(4). pp 551-553.

Example 1 :Time of Flight Calculations

This Example demonstrate the time of flight calculation technique on real data acquired during CO_2 laser bone ablation using MAthCAD.

Acquired Data

$\mathbf{n} := 700..1200$

$\mathbf{LP} :=$

	0	1
0	-0.04168	-1.69
1	-0.04167	-1.7
2	-0.04167	-1.71

$\mathbf{AFB} :=$

	0	1
0	-0.04168	-0.03
1	-0.04167	-0.02
2	-0.04167	0

$$\mathbf{LPI}_{\mathbf{n},0} := \mathbf{LP}_{\mathbf{n},0} - \mathbf{LP}_{0,0}$$

$$\mathbf{Time}_{\mathbf{n}} := \mathbf{LPI}_{\mathbf{n},0}$$

LP is the Laser Pulse
AFB is the acoustic Feedback
column (0) represent the time

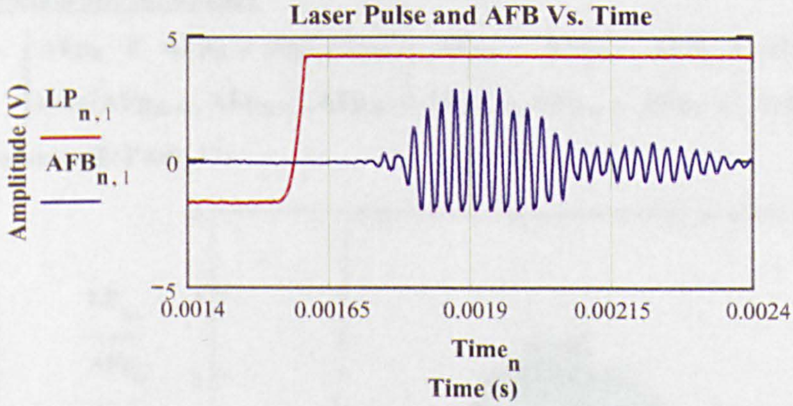

Data Analysis Processing

DC Offset Null and Setting a Zero Base Line

Removing the DC offset from Laser Pulse (LP) and the Acoustic Feedback (AFB)

$$\mathbf{AFbase} := \mathbf{mean}\left(\mathbf{AFB}_{600,1}, \mathbf{AFB}_{550,1}, \mathbf{AFB}_{500,1}, \mathbf{AFB}_{450,1}, \mathbf{AFB}_{400,1}, \mathbf{AFB}_{350,1}\right)$$

$$\mathbf{AF}_{\mathbf{n},1} := \mathbf{AFB}_{\mathbf{n},1} - \mathbf{AFbase}$$

$$\mathbf{LPbase} := \mathbf{mean}\left(\mathbf{LP}_{600,1}, \mathbf{LP}_{550,1}, \mathbf{LP}_{500,1}, \mathbf{LP}_{450,1}, \mathbf{LP}_{400,1}, \mathbf{LP}_{350,1}\right)$$

$$\mathbf{LP}_{\mathbf{n},1} := \mathbf{LP}_{\mathbf{n},1} - \mathbf{LPbase}$$

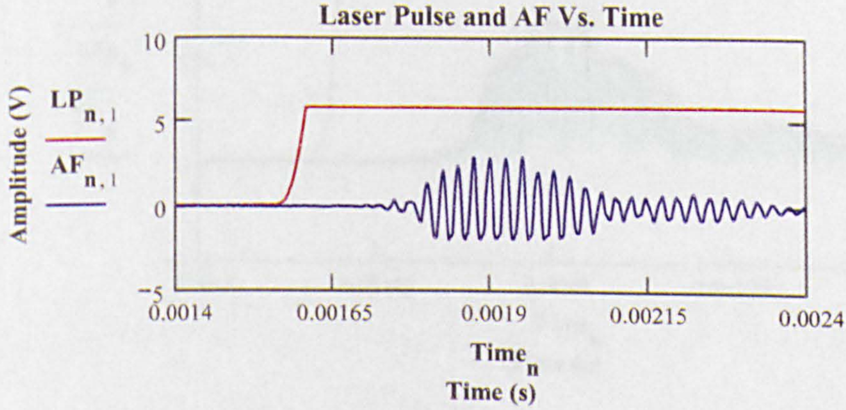

Rectifying the Acoustic Signal

Inverting the negative side of the acoustic signal

$$AFp_n := \left|AF_{n,1}\right|$$

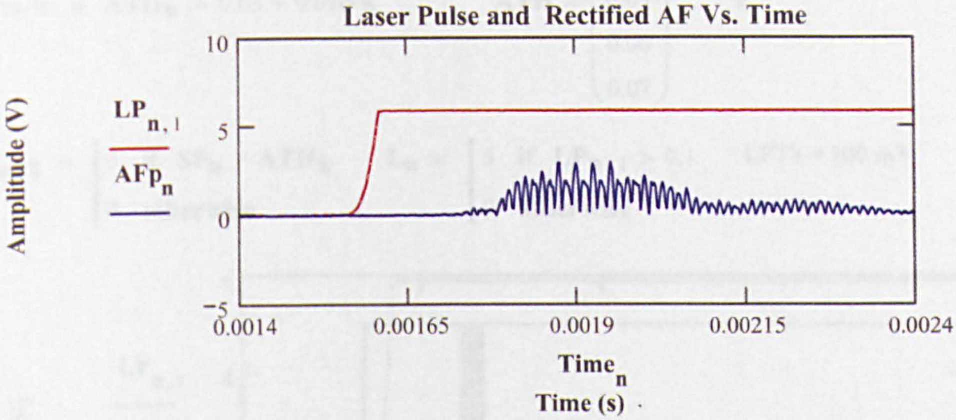

Peak Detection and Smoothing

$$Peak_n := \begin{cases} AFp_n & \text{if } AFp_n > \max(AFp_{n-1}, AFp_{n-2}, AFp_{n-3}, AFp_{n-4}, AFp_{n-5}, AFp_{n-6}) \\ \max(AFp_{n-1}, AFp_{n-2}, AFp_{n-3}, AFp_{n-4}, AFp_{n-5}, AFp_{n-6}) & \text{otherwise} \end{cases}$$

$$SP := \text{medsmooth}(Peak, 37)$$

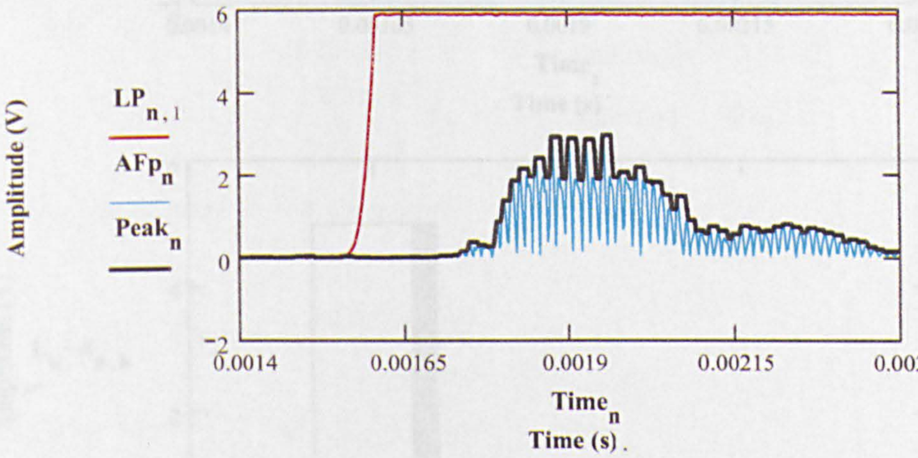

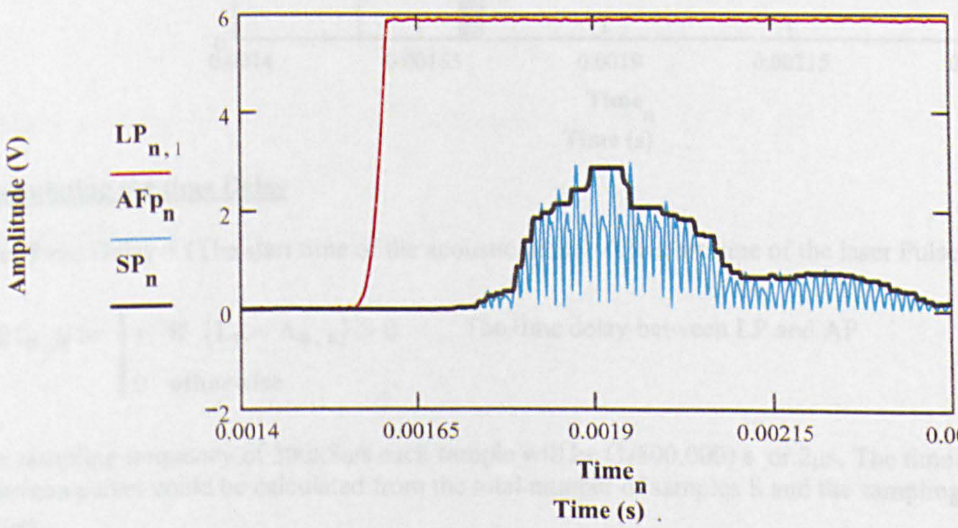

Normalising the Acoustic Feedback according to a threshold level

$$k := 0..4 \quad ATH_k := 0.03 + 0.010 \cdot k \qquad ATH = \begin{pmatrix} 0.03 \\ 0.04 \\ 0.05 \\ 0.06 \\ 0.07 \end{pmatrix} \ V$$

$$A_{n,k} := \begin{vmatrix} 5 \ \text{if} \ SP_n > ATH_k \\ 0 \ \text{otherwise} \end{vmatrix} \qquad L_n := \begin{vmatrix} 5 \ \text{if} \ LP_{n,1} > 0.1 \\ 0 \ \text{otherwise} \end{vmatrix} \qquad LPTh = 100 \ mV$$

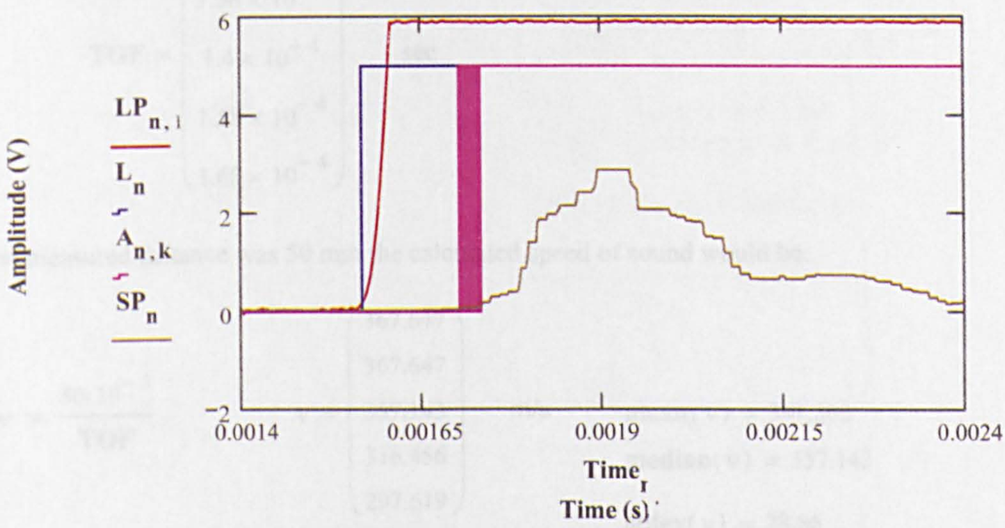

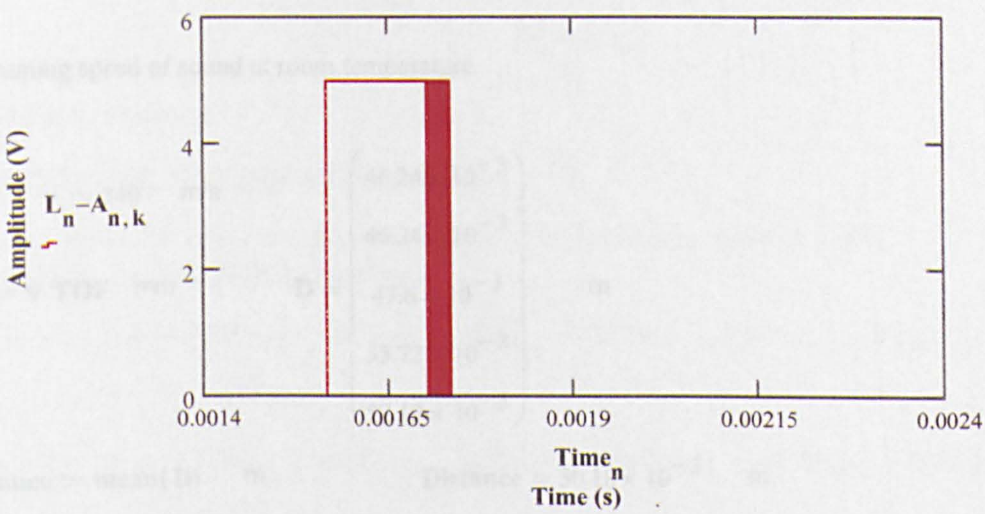

Calculating the time Delay

The Time Delay = (The start time of the acoustic pulse) -(the start time of the laser Pulse)

$$\theta 1_{n,k} := \begin{vmatrix} 1 \ \text{if} \ \left(L_n - A_{n,k}\right) > 0 \\ 0 \ \text{otherwise} \end{vmatrix} \qquad \text{The time delay between LP and AP}$$

for sampling frequency of 500kSa/s each sample will be (1/500,000) s or 2μs. The time delay between pulses could be calculated from the total number of samples S and the sampling time (2μs).

$$\mathbf{SR} := 500\cdot 10^3 \qquad \lambda := \frac{1}{\mathbf{SR}} \qquad \mathbf{TOF} := \mathbf{S}\cdot\lambda$$

$$\mathbf{S_k} := \sum_{\mathbf{n}} \theta\mathbf{1}_{\mathbf{n},\mathbf{k}} \qquad \mathbf{S} = \begin{pmatrix} 68 \\ 68 \\ 70 \\ 79 \\ 84 \end{pmatrix} \qquad \mathbf{TOF} := \mathbf{S}\cdot\lambda$$

$$\mathbf{TOF} = \begin{pmatrix} 1.36\times 10^{-4} \\ 1.36\times 10^{-4} \\ 1.4\times 10^{-4} \\ 1.58\times 10^{-4} \\ 1.68\times 10^{-4} \end{pmatrix} \quad \mathbf{sec}$$

The measured distance was 50 mm the calculated speed of sound would be:

$$\mathbf{v} := \frac{50\cdot 10^{-3}}{\mathbf{TOF}} \qquad \mathbf{v} = \begin{pmatrix} 367.647 \\ 367.647 \\ 357.143 \\ 316.456 \\ 297.619 \end{pmatrix} \ \mathrm{m/s}$$

$$\mathbf{mean(v)} = 341.302$$

$$\mathbf{median(v)} = 357.143$$

$$\mathbf{stdev(v)} = 28.86$$

Assuming speed of sound at room temperature

For $\mathbf{v} := 340$ m/s

$$\mathbf{D} := \mathbf{v}\cdot\mathbf{TOF} \ \mathrm{mm} \qquad \mathbf{D} = \begin{pmatrix} 46.24\times 10^{-3} \\ 46.24\times 10^{-3} \\ 47.6\times 10^{-3} \\ 53.72\times 10^{-3} \\ 57.12\times 10^{-3} \end{pmatrix} \ \mathrm{m}$$

$$\mathbf{Distance} := \mathbf{mean(D)} \ \mathrm{m} \qquad \mathbf{Distance} = 50.18\times 10^{-3} \ \mathrm{m}$$

$$\mathbf{median(D)} = 47.6\times 10^{-3} \ \mathrm{m}$$

$$\sigma := \mathbf{stdev(D)} \qquad \sigma = 4.436\times 10^{-3} \ \mathrm{m}$$

Example 2: Photo-Acoustic Phase Shift Calculations

This example demonstrates the Photo-Acoustic feedback Phase Shift (APS) during CO_2 laser bone ablation

Acquired Data

$\mathbf{n} := 100 .. 9000$

$\mathbf{LP} :=$

	0	1
0	-0.05154	-1.78
1	-0.05154	-1.77
2	-0.05153	-1.76

$\mathbf{AFB} :=$

	0	1
0	-0.05154	0
1	-0.05154	0
2	-0.05153	-0.01

$$\mathbf{LPI_{n,0}} := \mathbf{LP_{n,0}} - \mathbf{LP_{0,0}}$$

LP is the Laser Pulse
AFB is the acoustic Feedback

$$\mathbf{Time_n} := \mathbf{LPI_{n,0}}$$

column (0) represent the time

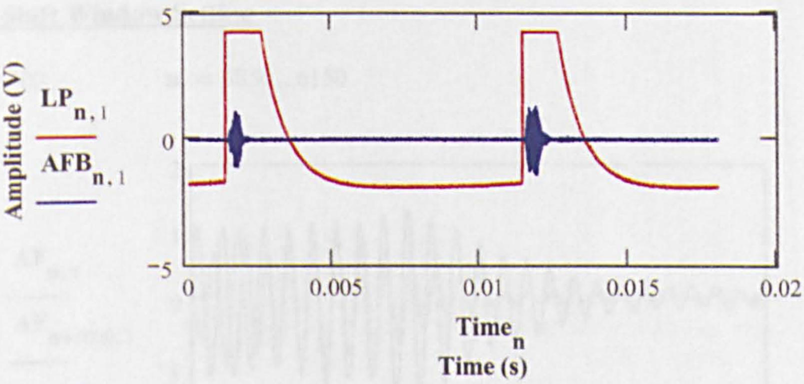

Signal Processing

DC Offset Null and Setting a Zero Base Line

Removing the DC offset from Laser Pulse (LP) and the Acoustic Feedback (AFB)

Setting the Acoustic base line position

$$\mathbf{AFbase1} := \mathbf{mean}\left(\mathbf{AFB_{500,1}}, \mathbf{AFB_{450,1}}, \mathbf{AFB_{400,1}}, \mathbf{AFB_{350,1}}, \mathbf{AFB_{300,1}}, \mathbf{AFB_{250,1}}\right)$$

$$\mathbf{AF_{n,1}} := \mathbf{AFB_{n,1}} - \mathbf{AFbase1}$$

$$\mathbf{AFbase2} := \mathbf{mean}\left(\mathbf{AFB_{5500,1}}, \mathbf{AFB_{5450,1}}, \mathbf{AFB_{5400,1}}, \mathbf{AFB_{5350,1}}, \mathbf{AFB_{5300,1}}, \mathbf{AFB_{5250,1}}\right)$$

$$\mathbf{AF_{n+5000,1}} := \mathbf{AFB_{n,1}} - \mathbf{AFbase2}$$

Setting the Laser Pulse base line position

$$\mathbf{LPbase1} := \mathbf{mean}\left(\mathbf{LP_{500,1}}, \mathbf{LP_{450,1}}, \mathbf{LP_{400,1}}, \mathbf{LP_{350,1}}, \mathbf{LP_{300,1}}, \mathbf{LP_{250,1}}\right)$$

$$\mathbf{LP_{n,1}} := \mathbf{LP_{n,1}} - \mathbf{LPbase1}$$

$$\mathbf{LPbase2} := \mathbf{mean}\left(\mathbf{LP_{5500,1}}, \mathbf{LP_{5450,1}}, \mathbf{LP_{5400,1}}, \mathbf{LP_{5350,1}}, \mathbf{LP_{5300,1}}, \mathbf{LP_{5250,1}}\right)$$

$$\mathbf{LP_{n+5000,1}} := \mathbf{LP_{n,1}} - \mathbf{LPbase2}$$

Laser Pulse Synchronisation

$\mathbf{n} := 5600 .. 6200$

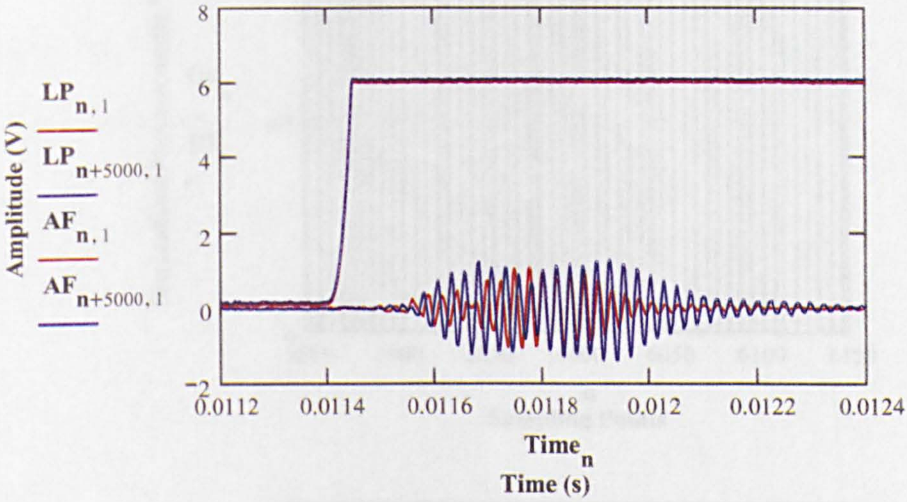

Phase Shift Window Setting

$\mathbf{w} := 200$ $\mathbf{n} := 5850 .. 6150$

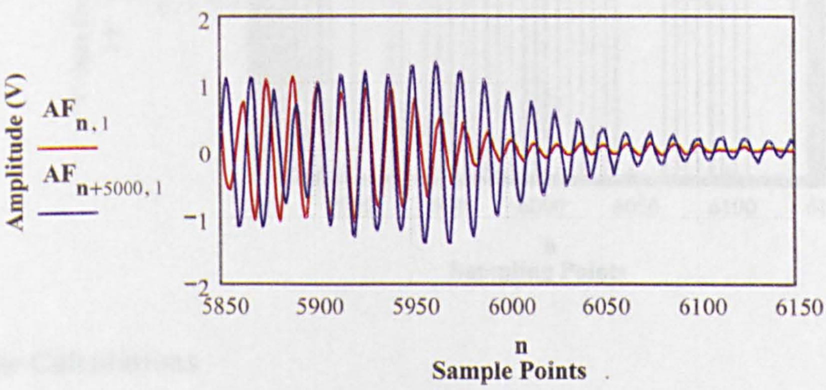

$$\mathbf{U0_n} := \begin{cases} 1 & \textbf{if } \mathbf{AF_{n,1}} > 0 \\ 0 & \textbf{otherwise} \end{cases} \qquad \mathbf{U1_n} := \begin{cases} 1 & \textbf{if } \mathbf{AF_{n+5000,1}} > 0 \\ 0 & \textbf{otherwise} \end{cases}$$

$$\mathbf{POP_n} := \left|\mathbf{U0_n} - \mathbf{U1_n}\right| \qquad \mathbf{POP_n} := \begin{cases} 1 & \textbf{if } \left|\mathbf{U0_n} - \mathbf{U1_n}\right| > 0 \\ 0 & \textbf{otherwise} \end{cases}$$

where

U0 and U1:	are the normalised values of all points above 0 level in both signals
POP:	is the difference between the normalised points relative to real time
SReal:	is the total number points representing the phase shift
PHASE:	is the phase shift in radians
PHASE_deg:	is the phase shift in degrees

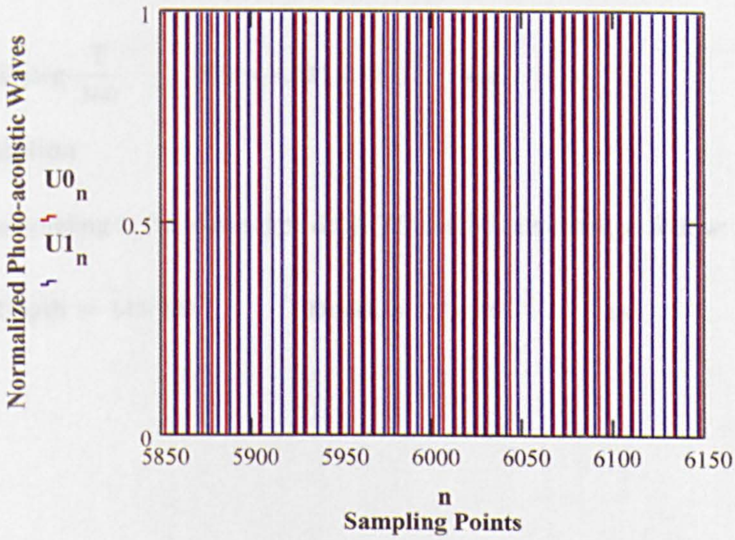

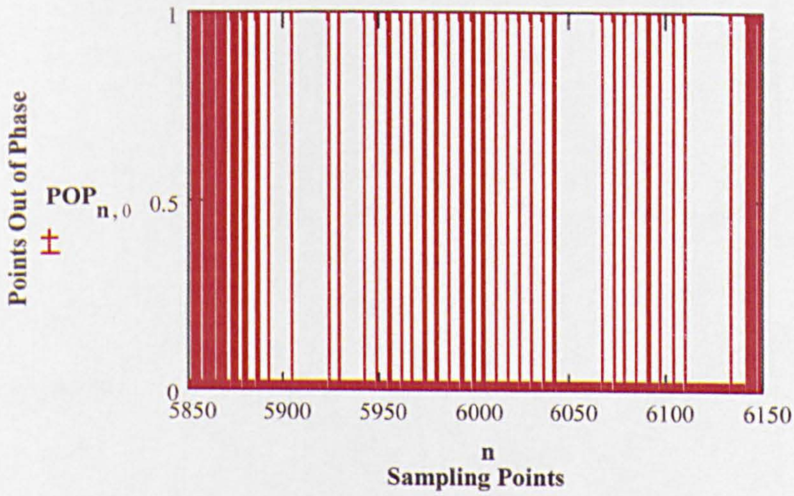

Phase Calculations

$$\mathbf{SReal} := \sum_{n} \mathbf{POP}_{n,0} \qquad \mathbf{SReal} = 71$$

The calculated value of the phase would be

$$\mathbf{PHASE} := \frac{\mathbf{SReal}\pi}{\mathbf{w}} \qquad \mathbf{PHASE} = 1.115 \quad \mathbf{rad}$$

In degrees

$$\mathbf{PHASE\_deg} := \mathbf{SReal} \cdot \frac{180}{\mathbf{w}} \qquad \mathbf{PHASE\_deg} = 63.9 \quad \mathbf{Deg.}$$

Time Delay Calculations

The time delay can be calculated as follow

given the frequency of the data = 36.03 kHz and T = 27.76 ms

$$T := 27.76 \cdot 10^{-6} \quad \mathbf{sec}$$

$$TD := PHASE\_deg \cdot \frac{T}{360} \qquad TD = 4.927 \times 10^{-6} \quad \mathbf{sec}$$

Depth Calculation

The depth corresponding to the above time delay TD can be calculated as follow:

$$Depth := 345 \cdot TD \qquad Depth = 1.7 \times 10^{-3} \quad \mathbf{m}$$

Example 3: Magnitude effects on Phase Shift Measurement

This example gives an illustration of Phase Shift measurement between two out of phase signals (x and y) having the same frequency yet different magnitudes

$i := 0..100 \quad \theta_i := i \cdot \frac{\pi}{10} \qquad \Delta\theta := \frac{\pi}{5} \qquad \Delta\theta = 0.628 \qquad \Delta\theta\_Deg := \Delta\theta \cdot \frac{180}{\pi} \qquad \Delta\theta\_Deg = 36 \quad \mathbf{Deg}$

$x_i := 10\sin(\theta_i)$

$y_i := 3\sin(\theta_i - \Delta\theta)$

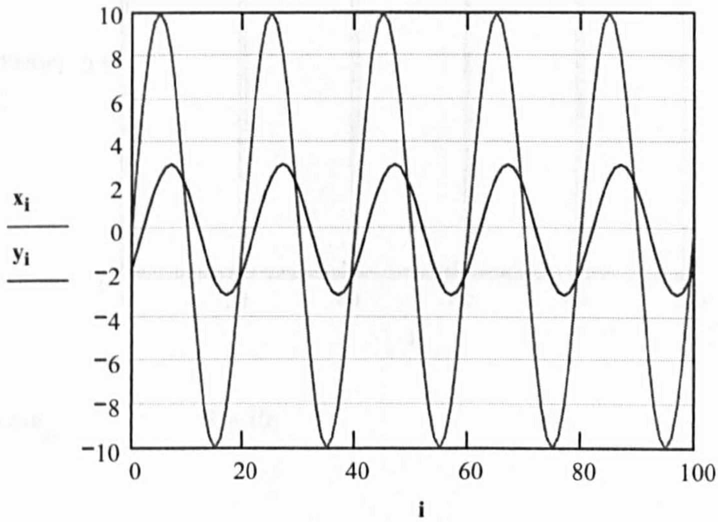

Waves Normalising

$X_i := \begin{cases} 1 & \text{if } x_i > 0 \\ 0 & \text{otherwise} \end{cases} \qquad Y_i := \begin{cases} 1 & \text{if } y_i > 0 \\ 0 & \text{otherwise} \end{cases}$

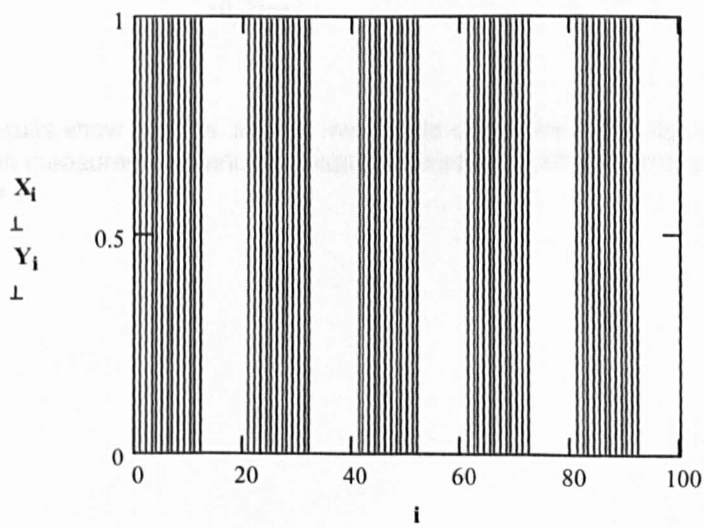

Samples out of Phase

$$\mathbf{Phase_i} := \begin{cases} 1 & \text{if } \mathbf{X_i - Y_i > 0} \\ 0 & \text{otherwise} \end{cases}$$

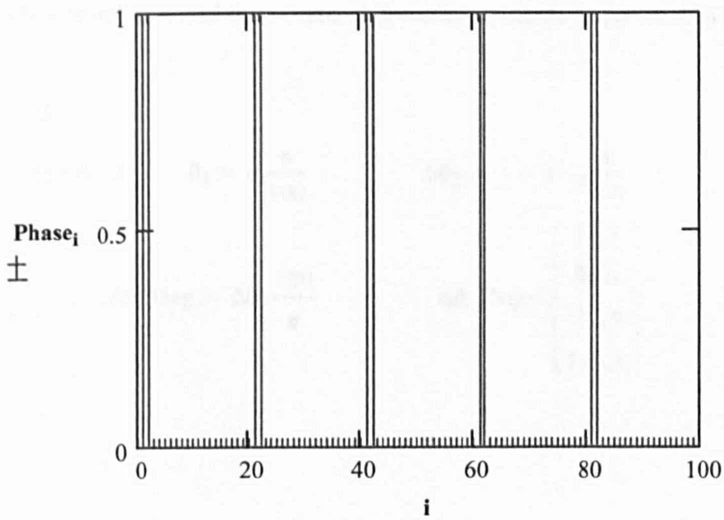

$$\mathbf{S} := \sum_{\mathbf{i}} \mathbf{Phase_i} \qquad \mathbf{S = 10}$$

Phase Calculation

$$\mathbf{PHASE} := \frac{\mathbf{S \cdot 2\pi}}{\mathbf{100}} \qquad \mathbf{PHASE = 0.628}$$

$$\mathbf{PHASE\_Deg := PHASE \cdot \frac{180}{\pi}} \qquad \mathbf{PHASE\_Deg = 36} \quad \mathbf{Deg}$$

$$\mathbf{\%PSError} := \frac{\mathbf{(PHASE\_Deg - \Delta\theta\_Deg) \cdot 100\%}}{\mathbf{\Delta\theta\_Deg}} \qquad \mathbf{\%PSError = 0}$$

Conclusion

The above results show that the signals magnitude difference in the signals has no effect on the phase shift measurements and technique showed zero percent error in the Phase shift measurement.

Example 4: Group Phase Shift Measurements (GPSM)

This example gives an illustration of using the phase shift measurement technique for group phase measurements. The example shows four waves having similar frequencies and wave form yet they have different magnitudes and phase. The example shows phase measurements for the y waves with respect to x and the phase shift measurements between the individual y signals

Assume the following

$i := 0..999$ $\quad j := 0..3$ $\quad \theta_i := i\cdot\frac{\pi}{100}$ $\quad \Delta\theta_j := 1 + j - j\frac{\pi}{10}$

$$\Delta\theta = \begin{pmatrix} 1 \\ 1.69 \\ 2.37 \\ 3.06 \end{pmatrix} \qquad \Delta\theta\_Deg := \Delta\theta\cdot\frac{180}{\pi} \qquad \Delta\theta\_Deg = \begin{pmatrix} 57.3 \\ 96.6 \\ 135.9 \\ 175.2 \end{pmatrix}$$

$x_i := 10\sin(\theta_i)$

$y_{i,j} := 6\cdot(j + 0.5)\sin(\theta_i - \Delta\theta_j)$

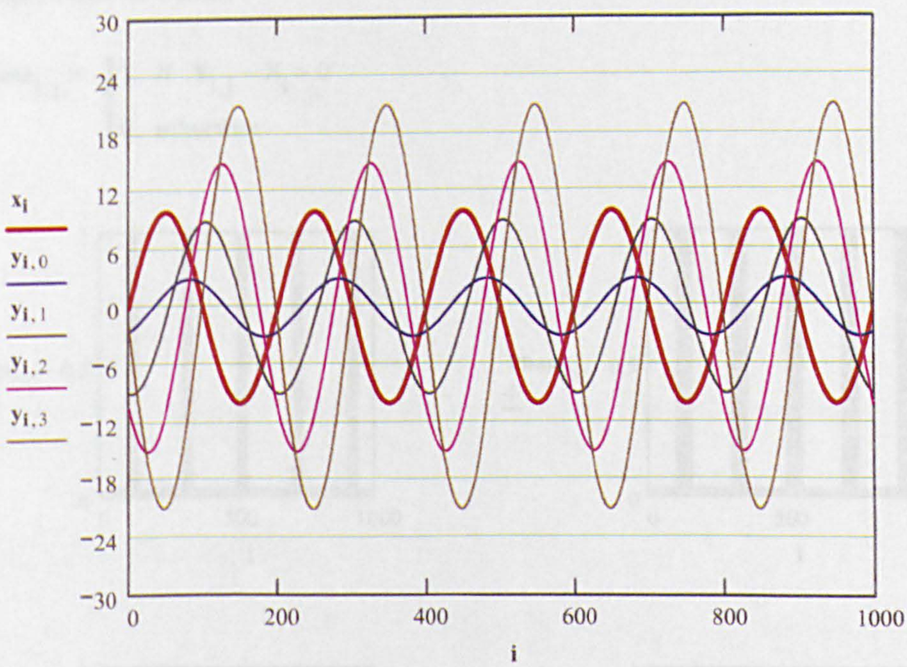

Waves Normalising

$$X_i := \begin{cases} 1 & \text{if } x_i > 0 \\ 0 & \text{otherwise} \end{cases} \qquad Y_{i,j} := \begin{cases} 1 & \text{if } y_{i,j} > 0 \\ 0 & \text{otherwise} \end{cases}$$

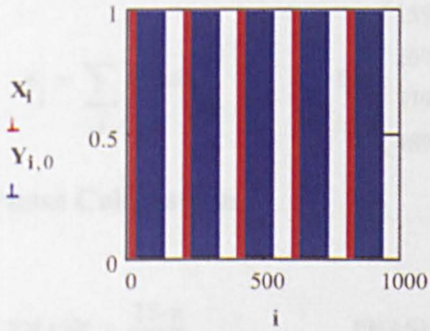

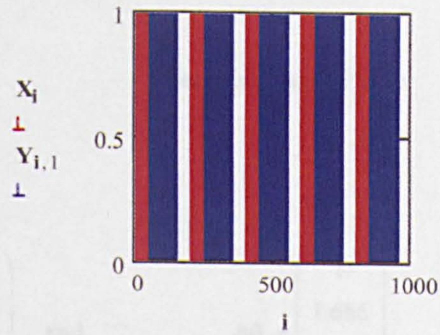

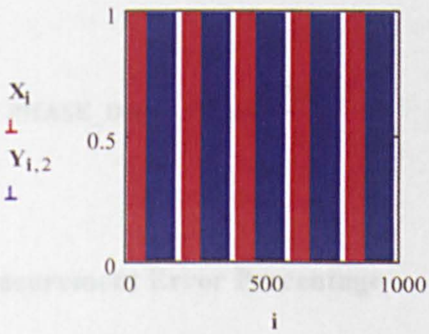

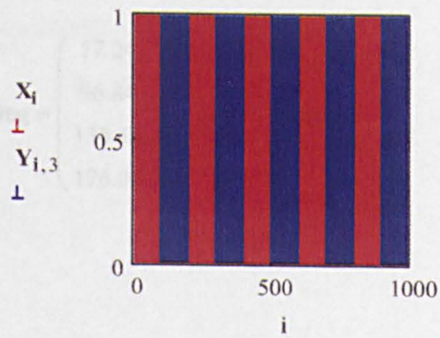

Samples out of Phase

$$\mathbf{Phase}_{i,j} := \left| \begin{array}{l} 1 \ \ \textbf{if} \ \ Y_{i,j} - X_i > 0 \\ 0 \ \ \textbf{otherwise} \end{array} \right.$$

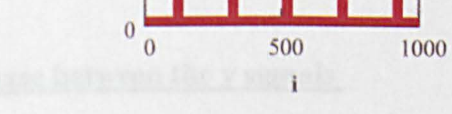

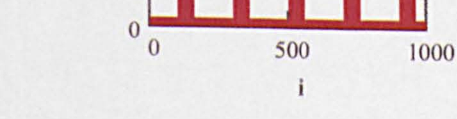

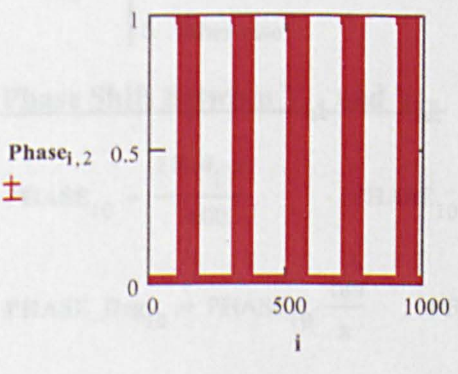

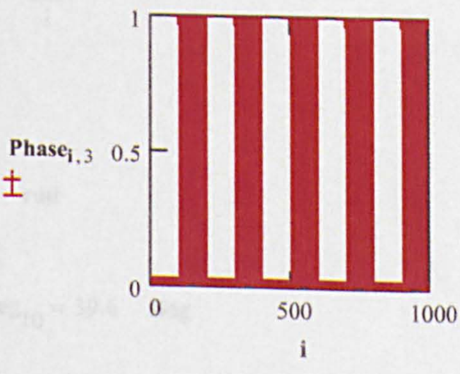

$$S_j := \sum_i \mathbf{Phase}_{i,j} \qquad S = \begin{pmatrix} 159 \\ 269 \\ 379 \\ 489 \end{pmatrix}$$ Samples out of Phase

Phase Calculations

$$\mathbf{PHASE} := \frac{2S\cdot\pi}{1000} \qquad \mathbf{PHASE} = \begin{pmatrix} 0.999 \\ 1.69 \\ 2.381 \\ 3.072 \end{pmatrix} \ \mathbf{rad} \qquad \Delta\theta = \begin{pmatrix} 1 \\ 1.686 \\ 2.372 \\ 3.058 \end{pmatrix}$$

$$\mathbf{PHASE\_Deg} := \mathbf{PHASE}\cdot\frac{180}{\pi} \qquad \mathbf{PHASE\_Deg} = \begin{pmatrix} 57.24 \\ 96.84 \\ 136.44 \\ 176.04 \end{pmatrix}$$ **Degree**

Measurement Error Percentage

$$\mathbf{\%PError}_j := \frac{\left(\mathbf{PHASE\_Deg}_j - \Delta\theta\mathbf{\_Deg}_j\right)\cdot 100}{\Delta\theta\mathbf{\_Deg}_j} \quad \%$$

$$\mathbf{\%PError}_j = \begin{pmatrix} -0.1 \\ 0.26 \\ 0.41 \\ 0.49 \end{pmatrix} \quad \%$$

The above results show highly accurate phase measurements with percentage errors not exceeding 0.5% this is mainly due to sample points overlap.

<u>Phase between the y signals</u>

$$\mathbf{Phase}_{i,j} := \begin{cases} 1 & \text{if } Y_{i,1} - Y_{i,0} > 0 \\ 0 & \text{otherwise} \end{cases} \qquad \mathbf{S10}_j := \sum_i \mathbf{Phase}_{i,j} \qquad \mathbf{S10}_1 = 110$$

<u>Phase Shift Between $Y_{i,1}$ and $Y_{i,0}$</u>

$$\mathbf{PHASE}_{10} := \frac{2\,\mathbf{S10}_1\cdot\pi}{1000} \qquad \mathbf{PHASE}_{10} = 0.691 \quad \mathbf{rad}$$

$$\mathbf{PHASE\_Deg}_{10} := \mathbf{PHASE}_{10}\cdot\frac{180}{\pi} \qquad \mathbf{PHASE\_Deg}_{10} = 39.6 \quad \mathbf{Deg}$$

$$\mathbf{Phase}_{i,j} := \begin{cases} 1 & \text{if } Y_{i,3} - Y_{i,0} > 0 \\ 0 & \text{otherwise} \end{cases} \qquad \mathbf{S30}_j := \sum_i \mathbf{Phase}_{i,j} \qquad \mathbf{S30}_1 = 330$$

Phase Shift Between $Y_{i,3}$ and $Y_{i,0}$

$$\mathbf{PHASE}_{30} := \frac{2\,\mathbf{S30}_1 \cdot \pi}{1000} \qquad \mathbf{PHASE}_{30} = 2.073 \quad \mathbf{rad}$$

$$\mathbf{PHASE\_Deg}_{30} := \mathbf{PHASE}_{30} \cdot \frac{180}{\pi} \qquad \mathbf{PHASE\_Deg}_{30} = 118.8 \quad \mathbf{Deg}$$

Similarly the phase between any two signals can be calculated

Example 5: The Effect on Noise on Phase Shift Measurement (NPSM)

The aim of this example is study the effect of random noise on phase measurement assuming the noise only effects the amplitude and not the frequency.

Assume the following

$i := 0..99$ $\quad \theta_i := i\cdot\frac{\pi}{10}$ $\quad \Delta\theta := \frac{\pi}{5}$ $\quad \Delta\theta = 0.628$ **rad** [Assumed Phase Shift]

Signals with no Noise

$X_i := 30\cdot\sin(\theta_i)$

$Y_i := (20\cdot\sin(\theta_i - \Delta\theta))$

Signal with Random Noise

$yN_i := (20\cdot\sin(\theta_i - \Delta\theta))\cdot(2\,\mathbf{rnd}(0.5))$

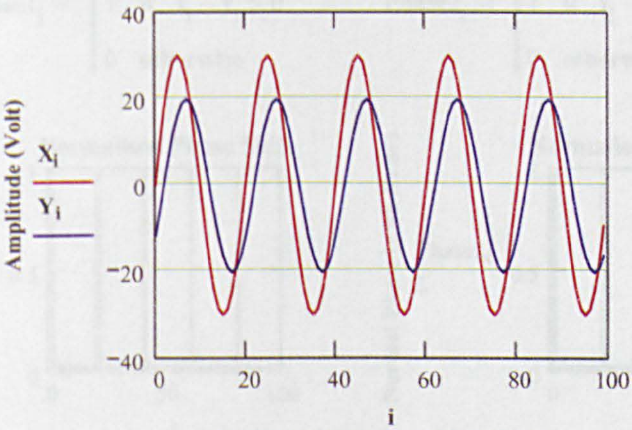

Fig.1: Normal Signals Out of Phase

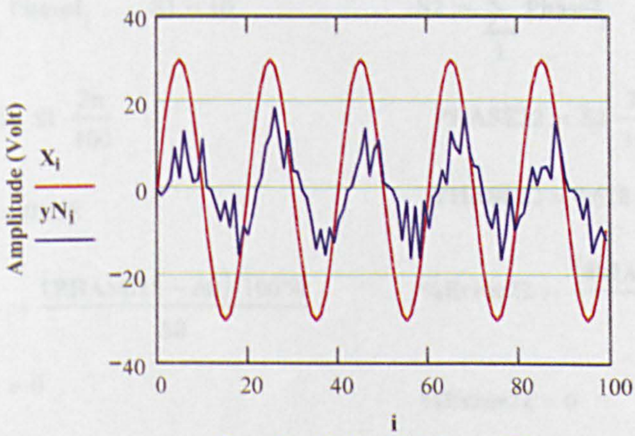

Fig.2:Effect of Amplitude Noise on Phase

Normalising the positive values of the data

$x_i := \begin{cases} 1 & \text{if } X_i > 0 \\ 0 & \text{otherwise} \end{cases}$ $\quad y_i := \begin{cases} 1 & \text{if } Y_i > 0 \\ 0 & \text{otherwise} \end{cases}$ $\quad YN_i := \begin{cases} 1 & \text{if } yN_i > 0 \\ 0 & \text{otherwise} \end{cases}$

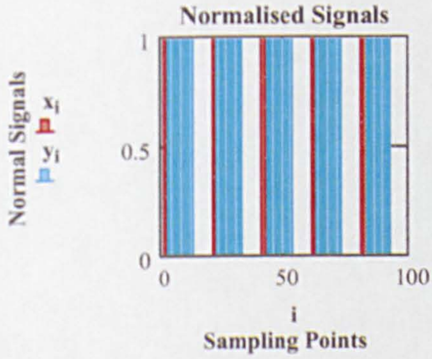

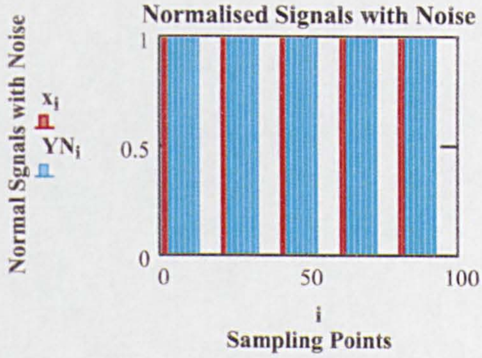

Phase clculations

$$\text{Phase1}_i := \begin{vmatrix} 1 & \text{if } x_i - y_i > 0 \\ 0 & \text{otherwise} \end{vmatrix} \qquad \text{Phase2}_i := \begin{vmatrix} 1 & \text{if } x_i - YN_i > 0 \\ 0 & \text{otherwise} \end{vmatrix}$$

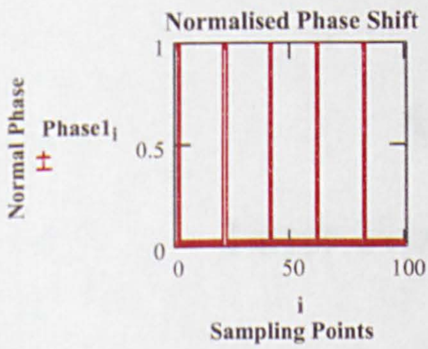

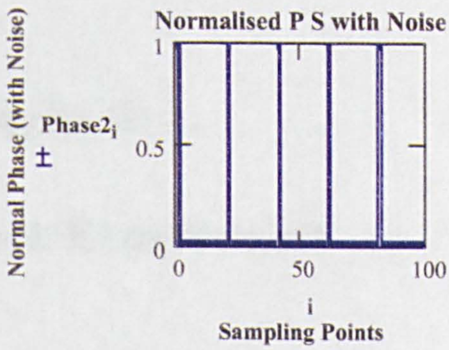

$$S1 := \sum_i \text{Phase1}_i \qquad S1 = 10 \qquad\qquad S2 := \sum_i \text{Phase2}_i \qquad S2 = 10$$

$$\text{PHASE11} := S1 \cdot \frac{2\pi}{100} \qquad\qquad \text{PHASE22} := S2 \cdot \frac{2\pi}{100}$$

$$\text{PHASE11} = 0.628 \qquad\qquad \text{PHASE22} = 0.628$$

$$\%\text{Error11} := \frac{(\text{PHASE11} - \Delta\theta) \cdot 100\%}{\Delta\theta} \qquad\qquad \%\text{Error22} := \frac{(\text{PHASE22} - \Delta\theta)}{\Delta\theta} \cdot 100\%$$

$$\%\text{Error11} = 0 \qquad\qquad \%\text{Error22} = 0$$

The above results demonstrates the immunity of the phase shift calculation technique to amblitude noise

Appendix B:

Laser Feedback Experiments

Laser Feedback Experiments

Objective

The aim of these experiments is to investigate the possibility of detecting laser front position during laser tissue interaction and measure the laser penetration depth. They also aim to device a control mechanism for the laser End-Effector.

Introduction

Detection of laser front inside tissue during laser tissue interaction is not an easy and straightforward process. It requires a full understanding of the nature of the laser tissue interaction and the identification of the laser parameters, tissue type, plume components and the heat and sound propagation properties.

Current surgical laser applications are open loop; in which no direct feedback mechanism is available. The process of laser feedback helps surgeons in determining the position of the laser front during surgery, and aids in setting the laser control and manipulation parameters.

The feedback techniques presented in these experiments include: Detection of laser front during laser tissue-interaction via acoustic feedback. This technique investigates the possibility of providing position feedback of the laser front inside tissue, using the acoustic waves generated by the laser tissue-interaction.

Experiment I: Acoustic Detection of Laser Front on the bone surface

Objective

The main objective of this experiment is to investigate the detection of the laser front on the surface of the bone during laser-bone interaction.

Equipments

- Oscilloscope
- Ultrasound piezoelectric transducers
- Wideband amplifier with power source
- Infrared (IR) Photoconductive detector
- IR Laser source (Er: YAG or Medical-CO_2)
- Smoke removal system (Vacuum)
- Bone Sample (or Bone Analogue)

Experimental setup

Figure 1 shows the experimental setup.

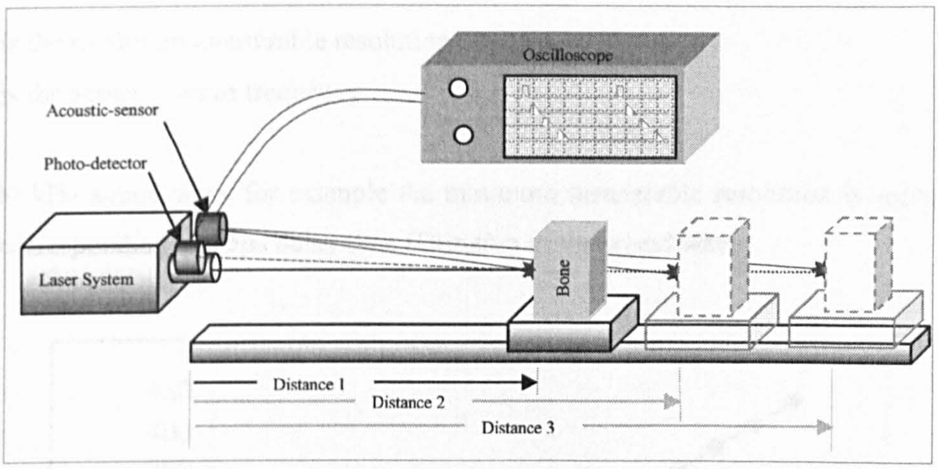

Figure 1: Experimental setup of the acoustic feedback system of laser front from the bone surface.

Procedure

In this experiment the targeted bone is placed on an optical rail in line with the laser beam at fixed distances from the laser front-end as shown in Figure 1. The acoustic and optical sensors are placed at fixed positions relative to the laser front-end in line with the optical rail and facing the laser tissue interaction point. As laser pulses hit the targeted bone the reflected light and acoustic waves generated by the laser-tissue interaction are detected by the photo-detector (photo-sensor) and the acoustic sensor respectively. Because of the relatively small distance between the laser front-end and the targeted bone the light pulses detected by the photo-sensor can represent the real time laser pulses. And due to the relatively slow speed of sound (relative to the speed of light) there would be some time delay before the laser-bone interaction acoustic waves are detected by the acoustic-sensor (Bi-Morph element). This time delay as shown in Figure 2 is directly related to the distance between the laser tissue-interaction point on the bone surface and the acoustic sensor and can be calculated by the following equation:

Equation B1

$$d = t \cdot v$$

where

d is the displacement distance

t is the time delay

v is speed of sound (~340m/s)

The minimum measurable resolution depends on the frequency of the acoustic waves generated by the interaction can be calculated as follow

Equation B2

$$R_{\min} = \frac{V}{f}$$

where

$R_{\min}$ is the minimum measurable resolution

f is the acoustic wave frequency

For a 200 kHz sound wave for example the minimum measurable resolution is approximately 1.7 mm corresponding to a 5μs delay time (Duration of the sound wave).

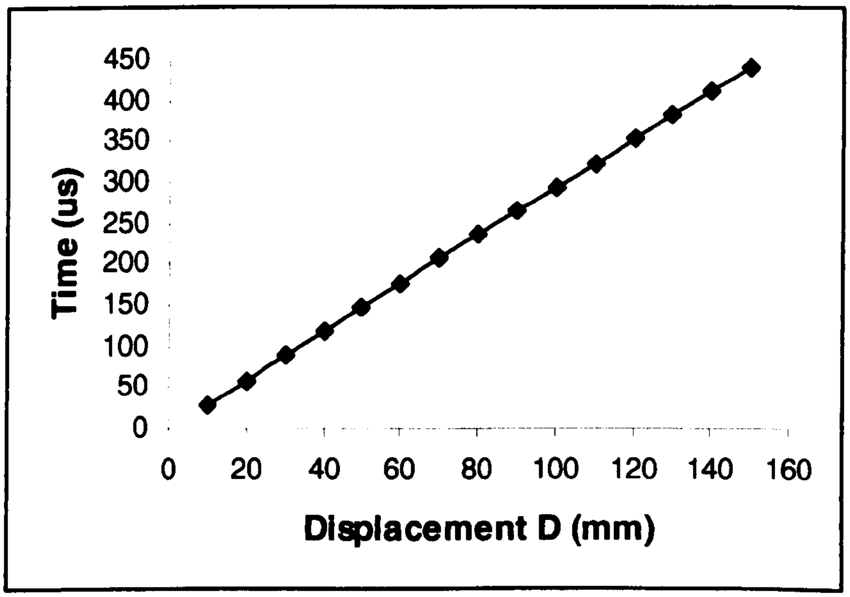

Figure 2: Acoustic delay time as a function of displacement (distance from the laser front-end to the interaction point at the target bone)

Measurements

Initial measurements can be made using the optical and acoustic sensors and a high frequency (100 MHz) memory storage oscilloscope. Signals generated by the sensors are measured by the oscilloscope in real time during laser tissue interaction; where the time delay between the signals is measured (Figure 3) and recorded. The measured time delay can then be used to calculate the distance between the bone and the laser front-end using Equation B1. Figure 3 shows the optical and acoustic signals for three known distance positions for the target bone from the laser front-end.

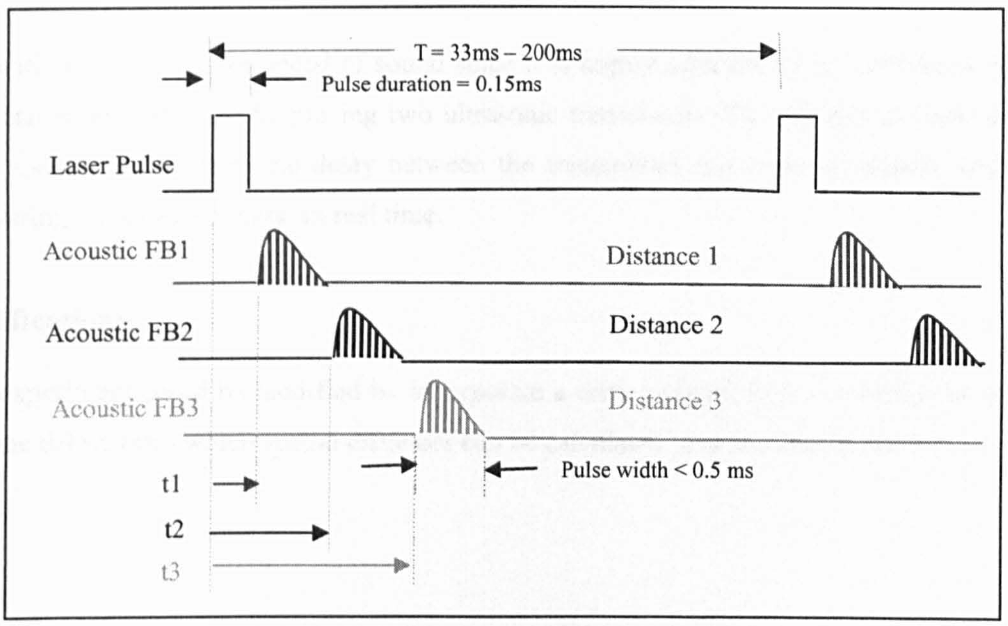

Figure 3: Delay time measurements

Experimental setup for deep drilling

To be able to do similar measurements as above while drilling deep inside bone we may have to alter the setup. This is so because as the drilled hole gets deeper inside the bone the optical sensor may not function properly (It may not pick up directly reflected interaction light waves). In this case we may use a beam splitter with different reflection ratios to allow the high percentage of the laser light to pass to the target bone while reflecting a fraction of beam toward an optical sensor placed perpendicular to laser beam as shown in Figure 4. Deep drilling may also effect the acoustic measurement which may require some modification to Equation B1.

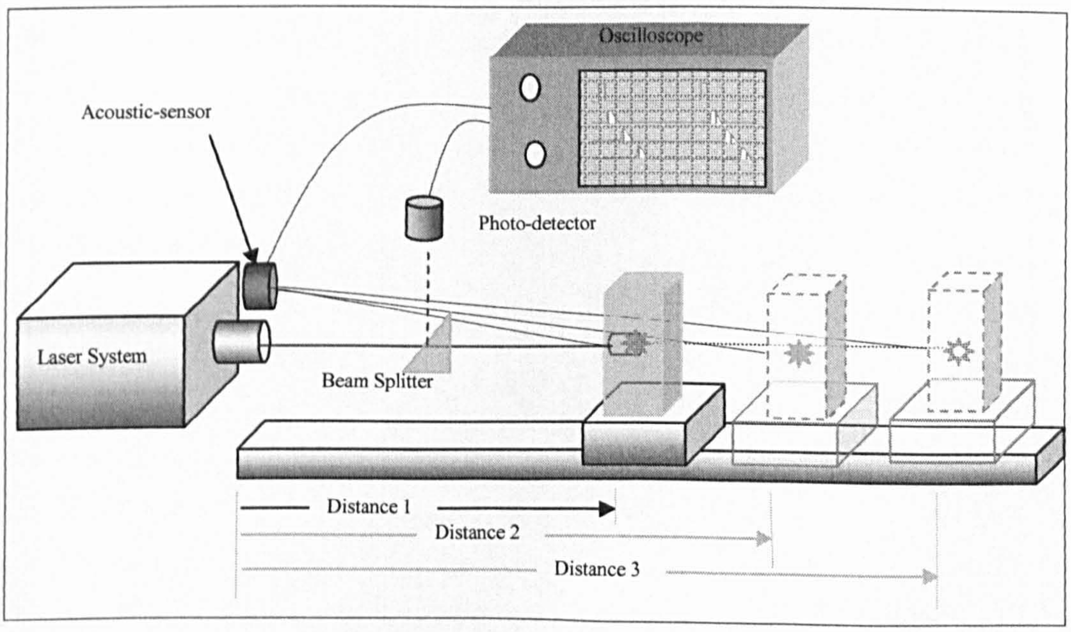

Figure 4: Experimental setup of the acoustic feedback system of laser front for deep drilling.

Calibration

Calibration is required for speed of sound since it is highly affected by environmental factors. This can simply be done by placing two ultrasonic transducers (Tx and Rx) at fixed distance apart and measuring the time delay between the transmitted and received signals and hence calculating the speed of sound in real time.

Modifications

This experiment could be modified by incorporate a timing circuit and a computer to measure the time delay, from which spatial distances can be calculated and monitored in real time

Appendix C:

AutoCAD Blueprints

Blueprints of the Laser End-Effector Design Components

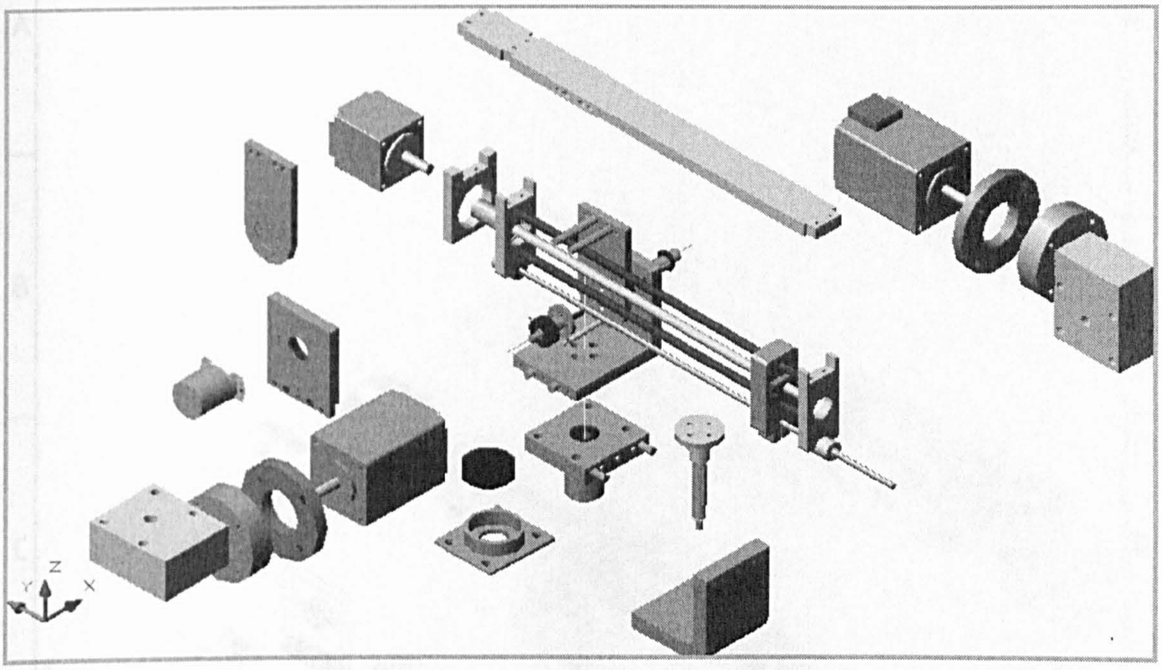

Figure AC1: Un-assembled Laser End-Effector Design Components

Figure AC2: Laser End-Effector

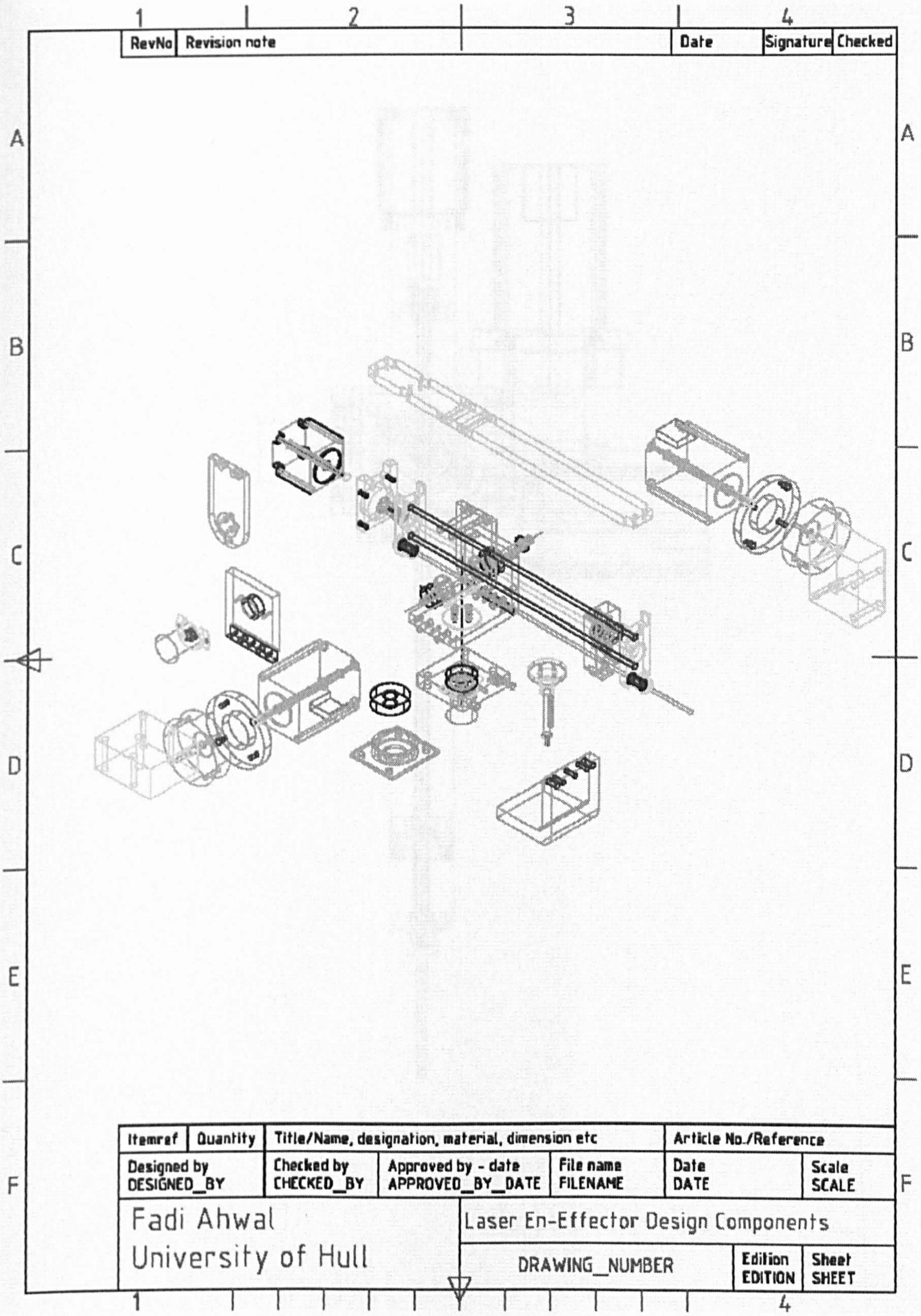

Figure AC3: A blueprint of the laser End-Effector design components

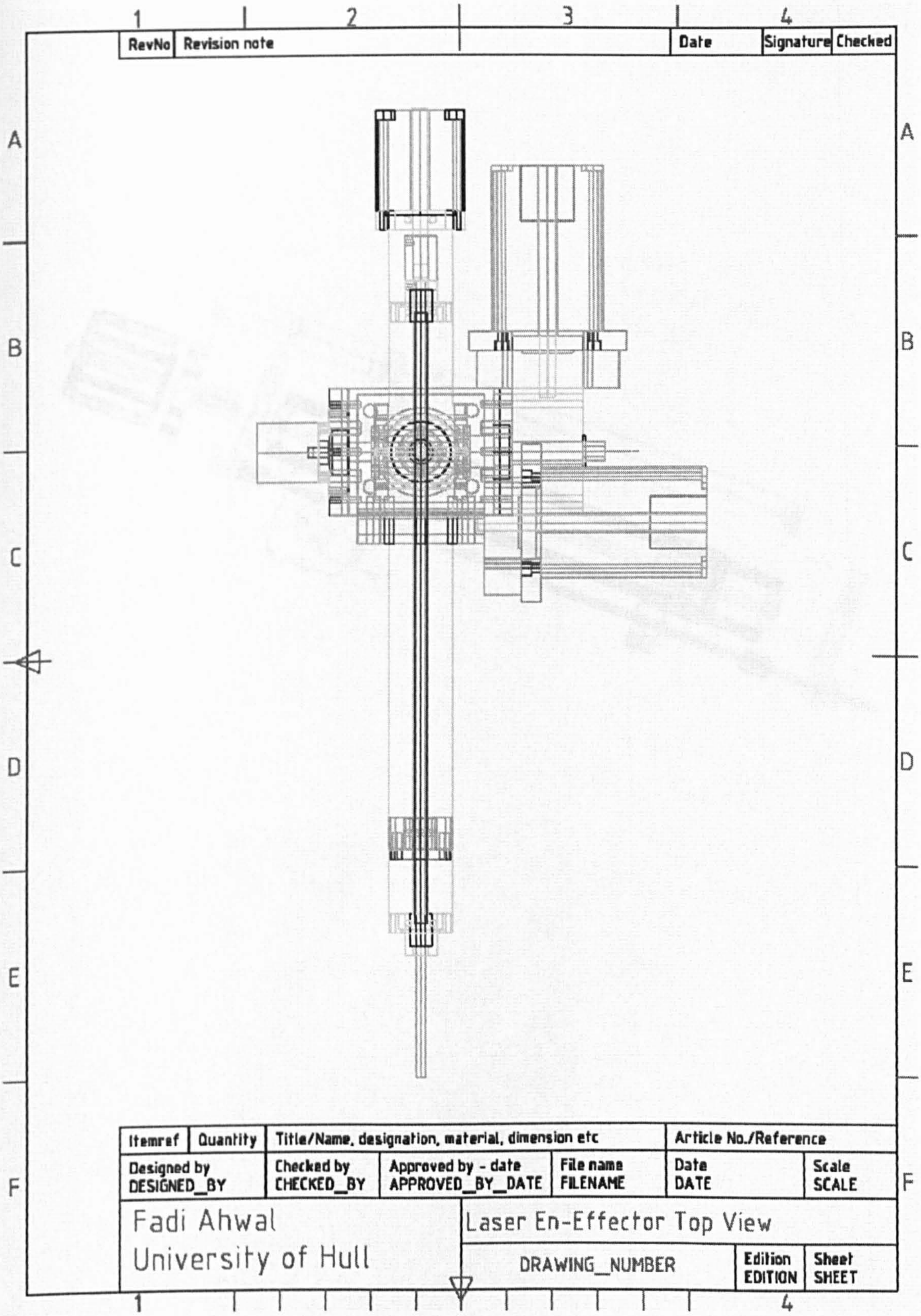

Figure AC4: A blueprint of the Laser End-Effector top view

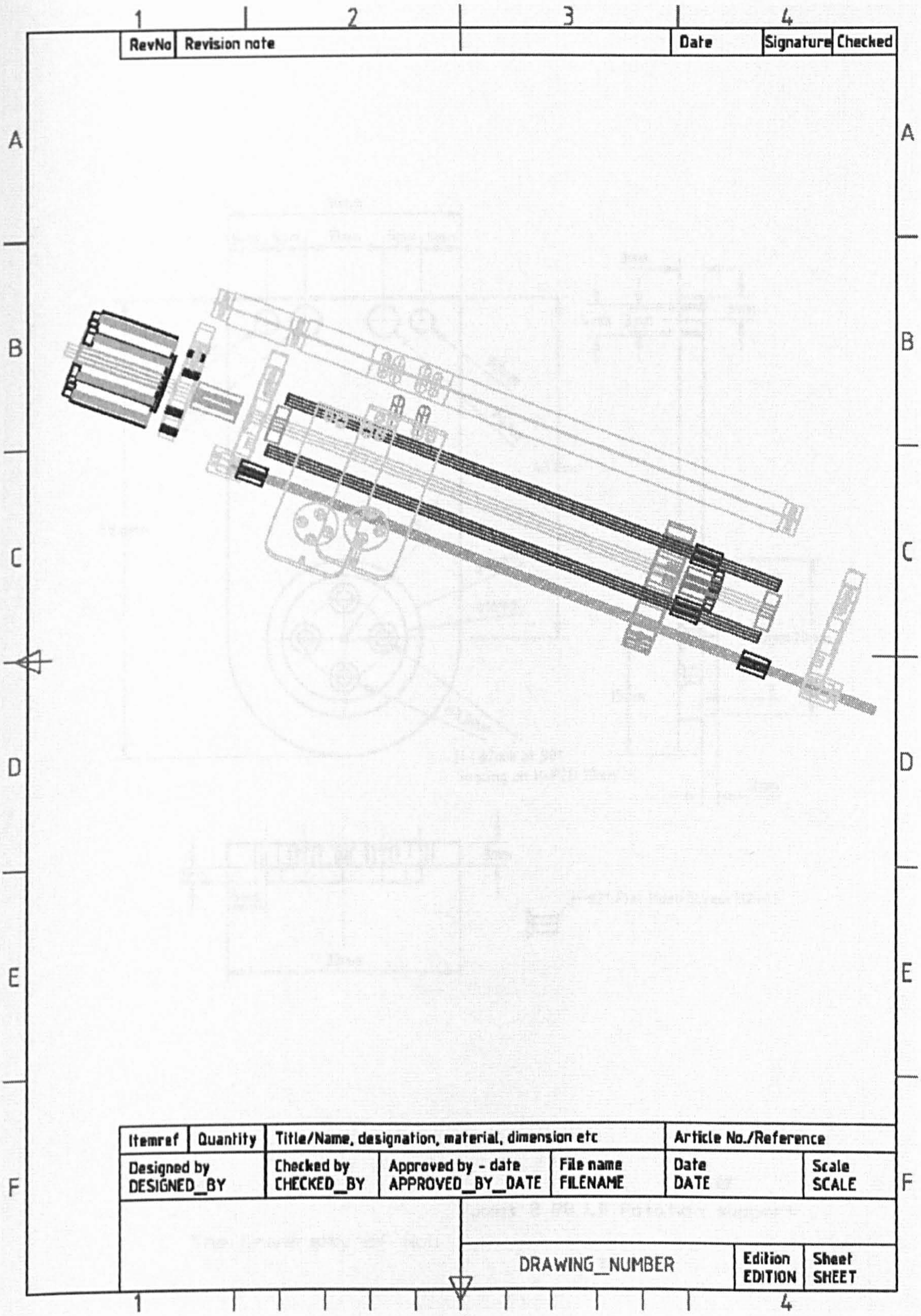

Figure AC5: Un-assembled linear drive design components

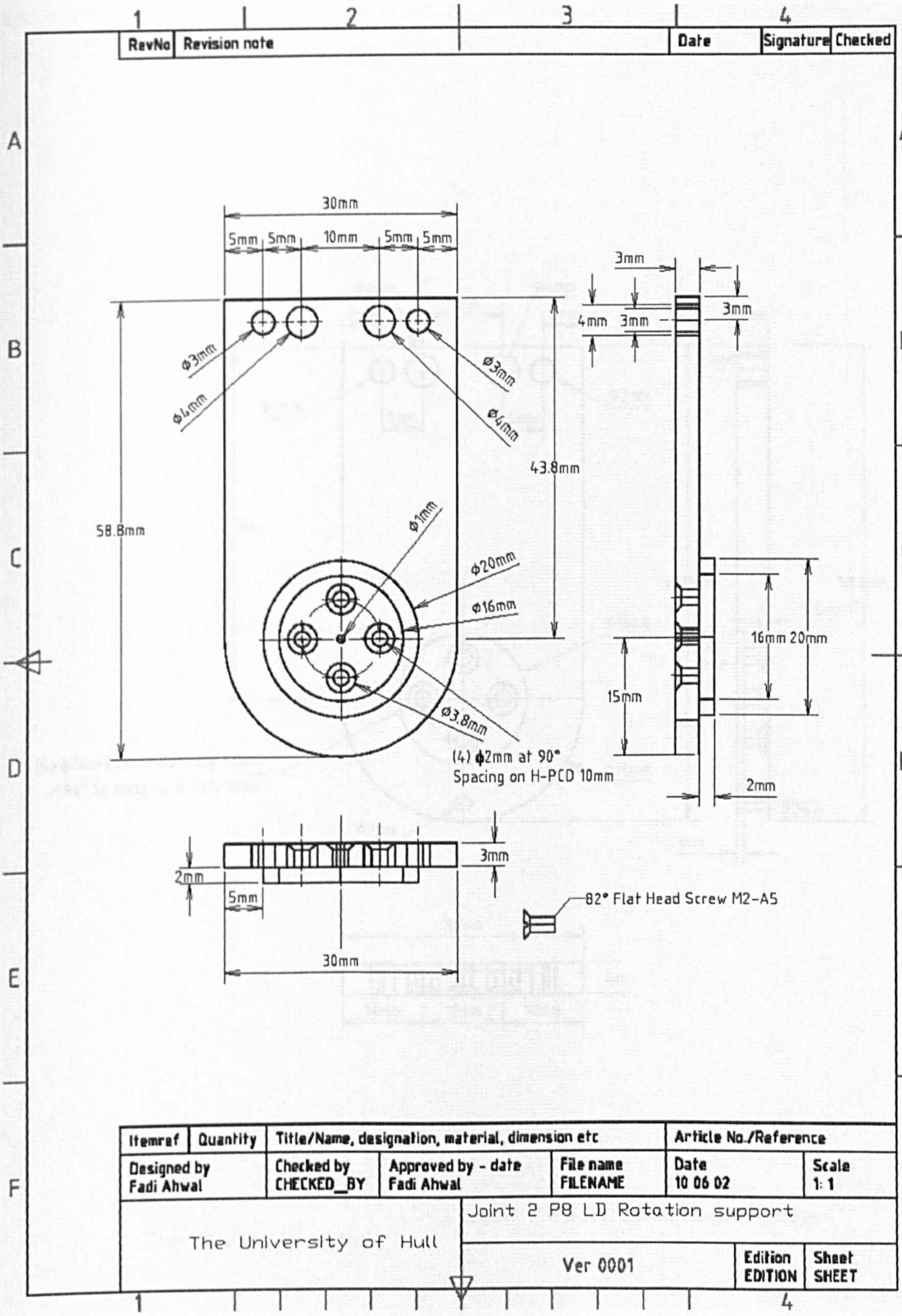

Figure AC6: Linear drive vertical rotation support L- side

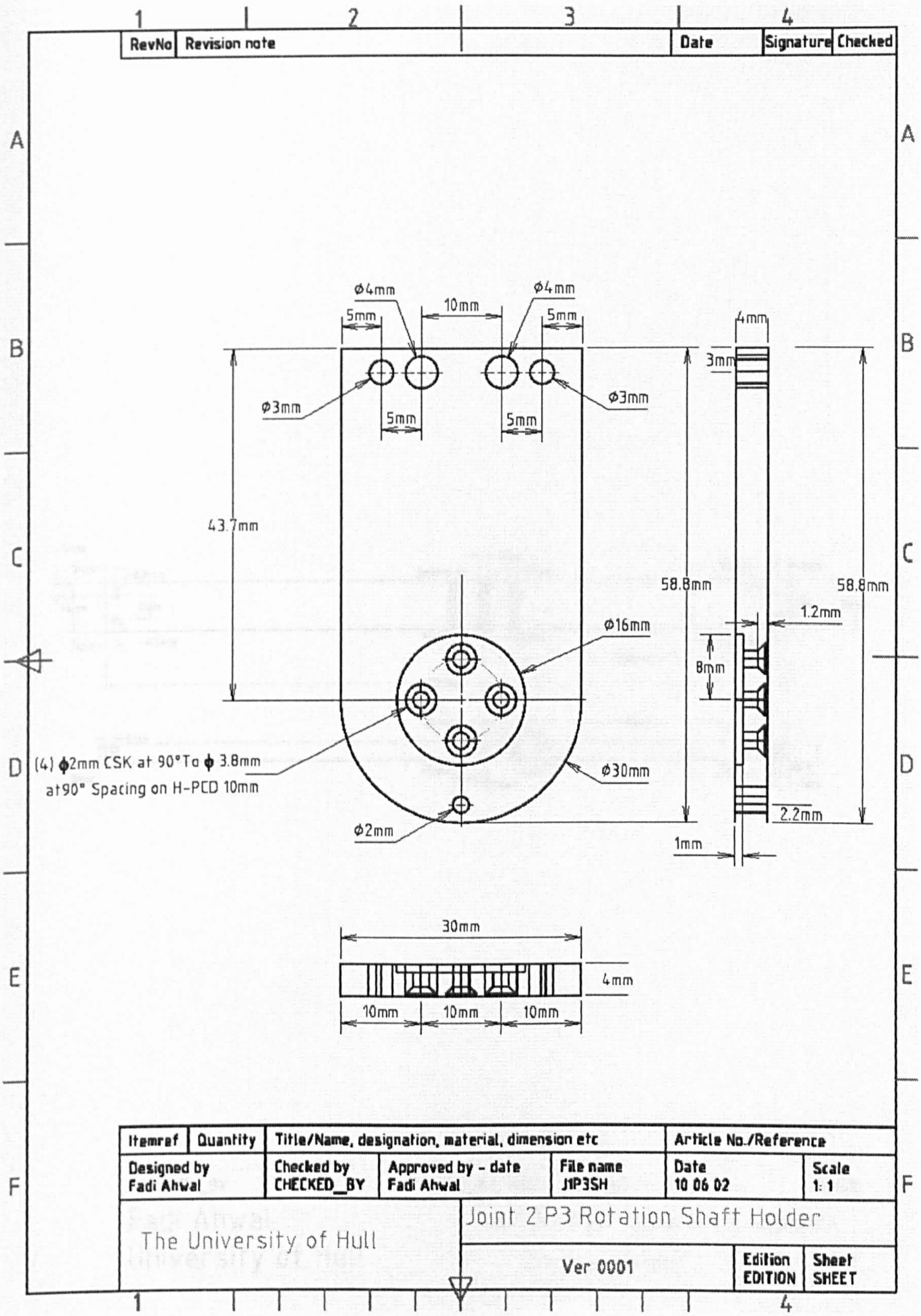

Figure AC7: Linear drive vertical rotation support (Joint2 rotation shaft holder) R-side

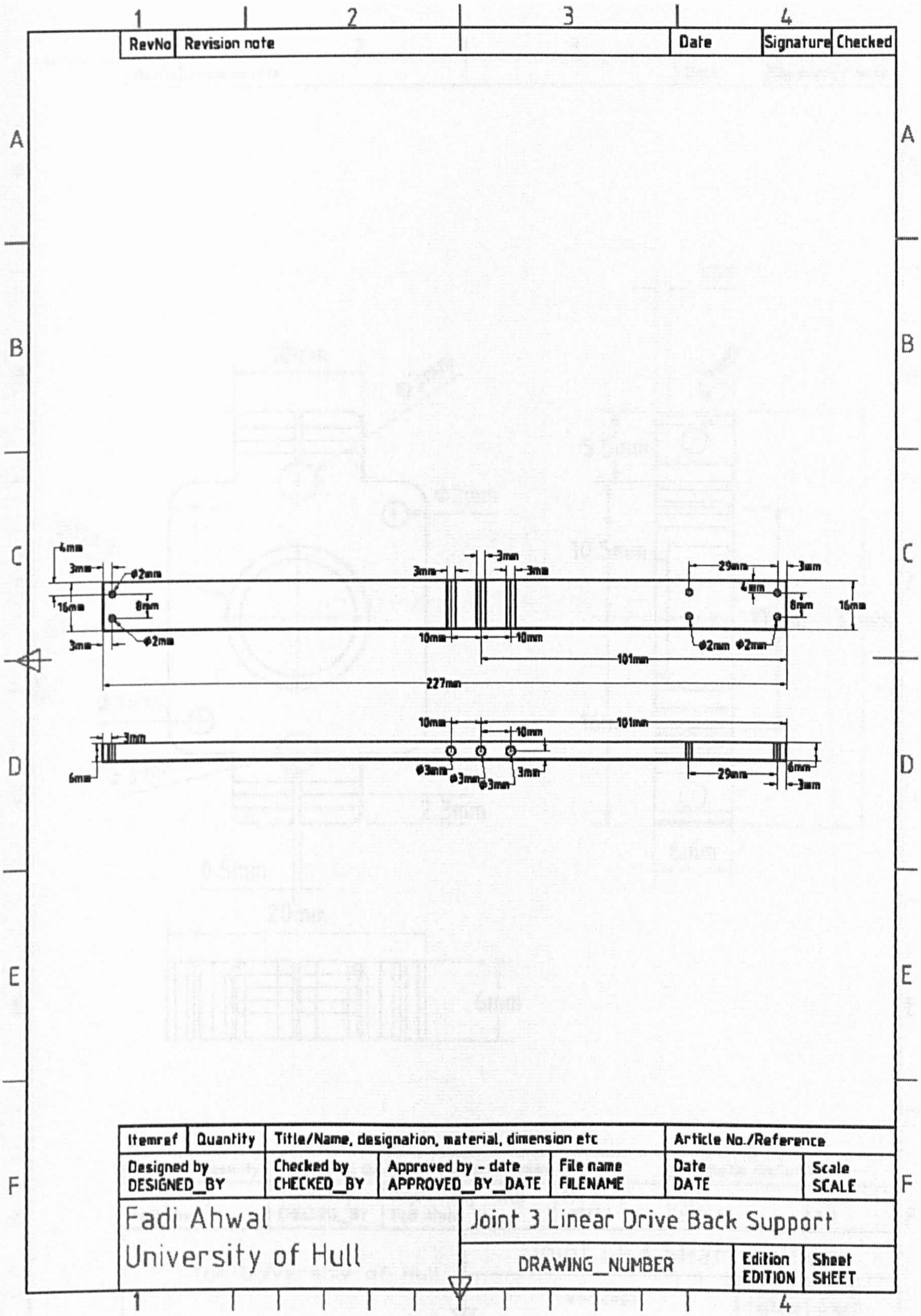

Figure AC8: linear drive back support

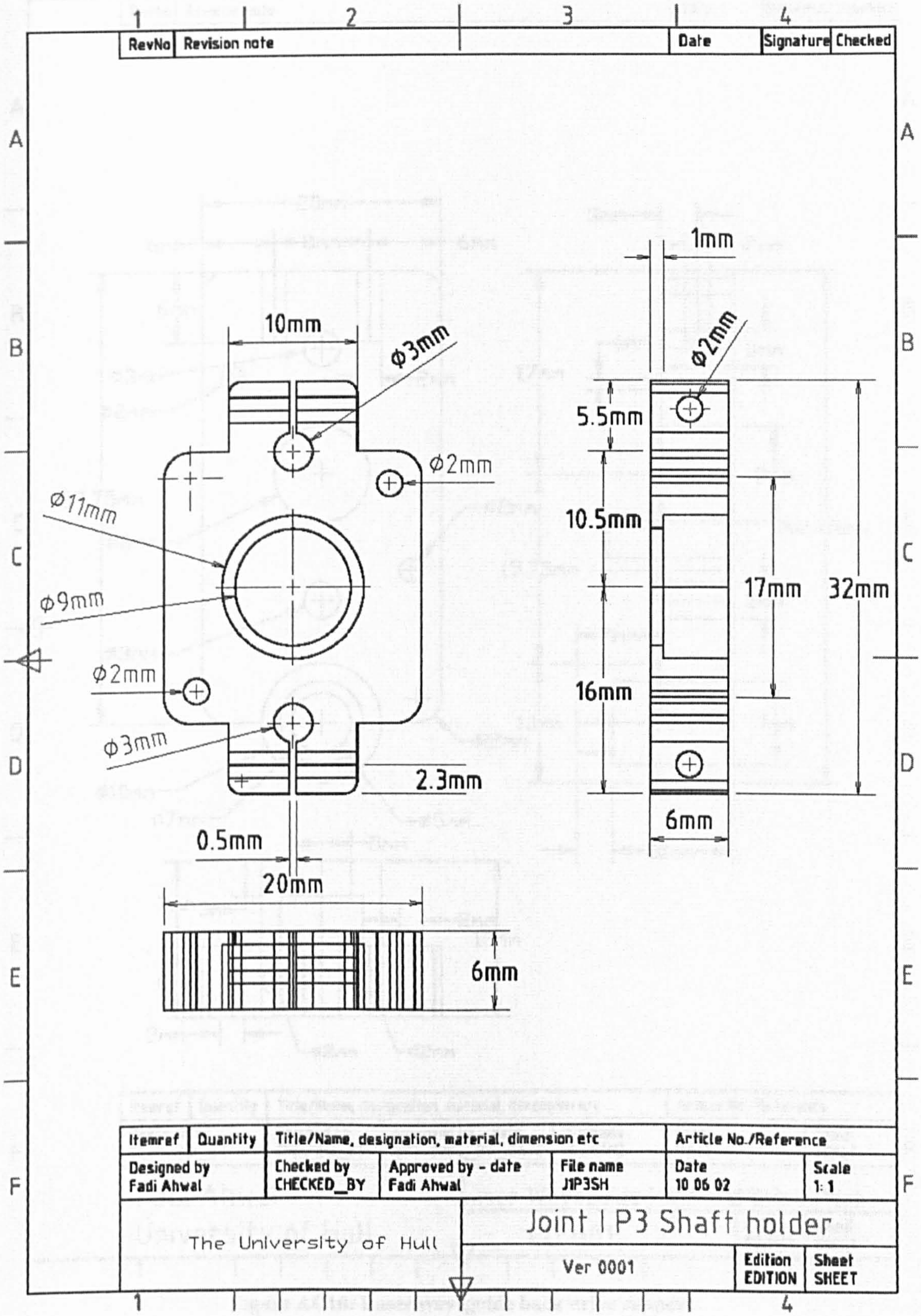

Figure AC9: Linear drive leadscrew and sliding shafts support

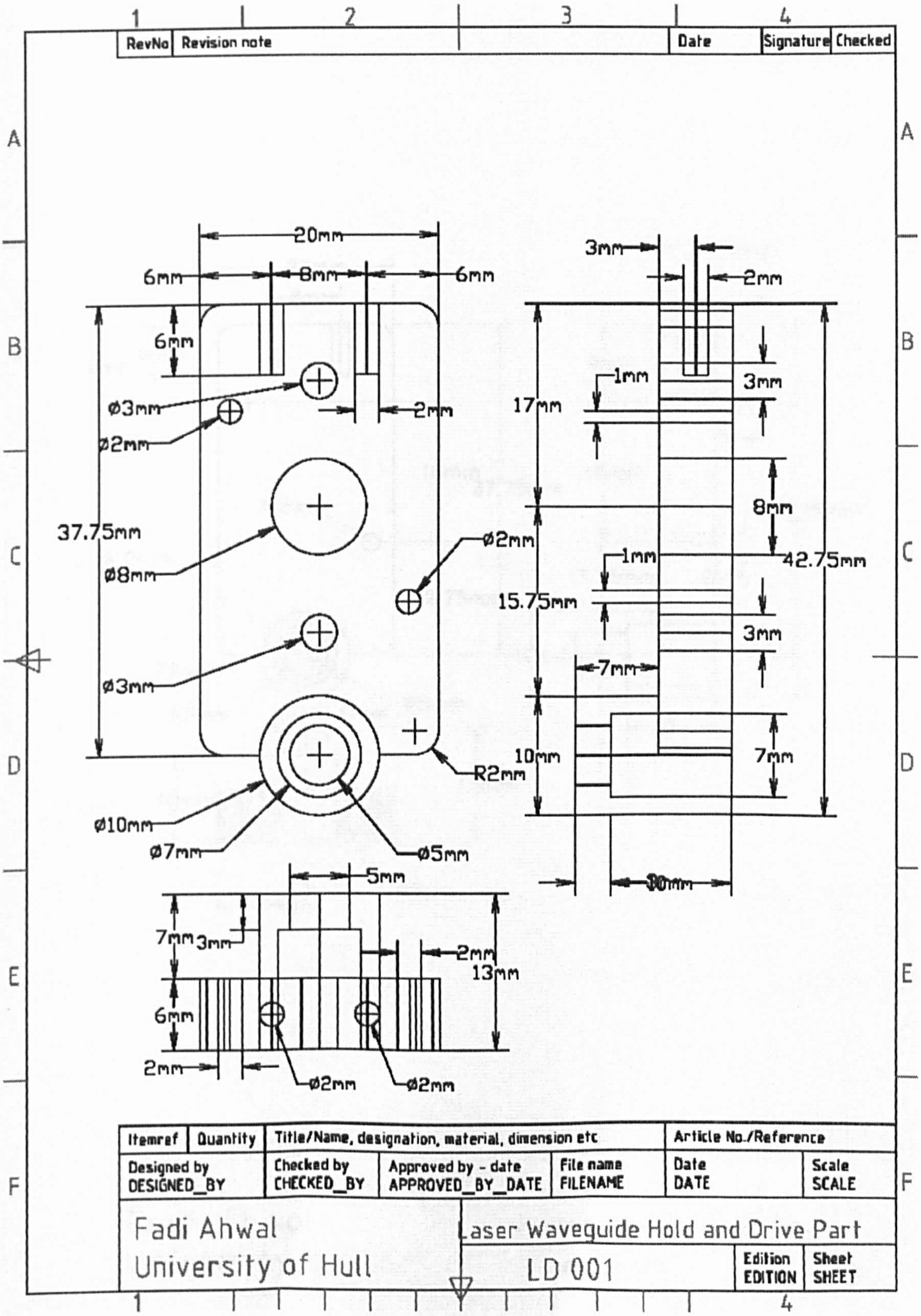

Figure AC10: Laser waveguide back drive support

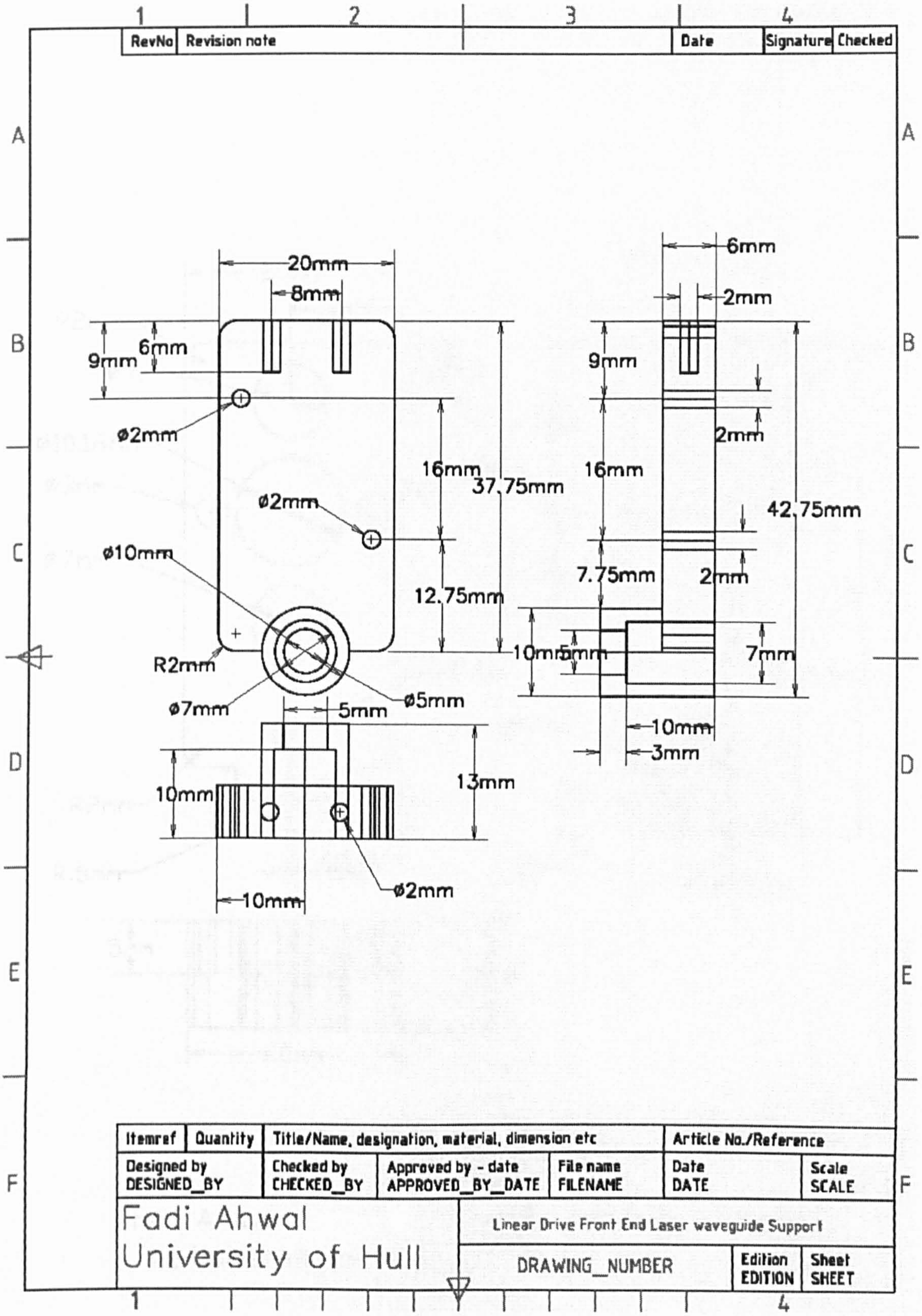

Figure AC11: Laser waveguide front end support

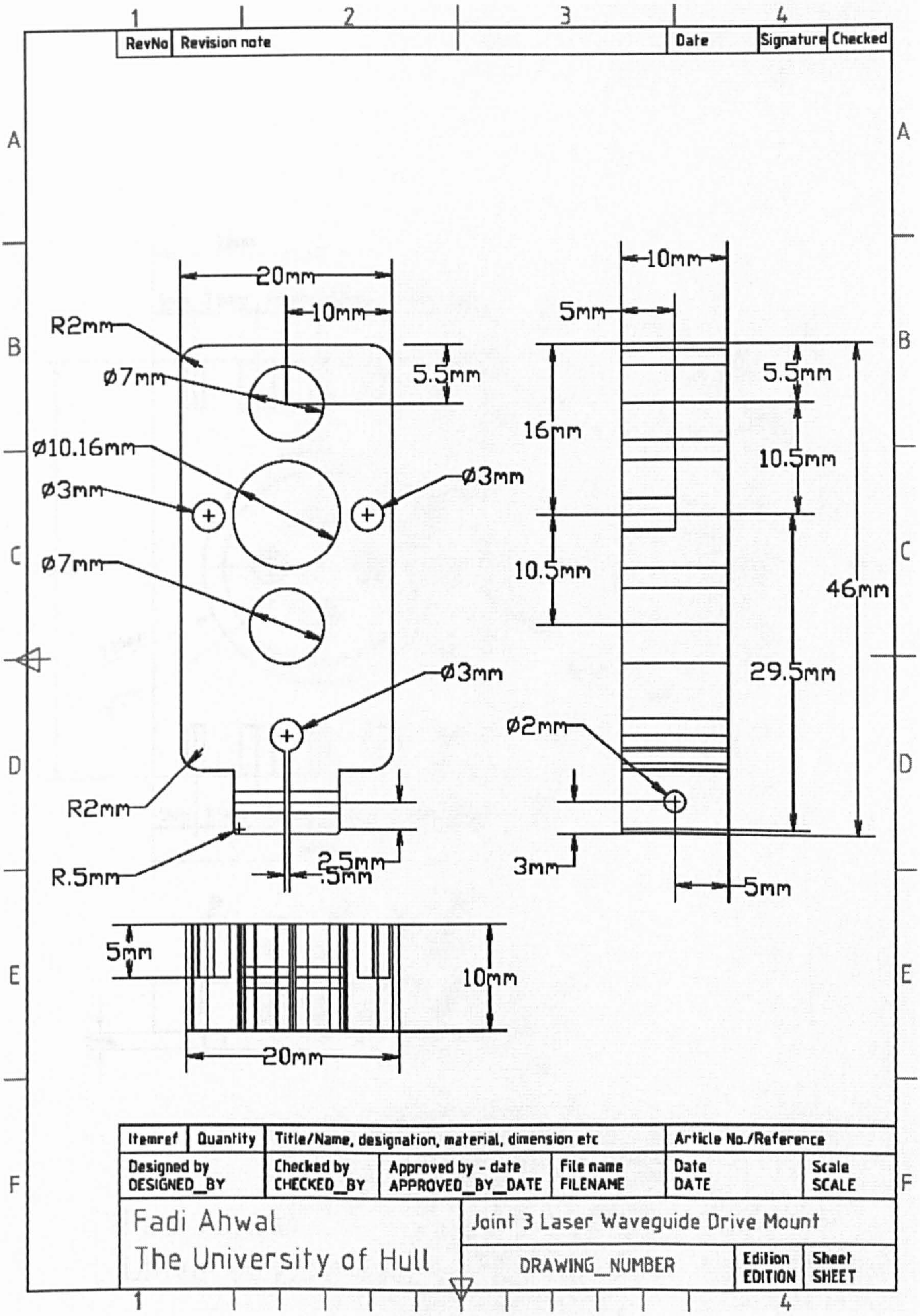

Figure AC12: laser waveguide drive mount

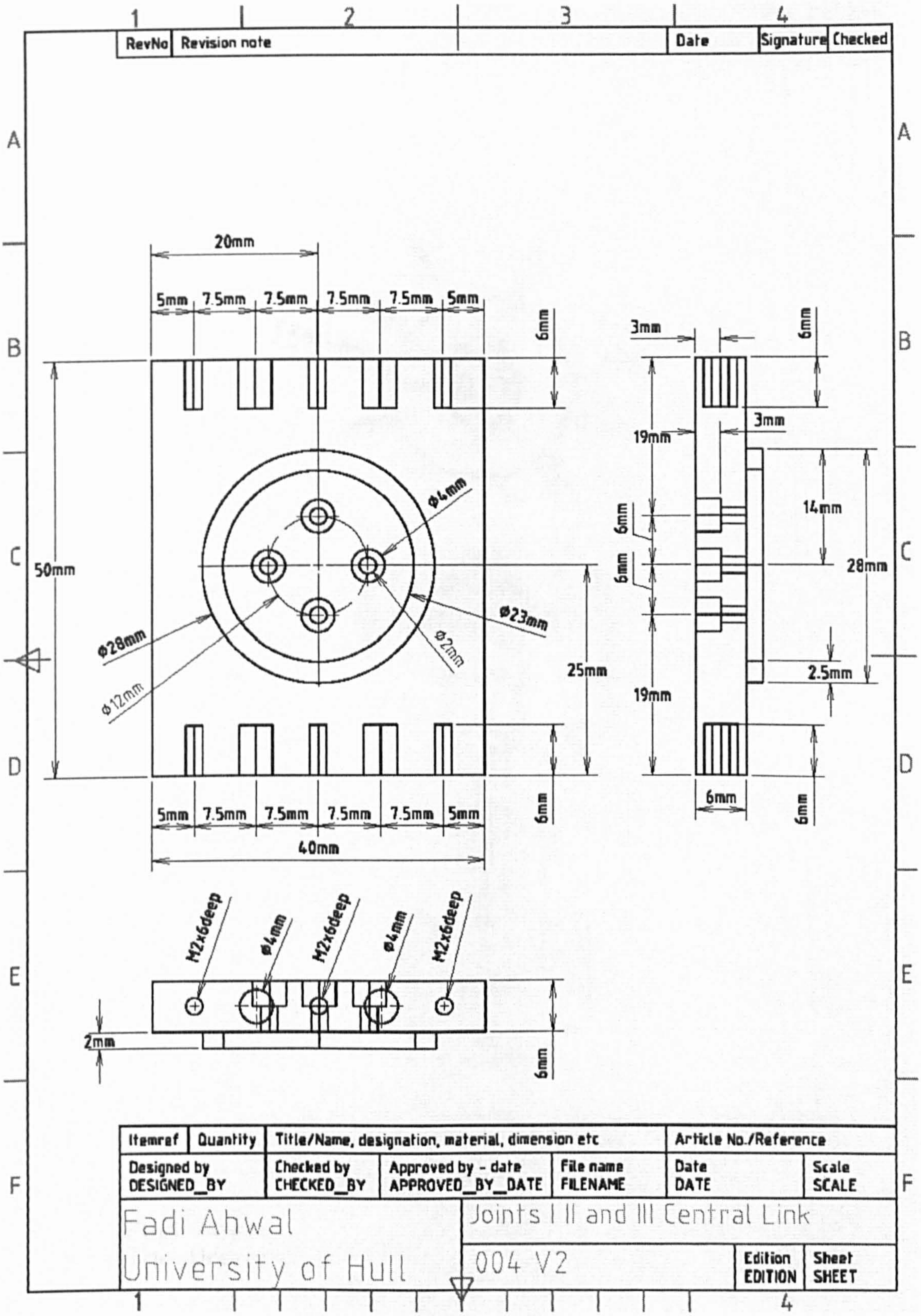

Figure AC13: Central link component (Joints I,II and III)

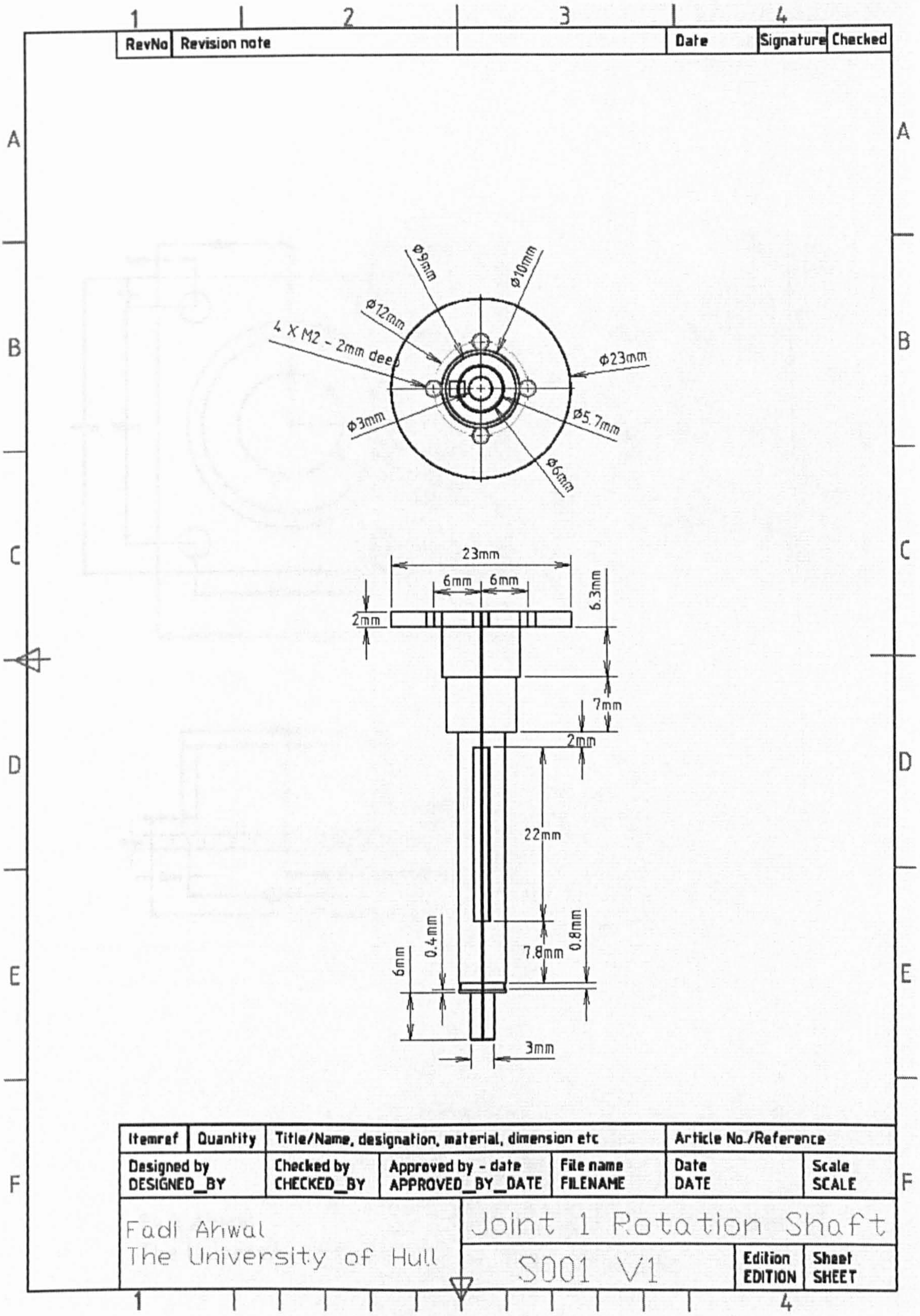

Figure AC14: Joint 1: Rotational shaft

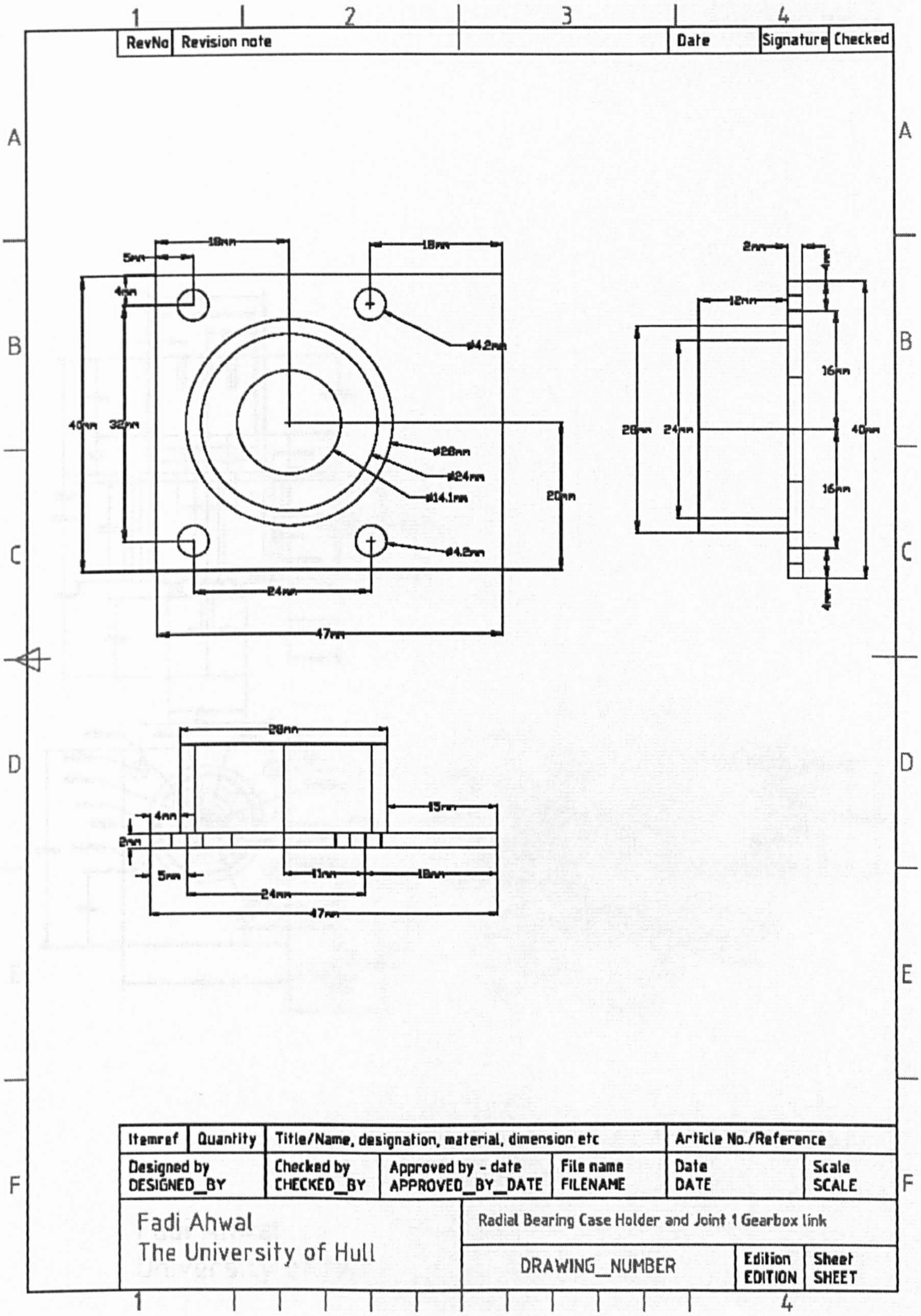

Figure AC15: Radial bearing case holder and joint 1 gearbox link

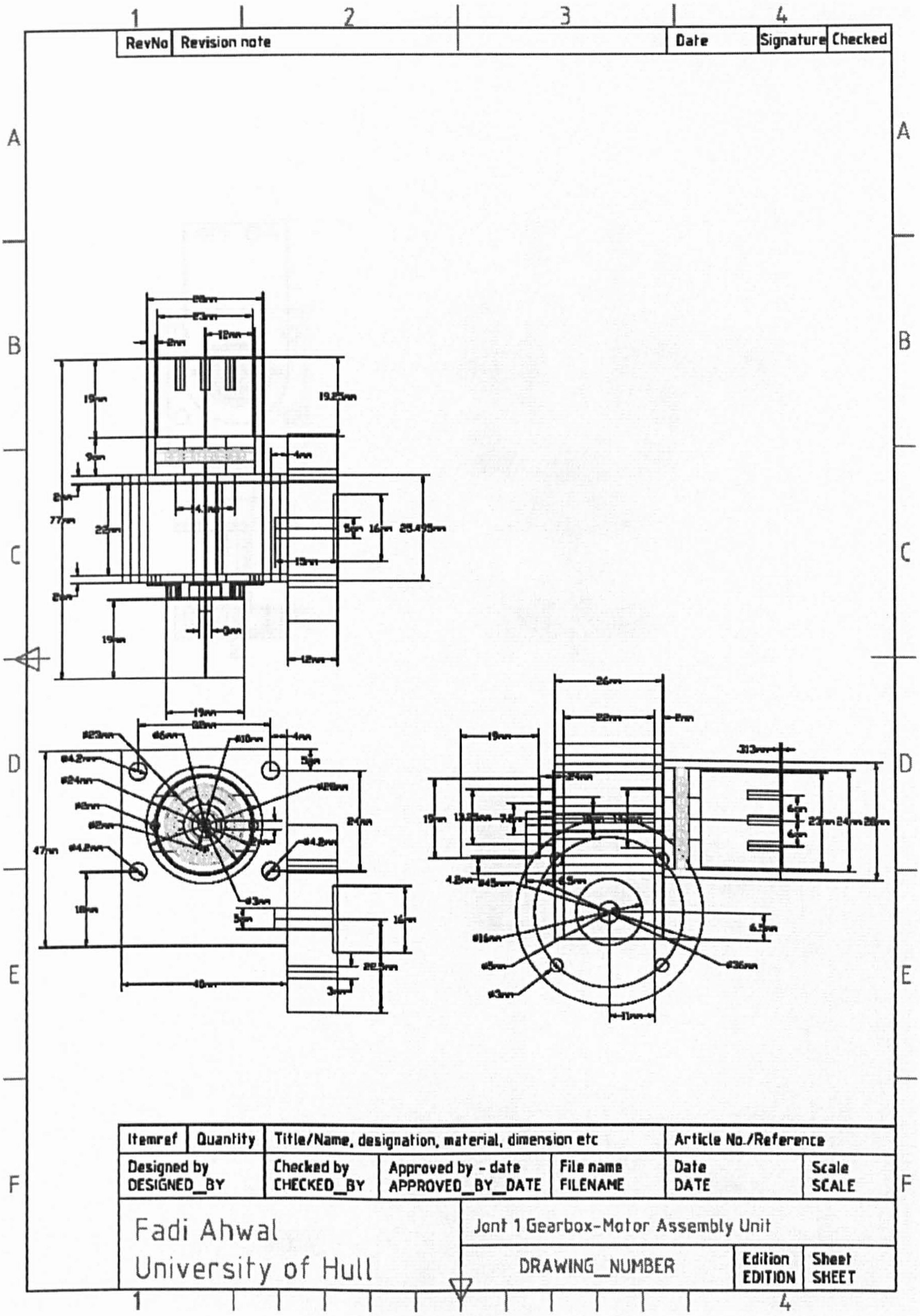

Figure AC16: Joint 1 Gearbox-Motor assembly unit

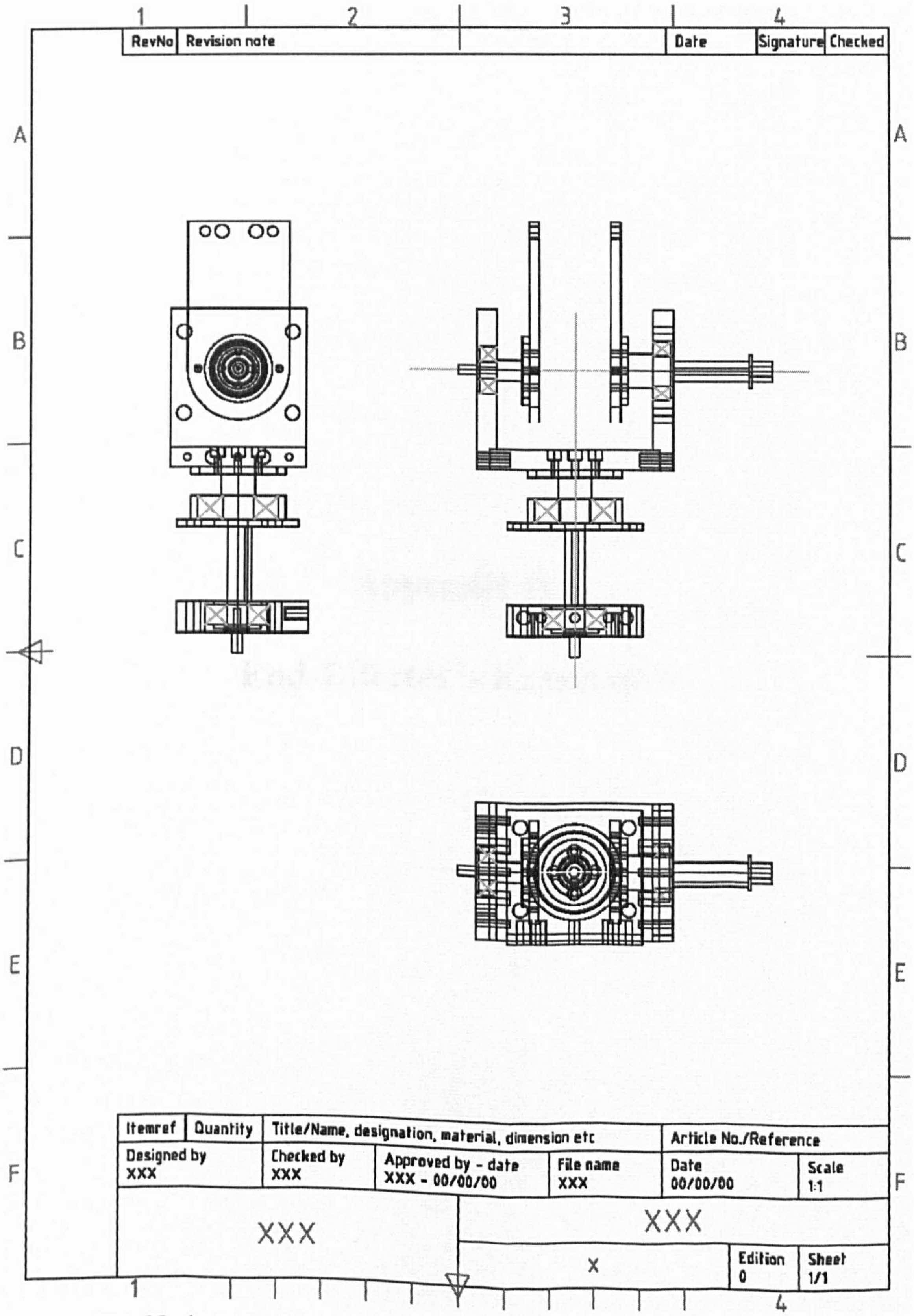

Figure AC17: Manipulation links of Joints I and II illustrating the End-Effectors Origin of manipulation

Appendix D:

End-Effector's Kinematics

Denavit - Harttenburg Representation

The following is the End-Effector's kinematic analysis using the D-H representation

Let

θ_i is the angle of rotation about the Z_{i-1} axis to align the X_{i-1} axis with the X_i axis (i.e X_{i-1} axis is in parallel to X_i and pointing in the same direction).

d_i is the translation distance along the $Z_{i-1}$to bring the X_{i-1} axis with the X_i axis into co incidence

a_i is the translation distance along the X_i axis to bring the two origins as well as the X axis into coincidence.

α_i is the angle of rotation about the X_i axis to bring the two co-ordinate systems into coincidence

The basic homogeneous rotation-translation matrix of the D-H representation

$Tz\theta$ Rotation about the Z_{i-1} axis

Tzd Translation along the the Z_{i-1} axis

Txa Translation along the X_i axis

$Tx\alpha$ Rotation about the X_i axis

$$Tzd := \begin{pmatrix} 1 & 0 & 0 & 0 \\ 0 & 1 & 0 & 0 \\ 0 & 0 & 1 & d_i \\ 0 & 0 & 0 & 1 \end{pmatrix} \qquad Tz\theta := \begin{pmatrix} \cos(\theta_i) & -\sin(\theta_i) & 0 & 0 \\ \sin(\theta_i) & \cos(\theta_i) & 0 & 0 \\ 0 & 0 & 1 & 0 \\ 0 & 0 & 0 & 1 \end{pmatrix}$$

$$Txa := \begin{pmatrix} 1 & 0 & 0 & a_i \\ 0 & 1 & 0 & 0 \\ 0 & 0 & 1 & 0 \\ 0 & 0 & 0 & 1 \end{pmatrix} \qquad Tx\alpha := \begin{pmatrix} 0 & 0 & 0 & 0 \\ 0 & \cos(\alpha_i) & -\sin(\alpha_i) & 0 \\ 0 & \sin(\alpha_i) & \cos(\alpha_i) & 0 \\ 0 & 0 & 0 & 1 \end{pmatrix}$$

The D-H Transformation matrix for the adjacent co-ordinate frames i and i-1 is $A_{(i-1)i}$

$$A_{(i-1)i} := Tzd \cdot Tz\theta \cdot Txa \cdot Tx\alpha$$

$$A_{(i-1)i} := \begin{pmatrix} \cos(\theta_i) & -\cos(\alpha_i)\cdot\sin(\theta_i) & \sin(\alpha_i)\cdot\sin(\theta_i) & a_i\cdot\cos(\theta_i) \\ \sin(\theta_i) & \cos(\alpha_i)\cdot\sin(\theta_i) & -\sin(\alpha_i)\cdot\cos(\theta_i) & a_i\cdot\sin(\theta_i) \\ 0 & \sin(\alpha_i) & \cos(\alpha_i) & d_i \\ 0 & 0 & 0 & 1 \end{pmatrix}$$

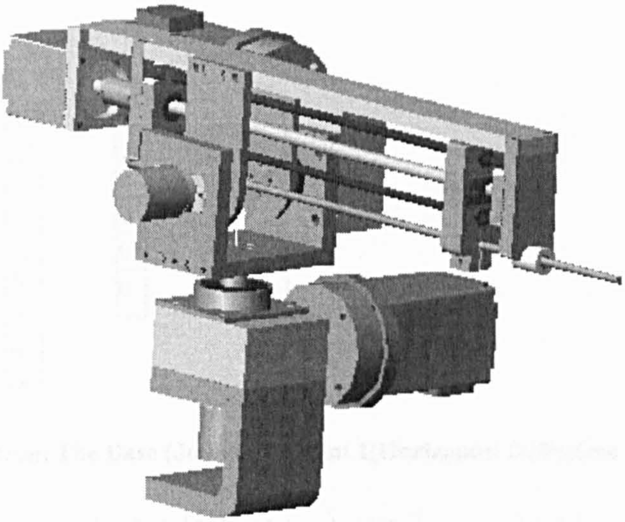

Figure 1: End Effector

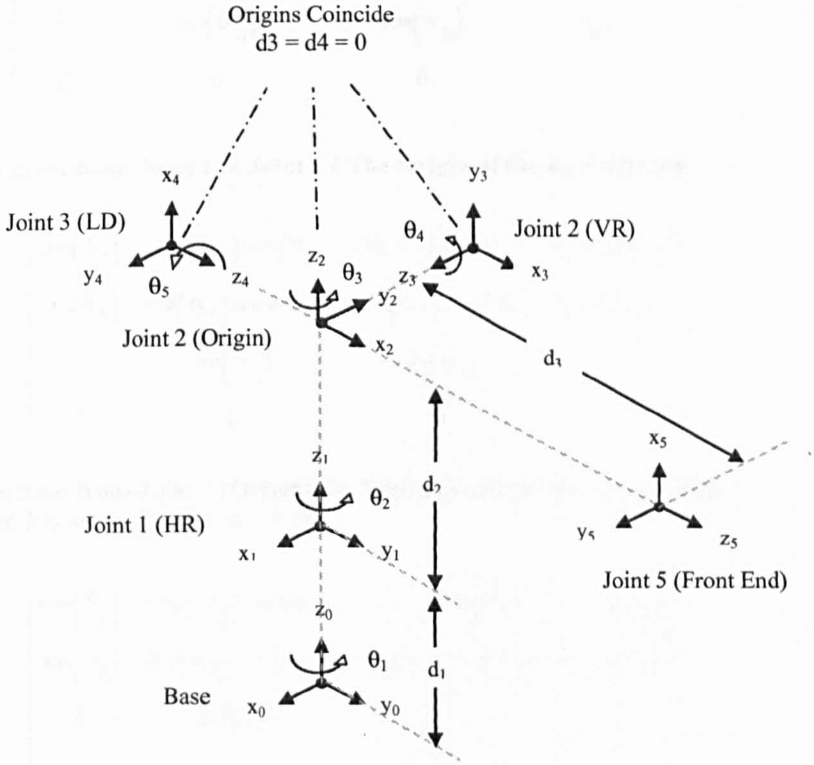

Figure 2: End-Effector Link coordinate system

End Effector link parameters				
Joint *i*	θ_i *rad*	α_i *rad*	a_i *(mm)*	d_i *(mm)*
1	0	0	0	59
2	$\pi/2$	0	0	57.25
3	0	$\pi/2$	0	0
4	$\pi/2$	$\pi/2$	0	0
5	0	0	0	360

Figure 3: End Effecor link coordinate parameters

$i := 0 .. 5$

$$\theta_i := \begin{pmatrix} 0 \\ \frac{\pi}{2} \\ 0 \\ \frac{\pi}{2} \\ 0 \end{pmatrix} \qquad \alpha_i := \begin{pmatrix} 0 \\ 0 \\ \frac{\pi}{2} \\ \frac{\pi}{2} \\ 0 \end{pmatrix} \qquad a_i := \begin{pmatrix} 0 \\ 0 \\ 0 \\ 0 \\ 0 \end{pmatrix} \qquad d_i := \begin{pmatrix} 59 \\ 57.25 \\ 0 \\ 0 \\ 280 \end{pmatrix}$$

Transformation from The Base (Joint 0) to Joint 1(Horizontal Deflection unit)

$$A_{0,1} := \begin{pmatrix} \cos(\theta_0) & -\cos(\alpha_0)\cdot\sin(\theta_0) & \sin(\alpha_0)\cdot\sin(\theta_0) & a_3\cdot\cos(\theta_0) \\ \sin(\theta_0) & \cos(\alpha_0)\cdot\cos(\theta_0) & -\sin(\alpha_0)\cdot\cos(\theta_0) & a_1\cdot\sin(\theta_0) \\ 0 & \sin(\alpha_0) & \cos(\alpha_0) & d_0 \\ 0 & 0 & 0 & 1 \end{pmatrix}$$

Transformation from Joint 1 to Joint 2 (The Origin of the End Effector)

$$A_{1,2} := \begin{pmatrix} \cos(\theta_1) & -\cos(\alpha_1)\cdot\sin(\theta_1) & \sin(\alpha_1)\cdot\sin(\theta_1) & a_1\cdot\cos(\theta_1) \\ \sin(\theta_1) & \cos(\alpha_1)\cdot\cos(\theta_1) & -\sin(\alpha_1)\cdot\cos(\theta_1) & a_1\cdot\sin(\theta_1) \\ 0 & \sin(\alpha_1) & \cos(\alpha_1) & d_1 \\ 0 & 0 & 0 & 1 \end{pmatrix}$$

Transformation from Joint 2 (Origin) To Joint 3 (Vertical Deflection Unit)
Note:- Joint 3 is at the Origin (i.e. d = 0)

$$A_{2,3} := \begin{pmatrix} \cos(\theta_2) & -\cos(\alpha_2)\cdot\sin(\theta_2) & \sin(\alpha_2)\cdot\sin(\theta_2) & a_2\cdot\cos(\theta_2) \\ \sin(\theta_2) & \cos(\alpha_2)\cdot\cos(\theta_2) & -\sin(\alpha_2)\cdot\cos(\theta_2) & a_1\cdot\sin(\theta_2) \\ 0 & \sin(\alpha_2) & \cos(\alpha_2) & d_2 \\ 0 & 0 & 0 & 1 \end{pmatrix}$$

Transformation from Joint 3 (Vertical Deflection Unit) to Joint 4 (Linear Drive Unit)
Note:- Joint 4 is also at the Origin (i.e. d = 0) as shown in Figure 1

$$A_{3,4} := \begin{pmatrix} \cos(\theta_3) & -\cos(\alpha_3)\cdot\sin(\theta_3) & \sin(\alpha_3)\cdot\sin(\theta_3) & a_3\cdot\cos(\theta_3) \\ \sin(\theta_3) & \cos(\alpha_3)\cdot\cos(\theta_3) & -\sin(\alpha_3)\cdot\cos(\theta_3) & a_1\cdot\sin(\theta_3) \\ 0 & \sin(\alpha_3) & \cos(\alpha_3) & d_3 \\ 0 & 0 & 0 & 1 \end{pmatrix}$$

Transformation from Joint 4 (The Linear Drive) to Joint 5 (The laser waveguide Front End)

$$A_{4,5} := \begin{pmatrix} \cos(\theta_4) & -\cos(\alpha_4)\cdot\sin(\theta_4) & \sin(\alpha_4)\cdot\sin(\theta_4) & a_4\cdot\cos(\theta_4) \\ \sin(\theta_4) & \cos(\alpha_4)\cdot\cos(\theta_4) & -\sin(\alpha_4)\cdot\cos(\theta_4) & a_1\cdot\sin(\theta_4) \\ 0 & \sin(\alpha_4) & \cos(\alpha_4) & d_4 \\ 0 & 0 & 0 & 1 \end{pmatrix}$$

$$A_{0,1} = \begin{pmatrix} 1 & 0 & 0 & 0 \\ 0 & 1 & 0 & 0 \\ 0 & 0 & 1 & 59 \\ 0 & 0 & 0 & 1 \end{pmatrix} \qquad A_{1,0} := \left(A_{0,1}\right)^{-1} \qquad A_{1,0} = \begin{pmatrix} 1 & 0 & 0 & 0 \\ 0 & 1 & 0 & 0 \\ 0 & 0 & 1 & -59 \\ 0 & 0 & 0 & 1 \end{pmatrix}$$

$$A_{1,2} = \begin{pmatrix} 0 & -1 & 0 & 0 \\ 1 & 0 & 0 & 0 \\ 0 & 0 & 1 & 57.25 \\ 0 & 0 & 0 & 1 \end{pmatrix} \qquad A_{2,1} := \left(A_{1,2}\right)^{-1} \qquad A_{2,1} = \begin{pmatrix} 0 & 1 & 0 & 0 \\ -1 & 0 & 0 & 0 \\ 0 & 0 & 1 & -57.25 \\ 0 & 0 & 0 & 1 \end{pmatrix}$$

$$A_{2,3} = \begin{pmatrix} 1 & 0 & 0 & 0 \\ 0 & 0 & -1 & 0 \\ 0 & 1 & 0 & 0 \\ 0 & 0 & 0 & 1 \end{pmatrix} \qquad A_{3,2} := \left(A_{2,3}\right)^{-1} \qquad A_{3,2} = \begin{pmatrix} 1 & 0 & 0 & 0 \\ 0 & 0 & 1 & 0 \\ 0 & -1 & 0 & 0 \\ 0 & 0 & 0 & 1 \end{pmatrix}$$

$$A_{3,4} = \begin{pmatrix} 0 & 0 & 1 & 0 \\ 1 & 0 & 0 & 0 \\ 0 & 1 & 0 & 0 \\ 0 & 0 & 0 & 1 \end{pmatrix} \qquad A_{4,3} := \left(A_{3,4}\right)^{-1} \qquad A_{4,3} = \begin{pmatrix} 0 & 1 & 0 & 0 \\ 0 & 0 & 1 & 0 \\ 1 & 0 & 0 & 0 \\ 0 & 0 & 0 & 1 \end{pmatrix}$$

$$A_{4,5} = \begin{pmatrix} 1 & 0 & 0 & 0 \\ 0 & 1 & 0 & 0 \\ 0 & 0 & 1 & 280 \\ 0 & 0 & 0 & 1 \end{pmatrix} \qquad A_{5,4} := \left(A_{4,5}\right)^{-1} \qquad A_{5,4} = \begin{pmatrix} 1 & 0 & 0 & 0 \\ 0 & 1 & 0 & 0 \\ 0 & 0 & 1 & -280 \\ 0 & 0 & 0 & 1 \end{pmatrix}$$

Front End to Base

The homogeneous matrix T_{05} specifies the location of the 5th co-ordinate frame with respect to the base co-ordinate system

$$T_{0,5} := A_{0,1}\cdot A_{1,2}\cdot A_{2,3}\cdot A_{3,4}\cdot A_{4,5} \qquad T_{5,0} := \left(T_{0,5}\right)^{-1}$$

$$T_{0,5} = \begin{pmatrix} 0 & 1 & 0 & 0 \\ 0 & 0 & 1 & 280 \\ 1 & 0 & 0 & 116.25 \\ 0 & 0 & 0 & 1 \end{pmatrix} \qquad T_{5,0} = \begin{pmatrix} 0 & 0 & 1 & -116.25 \\ 1 & 0 & 0 & -0 \\ 0 & 1 & 0 & -280 \\ 0 & 0 & 0 & 1 \end{pmatrix}$$

The homogeneous matrix T_{25} specifies the location of the 5th co-ordinate frame with respect to the Origin co-ordinate system

$$T_{2,5} := A_{2,3}\cdot A_{3,4}\cdot A_{4,5} \qquad T_{5,2} := \left(T_{2,5}\right)^{-1}$$

$$T_{2,5} = \begin{pmatrix} 0 & 0 & 1 & 280 \\ 0 & -1 & 0 & -0 \\ 1 & 0 & 0 & -0 \\ 0 & 0 & 0 & 1 \end{pmatrix} \qquad T_{5,2} = \begin{pmatrix} 0 & 0 & 1 & 0 \\ 0 & -1 & 0 & 0 \\ 1 & 0 & 0 & -280 \\ 0 & 0 & 0 & 1 \end{pmatrix}$$

Forward Kinematics Equation for the Laser End-Effector

The homogeneous matrix T_{0i} which specifies the location of the ith coordinate fram with respect to the base coordinate system is the chain product of successive coordinate transformation matrices of $A_{(i-1)i}$ and expressed as

$$T_{0,5} := A_{0,1} A_{1,2} A_{2,3} A_{3,4} A_{4,5} \qquad G := T_{0,5}$$

$$T_{i,(i+1)} := \begin{pmatrix} x_i & y_i & z_i & p_i \\ 0 & 0 & 0 & 1 \end{pmatrix} \qquad T_{0,5} := \begin{pmatrix} R_{05} & p_{05} \\ 0 & 1 \end{pmatrix}$$

Where

$[x_i, y_i, z_i]$ is the orentation matrix of the i^{th} coordinate system established at link i with respect to the base coordinate system. It is the upper left 3 xl3 partitioned marix of T_{0i}

P_i is the position vector which points from the originof the base coorinate system to the origin of the ith coordinate system. It is the upper right 3 x 1 partionend matrix of T_{0i}

<u>In general</u>

$$A_{i,(i+1)} := \begin{pmatrix} \cos(\theta_i) & -\cos(\alpha_i)\cdot\sin(\theta_i) & \sin(\alpha_i)\cdot\sin(\theta_i) & a_i\cdot\cos(\theta_i) \\ \sin(\theta_i) & \cos(\alpha_i)\cdot\sin(\theta_i) & -\sin(\alpha_i)\cdot\cos(\theta_i) & a_i\cdot\sin(\theta_i) \\ 0 & \sin(\alpha_i) & \cos(\alpha_i) & d_i \\ 0 & 0 & 0 & 1 \end{pmatrix}$$

$$C_i := \cos(\theta_i) \qquad S_i := \sin(\theta_i)$$

Thus

$$A_{0,1} := \begin{pmatrix} C_0 & -S_0 & 0 & 0 \\ S_0 & C_0 & 0 & 0 \\ 0 & 0 & 1 & d_0 \\ 0 & 0 & 0 & 1 \end{pmatrix} \qquad A_{1,2} := \begin{pmatrix} C_1 & -S_1 & 0 & 0 \\ S_1 & C_1 & 0 & 0 \\ 0 & 0 & 1 & d_1 \\ 0 & 0 & 0 & 1 \end{pmatrix} \qquad A_{2,3} := \begin{pmatrix} C_2 & 0 & S_2 & 0 \\ S_2 & 0 & -C_2 & 0 \\ 0 & 1 & 0 & d_2 \\ 0 & 0 & 0 & 1 \end{pmatrix}$$

$$A_{3,4} := \begin{pmatrix} C_3 & 0 & S_3 & 0 \\ S_3 & 0 & -C_3 & 0 \\ 0 & 1 & 0 & d_3 \\ 0 & 0 & 0 & 1 \end{pmatrix} \qquad A_{4,5} := \begin{pmatrix} C_4 & -S_4 & 0 & 0 \\ S_4 & C_4 & 0 & 0 \\ 0 & 0 & 1 & d_4 \\ 0 & 0 & 0 & 1 \end{pmatrix}$$

Let $T_1 := A_{0,1}\cdot A_{1,2}\cdot A_{2,3}$ and $T_2 := A_{3,4}\cdot A_{4,5}$

This will lead to

$$T_1 := \begin{bmatrix} \left[C_2\cdot(C_0\cdot C_1 - S_0\cdot S_1)\right] - S_2\cdot(C_0 S_1 + S_0 C_1) & 0 & S_2(C_0 C_1 - S_0 S_1) + C_2(C_0 S_1 - S_0 C_1) & 0 \\ C_2(S_0 C_1 + C_0 S_1) - S_0 S_1 S_2 - C_0 C_1 S_2 & 0 & S_2(S_0 C_1 + C_0 S_1) + C_2(S_0 S_1 - C_0 C_1) & 0 \\ 0 & 1 & 0 & 116.25 \\ 0 & 0 & 0 & 1 \end{bmatrix}$$

Let

$$U11 := \left[C_2\cdot(C_0\cdot C_1 - S_0\cdot S_1)\right] - S_2\cdot(C_0\cdot S_1 + S_0\cdot C_1)$$

$$U13 := S_2\cdot(C_0\cdot C_1 - S_0\cdot S_1) + C_2\cdot(C_0\cdot S_1 - S_0\cdot C_1)$$

$$U21 := C_2\cdot(S_0\cdot C_1 + C_0\cdot S_1) - S_0\cdot S_1\cdot S_2 - C_0\cdot C_1\cdot S_2$$

$$U23 := S_2\cdot(S_0\cdot C_1 + C_0\cdot S_1) + C_2\cdot(S_0\cdot S_1 - C_0\cdot C_1)$$

$$T_2 := \begin{pmatrix} C_3 & 0 & S_3 & 0 \\ S_3 & 0 & -C_3 & 0 \\ 0 & 1 & 0 & d_3 \\ 0 & 0 & 0 & 1 \end{pmatrix}\cdot\begin{pmatrix} C_4 & -S_4 & 0 & 0 \\ S_4 & C_4 & 0 & 0 \\ 0 & 0 & 1 & d_4 \\ 0 & 0 & 0 & 1 \end{pmatrix} \qquad \text{Then} \qquad T_2 := \begin{pmatrix} C_3C_4 & -S_4C_3 & S_3 & d_4S_3 \\ S_3C_4 & -S_3S_4 & -C_3 & -d_4C_3 \\ S_4 & C_4 & 0 & 0 \\ 0 & 0 & 0 & 1 \end{pmatrix}$$

$$T := \begin{pmatrix} U11 & 0 & U13 & 0 \\ U21 & 0 & U23 & 0 \\ 0 & 1 & 0 & 116.25 \\ 0 & 0 & 0 & 1 \end{pmatrix}\cdot\begin{pmatrix} C_3C_4 & -S_4C_3 & S_3 & d_4S_3 \\ S_3C_4 & -S_3S_4 & -C_3 & -d_4C_3 \\ S_4 & C_4 & 0 & 0 \\ 0 & 0 & 0 & 1 \end{pmatrix}$$

$$T := \begin{bmatrix} U11\cdot(C_3C_4) + U13\cdot(S_4) & -U11\cdot(S_4C_3) + U13\cdot(C_4) & U11\cdot(S_3) & U11\cdot(d_4S_3) \\ U21\cdot(C_3C_4) + U23\cdot(S_4) & -U21\cdot(S_4C_3) + U23\cdot(C_4) & U21\cdot(S_3) & U21\cdot(d_4S_3) \\ S_3C_4 & -S_3S_4 & -C_3 & -d_4C_3 + 116.25 \\ 0 & 0 & 0 & 1 \end{bmatrix}$$

Thus the vector X (nx,ny,nz) can be calculated from the following

$$nx := U11\cdot(C_3\cdot C_4) + U13\cdot(S_4)$$

$$ny := U21\cdot(C_3\cdot C_4) + U23\cdot(S_4)$$

$$nx := \left[C_2\cdot(C_0\cdot C_1 - S_0\cdot S_1) - S_2\cdot(C_0\cdot S_1 + S_0\cdot C_1)\right]\cdot C_3\cdot C_4 + S_4\cdot\left[S_2\cdot(C_0\cdot C_1 - S_0\cdot S_1) + C_2\cdot(C_0\cdot S_1 - S_0\cdot C_1)\right]$$

$$ny := \left[C_2\cdot(S_0\cdot C_1 + C_0\cdot S_1) - S_0\cdot S_1\cdot S_2 - C_0\cdot C_1\cdot S_2\right]\cdot C_3C_4 + S_4\left[S_2\cdot(S_0\cdot C_1 + C_0\cdot S_1) + C_2\cdot(S_0\cdot S_1 - C_0\cdot C_1)\right]$$

$$nz := S_3C_4$$

$$X := (nx \;\; ny \;\; nz)^T \qquad X = \begin{pmatrix} 0 \\ 0 \\ 1 \end{pmatrix}$$

The vector Y (sx,sy,sz) can be calculated from the following

$$sx := -U11\cdot(S_4\cdot C_3) + U13\cdot(C_4)$$

$$sy := -U21\cdot(S_4\cdot C_3) + U23\cdot(C_4)$$

Hence

$$sx := \left[C_2\cdot(C_0\cdot C_1 - S_0\cdot S_1) - S_2\cdot(C_0\cdot S_1 + S_0\cdot C_1)\right]\cdot(-S_4\cdot C_3) + C_4\cdot\left[S_2\cdot(C_0\cdot C_1 - S_0\cdot S_1) + C_2\cdot(C_0\cdot S_1 - S_0\cdot C_1)\right.$$

$$sy := \left[C_2\cdot\left(S_0\cdot C_1 + C_0\cdot S_1\right) - S_0\cdot S_1\cdot S_2 - C_0\cdot C_1\cdot S_2\right]\cdot S_4 C_3 + C_4\left[S_2\cdot\left(S_0\cdot C_1 + C_0\cdot S_1\right) + C_2\cdot\left(S_0\cdot S_1 - C_0\cdot C_1\right)\right]$$

$$sz := -S_3 S_4$$

$$Y := (sx \;\; sy \;\; sz)^T \qquad Y = \begin{pmatrix} 1 \\ 0 \\ 0 \end{pmatrix}$$

The Vector Z(ax,ay,az) can be be found from the following

$$ax := U11\cdot\left(S_3\right)$$

$$ay := U21\cdot\left(S_3\right)$$

Hence

$$ax := S_3\cdot\left[C_2\cdot\left(C_0\cdot C_1 - S_0\cdot S_1\right) - S_2\cdot\left(C_0\cdot S_1 + S_0\cdot C_1\right)\right]$$

$$ay := S_3\cdot\left[C_2\cdot\left(S_0\cdot C_1 + C_0\cdot S_1\right) - S_0\cdot S_1\cdot S_2 - C_0\cdot C_1\cdot S_2\right]$$

$$az := -C_3$$

$$Z := (ax \;\; ay \;\; az)^T \qquad Z = \begin{pmatrix} 0 \\ 1 \\ 0 \end{pmatrix}$$

The Rotation matrix R is

$$R := (X \;\; Y \;\; Z) \qquad R = \left[\begin{pmatrix} 0 \\ 0 \\ 1 \end{pmatrix} \begin{pmatrix} 1 \\ 0 \\ 0 \end{pmatrix} \begin{pmatrix} 0 \\ 1 \\ 0 \end{pmatrix}\right]$$

And the Position Vector P (px,py,pz) can be found from the following

$$px := U11\cdot\left(d_4 S_3\right)$$

$$py := U21\cdot\left(d_4 S_3\right)$$

$$pz := -d_4 C_3 + 116.25$$

$$px := d_4\cdot S_3\cdot\left[C_2\cdot\left(C_0\cdot C_1 - S_0\cdot S_1\right) - S_2\cdot\left(C_0\cdot S_1 + S_0\cdot C_1\right)\right]$$

$$py := d_4 S_3\cdot\left[C_2\cdot\left(S_0\cdot C_1 + C_0\cdot S_1\right) - S_0\cdot S_1\cdot S_2 - C_0\cdot C_1\cdot S_2\right]$$

$$P := (px \;\; py \;\; pz)^T \qquad P = \begin{pmatrix} 0 \\ 280 \\ 116.25 \end{pmatrix}$$

The homogeneous transformation matrix T is

$$T := \begin{pmatrix} nx & sx & ax & px \\ ny & sy & ay & py \\ nz & sz & az & pz \\ 0 & 0 & 0 & 1 \end{pmatrix}$$

As a check for the End- Effector Home Position

$$T = \begin{pmatrix} 0 & 1 & 0 & 0 \\ 0 & 0 & 1 & 280 \\ 1 & 0 & 0 & 116.25 \\ 0 & 0 & 0 & 1 \end{pmatrix}$$

Note:- that maximum rotation angles are +/- 30 degrees H & V and the laser waveguide ranges from 200-360 mm in length

For

$$\theta_i := \begin{pmatrix} 0 \\ \frac{\pi}{2}+\frac{\pi}{18} \\ 0 \\ \frac{\pi}{2}+\frac{\pi}{9} \\ 0 \end{pmatrix} \quad \alpha_i := \begin{pmatrix} 0 \\ 0 \\ 0 \\ 0 \\ 0 \end{pmatrix} \quad d_i := \begin{pmatrix} 59 \\ 57.25 \\ 0 \\ 0 \\ 200 \end{pmatrix} \quad a_i := \begin{pmatrix} 0 \\ 0 \\ 0 \\ 0 \\ 0 \end{pmatrix} \quad C_i := \cos(\theta_i) \quad S_i := \sin(\theta_i)$$

$\vec{X}$

$$nx := \left[C_2\cdot(C_0\cdot C_1 - S_0\cdot S_1) - S_2\cdot(C_0\cdot S_1 + S_0\cdot C_1)\right]\cdot C_3\cdot C_4 + S_4\cdot\left[S_2\cdot(C_0\cdot C_1 - S_0\cdot S_1) + C_2\cdot(C_0\cdot S_1 - S_0\cdot C_1)\right]$$

$$ny := \left[C_2\cdot(S_0\cdot C_1 + C_0\cdot S_1) - S_0\cdot S_1\cdot S_2 - C_0\cdot C_1\cdot S_2\right]\cdot C_3 C_4 + S_4\left[S_2\cdot(S_0\cdot C_1 + C_0\cdot S_1) + C_2\cdot(S_0\cdot S_1 - C_0\cdot C_1)\right]$$

$$nz := S_3 C_4$$

$\vec{Y}$

$$sx := \left[C_2\cdot(C_0\cdot C_1 - S_0\cdot S_1) - S_2\cdot(C_0\cdot S_1 + S_0\cdot C_1)\right]\cdot(-S_4\cdot C_3) + C_4\cdot\left[S_2\cdot(C_0\cdot C_1 - S_0\cdot S_1) + C_2\cdot(C_0\cdot S_1 - S_0\cdot C_1)\right.$$

$$sy := \left[C_2\cdot(S_0\cdot C_1 + C_0\cdot S_1) - S_0\cdot S_1\cdot S_2 - C_0\cdot C_1\cdot S_2\right]\cdot S_4 C_3 + C_4\left[S_2\cdot(S_0\cdot C_1 + C_0\cdot S_1) + C_2\cdot(S_0\cdot S_1 - C_0\cdot C_1)\right]$$

$$sz := -S_3 S_4$$

$\vec{Z}$

$$ax := S_3\cdot\left[C_2\cdot(C_0\cdot C_1 - S_0\cdot S_1) - S_2\cdot(C_0\cdot S_1 + S_0\cdot C_1)\right]$$

$$ay := S_3\cdot\left[C_2\cdot(S_0\cdot C_1 + C_0\cdot S_1) - S_0\cdot S_1\cdot S_2 - C_0\cdot C_1\cdot S_2\right]$$

$$az := -C_3$$

$\vec{P}$

$$px := d_4\cdot S_3\cdot\left[C_2\cdot(C_0\cdot C_1 - S_0\cdot S_1) - S_2\cdot(C_0\cdot S_1 + S_0\cdot C_1)\right]$$

$$py := d_4 S_3\left[C_2\cdot(S_0\cdot C_1 + C_0\cdot S_1) - S_0\cdot S_1\cdot S_2 - C_0\cdot C_1\cdot S_2\right]$$

$$pz := -d_4 C_3 + 116.25$$

$$P := (px \;\; py \;\; pz)^T \qquad P = \begin{pmatrix} 0 \\ 200 \\ 116.25 \end{pmatrix}$$

The homogeneous transformation matrix T is

$$Ttest := \begin{pmatrix} nx & sx & ax & px \\ ny & sy & ay & py \\ nz & sz & az & pz \\ 0 & 0 & 0 & 1 \end{pmatrix}$$

$$Ttest = \begin{pmatrix} 0 & 1 & 0 & 0 \\ 0 & 0 & 1 & 200 \\ 1 & 0 & 0 & 116.25 \\ 0 & 0 & 0 & 1 \end{pmatrix} \qquad Ttest^{-1} = \begin{pmatrix} 0 & 0 & 1 & -116.25 \\ 1 & 0 & 0 & 0 \\ 0 & 1 & 0 & -200 \\ 0 & 0 & 0 & 1 \end{pmatrix}$$

Since $\theta_0 = \theta_2 = \theta_4 = 0$

$$C_0 = 1 \qquad S_0 = 0$$
$$C_2 = 1 \qquad S_2 = 0$$
$$C_4 = 1 \qquad S_4 = 0$$

This will lead to

$\vec{n}$	$\vec{s}$	$\vec{a}$	$\vec{p}$
$nx := C_1 \cdot C_3$	$sx := S_1$	$ax := S_3 \cdot C_1$	$px := d_4 \cdot S_3 \cdot C_1$
$ny := S_1 \cdot C_3$	$sy := -C_1$	$ay := S_3 \cdot S_1$	$py := d_4 \cdot S_3 \cdot S_1$
$nz := S_3$	$sz := 0$	$az := -C_3$	$pz := -d_4 C_3 + 116.25$

And the homogeneous transformation matrix TR would be

$$TR := \begin{pmatrix} C_1 \cdot C_3 & S_1 & S_3 \cdot C_1 & d_4 \cdot S_3 \cdot C_1 \\ S_1 \cdot C_3 & -C_1 & S_3 \cdot S_1 & d_4 \cdot S_3 \cdot S_1 \\ S_3 & 0 & -C_3 & -d_4 C_3 + 116.25 \\ 0 & 0 & 0 & 1 \end{pmatrix} \qquad TR = \begin{pmatrix} 0 & 1 & 0 & 1.225 \times 10^{-14} \\ 0 & 0 & 1 & 200 \\ 1 & 0 & 0 & 116.25 \\ 0 & 0 & 0 & 1 \end{pmatrix}$$

From the above we can sea that

$$nz := \sin(\theta_3) \qquad sx := \sin(\theta_1) \qquad sy := -\cos(\theta_1) \qquad az := -\cos(\theta_3)$$

Hence

$nx := C_1 C_3$	$nx := sy \cdot az$	$sx := S_1$	$sx := sx$
$ny := S_1 C_3$	$ny := -sx \cdot az$	$sy := -C_1$	$sy := sy$
$nz := S_3$	$nz := nz$	$sz := 0$	$sz := 0$
$ax := S_3 \cdot C_1$	$ax := -nz \cdot sy$	$Px := d_4 \cdot S_3 \cdot C_1$	$Px := -d_4 nz \cdot sy$
$ay := S_3 S_1$	$ay := nz \cdot sx$	$Py := d_4 \cdot S_3 \cdot S_1$	$Py := d_4 \cdot nz \cdot sx$
$az := -C_3$	$az := az$	$Pz := -d_4 C_3 + 116.25$	$Pz := d_4 \cdot az + 116.25$

Therefore homogeneous transformation matrix HTM would be

$$HTM := \begin{pmatrix} sy \cdot az & sx & -nz \cdot sy & -d_4 \cdot nz \cdot sy \\ -sx \cdot az & sy & nz \cdot sx & d_4 \cdot nz \cdot sx \\ nz & 0 & az & d_4 \cdot az + 116.25 \\ 0 & 0 & 0 & 1 \end{pmatrix} \qquad HTM = \begin{pmatrix} 0 & 1 & 0 & 0 \\ 0 & 0 & 1 & 200 \\ 1 & 0 & 0 & 116.25 \\ 0 & 0 & 0 & 1 \end{pmatrix}$$

Inverse Kinematics

Given the homogeneous transformation matrix by the Optical Tracking system with reference to the dynamic reference frame coordinate system, one can drive the homogeneous transformation matrix **HTM** in the base coordinate system from which the angles of rotation and displacements can be calculated.

Note: Assuming the rotation matrix given by the Optic tracing system is given in unit vectors

Inverse Kinematics Example:-

Given the following HTM calculate θ1, θ2 and D

$$HTM := \begin{pmatrix} C_1 \cdot C_3 & S_1 & S_3 \cdot C_1 & d_4 \cdot S_3 \cdot C_1 \\ S_1 \cdot C_3 & -C_1 & S_3 \cdot S_1 & d_4 \cdot S_3 \cdot S_1 \\ S_3 & 0 & -C_3 & -d_4 C_3 + 116.25 \\ 0 & 0 & 0 & 1 \end{pmatrix} \qquad HTM := \begin{pmatrix} sy \cdot az & sx & -nz \cdot sy & -d_4 \cdot nz \cdot sy \\ -sx \cdot az & sy & nz \cdot sx & d_4 \cdot nz \cdot sx \\ nz & 0 & az & d_4 \cdot az + 116.25 \\ 0 & 0 & 0 & 1 \end{pmatrix}$$

Giving that

$$\theta 1 := \theta_1 - \frac{\pi}{2} \qquad \text{and} \qquad \theta 3 := \theta_3 - \frac{\pi}{2} \qquad HTM = \begin{pmatrix} 0 & 1 & 0 & 1.225 \times 10^{-14} \\ 0 & 0 & 1 & 200 \\ 1 & 0 & 0 & 116.25 \\ 0 & 0 & 0 & 1 \end{pmatrix}$$

where

θ1	is the rotation angle about the Z axis at the origin (Joint 2) ranging from -(π/6 to π/6)
θ3	is the rotation angle about the X axis at the origin (Joint 2) ranging from -(π/6 to π/6)
d_4	is the displacement of the End Effector in the direction of application ranging from 200mm to 360 mm

Also knowing that from homogeneous transformation matrix HTM

$sx := \sin(\theta_1)$ $\quad sy := -\cos(\theta_1)$ $\quad$ And $\quad nz := \sin(\theta_3)$ $\quad az := -\cos(\theta_3)$

$\theta_1 := \text{acos}(-sy)$ $\qquad \theta_1 = 1.745$ rad

$\theta 1 = 0.175$ rad $\qquad \theta 1 := 0.175 \cdot \frac{180}{\pi}$ $\qquad \theta 1 = 10$ Deg

$\theta_3 := \text{acos}(-az)$ $\qquad \theta_3 = 1.92$ rad

$\theta 3 = 0.349$ rad $\qquad \theta 3 := 0.349 \cdot \frac{180}{\pi}$ $\qquad \theta 3 = 20$ Deg

$Pz = 116.25$

$Pz := d_4 \cdot az + 116.25$

$$d_4 := \frac{(Pz - 116.25)}{az}$$

$d_4 = 200$

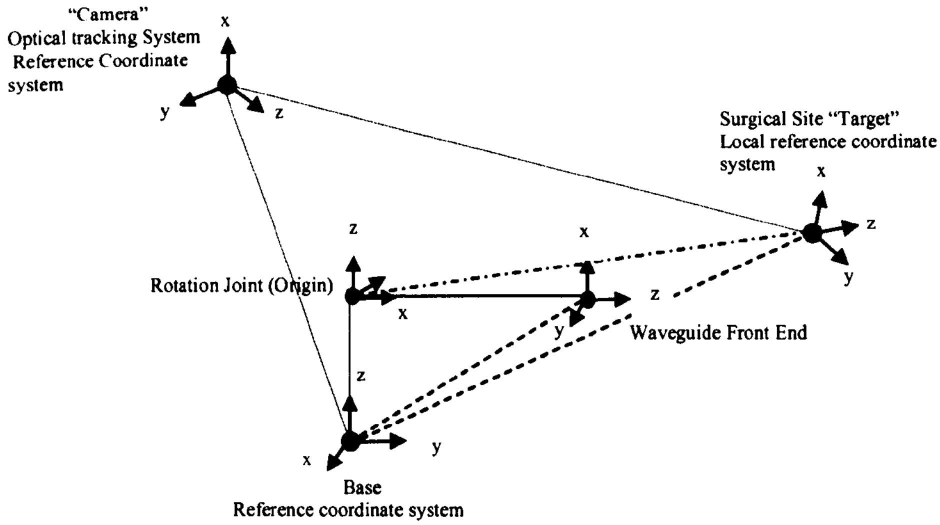

Figure 4:Feedback mechanism relating the surgical site or target and End Effector base to the camera coordinate system

The Figure above relates the local coordinate systems of both the End Effector's base and the surgical site to the camera or optical track coordinate system. The camera is able to see the two coordinate systems and generate a transformation matrix for each of the target and the base relative to its own coordinate system

Given a homogeneous transformation matrix of the surgical site (Target) by the optical tracking system (camera) relative to its origin, one has to drive the homogeneous transformation matrix of the Target relative the base coordinate system of the End-Effector HTM. Hence, given the HTM and using the drived equations above one can calculate the horizontal and vertical rotation angles q1 and q2, and the linear translation displacement of the laser waveguide in the direction of application d_4.

$$T_{Camera-Target} := \begin{pmatrix} n & s & a & p \\ 0 & 0 & 0 & 1 \end{pmatrix} \qquad T_{Camera-Base} := \begin{pmatrix} N & S & A & P \\ 0 & 0 & 0 & 1 \end{pmatrix}$$

where

n, s, a are the rotation (orientation) vectors of the Target with respect to the Cameras' coordinate system

p is the position vector of the Target relative to the Camera coordinate system

N, S, A are the orientation vectors of the Base with respect to the Camera coordinate system

P is the Position vector of the Base with respect to the Camera coordinate system

The above matrices can also be expressed as follow

$$T_{Camera-Target} := \begin{pmatrix} n_x & s_x & a_x & p_x \\ n_y & s_y & a_y & p_y \\ n_z & s_z & a_z & p_z \\ 0 & 0 & 0 & 1 \end{pmatrix} \qquad T_{Camera-Base} := \begin{pmatrix} N_x & S_x & A_x & P_x \\ N_y & S_y & A_y & P_y \\ N_z & S_z & A_z & p_z \\ 0 & 0 & 0 & 1 \end{pmatrix}$$

$$T_{Base-Target} := T_{Base-Camera} \cdot T_{Camera-Target}$$

$$T_{Base-Target} := \left(T_{Camera-Base}\right)^{-1} \cdot T_{Camera-Target}$$

$$T_{Base-Camera} := \begin{pmatrix} n_x & n_y & n_z & -n^T p \\ s_x & s_y & s_z & -s^T p \\ a_x & a_y & a_z & -a^T p \\ 0 & 0 & 0 & 1 \end{pmatrix}$$

Then

$$T_{Base-Target} := \begin{pmatrix} n_x & n_y & n_z & -n^T p \\ s_x & s_y & s_z & -s^T p \\ a_x & a_y & a_z & -a^T p \\ 0 & 0 & 0 & 1 \end{pmatrix} \cdot \begin{pmatrix} N_x & S_x & A_x & P_x \\ N_y & S_y & A_y & P_y \\ N_z & S_z & A_z & p_z \\ 0 & 0 & 0 & 1 \end{pmatrix}$$

where

$$n^T := \begin{pmatrix} n_x & n_y & n_z \end{pmatrix} \qquad s^T := \begin{pmatrix} s_x & s_y & s_z \end{pmatrix} \qquad a^T := \begin{pmatrix} a_x & a_y & a_z \end{pmatrix} \qquad p := \begin{pmatrix} p_x \\ py \\ pz \end{pmatrix}$$

Therefore

$$-n^T P := -\left(n_x p_x + n_y p_y + n_z p_z\right)$$

$$-s^T P := -\left(s_x p_x + s_y p_y + s_z p_z\right)$$

$$-a^T P := -\left(a_x p_x + a_y p_y + a_z p_z\right)$$

Now let

$$T_{Base-Target} := T_{BT}$$

Then

$$T_{BT} := \begin{pmatrix} n_x N_x + n_y N_y + n_z N_z & n_x \cdot S_x + n_y \cdot S_y + n_z \cdot S_z & n_x \cdot A_x + n_y \cdot A_y + n_z \cdot A_z & n_x \cdot P_x + n_y \cdot P_y + n_z \cdot P_z - n^T p \\ s_x \cdot N_x + s_y \cdot N_y + s_z \cdot N_z & s_x \cdot S_x + s_y \cdot S_y + s_z \cdot S_z & s_x \cdot A_x + s_y \cdot A_y + s_z \cdot A_z & s_x \cdot P_x + s_y \cdot P_y + s_z \cdot P_z - s^T p \\ a_x \cdot N_x + a_y \cdot N_y + a_z \cdot N_z & a_x \cdot S_x + a_y \cdot S_y + a_z \cdot S_z & a_x \cdot A_x + a_y \cdot A_y + a_z \cdot A_z & a_x \cdot P_x + a_y \cdot P_y + a_z \cdot P_z - a^T p \\ 0 & 0 & 0 & 1 \end{pmatrix}$$

Which can also be expressed as follow

$$T_{BT} := \begin{bmatrix} n^T N & n^T S & n^T A & n^T (P - p) \\ s^T N & s^T S & s^T A & s^T (P - p) \\ a^T N & a^T S & a^T A & a^T (P - p) \\ 0 & 0 & 0 & 1 \end{bmatrix}$$

where

$$n := \begin{pmatrix} n_x \\ n_y \\ n_z \end{pmatrix} \qquad s := \begin{pmatrix} s_x \\ s_y \\ s_z \end{pmatrix} \qquad a := \begin{pmatrix} a_x \\ a_y \\ a_z \end{pmatrix} \qquad p := \begin{pmatrix} p_x \\ p_y \\ p_z \end{pmatrix}$$

$$N := \begin{pmatrix} N_x \\ N_y \\ N_z \end{pmatrix} \qquad S := \begin{pmatrix} S_x \\ S_y \\ S_z \end{pmatrix} \qquad A := \begin{pmatrix} A_x \\ A_y \\ A_z \end{pmatrix} \qquad P := \begin{pmatrix} P_x \\ P_y \\ P_z \end{pmatrix}$$

Comparing the above matrix with the Homogeneous Transformation Matrix of the End Effector base co-ordinates

$$HTM := \begin{pmatrix} C_1 \cdot C_3 & S_1 & S_3 \cdot C_1 & d_4 \cdot S_3 \cdot C_1 \\ S_1 \cdot C_3 & -C_1 & S_3 \cdot S_1 & d_4 \cdot S_3 \cdot S_1 \\ S_3 & 0 & -C_3 & -d_4 C_3 + 116.25 \\ 0 & 0 & 0 & 1 \end{pmatrix}$$

$$\begin{bmatrix} n^T N & n^T S & n^T A & n^T (P-p) \\ s^T N & s^T S & s^T A & s^T (P-p) \\ a^T N & a^T S & a^T A & a^T (P-p) \\ 0 & 0 & 0 & 1 \end{bmatrix} \equiv \begin{pmatrix} C_1 \cdot C_3 & S_1 & S_3 \cdot C_1 & d_4 \cdot S_3 \cdot C_1 \\ S_1 \cdot C_3 & -C_1 & S_3 \cdot S_1 & d_4 \cdot S_3 \cdot S_1 \\ S_3 & 0 & -C_3 & -d_4 C_3 + 116.25 \\ 0 & 0 & 0 & 1 \end{pmatrix}$$

Then

$a^T N := \sin(\theta_3)$ $\qquad a^T A := -\cos(\theta_3)$ $\qquad a^T S := 0$

$n^T S := \sin(\theta_1)$ $\qquad s^T S := -\cos(\theta_1)$

$n^T (P-p) := d_4 \cdot S_3 \cdot C_1$

$s^T (P-p) := d_4 \cdot S_3 \cdot S_1$

$a^T (P-p) := -d_4 C_3 + 116.25$

For The Inverse Kinematics of the Laser End Effector

$\theta_1 := \operatorname{asin}(a^T S)$ or $\theta_1 := \operatorname{acos}[-(s^T S)]$ and $\theta 1 := \theta_1 - \frac{\pi}{2}$

$\theta_3 := \operatorname{asin}(a^T N)$ or $\theta_3 := \operatorname{acos}[-(a^T A)]$ and $\theta 3 := \theta_1 - \frac{\pi}{2}$

$d_4 := \dfrac{[[a^T \cdot (P-p)] - 116.25]}{-\cos(\theta_3)}$ or $d_4 := \dfrac{[n^T \cdot (P-p)]}{\sin(\theta_3) \cdot \cos(\theta_1)}$ or $d_4 := \dfrac{[s^T \cdot (P-p)]}{\sin(\theta_3) \cdot \sin(\theta_1)}$

Hence given the transformation Matrices of the Target and the Base with respect to the Camera co-ordinate system one can drive the transformation matrix of the Target with respect the base co-ordinates. he/she can also calculate the required kinematic parameters of the End - Effector.

Inverse Kinematics Example:-

A Target is placed within the workspace of the laser End Effector and its origin can be seen by an optical tracking system (Camera). The Camera can also see the origin of the Base coordinate system of the End Effector. If the local coordinate system has been established at origin of the Target, this coordinate as seen by the Camera can be represented by a homogeneous transformation matrix T_{ct}. The origin of the Base coordinate system can also be expressed by a homogeneous coordinate matrix T_{cb} with respect to the Camera coordinate system.

Assuming $\alpha 1 := 20$ $\qquad \alpha 2 := 10$

$$Tct := \begin{pmatrix} 0.059 & 0.342 & 0.059 & 50 \\ -0.163 & -0.94 & 0.925 & 110 \\ 0.985 & 0 & 0.1736 & 10 \\ 0 & 0 & 0 & 1 \end{pmatrix} \quad \text{and} \quad Tcb := \begin{pmatrix} 0 & 1 & 0 & 100 \\ 1 & 0 & 0 & 20 \\ 0 & 0 & 1 & 129 \\ 0 & 0 & 0 & 1 \end{pmatrix}$$

Solution

To find the position and orientation (Tbt)of the Target with respect to the End Effector Base coordinate system we use the following chain product

$$Tbt := Tcb^{-1} \cdot Tct$$

$$Tcb^{-1} = \begin{pmatrix} 0 & 1 & 0 & -20 \\ 1 & 0 & 0 & -100 \\ 0 & 0 & 1 & -129 \\ 0 & 0 & 0 & 1 \end{pmatrix} \quad \text{Thus} \quad Tbt = \begin{pmatrix} -0.163 & -0.94 & 0.925 & 90 \\ 0.059 & 0.342 & 0.059 & -50 \\ 0.985 & 0 & 0.174 & -119 \\ 0 & 0 & 0 & 1 \end{pmatrix}$$

Knowing that

$$Tbt := \begin{pmatrix} C_1 \cdot C_3 & S_1 & S_3 \cdot C_1 & d_4 \cdot S_3 \cdot C_1 \\ S_1 \cdot C_3 & -C_1 & S_3 \cdot S_1 & d_4 \cdot S_3 \cdot S_1 \\ S_3 & 0 & -C_3 & -d_4 C_3 + 116.25 \\ 0 & 0 & 0 & 1 \end{pmatrix} \quad \text{or} \quad Tbt := \begin{bmatrix} n^T N & n^T S & n^T A & n^T (P-p) \\ s^T N & s^T S & s^T A & s^T (P-p) \\ a^T N & a^T S & a^T A & a^T (P-p) \\ 0 & 0 & 0 & 1 \end{bmatrix}$$

$$\theta_1 := \mathrm{acos}\left[-\left(s^T S\right)\right] \quad \text{and} \quad \theta 1 := \theta_1 - \frac{\pi}{2} \qquad d_4 := \frac{\left[\left[a^T \cdot (P-p)\right] - 116.25\right]}{-\cos(\theta_3)}$$

$$\theta_3 := \mathrm{acos}\left[-\left(a^T A\right)\right] \quad \text{and} \quad \theta 3 := \theta_1 - \frac{\pi}{2}$$

Using the above equations

$$\theta 3 := \mathrm{acos}(-0.174) - \frac{\pi}{2} \qquad \theta 3 = 0.175 \ \text{rad} \qquad \theta 3 := 0.175 \cdot \frac{180}{\pi} \qquad \theta 3 = 10.027 \ \text{Deg}$$

$$\theta 1 := \mathrm{acos}(-0.342) - \frac{\pi}{2} \qquad \theta 1 = 0.349 \ \text{rad} \qquad \theta 1 := 0.349 \cdot \frac{180}{\pi} \qquad \theta 1 = 19.996 \ \text{Deg}$$

$$d_4 := \frac{(-119 - 116.25)}{-\cos(0.174)} \qquad d_4 = 238.857 \ \text{mm} \qquad \Delta d := d_4 - 200 \qquad \Delta d = 38.857 \ \text{mm}$$

End Effector Workspace

Basic Requirements and Limitations

One of the major requirements of the End Effector applications is that, the surgical site should be within the reachability or the workspace of the laser End Effector which is limited in the angular and displacement movements and the number of degrees of freedom.

End Effector's Workspace Limitations

- Maximum rotation angle is 60 degrees ($\pi/6$) ranging from ($-\pi/6$ to $\pi/6$) vertical or Horizontal
- Maximum linear displacement of the laser waveguide is 160mm ranging from 200 - 360 mm

Given

$j := 0..20 \qquad i := 0..20 \qquad k := 0..5 \qquad D_k :=$

$$\theta_i := \frac{\pi}{2} + \frac{(i-10)\cdot\pi}{60} \qquad \theta 1_i := \frac{(i-10)\cdot\pi}{60}$$

$$\theta_j := \frac{\pi}{2} + \frac{(j-10)\cdot\pi}{60} \qquad \theta 3_j := \frac{(j-10)\cdot\pi}{60}$$

59
57.25
0
0
200

where

$\theta 1$ is the rotation angle about the Z axis at the origin (Joint 2) ranging from -($\pi/6$ to $\pi/6$)

$\theta 3$ is the rotation angle about the X axis at the origin (Joint 2) ranging from -($\pi/6$ to $\pi/6$)

D is the displacement of the End Effector in the direction of application ranging from 200mm to 360 mm

Let

$C_i := \cos(\theta_i) \qquad S_i := \sin(\theta_i) \qquad d := D_4 \qquad C_j := \cos(\theta_j) \qquad S_j := \sin(\theta_j)$

Given the homogeneous transformation matrix HTm

$$HTm_{i,j} := \begin{pmatrix} C_i \cdot C_j & S_i & S_j \cdot C_i & d \cdot S_j \cdot C_i \\ S_i \cdot C_j & -C_i & S_j \cdot S_i & d \cdot S_j \cdot S_i \\ S_j & 0 & -C_j & -d\,C_j + 116.25 \\ 0 & 0 & 0 & 1 \end{pmatrix}$$

Thus

$$P1x_{i,j} := d \cdot S_j \cdot C_i$$
$$P1y_{i,j} := d \cdot S_j \cdot S_i$$
$$P1z_{i,j} := -d\,C_j + 116.25$$

For maximum displacemen where d = 365

$d := 365$

$$HTm2_{i,j} := \begin{pmatrix} C_i \cdot C_j & S_i & S_j \cdot C_i & d \cdot S_j \cdot C_i \\ S_i \cdot C_j & -C_i & S_j \cdot S_i & d \cdot S_j \cdot S_i \\ S_j & 0 & -C_j & -d\,C_j + 116.25 \\ 0 & 0 & 0 & 1 \end{pmatrix}$$

Thus

$$P2x_{i,j} := d \cdot S_j \cdot C_i$$
$$P2y_{i,j} := d \cdot S_j \cdot S_i$$
$$P2z_{i,j} := -d\,C_j + 116.25$$

Figure 5 shows the workspace of the end Laser End-Effector

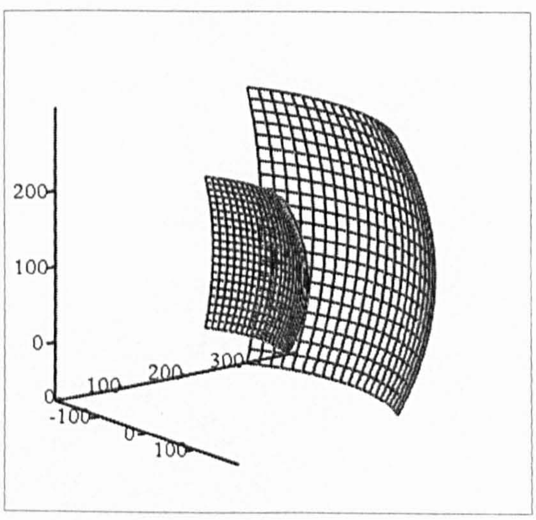

(P1x, P1y, P1z), (P2x, P2y, P2z)

Figure 5: The workspace of the laser End-Effector

Appendix E:

End-Effector's Design Components Data Sheets

End-Effector Design Electrical and Mechanical Components

GEARBOXES

CAD Drawings Available **PF20DU**

NEW Worm & Wheel Reduction Gearbox

Fitted with 24V DC Motor (0.50Nm - 2.10Nm)

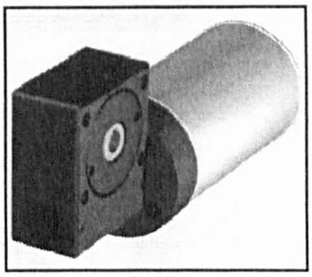

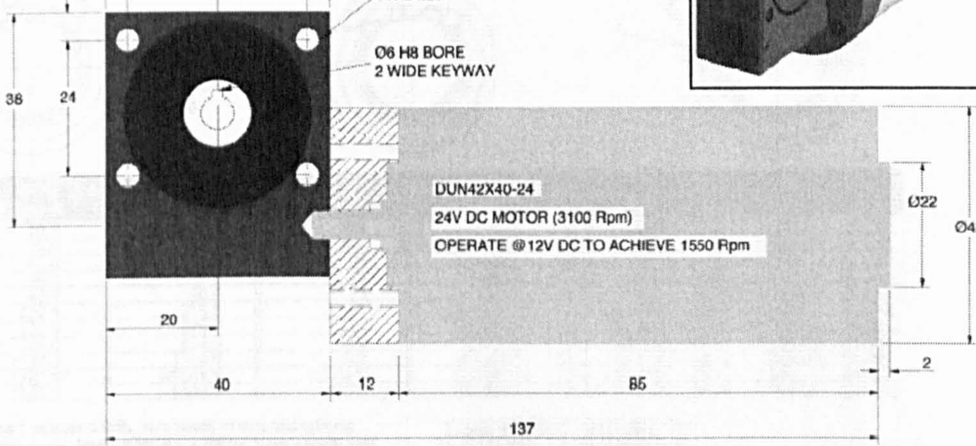

Part Number	Ratio	Input Speed Rpm	Nom. Output Rpm	Efficiency at 1000 Rpm	Nm Output at 1550Rpm Input	DC Motor	Price Each 1 - 5
PF20DU-10	10:1	1550	155.0	86%	0.50	DUN42x40-24	£200.52
PF20DU-12	12:1	1550	129.0	85%	0.70	DUN42x40-24	£200.52
PF20DU-15	15:1	1550	103.0	84%	0.80	DUN42x40-24	£200.52
PF20DU-20	20:1	1550	77.5	78%	1.10	DUN42x40-24	£200.52
PF20DU-30	30:1	1550	51.0	71%	1.70	DUN42x40-24	£200.52
PF20DU-60	60:1	1550	25.0	60%	2.10	DUN42x40-24	£200.52
PF20DU-120	120:1	1550	13.0	32%	1.25	DUN42x40-24	£200.52
PF20DU-SP	5:1 - 120:1	1550 Special Ratios: Replace **SP** with required ratio				DUN42x40-24	£228.21

Motor Part Number	Voltage (V)	No Load Speed (Rpm)	No Load Current (A)	Nominal Current (A)	Max. Efficiency	Nominal Torque (Ncm)	Nom. Speed (Rpm)	Moment of Inertia (gcm²)
DUN42x40-24	24	3800	0.175	1.22	63%	5.7	3100	110

Other input speeds available. For details of PF20 Gearbox or to purchase seperately, see page. For details of DUN42 DC Motor or to purchase seperately, see page.

24V DC Motor

Commutation: Graphite **Number of Sectors:** 12 **Brushes:** Rotary **Magnets:** Ferrite **Axial Backlash:** <0.15mm **Radial Backlash:** <0.15mm **Maximum Axial Load:** 30N **Maximum Radial Load at 20mm:** 60N **Maximum Shaft Push Pressure:** 200N **Operating Temperature Range:** -20°C to +85°C **Mass:** 0.49kg **Maximum Housing Temperature:** +85°C **Starting Voltage:** 1V.

Discounts

Qty.	1+	6+	20+
Disc	list	-8%	-14%

Other Info.

Motor performance data is based upon an operating temperature of +25°C. Testing in your applications is necessary.
You will need to assess duty, cycles and confirm gearbox suitability with your own calculations. Torque figures are to be used for guidance only.

PF Type only.

Tapped holes on input flange are not relative in position to the gearbox body and will alter from box to box. This also applies to the motor leads. However, we can machine the tapped holes after assembly so they are relative in position to the gearbox body. This will affect delivery.

sales@ondrives.com www.ondrives.com ondrives

LB
LBE

LINEAR MOTION

Linear Bearings/Bushings

With Seals ***For Use with Linear Shafting***

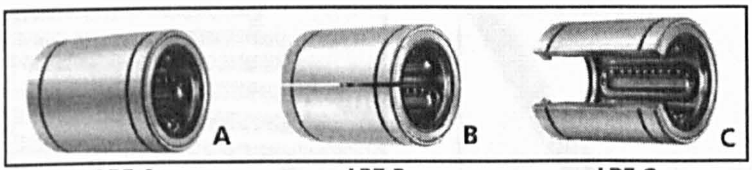

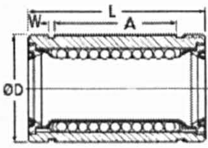

LBE-A Closed (Standard) **LBE-B Adjustable Clearance** **LBE-C Open**

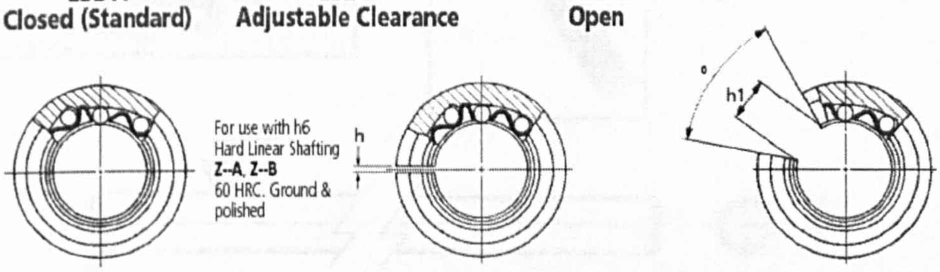

Part Number	Wt. g Type A	A-Ball Circs.	Wt. g Type B	B-Ball Circs.	Wt. g TypeC	C-Ball Circs.	ØB	Tol. µm	ØD	Tol. µm	L	Tol. µm
LB/LBE5	10.0	4	9.5	4	N/A	N/A	5	+8/-0	12	0/-8	22	0/-210
LB/LBE8	20.0	4	19.0	4	N/A	N/A	8	+8/-0	16	0/-8	25	0/-210
LB/LBE12	41.0	4	40.0	4	32	3	12	+8/-0	22	0/-9	32	0/-250
LB/LBE16	56.5	4	54.5	4	44	3	16	+9/-1	26	0/-9	36	0/-250
LB/LBE20	92.0	5	90.0	5	75	4	20	+9/-1	32	0/-11	45	0/-250
LB/LBE25	220.0	6*	215.0	6*	181	5*	25	+11/-1	40	0/-11	58	0/-300
LB/LBE30	325.0	6	320.0	6	272	5	30	+11/-1	47	0/-11	68	0/-300
LB/LBE40	705.0	6	694.0	6	600	5	40	+13/-2	62	0/-13	80	0/-300
LB/LBE50	1130.0	6	1110.0	6	970	5	50	+13/-2	75	0/-13	100	0/-350
LB/LBE60**	2050/1860	6	2000/1820	6	1580/1610	5	60	+13/-2	90	0/-15	125	0/-400
LB/LBE80	5140.0	6	5100.0	6	4350	5	80	+16/-4	120	0/-15	165	0/-400

*** Seals marked * extrude a little from width of external cylinder**
**** Not available sealed 1kgf = 9.807N = 2.205lbs. 1mm = 0.039 inch.**

Part Number	A	Tol. µm	W	ØG Groove	h	h1	° Deg.	Ecc. max µm	BASIC DYNAMIC LOAD RATING - C Load Direction A (N)	B (N)	BASIC STATIC LOAD RATING - Co Load Direction A (N)	B (N)	Price Each 1 - 5 Type A Closed	Type B Adj.	Type C Open
CARBON STEEL (Balls and external cylinder) (Ball retainer is resin and seals are rubber)															
LBE5	12	0/+270	1.10	11.50	1.00	-	-	12	90.8	104	219	310	£19.13	£21.18	-
LBE8	14	0/+270	1.10	15.20	1.00	-	-	12	121.0	139	255	361	£19.63	£21.96	-
LBE12	20	0/+330	1.30	21.00	1.50	7.50	78°	12	259.0	298	503	711	£19.89	£22.22	£24.54
LBE16	22	0/+330	1.30	24.90	1.50	10.00	78°	12	283.0	325	514	726	£24.54	£27.13	£28.42
LBE20	28	0/+330	1.60	30.30	2.00	10.00	60°	15	562.0	668	1010	1470	£26.36	£29.21	£33.07
LBE25	40	0/+390	1.85	37.50	2.00	12.50	60°	15	920.0	974	1780	2280	£30.50	£33.60	£40.83
LBE30	48	0/+390	1.85	44.50	2.00	12.50	50°	15	1350.0	1430	2500	3200	£41.87	£47.04	£51.68
LBE40	56	0/+460	2.15	59.00	3.00	16.80	50°	17	2030.0	2150	3620	4640	£69.78	£76.25	£80.12
LBE50	72	0/+460	2.65	72.00	3.00	21.00	50°	17	3940.0	4180	7130	9120	£87.87	£98.21	£103.39
LBE60	95	0/+400	3.15	86.50	3.00	27.20	54°	20	4760.0	5040	8150	10400	£216.02	£241.27	£263.07
LBE80	125	0/+400	4.15	116.00	3.00	36.30	54°	20	8710.0	9220	14500	18500	£449.83	£499.47	£560.56
STAINLESS STEEL 440C (Balls and external cylinder) (Ball retainer is resin and seals are rubber)															
LB5	12	0/+270	1.10	11.50	1.00	-	-	12	90.8	104	219	310	£40.74	£46.02	-
LB8	14	0/+270	1.10	15.20	1.00	-	-	12	121.0	139	255	361	£40.74	£46.02	-
LB12	20	0/+330	1.30	21.00	1.50	7.50	78°	12	259.0	298	503	711	£40.74	£46.02	£51.43
LB16	22	0/+330	1.30	24.90	1.50	10.00	78°	12	283.0	325	514	726	£61.74	£66.17	£66.33
LB20	28	0/+330	1.60	30.30	2.00	10.00	60°	15	562.0	668	1010	1470	£76.70	£93.25	-
LB25	40	0/+390	1.85	37.50	2.00	12.50	60°	15	920.0	974	1780	2280	£159.70	£169.24	-

Material

LBE: Hardened Steel **LB:** Hard Stainless Steel similar to 440C

Performance

Shaft Tolerance: h6 (Normal Fit) j6 (Closer Fit)
Housing Tolerance: H7 (Clearance Fit) J7 (Interference Fit)
Maximum Operating Temperature: +100°C (intermittent)
+80°C (continuous)

Other Info.

LBE60 & LBE80 are not sealed and are fitted with metal ball retainers. Other sizes have resin retainers fitted as standard - metal retainers available on request, P.O.A.

Discounts

Qty.	1+	6+
Disc	list	-10%

Z-A

LINEAR MOTION

Linear Shafting, Steel Hardened & Ground

h6 tolerance ***For use with Linear Bearings***

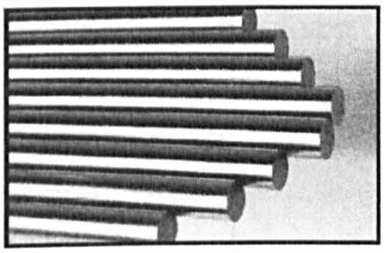

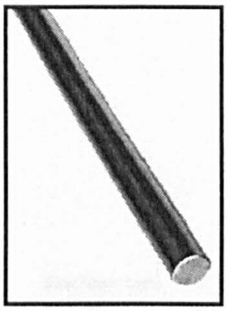

Specials to order

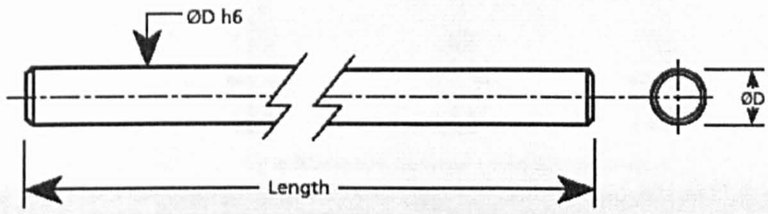

Part Number	Nom. Dia. ØD h6	Tolerance µm	Standard Length	Maximum Length	Weight per m Kg	Depth of Hardening	Price Each 1 - 5 per std. length
Z-3-300A	3	-	300	-	-	-	£53.82
Z-4-300A	4	-	300	-	-	-	£42.08
Z-5-1000A	5	0/-8	1000	3800	0.15	0.80	£18.90
Z-6-1000A	6	0/-8	1000	3800	0.22	0.80	£18.90
Z-8-1000A	8	0/-9	1000	3800	0.39	1.00	£18.90
Z-10-1000A	10	0/-9	1000	3800	0.61	1.00	£24.04
Z-12-1000A	12	0/-11	1000	3800	0.89	1.30	£24.04
Z-14-1000A	14	0/-11	1000	3800	1.21	1.30	£29.21
Z-15-1000A	15	0/-11	1000	3800	1.37	1.30	£41.48
Z-16-1000A	16	0/-11	1000	3800	1.57	1.60	£27.48
Z-18-1000A	18	0/-11	1000	3800	1.98	1.60	£30.92
Z-20-1000A	20	0/-13	1000	7000	2.45	1.60	£30.92
Z-22-1000A	22	0/-13	1000	7800	-	1.80	£77.32
Z-25-1000A	25	0/-13	1000	7800	3.83	1.80	£44.66
Z-30-1000A	30	0/-13	1000	7600	5.51	2.00	£54.98
Z-40-1000A	40	0/-16	1000	7600	9.80	2.50	£108.84
Z-50-1000A	50	0/-16	1000	7600	15.30	3.00	£139.44
Z-60-1000A	60	0/-19	1000	7600	22.10	3.00	£198.52
Z-80-1000A	80	0/-19	1000	7600	39.20	3.00	£233.98

Material

Ck53 / Cf53 Steel 62 HRC

Performance

Surface Finish: <0.30µm Ra **Straightness:** 0.10mm/m

Extras

Special machining available on shafting, special tolerances on length.

Linear shafting designed to be used with our linear bearings
- **LBE, LSP, LSB, LSTB**, etc.

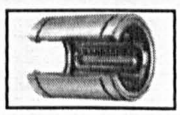

Discounts

Qty.	1+	6+	10+	20+	50+	100+
Disc	list	-20%	-25%	-30%	-40%	-42%
Qty.	200+					
Disc	-45%					

rino

Search Site

Bearings » Deep Groove Bearings

6 & 16 : Single Row Ø10 to Ø22

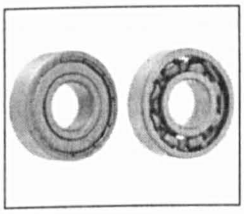

Material:
•Steel

Ordering Information:
Add -ZZ for shielded bearings
Add -LLU for sealed bearings

Open Type **Shielded Type ZZ** **Contact Sealed Type LLU**

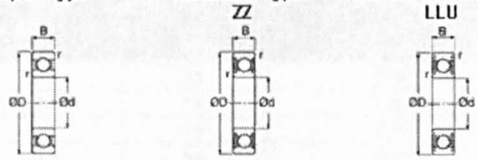

Up to 800mm bore diameters are available upon request

Part Number	Boundary Dimensions (mm)			Basic Radial Load Ratings (N)		Limiting Speeds (rpm)			Mass (kg)
						Grease		Oil	
Open	Ød	ØD	B	dynamic Cr	static Cor	Open ZZ	LLU	Open	(approx.)
6800	10	19	5	1720	840	34000	N/A	40000	0.005
6900	10	22	6	2700	1270	32000	N/A	38000	0.009
6000	10	26	8	4550	1970	30000	22000	36000	0.018
6200	10	30	9	5100	2390	24000	18000	30000	0.031
6300	10	35	11	8100	3450	22000	17000	26000	0.051
6801	12	21	5	1920	1040	32000	N/A	38000	0.006
6901	12	24	6	2890	1460	30000	N/A	36000	0.010
16001	12	28	7	5100	2370	28000	N/A	32000	0.019
6001	12	28	8	5100	2370	28000	18000	32000	0.022
6201	12	32	10	6800	3050	22000	17000	28000	0.037
6301	12	37	12	9700	4200	20000	16000	24000	0.060
6802	15	24	5	2070	1260	28000	N/A	34000	0.007
6902	15	28	7	4350	2260	26000	N/A	30000	0.015
16002	15	32	8	5600	2830	24000	N/A	28000	0.027
6002	15	32	9	5600	2830	24000	15000	28000	0.031
6202	15	35	11	7650	3750	20000	14000	24000	0.045
6302	15	42	13	11400	5450	17000	13000	20000	0.083
6803	17	26	5	2630	1570	26000	N/A	30000	0.007
6903	17	30	7	4600	2550	24000	15000	28000	0.017
16003	17	35	8	6000	3250	22000	N/A	26000	0.033
6003	17	35	10	6000	3250	22000	13000	26000	0.041
6203	17	40	12	9550	4800	17000	12000	20000	0.067
6303	17	47	14	13600	6650	15000	11000	18000	0.113
6804	20	32	7	4000	2470	22000	N/A	26000	0.017
6904	20	37	9	6400	3700	19000	12000	22000	0.037
16004	20	42	8	7900	4450	18000	N/A	20000	0.048
6004	20	42	12	9400	5000	18000	11000	20000	0.068
6204	20	47	14	12800	6600	15000	11000	18000	0.107
6304	20	52	15	15900	7900	14000	10000	17000	0.146

Couplings & Clamps » Miniature Rigid Couplings

MRG : Aluminium with Set Screw

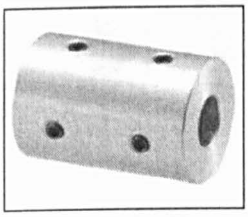

Material: (all Sizes)
•Aluminium alloy, Anodic Oxide coated

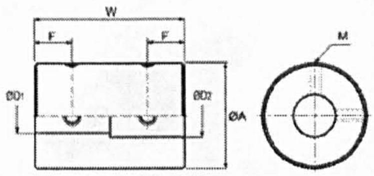

Part Number	Wrench Torque (Nm)	Rated Torque (Nm)	Max. Torque (Nm)	Max. rev. per min (rpm) (min^{-1})	Moment of Inertia $(kg{\cdot}m^2)$	Mass (g)
MRG-16	0.7	0.3	0.6	24000	4.4×10^{-7}	11
MRG-20	0.7	0.5	1.0	19000	1.3×10^{-6}	20
MRG-25	1.7	1.0	2.0	15000	3.9×10^{-6}	39
MRG-32	1.7	2.0	4.0	12000	1.2×10^{-5}	71

The maximum torque of the miniature coupling is two-fold of the rated torque. Select a type in which torque generated during continuous operation does not exceed the rated torque of the miniature coupling.

Part Number	Standard Bores		Max. Bore (mm)	Dimensions (mm)					
	$ØD_1$ (mm)	$ØD_2$ (mm)		ØA	L	W	F	G	M
MRG-16	3	3	8	16	-	24	6	-	M3
MRG-20	5	5	10	20	-	30	7	-	M3
MRG-25	8	8	12	25	-	36	9	-	M4
MRG-32	12	12	16	32	-	41	10	-	M4

These rigid couplings transmit the torque and rotational angles while absorbing misalignments. When the misalignment exceeds allowable values, vibration may result or the life of the coupling may become shortened. Make sure to adjust the alignment accordingly.
There are three types of shaft misalignment, namely in terms of parallel misalignment, angular misalignment and shaft end-play. Adjust the alignment to be below allowable values listed in the specification table.
The maximum misalignment is the allowable value when only one of the misalignments exists alone. In case two or more misalignments exist at the same time, the allowable values shall be less than half of the maximum misalignment listed in the specification table.
We recommend you to adjust the shaft misalignment to be below 1/3 of maximum values for the elongation of the life of the coupling.
IMPORTANT:- Couplings and other rotational parts should be protected by covers for safety operation. Also, take note that operation under misalignment exceeding maximum values and excessive torque may result in shorter life of the coupling due to plastic deformation.

Features
•Lightweight
•High response
•Minimum moment of inertia
•Maintenance-free and excellent resistance to oil and chemicals
•Max. temperature (approx.) 100°C

Options
•Also available in stainless steel (SUS303).
•One-piece clamp type
•Two-piece clamp type

Ordering Information:
e.g.
MRG-25 - Ø8 x Ø10
Type
ØD1
ØD2

The MRG coupling can be bored out for larger bore sizes.

Anti-backlash Miniature Leadscrews

Sizes 3, 5 & 6

General Information

All dimensions in mm
General tolerances: ±0.13mm
Material:
Screw - Stainless steel 303.
Nut - Polyacetal
Standard lead:
Right hand

Associated Products

Reli-a-Flex® couplings
Linear bearings
Linear slides
Stepper motors
Plain bearings

Visit our online catalogue for associated products

Anti-backlash, sizes 3 & 5

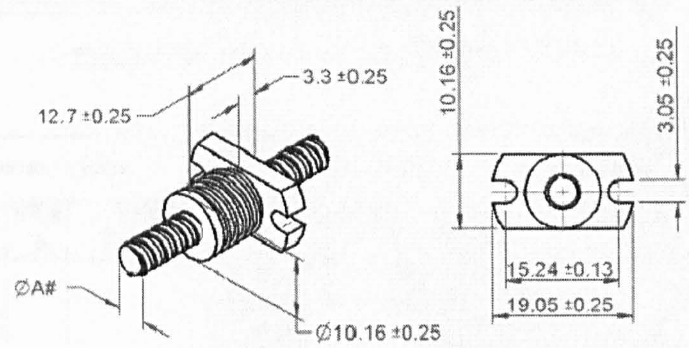

Anti-backlash, size 6

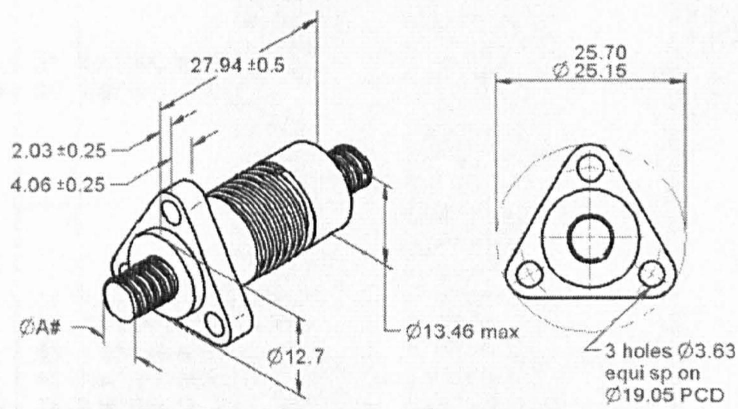

- Precision rolled thread for greater accuracy.
- Polyacetal nut with lubricating additive for longer life.
- Standard lead accuracy 0.0006mm/mm.
- Repeatability 0.0015mm.

Non-standard options, please enquire....

- Low friction TFE coating extends nut life by 300%, add **-TFE** to part number.
- Some leadscrews available with left hand thread, † add **-LH** to part number.

www.rpmechatronics.co.uk

Standard Product Sales : +44 (0)1484 601060 +44 (0)1484 601061
www.rpmechatronics.co.uk sales@rpmechatronics.co.uk

Sizes 3, 5 & 6

Anti-backlash Miniature Leadscrews

Part number selection table

Example Part No:- LNTBF5-M005 - 100mm or LNTBF5-0192 - 100mm

Leadscrew Dia ØA# (Series)	Metric Leads: Lead	Eff.‡ %	Basic Part No.	Inch Leads: Lead	Eff.‡ %	Basic Part No.	Unloaded Friction Torque
3.18mm (LNTBF3) (size 3)				0.0120"	26	LNTBF3-0012	
				0.0240"	43	LNTBF3-0024	
				0.0480"	61	LNTBF3-0048	<0.007Nm
				0.0750"	70	LNTBF3-0075	
				0.0960"	75	LNTBF3-0096	
				0.3750"	85	LNTBF3-0375	
4.76mm (LNTBF5) (size 5)				0.0240"	31	LNTBF5-0024	
				0.0313"	39	LNTBF5-0031	
				0.0480"	50	LNTBF5-0048	
	0.50mm	30	LNTBF5-M005	0.0500"	52	LNTBF5-0050	
	10.85mm	85	LNTBF5-M109	0.0960"	66	LNTBF5-0096	<0.007Nm
				0.1875"	78	LNTBF5-0188	
				0.1920"	78	LNTBF5-0192	
				0.2500"	81	LNTBF5-0250	
				0.3750"	84	LNTBF5-0375	
6.35mm (LNTBF6) (size 6)				0.0250"	30	LNTBF6-0025	
				0.0357"	35	LNTBF6-0036	
				0.0500"†	46	LNTBF6-0050	
	1.0mm	40	LNTBF6-M010	0.0625"	52	LNTBF6-0063	
	1.5mm	52	LNTBF6-M015	0.1000"	62	LNTBF6-0100	
	2.0mm	59	LNTBF6-M020	0.2000"	65	LNTBF6-0200	<0.007Nm
	3.0mm	68	LNTBF6-M030	0.2500"†	79	LNTBF6-0250	
	10.0mm	78	LNTBF6-M100	0.4000"	84	LNTBF6-0400	
				0.5000"†	85	LNTBF6-0500	
				0.7500"	86	LNTBF6-0750	
				1.0000"	84	LNTBF6-1000	

‡ Efficiencies quoted are maximum theoretical - see page 54.
# Thread dimensions are lead dependant - see page 14.

For leadscrew lengths up to 450mm for LNTBF3 & LNTBF5 and lengths up to 1000mm for LNTBF6, add required length to basic part number.

General Information

All dimensions in mm
General tolerances: ±0.13mm
Material:
Screw - Stainless steel 303.
Nut - Polyacetal
Standard lead: Right hand

Associated Products

Reli-a-Flex® couplings
Linear bearings
Linear slides
Stepper motors
Plain bearings

Visit our online catalogue for associated products

www.rpmechatronics.co.uk

Leadscrews

Technical Information

FEATURES

Reliance precision leadscrew assemblies are designed specifically for motion control applications where accuracy must be maintained. Rather than being adaptations of general purpose screw or nuts they have a precision rolled screw thread which has been designed for maximum life and quiet operation.
A further enhancement available on stainless steel leadscrews up to 2.4 metres long is a specially formulated TFE coating which can extend normal nut life by up to 300%.

Innovative anti-backlash nut designs provide assemblies which are wear compensating with low frictional drag torques and excellent positional repeatability.

Reliance stainless steel leadscrews offer the following:

1. High Accuracy
Precision thread rolling process provides a standard lead accuracy of 0.0006mm/mm.
Higher accuracies up to 0.0001mm/mm can be provided.
The unloaded repeatability of anti-backlash assemblies is within 0.0013mm.

2. Long Life
More than 7.5 million metres of travel can be expected.

3. Low Drag Torque
An anti-backlash nut design which does not require high spring forces to maintain bidirectional anti-backlash characteristics gives a very low nut to screw friction.

4. Low Maintenance
Self lubricating and wear compensating nuts eliminate the need for repeated lubrication or adjustment.

5. Wide Range
Diameters from 3.2mm to 16mm.
Leads from 0.30mm to 25mm.
Lengths up to 1 metre.

6. Custom Thread Design
Unique thread form designed specifically for leadscrews in anti-backlash applications.

7. Smooth Quiet Operation
No recirculating ball noise or metal to metal contact.

8. Lower Cost
Less then comparable ball screws or ground leadscrews, while still providing high accuracy and long life.

9. Modifications
Special leadscrew ends, aluminium alloy shafts and other leads are available on the stainless steel leadscrew range in selected sizes. Please contact Reliance Technical Sales or refer to the leadscrews modification section of this brochure.

Standard Product Sales : +44 (0)1484 601060 +44 (0)1484 601061
www.rpmechatronics.co.uk sales@rpmechatronics.co.uk

Technical Information — Leadscrews

ENGINEERING DATA

1. Lead
The lead of the screw is the amount of linear movement of the nut for one revolution of the leadscrew.

2. Drive Torque
The required motor torque to drive a leadscrew assembly is the sum of three components: inertial torque, static friction torque and torque to move the load. Additional torque associated with driving and supporting the leadscrew must also be considered.

Inertial torque: $T = I\alpha$

I = Inertia of leadscrew (kgm^2)
α = Angular acceleration ($rads/s^2$)

Static friction Torque: Anti-backlash leadscrews are typically supplied with a static frictional torque of 0.007 - 0.05Nm. Higher pre-load forces lead to higher frictional drag torques but better anti-backlash characteristics.

Torque to move load: The torque to move a certain load is a function of the lead and efficiency of the leadscrew assembly.

$$\text{Torque} = \frac{\text{Load} \times \text{Lead}}{2\pi \times \text{Efficiency}}$$

Torque = Newton metres
Load = Newtons
Lead = Metres

(Note - efficiency of 70% would require 0.7 in these equations)

4. Backdriving
In general when the screw pitch is less than 1/3 its diameter, backdriving will not occur. For higher leads where backdriving is likely, the torque required for holding a load is as follows:

$$\text{Backdrive torque} = \frac{\text{Load} \times \text{Lead} \times \text{Efficiency}}{2\pi}$$

Torque = Newton metres
Load = Newtons
Lead = Metres

5. Traverse Speed
The Polyacetal nut materials provide long wear-life over a wide variety of conditions, but very high loads and/or high speeds will accelerate nut wear. We recommend the following maximum linear traversing speeds for optimum life:

Lead	Maximum traverse speed
2.5mm - 12mm	100mm/sec
12mm - 25mm	250mm/sec

www.rpmechatronics.co.uk

Leadscrews

Technical Information

6. Critical Speed
This is the rotational speed at which a leadscrew will experience vibration or other dynamic problems. See the critical speed chart below to determine if the application parameters result in speeds approaching critical.
To minimise critical speed problems use a longer lead, choose a larger diameter screw or increase the bearing mount support.

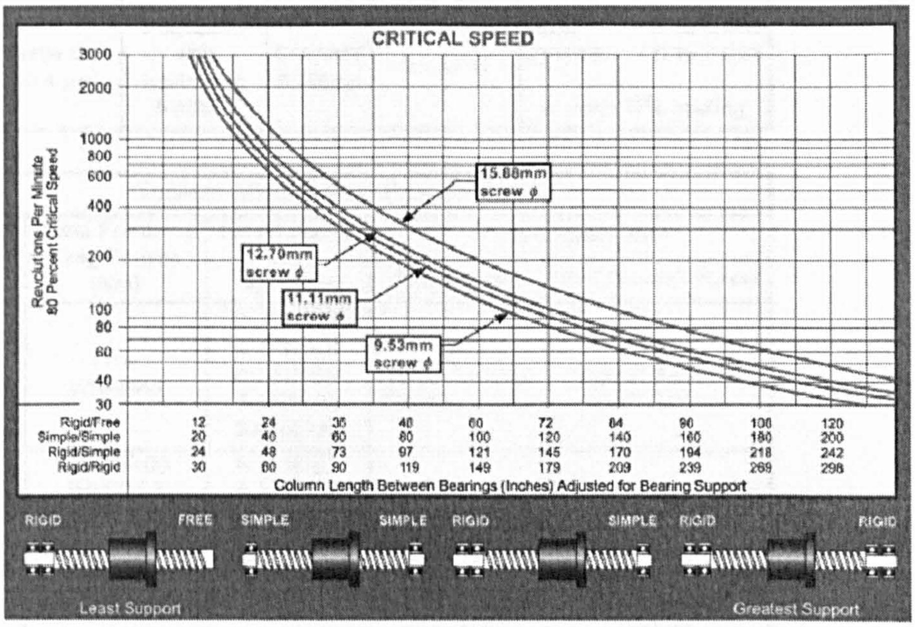

7. Maximum Load
Although the leadscrew assemblies are able to withstand relatively high loads without catastrophic failure, these units have been designed to operate with the loads shown on the product pages.

8. Efficiency
The efficiency of a leadscrew varies with the lead angle of the screw. The theoretical maximum efficiencies of all our leadscrews are given in the part number tables on the product pages. These have been calculated using the static coefficient of friction 0.08. For applications where the dynamic efficiency is critical please contact Reliance Technical Sales.

9. Leadscrew Inertia
Values of leadscrew inertia are given in the Typical Mechanical Properties chart on the next page.

10. Screw Straightness
Typical screw straightness is 0.25mm/metre.

11. Leadscrew Interfacing
A table of leadscrew minor diameters and examples of options for machined ends can be found on pages 14 and 15 .

Technical Information

Leadscrews

Physical Properties					
Leadscrew		**Nuts**		**Assembly**	
Material	**Surface Finish**	**Material**	**Tensile Strength**	**Operating Temp. Range**	**Coefficient of Friction Nut to Screw**
Stainless steel 303 series	Better than 0.4 µm	Polyacetal with lubricating Additive	$67 N/mm^2$ 9,700psi	0 - 93°C	Static = 0.08 0.08# Dynamic = 0.15 0.09# # - with TFE coating

Typical Mechanical Properties				
Leadscrew Series	**Static Frictional Drag Torque (Nm)**	**Screw Inertia Kg m^2/m**	**Anti-backlash life +**	
			Plain Screw	**TFE Coated Screw**
LPX6 LPX10 LPX11 LPX13 LPX16	Free Wheeling	8.341E-07 4.171E-06 9.731E-06 1.446E-05 3.948E-05	N/A Typical Backlash 0.076-0.25mm	N/A Typical Backlash 0.076-0.25mm
LAF6 LAF10 LAF11 LAF13 LAF16	0.007-0.03 0.01-0.03 0.02-0.04 0.02-0.04 0.03-0.05	8.341E-07 4.171E-06 9.731E-06 1.446E-05 3.948E-05	1.0 - 1.5 million metres	3.8 - 5.0 million metres
LAK10	0.007-0.02	4.171E-06	2.0 - 2.5 million metres	4.5 - 5.8 million metres
LAX13 LAX16	0.01-0.04 0.01-0.04	1.446E-05 3.948E-05	5.0 - 5.7 million metres	7.6 - 8.8 million metres

+ Life will vary with loading, operating environment and duty cycle.
  Longer screw leads generally give longer life.

TFE Coated Leadscrew Assemblies

The TFE coating is designed to supply a more even distribution of lubricant than is normally achieved when using standard self lubricating plastics on steel. The entire screw surface is coated which gives an extremely even lubrication distribution, and an expected increase in normal nut life of up to 300%. Lubrication to the screw/nut interface occurs by the nut picking up TFE particles from the coating as well as from migration of the internal lubricant from within the plastic nut.

Although care should be taken to ensure that chips and voids do not occur in the coating, small voids have been shown to have little effect on the system performance. The lubricant, although solid, has some of the "spreading" ability of fluid lubricants. When machining for bearing ends, soft fixtures are recommended.

TFE coated screws provide the maximum level of self-lubrication and should not be additionally lubricated or used in environments where oils or other lubricant contamination is possible.

1.8° SIZE 11 STANDARD MOTOR

LIN ENGINEERING
Step Motor Specialists
ISO 9001

211

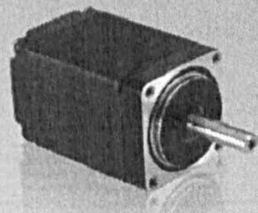

- NEMA Size 11 Mounting
- Small Package
- Cost Effective
- Custom Windings Available (No Additional Cost)

SPECIFICATIONS

BIPOLAR Dimension "A" Max	Model #	Amps/ Phase	Torque oz-in	Torque N-m	Resistance Ohm/Phase	Inductance mH/Phase	Inertia oz-in²	Weight Lbs.	Number of Leads
1.26" 32 mm	211-13-01	0.67	9.2	0.06	5.6	3.4	0.05	0.24	4
	211-13-02	1.30	9.2	0.06	1.7	1.1	0.05	0.24	4
1.77" 45 mm	211-18-01	0.67	13.7	0.10	7.1	4.8	0.07	0.31	4
	211-18-02	1.30	13.7	0.10	1.3	0.8	0.07	0.31	4
2.01" 51.1 mm	211-20-01	0.67	16.6	0.14	8.6	6.7	0.10	0.44	4
	211-20-02	1.30	16.6	0.14	1.9	1.7	0.10	0.44	4

- Please complete our application data sheet for different windings.
- Power supply voltage can be any value as long as the driver output current is controlled at the motor's rated current.
- Call Lin Engineering for additional Bipolar torque curves.
- Performance, use, and appearance specifications of the products listed here are subject to change without notice.
- For operating temperatures, see page 94.

DIMENSIONS (inches)

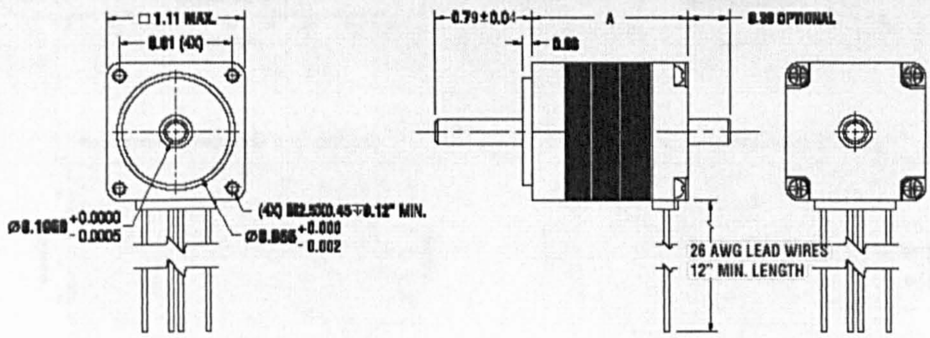

DID YOU KNOW...

TORQUE CURVES

211-13-01 24vDC, 0.67 Amps/Phase, Bipolar, 1/2 Stepping

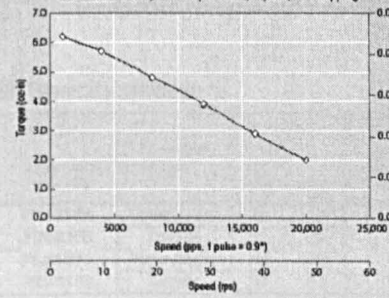

211-13-02 24vDC, 1.3 Amps/Phase, Bipolar, 1/2 Stepping

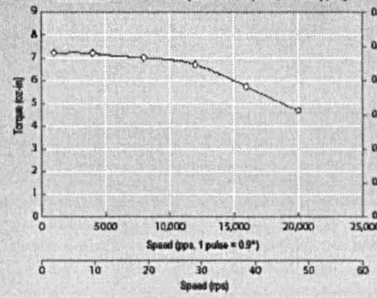

211-18-01 24vDC, 0.67 Amps/Phase, Bipolar, 1/2 Stepping

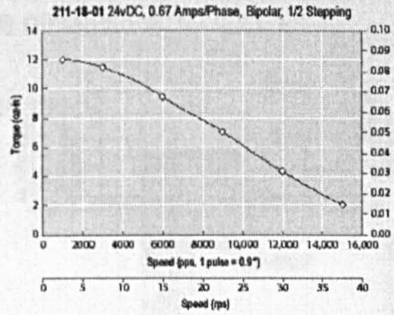

211-18-02 24vDC, 1.3 Amps/Phase, Bipolar, 1/2 Stepping

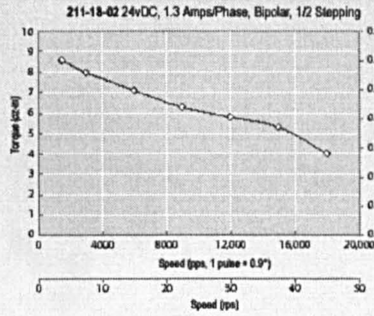

211-20-01 24vDC, 0.67 Amps/Phase, Bipolar, 1/2 Stepping

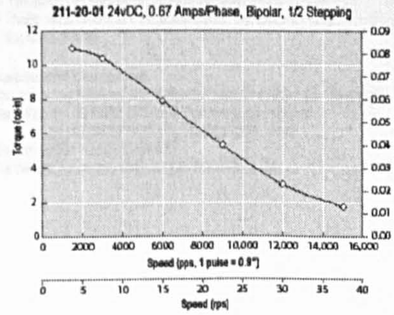

211-20-02 24vDC, 1.3 Amps/Phase, Bipolar, 1/2 Stepping

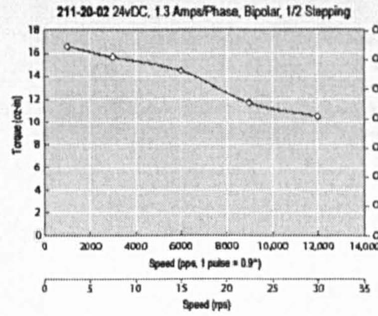

□ 1.38 in. (□ 35 mm)

Step Angle 1.8°

PK Series Standard P Type (High Torque)

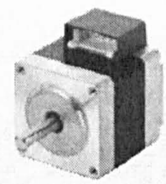

■ Specifications

Model Single Shaft Double Shaft	Connection Type	Holding Torque oz-in	Holding Torque N·m	Current per Phase A/phase	Voltage VDC	Resistance per Phase Ω/phase	Inductance mH/phase	Rotor Inertia J oz-in²	Rotor Inertia J kg·m²	Lead Wires (Pins)
PK233PA	Bipolar (Series)	28	0.2	0.85	4.6	5.4	5.6	0.131	24×10^{-7}	6
PK233PB	Unipolar	22	0.16	1.2	3.24	2.7	1.4			
PK235PA	Bipolar (Series)	52	0.37	0.85	5.8	6.8	8	0.27	50×10^{-7}	6
PK235PB	Unipolar	42	0.3	1.2	4.08	3.4	2			

How to Read Specifications →Page C-9
Motor Wiring Diagrams →Page C-189

■ Dimensions Scale 1/2, Unit = **inch** (mm)

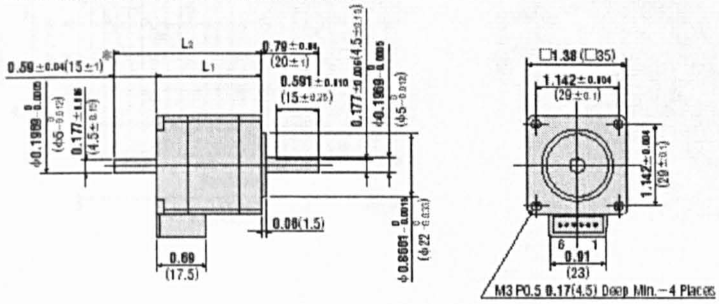

∗ The length of machining on double shaft model is 0.591±0.010 (15±0.25).
● These dimensions are for double shaft models. For single shaft models, ignore the shaded area.

Model	L1 inch (mm)	L2 inch (mm)	Weight lb. (kg)	DXF
PK233PA	1.46 (37)	—	0.4 (0.18)	B329
PK233PB		2.05 (52)		
PK235PA	2.05 (52)	—	0.63 (0.285)	B330
PK235PB		2.64 (67)		

Applicable Connector
The following housing and contacts must be purchased separately.
Housing: 51103-0600 (MOLEX, Positive Lock Type) or
51102-0600 (MOLEX, Friction Lock Type)
Contact: 50351-8100 (MOLEX)
Connector Assembly Tool: 57295-5000 (MOLEX)

Features C-184 Accessories C-185

Speed–Torque Characteristics

How to Read Speed-Torque Characteristics →Page C-10

● **PK233PB** Bipolar (Series)

Bipolar Constant Current Driver
With Damper **D4CL-5.0F**: J_L = 0.186 oz-in² (34×10⁻⁷ kg·m²)
Step Angle: 1.8°/step

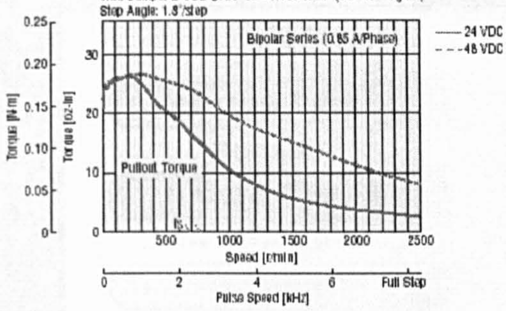

● **PK233PB** Unipolar

Power Input: 24 VDC Unipolar Constant Current Driver
With Damper **D4CL-5.0F**: J_L = 0.186 oz-in² (34 × 10⁻⁷ kg·m²)
Step Angle: 1.8°/step

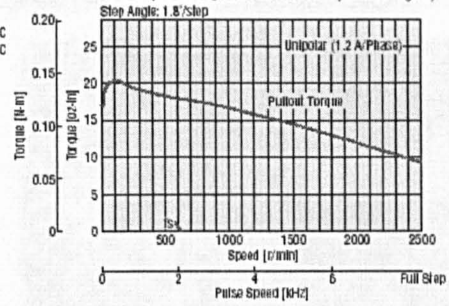

● **PK235PB** Bipolar (Series)

Bipolar Constant Current Driver
With Damper **D4CL-5.0F**: J_L = 0.186 oz-in² (34×10⁻⁷ kg·m²)
Step Angle: 1.8°/step

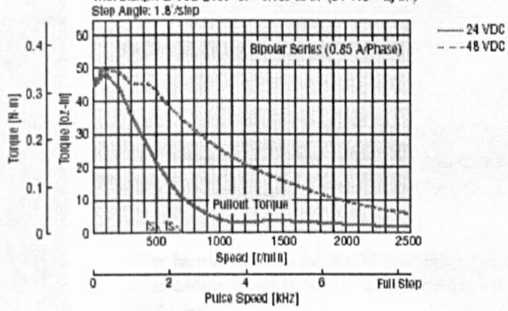

● **PK235PB** Unipolar

Power Input: 24 VDC Unipolar Constant Current Driver
With Damper **D4CL-5.0F**: J_L = 0.186 oz-in² (34 × 10⁻⁷ kg·m²)
Step Angle: 1.8°/step

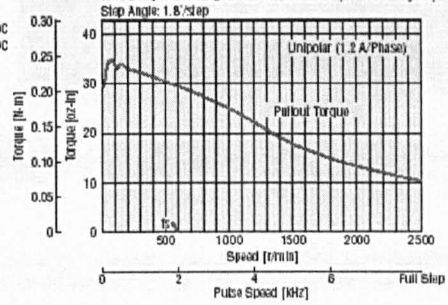

Motor Cables (Sold separately)

These cables make it easy to connect the Standard **P** type motor. The crimped connectors eliminate the need for assembly. There are two cable lengths to choose from.

Model	Cable Length feet (m)	Number of Leads	Lead Specifications UL Style No.	Lead Specifications AWG No.
LC2U06B	2 (0.6)	6 Leads	3265	24
LC2U10B	3.3 (1)			

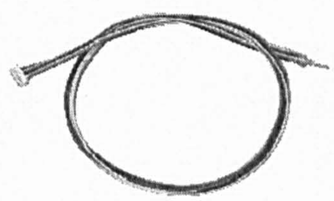

Connection Diagrams C-180 General Specifications C-240

GURLEY MODELS R119 AND R120
ROTARY INCREMENTAL MINI-ENCODERS

MOTION TYPE:
ROTARY

USAGE GRADE:
LIGHT INDUSTRIAL

OUTPUT:
INCREMENTAL

MAX RESOLUTION:
65,536 COUNTS/REV

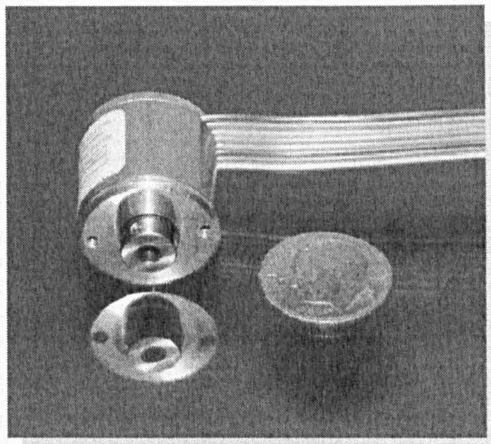

MINIATURE HIGH-RESOLUTION ENCODER

The Models **R119** and **R120** optical incremental encoders are designed for light industrial applications that require high resolution in a very small package. The two models share these features:

- Represent either shafted or blind-hollow shaft version
- LED illumination for long life (>100,000 hours)
- Differential photo-detectors for signal stability
- Single-board, surface-mount electronics for reliability
- RS-422 differential line driver output for noise immunity
- Zero index signal
- Monolithic integrated ASIC for internally interpolated resolutions up to 16,384 cycles/rev (65,536 counts/rev)

R119: ϕ19-mm body; ribbon cable
R120: ϕ20-mm body; round cable with shielded twisted pairs

ingenuity@work®

ISO 9001 CERTIFIED

Gurley Precision Instruments
514 Fulton Street
Troy, NY 12180 U.S.A.
(800) 759-1844, (518) 272-6300, fax (518) 274-0336,
Online at www.gurley.com, e-mail: info@gurley.com

GPI

SPECIFICATIONS

	See Note	Models R119 and R120
Maximum line count on disc		1024
Maximum cycles /rev (quad sq waves)		16,384
Max counts/rev (after quad decode)		65,536
Internal square wave interpolation		1x, 2x, 5x, 10x, or 16x
Instrument error, ±arcminutes	1, 2	4
Quadrature error, ±electrical degrees	1, 3	24
Interpolation error, ±quanta	1, 4	0.15
Maximum output frequency, kHz		
1x square waves		100
2x square waves		150
5x square waves		300
10x, 16x square waves		500
Starting torque, in-oz (N-m) @20°C		0.07 (5×10^{-4})
Running torque, in-oz (N-m) @20°C		0.04 (2.9×10^{-4})
Moment of inertia, in-oz-s2 (g-cm^2)		5.7×10^{-6} (0.4)
Maximum weight, oz (g)		1 (30)
Sealing		IP50
Max. Radial or axial shaft load, lb (N)	5	0.7 (3)
Bearing life with 0.25 lb radial load	6	1×10^{10} rev
Operating temperature, °F (°C)		32 to 158 (0 to 70)
Storage temperature, °F(°C)		-22 to 185 (-30 to 85)
Humidity, % rh, non-condensing		98
Shock		30g (300m/s2)
Vibration		10g (100m/s2)

Notes:

1. Total Optical Encoder Error is the algebraic sum of *Instrument Error + Quadrature Error + Interpolation Error*. Typically, these error sources sum to a value less than the theoretical maximum. Error is defined at the signal transitions and therefore does not include quantization error, which is ±1/2 quantum. ("Quantum" is the final resolution of the encoder, after user's 4X quadrature decode.) Accuracy is guaranteed at 20°C.

2. *Instrument Error* is the sum of disc pattern errors, disc eccentricity, bearing runout and other mechanical imperfections within the encoder. This error tends to vary slowly around a revolution.

3. *Quadrature Error* is the combined effect of phasing and duty cycle tolerances and other variables in the basic analog signals. This error applies to data taken at all four transitions within a cycle; if data are extracted from 1X square waves on a 1X basis (i.e., at only one transition per cycle), this error can be ignored.

   Error in arcminutes = (60) x (error in electrical degrees) (disc line count)

4. *Interpolation Error* is present only when the resolution has been electronically increased to more than four data points per optical cycle. It is the sum of all the tolerances in the electronic interpolation circuitry.

   Error in arcminutes = (21600) x (error in quanta) (counts/rev)

5. The maximum recommended shaft load is based on bearing life considerations. If accuracy is critical, shaft loads should be kept as low as possible.

6. Bearing life is based on fatigue failure criteria. In many long-duration applications, lubrication retention becomes the determining factor.

As part of our continuing product improvement program, all specifications are subject to change without notice

R119S/R120B
PAGE 2 OF 6
V3.1

Gurley Precision Instruments
514 Fulton Street
Troy, NY 12180 U.S.A.
(800) 759-1844, (518) 272-6300, fax (518) 274-0336,
Online at www.gurley.com, e-mail: info@gurley.com

GPI

SPECIFICATIONS

INPUT POWER
+5 VDC ±0.25 V @100 mA max.

SQUARE WAVE OUTPUT
Quadrature square waves at 1, 2, 5, 10, or 16 times the line count on the disc. On all channels: EIA/RS-422 balanced differential line driver, protected to survive an extended-duration short circuit across its output. May be used single-ended for TTL-compatible inputs. Index is ¼-cycle wide, gated with the high states of channels A and B.

OUTPUT WAVEFORMS (CW rotation shown)

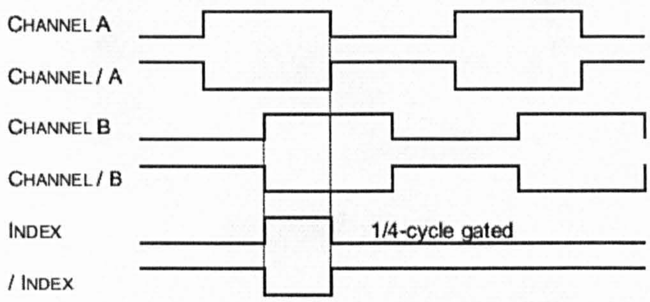

ELECTRICAL CONNECTIONS

	R119		R120	
Output Functions	Wire Colors Conn. Code **P**	Ribbon conn Conn. Code **Y**	Wire Colors Conn. Code **P**	Ribbon conn Conn. Code **Y**
A	Orange	2	Yellow	4
/ A	Yellow	3	Brown	8
B	Violet	6	Green	3
/ B	Gray	7	Orange	7
IND	Green	4	Blue	2
/ IND	Blue	5	White	6
+V	Red	1	Red	5
COMMON	White	8	Black	9
CASE			Bare (shield)	1

NOTE: Channel A leads Channel B for clockwise rotation, looking at the shaft end.

FLEXIBLE SHAFT COUPLINGS

	Tether Mount for **-B** version	**SCD** Coupling for **-S** version
Maximum parallel offset, in (mm)	0.002 (.05)	0.008 (0.2)
Maximum axial extension or compression, in (mm)	0.008 (0.2)	0.008 (0.2)
Maximum angular misalignment, degrees	2.0	0.5

See separate data sheet for specifications and ordering information for the Model **SCD** coupling.

NOTE: Flexible couplings are intended to absorb normal installation misalignments and run-outs in order to prevent undue loading of the encoder bearings. To realize all the accuracy inherent in the encoder, the user should minimize misalignments as much as possible.

Gurley Precision Instruments
514 Fulton Street
Troy, NY 12180 U.S.A.
(800) 759-1844, (518) 272-6300, fax (518) 274-0336,
Online at www.gurley.com, e-mail: info@gurley.com

R119 DIMENSIONS

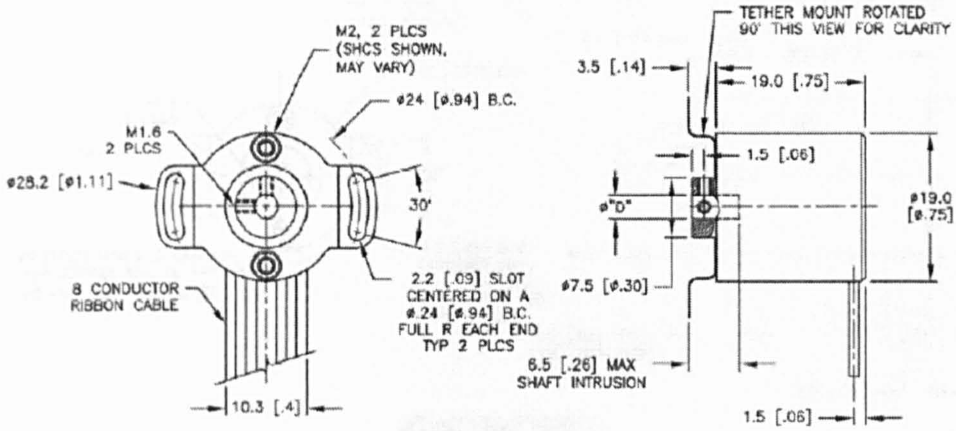

R119B (BASE CODE A)

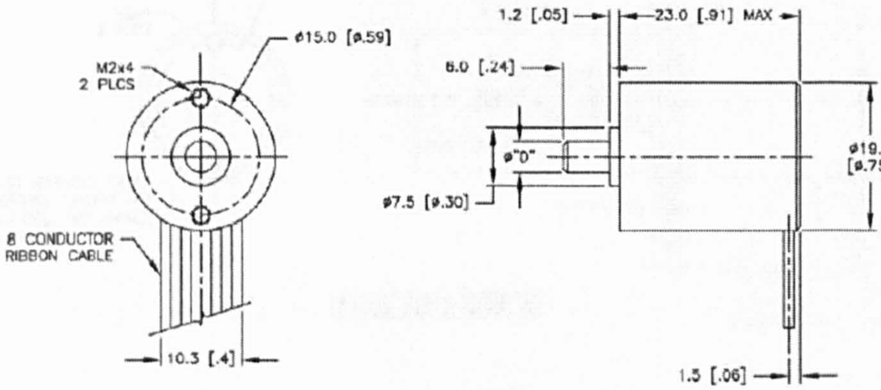

R119S (BASE CODE B)

ø"D" TABLE		
"DIA" CODE	R119S	R119B
D4M	ø4mm h6	N/A
03M	ø3mm h6	ø3mm H7
02E	ø0.125" +.0000/−.0003	ø0.125" +.0005/−.0000

ALL DIMENSIONS IN MM [INCHES]

Gurley Precision Instruments
514 Fulton Street
Troy, NY 12180 U.S.A.
(800) 759-1844, (518) 272-6300, fax (518) 274-0336,
Online at www.gurley.com, e-mail: info@gurley.com

R120 Dimensions

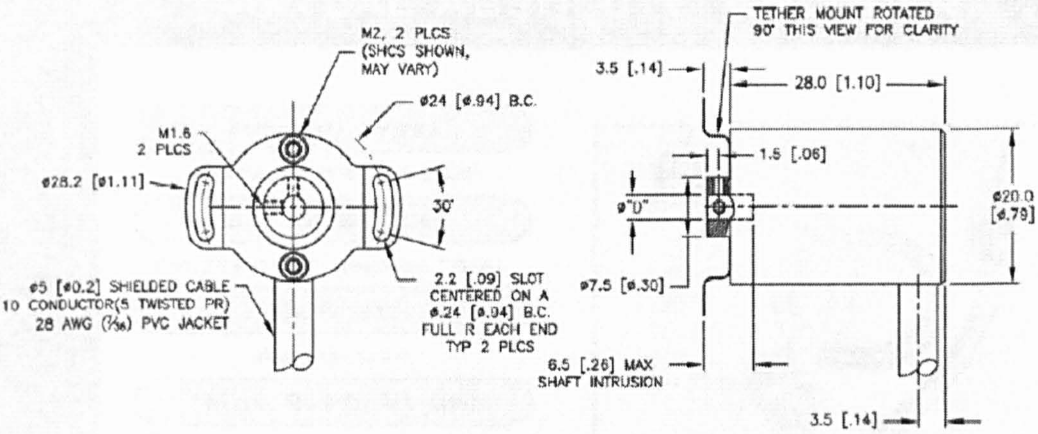

R120B (BASE CODE A)

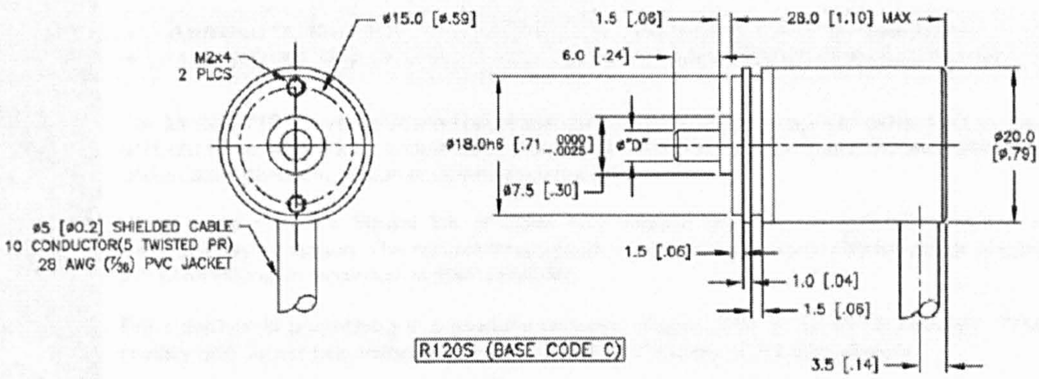

R120S (BASE CODE C)

ø"D" TABLE		
"DIA" CODE	R120S	R120B
04M	ø4mm h6	N/A
03M	ø3mm h6	ø3mm H7
02E	ø0.125" +.0000 -.0003	ø0.125" +.0005 -.0000

ALL DIMENSIONS IN MM [INCHES]

Gurley Precision Instruments
514 Fulton Street
Troy, NY 12180 U.S.A.
(800) 759-1844, (518) 272-6300, fax (518) 274-0336,
Online at www.gurley.com, e-mail: info@gurley.com

GURLEY MODEL 9710
VIRTUAL ABSOLUTE® ENCODER

MOTION TYPE:

ROTARY OR LINEAR

USAGE GRADE:

PROTECTED INDUSTRIAL

OUTPUT:

ABSOLUTE

***MAX RESOLUTION:**

2^{22} STEPS/REV. (~0.3 ARCS)

0.25 μM

*W/EXTERNAL ELECTRONICS

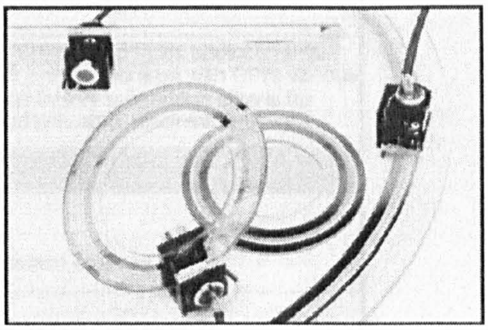

- ABSOLUTE OUTPUT
- MANY DISC SIZES
- FRICTION FREE OPERATION
- VACUUM-COMPATIBLE OPTION

The Model **9710** is a versatile read head that can be configured for use with either a rotary disc or linear scale. Its modular construction provides friction-free operation, and the wide selection of disc sizes gives the design engineer great flexibility
.

When used with the **Model VA** or other interpolating decoder, its optical resolution is electronically increased. The natural-binary position output is augmented by a number of built-in test functions for maximum system reliability.

For incremental positioning in a modular encoder, please refer to the **9710 (rotary), 7700 (rotary and linear in a compact package), and 9717 (linear only) datasheets**

ingenuity@work®

ISO
9001
CERTIFIED

Gurley Precision Instruments
514 Fulton Street
Troy, NY 12180 U.S.A.
(800) 759-1844, (518) 272-6300, fax (518) 274-0336,
Online at www.gurley.com, e-mail: info@gurley.com

SPECIFICATIONS

Electrical	
Input Power	V_{CC}: +5VDC 0.25 VDC@ 10 mA I_{LED}: +20mA regulated DC current source
Light Source	Screened infra-red LED; rated life > 100,000 hours
Output Signals	High-output differential Sine, Cosine, and Index photocurrents. Signal levels are designed for proper operation with GPI's various electronics packages. Consult factory to establish criteria for waveforms when 9710 is used with other electronics.
Mechanical	
Materials Encoder Body Scale of Disk	 Aluminum Vacuum-deposited chrome pattern on glass
Weight Read Head Scale	 1.7 oz (49g) + cable @ 0.034 oz/in (0.04 g/mm) 0.31 oz/in (0.34 g/mm) (1.125" x 0.189" cross-section)
Performance	
Frequency Response	50 kHz, all channels (Max. Speed may be limited by subsequent electronics; see data sheet for Model VA interpolating decoder.)
Quadrature Error	±30° typical (depends on user's installation)
Scale Accuracy Standard Optional	 ±0.0001 in/ft (8 μm/m) ±0.00005 in/ft (4 μm/m)
Disc Accuracy Dia ≤ 3" Dia > 3"	 ±10 arcs ±5 arcs
Environmental	
Operating Temp. Humidity Shock Vibration	-40 F to +185 F (40 C to +85 C) 98% rh, non-condensing 50g, 11 ms 2g, 0-2000 Hz

As part of our continuing product improvement program, all specifications are subject to change without notice.

9710 VA
PAGE 2 OF 6
V3.1

Gurley Precision Instruments
514 Fulton Street
Troy, NY 12180 U.S.A.
(800) 759-1844, (518) 272-6300, fax (518) 274-0336,
Online at www.gurley.com, e-mail: info@gurley.com

9710 VA THEORY

THEORY OF OPERATION - SHORT VERSION

Virtual Absolute (VA) discs and scales are similar to incremental discs and scales in that they contain a cyclic track and an index track. In an incremental encoder, the index occurs at one place in the full travel, but in a *VA* encoder, the index track is a continuous serial code (similar in appearance to a bar code). You don't know position immediately upon start-up, as you do in a conventional absolute, but after a very short travel, *in either direction and starting from anywhere*, you know exactly where you are. In a rotary *VA*, this *initialization* angle is typically about one degree, depending on the encoder's line count; in a linear *VA* encoder, less than 1 mm motion is needed. From then on, the encoder is truly absolute. (There are ways to build a pseudorandom encoder so that absolute information is available on power-up without initializing, but these techniques require far more complex sensing hardware; they often impose slower operation as well. And none of them offers the sophisticated built-in testing of GPI's *VirtualAbsolute* technology.)

To complete the system, the **9710** is used with one of Gurley's **Interpolating Decoders**. The size of a credit card, it contains patented high-speed circuitry to decode the special serial index track and interpolation to increase the final resolution. In addition to the natural binary position output, a *Status* bit is provided to tell you when the encoder is initialized. This bit is at a logic high whenever the initializing motion is not yet complete, or when some other problem such as supply voltage interruption, electrical noise, damage, or fouling of the disc interferes with the proper code sequence from the index track. When these self-tests are all satisfied, the status bit is low, indicating the position data output is valid. The **9710** is usually used with the **Model VA** interpolating decoder, but other versions are added from time to time.

For a more thorough discussion, refer to the data sheet for the **Model VA**.

DISCS

Gurley does not offer disc hubs as catalog items, but we will mount discs to customer-furnished hubs, and we can provide hubs designed for your specific application. Even if we are not providing the mounting or the hub, we strongly suggest that you consult with us regarding the proper design of the disc/hub assembly and mounting of the **9710** Read Head.
All dimensions are in inches (mm). Consult factory for other sizes or line counts (including non-binary numbers).

O.D.	I.D.	Thick	#Lines (1)	Init. angle	Throat	CL-Mntg	P/N
3.13 (79.502)	1.45 (36.830)	0.125 (3.175)	**4096 R**	1.05°	0.105 (2.667)	1.918 (48.717)	CX01327
4.30 (109.220)	2.78 (70.612)	0.100 (2.540)	**4096 R**	1.05°	0.100 (2.540)	2.500 (63.500)	CX01115
4.80 (121.920)	2.90 (73.630)	0.120 (3.048)	**4096 R**	1.05°	0.105 (2.667)	2.755 (69.977)	CX01071
6.40 (162.560)	4.40 (111.760)	0.125 (3.175)	**4096 R**	1.05°	0.106 (2.692)	3.556 (90.322)	CX01258
9.00 (228.600)	6.00 (152.400)	0.250 (6.350)	**16384 R (2)**	0.31°	0.062 (1.575)	4.812 (122.225)	CX01296
16.25 (412.750)	14.00 (355.600)	0.235 (5.969)	**4096 S**	1.05°	n/a	6.650 (168.910)	CX01346
19.50 (495.300)	15.50 (393.700)	0.010 (.0254)	**2048 R**	1.94°	0.105 (2.667)	9.480 (240.792)	BX02049

(1) R means read head straddles disc O.D.; this is the preferred method.
S means read head straddles disc I.D.; consult factory.

(2) This disc requires an interpolating decoder other than the **Model VA**; consult factory.

Gurley Precision Instruments
514 Fulton Street
Troy, NY 12180 U.S.A.
(800) 759-1844, (518) 272-6300, fax (518) 274-0336,
Online at www.gurley.com, e-mail: info@gurley.com

DRAWINGS

SCALES

The following scales are available from existing masters. Additional standard scales may be added periodically; we can always make special scales on a custom basis.

Scale pitch	Maximum resolution *	Max. measuring length	Cross-section	Initialization distance
64 µm	0.25 µm	262.144 mm (10.32")	1.125" x 0.125" (28.575 x 3.175 mm)	768 µm (0.030")

* with **Model VA** support electronics

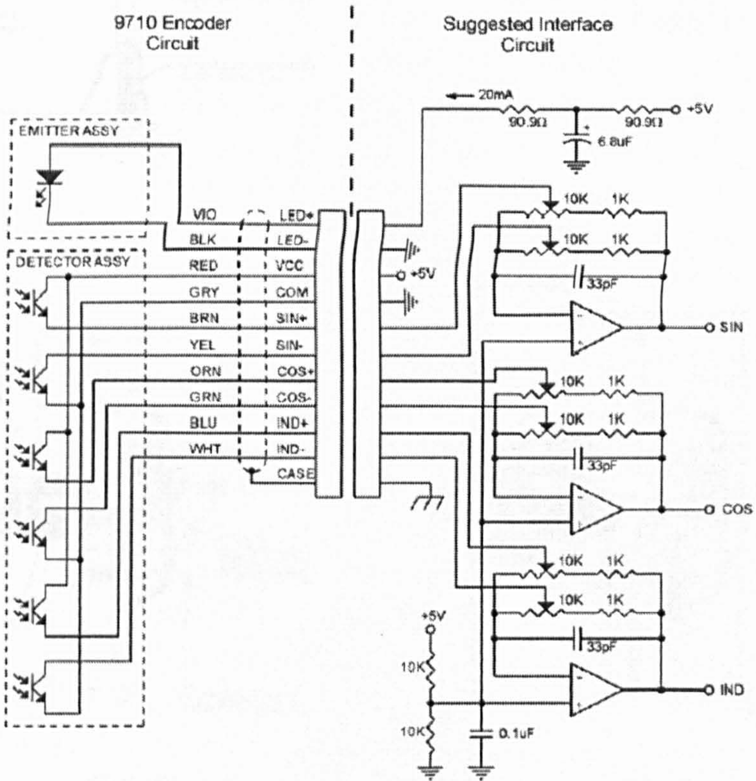

Gurley Precision Instruments
514 Fulton Street
Troy, NY 12180 U.S.A.
(800) 759-1844, (518) 272-6300, fax (518) 274-0336,
Online at www.gurley.com, e-mail: info@gurley.com

DRAWINGS

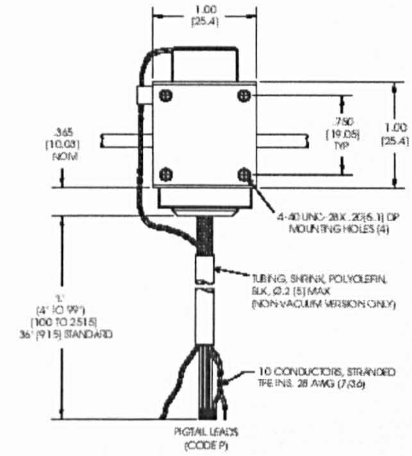

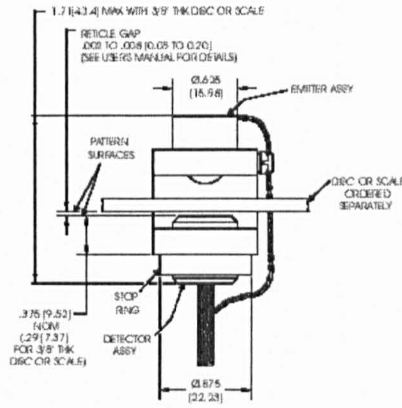

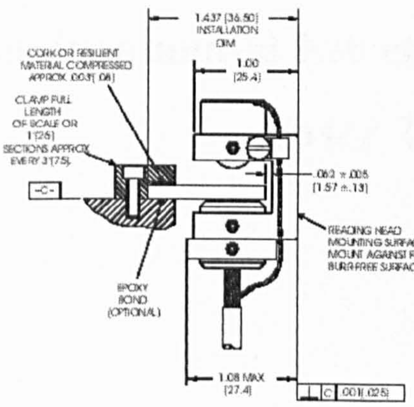

LINEAR APPLICATIONS

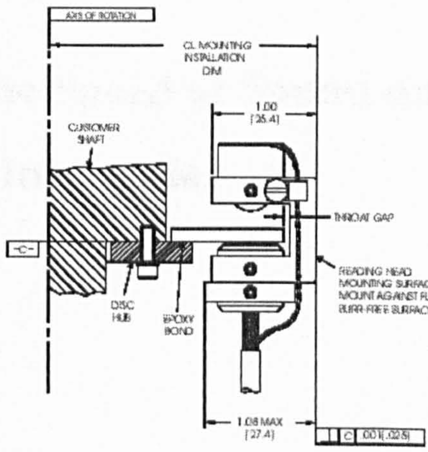

ROTARY APPLICATIONS

SUGGESTED MOUNTING METHODS

Gurley Precision Instruments
514 Fulton Street
Troy, NY 12180 U.S.A.
(800) 759-1844, (518) 272-6300, fax (518) 274-0336,
Online at www.gurley.com, e-mail: info@gurley.com

Appendix F:

Environmental Effects on the Speed of Sound during Laser Tissue Interaction

Environmental Effects on the Speed of Sound during laser tissue Interaction

It is evident that the speed of sound is highly affected by temperature variation. Researches also showed that the speed of sound is highly dependent on the humidity the molecular weight of the medium and the pressure.

Temperature Effects on the Speed of Sound

The speed of sound is seen to increase as the square root of the absolute temperature. and it can be calculated as follow:

$t := 0..600 \qquad v_0 := 331$

$$v_t := v_0 \cdot \sqrt{1 + \frac{t}{273}} \qquad \text{[BOHN 88]}$$

where

t	is the temperature in degrees C
vt	is the speed of sound at temperature (t)
v0	is the speed of sound at 0 degree C

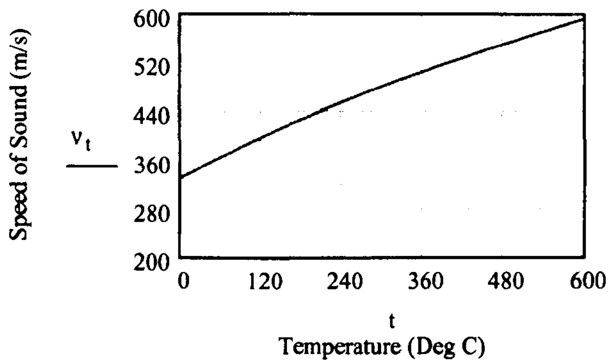

Figure 1: Speed of Sound vs.Temperature

The percent increase of the speed of sound due to temperature can be calculated as follows

$$\%VT_t := \frac{(v_t - v_0) \cdot 100}{v_0}$$

Humidity Effects on the Speed of Sound

To accurately determine the humidity effect on the speed of sound one must take into account the specific **heat ratio** γ and the average **molecular weight** of the different types of molecules in the air **M**. The affect of humidity on the speed of sound can be calculated as follow [BOHN 88]

$i := 0..7 \qquad Temp_i := 5\cdot(i+1) \qquad k := 0..20 \qquad RH_k := 5\cdot k$

$P := 1.013\cdot 10^5 \text{ Pa} \qquad d := 5 \text{ DOF}$

$et_i :=$

872
1228
1705
2338
3169
4243
5627
7376

$$Temp = \begin{pmatrix} 5 \\ 10 \\ 15 \\ 20 \\ 25 \\ 30 \\ 35 \\ 40 \end{pmatrix}$$

$$h_{i,k} := \frac{(0.01\, RH_k \cdot et_i)}{P}$$

$$\gamma_{i,k} := \frac{(d + 2 + h_{i,k})}{d + h_{i,k}}$$

$$M := 29 - 11 \cdot h$$

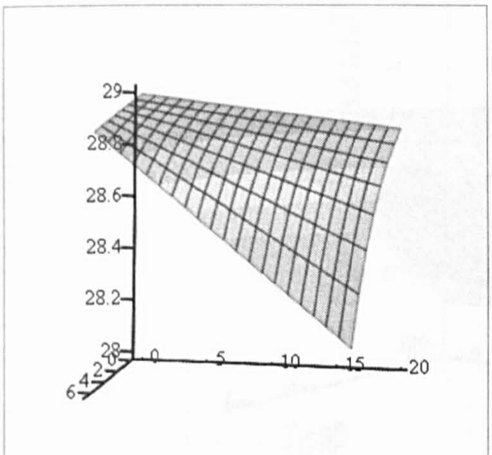

Figure.2: Molecular Weight vs H & T.

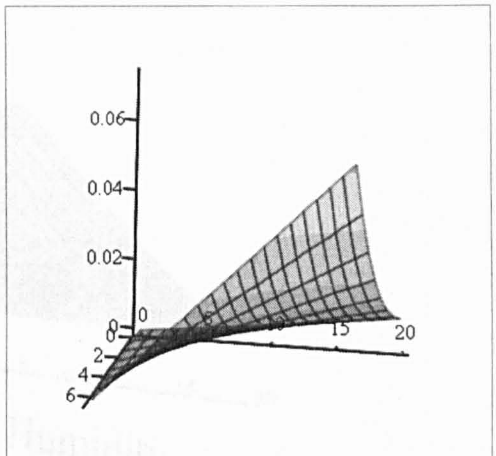

Figure 3: % of water molecules vs H & T

And the increase of speed of sound due to Humidity is as follow: [BOHN 88]

$$\%Vh_{i,k} := \left(455.13 \cdot \sqrt{\frac{\gamma_{i,k}}{M_{i,k}}}\right) - 100$$

where $\%Vh$ is the percent increase in the speed of sound due to humidity

Hence the speed of sound due to humidity effect (only) would be as follow:

$$vH_{i,k} := \left[\frac{\left(\%Vh_{i,k}\right)}{100} + 1\right] \cdot v_0$$

Figure 4: Speed of Sound vs Humidity

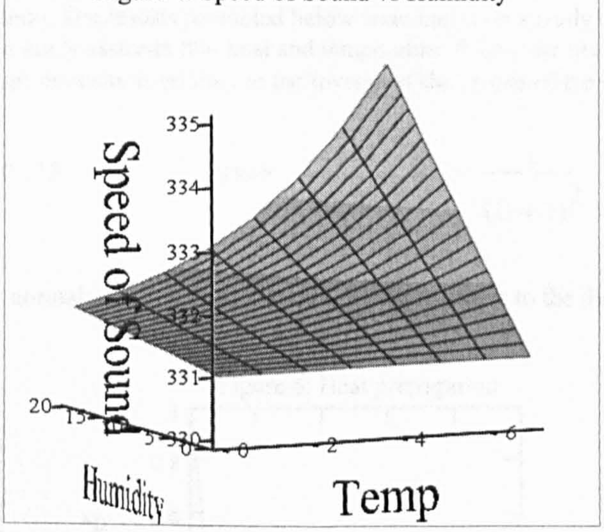

The speed of sound due to Temperature and Humidity effect combined would be as follow:

$$vTemp_i := v_0 \cdot \sqrt{1 + \frac{Temp_i}{273}} \qquad vTH_{i,k} := \left[1 + \frac{\left(\%Vh_{i,k}\right)}{100}\right] \cdot vTemp_i$$

Figure 5: Speed of Sound vs. H & T

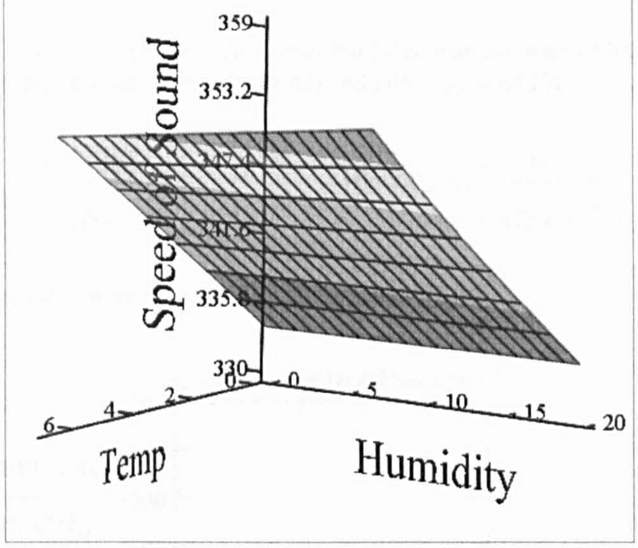

Note

It is evident the speed of sound is highly effected by temperature variations and with lesser extend by humidity as shown in Figures 4 and 5

Acoustic Feedback of laser tissue ablation

Experimental results showed that it is possible to the determine the laser front position during laser tissue interaction using the photo-acoustic feedback technique. However this feedback mechanism is govern by some factors which limit its functionality and impose limitations on its accuracy. these factors include environmental effects on the speed of sound as well factors related to the nature of the laser tissue interaction (Type of laser, type of tissue, and other laser and tissue parameters).

The following model discusses the effect of heat propagation due to laser tissue interaction on the speed of sound, while ignoring the effect of humidity, pressure and molecular weight of the transmitting medium. The results presented below were based on a study made using CO_2 laser for bone drilling. The study assumes that heat and temperature follow the **inverse square law, (i.e.** heat or temperature intensity is relative to the inverse of the square of the travelled distance).

Let $D := 0..15$ Then $x_D := \frac{1}{(D+1)^2}$

where

x is the normalised temperature (heat intensity) relative to the distance d

Figure 6: Heat prepagation

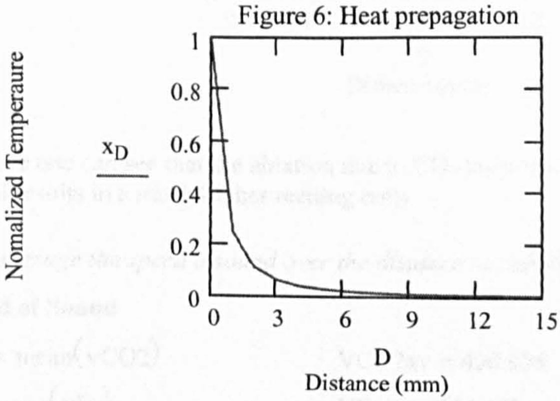

Taking the above into account, and assuming that the ablation temperature is 400 deg C (due to laser tissue interaction), The speed of sound would be affected as follow.

For a Temperature of (400 Deg C Er: YAG Laser-hard tissue ablation and 1500 C for CO2 laser- hard tissue ablation) the Heat propagation (HPErYAG and HPCO2) would be

$$HPErYAG_D := \left[\frac{400}{(D+1)^2} \right] \qquad HPCO2_D := \left[\frac{1500}{(D+1)^2} \right]$$

Note: heat propagation time is also an important factor here

Figure 7: Laser Heat Prepagation

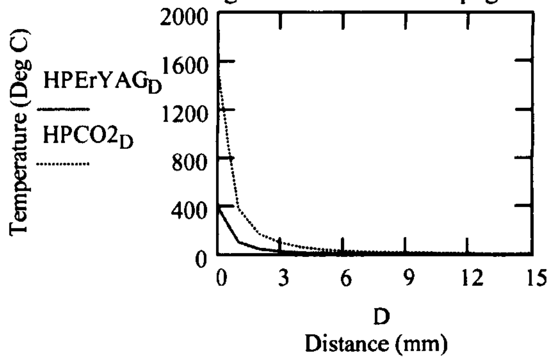

Assuming the speed of sound at room temperature is nRT = 340 m/s

$$vEr_D := \left(v_0 \cdot \sqrt{1 + \frac{HPErYAG_D}{273}} \right) + 9$$

$$vCO2_D := \left(v_0 \cdot \sqrt{1 + \frac{HPCO2_D}{273}} \right) + 9$$

Speed of Sound due to Laser Abaltion

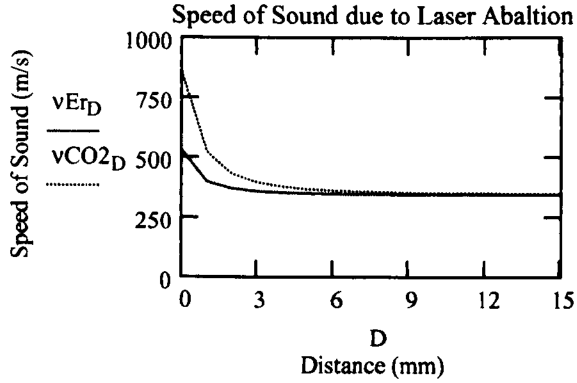

From the above one can see that the ablation due to CO_2 laser results in a much higher effect on the speed and results in a much higher reading error

NOTE must Average the speed o sound over the distance to reduce the error

Average speed of Sound

$VCO2av := mean(vCO2)$ $\qquad VCO2av = 400.956$

$VErav := mean(vEr)$ $\qquad VErav = 360.252$

References

[BOHN 88] Bohn D. A., 1998. Environmental Effect on the Speed of Sound. *J. Audio Eng. soc., 36(4).*